University of Rochester
Laboratory for Laser Energetics

DOE/NA/1944-1314
February 2017

LLE 2016 Annual Report

October 2015 – September 2016

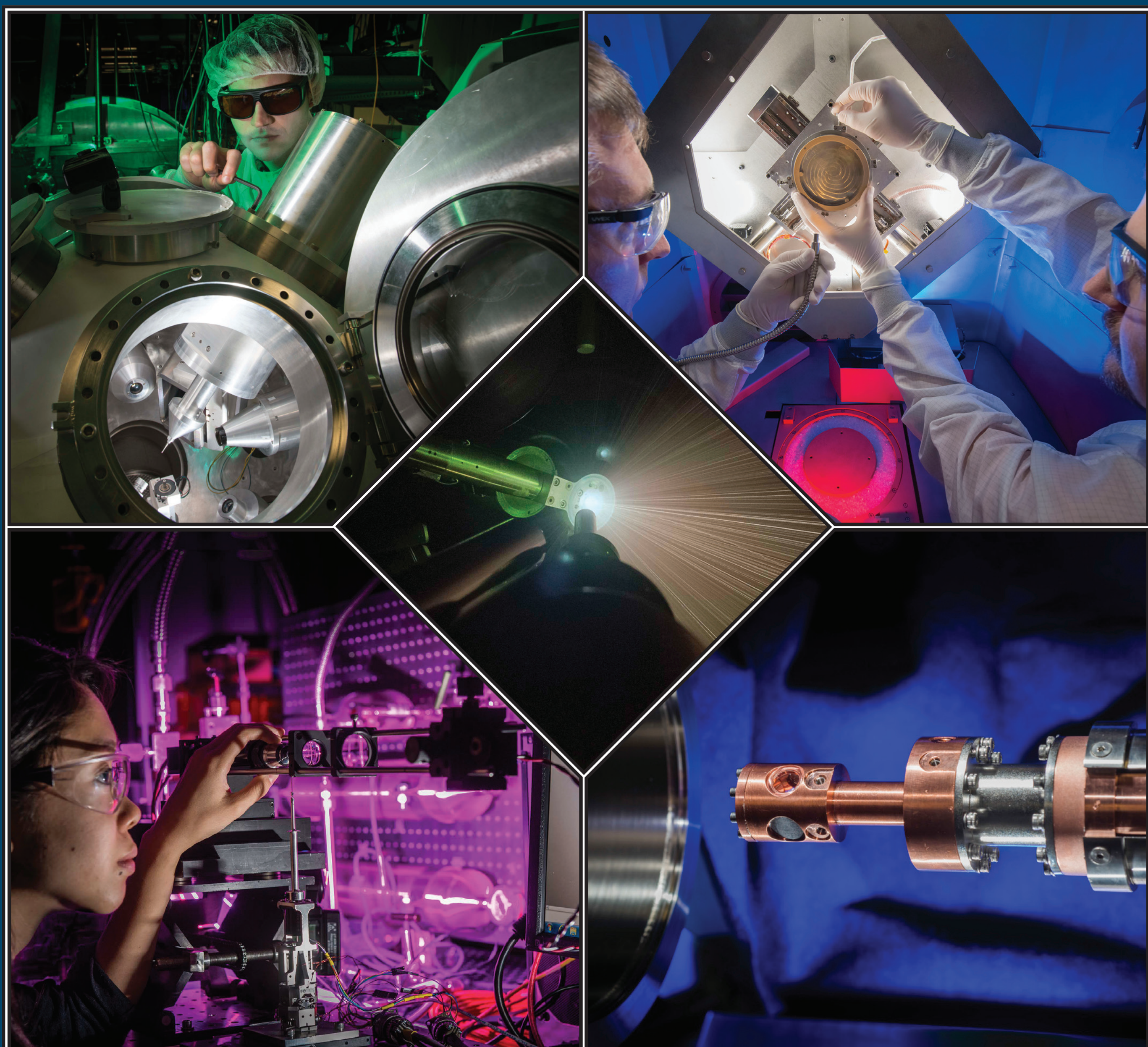

Cover Photos

Top Left: Dr. Steven Ivancic is shown securing the extreme-ultraviolet (EUV) spectrometer to the Multi-Terawatt (MTW) laser target chamber. The EUV spectrometer measures emission from targets rapidly heated by the subpicosecond MTW laser pulse.

Top Right: Optical manufacturing process engineer, John Spaulding, and Coating Operator, Justin Foster, are shown installing an optic on a new prototype stage built to support research and development work on glancing-angle–deposition (GLAD) coatings.

Center: Photograph of a diamond-anvil cell experiment conducted on OMEGA. These experiments generate ultrahigh pressures in mixtures of hydrogen and helium to simulate the conditions inside Saturn's atmosphere. Analysis of these experiments points to possible "helium rain" inside Saturn's atmosphere that may account for its unexpectedly high brightness. The work was presented at an American Geophysical Union meeting and was highlighted in a Science Magazine article in December 2015.

Bottom Left: Summer High School intern, Joy Zhang of Penfield High School is shown adjusting a digital microscope that is being developed for use on the target Fill/Transfer Station to view target defects.

Bottom Right: Photograph of a new layering sphere designed to fill targets with liquid D_2 (and DT) through a 10-μm-diam tube. The new design is required for the project to demonstrate compressed direct-drive implosion pressures of 100 Gbar in cryogenic targets.

Prepared for
U.S. Department of Energy
Albuquerque Service Center
DOE/NA/1944-1314

Distribution Category
October 2015 – September 2016

Printed in the United States of America
Available from
National Technical Information Services
U.S. Department of Commerce
5285 Port Royal Road
Springfield, VA 22161
www.ntis.gov

The work described in this volume includes current research at the Laboratory for Laser Energetics, which is supported by New York State Energy Research and Development Authority, the University of Rochester, the U.S. Department of Energy Office of Inertial Confinement Fusion under Cooperative Agreement No. DE-NA0001944, and other agencies.

For questions or comments, Laboratory for Laser Energetics,
250 East River Road, Rochester, NY 14623-1299, (585) 275-5286.
www.lle.rochester.edu

University of Rochester
Laboratory for Laser Energetics

DOE/NA/1944-1314
February 2017

LLE 2016 Annual Report

UR LLE

October 2015 – September 2016

Inertial Fusion Program and
National Laser Users' Facility Program

Contents

Executive Summary

The fiscal year ending September 2016 (FY16) concluded the first 42 months of the fourth five-year renewal of Cooperative Agreement DE-NA0001944 with the U.S. Department of Energy (DOE). This annual report summarizes work carried out under the Cooperative Agreement at the Laboratory for Laser Energetics (LLE) during the past fiscal year including work on the Inertial Confinement Fusion (ICF) Campaign; laser, optical materials, and advanced technology development; operation of the Omega Laser Facility for the ICF and High-Energy-Density (HED) Campaigns, the National Laser Users' Facility (NLUF), the Laboratory Basic Science (LBS) Program, and other external users; and programs focusing on the education of high school, undergraduate, and graduate students during the year.

Inertial Confinement Fusion Research

One of LLE's principal missions is to conduct research in ICF with particular emphasis on supporting the goal of achieving ignition at the National Ignition Facility (NIF). This program uses the Omega Laser Facility and the full experimental, theoretical, and engineering resources of the Laboratory. During FY16, a record 2193 target shots were taken at the Omega Laser Facility (comprised of the 60-beam OMEGA UV laser and the four-beam, high-energy petawatt OMEGA EP laser). Nearly 72% of the facility's FY16 target shots were designated for ICF or HED campaigns. LLE plays a lead role in validating the performance of cryogenic target implosions, essential to all forms of ICF ignition. LLE is responsible for a number of critical elements within the integrated experimental teams that support the demonstration of indirect-drive ignition on the NIF and is the lead laboratory for the validation of direct-drive ignition. LLE has also developed, tested, and constructed a number of diagnostics currently being used at both the Omega Laser Facility and on the NIF. During this past year, progress in the Inertial Confinement Fusion Research Program continued in three principal areas: ICF experiments and experiments in support of ICF; theoretical analysis and design efforts aimed at improving direct-drive–ignition capsule designs (including direct-drive–ignition designs) and advanced ignition concepts such as shock ignition and fast ignition; and development of diagnostics for experiments on the NIF, OMEGA, and OMEGA EP.

1. Inertial Confinement Fusion Experiments in FY16

The Laboratory for Laser Energetics' (LLE's) investigations of direct-drive implosions at the National Ignition Facility to validate models related to implosion velocities and the magnitude of hot-electron preheat are addressed beginning on p. 1. Implosion experiments indicate that the energetics are well modeled when cross-beam energy transfer (CBET) is included in the simulation. Trajectories from backlit images are also well predicted, although with lower velocities than theory, with discrepancies likely caused by nonuniformity growth seeded by laser imprint.

Experiments on the OMEGA Laser System to evaluate cryogenic implosions that are hydrodynamically equivalent to spherical ignition designs for the NIF are described (p. 30). Current cryogenic implosions on OMEGA have reached 56 Gbar, and implosions with a shell convergence (CR) < 17 and a fuel adiabat (α) > 3.5 perform close to one-dimensional (1-D) predictions. Demonstrating hydrodynamic equivalence on OMEGA will require reduced coupling losses caused by CBET and minimized long-wavelength nonuniformity. Ignition in a direct-drive cryogenic implosion on the NIF will require central stagnation pressures in excess of 100 Gbar.

During FY16 LLE researchers performed polar-direct-drive experiments (p. 57) on the NIF to quantify CBET. The polar-direct-drive laser configuration was used to limit CBET at the target poles while maintaining its influence at the equator. This combination of low- and high-CBET conditions in a single implosion made it possible to determine the effects of CBET on the ablation rate and ablation pressure. Hydrodynamic simulations performed without CBET agree with the measured ablation rate and ablation-front trajectory at the target pole, confirming that the CBET effects at the pole are small. CBET simulations incorporating a gain multiplier lead to excellent agreement with both polar and equatorial measurements.

A unique approach for filling nonpermeable ICF target capsules with deuterium–tritium (DT) by permeation if presented beginning on p. 90. This process uses a permeable capsule coupled into the final target capsule with a tapered 0.1- or 0.08-mm-diam fill tube. Such an approach makes is possible to fill new target materials without requiring the design and construction of a fill-tube–based DT filling station. Permeation filling of glow-discharge polymerization (GDP) targets using this method as well as ice layering of the target, has been successfully demonstrated, yielding an inner ice surface roughness of <1-μm rms.

Measurements of the maximum in-flight shell thickness, which decreased from 75±2 nm to 60±2 nm in direct-drive implosions on OMEGA when the shell adiabat was reduced from 6 to 4.5, are presented (p. 109). When the adiabat was decreased farther (to α = 1.8), the shell thickness increased to 75±2 nm. Two-dimensional (2-D) simulations that included laser imprint, nonlocal thermal transport, cross-beam energy transfer, and first-principles equation-of-state models reproduced the measured shell thickness, shell trajectories, minimum core radius, and neutron yield and showed that the increased shell thickness for $\alpha \le 3$ was caused by laser imprint.

Optical smoothing of laser imprinting in planar-target experiments on OMEGA EP using 1-D multi-FM smoothing by spectral dispersion (SSD) has been demonstrated (p. 115). Direct-drive ignition on the NIF requires single-beam smoothing to minimize imprinting of laser nonuniformities that can negatively affect implosion performance. One-dimensional, multi-FM SSD has been proposed to provide the required smoothing. A prototype multi-FM SSD system has been integrated into the NIF-like beamline of the OMEGA EP Laser System. Experiments have been performed to verify the smoothing performance by measuring Rayleigh–Taylor growth rates in planar targets of laser-imprinted and preimposed surface modulations. One-dimensional, multi-FM SSD has been observed to reduce imprint levels by +50% compared to the nominal OMEGA EP SSD system. The experimental results are in agreement with 2-D *DRACO* simulations using realistic, time-dependent, far-field spot-intensity calculations that emulate the effect of SSD.

We report on plasma characterization using ultraviolet Thomson scattering from ion-acoustic and electron plasma waves (p. 125). Collective Thomson scattering is a technique that measures the plasma conditions in laser-plasma experiments. Simultaneous measurements of ion-acoustic and electron plasma wave spectra were obtained using a 263.25-nm Thomson-scattering probe beam. A fully reflective collection system was used to record light scattered from electron plasma waves at electron densities greater than 10^{21} cm^{-3}, which produced scattering peaks near 200 nm. An accurate analysis of the experimental Thomson-scattering spectra required accounting for plasma gradients, instrument sensitivity, optical effects, and background radiation. Practical techniques for including these effects when fitting Thomson-scattering spectra are presented and applied to the measured spectra to show the improvement in plasma characterization.

Measurements of hot-electron temperature in laser-irradiated plasmas are discussed beginning on p. 134. The total energy of hot electrons produced by the interaction of OMEGA nanosecond wide pulses with planar CH-coated molybdenum targets, using Mo K_α emission, was reported in 2012. The temperature of the hot electrons in that work was determined by the high-energy bremsstrahlung spectrum measured by a three-channel fluorescence-photomultiplier hard x-ray detector (HXRD). In the 2016 work, the HXRD was replaced with a nine-channel image-plate–based detector. For the same conditions (irradiance of the order of 10^{14} W/cm^2; 2-ns pulses), the measured temperatures were consistently lower than those measured by the HXRD (by a factor ~1.5 to 1.7). This measurement was supplemented with three experiments that measured the hot-electron temperature using K_α emission from high-Z target layers, independent of the hard x-ray emission. These experiments yielded temperatures that were consistent with those measured by the bremsstrahlung. For a given x-ray emission in ICF compression experiments, this result would lead to a higher total energy in hot electrons, but to a lower preheat of the compressed fuel, because of the reduced hot-electron range.

Beginning on p. 150, the influence of surface modifications on the adsorption and absorption of tritium into stainless-steel 316 is discussed. Tritium dissolution within the adsorbed water layers on stainless-steel surfaces can contribute a significant fraction to the total quantity of tritium absorbed during an exposure to tritium-containing gas. Additionally, these water layers govern the migration of tritium from the stainless-steel lattice to the metal surface after the surface is cleaned. The adsorbed water layers are sensitive to the conditions of the metal surface; different pretreatments can lead to different surface concentrations of water. In the reported work, the effect of altering the metal surface by mechanical polishing, electropolishing, Fe or Cr oxidation, gold plating, and nitric-acid treatments was studied using linear thermal desorption and plasma-induced ion sputtering. The results demonstrate that altering the metal surface can reduce tritium absorption by ≥35%. Finally, a quantitative migration model accurately describes the migration of tritium out of the stainless-steel lattice after the surface is cleaned.

The following advantages of the laser direct-drive (DD) approach to ignition are discussed (p. 172): the increased fraction of laser drive energy coupled to the hot spot and relaxed hot-spot requirements for the peak pressure and convergence ratios relative to the indirect-drive approach at equivalent laser energy. With the goal of successfully demonstrating ignition by using direct drive, the recently established national strategy has several elements and involves multiple national and international institutions. These elements include the experimental demonstration on OMEGA cryogenic implosions of hot-spot conditions relevant for ignition at MJ-scale energies available on the NIF and developing an understanding of laser–plasma interactions and laser coupling using DD experiments on the NIF. Direct-drive designs require reaching central stagnation pressures in excess of 100 Gbar. The current experiments on OMEGA have achieved inferred peak pressures of 56 Gbar. Extensive analysis of the cryogenic target experiments and in addition to 2-D and 3-D simulations suggests that power balance, target offset, and target quality are the main limiting factors in target performance. In addition, CBET has been identified as the main mechanism for reducing laser coupling. Reaching the goal of demonstrating hydrodynamic equivalence on OMEGA includes improving laser power balance, target position, and target quality at shot time. CBET must also be significantly reduced and several strategies have been identified to address this issue.

2. Theoretical Design and Analysis

Hydrodynamic simulations to design a new experimental platform to investigate two-plasmon decay and other laser–plasma instabilities are presented (p. 15). Proposed experiments will use planar plastic targets with an embedded Mo layer to characterize the generation of hot electrons through Mo K_{α} fluorescence and hard x-ray emission, approximating conditions near both the equator and the pole of a polar-direct-drive implosion.

First-principles investigations of the ionization and thermal conductivity of polystyrene (CH) over a wide range of plasma conditions (t = 0.5 to 100 g/cm^3 and T = 15,625 to 500,000 K) are being conducted (p. 19). Hydrodynamic simulations of cryogenic deuterium–tritium targets with CH ablators on OMEGA and the NIF predict an ~20% variation in target performance in terms of hot-spot pressure and neutron yield (gain) relative to traditional model simulations.

3. Diagnostics

A next-generation neutron temporal diagnostic (NTD) that will determine the hot-spot pressure achieved in ICF experiments and will assess the implosion quality has been installed at the Omega Laser Facility (p. 36). This NTD is based on a fast-rise-time plastic scintillator, which converts the neutron kinetic energy to 350- to 450-nm-wavelength light that is relayed to a streak camera. An ~200-fold reduction in neutron background was observed during the first high-yield DT cryogenic implosions compared to the current NTD installation on OMEGA. An impulse response of ~40±10 ps was measured in a dedicated experiment with a 10-ps pulse from the OMEGA EP laser.

A newly designed pulse-front-tilt–compensated streaked optical spectrometer with high throughput and picosecond time resolution is described (p. 143). A high-throughput, broadband optical spectrometer coupled to the Rochester Optical Streak System equipped with a Photonis P820 streak tube has been designed to record time-resolved spectra with 1-ps time resolution. Spectral resolution of 0.8 nm was achieved over a wavelength coverage range of 480 to 580 nm, using a 300-groove/mm diffraction grating in conjunction with a pair of 225-mm-focal-length doublets operating at an f/2.9 aperture. Overall pulse-front tilt across the beam diameter generated by the diffraction grating can be reduced by preferentially delaying discrete segments of the collimated input beam using a 34-element reflective echelon optic. The introduced delay temporally aligns the beam segments and the net pulse-front tilt is limited to the accumulation across an individual sub-element. The resulting spectrometer design balances resolving power and pulse-front tilt while maintaining high throughput.

The design of an extreme ultraviolet spectrometer suite to characterize rapidly heated solid matter is reported (p. 146). An ultrafast, streaked, extreme-ultraviolet (XUV) spectrometer (5 to 20 nm) has been developed to measure the temperature dynamics in rapidly heated samples. Rapid heating makes it possible to create exotic states of matter that can be probed during their inertial confinement time—tens of picoseconds in the case of micron-sized targets. In contrast to other forms of pyrometry, where the temperature is inferred from bulk x-ray emission, XUV emission is restricted to the sample surface, allowing one to measure temperature at the material–vacuum interface. Measuring the surface temperature constrains models for the release of high-energy-density material. Coupling the XUV spectrometer to an ultrafast (<2-ps) streak camera provided an evolution in the picosecond time scale of the surface-layer emission. Two high-throughput XUV spectrometers have been designed to simultaneously measure the time-resolved and absolute XUV emission.

An x-ray detection system (XDS) has been developed and commissioned at LLE with the intent of nondestructively extrapolating the pressure of tritium-filled targets from their measured activity (p. 186). The x-ray emission from silica (SiO_2) and plastic (CH and CD) targets have been measured in the helium environment of the XDS in OMEGA and ICF implosions. The T_2 permeation half-lives were measured for three plastic targets, allowing for the actual initial-fill pressures of those targets to be calculated based on the slope of the pressure versus activity. The half-lives measured by the XDS are compared with values reported by the target manufacturer, differing with a range of up to 2.3×.

High-Energy-Density Science

We report on measurements of the equation of state of carbon at extreme pressures (p. 159). These measurements are of interest to studies of planetary ice giants and white dwarfs and to ICF. Knowledge of the high-pressure shock-and-release responses of diamond is necessary to accurately model an ICF implosion and design ignition targets. The article presents Hugoniot and release data for both single-crystal diamond and high-density carbon (HDC), comprised of nanometer-scale grains, used as a NIF ablator. Diamond was shock compressed to multimegabar pressures and then released into reference materials with known Hugoniots at the Omega Laser Facility. Hugoniot results indicate that HDC, which is ultrananocrystalline and ~4% less dense than single-crystal diamond, has a stiffer response than single-crystal diamond.

Lasers, Optical Materials, and Advanced Technology

The contribution of thin-film interfaces to the near-ultraviolet absorption and pulsed-laser–induced damage for ion-beam–sputtered and electron-beam–evaporated coatings is discussed beginning on p. 43. Film characterization shows a small contribution to total absorption from the interfaces relative to that of the HfO_2 film material, with a higher damage resistance in the seven-layer coating compared to the single-layer HfO_2 film. The results indicate a similarity of interfacial film structure with that formed during the co-deposition of HfO_2 and SiO_2 materials.

A simple diagnostic to characterize 1-D chromatic aberrations in a broadband beam is discussed (p. 52). A Ronchi grating is placed in front of a spectrometer entrance slit to provide spatially coupled spectral phase information. The phase-offset variation in the interferogram along the wavelength axis contains the information on chromatic aberrations that can be extracted using Fourier analysis. The radial-group delay of a refractive system and the pulse-front delay of a wedged glass plate have been accurately characterized in a demonstration.

A description of an eight-channel, time-multiplexed pulse-shaping system that generates, demultiplexes, and retimes optical waveforms from a single pulse-shaping unit begins on p. 68. This system can provide pulses to multiple optical systems with low relative jitter and lower cost. Losses of less than 5 dB and extinction ratios of the order of 50 dB for an eight-channel system were measured for the system. By operating with only four channels, this system can provide a contrast of the order of 70 dB by using the final stage of the demultiplexer to enhance the contrast in the output.

A new design approach to continuous distributed phase plates (DPP's) using the code *Zhizhoo'* has been developed (p. 74). *Zhizhoo'* produces DPP designs with exceptional control of the envelope shape, spectral and gradient control, and robustness from near-field phase aberrations. This code leads to rapid DPP design optimization, with achieved focal-spot shapes having high fidelity relative to the design objective. Using a personal computer, phase-dislocation–free DPP designs with low near-field modulation can be achieved with a less-than-1%-to-2% weighted σ_{rms} error of the far-field spot shape in a few minutes.

Experimental efforts were made to correlate the mechanical properties of multilayer diffraction gratings to laser-induced–damage thresholds (LIDT's) (p. 78). Nanoindentation of holographic diffraction gratings etched into silica provides the penetration depth, brittleness, and yield strength of the structure; lower LIDT's are strongly correlated with greater measured yield stresses and lower penetration depths for the evaluated samples. This work indicates that mechanical testing may provide guidance on grating cleanliness and damage thresholds for use in high-intensity laser systems.

The first complete set of measurements of a laser–plasma optical system's refractive index, as seen by an independent probe laser beam, as a function of the relative wavelength shift between the two laser beams have been made (p. 181). Both the imaginary and real refractive-index components have been found to be in good agreement with linear theory using plasma parameters measured by optical Thomson scattering and interferometry; the former is in contrast to previous work and has implications for cross-beam energy transfer in indirect-drive inertial confinement fusion, and the latter is measured for the first time. The data include the first demonstration of a laser-plasma polarizer with 85% to 87% extinction for the particular laser and plasma parameters used in this experiment, complementing the existing suite of high-power, tunable, and ultrafast plasma-based photonic devices.

Omega Laser Facility Users Group (OLUG)

The Eighth Omega Laser Facility Users Group (OLUG) Workshop, held on 27–29 April 2016, attracted more than 110 scientists, postdoctoral fellows (postdocs), and students from institutions in the U.S. and abroad. OLUG consists of over 430 members from 55 universities and 35 research centers and national laboratories from 21 nations covering 4 continents. As has been the case in previous workshops, postdocs and students received travel support for the workshop from DOE's National Nuclear Security Administration (NNSA).

The purpose of the 2.5-day workshop was to facilitate communications and exchanges among individual OMEGA users, and between users and LLE management; to present ongoing and proposed research; to encourage research opportunities and collaborations that could be undertaken at the Omega Laser Facility and in a complementary fashion at other facilities [such as the NIF or the Laboratoire pour l'Utilisation des Lasers Intenses (LULI)]; to provide an opportunity for students, postdoctoral fellows, and young researchers to present their research in an informal setting; and to provide feedback from the users to LLE management about ways to improve and keep the facility and future experimental campaigns at the cutting edge.

The workshop program included an overview on the National ICF Program presented by Keith LeChien from NNSA; four review and science talks by Craig Sangster (National ICF Direct-Drive Program), Carlo Graziani (Inferring Morphology and Strength of Magnetic Fields from Proton Radiographs), Philip Nilson (High-Resolving-Power, Ultrafast Streaked X-Ray Spectroscopy on OMEGA EP), and Jonathan Davies (An Overview on Laser-Driven Magnetized Liner Inertial Fusion on OMEGA); one Omega Laser Facility talk given Samuel Morse (Progress on Recommendations and Items of General Interest); three poster sessions including a total of 76 research posters and 15 Omega Laser Facility posters (the majority of the contributed posters were presented by postdocs and students); two mini-workshop sessions dedicated to streak cameras (organized by Charles Sorce) and magneto-inertial fusion electrical discharge system (MIFEDS) (organized by Gennady Fiksel); a students and postdocs panel discussion; a discussion and presentation of the Findings and Recommendations; and research and career opportunity talks by representatives from Lawrence Livermore National Laboratory (LLNL) (Robert Heeter), Los Alamos National Laboratory (LANL) (S. Batha), Sandia National Laboratories (SNL) (P. Knapp), and LLE (Michael Campbell).

Detailed reporting on the workshop and the Findings and Recommendations may be found in an article beginning on p. 193.

Education

As the only major university participant in the National ICF Program, education continues as an important mission for LLE. The Laboratory's education programs cover the range from high school (p. 200) to graduate education.

1. High School Program

During the summer of 2016, 13 students from Rochester-area high schools participated in the Laboratory for Laser Energetics' Summer High School Research Program. The goal of this program is to excite a group of high school students about careers in the areas of science and technology by exposing them to research in a state-of-the-art environment. Too often, students are exposed to "research" only through classroom laboratories, which have prescribed procedures and predictable results. In LLE's summer program, the students experience many of the trials, tribulations, and rewards of scientific research. By participating in research in a real environment, the students often become more excited about careers in science and technology. In addition, LLE gains from the contributions of the many highly talented students who are attracted to the program. Three hundred and fifty-three high school students have now participated in the program since it began in 1989. This year's students were selected from approximately 60 applicants.

2. Undergraduate Student Program

Thirty-nine undergraduate students participated in work or research projects at LLE this past year. Student projects include operational maintenance of the Omega Laser Facility; work in laser development, materials, and optical thin-film coating laboratories; computer programming; image processing; and diagnostics development. This is a unique opportunity for students, many of whom will go on to pursue a higher degree in the area in which they gained experience at LLE.

3. Graduate Student Program

Graduate students are using the Omega Laser Facility as well as other LLE facilities for fusion and HED physics research and technology development activities. These students are making significant contributions to LLE's research program. Twenty-six faculty members from five University of Rochester academic departments collaborate with LLE scientists and engineers. In FY16, 62 graduate students were involved in research projects at LLE, and LLE directly sponsored 35 students pursuing Ph.D. degrees via the NNSA-supported Frank Horton Fellowship Program in Laser Energetics. Their research includes theoretical and experimental plasma physics, HED physics, x-ray and atomic physics, nuclear fusion, ultrafast optoelectronics, high-power–laser development and applications, nonlinear optics, optical materials and optical fabrication technology, and target fabrication. In addition, LLE directly funds research programs within the Massachusetts Institute of Technology (MIT) Plasma Science and Fusion Center, the State University of New York (SUNY) at Geneseo, and the University of Wisconsin. These programs involve a total of approximately 6 graduate students, 25 to 30 undergraduate students, and 10 faculty members. Over 330 graduate students have now conducted their graduate research work at LLE since its graduate research program began. In addition, 170 graduate students and post-graduate fellows from other universities have conducted research at the Omega Laser Facility as part of the NLUF program. Over 60 graduate students and undergraduate students were involved in research at the Omega Laser Facility as members of participating NLUF teams in FY16.

FY16 Omega Laser Facility Operations

During FY16, the Omega Laser Facility conducted 1414 target shots on OMEGA and 779 target shots on OMEGA EP for a total of 2193 target shots (see Tables 148.IX and 148.X, p. 202). OMEGA averaged 11.7 target shots per operating day with Availability and Experimental Effectiveness averages for FY16 of 95.6% and 96.6%, respectively. OMEGA EP was operated extensively in FY16 for a variety of internal and external users. A total of 718 target shots were taken in the OMEGA EP target chamber and 61 joint target shots were taken in the OMEGA target chamber. OMEGA EP averaged 7.9 target shots per operating day with Availability and Experimental Effectiveness averages for FY16 of 96.9% and 95.8%, respectively. Per the guidance provided by DOE/NNSA, the facility provided target shots for the ICF, HED, NLUF, and LBS programs. The facility also provided a small number of shots for the Commissariat à l'énergie atomique et aux energies (CEA) of France (see Fig. 1). In FY16, 72% of the target shots were taken for the ICF and HED programs.

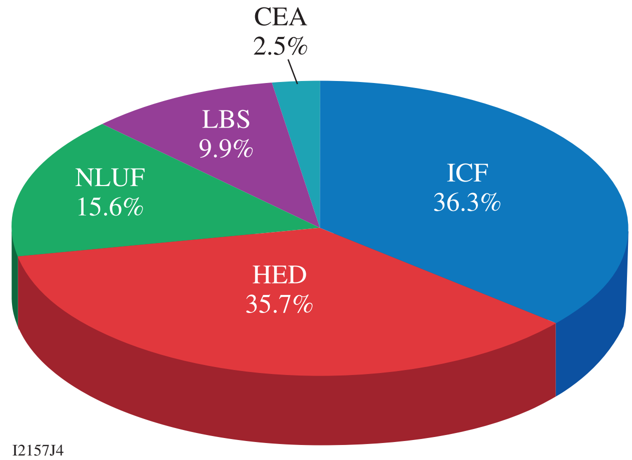

Figure 1
The distribution of non-maintenance Omega Laser Facility target shots by program in FY16.

Details of this work are contained in an article beginning on p. 202. Highlights of the Omega Laser Facility activities in FY16 included the following:

- Improved energy balance over 100-ps segments of the pulse shape
- Changed the equivalent-target-plane diagnostic from Beamline 46 to Beamline 56
- Synchronized the SSD modulators to the laser pulse shape
- Improved the beam-timing system
- Provided an alternative beam path for Beamline 35 to support magnetized liner inertial fusion experiments
- Augmented the lower-compressor diagnostic beam path on OMEGA EP
- Overhauled the OMEGA EP stimulated Brillouin scattering suppression system
- Improved the OMEGA EP short-pulse diagnostic package
- Added a low-yield neutron time of flight diagnostic on OMEGA

National Laser Users' Facility and External Users Programs

Under the facility governance plan implemented in FY08 to formalize the scheduling of the Omega Laser Facility as an NNSA User Facility, Omega Laser Facility shots are allocated by campaign. The majority (71.9%) of the FY16 target shots were allocated to the ICF Campaign conducted by integrated teams from LLNL, LANL, NRL (Naval Research Laboratory), SNL, and LLE. The HED Campaigns were conducted by teams led by scientists from the national laboratories, some with support from LLE.

The Fundamental Science Campaigns accounted for 25.5% of the Omega Laser Facility target shots taken in FY16. Over 61% of these shots were dedicated experiments under the NLUF Program, and the remaining shots were allotted to the LBS Program, comprising peer-reviewed fundamental science experiments conducted by the national laboratories and by LLE.

The Omega Laser Facility was also used for several campaigns by teams from CEA. These programs are conducted at the facility on the basis of special agreements put in place by DOE/NNSA and participating institutions.

The facility users during this year included 13 collaborative teams participating in the NLUF Program; 14 teams led by LLNL and LLE scientists participating in the LBS Program; many collaborative teams from the national laboratories and LLE conducting ICF experiments; investigators from LLNL, LANL, and LLE conducting experiments for high-energy-density–physics programs; and scientists and engineers from CEA.

FY16 NLUF Program

FY16 was the second of a two-year period of performance for the NLUF projects approved for FY15–FY16 funding and Omega Laser Facility shot allocation. Thirteen NLUF projects (see Table 148.XI, p. 206) were allotted Omega Laser Facility shot time and conducted a total of 342 target shots at the facility. The FY16 NLUF experiments are summarized in the section beginning on p. 205.

FY16 Laboratory Basic Science Studies

In FY16, LLE issued a solicitation for LBS proposals to be conducted in FY17. A total of 23 proposals were submitted. An independent committee reviewed and ranked the proposals; on the basis of these scores, 14 proposals were allocated 20 shot days at the Omega Laser Facility in FY17. Table 148.XII, p. 226, lists the approved FY17 LBS proposals.

Fourteen LBS projects previously approved for FY16 target shots were allotted Omega Laser Facility shot time and conducted a total of 218 target shots at the facility in FY16 (see Table 148.XIII, p. 227). The FY16 LBS experiments are summarized in a section beginning on p. 225.

1. FY16 LLNL Experimental Programs

In FY16, LLNL's HED Physics and Indirect-Drive Inertial Confinement Fusion (ICF-ID) Programs conducted several campaigns on the OMEGA and OMEGA EP Laser Systems, as well as campaigns that used the OMEGA and OMEGA EP beams jointly. Overall, these LLNL programs led 430 target shots in FY16, with 304 shots using only OMEGA and 126 shots using only OMEGA EP. Approximately 21% of the total number of shots (77 OMEGA shots and 14 OMEGA EP shots) supported the ICF-ID Campaign. The remaining 79% (227 OMEGA shots and 112 OMEGA EP shots) were dedicated to experiments for the HED Physics Campaign. Highlights of the various HED and ICF campaigns are summarized beginning on p. 238.

In addition to these experiments, LLNL Principal Investigators (PI's) led a variety of Laboratory Basic Science Campaigns using OMEGA and OMEGA EP, including 81 target shots using only OMEGA and 42 shots using only OMEGA EP.

2. FY16 LANL Experimental Campaigns

In FY16, LANL scientists carried out 22 shot days on the OMEGA and OMEGA EP Laser Systems in the areas of HED science and ICF. The HED shots focused on the areas of radiation flow, hydrodynamic turbulent mix and burn, the equations of state of warm dense matter, and coupled Kelvin–Helmholtz/Richtmyer–Meshkov instability growth. The ICF campaigns focused on the priority research directions of implosion phase mix and stagnation and burn, specifically as they pertain to laser direct drive. Several of the shot days also focused on transport properties in the kinetic regime. LANL continues to develop advanced diagnostics such as neutron imaging, gamma reaction history, and gas Cherenkov detectors. The reports starting on p. 261 summarize the LANL campaigns, their motivation, and the main results from FY16.

FY16 NRL Experimental Campaigns

During FY16, NRL/LLE collaboration on laser imprint led to three successful shot days on OMEGA EP. A new method was devised to produce smooth preheating of the coating without installing a dedicated laser for preheating. It utilized soft x rays generated by a low-energy laser pulse on an auxiliary gold foil to heat and expand the coating on the main target. Streaked x-ray radiography shows that the x rays successfully expanded the coating in front of the plastic foil prior to the arrival of the main laser drive. Well-resolved measurements of Rayleigh–Taylor–amplified laser imprint (Fig. 148.136, p. 274) were obtained on OMEGA EP, showing significant reduction of the target perturbations with the gold overcoat. Initial analysis shows further reduction when the coating is pre-expanded by the prepulse (Fig. 148.137, p. 274).

FY16 CEA Experiments

CEA conducted 55 target shots on the OMEGA laser in FY16 for the campaigns discussed starting on p. 274.

Robert L. McCrory
Director, Laboratory for Laser Energetics
Vice President, University of Rochester

Direct Drive: Simulations and Results from the National Ignition Facility

Introduction

In direct-drive inertial confinement fusion[1] nominally identical laser beams are incident on a capsule containing a layer of frozen deuterium–tritium (DT) within a shell made of an ablator such as plastic (CH). The beams ablate the outer material, driving the cryogenic DT layer inward. The shell accelerates during the laser pulse as a result of the pressure from the laser energy deposited in the corona and then decelerates when an outgoing shock is launched once the pressure in the vapor region is higher than the pressure in the inward-moving shell. The shell kinetic energy is then converted to the internal hot-spot energy during stagnation. Ignition requires that the temperature and areal density of the hot spot should be sufficient to generate heating by the alpha particles produced from the D–T fusion reaction. Several measures of target performance have been presented in the literature.[2,3] The minimum fuel energy required for ignition $E_{\min}$ considered here is given by[3]

$$E_{\min}(\mathrm{kJ}) = 50.8\,\alpha_{\mathrm{inn}}^{1.88}\left(\frac{V_{\mathrm{imp}}}{3\times 10^{7}\,\mathrm{cm/s}}\right)^{-5.89} \times\left(\frac{P}{100\ \mathrm{Mbar}}\right)^{-0.77}, \tag{1}$$

where α_{inn} is the adiabat defined as the ratio of the pressure to the Fermi-degenerate pressure in the inner surface of the shell, V_{imp} is the implosion (peak) velocity of the shell, and P is the ablation pressure. Direct drive couples ~3 to 5× more laser energy into the imploding shell than x-ray drive, resulting in larger values of V_{imp} for the same laser energy. From Eq. (1), for the same $E_{\min}$ and with larger values of V_{imp}, ignition designs with larger values of α_{inn} are possible in direct drive than from x-ray drive. Direct drive, for example, requires convergence ratios of $\gtrsim$22 (defined as the ratio of initial radius to hot-spot radius at peak neutron production) to be ignition relevant, whereas x-ray drive requires convergence ratios of 30 to 40. Designs with higher adiabats are more robust to shock mistiming, preheat from fast electrons, or radiation. Higher-adiabat direct-drive designs also benefit greatly from reduced Rayleigh–Taylor (RT)[4] growth. The high power of the velocity term in Eq. (1) $\left(\sim V_{\mathrm{imp}}^{-5.89}\right)$ also indicates that robust predictions of ignition require knowledge of the shell's velocity to very high precision; a 5% decrease in velocity increases the minimum energy required for ignition by nearly 35%.

In direct drive, the implosion velocity and the ablation pressure are primarily determined by coupling the laser into the coronal plasma and the conduction of heat to the ablation surface. The equation of state has been shown to influence these quantities, although to a smaller extent.[5] While the dominant mechanism for laser-energy absorption is collisional absorption (or inverse bremsstrahlung), because of cross-beam energy transfer (CBET)[6] modifications in simulation codes are required to explain observables including capsule trajectory, scattered-light spectra and time histories, and bang times in OMEGA experiments.[7]

In CBET, ion-acoustic waves in the plasma mediate the transfer of energy from an incoming (pump) ray to an outgoing (probe) ray, reducing the energy available for deposition by the most hydrodynamically efficient incoming rays. The CBET gain factor scales as[6,7]

$$\mathrm{d}\tau_{\mathrm{CBET}} = f_{\mathrm{CBET}}\,\zeta_{\mathrm{pol}}\left[\frac{e^{2}}{c^{3}m_{\mathrm{e}}}\,\frac{n_{\mathrm{e}}}{1-n_{\mathrm{e}}}\,\frac{\lambda_{0}\langle Z\rangle}{\langle Z\rangle T_{\mathrm{e}}+3T_{\mathrm{i}}}\right] \times P(\eta)\,I_{\mathrm{pump}}\,\mathrm{d}s\,, \tag{2}$$

where f_{CBET} is an *ad hoc* multiplier used to explore sensitivity to the model; $\zeta_{\mathrm{pol}} = 1/4\left[1+(\hat{k}_{\mathrm{pump}}\cdot\hat{k}_{\mathrm{probe}})^{2}\right]$ is the polarization factor; e is the electron charge; c is the speed of light; m_{e} and n_{e} are the electron mass and electron density, respectively; λ_{0} is the laser wavelength; $\langle Z\rangle$ is the average ionization of the material; T_{e} and T_{i} are the electron and ion temperatures, respectively; $P(\eta)=\eta\nu_{\alpha}\Big/\left[(\eta\nu_{\alpha})^{2}+(1-\eta)^{2}\right]$ is the resonance function with $\eta=(\omega_{\mathrm{pump}}-\omega_{\mathrm{probe}})-k_{\alpha}\cdot V_{\mathrm{fluid}}\Big/\left|k_{\alpha}\right|c_{\alpha}$, where ω_{pump} and ω_{probe} are the pump and probe frequencies, and k_{α} is the wave number of the ion-acoustic wave given by the wave-matching condition with sound speed c_{α} and the dimensionless ion-wave damping coefficient ν_{α}; and V_{fluid} is the fluid velocity. The energy gained or lost is given by $E_0\left[e^{\mathrm{d}\tau_{\mathrm{CA}}}e^{\mathrm{d}\tau_{\mathrm{CBET}}}-1\right]$, where $\mathrm{d}\tau_{\mathrm{CA}}$ is the absorption factor caused by collisional absorption. This model was implemented in the spherically symmetric code *LILAC*[8] and the axisymmetric code *DRACO*.[9] This CBET model was compared to 60-beam OMEGA implosions and, at this time, an overall multiplier f_{CBET} = 1.5 is required in *DRACO* to reproduce the observed neutron rates and scattered light. The reason for an overall multiplier is unknown. This fixed value of 1.5 is used in all *DRACO* simulations described in this article.

Differences between OMEGA[10] and National Ignition Facility (NIF)[11] implosions motivate the current experiments on the NIF. The simulated coronal temperature in NIF implosions is ~3.2 keV compared to ~2.75 keV in OMEGA implosions. Additionally, the path lengths d*s* for the rays [Eq. (2)] in the NIF corona are significantly longer; the volume in the NIF corona is approximately a factor of 1.5× larger than OMEGA-scale implosions. Therefore, it is expected that the CBET effect will be considerably larger on the NIF scale. As will be shown later, for the ongoing experiments, CBET decreases implosion velocity by ~18% and the ablation pressure by ~57%, significantly increasing E_{min}. Validating such a model and demonstrating mitigation of CBET are important to the larger direct-drive–ignition program.

The electron-heat conduction from the laser-deposition region to the ablation surface sets up the ablation pressure in direct drive. Nonlocal heat conduction[12] has been shown to play an important role in shock timing in cryogenic DT OMEGA experiments and, in combination with CBET, is required to reproduce all observables related to energetics including trajectories, bang times, time-resolved scattered light, and scattered-light spectra. It is expected that nonlocal electron thermal transport should also play an important role in NIF-scale experiments.

Preheat from two-plasmon decay (TPD)[13] is expected to be larger on the NIF scale compared to OMEGA implosions. In TPD, plasma waves accelerate electrons to energies (≥30 keV) with sufficiently long mean free paths so that their energy can be deposited in the cold shell, compromising compression or α_{inn}. TPD is a multibeam instability that requires the overlap of several beams to cooperatively overcome the threshold. In OMEGA implosions, the magnitude of the energy in the source of energetic electrons has been shown to scale with the threshold parameter η:[13]

$$\eta=\frac{I_{n_{\mathrm{c}}/4}\left(\times 10^{14}\,\mathrm{W/cm^2}\right)L_{n_{\mathrm{c}}/4}(\mu\mathrm{m})}{233\,T_{\mathrm{e}}(\mathrm{keV})}, \tag{3}$$

where $I_{n_{\mathrm{c}}/4}$, $L_{n_{\mathrm{c}}/4}$, and T_{e} are the intensity, density scale length, and electron temperature at the quarter-critical surface, respectively. As mentioned earlier, NIF implosions are characterized by higher coronal temperatures; however, the scale length is also larger—350 μm in the current experiments compared to 150 μm in OMEGA implosions. Note that since the target sizes in the ongoing experiments are determined by the phase plates on the NIF, the scale lengths are smaller than those in ignition-relevant designs (~500 to 600 μm). The extrapolation to longer scale lengths suggests that a larger source of hot electrons is expected on the NIF; however, beam polarizations and beam angles also influence the extent of this instability. One significant difference between OMEGA and NIF experiments is that the ongoing NIF implosions are performed in the polar-direct-drive (PDD) geometry.[14] Beams displaced toward the equator to improve symmetry are incident at oblique angles onto the target. More beams are overlapped in the NIF geometry than on OMEGA but with variations in the beam polarizations and incident angles. These differences motivate experiments on the NIF to estimate the TPD source and its effect on the imploding capsule.

This work presents results from implosion experiments on the NIF. While a subset of results presented in this work has appeared previously,[15] a more-complete analysis that includes the validation of the CBET model in OMEGA PDD implosions, comparison of scattered-light spectra, and time histories with updated simulations that include a first-principles equation of state (FPEOS)[5] is presented here. Also included is a discussion on the reasons for possible differences between simulation and experiment.

This article discusses (1) the target design and (2) results from the experiments, organized by the physics topics—energetics and preheat. Simulated scattered-light spectra show similar trends as observed; trajectories from backlit images and the shapes of the imploding core agree very well, although the trajectory from self-emission images lags the simulation in the experiment. These results and sensitivity analyses to possible errors in CBET modeling, the effect of laser imprint, and fast-electron preheat are examined and future work and conclusions are presented.

NIF Target Design

The primary target type considered in this article has an outer radius of ~1100 μm with an ~100-μm-thick, all-plastic (CH) shell filled with 20 atm of deuterium (D_2) gas [Fig. 145.1(a)]. The capsule is irradiated with a laser pulse shape whose temporal history includes a flat foot rising to a main pulse at varying laser intensities.[16,17] The shock launched

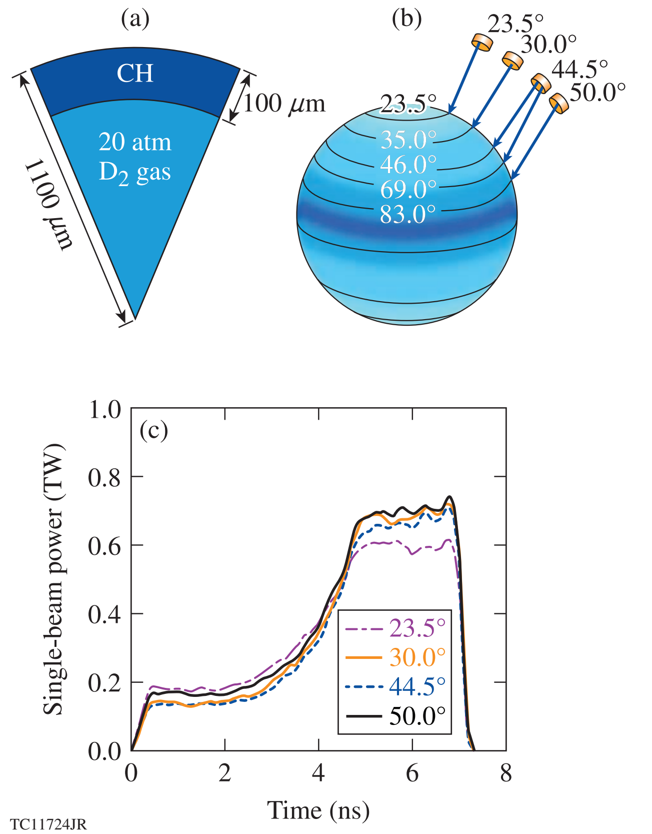

Figure 145.1
(a) Schematic of the target used in a typical polar-direct-drive (PDD) National Ignition Facility (NIF) implosion. (b) The pointing scheme in polar angle used for the PDD implosions. The four original cones at 23.5°, 30.0°, 44.5°, and 50.0° are repointed to the locations shown on the target. (c) Pulse shapes for each of the cones.

during the foot of the pulse shape sets the implosion at an ignition-relevant adiabat $\alpha_{\text{inn}} \sim 3$. The implosions have a low convergence ratio of ~13 (compared to ≳22 for direct-drive ignition), defined as the ratio of the initial radius of the fuel–shell interface to the final fuel radius at peak neutron production. The laser energy on target varies from ~350 kJ (for a pulse shape with an intensity of $\sim 4 \times 10^{14}$ W/cm^2 at the initial target radius) to ~650 kJ (corresponding to an on-target intensity of $\sim 1.2 \times 10^{15}$ W/cm^2). The pulse shapes are similar although they differ in the duration of the main pulse. The shell is deliberately set at a low implosion velocity of 1.8 to 2.2×10^7 cm/s, compared to ignition-relevant values of $\gtrsim 3.5 \times 10^7$ cm/s. The low velocity reduces the instability growth of the most-dangerous modes, which scale linearly with the implosion velocity.[18] This conservative design was chosen because the growth of single-beam nonuniformity (laser imprint) is expected to significantly compromise shell integrity in these implosions (also discussed in **Future Work**, p. 12); the existing laser-beam smoothing is insufficient to drive high-performing implosions. Beam profiles used in the x-ray drive ignition campaigns[19] are used in the design. The on-target beam profile is calculated by forward propagating the near-field phase-front information using the code *Waasikwa'*.[20] The laser beams are also defocused by 1 cm to improve symmetry, which is taken into account in the calculation. Since only one set of near-field beam phase-front information is available for each cone, the same calculated profiles are used for all of the beams within a cone.

The beam geometry on the NIF is configured for the axisymmetric x-ray-drive configuration [Fig. 145.1(b)]. To improve irradiation symmetry, the equator requires additional drive. This is achieved by displacing the beams toward the equator as illustrated in Fig. 145.1(b). The beams on the NIF are arranged in cones at 23.5°, 30°, 44.5°, and 50°. In this PDD geometry, for example, the outer cone located at 50° is displaced to irradiate the target at 83°. The beam configuration in Fig. 145.1(b) is obtained by iteratively adjusting the combination of beam displacements, beam defocus, and beam pulse shapes to reduce shell asymmetry.[16] In addition, beams in cones 44.5° and 50° are displaced azimuthally to improve symmetry. Typical laser pulse shapes for the different cones are shown in Fig. 145.1(c). Notice that the 50° cone is driven with the highest power to provide additional drive in that region. The PDD configuration differs from the spherical-direct-drive (SDD) implosion studies on OMEGA,[16,21] where models have been validated. The lack of drive at the equator is deliberately compensated by displacing beams toward the equator. These beams displaced toward the equator scatter around the target and, consequently, more scattered light appears near the poles in PDD than SDD. SDD is quasi-symmetric; simulations indicate that the scattered light around the target chamber varies by less than 1% rms (root mean square), significantly smaller than PDD. CBET, in particular, is influenced by the PDD beam displacements. More ray crossings occur over a region around the equator; therefore, CBET influences the laser-energy deposition in the region over the equator. As the schematic in Fig. 145.2(a) indicates, an outgoing ray (probe) from the southern hemisphere near the equator acquires energy from an incoming ray (pump) in the northern hemisphere; this excess energy in the outgoing ray can appear as scattered light over the northern polar region. This is also shown in Fig. 145.2(b) in the contour plot of the CBET energy gained per unit volume and normalized to the hydrodynamic time step. The contour plot shows the region where CBET dominates. Most of the energy gain in the rays occurs away from the poles and in a range of polar angles closer to the equator. The projected scattered light around the target chamber is shown in Fig. 145.3 for an OMEGA PDD implosion. The hydrodynamic code *DRACO* with a full three-dimensional

(3-D) ray trace[22] that includes collisional absorption, nonlocal heat conduction,[23] and FPEOS[5] is used to simulate the PDD implosion. When the effect of CBET is included in the calculation [Fig. 145.3(b)], significantly more scattered light appears near the poles than when only collisional absorption is used to model the laser-energy deposition [Fig. 145.3(a)]. Scattered-light flux around the target chamber as a function of polar angle, collected using calorimeters in a PDD implosion irradiated with a pulse shape similar to one used in NIF implosions,[24] is shown in Fig. 145.3(c). The locations of the calorimeters are shown as

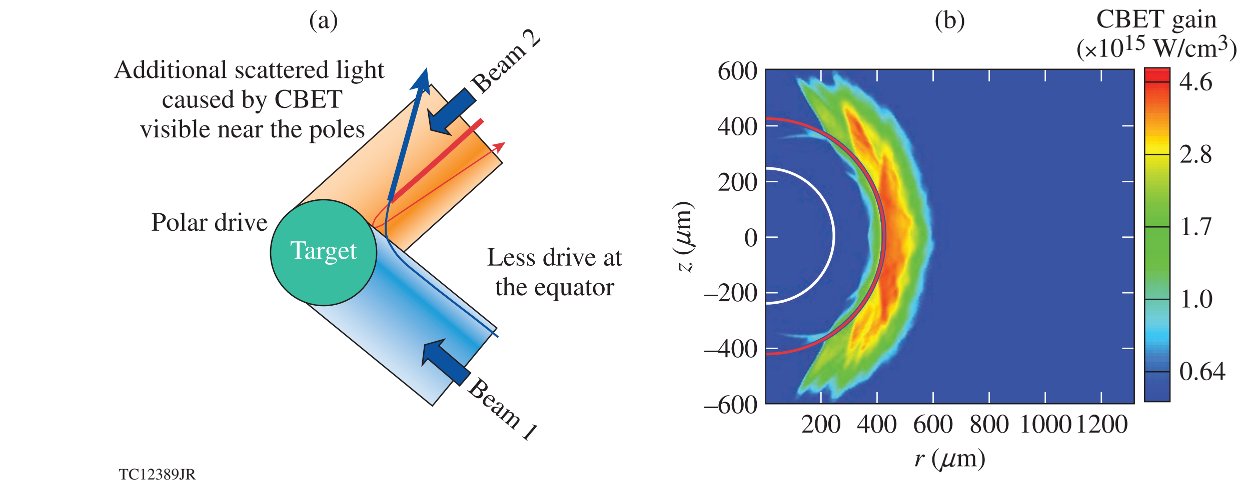

Figure 145.2
(a) Schematic of cross-beam energy transfer (CBET) in the PDD geometry. The dominant transfer occurs when energy is transferred from an incoming ray to an outgoing ray. (b) Contour plot of energy gained from CBET. The transfer occurs away from the poles; more ray intersections occur away from the poles because of PDD beam displacements.

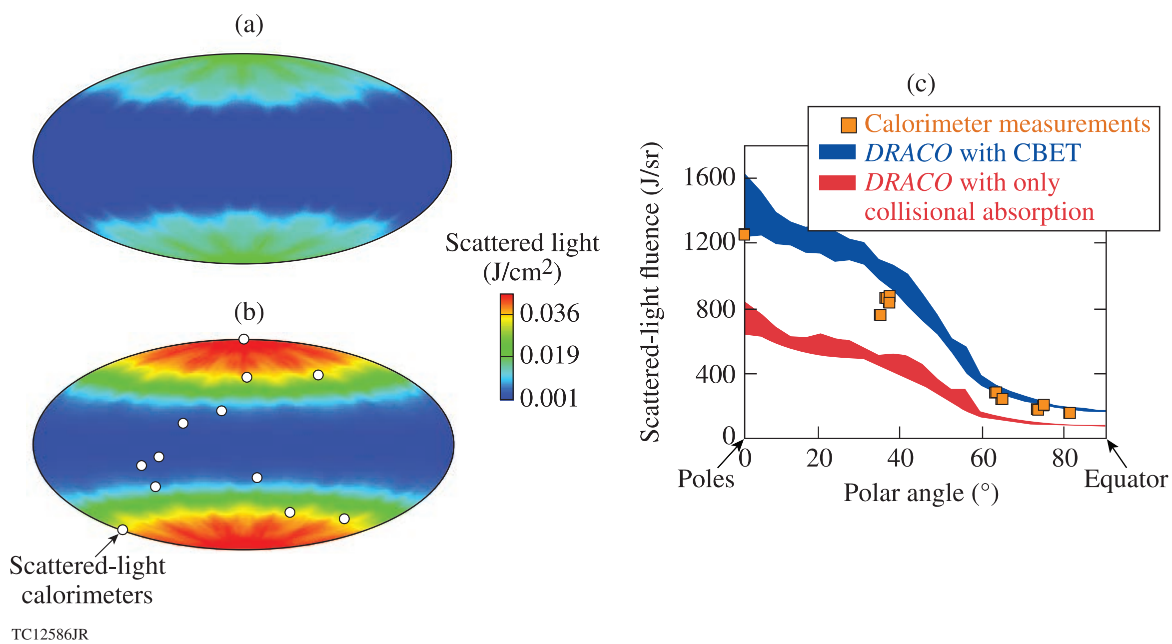

Figure 145.3
Projected scattered light in the OMEGA target chamber from a simulation that includes (a) only the effect of collisional absorption and (b) the effect of CBET. Circles indicate the locations of the calorimeters in the OMEGA chamber. (c) Scattered-light fluence at the calorimeters in shot 64099 on OMEGA (symbols). The simulation is shown as shaded regions, indicating the minimum and maximum scattered light along the azimuthal angle. Red corresponds to (a)—only the effect of collisional absorption is included. Blue corresponds to (b)—the effect of CBET is also included in the simulation.

circles on Fig. 145.3(b). As the figure indicates, significantly more scattered light appears near the poles when CBET is included in the calculation (blue) compared to when only collisional absorption is included (red). The shaded regions indicate the minimum and maximum light along the azimuth as calculated by the 3-D ray trace. The additional polar light agrees well with observations (symbols), which also show the same trend.

Simulations indicate that the energy transfer from the incoming rays occurs at the center of the beam for rays with the smallest incident angles that are the most hydrodynamically efficient. This results in less drive around the equatorial region; therefore, CBET makes the implosion more oblate than collisional only absorption as seen by the synthetic self-emission images of the imploding shell (Fig. 145.4). Requiring simulations to reproduce the observed shape of the imploding core, i.e., the drive as a function of polar angle, makes PDD a more-stringent test of direct-drive implosion physics than SDD.

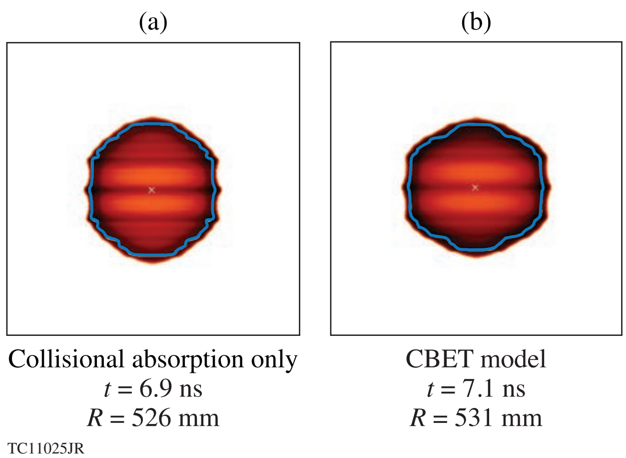

Figure 145.4
Simulated self-emission images from N150118-002 with (a) only collisional absorption laser deposition included in the calculation and (b) the effect of CBET also included in the calculation.

Results and Discussion

1. Energetics

a. Results. Energetics on the NIF is inferred from time-resolved scattered light measured using fast diodes[25] and a streak camera.[25] The time-resolved scattered light is plotted in Fig 145.5. The simulation tracks the observations very closely with deviations between 5 and 7 ns. The implication of the excess simulated scattering is unclear. Additional information is also available from the two full-aperture backscatter stations (FABS)[25] that measure the spectrum of scattered light. Figure 145.6(a) shows the spectra observed by the FABS. Features characteristic of implosions are observed in the spectra:

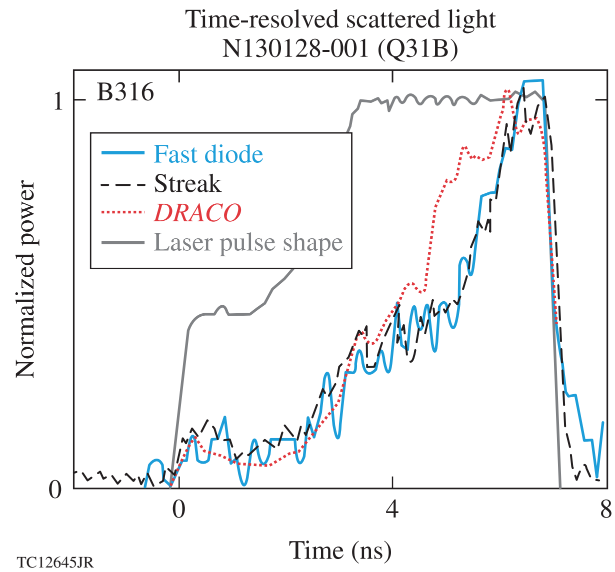

Figure 145.5
Time-resolved scattered light measured at one location, corresponding to B316, from fast diodes (blue solid line) and optical streak cameras (black dashed and solid lines). Time-resolved scattered light from a simulation including the effect of CBET is also shown (red dotted line).

a rapid blue shift is observed early in time corresponding to corona formation; the red shift at ~2 ns corresponds to the onset of inward motion of the corona during the acceleration phase. Very similar trends are observed in the *DRACO* simulation [Fig. 145.6(b)]. Similar agreement is obtained with the spectra from the other FABS location. Quantitative inferences of the energy in the scattered-light spectrum and the time-resolved light are in progress and are important to further validate the modeling (discussed in the next section).

Trajectories of the converging shell provide information about the laser energy coupled to the target and are measured in two ways: the first uses a gated framing cameras with a 1-mil-thick Be filter (~25 μm) to measure the self-emission of the target,[26] corresponding to photon energies ≳1 keV; the second uses a gated framing camera to measure a radiograph obtained by backlighting an implosion[27] using Fe (~6.7 keV). Excellent agreement is obtained with the CBET model on OMEGA to replicate observed trajectories from self-emission images,[21] while trajectories from backlit images have been explored to a more-limited extent.[27] The design for a backlit implosion requires changes to the beam configuration. Two quads (one from each hemisphere) are removed to irradiate an iron backlighter. The energies of eight neighboring quads and their pointing are adjusted to improve symmetry. Figure 145.7 shows typical images obtained from the framing cameras. The view from the pole records the self-emission. Simulations show that the location of the steepest gradient corresponds closely to the ablation surface.[26] This location is shown on a typical simulated density profile of the implosion. Notice the circular polar image indicating that the nonuniformity imposed by the removal of quads to irradiate the backlighter has been adequately compensated by the increased energies and repointing of the eight neighboring quads. The view from the equator records the backlit image. The surface of greatest absorption corresponds to the location of the fuel–shell interface, as shown on the same density profile; therefore, the difference in the location of the two surfaces can be interpreted as the thickness of the imploding shell.

Trajectories for different shots are plotted in Fig. 145.8. Simulations are post-processed using the code *Spect3D*[28] to create the self-emission and backlit images. The finite spatial resolution (~20- to 30-μm pinhole size depending on the shot) and gating time window of the cameras (~100 ps) are included in the simulated images. The same analysis is used to extract average radii from the synthetic and measured images.[26,27] The black solid line from the backlit image reproduces the inferred trajectory very well, whereas the red dashed line from self-emission images apparently overestimates the drive. The slopes of the two trajectories indicate that the velocity from the backlit trajectory

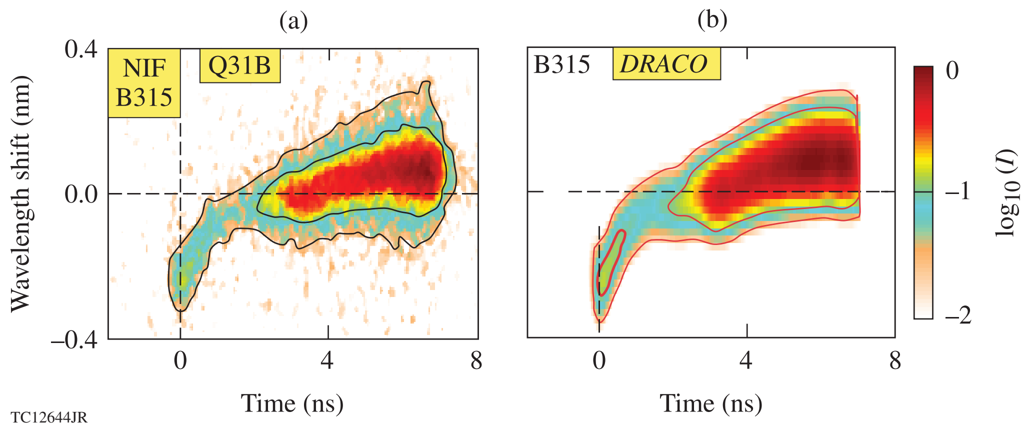

Figure 145.6
Scattered-light spectrum measured using the full-aperture backscatter station (FABS) diagnostic at one location and corresponding to the same location as the diodes. (a) Measured scattered-light spectrum and (b) spectrum from a simulation including the effect of CBET.

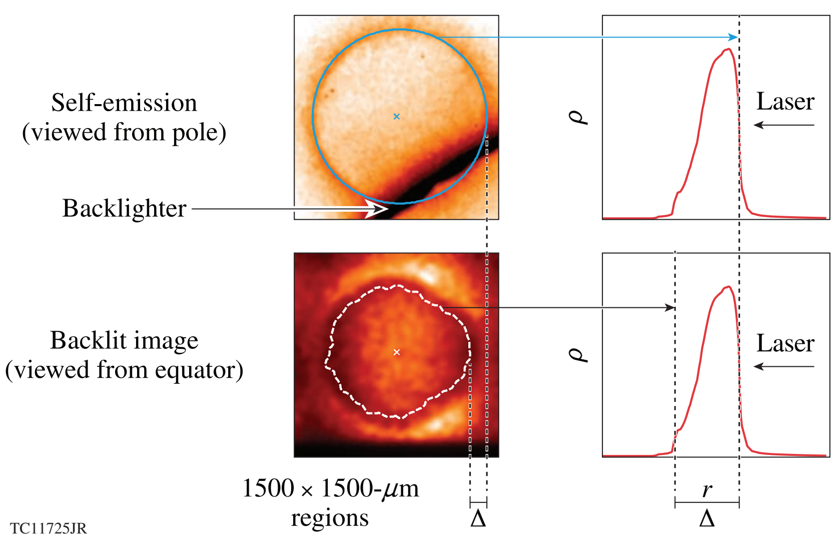

Figure 145.7
Typical self-emission image viewed from the pole and backlit image viewed from the equator (shot N140612-001). Absorption images are obtained at 6.7 keV by backlighting the implosion with Fe. Self-emission images are viewed at ≳1 keV with a Be filter of 1-mil thickness. The lineouts point to the surfaces in the density profile (right) that are extracted from the image.

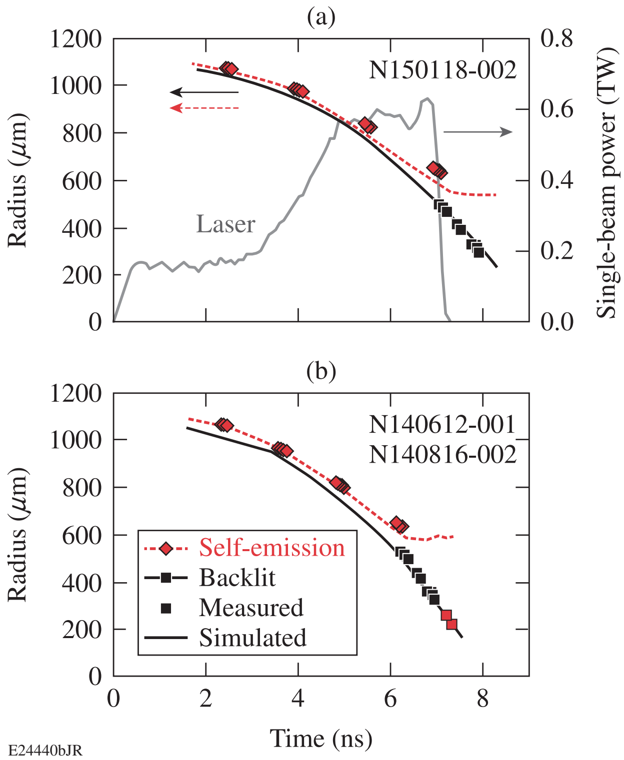

Figure 145.8
(a) Trajectories from backlit images from measurements (black squares) and simulations (black solid line). Trajectories from self-emission images from measurements (diamonds) and simulations (red dashed line) for shot N150118-002. (b) Same as (a) but for shots N140612-001 and N140816-002.

is reproduced to within 1% by the simulation, whereas the trajectory from the self-emission images is overestimated by ~9%. If the self-emission trajectory was representative of the velocity, this would significantly increase E_{min}, compromising ignition. It is, therefore, important to resolve the difference and identify which trajectory, if either, is representative of the true implosion velocity. Note that the inferred shell thickness estimated using the procedure in Fig. 145.7 is larger than the simulated value. The trajectories and shell thickness can be influenced by both 1-D and multidimensonal physics. One-dimensional physics energy includes coupling models and preheat (radiative or fast electron). Multidimensional physics such as Rayleigh–Taylor growth seeded by imprint can also change the location of peak emission or absorption of x rays. It is important to understand if the differences are caused by errors in the 1-D modeling since they influence models used to predict ignition. If imprint was the cause, it is expected to be of less concern since improved beam smoothing[29] and target designs with doped-CH overcoats[30] or Au layers[31] have been shown to mitigate this effect. Each of these factors is discussed below—first qualitatively and then collated in a plot showing the relative magnitude of each of these effects.

b. Sensitivity analysis. Overestimating the predicted velocity of the early shock (resulting from inaccuracies in the modeling of laser coupling or equation of state) can delay the trajectory. If the shock was slower than simulated, the breakout of the shock into the gas would be delayed, postponing the onset of acceleration. Shock mistiming can thicken the converging shell: a higher adiabat results in a lower-density shell that occupies a larger volume during convergence. However, for this pulse shape, the absorption during the low-intensity foot is very high (~95%). The mechanism for absorption during this time is primarily collisional absorption; so any mistiming of the shock is small and its effect on shell thickness and trajectory is insignificant. For example, mistiming the shock during the foot by using a flux-limited diffusive heat-conduction model with flux limiter $f = 0.06$ (Ref. 32) instead of the nonlocal transport delays the shock breakout by less than 20 ps, which only marginally influences trajectory and shell thickness. Therefore, it is hypothesized that the observations cannot be explained by shock mistiming alone.

Sensitivity analysis to the CBET model is examined using the spherically symmetric code *LILAC* by using a multiplier, $f_{CBET} = 2$, in the gain factor [Eq. (2)]. Figure 145.9 shows the density profiles in the simulation of a NIF-type implosion at different times when the inner surface of the shell has traveled the same distance. The shell becomes increasingly decompressed and the ablation pressure is reduced as the extent of CBET is increased in the modeling (Table 145.I). This also significantly reduces the absorption fraction, suggesting that

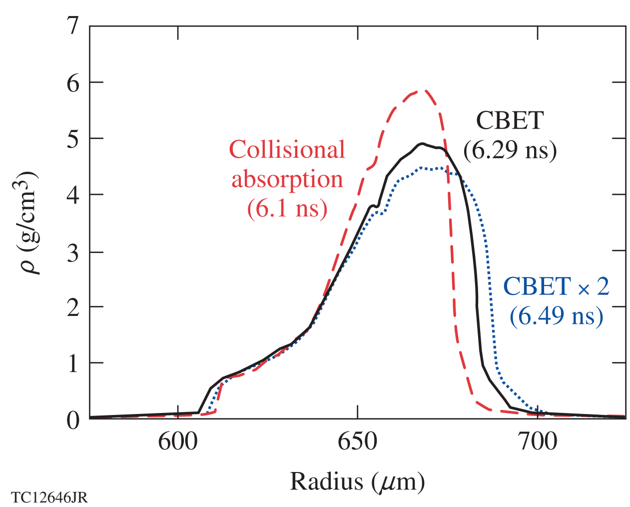

Figure 145.9
Density profiles showing the sensitivity of the shell thickness to different extents of CBET (red dashed line: collisional absorption only; black solid line: CBET with $f_{CBET} = 1$; blue dotted line: CBET × 2 with $f_{CBET} = 2$).

a detailed quantification of the scattered light is crucial to achieve higher accuracy in the laser-deposition CBET modeling. The implosion velocity, which decreases as the extent of CBET increases in the model, is listed in Table 145.I. This is also shown in Fig. 145.10 through the trajectories of the two surfaces; CBET reduces the velocity of both the surfaces while decompressing the shell. Agreement with the experimentally inferred trajectories requires that the backlit trajectory remains unchanged, whereas the self-emission trajectory becomes apparently slower; therefore, an error in the CBET modeling alone is insufficient to explain the observation.

Preheat from energetic "hot" electrons can also potentially influence the trajectories. The energy in hot electrons is inferred in NIF implosions from the filter-fluorescence x-ray (FFLEX)[33] diagnostic. FFLEX measures the time-resolved x-ray emission in ten channels ranging from ~20 keV to 250 keV. The inferred total cumulative energy E_{hot} is calculated assuming that the entire observed x-ray emission results from the deposition of the fast-electron energy in the CH ablator. A value of $E_{hot} \sim 2.5 \pm 0.3$ kJ is, therefore, obtained corresponding to ~0.4% of the total laser energy. The hot-electron temperature is inferred by fitting the measured time-integrated x-ray spectrum for the various FFLEX channels. The fit yields a value of 46±3 keV for the shots considered here.[15] This is consistent with temperature measurements on OMEGA.[34] A straight-line deposition formula is used in *LILAC* to simulate the effect of this distribution of electrons on the trajectory and shell thickness.[35] A wide angular divergence of the electrons (240°) is assumed in the model. Studies of TPD in SDD OMEGA implosions using Mo balls of different radii suggest that the electrons are produced at a large divergence angle.[34] Indications of isotropy were also observed in NIF PDD implosions in the DIME[36] (defect-induced mix experiment) campaign.[35] Energetic x rays produced in the DIME NIF PDD implosions are observed via pinhole images and are also isotropic.[37] Therefore, a straight model in the spherically symmetric code *LILAC* is expected to reproduce the sensitivity of the NIF implosion to fast-electron preheat. The observed time-resolved history of the x-ray emission (Fig. 13 in Ref. 15) is calculated by the model—almost no emission is observed until ~4 ns.

Table 145.I: The effect of selected implosion parameters with increasing extents of CBET using the spherically symmetric code *LILAC*. CBET × 2 corresponds to $f_{CBET} = 2$ in Eq. (2). The numbers in parentheses indicate the values (in %) of the quantity relative to the collisional absorption value.

Model	P_{abl} (Mbar)	M_{abl} ($\times 10^6$ cm/s)	V_{imp} ($\times 10^7$ cm/s)	f_{abs}(%)
Collisional absorption	70	1.4	2.2	95
CBET	30 (43%)	0.8 (57%)	1.8 (82%)	75 (79%)
CBET × 2	15 (21%)	0.6 (43%)	1.5 (68%)	64 (67%)

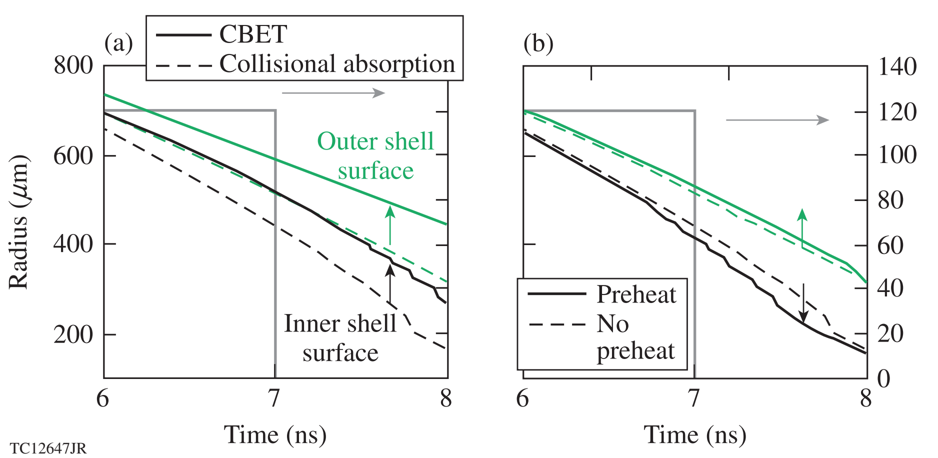

Figure 145.10
Dependence of the backlit and self-emission trajectory to models with (a) collisional absorption only (dashed lines), including the effect of CBET (solid lines) and (b) collisional absorption only (dashed line), including the effect of preheat (solid line). The laser pulse, corresponding to the right axis, is shown for reference.

The emission then increases during the main pulse and stops at approximately the end of the laser pulse. The effect of these electrons on the implosion is shown in Fig. 145.10. A factor of ~2 more electron energy (4.6 kJ) than experimentally inferred is required in the simulation to make the effect more visible on the plot. Preheat increases the shell thickness and decreases the slope of the self-emission trajectory as required to match the observations; however, note that it also increases the slope of the backlit trajectory contrary to what is required to match the observations. The significantly larger magnitude of the preheat source required to observably change trajectories and shell thickness suggests that preheat alone is not likely the cause of the observed discrepancies between simulation and measurements. A comparison of the simulated and inferred self-emission trajectory from a low-intensity shot (~4×10^{14} W/cm^2 at the initial target radius) also indicates the apparent slowing down of the self-emission trajectory (Fig. 145.11). At this intensity, the energy in fast electrons is estimated to be less than 0.05% of the laser energy at the noise level of the FFLEX instrument—a value that has an insignificant effect on the implosion. This also suggests that fast-electron preheat is less likely a cause for the apparent shell decompression. Fast-electron preheat can be conclusively ruled out only if the backlit trajectory is also well reproduced at the low intensity and the trend in the discrepancy at the two different intensities stays the same. This is being investigated with a low-intensity implosion where a backlit trajectory is also available.

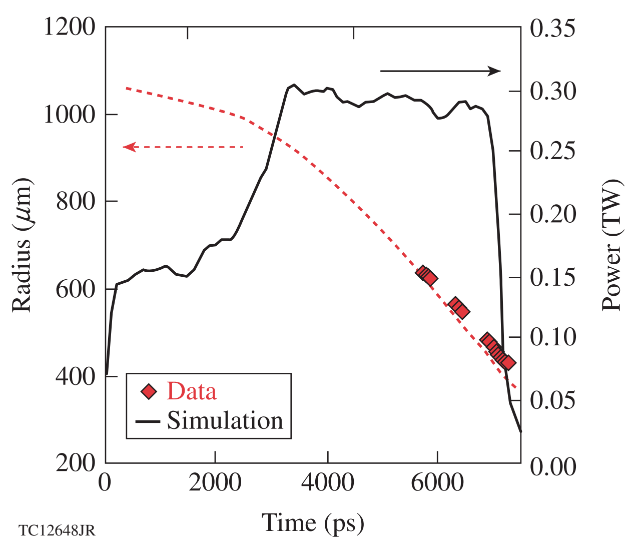

Figure 145.11
Trajectories from a low-intensity implosion (~4×10^{14} W/cm^2 average on-target intensity at the initial target radius), N130128-001. Only the self-emission trajectory is measured for this shot (red diamonds). The simulated trajectory, including the effect of CBET, is shown as the black solid line.

Finally, multidimensional effects are discussed. Single-beam laser nonuniformity imposes perturbations on the target starting at short wavelengths corresponding to ~10 μm ($\ell \sim$ 600 at the initial target radius).[9] The effect of laser imprint and the subsequent RT growth is modeled using *DRACO*. Density contours at the end of the acceleration phase for a NIF implosion are shown in Fig. 145.12(a). To make the simulation tractable, only modes up to $\ell \sim 200$ are included in the calculation. The shell is significantly distorted with a relatively intact inner shell. Trajectories from simulated images [Fig. 145.12(b)] indicate that the backlit trajectory is unchanged relative to a simulation with no distortions, whereas the self-emission region moves

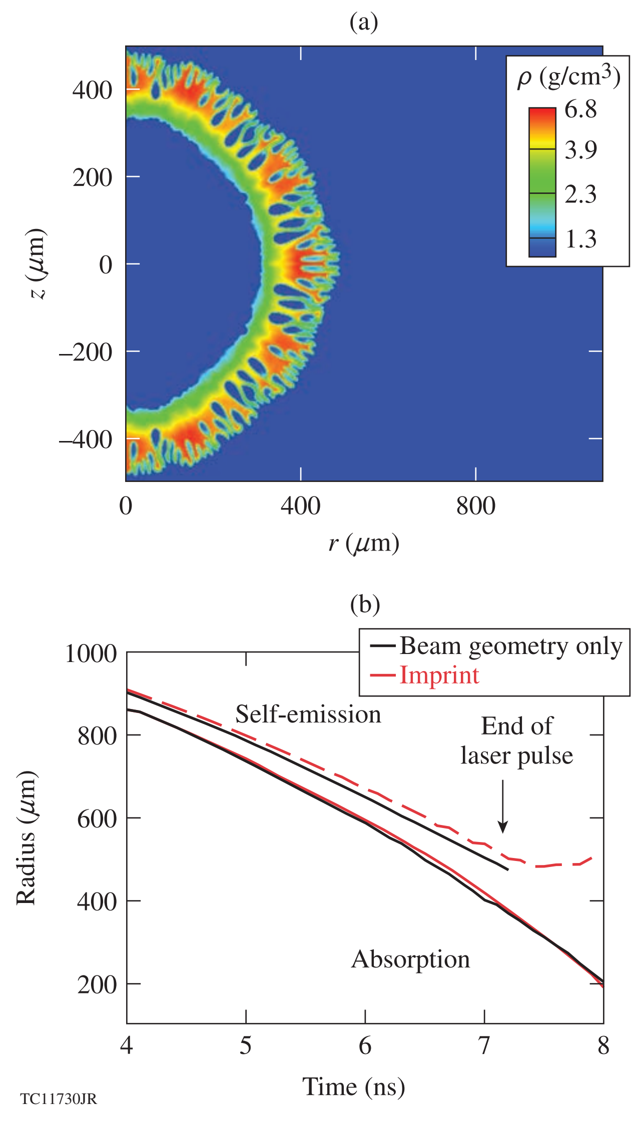

Figure 145.12
The effect of single-beam nonuniformity (laser imprint) is shown as (a) density contours at the end of the acceleration phase and (b) trajectories extracted from post-processed synthetic images of the simulation shown in (a).

farther outward, leading to an apparent decompression of the shell. This trend is consistent with experiments. A larger-scale simulation including modes up to $\ell \leq 600$ is being performed to study the influence of shorter wavelengths on the trajectory and shell thickness. Of the three sources of modeling uncertainty considered so far, only laser imprint shows the correct trends of keeping the backlit trajectory relatively unchanged and causing an apparent slowing down of the self-emission trajectory.

The results from these sensitivity studies are summarized in Fig. 145.13. The percentage increase in shell thickness over the nominal implosion (defined as including CBET, nonlocal transport, and FPEOS) is plotted against the percentage of preheat energy in the fast-electron source. To explore the sensitivity to angular divergence, electrons are launched isotropically and with an angular divergence of 240°. Shell thickness increases slowly with increasing preheat. The observed shell thickness, shown for two shots, is significantly higher than the increase caused by preheat, indicating that preheat alone is insufficient to explain the observed thickness. The increase in thickness from $f_{\mathrm{CBET}} = 2$ is also shown in Fig. 145.13. The relatively small change in shell thickness resulting from any possible error in the CBET model also suggests that energetics are well modeled and is not likely the cause for the observed differences. The increase in shell thickness caused by imprint is shown in Fig. 145.13. Of all the sources considered, imprint is the dominant contributor to the increase in shell thickness. Imprint also leaves the backlit trajectory unchanged, which is required for consistency with the measurements. It is hypothesized that some combination of the various sources of error and imprint will explain the observations with imprint as the dominant source.

A further indication that the laser drive is well modeled is obtained from the shape of the imploding core. Simulated and observed backlit images are shown in Fig. 145.14 for approximately the same convergence. Note that the shapes are far from round. This is a limitation of the available beam profiles on the NIF. Significantly improved implosions can be obtained with custom beam profiles.[38] The observed shape is very well reproduced by simulations. This is quantified by the radial deviation about the mean radius in Fig. 145.14(c), where the observed and simulated lineouts of the radial deviation are overlaid. Excellent agreement is obtained, suggesting that energetics is well modeled. Small deviations are observed near the pole. This difference is also observed on a lower-

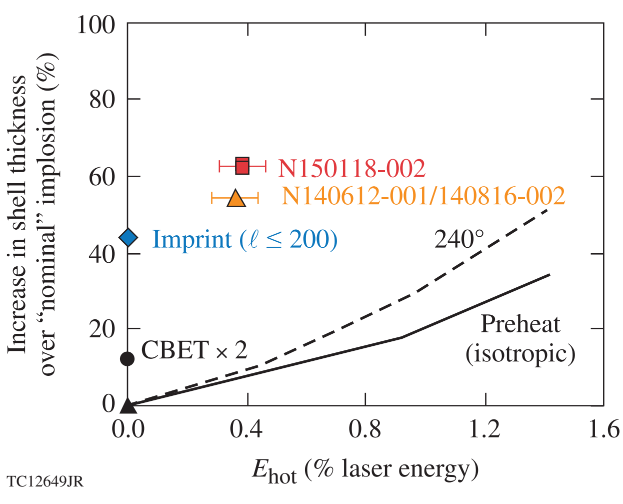

Figure 145.13
Increase in shell thickness (in %) over the nominal implosion defined as one including the effects of CBET, FPEOS, and nonlocal transport. The symbols with error bars correspond to measured values from framing-camera images. The dashed and solid lines correspond to the simulated effect of preheat. The circle indicates the effect of $f_{\mathrm{CBET}} = 2$ in the CBET model. The diamond indicates the effect of imprint.

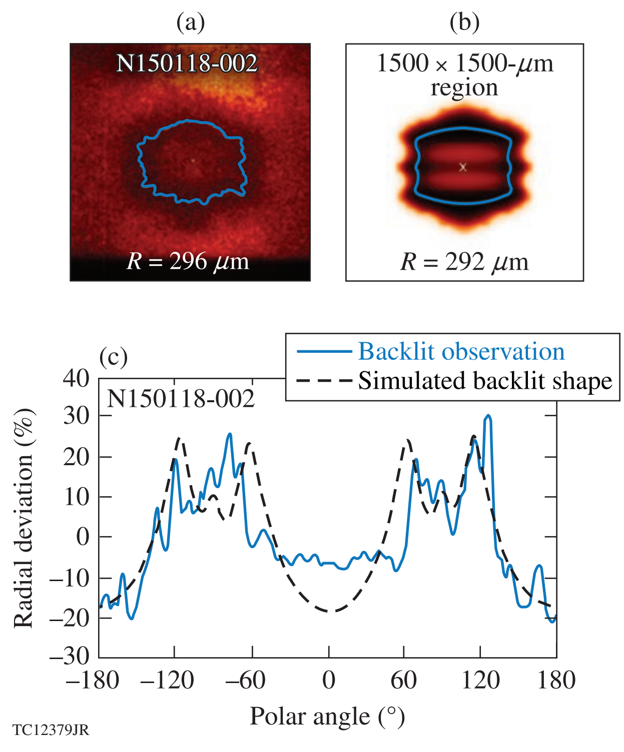

Figure 145.14
(a) Measured backlit image using the Fe line at 6.7 keV. The blue line indicates the surface of maximum absorption. (b) Simulated backlit image. The line shows the surface of maximum absorption. (c) Lineout in polar angle of the radial deviation about the mean at approximately the same convergence for measurements (solid) and simulations (dashed) for shot N150118-002.

intensity shot (Fig. 145.15). The measured and simulated images at the low intensity show reasonable agreement in the shape [Figs. 145.15(a) and 145.15(b)]. The deviation of the lineout about the average radius versus polar angle is shown in Fig. 145.15(c). The gross shape is well reproduced, although the polar region is driven significantly more in the simulation compared to experiment. Since this difference is systematic between two shots, a plausible reason for this difference could be incomplete knowledge of the calculated defocused beam profiles. No measurements of these profiles are available at this time. Moreover, as mentioned earlier, while different beam profiles are calculated for each cone, the same profile is used for all of the beams within the cone. Beam-to-beam variations are not included in the calculation since this information is unavailable.

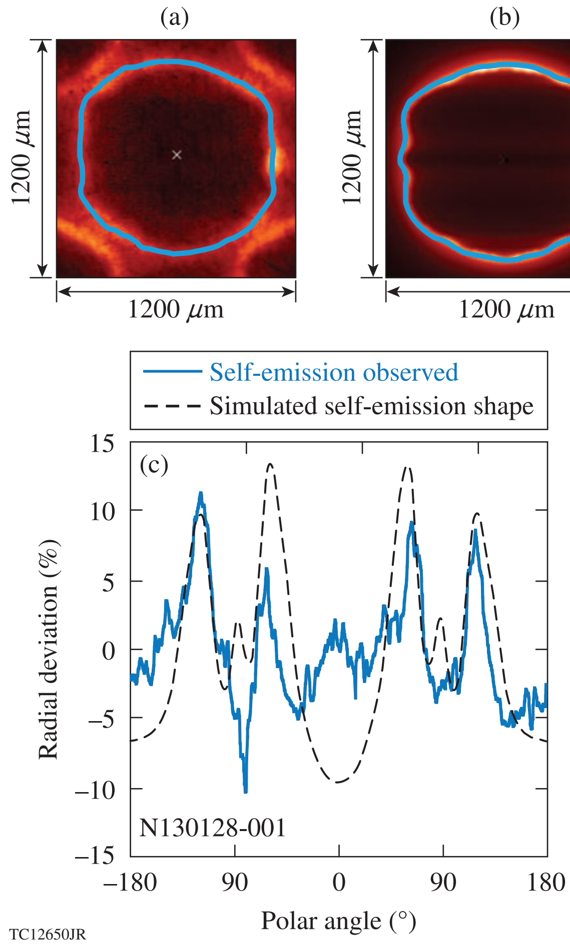

Figure 145.15
(a) Measured self-emission image. The blue line indicates the surface of steepest gradient of emission. (b) Simulated image. The blue line shows the surface of maximum absorption. (c) Lineout in polar angle of the radial deviation about the mean at approximately the same convergence for measurements (blue solid line) and simulations (black dashed line) for shot N130128-001.

c. Preheat. Estimates from FFLEX measurements in NIF implosions indicate that ~0.4% of the laser energy is converted into electron energy at intensities of 8×10^{14} W/cm^2 (the lowest ignition-relevant intensity).[15] Preheat results inferred from FFLEX for shots with varying intensity are summarized in Fig. 145.16. In integrated implosion experiments, typically only the preheat source is inferred from the measurement of bremsstrahlung x rays emitted by the fast electrons. The energy deposited in the cold shell, which is the relevant quantity for designs, is usually calculated using models[35] or estimated from complementary experiments.[39] It has been shown previously from semi-analytic estimates that ignition fails if ≥1.5% of the shell's kinetic energy is deposited as the preheat energy into the shell.[40] A typical ignition design at 1.5 MJ of laser energy, with ~80 kJ of the shell's kinetic energy, can tolerate a maximum of 1.2 kJ or 0.08% of the laser energy deposited in the cold shell without significantly compromising ignition. A similar fraction of ≲1% of the laser energy deposited in the cold shell has been previously obtained from *LILAC* simulations.[41]

The deposited energy in experiments described in this work is estimated using OMEGA implosions. A combination of room-temperature and cryogenic implosions of equivalent mass has been used to infer the energy deposited in the cold shell.[39] This work estimates that ~1/7th of the electron source energy is deposited in the high-density shell. The same ratio is applied to the NIF implosions; the same energy estimated from FFLEX is

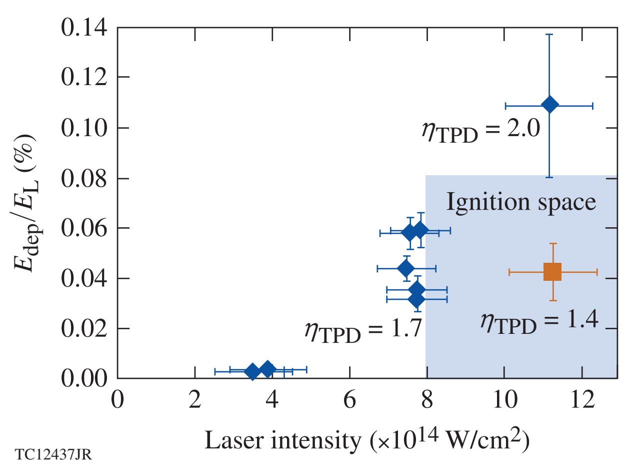

Figure 145.16
Estimated deposited energy from energetic electrons from two-plasmon decay (TPD) as a fraction of the total laser energy versus the polar-angle–averaged, on-target laser intensity during the peak of the laser pulse (measured at the initial target radius) for CH ablators (diamonds) and a target with an outer Si layer (square). The shaded region shows the range of acceptable preheat from fast electrons.

multiplied by this ratio to obtain the hot-electron energy deposited in the shell. Figure 145.16 shows this energy as a fraction of the total laser energy plotted against the on-target intensity (calculated at the initial target radius). The shaded region in the figure shows the acceptable range of intensity and deposited energy based on the analysis presented above. The preheat scales with the calculated values for the threshold parameter, η_{TPD}, consistent with OMEGA implosions. The figure shows that preheat for CH ablators is tolerable at intensities closer to 8×10^{14} W/cm^2, whereas it is clearly at an unacceptable value for ignition at higher intensities. Simulations indicate that with full CBET mitigation, η_{TPD} will increase by nearly 60% to 2.6, possibly resulting in preheat closer to the value at the higher intensity of 1.2×10^{14} W/cm^2. This would result in failure of ignition.

The presence of a mid-*Z* layer such as Si at the quarter-critical surface during the time of TPD production (the latter part of the main pulse) (Fig. 13 in Ref. 15) has been shown to reduce the preheat source in OMEGA implosions.[42] The reduction in the preheat source is primarily from the higher temperature in the corona because of the high atomic number of Si. A similar NIF experiment with an outer 14 μm of Si overlaid on a CH layer is also shown in Fig. 145.16. In this design, Si is present in the quarter-critical surface throughout the implosion. This clearly reduces the shell preheat to tolerable levels. A similar implosion will be repeated after CBET mitigation to study mitigation of fast-electron preheat.

Future Work

Future work related to NIF experiments will focus on continued model validation. As mentioned earlier, quantification of scattered light is important to disentangle the various effects discussed above and could potentially explain the discrepancy in the self-emission trajectories. Further validation requires larger-scale imprint simulations to isolate the effect of imprint. Measurements of imprint in cone-in-shell geometry[43] will be performed over the next year on the NIF. These experiments will also serve as platforms for future studies of imprint and its mitigation when improved beam smoothing[29] is installed on the NIF. As Table 145.I shows, CBET decreases the mass ablation rate and implosion velocity. Mitigation of CBET is important to recover robust ignition designs. As Eq. (2) shows, detuning the wavelengths of the pump and probe beams will detune the resonance and reduce the volume over which CBET can occur, reducing the magnitude of the effect. This will be studied using the available tunable wavelength capability of the NIF: a maximum of ± 2.3 Å in the UV.[44] This value is smaller than what is required to recover more than 50% of the CBET energy lost in simulations ($\gtrsim 6$ Å in the UV).[44] Simulations predict, however, that differences in the shape, trajectory, and the magnitude of scattered light should be observable in the experiment.[44] Other means to improve mass ablation rates such as Be ablators[45] will be explored in the coming year. Finally, TPD mitigation will be studied with a mid-*Z* layer such as Si after CBET has been mitigated.

The longer-term pre-ignition goal on the NIF is to implode a multilayer target such as the one described in Ref. 21. A mass-equivalent CH layer will replace the cryogenic DT layer in the room-temperature equivalent of the cryogenic target described in Ref. 21. A multilayer target will permit imprint mitigation (through the use of doped ablators such as CHSi or Au layers), the reduction of TPD through the use of a thin Si layer that would be present at the quarter-critical surface only during the latter part of the main pulse (where TPD is evident from fast electrons), and a Be layer to provide an improved mass ablation rate. A high-convergence implosion is not expected from this design since the outer layers of Si radiatively preheat the inner CH layer. This effect is small when a DT layer is used instead of the inner CH layer because of its low opacity. High-convergence direct-drive NIF implosions with CBET and TPD mitigation are possible only in cryogenic DT layered targets.

Ignition attempts require additional investments in hardware on the NIF including improved beam smoothing,[29] custom phase plates,[38] cryogenic target layering, delivery systems, etc. At this time, it is unclear if such an attempt would involve SDD or PDD. A future study will explore the facility and mission impacts of moving some of the NIF beams to enable spherical illumination. The NIF target chamber has ports for such beam placement. The results presented in this work apply to either scheme. Estimating imprint and the effect of laser–plasma interactions at long scale lengths on implosions and their mitigation is a critical component of studying the viability of direct drive as an ignition option.

Conclusions

Results from NIF PDD implosion experiments have been presented. The goal is to test the modeling of energetics and measure the extent of preheat in NIF implosions that have longer coronal density scale lengths than comparable implosions at the Omega Laser Facility. Observables such as the shape of the scattered-light spectrum, time-resolved scattered light, trajectories from backlit images, and the shape of the imploding shell agree very well with simulations. However, the trajectory from self-emission images lags simulations, suggesting a slower trajectory from self-emission or a thicker shell than simulated. While the cause for this discrepancy is unknown, sensitivity analyses for the various effects that might result in an effectively decompressed shell indicate that errors in energetics modeling, such as those in the CBET model, are likely not the cause. Laser imprint and subsequent Rayleigh–Taylor growth appear to be the dominant source of the observed difference. The CBET model that best reproduces the observations requires the same overall multiplier to the gain factor for both OMEGA and NIF simulations. It is expected that quantifying the scattered light on the NIF will help to identify, if this is indeed the case, and further test model predictability. The fast-electron preheat source in ongoing implosions is at a tolerable level (~0.4% of laser energy at an ignition-relevant intensity of 8×10^{14} W/cm^2 at the initial target radius) corresponding to ~0.06% of the energy deposited in the cold shell. While this is believed to be tolerable for ignition, it is expected that with the mitigation of CBET, the preheat source will increase, leading to more energy deposited in the cold shell. Implosions with mid-Z layers have been shown to reduce the preheat source (by nearly a factor of 3). Future pre-ignition plans on the NIF include continued validation of models through measurements of imprint and mitigation of CBET and TPD. All of these mitigation strategies will be studied in an integrated room-temperature implosion involving a target with multiple layers.

ACKNOWLEDGMENT

This material is based upon work supported by the Department of Energy National Nuclear Security Administration under Award Number DE-NA0001944, the University of Rochester, and the New York State Energy Research and Development Authority. The support of DOE does not constitute an endorsement by DOE of the views expressed in this article.

REFERENCES

1. J. Nuckolls *et al*., Nature **239**, 139 (1972).
2. S. W. Haan *et al*., Phys. Plasmas **18**, 051001 (2011); P. Y. Chang, R. Betti, B. K. Spears, K. S. Anderson, J. Edwards, M. Fatenejad, J. D. Lindl, R. L. McCrory, R. Nora, and D. Shvarts, Phys. Rev. Lett. **104**, 135002 (2010).
3. M. C. Herrmann, M. Tabak, and J. D. Lindl, Nucl. Fusion **41**, 99 (2001).
4. Lord Rayleigh, Proc. London Math Soc. **XIV**, 170 (1883); G. Taylor, Proc. R. Soc. London Ser. A **201**, 192 (1950).
5. S. X. Hu, L. A. Collins, V. N. Goncharov, J. D. Kress, R. L. McCrory, and S. Skupsky, Phys. Rev. E **92**, 043104 (2015).
6. C. J. Randall, J. R. Albritton, and J. J. Thomson, Phys. Fluids **24**, 1474 (1981).
7. I. V. Igumenshchev, W. Seka, D. H. Edgell, D. T. Michel, D. H. Froula, V. N. Goncharov, R. S. Craxton, L. Divol, R. Epstein, R. Follett, J. H. Kelly, T. Z. Kosc, A. V. Maximov, R. L. McCrory, D. D. Meyerhofer, P. Michel, J. F. Myatt, T. C. Sangster, A. Shvydky, S. Skupsky, and C. Stoeckl, Phys. Plasmas **19**, 056314 (2012).
8. J. Delettrez, R. Epstein, M. C. Richardson, P. A. Jaanimagi, and B. L. Henke, Phys. Rev. A **36**, 3926 (1987).
9. P. B. Radha, V. N. Goncharov, T. J. B. Collins, J. A. Delettrez, Y. Elbaz, V. Yu. Glebov, R. L. Keck, D. E. Keller, J. P. Knauer, J. A. Marozas, F. J. Marshall, P. W. McKenty, D. D. Meyerhofer, S. P. Regan, T. C. Sangster, D. Shvarts, S. Skupsky, Y. Srebro, R. P. J. Town, and C. Stoeckl, Phys. Plasmas **12**, 032702 (2005).
10. T. R. Boehly, D. L. Brown, R. S. Craxton, R. L. Keck, J. P. Knauer, J. H. Kelly, T. J. Kessler, S. A. Kumpan, S. J. Loucks, S. A. Letzring, F. J. Marshall, R. L. McCrory, S. F. B. Morse, W. Seka, J. M. Soures, and C. P. Verdon, Opt. Commun. **133**, 495 (1997).
11. J. D. Lindl and E. I. Moses, Phys. Plasmas **18**, 050901 (2011).
12. V. N. Goncharov, O. V. Gotchev, E. Vianello, T. R. Boehly, J. P. Knauer, P. W. McKenty, P. B. Radha, S. P. Regan, T. C. Sangster, S. Skupsky, V. A. Smalyuk, R. Betti, R. L. McCrory, D. D. Meyerhofer, and C. Cherfils-Clérouin, Phys. Plasmas **13**, 012702 (2006).
13. A. Simon, R. W. Short, E. A. Williams, and T. Dewandre, Phys. Fluids **26**, 3107 (1983).
14. S. Skupsky, J. A. Marozas, R. S. Craxton, R. Betti, T. J. B. Collins, J. A. Delettrez, V. N. Goncharov, P. W. McKenty, P. B. Radha, T. R. Boehly, J. P. Knauer, F. J. Marshall, D. R. Harding, J. D. Kilkenny, D. D. Meyerhofer, T. C. Sangster, and R. L. McCrory, Phys. Plasmas **11**, 2763 (2004).
15. M. Hohenberger, P. B. Radha, J. F. Myatt, S. LePape, J. A. Marozas, F. J. Marshall, D. T. Michel, S. P. Regan, W. Seka, A. Shvydky, T. C. Sangster, J. W. Bates, R. Betti, T. R. Boehly, M. J. Bonino, D. T. Casey, T. J. B. Collins, R. S. Craxton, J. A. Delettrez, D. H. Edgell, R. Epstein, G. Fiksel, P. Fitzsimmons, J. A. Frenje, D. H. Froula, V. N. Goncharov, D. R. Harding, D. H. Kalantar, M. Karasik, T. J. Kessler, J. D. Kilkenny, J. P. Knauer, C. Kurz, M. Lafon, K. N. LaFortune, B. J. MacGowan, A. J. Mackinnon, A. G. MacPhee, R. L. McCrory, P. W. McKenty, J. F. Meeker, D. D. Meyerhofer, S. R. Nagel, A. Nikroo, S. Obenschain, R. D. Petrasso, J. E. Ralph, H. G. Rinderknecht, M. J. Rosenberg, A. J. Schmitt, R. J. Wallace, J. Weaver, C. Widmayer, S. Skupsky, A. A. Solodov, C. Stoeckl, B. Yaakobi, and J. D. Zuegel, Phys. Plasmas **22**, 056308 (2015).
16. P. B. Radha, J. A. Marozas, F. J. Marshall, A. Shvydky, T. J. B. Collins, V. N. Goncharov, R. L. McCrory, P. W. McKenty, D. D. Meyerhofer, T. C. Sangster, and S. Skupsky, Phys. Plasmas **19**, 082704 (2012).
17. P. B. Radha, C. Stoeckl, V. N. Goncharov, J. A. Delettrez, D. H. Edgell, J. A. Frenje, I. V. Igumenshchev, J. P. Knauer, J. A. Marozas, R. L. McCrory, D. D. Meyerhofer, R. D. Petrasso, S. P. Regan, T. C. Sangster, W. Seka, and S. Skupsky, Phys. Plasmas **18**, 012705 (2011).
18. C. D. Zhou and R. Betti, Phys. Plasmas **14**, 072703 (2007).
19. L Divol, Lawrence Livermore National Laboratory, private communication (2012); D. A. Callahan *et al*., J. Phys.: Conf. Ser. **112**, 022021 (2008).
20. J. A. Marozas, S. P. Regan, J. H. Kelly, D. D. Meyerhofer, W. Seka, and S. Skupsky, J. Opt. Soc. Am. B **19**, 7 (2002).

21. V. N. Goncharov, T. C. Sangster, R. Betti, T. R. Boehly, M. J. Bonino, T. J. B. Collins, R. S. Craxton, J. A. Delettrez, D. H. Edgell, R. Epstein, R. K. Follet, C. J. Forrest, D. H. Froula, V. Yu. Glebov, D. R. Harding, R. J. Henchen, S. X. Hu, I. V. Igumenshchev, R. Janezic, J. H. Kelly, T. J. Kessler, T. Z. Kosc, S. J. Loucks, J. A. Marozas, F. J. Marshall, A. V. Maximov, R. L. McCrory, P. W. McKenty, D. D. Meyerhofer, D. T. Michel, J. F. Myatt, R. Nora, P. B. Radha, S. P. Regan, W. Seka, W. T. Shmayda, R. W. Short, A. Shvydky, S. Skupsky, C. Stoeckl, B. Yaakobi, J. A. Frenje, M. Gatu-Johnson, R. D. Petrasso, and D. T. Casey, Phys. Plasmas **21**, 056315 (2014).

22. J. A. Marozas, F. J. Marshall, R. S. Craxton, I. V. Igumenshchev, S. Skupsky, M. J. Bonino, T. J. B. Collins, R. Epstein, V. Yu. Glebov, D. Jacobs-Perkins, J. P. Knauer, R. L. McCrory, P. W. McKenty, D. D. Meyerhofer, S. G. Noyes, P. B. Radha, T. C. Sangster, W. Seka, and V. A. Smalyuk, Phys. Plasmas **13**, 056311 (2006).

23. D. Cao, G. Moses, and J. Delettrez, Phys. Plasmas **22**, 082308 (2015).

24. D. H. Edgell, P. B. Radha, V. N. Goncharov, I. V. Igumenshchev, J. A. Marozas, J. F. Myatt, W. Seka, and D. H. Froula, Bull. Am. Phys. Soc. **57**, 343 (2012).

25. D. E. Bower, T. J. McCarville, S. S. Alvarez, L. E. Ault, M. D. Brown, M. P. Chrisp, C. M. Damian, W. J. DeHope, D. H. Froula, S. H. Glenzer, S. E. Grace, K. Gu, F. R. Holdener, C. K. Huffer, J. H. Kamperschroer, T. M. Kelleher, J. R. Kimbrough, R. Kirkwood, D. W. Kurita, A. P. Lee, F. D. Lee, I. T. Lewis, F. J. Lopez, B. J. MacGowan, M. W. Poole, M. A. Rhodes, M. B. Schneider, N. R. Sewall, F. Y. Shimamoto, S. J. Shiromizu, D. Voloshin, A. L. Warrick, C. R. Wendland, and B. K. Young, Rev. Sci. Instrum. **75**, 4177 (2004); J. D. Moody *et al*., Rev. Sci. Instrum. **81**, 10D921 (2010); P. Datte *et al*., Proc. SPIE **8850**, 885003 (2013).

26. D. T. Michel, C. Sorce, R. Epstein, N. Whiting, I. V. Igumenshchev, R. Jungquist, and D. H. Froula, Rev. Sci. Instrum. **83**, 10E530 (2012).

27. F. J. Marshall, P. W. McKenty, J. A. Delettrez, R. Epstein, J. P. Knauer, V. A. Smalyuk, J. A. Frenje, C. K. Li, R. D. Petrasso, F. H. Séguin, and R. C. Mancini, Phys. Rev. Lett. **102**, 185004 (2009).

28. J. J. MacFarlane *et al*., High Energy Density Phys. **3**, 181 (2007).

29. *LLE Review Quarterly Report* **91**, 116, Laboratory for Laser Energetics, University of Rochester, Rochester, NY, LLE Document No. DOE/SF/19460-458, NTIS Order No. PB2006-106662 (2002). Copies may be obtained from the National Technical Information Service, Springfield, VA 22161.

30. G. Fiksel, S. X. Hu, V. N. Goncharov, D. D. Meyerhofer, T. C. Sangster, V. A. Smalyuk, B. Yaakobi, M. J. Bonino, and R. Jungquist, Phys. Plasmas **19**, 062704 (2012).

31. A. N. Mostovych, D. G. Colombant, M. Karasik, J. P. Knauer, A. J. Schmitt, and J. L. Weaver, Phys. Rev. Lett. **100**, 075002 (2008).

32. R. C. Malone, R. L. McCrory, and R. L. Morse, Phys. Rev. Lett. **34**, 721 (1975); J. Delettrez, Can. J. Phys. **64**, 932 (1986).

33. M. Hohenberger, F. Albert, N. E. Palmer, J. J. Lee, T. Döppner, L. Divol, E. L. Dewald, B. Bachmann, A. G. MacPhee, G. LaCaille, D. K. Bradley, and C. Stoeckl, Rev. Sci. Instrum. **85**, 11D501 (2014).

34. B. Yaakobi, A. A. Solodov, J. F. Myatt, J. A. Delettrez, C. Stoeckl, and D. H. Froula, Phys. Plasmas **20**, 092706 (2013).

35. J. A. Delettrez, T. J. B. Collins, and C. Ye, Bull. Am. Phys. Soc. **59**, 150 (2014).

36. T. J. Murphy, N. S. Krasheninnikova, G. A. Kyrala, P. A. Bradley, J. A. Baumgaertel, J. A. Cobble, P. Hakel, S. C. Hsu, J. L. Kline, D. S. Montgomery, K. A. D. Obrey, R. C. Shah, I. L. Tregillis, M. J. Schmitt, R. J. Kanzleiter, S. H. Batha, R. J. Wallace, S. D. Bhandarkar, P. Fitzsimmons, M. L. Hoppe, A. Nikroo, M. Hohenberger, P. W. McKenty, H. G. Rinderknecht, M. J. Rosenberg, and R. D. Petrasso, Phys. Plasmas **22**, 092707 (2015); N. S. Krasheninnikova *et al*., Phys. Plasmas **21**, 042703 (2014).

37. T. J. Murphy, Los Alamos National Laboratory, private communication (2015).

38. F. Weilacher, P. B. Radha, T. J. B. Collins, and J. A. Marozas, Phys. Plasmas **22**, 032701 (2015); D. Cao, J. A. Marozas, T. J. B. Collins, P. B. Radha, and P. W. McKenty, Bull. Am. Phys. Soc. **60**, 29 (2015).

39. A. R. Christopherson, R. Betti, W. Theobald, and J. Howard, the Ninth International Conference on Inertial Fusion Sciences and Applications (IFSA 2015), Seattle, WA, 20–25 September 2015 (Paper Th.O.2.2).

40. *LLE Review Quarterly Report* **130**, 72, Laboratory for Laser Energetics, University of Rochester, Rochester, NY, LLE Document No. DOE/NA/28302-1058 (2012).

41. *LLE Review Quarterly Report* **79**, 121, Laboratory for Laser Energetics, University of Rochester, Rochester, NY, LLE Document No. DOE/SF/19460-317, NTIS Order No. DE2002762802 (1999). Copies may be obtained from the National Technical Information Service, Springfield, VA 22161.

42. W. Seka, D. H. Edgell, J. F. Myatt, A. V. Maximov, R. W. Short, V. N. Goncharov, and H. A. Baldis, Phys. Plasmas **16**, 052701 (2009).

43. M. Hohenberger, A. Shvydky, P. B. Radha, M. J. Rosenberg, V. N. Goncharov, F. J. Marshall, J. P. Knauer, S. P. Regan, T. C. Sangster, A. Nikroo, and R. J. Wallace, Bull. Am. Phys. Soc. **60**, 164 (2015); A. Shvydky, M. Hohenberger, P. B. Radha, M. J. Rosenberg, R. S. Craxton, V. N. Goncharov, J. A. Marozas, F. J. Marshall, P. W. McKenty, S. P. Regan, and T. C. Sangster, Bull. Am. Phys. Soc. **60**, 118 (2015).

44. J. A. Marozas, T. J. B. Collins, J. D. Zuegel, P. B. Radha, F. J. Marshall, and W. Seka, presented at the 44th Annual Anomalous Absorption Conference, Estes Park, CO, 8–13 June 2014.

45. D. T. Michel, V. N. Goncharov, I. V. Igumenshchev, R. Epstein, and D. H. Froula, Phys. Rev. Lett. **111**, 245005 (2013).

Hydrodynamic Simulations of Long-Scale-Length Plasmas for Two-Plasmon–Decay Planar-Target Experiments at the National Ignition Facility

Introduction

Coronal plasmas of direct-drive–ignition designs with a baseline plastic ablator are characterized by long density scale lengths $L_n \sim 500$ to $600\ \mu$m. Understanding and controlling the impact of laser–plasma interaction (LPI) instabilities in such plasmas are key requirements of inertial confinement fusion (ICF) research. One of the instabilities driven by multiple laser beams that can exceed the instability threshold is two-plasmon decay (TPD).[1–4] In TPD, the overlapping intense laser beams excite large-amplitude electron plasma waves in the region near the quarter-critical density (n_{qc}) surface, leading to extra laser absorption and hot-electron production. The extra absorption at n_{qc} may reduce, however, the laser intensity reaching critical density, thereby decreasing the hydroefficiency. The hot-electron generation from TPD may negatively affect target compression because of the possible preheat of the imploding shell, which must remain on a low adiabat for efficient compression. Other LPI instabilities, such as multibeam stimulated Raman scattering (SRS), can also lead to anomalous laser-energy dissipation before the n_{qc} surface and/or hot-electron generation.

To support direct-drive ICF experiments at the National Ignition Facility (NIF) in its indirect-drive beam configuration, the polar-direct-drive (PDD) concept was proposed.[5] The impact of laser parametric instabilities on the PDD implosions has been recently tested in experiments on the NIF.[6] To investigate the scaling of TPD-induced hot electrons to the laser intensity and plasma conditions, a series of planar experiments has also been conducted at the Omega Laser Facility.[7] The plasma parameters at the n_{qc} surface achieved in those experiments (as predicted by simulations using the code *DRACO*[8]) are summarized in Table 145.II. The coronal plasma parameters in the NIF PDD-ignition design developed at the Laboratory for Laser Energetics[9] are also shown. Table 145.II shows that all parameters in the previous experiments [the overlapped laser intensity (I), density scale length (L_n), and electron temperature (T_e) at the n_{qc} surface] are still ~1.5 to 2× below that in the ignition design. The empirical TPD threshold parameter $\eta = I_{14} L_{n,\mu m} / (230\ T_{e,keV})$, often used to evaluate the effect of TPD,[2,10] is ~2× less than in the ignition design. Importantly, cross-beam energy transfer (CBET) reduces the laser beam energy, reaching the n_{qc} surface in current NIF implosion experiments, so that current implosion experiments do not achieve ignition-relevant coronal plasma conditions.

In this article, hydrodynamic simulations using *DRACO* are presented to show that coronal plasma conditions in the ignition PDD design can be approached in planar-target experiments on the NIF (Table 145.II). Since planar targets exhibit a very high absorption efficiency, CBET seeded by backscattered light represents a negligible source of losses in laser energy. It is speculated that because of the characteristics of the NIF beam overlap on the target, the TPD instability will be able to share decay waves most effectively along the polar axis and around the equatorial region of a PDD implosion. Two planar-target simulations that differ by the NIF beam irradiation geometry are presented: (1) irradiation by the NIF inner-cone beams only (23.5° and 30° incidence angle with respect to target normal) and (2) irradiation by the outer-cone beams (44.5° and 50°). The higher-angle cones approximate irradiation conditions near the equator of a PDD implosion, while the lower-angle cones correspond to those near the poles.

Table 145.II: Plasma parameters at the n_{qc} surface and two-plasmon–decay (TPD) threshold in OMEGA and NIF experiments, ignition NIF PDD design, and planar targets in this article, as predicted by *DRACO* simulations.

Parameters at n_{qc} surface	OMEGA	Current NIF PDD	Ignition NIF PDD	Planar NIF
I (W/cm^2)	$<4 \times 10^{14}$	$<4.5 \times 10^{14}$	8 to 10×10^{14}	6 to 8×10^{14}
L_n (μm)	<350 μm	<350 μm	600 μm	550 to 600 μm
T_e (keV)	<2.5 keV	<3.5 keV	5 keV	3.2 keV
η	<2.4	<2	4.7	4.5 to 5.5

Proposed Experimental Configuration

The planar-target design is shown schematically in Fig. 145.17. The target is an ~5-mm-diam, ~500-μm-thick plastic CH disk. A 30-μm-thick, ~4-mm-diam Mo disk is buried 40 μm behind the target's front surface. The target is oriented in the equatorial plane of the NIF chamber and irradiated by a subset of NIF beams from the south pole. Hot electrons generated by the LPI instability in the coronal plasma flow into the target. Time-resolved K_α line emission and the hard x-ray bremsstrahlung from Mo are used as the main hot-electron diagnostics. The Mo thickness is equal to the range of electrons of a typical energy of ~120 keV. Hot electrons that are not stopped in Mo are slowed down in the back CH, so that electron recirculation is minimal in this experiment. The front CH layer is chosen to be thick enough to avoid a burnthrough to the Mo layer, while sufficiently thin to reduce collisional energy losses of hot electrons on the way toward the Mo. For the proposed target thickness, the laser-induced shock does not reach the back of the target, and the target is not accelerated when the laser pulse is on. The simulations use laser pulses with a 2-ns linear power rise from zero to the maximum value and flattop after that, with a total duration of 5.5 to 7.5 ns.

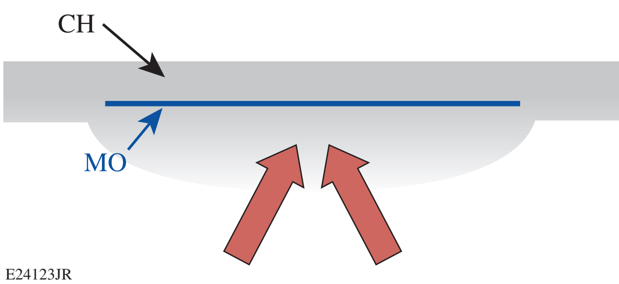

Figure 145.17
The proposed target design.

The measurements can be performed using the NIF x-ray spectrometer[11] to measure the time-resolved Mo K_α emission and the filter-fluorescer x-ray diagnostic[12] to measure the time-resolved hard x-ray emission. NIF optical spectrometers can measure the half-frequency $\left(\omega_L/2\right)$ harmonic of the incident light, which is a characteristic signature of TPD, and SRS spectra.

***DRACO* Simulations**

The simulations were performed using the Eulerian version of *DRACO*[8] in cylindrically symmetric geometry. *DRACO* includes a full three-dimensional (3-D) laser ray trace, a flux-limited heat-conduction model (with a flux limiter f = 0.1), multigroup diffusive radiation transport, and *SESAME* equation of state. For the low-Z plastic CH ablator, the Astrophysics Opacity Table was applied; the average-ion model, which is a collisional-radiative-equilibrium model, was used for the high-Z Mo.

The simulations used the actual measured focal-spot shapes of the indirect-drive NIF beams. The beams are used at best focus and pointed at the averaged-over-time longitudinal position of the n_{qc} surface—320 μm in front of the target surface. The simulations are designed to have similar plasma parameters at the n_{qc} surface, with flattop total powers of 17 TW and 15 TW, durations of 5.5 ns and 7.5 ns in the inner- (32 beams at 23.5° and 30°) and outer-cone beam (64 beams at 44.5° and 50°) simulations, respectively. The duration of the flattop used in the inner-cone beam simulation is chosen to be the longest allowable while still avoiding laser damage on the NIF.

Figure 145.18 presents the electron density and electron temperature in the coronal plasma at t = 4.5 ns in the inner-cone

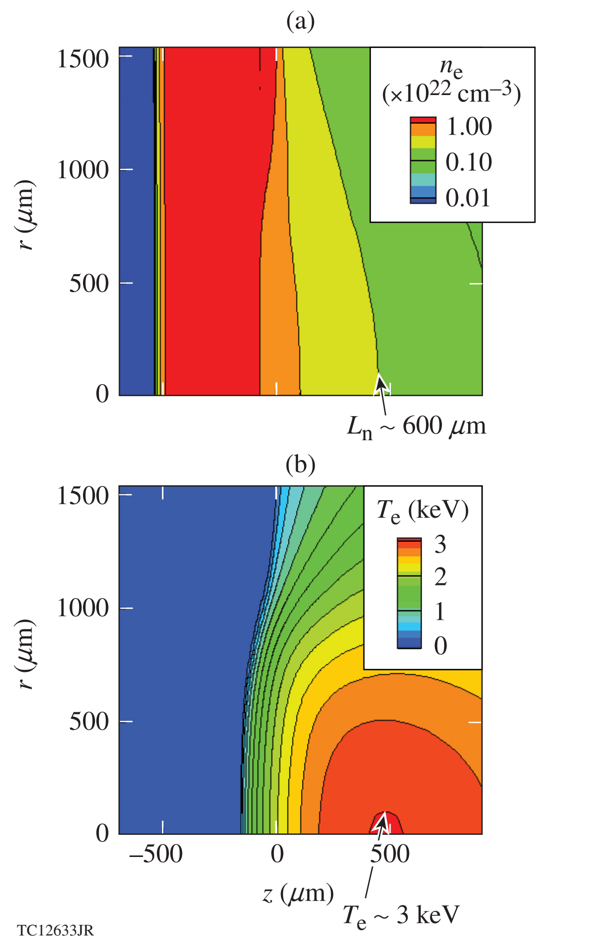

Figure 145.18
The (a) electron density and (b) electron temperature in the coronal plasma at t = 4.5 ns in the inner-cone beam simulation.

beam simulation. The outer-cone beam simulation predicts similar results (with a slightly higher peak temperature of 3.15 keV) and is not shown.

Figure 145.19 shows the time evolution of the plasma parameters at the n_{qc} surface and TPD threshold parameter at $r = 0$ in both simulations. The density scale length and electron temperature are almost stationary at $t > 2.5$ ns with $L_n = 500$ to 600 μm and $T_e \sim 3$ to 3.3 keV. Laser intensity slowly decreases with time, with $I = 5$ to 6.5×10^{14} W/cm^2 in the inner-cone beam and $I = 6$ to 8×10^{14} W/cm^2 in the outer-cone beam simulation. Notably, the empirical TPD threshold is greatly exceeded in these simulations—$\eta \sim 4$ to 5.

Discussion and Conclusions

Overall, a similar evolution of the plasma parameters at the n_{qc} surface is predicted by *DRACO* simulations for the inner- and outer-cone beams. Planar-target experiments on the NIF, therefore, can study the effect of a beam's incidence angle on TPD instability and hot-electron generation. Simulations of TPD using the 3-D laser–plasma interaction code *LPSE*[13] have been performed using the NIF irradiation geometry and plasma parameters at the n_{qc} surface predicted by *DRACO*. *LPSE* models the TPD instability in a small volume of plasma (200 μm × 30 μm × 30 μm) close to the n_{qc} surface. *LPSE* simulations confirm the onset of TPD instability when the TPD threshold (η) exceeds unity in *DRACO* simulations for both irradiation geometries. The mechanisms of saturation of the TPD instability (such as pump depletion) are currently under implementation in *LPSE*. *LPSE* will be used to study hot-electron production and laser absorption at the nonlinear stage of TPD.

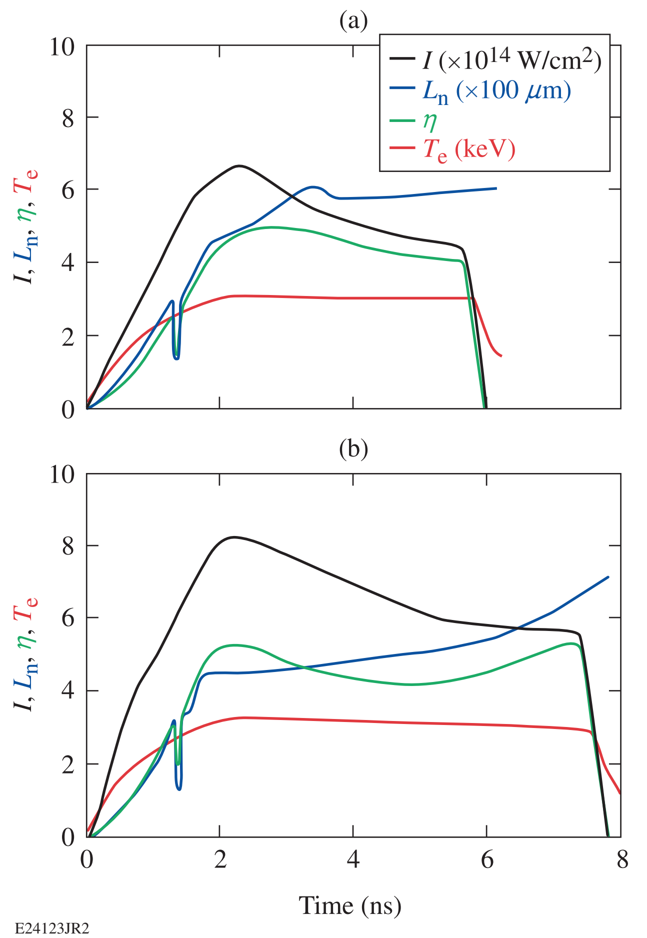

Figure 145.19
Time evolution of the plasma parameters at the n_{qc} surface and TPD threshold parameter at $r = 0$ in the (a) inner- and (b) outer-cone beam simulations.

Table 145.II shows that the plasma parameters at the n_{qc} surface in the present simulations are closer to the PDD-ignition design than in the OMEGA and current NIF PDD implosion experiments, with the exception of the electron temperature. In particular, the plasma density scale length is as long as that in the ignition design. A relatively low temperature is explained by higher transversal thermoconduction losses in planar experiments compared to those in spherical implosions. The laser power can be further increased, provided the optics' damage threshold is not exceeded. This can allow one to study TPD at higher overlapped laser intensity (equal or exceeding that in the ignition design) and electron temperature at the n_{qc} surface. The power can be increased by up to a factor of 2 in the outer-beam configuration. The power can also be increased at the expense of decreased pulse duration in the inner-beam configuration.

In conclusion, hydrodynamic simulations suggest that planar-target experiments on the NIF can be a powerful tool in the study of TPD and other LPI processes in the plasma conditions relevant to the ignition direct-drive designs. While current NIF PDD experiments suffer from CBET, which reduces the laser absorption, planar NIF experiments can provide a first look at the effect of TPD in NIF PDD implosions when CBET has been mitigated. Subsequently, the NIF planar platform can be used to study TPD mitigation strategies by using different ablator materials.

ACKNOWLEDGMENT

This material is based upon work supported by the Department of Energy National Nuclear Security Administration under Award Number DE-NA0001944, the University of Rochester, and the New York State Energy Research and Development Authority. The support of DOE does not constitute an endorsement by DOE of the views expressed in this article.

REFERENCES

1. M. N. Rosenbluth, Phys. Rev. Lett. **29**, 565 (1972).
2. A. Simon, R. W. Short, E. A. Williams, and T. Dewandre, Phys. Fluids **26**, 3107 (1983).
3. D. T. Michel, A. V. Maximov, R. W. Short, S. X. Hu, J. F. Myatt, W.Seka, A. A. Solodov, B. Yaakobi, and D. H. Froula, Phys. Rev. Lett. **109**, 155007 (2012).
4. J. Zhang, J. F. Myatt, R. W. Short, A. V. Maximov, H. X. Vu, D. F. DuBois, and D. A. Russell, Phys. Rev. Lett. **113**, 105001 (2014).
5. S. Skupsky, J. A. Marozas, R. S. Craxton, R. Betti, T. J. B. Collins, J. A. Delettrez, V. N. Goncharov, P. W. McKenty, P. B. Radha, T. R. Boehly, J. P. Knauer, F. J. Marshall, D. R. Harding, J. D. Kilkenny, D.D. Meyerhofer, T. C. Sangster, and R. L. McCrory, Phys. Plasmas **11**, 2763 (2004).
6. M. Hohenberger, P. B. Radha, J. F. Myatt, S. LePape, J. A. Marozas, F. J. Marshall, D. T. Michel, S. P. Regan, W. Seka, A. Shvydky, T. C. Sangster, J. W. Bates, R. Betti, T. R. Boehly, M. J. Bonino, D. T. Casey, T. J. B. Collins, R. S. Craxton, J. A. Delettrez, D. H. Edgell, R. Epstein, G. Fiksel, P. Fitzsimmons, J. A. Frenje, D. H. Froula, V. N. Goncharov, D. R. Harding, D. H. Kalantar, M. Karasik, T. J. Kessler, J. D. Kilkenny, J. P. Knauer, C. Kurz, M. Lafon, K. N. LaFortune, B. J. MacGowan, A. J. Mackinnon, A. G. MacPhee, R. L. McCrory, P. W. McKenty, J. F. Meeker, D. D. Meyerhofer, S. R. Nagel, A. Nikroo, S. Obenschain, R. D. Petrasso, J. E. Ralph, H. G. Rinderknecht, M. J. Rosenberg, A. J. Schmitt, R. J. Wallace, J. Weaver, C. Widmayer, S. Skupsky, A. A. Solodov, C. Stoeckl, B. Yaakobi, and J. D. Zuegel, Phys. Plasmas **22**, 056308 (2015).
7. B. Yaakobi, P.-Y. Chang, A. A. Solodov, C. Stoeckl, D. H. Edgell, R. S. Craxton, S. X. Hu, J. F. Myatt, F. J. Marshall, W. Seka, and D. H. Froula, Phys. Plasmas **19**, 012704 (2012).
8. P. B. Radha, T. J. B. Collins, J. A. Delettrez, Y. Elbaz, R. Epstein, V. Yu. Glebov, V. N. Goncharov, R. L. Keck, J. P. Knauer, J. A. Marozas, F. J. Marshall, R. L. McCrory, P. W. McKenty, D. D. Meyerhofer, S. P. Regan, T. C. Sangster, W. Seka, D. Shvarts, S. Skupsky, Y. Srebro, and C. Stoeckl, Phys. Plasmas **12**, 056307 (2005).
9. T. J. B. Collins, J. A. Marozas, K. S. Anderson, R. Betti, R. S. Craxton, J. A. Delettrez, V. N. Goncharov, D. R. Harding, F. J. Marshall, R. L. McCrory, D. D. Meyerhofer, P. W. McKenty, P. B. Radha, A. Shvydky, S. Skupsky, and J. D. Zuegel, Phys. Plasmas **19**, 056308 (2012).
10. W. Seka, D. H. Edgell, J. F. Myatt, A. V. Maximov, R. W. Short, V. N. Goncharov, and H. A. Baldis, Phys. Plasmas **16**, 052701 (2009).
11. S. P. Regan, K. B. Fournier, M. J. Bedzyk, A. Agliata, S. L. Ayers, M. A. Barrios, P. M. Bell, D. K. Bradley, H. Chen, J. A. Emig, R. K. Jungquist, G. E. Kemp, J. D. Kilkenny, D. D. Meyerhofer, F. Perez, J. Pino, T. C. Sangster, and M. J. Shoup III, SPIE Optics and Photonics 2014, San Diego, CA, 17–21 August 2014 (Paper 9211-15).
12. M. Hohenberger, F. Albert, N. E. Palmer, J. J. Lee, T. Döppner, L. Divol, E. L. Dewald, B. Bachmann, A. G. MacPhee, G. LaCaille, D. K. Bradley, and C. Stoeckl, Rev. Sci. Instrum. **85**, 11D501 (2014).
13. J. F. Myatt, J. G. Shaw, V. N. Goncharov, J. Zhang, A. V. Maximov, R. W. Short, R. K. Follett, W. Seka, D. H. Edgell, and D. H. Froula, "Laser–Plasma Interaction in Direct-Drive Inertial Confinement Fusion," submitted to the Journal of Physics: Conference Series.

First-Principles Investigations on Ionization and Thermal Conductivity of Polystyrene (CH) for Inertial Confinement Fusion Applications

Introduction

Controlled inertial confinement fusion (ICF) has been pursued in laboratories for decades, in both indirect-drive[1–3] and direct-drive[4–6] schemes. A typical ICF target consists of layered solid deuterium–tritium (DT) covered with an ablator layer.[7] The ablator layer is used to convert the laser and/or x-ray energy to the kinetic energy of the imploding shell (besides compressing it) by the rocket effect through the ablation process. Polystyrene (CH) is often chosen as the ablator material[7] since it is inexpensive and easy to make. Upon x-ray or laser ablation, the CH ablator can be shocked to pressures up to tens of Mbars. The target convergence can further bring the CH-layer pressure to Gbars, or even hundreds of Gbars at peak compression. Besides ICF applications, CH is also often used as an effective ablator for high-energy-density–physics (HEDP) experiments.[8–10] The properties of CH plasmas under such high-energy-density conditions are essential for understanding ICF and HEDP experiments involving CH ablators.

Because of its importance to ICF, the plasma properties of polystyrene have been extensively studied in both experiment and theory. For example, the principal Hugoniot of CH has been measured using gas-gun experiments[11] and laser/x-ray–launched shocks.[12–16] The measured pressures, temperatures, and reflectivity of shocked CH compare well with state-of-the-art calculations using first-principles methods[17–19] along the principal Hugoniot. The original *SESAME* model (Table 7593 for CH) gave a reasonable Hugoniot in the pressure range that experiments explored, while it overestimated the Hugoniot temperatures.[18,19] Off the principal Hugoniot, we calculated the equations of state over a wide range of CH-plasma conditions and constructed a first-principles equation-of-state (FPEOS) table of CH for ICF applications. The FPEOS of CH has shown significant differences for warm-dense-plasma conditions[19] when compared to the original *SESAME* model. Its effect on ICF implosions has been examined in hydrodynamic simulations: a smaller mass ablation rate was predicted with the CH FPEOS. This prompts us to consider other plasma properties such as ionization and thermal conductivity that can be self-consistently extracted from such first-principles calculations for ICF and HEDP applications.

Thermal conductivity (κ) is an important plasma property that is needed in ICF simulations because it determines the heat transport in ICF plasmas and affects the hydrodynamic instability growth in ICF implosions.[20] In traditional ICF simulations, plasma-physics models of thermal conductivity were adopted in hydrocodes. For example, the Spitzer model[21] has been extensively used for classical plasmas. However, such an analytical model breaks down in warm-dense-plasma conditions since the Spitzer Coulomb logarithm becomes negative for low-temperature and high-density plasmas. To overcome this difficulty of computing κ for warm dense plasmas, the Lee–More model[22] was developed in the 1980s with the first-order approximation to the Boltzmann equation. The Purgatorio model[23] and the SCAALP model,[24] developed about a decade ago, are both based on the average atom model. In the past, quantum-molecular dynamics (QMD) calculations of κ have been performed for ICF-relevant materials of deuterium[25–29] and CH/CH_2 (Refs. 30–32). These first-principles calculations have indicated a larger κ for warm dense D_2 and CH plasmas than the predictions of the Lee–More model that was widely adopted in hydrocodes for ICF simulations. These QMD calculations, however, have been performed for only a few specific density−temperature conditions of CH plasmas. To test whether or not such an enhanced κ of CH will affect ICF simulations, one must extend such QMD calculations to a wide range of plasma conditions, similar to the deuterium case in Ref. 29. In this article, we report on such an endeavor to "gauge" the global behavior of CH thermal conductivity from direct QMD calculations of κ for a wide range of CH plasma conditions. The obtained analytical form of κ, fitted with the generalized QMD Coulomb logarithm, has then been used in hydrodynamic simulations to explore its effect in ICF implosions. Our results show that the κ_{QMD} simulations give an ~20% variation in neutron yield and peak hot-spot pressure when compared to the use of the traditional Lee–More model.

A brief description of the QMD method is presented that combines the orbital-based Kohn–Sham molecular dynamics (KSMD) method with the orbital-free molecular dynamics (OFMD). Since all physics models of the thermal conductivity invoked the use of an effective ionic charge in single-fluid ICF simulations, we first present the OFMD calculations of the average ionization $\left(\langle Z\rangle \text{ and } \langle Z^2\rangle\right)$ of CH over a wide range of plasma densities and temperatures. The obtained $\langle Z\rangle$ and $\langle Z^2\rangle$ are then fitted with a Saha-type model, while the KSMD-derived thermal conductivities of CH are compared with the Lee–More model and fitted with the generalized Coulomb logarithm [$(\ln\Lambda)_{\text{QMD}}$]. The κ_{QMD} effects on ICF implosions for both OMEGA and National Ignition Facility (NIF) targets are presented, followed by the conclusions.

The Quantum-Molecular Dynamics Method

The QMD method is an effective first-principles method for simulating warm dense plasmas,[33–36] where quantum mechanics is used to describe the dynamics of electrons in combination with classical molecular dynamics for the ion motion. To make the quantum-mechanical computations of a many-electron system feasible, the traditional QMD method is based on the density functional theory (DFT).[37–39] Depending on the choice of DFT implementation, the QMD method can be either orbital based or orbital free. For instance, the KSMD method uses the plane-wave basis in a finite-temperature DFT format, which has been implemented in the Vienna *ab-initio* simulation package (VASP),[40–42] while the OFMD method[43] represents the electronic free energy as a direct function of the electronic density through a semiclassical expansion of the Mermin functional. The KSMD method can handle dense plasmas, but only up to the Fermi temperature; the large number of basis functions needed for high-T plasmas renders KSMD as computationally impractical. In contrast, the OFMD method is suitable for high-T plasma simulations. Combining the two first-principles methods of KSMD and OFMD, we are able to simulate a wide range of plasma conditions. Since both methods have been documented elsewhere, only a brief description follows.

1. KSMD

The KSMD method implemented in VASP is based on the finite-temperature density functional theory (FTDFT). To be specific, the electrons are treated quantum-mechanically by plane-wave FTDFT calculations using the Perdew–Burke–Ernzerhof exchange-correlation functional[44] in the generalized gradient approximation. The electron–ion interaction is modeled by a projector-augmented wave (PAW) pseudopotential. The system was assumed to be in local thermodynamical equilibrium with equal electron and ion temperatures ($T_e = T_i$). The ion temperature was kept constant through simple velocity scaling during a molecular-dynamics simulation.

A periodically replicated cubic cell is used with equal numbers of C and H atoms. The plasma density and the number of atoms determine the volume of the cell. For the present simulations of densities below $\rho = 17.5$ g/cm^3, we have employed 250 atoms in total, while a total of 432 atoms were used for densities of $\rho \geq 25$ g/cm^3. For each molecular-dynamics (MD) step, a set of electronic-state functions for each k point is self-consistently determined for an ionic configuration. Under the Born–Oppenheimer approximation, the ions are moved classically with a velocity Verlet algorithm, according to the combined ionic and electronic forces. Repeating the two steps propagates the system in time, resulting in a set of self-consistent ion configurations and electronic-state functions. These trajectories provide a consistent set of static, dynamic, and optical properties of the simulated CH plasmas.

The Γ-point sampling of the first Brillion zone in the cubic cell was employed and tested with a $2 \times 2 \times 2$ Monkhorst–Pack k-point grid. It was found that the resulting thermal conductivity varies <5%. To converge the plasma property calculations, the plane-wave cutoff energy was set to $E_{\max} = 1000$ eV and the PAW potentials were adopted with tight cores (core radii of 1.1 and 0.8 atomic units for C and H, respectively). A large number of energy bands (up to $N_b = 11{,}000$) have been included to ensure that the population of the highest energy band is $<10^{-4}$. For the lowest temperature, 500 bands and a time step of $\Delta t = 0.5$ fs were used, while at the highest temperature, a larger number of bands (11,000) and a small time step of $\Delta t = 0.011$ fs were used.

To calculate the electronic thermal conductivity of CH plasmas, the linear response of the plasma to an electric field $\mathbf{E}$ and a temperature gradient ∇T are considered, which induce the electric current $\mathbf{j}_e$ and the heat flux $\mathbf{j}_q$:

$$\mathbf{j}_e = \left(eL_{11}\mathbf{E} - \frac{L_{12}\nabla T}{T}\right)\Big/ e\,, \tag{1}$$

$$\mathbf{j}_q = \left(eL_{21}\mathbf{E} - \frac{L_{22}\nabla T}{T}\right)\Big/ e\,. \tag{2}$$

For plasmas having no electric current ($\mathbf{j}_e = 0$), the above equations in combination with the definition of $\mathbf{j}_q = -\kappa\nabla T$ give the thermal conductivity

$$\kappa = \frac{1}{T}\left(L_{22} - \frac{L_{12}^2}{L_{11}}\right) \tag{3}$$

with the Onsager coefficients given by $L_{ij} \equiv L_{ij}(0)$. The frequency-dependent Onsager coefficients can be calculated using the Kubo–Greenwood formalism[45,46]

$$L_{ij}(\omega) = \sum_{mn} \frac{2\pi(-e)^{4-i-j}}{3Vm_e^2\omega} \mathrm{F}_{mn} |D_{mn}|^2$$

$$\times \left(\frac{E_m + E_n}{2} - \mathrm{H}\right)^{i+j-2} \delta(E_m - E_n - \hbar\omega), \tag{4}$$

where V is the atomic volume, E_m (E_n) is the energy of the mth (nth) state, and H is the enthalpy (per atom) of the system. F_{mn} is the difference between the Fermi–Dirac distributions for the involved states m and n at temperature T. The velocity matrix elements D_{mn} can be evaluated from the VASP wave functions. In practical calculations, the δ function in Eq. (4) is approximated by a Gaussian function of width ΔE ($\simeq$0.1 to 0.5 eV). The resulting κ was averaged over at least five snapshots of uncorrelated configurations along the MD trajectories. The convergence of κ required a much larger number of energy bands (~2 to 3×) than for the MD simulation.

2. OFMD

The development of OFMD has been documented elsewhere.[43] In the OFMD method, the free energy is approximated by a direct function of the electronic density through a semiclassical expansion of the Mermin functional. The leading- and next-to-leading-order expansions, in terms of the Planck constant h, give the well-known finite-temperature Thomas–Fermi model. To preserve the electronic density beyond the cutoff radius, the OFMD method has introduced a norm-conserving regularization by imposing an analytical form to the electronic density within the cutoff volume. The local-density approximation (LDA) has been used for the electron exchange correlation functional in our OFMD simulations. The time steps used in these calculations vary from 2.4×10^{-2} fs to 4.8×10^{-3} fs, depending on the density and temperature of the CH plasma. The pressures calculated from both KSMD and OFMD methods at the temperature "boundary" of $T \simeq T_F$ are matched well (within <1%).

Since the OFMD method is not based on the plane-wave orbital expansion, it does not give wave functions as in KSMD; therefore, the transport properties of plasmas at high temperatures cannot be extracted directly from the current OFMD simulations. The OFMD method is used to calculate the static plasma properties such as pressure and internal energy. The OFMD simulations can be used to estimate the average ionization in CH plasmas. It is noted that all electrons (core and valence) are considered in the OFMD method. Although there is no operator for ionization in a quantum many-body system, the concept of average ionization $(\langle Z\rangle$ and $\langle Z^2\rangle)$ is extensively adopted in plasma physics models. To fit our KSMD-calculated thermal-conductivity results with a generalized Coulomb logarithm for its use in hydrocodes, we must apply the OFMD calculations to obtain $\langle Z\rangle$ and $\langle Z^2\rangle$ for a wide range of plasma conditions.

The OFMD calculations give the total pressure of CH plasmas. As described in previous references,[30,47] one can use the orbital-free average atom model in conjunction with the pressure-matching mixing rule to calculate the average charge states for C and H atoms, respectively. For the case of LDA exchange correlation, the pressure matching is equivalent to equalizing the free-electron density of C and H atoms. Once the effective charge states Z_C and Z_H are obtained, the average ionization quantities of $\langle Z\rangle$ and $\langle Z^2\rangle$ of CH plasmas can be computed as follows (as defined in our hydrocodes):

$$\langle Z\rangle = (Z_C + Z_H)/2, \tag{5}$$

$$\langle Z^2\rangle = (Z_C^2 + Z_H^2)/2, \tag{6}$$

for an equal mixture of C and H atoms. The effective charge extensively used in hydrocodes is $Z_{\text{eff}} = \langle Z^2\rangle/\langle Z\rangle$.

Results and Discussions

1. The Average Ionization $\langle Z\rangle$ and $\langle Z^2\rangle$ of CH

As described above, the OFMD method was used to estimate the average ionization of $\langle Z\rangle$ and $\langle Z^2\rangle$ for CH plasmas of densities varying from $\rho = 0.01$ g/cm^3 to $\rho = 100$ g/cm^3 and temperatures of $T \simeq 10.8$ to 344.7 eV. As an example, Fig. 145.20 shows the comparison of $\langle Z\rangle$ as a function of CH density between the OFMD prediction and the Astrophysics Opacity Table (AOT)[48] for two plasma temperatures of $T \simeq 10.8$ eV and $T \simeq 86.2$ eV. It is noted that the AOT model, usually patched with cold opacity in the warm-dense-plasma regime, is currently adopted in our hydrocodes for ICF simulations.[49] Figure 145.20 shows that at relatively low densities ($\rho < 1$ g/cm^3), the AOT model gives similar values of $\langle Z\rangle$ as the OFMD calculation for both temperatures, while significant differences are seen for higher densities at both temperatures. For instance, at $T \simeq 86.2$ eV

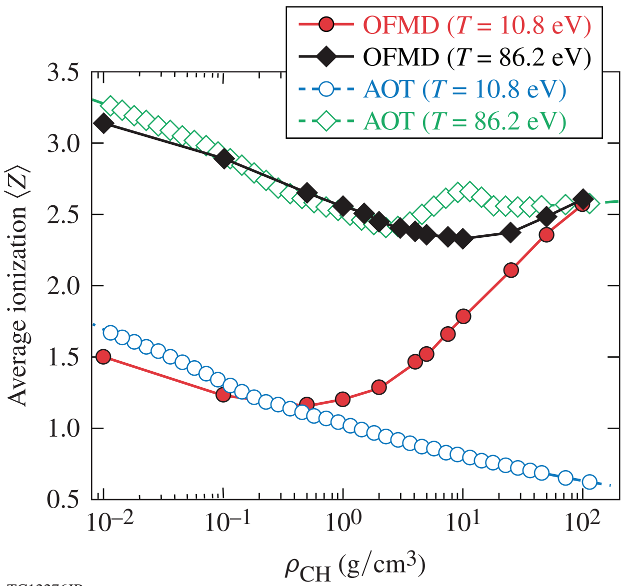

Figure 145.20
The orbital-free molecular dynamics (OFMD)–predicted average ionization $\langle Z\rangle$ as a function of CH density for two plasma temperatures of $T \simeq 10.8$ eV and $T \simeq 86.2$ eV, which are compared with the model predictions (open symbols) by the Astrophysics Opacity Table (AOT) currently used in our hydrocodes.

there are discrepancies in $\langle Z\rangle$ between AOT and OFMD for densities around ρ = 10 g/cm^3. Drastic differences are found for the case of a lower temperature at $T \simeq 10.8$ eV: the cold-opacity–patched AOT model does not give the correct behavior of pressure ionization when the CH density increases, which is in contrast to the OFMD prediction. Since low-temperature CH plasma conditions ($T \le 10$ eV) are often encountered in ICF implosions,[19] it is important that the correct $\langle Z\rangle$ be used for the thermal conductivity models in hydrocodes.

As discussed above, the average ionization of CH plasmas was calculated over a wide range of densities for four different temperatures of $T \simeq 10.8$ eV, 21.6 eV, 86.2 eV, and 344.7 eV. The resulting $\langle Z\rangle$ and $\langle Z^2\rangle$ are plotted in Figs. 145.21 and 145.22 as open symbols. To use these average-ionization quantities in hydrocodes for ICF simulations, a "Saha-type" ionization model for CH plasmas was derived in which the average-ionization fraction ξ is defined as

$$\frac{\xi^2}{1-\xi} = \frac{\alpha_0}{n_i \Lambda_e^3} \exp\left[-\frac{f_Z(\rho,T)}{kT}\right], \qquad (7)$$

where the ion density is defined as $n_i = \rho / A_{CH}$, the electron's thermal de Brogile wavelength is $\Lambda_e = h / \sqrt{2\pi m_e kT}$, with the

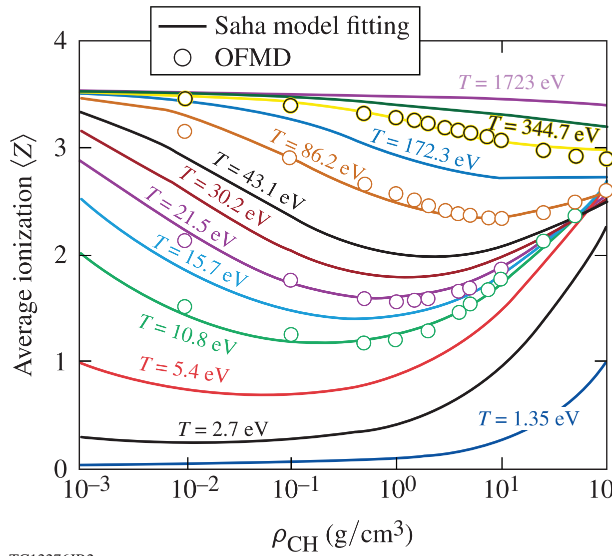

Figure 145.21
The OFMD-predicted average ionization $\langle Z\rangle$ as a function of CH density for plasma temperatures varying from $T \simeq 10.8$ eV to $T \simeq 344.7$ eV, which are fitted with the "Saha-type" ionization model described by Eq. (7).

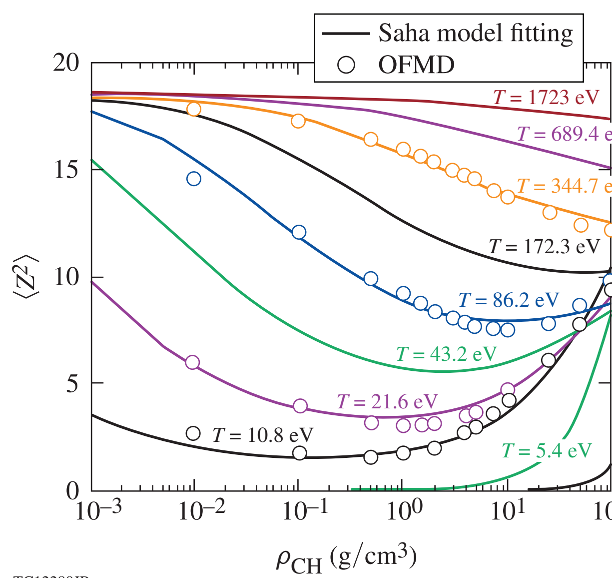

Figure 145.22
The OFMD-predicted average ionization square $\langle Z^2\rangle$ as a function of CH density for plasma temperatures varying from $T \simeq 10.8$ eV to $T \simeq 344.7$ eV, which are fitted with the Saha-type ionization model described by Eq. (9).

Planck constant h and the electron mass m_e, and the density/temperature–dependent average-ionization potential has the following form (kT in eV):

$$f_Z(\rho,T) = \alpha_1 + \alpha_2 \times kT \times \left[\left(1+\sqrt{3\Gamma_0}\right)^{1/4} - 1\right] + \alpha_3 \times (kT)^{0.9} + kT \times \left(\frac{\alpha_4}{r_0} + \frac{\alpha_5}{r_0^2} + \frac{\alpha_6}{r_0^3}\right) \quad (8)$$

with seven fitting parameters α_i. In Eq. (8), the second term accounts for the continuum lowering in the plasma similar to the Stewart–Pyatt form,[50] while the last term is for the pressure ionization. In Eq. (8), the ion–ion interdistance r_0 in terms of the Bohr radius α_B is defined as $n_i = \rho/A_{CH}$ and $r_0 = (1/\alpha_B)(3/4\pi n_i)^{1/3}$ with the ion density n_i. The average atomic weight $A_{CH} = (A_C + A_H)/2$ is used for CH. The quantity Γ_0 is proportional to the ion–ion coupling parameter, i.e., $\Gamma_0 = 1/r_0 kT$. Finally, the average ionization is expressed as $\langle Z \rangle = Z_{max} \times \xi$ with the maximum ionization of $Z_{max} = 3.5$ for the equal mixture of C and H. Performing a least-square fitting to the OFMD data with the above Saha model, we determined the following fitting parameters: $\alpha_0 = 87.222$, $\alpha_1 = 10.866$, $\alpha_2 = -28.412$, $\alpha_3 = 17.915$, $\alpha_4 = -2.422$, $\alpha_5 = 0.595$, and $\alpha_6 = -2.369 \times 10^{-2}$. The fitting is shown by lines in Fig. 145.21 for different temperatures varying from $T \simeq 1.35$ eV to $T \simeq 1723$ eV.

For the average ionization square $\langle Z^2 \rangle$, we adopted a similar model to fit the OFMD data, $\langle Z^2 \rangle = Z_{max}^2 \times \zeta$ with $Z_{max}^2 = 18.5$ for CH, and ζ is determined as

$$\frac{\zeta^2}{1-\zeta} = \frac{\beta_0}{n_i \Lambda_e^3} \exp\left[-\frac{f_{Z^2}(\rho,T)}{kT}\right] \quad (9)$$

with a different fitting function

$$f_{Z^2}(\rho,T) = \beta_1 + \beta_2 \times kT \times \left[\left(1+\sqrt{3\Gamma_0}\right)^{2/5} - 1\right] + \beta_3 \times (kT)^{3/4} + kT \times \left(\frac{\beta_4}{\sqrt{r_0}} + \frac{\beta_5}{r_0} + \frac{\beta_6}{r_0^{3/2}} + \frac{\beta_7}{r_0^2}\right). \quad (10)$$

The best fit to the OFMD results yielded the following parameters: $\beta_0 = 2.055 \times 10^{-3}$, $\beta_1 = 27.851$, $\beta_2 = -5.087$, $\beta_3 = 6.018$, $\beta_4 = -7.908$, $\beta_5 = 4.421$, $\beta_6 = -2.893$, and $\beta_7 = 0.961$. The model fitting of $\langle Z^2 \rangle$ is illustrated in Fig. 145.22 by colored lines, which all compared well with the OFMD results. With a fit for both $\langle Z \rangle$ and $\langle Z^2 \rangle$, we can now derive the effective charge of CH plasmas by $Z_{eff} = \langle Z^2 \rangle / \langle Z \rangle$ over a wide range of plasma conditions.

2. Thermal Conductivity κ_{QMD} of CH

Using the KSMD calculations with Eq. (3), we have calculated the thermal conductivity of CH plasmas for densities ranging from $\rho = 0.5$ g/cm^3 to $\rho = 100$ g/cm^3. For each density point, the κ_{QMD} calculations have been performed to the highest temperature approaching $T \simeq T_F$ $\left[\text{the Fermi temperature } T_F = \hbar^2/2mk \times \left(3\pi^2 n_e\right)^{2/3}\right]$. To test the effects of κ_{QMD} on ICF implosions, these results must be fitted in an analytical form. Similar to what we did for the deuterium case,[29] the following function is used for the fitting (in a similar format of κ_{LILAC} currently used in our hydrocode *LILAC*):[51]

$$\kappa_{QMD} = \frac{20 \times (2/\pi)^{3/2} k^{7/2} T^{5/2}}{\sqrt{m_e}\, e^4 Z_{eff}} \times \frac{0.095 \times (Z_{eff} + 0.24)}{1 + 0.24\, Z_{eff}} \times \frac{1}{(\ln\Lambda)_{QMD}}, \quad (11)$$

with the same Spitzer prefactor as used in κ_{LILAC}. Z_{eff} is the effective charge of CH plasmas that was determined in **The Average Ionization $\langle Z \rangle$ and $\langle Z^2 \rangle$ of CH**, p. 21. The generalized QMD Coulomb logarithm is a sixth-order polynomial function of ion–ion coupling and electron degeneracy parameters (Γ_i, θ_e), which has the following form:

$$(\ln\Lambda)_{QMD} = \exp\left\{\gamma_0 + \sum_{j=1}^{6}\left[\gamma_j (\ln\Gamma_i)^j + \sigma_j (\ln\theta_e)^j\right]\right\}, \quad (12)$$

with $\Gamma_i = \langle Z^2 \rangle e^2 / r_S kT$ and $\theta_e = T/T_F$, in which the Wigner–Seitz radius is defined as $r_S = r_0 \times \alpha_B$ and the free-electron density of $n_e = n_i \times \langle Z \rangle$. Using a multivariable least-square fitting to the κ_{QMD} data, we can determine the parameters γ_j and σ_j. To smoothly merge the κ_{QMD} results to the classical ideal plasma conditions ($\Gamma_i \ll 1$ and $\theta_e \gg 1$), we have added high-temperature κ_{LILAC} points into the dataset for the global fitting. The resulting fitting parameters are $\gamma_0 = -0.482$, $\gamma_1 = -0.150$ or $+0.275$, $\gamma_2 = +0.193$, $\gamma_3 = +8.364 \times 10^{-3}$, $\gamma_4 = -5.287 \times 10^{-3}$, $\gamma_5 = -3.191 \times 10^{-4}$, $\gamma_6 = +2.666 \times 10^{-5}$, $\sigma_1 = +1.00$ or $+1.20$, $\sigma_2 = -0.225$, $\sigma_3 = -4.652 \times 10^{-3}$, $\sigma_4 = +3.805 \times 10^{-3}$, $\sigma_5 = -7.643 \times 10^{-5}$, and $\sigma_6 = -1.391 \times 10^{-5}$. The choice for the two values of γ_1 and σ_1, either (γ_1, σ_1) = (−0.15,1.0) or (γ_1, σ_1) = (0.275,1.2), is to minimize the Coulomb logarithm for a better fit to the QMD results. The fitting results of $(\ln\Lambda)_{QMD}$ are plotted in Figs. 145.23(a) and 145.23(b) as functions of ln (Γ_i) and ln (θ_e), respectively. Overall, the global fitting with the above parameters gives only a small error of 5% or less.

Figures 145.24 and 145.25 compare the QMD-based thermal conductivities of CH plasmas with other models. The "hybrid" Lee–More model (κ_{LILAC}), which combined the Spitzer prefactor with the Lee–More Coulomb logarithm, is currently adopted in our hydrocode *LILAC*. The two others are the Ichimaru model[52] for dense plasmas and the Hubbard model[53] for fully degenerate electron gases. Figure 145.24 compares κ_{QMD} with the different model predictions as a function of plasma temperature for CH densities of $\rho = 1.05$ g/cm^3 (solid density) and $\rho = 4.0$ g/cm^3 (shocked CH). It is seen that κ_{QMD} is generally larger than κ_{LILAC} by a factor of ~2 to 10 at $T < 20$ eV. As indicated in Fig. 145.24(b), the Hubbard model gives reasonably good results in the low-T regime, where the electron degeneracy effect dominates transport behavior, while the Ichimaru model gives the correct trend for plasma temperatures approaching T_{F} and above. As seen in Fig. 145.23,

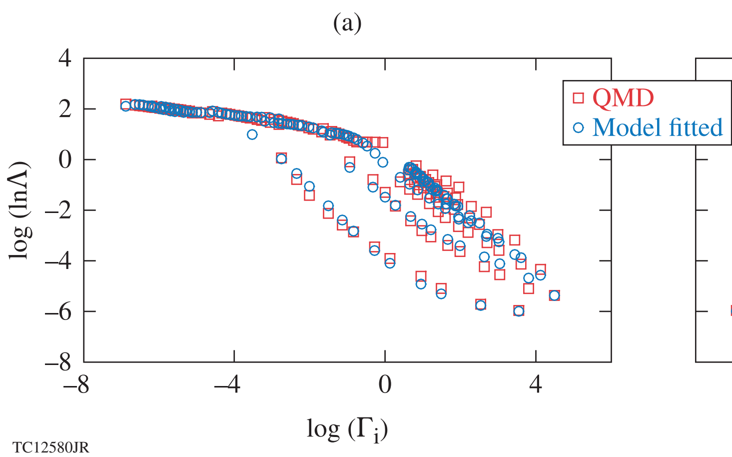

Figure 145.23
The generalized Coulomb logarithm, derived from QMD calculations of thermal conductivity, is fitted with a polynomial function of (a) the ion–ion coupling parameter (Γ_{i}) and (b) the electron degeneracy parameter (θ_{e}) of CH plasmas [Eq. (12)].

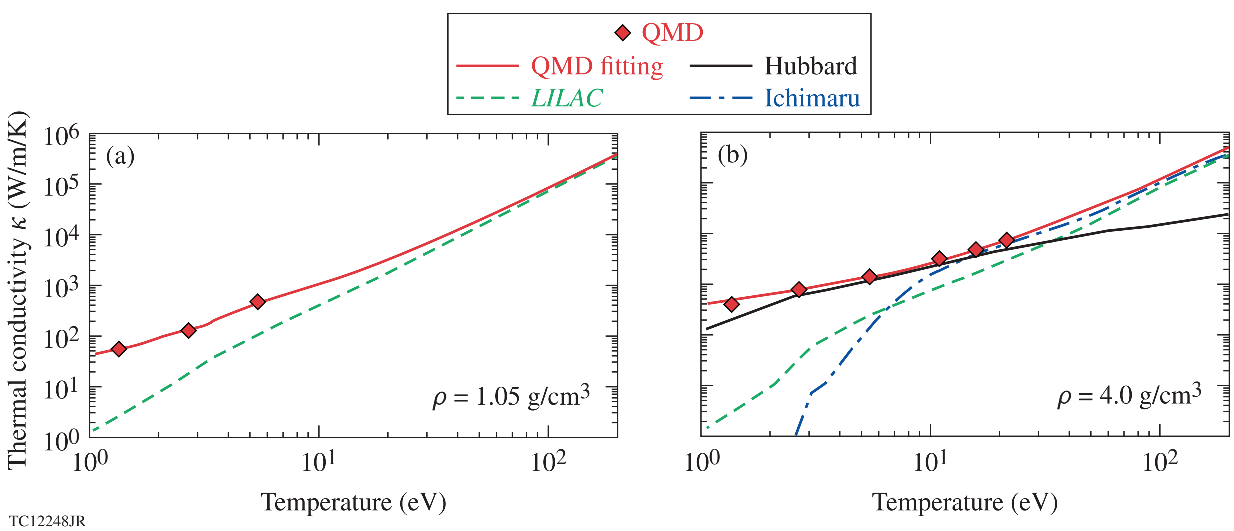

Figure 145.24
Comparison of thermal conductivities of CH plasmas as functions of temperature between QMD calculations and different thermal-conductivity models, for CH densities of (a) $\rho = 1.05$ g/cm^3 and (b) $\rho = 4.0$ g/cm^3. The hybrid *LILAC* model (green dashed lines) used in our hydrocodes adopted the Lee–More model for the Coulomb logarithm with a Spitzer prefactor. The Hubbard model was based on fully degenerate electron gas, while the Ichimaru model considered microfield corrections in dense plasmas.

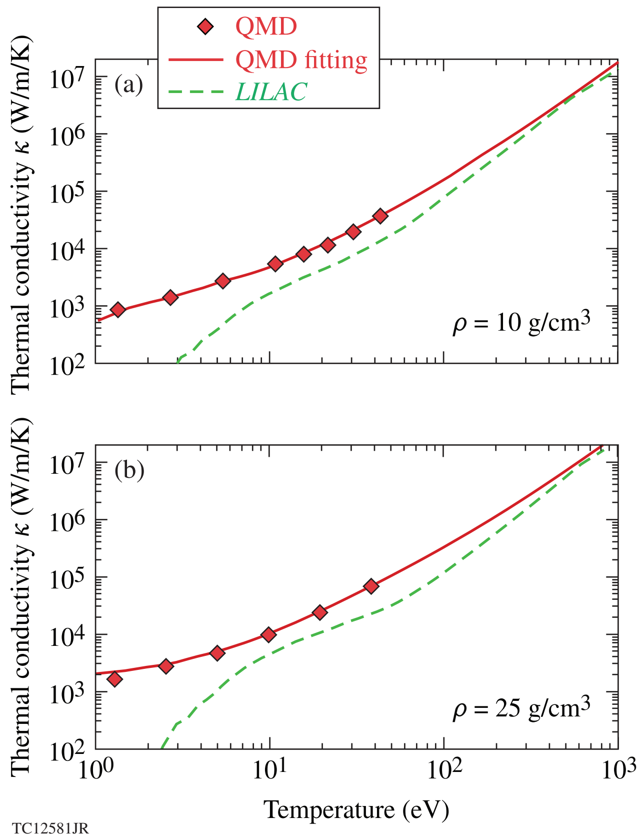

Figure 145.25
Similar to Fig. 145.24 but for CH densities of (a) ρ = 10 g/cm^3 and (b) ρ = 25 g/cm^3.

strongly coupled and degenerate plasmas ($\Gamma_i > 1$ and $\theta_e < 1$) lead to a smaller effective Coulomb logarithm that characterizes the electron collisions in plasmas, while the Lee–More model usually sets a minimum floor of $(\ln\Lambda)_{min} = 2$. The decrease in $(\ln\Lambda)_{QMD}$ means a larger mean free path for electrons, thereby leading to higher thermal conductivity in QMD calculations that account for coupling and degeneracy effects in warm dense CH plasmas. Figures 145.25(a) and 145.25(b) show similar comparisons for higher CH densities at ρ = 10 g/cm^3 and ρ = 25 g/cm^3, respectively. Overall, it is seen that our current hybrid Lee–More model (κ_{LILAC}) underestimates the electronic thermal conductivity when compared with κ_{QMD} in the warm dense plasma regime. The enhancement of κ in the warm dense CH plasmas may have implications in ICF simulations.

The Effect of κ_{QMD} on ICF Simulations

With the implementation of both Z_{eff} and κ_{QMD} into the hydrocode *LILAC* through the fitting formulas discussed above, their effects on ICF simulations may be examined. We first simulate a typical cryogenic DT implosion on OMEGA. Figure 145.26 shows the triple-picket laser pulse used for the implosion, while the inset illustrates the target dimensions. The cryogenic DT target on OMEGA has a 40-μm-thick DT ice layer covered by a 7.5-μm-thick deuterated-plastic (CD) ablator. The total target radius is ~432.5 μm. In the simulations a density scaling to obtain κ_{QMD} for CD from the above-derived κ_{QMD} for CH is used. The triple-picket pulse shape has been used extensively for implosions on OMEGA,[54–56] which enables one to better control shock timing.[57,58]

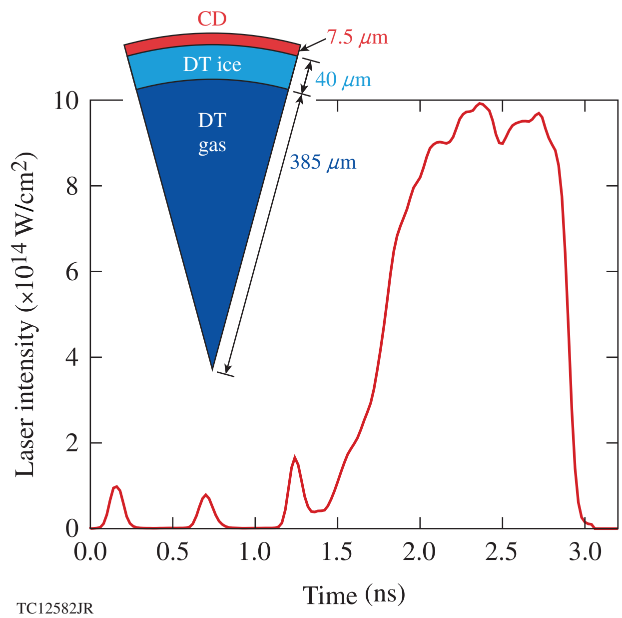

Figure 145.26
The pulse shape and target dimension for a typical cryogenic DT target implosion on OMEGA.

The 1-D *LILAC* hydro simulation results are displayed in Fig. 145.27. Figure 145.27(a) compares density profiles between the κ_{QMD} simulation and the traditional κ_{LILAC} simulation at the end of the laser pulse (t = 2.96 ns). At this time the thin CD layer has been ablated away from the shell. The density of the imploding DT shell is plotted as a function of target radius. One sees that the κ_{QMD} simulation (solid red line) predicts the DT shell being behind the κ_{LILAC} case (DT shell is moving inward); the κ_{QMD} simulation also gives a slightly lower density than the κ_{LILAC} simulation. In the two simulations, we have kept all inputs the same except for the different thermal-conductivity model. Namely, we have employed the FPEOS for both CH[19] and DT,[59] the first-principles opacity table for DT,[49] and a flux-limiter model for thermal transport. The larger value of κ_{QMD} causes more heat to flow into the high-density CD layer, while

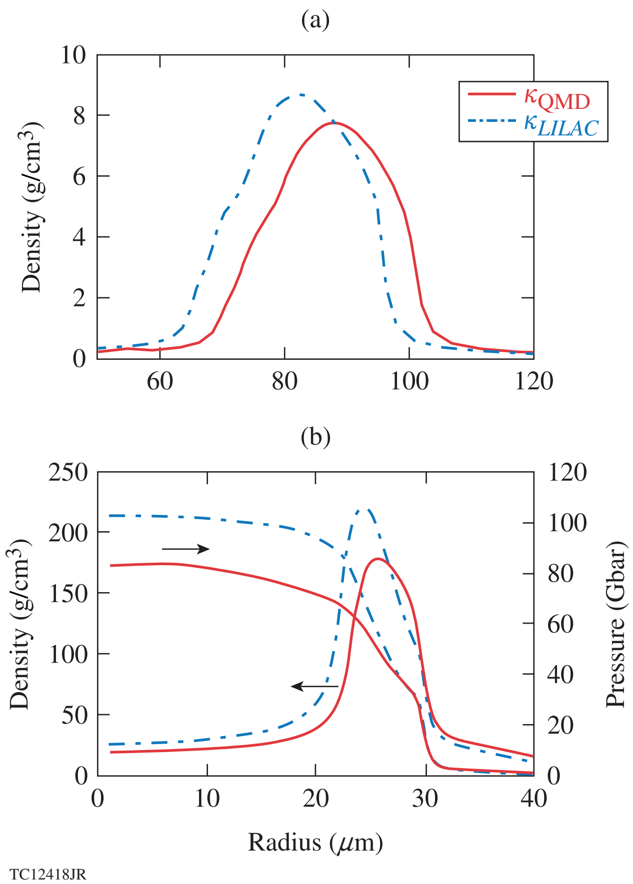

Figure 145.27
Comparison of density profiles and hot-spot pressures predicted by two hydrodynamic simulations using the new κ_{QMD} (red solid lines) and the traditional κ_{LILAC} (blue dashed–dotted lines), respectively. (a) The end of the pulse (t = 2.96 ns) and (b) the implosion reaching its peak neutron production (t = 3.14 ns). The overall target performances are compared in Table 145.III.

the electron temperature is reduced somewhat between the ablation front and the conduction zone when compared to the κ_{LILAC} case. This reduces the ablation efficiency, thereby leading to a slightly slower implosion. When the DT shell stagnates at t = 3.14 ns, the two simulations lead to certain differences in target performance. The comparisons are made in Fig. 145.27(b) for both peak densities in the shell and pressures in the hot spot. The peak density drops from $\rho_p \simeq 220$ g/cm^3 predicted by the κ_{LILAC} simulation to $\rho_p \simeq 180$ g/cm^3 in the κ_{QMD} simulation. Also, the hot-spot peak pressure decreases from $P \simeq 105$ Gbar (κ_{LILAC}) to $P \simeq 84$ Gbar (κ_{QMD}). Table 145.III summarizes the overall comparison in target performance from the two simulations with a variation in yield of ~20%.

The effects of κ_{QMD} are tested for a symmetric direct-drive–ignition design on the NIF, as seen in Figs. 145.28 and 145.29. The pulse shape is shown in Fig. 145.28, which is hydro-equivalently scaled from the above OMEGA target. It consists of a 180-μm-thick DT layer with a 35-μm CD ablator. The target diameter is about 3.43 mm, illustrated by the inset in Fig. 145.28. Results from the two simulations are shown in Fig. 145.29 for comparison. Figure 145.29(a) displays the DT shell's density as a function of target radius for both κ_{LILAC} (blue dashed–dotted line) and κ_{QMD} (red solid line) simulations. Similar to what was found for the implosion case on OMEGA, the NIF simulation using κ_{QMD} also indicates a slight slowdown in the implosion. This causes the difference seen in Fig. 145.29(b) at the start of the ignition burn. The comparison in target performance is summarized in Table 145.IV.

Table 145.III: Comparison of target performance of a typical cryogenic DT implosion on OMEGA simulated with κ_{QMD} versus κ_{LILAC} of CD. The subscript "n" represents neutron-averaged quantities.

OMEGA	κ_{LILAC}	κ_{QMD}
Yield	1.9×10^{14}	1.6×10^{14}
P_{peak}	105 Gbar	84 Gbar
$\langle T_i \rangle_n$	4.17 keV	4.07 keV
$\langle P \rangle_n$	78 Gbar	72 Gbar
$\langle \rho R \rangle_n$	213 mg/cm^2	208 mg/cm^2

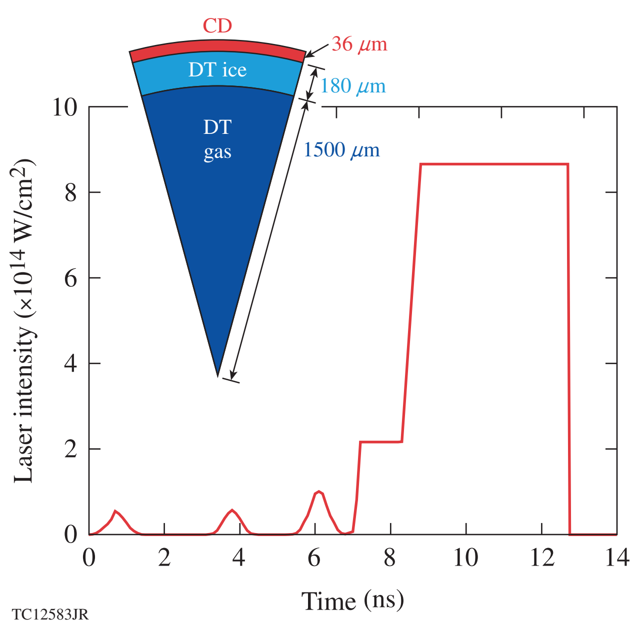

Figure 145.28
The pulse shape and target dimension for a symmetrical ignition design on the NIF.

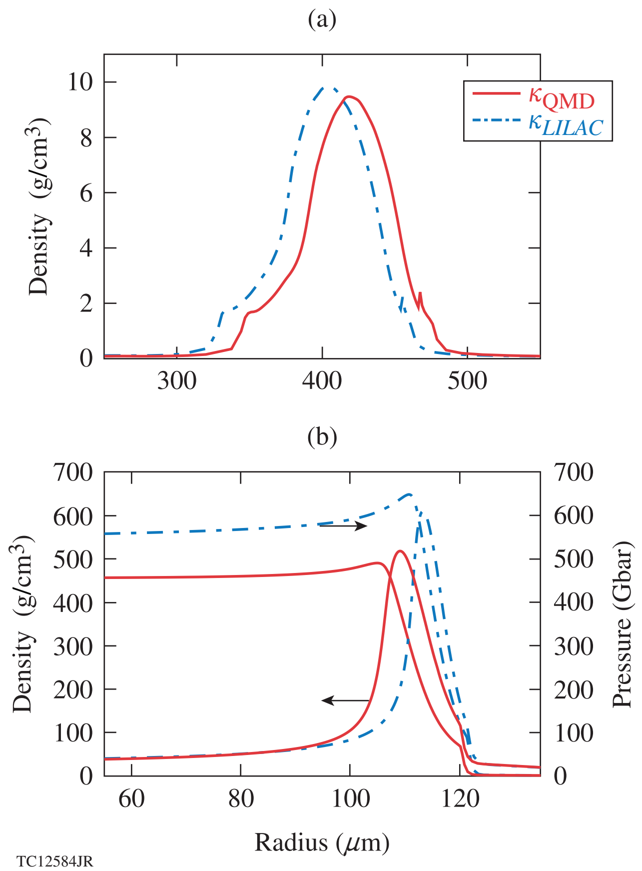

Figure 145.29
Simulation comparison of the NIF design in Fig. 145.28 using the new κ_{QMD} (red solid lines) and the traditional κ_{LILAC} (blue dashed–dotted lines), respectively. (a) The predicted density profiles at the peak velocity (t = 13 ns) and (b) hot-spot pressure and peak shell density compared for the two cases at t = 14 ns. The overall target performance is compared in Table 145.IV.

Table 145.IV: Comparison of a NIF ignition design simulated with κ_{QMD} versus κ_{LILAC} for CD.

NIF	κ_{LILAC}	κ_{QMD}
$\langle \rho R \rangle_n$	0.814 g/cm^2	0.786 g/cm^2
$\langle T_i \rangle_n$	20.8 keV	19.1 keV
$\langle P \rangle_n$	629 Gbar	546 Gbar
$\langle \rho \rangle_{peak}$	639.6 g/cm^3	586.6 g/cm^3
$R_{hot\ spot}$	74.1 μm	78.5 μm
$C_{hot\ spot}$	23.2	21.8
Yield	1.85×10^{19}	1.62×10^{19}
Gain	35	30

The target performance is overall degraded in the κ_{QMD} simulation when compared with the predictions from the traditional κ_{LILAC} simulation. The κ_{QMD} simulation predicts that the hot-spot radius $R_{hot\ spot}$ is slightly bigger and the hot-spot convergence ratio $C_{hot\ spot}$ decreases relative to the κ_{LILAC} case. The final gain is reduced by ~15% in the κ_{QMD} simulation.

Conclusion

Combining the first-principles methods of KSMD and OFMD, the ionization and thermal conductivity of CH plasmas for a wide range of ICF plasma conditions were investigated. The derived average ionization from OFMD calculations has large discrepancies with respect to the astrophysics model predictions in warm dense CH plasmas. The global behavior of $\langle Z \rangle$ and $\langle Z^2 \rangle$ has been fitted with a proposed Saha-type ionization model, which takes the continuum lowering and pressure ionization into account. The derived effective charge $Z_{eff} = \langle Z^2 \rangle / \langle Z \rangle$ is then applied to the global fitting of thermal conductivities κ_{QMD} of CH plasmas, using a generalized Coulomb logarithm $(\ln\Lambda)_{QMD}$. The QMD-based models of Z_{eff} and κ_{QMD} are implemented into our hydrocode for ICF simulations. Compared with the traditional simulations using AOT-based Z_{eff} and κ_{LILAC}, the new simulations with QMD-based Z_{eff} and κ_{QMD} have shown a 15% to ~20% reduction in target performance (yield and energy gain) for both OMEGA and NIF implosions. It is anticipated that these plasma properties of CH, derived from first-principles calculations, will improve the predictions of ICF implosions and other HEDP experiments involving CH ablators. It may also further stimulate the ongoing experimental efforts to measure thermal conductivity in high-energy-density plasmas.[60]

ACKNOWLEDGMENT

This material is based upon work supported by the Department of Energy National Nuclear Security Administration under Award Number DE-NA0001944, the University of Rochester, and the New York State Energy Research and Development Authority. The support of DOE does not constitute an endorsement by DOE of the views expressed in this article. This work was also supported by Scientific Campaign 10 at the Los Alamos National Laboratory, operated by Los Alamos National Security, LLC, for the National Nuclear Security Administration of the U.S. Department of Energy under Contract No. DE-AC52-06NA25396.

REFERENCES

1. S. W. Haan *et al.*, Phys. Plasmas **18**, 051001 (2011).

2. M. J. Edwards, J. D. Lindl, B. K. Spears, S. V. Weber, L. J. Atherton, D. L. Bleuel, D. K. Bradley, D. A. Callahan, C. J. Cerjan, D. Clark, G. W. Collins, J. E. Fair, R. J. Fortner, S. H. Glenzer, S. W. Haan, B. A. Hammel, A. V. Hamza, S. P. Hatchett, N. Izumi, B. Jacoby, O. S. Jones, J. A. Koch, B. J. Kozioziemski, O. L. Landen, R. Lerche, B. J. MacGowan, A. J. MacKinnon, E. R. Mapoles, M. M. Marinak,

M. Moran, E. I. Moses, D. H. Munro, D. H. Schneider, S. M. Sepke, D. A. Shaughnessy, P. T. Springer, R. Tommasini, L. Bernstein, W. Stoeffl, R. Betti, T. R. Boehly, T. C. Sangster, V. Yu. Glebov, P. W. McKenty, S. P. Regan, D. H. Edgell, J. P. Knauer, C. Stoeckl, D. R. Harding, S. Batha, G. Grim, H. W. Herrmann, G. Kyrala, M. Wilke, D. C. Wilson, J. Frenje, R. Petrasso, K. Moreno, H. Huang, K. C. Chen, E. Giraldez, J. D. Kilkenny, M. Mauldin, N. Hein, M. Hoppe, A. Nikroo, and R. J. Leeper, Phys. Plasmas **18**, 051003 (2011).

3. C. Cherfils-Clérouin *et al*., J. Phys.: Conf. Ser. **244**, 022009 (2010).
4. D. D. Meyerhofer, R. L. McCrory, R. Betti, T. R. Boehly, D. T. Casey, T. J. B. Collins, R. S. Craxton, J. A. Delettrez, D. H. Edgell, R. Epstein, K. A. Fletcher, J. A. Frenje, V. Yu. Glebov, V. N. Goncharov, D. R. Harding, S. X. Hu, I. V. Igumenshchev, J. P. Knauer, C. K. Li, J. A. Marozas, F. J. Marshall, P. W. McKenty, P. M. Nilson, S. P. Padalino, R. D. Petrasso, P. B. Radha, S. P. Regan, T. C. Sangster, F. H. Séguin, W. Seka, R. W. Short, D. Shvarts, S. Skupsky, J. M. Soures, C. Stoeckl, W. Theobald, and B. Yaakobi, Nucl. Fusion **51**, 053010 (2011).
5. R. L. McCrory, R. Betti, T. R. Boehly, D. T. Casey, T. J. B. Collins, R. S. Craxton, J. A. Delettrez, D. H. Edgell, R. Epstein, J. A. Frenje, D. H. Froula, M. Gatu-Johnson, V. Yu. Glebov, V. N. Goncharov, D. R. Harding, M. Hohenberger, S. X. Hu, I. V. Igumenshchev, T. J. Kessler, J. P. Knauer, C. K. Li, J. A. Marozas, F. J. Marshall, P. W. McKenty, D. D. Meyerhofer, D. T. Michel, J. F. Myatt, P. M. Nilson, S. J. Padalino, R. D. Petrasso, P. B. Radha, S. P. Regan, T. C. Sangster, F. H. Séguin, W. Seka, R. W. Short, A. Shvydky, S. Skupsky, J. M. Soures, C. Stoeckl, W. Theobald, B. Yaakobi, and J. D. Zuegel, Nucl. Fusion **53**, 113021 (2013).
6. R. S. Craxton, K. S. Anderson, T. R. Boehly, V. N. Goncharov, D. R. Harding, J. P. Knauer, R. L. McCrory, P. W. McKenty, D. D. Meyerhofer, J. F. Myatt, A. J. Schmitt, J. D. Sethian, R. W. Short, S. Skupsky, W. Theobald, W. L. Kruer, K. Tanaka, R. Betti, T. J. B. Collins, J. A. Delettrez, S. X. Hu, J. A. Marozas, A. V. Maximov, D. T. Michel, P. B. Radha, S. P. Regan, T. C. Sangster, W. Seka, A. A. Solodov, J. M. Soures, C. Stoeckl, and J. D. Zuegel, Phys. Plasmas **22**, 110501 (2015).
7. S. W. Haan, H. Huang, M. A. Johnson, M. Stadermann, S. Baxamusa, S. Bhandarkar, D. S. Clark, V. Smalyuk, and H. F. Robey, Phys. Plasmas **22**, 032708 (2015); T. C. Sangster, V. N. Goncharov, R. Betti, T. R. Boehly, D. T. Casey, T. J. B. Collins, R. S. Craxton, J. A. Delettrez, D. H. Edgell, R. Epstein, K. A. Fletcher, J. A. Frenje, V. Yu. Glebov, D. R. Harding, S. X. Hu, I. V. Igumenshchev, J. P. Knauer, S. J. Loucks, C. K. Li, J. A. Marozas, F. J. Marshall, R. L. McCrory, P. W. McKenty, D. D. Meyerhofer, P. M. Nilson, S. P. Padalino, R. D. Petrasso, P. B. Radha, S. P. Regan, F. H. Seguin, W. Seka, R. W. Short, D. Shvarts, S. Skupsky, V. A. Smalyuk, J. M. Soures, C. Stoeckl, W. Theobald, and B. Yaakobi, Phys. Plasmas **17**, 056312 (2010).
8. S. H. Glenzer and R. Redmer, Rev. Mod. Phys. **81**, 1625 (2009).
9. A. L. Kritcher *et al*., Phys. Rev. Lett. **107**, 015002 (2011).
10. L. B. Fletcher *et al*., Phys. Rev. Lett. **112**, 145004 (2014).
11. S. P. Marsh, ed. *LASL Shock Hugoniot Data*, Los Alamos Series on Dynamic Material Properties (University of California Press, Berkeley, CA, 1980).
12. R. Cauble *et al*., Phys. Plasmas **4**, 1857 (1997).
13. N. Ozaki *et al*., Phys. Plasmas **16**, 062702 (2009).
14. M. Koenig *et al*., Phys. Plasmas **10**, 3026 (2003).
15. M. A. Barrios, D. G. Hicks, T. R. Boehly, D. E. Fratanduono, J. H. Eggert, P. M. Celliers, G. W. Collins, and D. D. Meyerhofer, Phys. Plasmas **17**, 056307 (2010).
16. S. Hamel, L. X. Benedict, P. M. Celliers, M. A. Barrios, T. R. Boehly, G. W. Collins, T. Döppner, J. H. Eggert, D. R. Farley, D. G. Hicks, J. L. Kline, A. Lazicki, S. LePape, A. J. Mackinnon, J. D. Moody, H. F. Robey, E. Schwegler, and P. A. Sterne, Phys. Rev. B **86**, 094113 (2012).
17. C. Wang, X.-T. He, and P. Zhang, Phys. Plasmas **18**, 082707 (2011).
18. S. X. Hu, T. R. Boehly, and L. A. Collins, Phys. Rev. E **89**, 063104 (2014).
19. S. X. Hu, L. A. Collins, V. N. Goncharov, J. D. Kress, R. L. McCrory, and S. Skupsky, Phys. Rev. E **92**, 043104 (2015).
20. B. A. Hammel *et al*., High Energy Density Phys. **6**, 171 (2010).
21. L. Spitzer, Jr. and R. Härm, Phys. Rev. **89**, 977 (1953).
22. Y. T. Lee and R. M. More, Phys. Fluids **27**, 1273 (1984).
23. B. Wilson *et al*., J. Quant. Spectrosc. Radiat. Transf. **99**, 658 (2006).
24. G. Faussurier *et al*., Phys. Plasmas **17**, 052707 (2010); J. Clérouin *et al*., Phys. Rev. E **82**, 046402 (2010).
25. V. Recoules *et al*., Phys. Rev. Lett. **102**, 075002 (2009).
26. F. Lambert *et al*., Phys. Plasmas **18**, 056306 (2011).
27. B. Holst, M. French, and R. Redmer, Phys. Rev. B **83**, 235120 (2011).
28. C. Wang *et al*., Phys. Rev. E **88**, 013106 (2013).
29. S. X. Hu, L. A. Collins, T. R. Boehly, J. D. Kress, V. N. Goncharov, and S. Skupsky, Phys. Rev. E **89**, 043105 (2014).
30. F. Lambert and V. Recoules, Phys. Rev. E **86**, 026405 (2012).
31. C. E. Starrett *et al*., Phys. Plasmas **19**, 102709 (2012).
32. D. V. Knyazev and P. R. Levashov, Phys. Plasmas **22**, 053303 (2015).
33. L. Collins *et al*., Phys. Rev. E **52**, 6202 (1995).
34. J. G. Clérouin and S. Bernard, Phys. Rev. E **56**, 3534 (1997).
35. L. A. Collins *et al*., Phys. Rev. B **63**, 184110 (2001).
36. M. P. Desjarlais, Phys. Rev. B **68**, 064204 (2003).
37. P. Hohenberg and W. Kohn, Phys. Rev. **136**, B864 (1964).
38. W. Kohn and L. J. Sham, Phys. Rev. **140**, A1133 (1965).
39. N. D. Mermin, Phys. Rev. **137**, A1441 (1965).
40. G. Kresse and J. Hafner, Phys. Rev. B **47**, 558 (1993).

41. G. Kresse and J. Hafner, Phys. Rev. B **49**, 14,251 (1994).

42. G. Kresse and J. Furthmüller, Phys. Rev. B **54**, 11,169 (1996).

43. F. Lambert, J. Clérouin, and G. Zérah, Phys. Rev. E **73**, 016403 (2006).

44. J. P. Perdew, K. Burke, and M. Ernzerhof, Phys. Rev. Lett. **77**, 3865 (1996); **78**, 1396(E) (1997).

45. R. Kubo, J. Phys. Soc. Jpn. **12**, 570 (1957).

46. D. A. Greenwood, Proc. Phys. Soc. Lond. **71**, 585 (1958).

47. F. Lambert *et al*., Phys. Rev. E **77**, 026402 (2008).

48. W. F. Huebner *et al*., Los Alamos National Laboratory, Los Alamos, NM, Report LA-6760-M (1977).

49. S. X. Hu, L. A. Collins, V. N. Goncharov, T. R. Boehly, R. Epstein, R. L. McCrory, and S. Skupsky, Phys. Rev. E **90**, 033111 (2014).

50. J. C. Stewart and K. D. Pyatt, Jr., Astrophys. J. **144**, 1203 (1966).

51. J. Delettrez, R. Epstein, M. C. Richardson, P. A. Jaanimagi, and B. L. Henke, Phys. Rev. A **36**, 3926 (1987).

52. S. Ichimaru and S. Tanaka, Phys. Rev. A **32**, 1790 (1985); H. Kitamura and S. Ichimaru, Phys. Rev. E **51**, 6004 (1995).

53. W. B. Hubbard, Astrophys. J. **146**, 858 (1966).

54. V. N. Goncharov, T. C. Sangster, T. R. Boehly, S. X. Hu, I. V. Igumenshchev, F. J. Marshall, R. L. McCrory, D. D. Meyerhofer, P. B. Radha, W. Seka, S. Skupsky, C. Stoeckl, D. T. Casey, J. A. Frenje, and R. D. Petrasso, Phys. Rev. Lett. **104**, 165001 (2010).

55. S. X. Hu, V. N. Goncharov, P. B. Radha, J. A. Marozas, S. Skupsky, T. R. Boehly, T. C. Sangster, D. D. Meyerhofer, and R. L. McCrory, Phys. Plasmas **17**, 102706 (2010).

56. T. C. Sangster, V. N. Goncharov, R. Betti, P. B. Radha, T. R. Boehly, D. T. Casey, T. J. B. Collins, R. S. Craxton, J. A. Delettrez, D. H. Edgell, R. Epstein, C. J. Forrest, J. A. Frenje, D. H. Froula, M. Gatu-Johnson, V. Yu. Glebov, D. R. Harding, M. Hohenberger, S. X. Hu, I. V. Igumenshchev, R. Janezic, J. H. Kelly, T. J. Kessler, C. Kingsley, T. Z. Kosc, J. P. Knauer, S. J. Loucks, J. A. Marozas, F. J. Marshall, A. V. Maximov, R. L. McCrory, P. W. McKenty, D. D. Meyerhofer, D. T. Michel, J. F. Myatt, R. D. Petrasso, S. P. Regan, W. Seka, W. T. Shmayda, R. W. Short, A. Shvydky, S. Skupsky, J. M. Soures, C. Stoeckl, W. Theobald, V. Versteeg, B. Yaakobi, and J. D. Zuegel, Phys. Plasmas **20**, 056317 (2013).

57. T. R. Boehly, V. N. Goncharov, W. Seka, S. X. Hu, J. A. Marozas, D. D. Meyerhofer, P. M. Celliers, D. G. Hicks, M. A. Barrios, D. Fratanduono, and G. W. Collins, Phys. Plasmas **18**, 092706 (2011).

58. H. F. Robey, J. D. Moody, P. M. Celliers, J. S. Ross, J. Ralph, S. Le Pape, L. Berzak Hopkins, T. Parham, J. Sater, E. R. Mapoles, D. M. Holunga, C. F. Walters, B. J. Haid, B. J. Kozioziemski, R. J. Dylla-Spears, K. G. Krauter, G. Frieders, G. Ross, M. W. Bowers, D. J. Strozzi, B. E. Yoxall, A. V. Hamza, B. Dzenitis, S. D. Bhandarkar, B. Young, B. M. Van Wonterghem, L. J. Atherton, O. L. Landen, M. J. Edwards, and T. R. Boehly, Phys. Rev. Lett. **111**, 065003 (2013).

59. S. X. Hu, B. Militzer, V. N. Goncharov, and S. Skupsky, Phys. Rev. Lett. **104**, 235003 (2010); S. X. Hu, B. Militzer, V. N. Goncharov, and S. Skupsky, Phys. Rev. B **84**, 224109 (2011).

60. Y. Ping, A. Fernandez-Panella, H. Sio, A. Correa, R. Shepherd, O. Landen, R. A. London, P. A. Sterne, H. D. Whitley, D. Fratanduono, T. R. Boehly, and G. W. Collins, Phys. Plasmas **22**, 092701 (2015).

Demonstrating Ignition Hydrodynamic Equivalence in Direct-Drive Cryogenic Implosions on OMEGA

Introduction

The main approach to ignition by means of inertial confinement fusion (ICF)[1,2] currently pursued at the National Ignition Facility (NIF)[3] is x-ray (or indirect) drive, where the laser energy absorbed in a high-Z hohlraum is re-emitted in the form of x rays that drive the fuel capsule. In the other ICF approach—direct drive—the target is driven by laser irradiation directly coupled to the plasma blowing off the imploding capsule. The main advantage of the indirect-drive approach is reduced sensitivity of drive uniformity to short-scale beam nonuniformities. The main advantage of direct drive is a higher coupling efficiency (by factor of 3 to 5) of laser energy into kinetic energy of the shell (hydrodynamic efficiency) compared to that of x-ray drive. The OMEGA Laser System[4] and the KrF laser NIKE at the Naval Research Laboratory[5] have been the principal facilities for direct-drive experiments in the U.S.

Significant progress has been made over the last several decades in beam smoothing. This includes distributed phase plates (DPP's),[6] polarization smoothing with birefringent wedges,[7] smoothing by spectral dispersion (SSD),[8] and induced spatial incoherence.[9] In addition to these improvements, implementing adiabat shaping techniques[10,11] to significantly reduce Rayleigh–Taylor (RT) instability[12,13] growth during shell acceleration and demonstrating imprint mitigation with mid-Z–doped ablators[14] and high-Z target overcoats[15] make the direct-drive approach very attractive. The progress in direct-drive research and the challenges in achieving ignition on the NIF using x-ray drive suggests that direct drive as a viable alternative for developing a burning-plasma platform in the laboratory be considered.

Compared to x-ray drive, direct-drive targets couple a larger fraction of laser energy into shell kinetic energy and internal energy of the neutron-producing central region of the target (hot spot) at peak fuel compression. Larger hot-spot energy relaxes the requirement on shell convergence and hot-spot pressure in an igniting target. This can be shown with the help of a commonly used ignition condition according to which plasma self-heating is initiated by both PdV work and alpha-particle deposition inside the hot spot, given the product of areal density and ion temperature satisfies[1,2,16,17]

$$(\rho R)_{\mathrm{hs}} \times T \gtrsim 0.3\ \mathrm{g/cm}^2 \times 5\ \mathrm{keV}\,, \tag{1}$$

where ρ, R_{hs}, and T are the hot-spot density, radius, and temperature, respectively. Substituting expressions for the pressure $p_{\mathrm{hs}} = (1 + Z)\ \rho T/m_{\mathrm{i}}$ (Z is the average ion charge and m_{i} is the average ion mass) and internal energy $E_{\mathrm{hs}} = 3/2\ p_{\mathrm{hs}}V_{\mathrm{hs}}$ (V_{hs} is the neutron-averaged hot-spot volume) into Eq. (1) gives a minimum pressure requirement (threshold) for ignition,

$$p_{\mathrm{hs}} > p_{\mathrm{thr}} = 250\ \mathrm{Gbar}\left(\frac{E_{\mathrm{hs}}}{10\ \mathrm{kJ}}\right)^{-1/2}, \text{ or}$$

$$\overline{P} = \frac{p_{\mathrm{hs}}}{p_{\mathrm{thr}}} = \left(\frac{p_{\mathrm{hs}}}{250\ \mathrm{Gbar}}\right)\sqrt{\frac{E_{\mathrm{hs}}}{10\ \mathrm{kJ}}} > 1\,, \tag{2}$$

where $\overline{P}$ is the ignition pressure parameter.

Figure 145.30 shows the dependence of the threshold pressure p_{thr} on the hot-spot internal energy. Spherically symmetric direct-drive cryogenic designs on OMEGA couple up

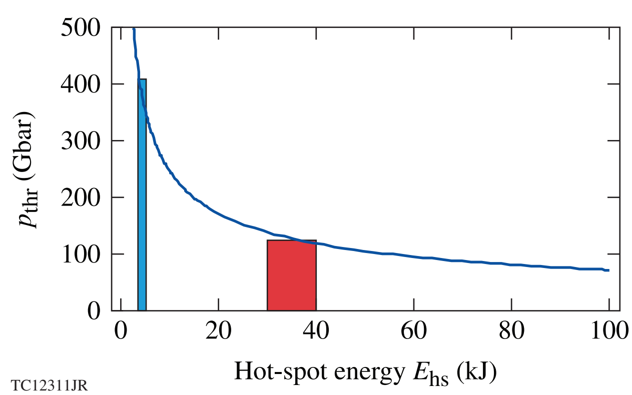

Figure 145.30
Threshold hot-spot pressure p_{thr} as a function of the hot-spot internal energy. A typical hot-spot energy in an indirect- and a direct-drive implosion for a National Ignition Facility (NIF)–scale laser energy is shown by the blue- and red-shaded regions, respectively.

to 0.44 kJ (out of 26-kJ incident laser energy) into the hot-spot internal energy. Hydrodynamically scaled to the NIF, with a laser energy of 1.5 MJ to 1.8 MJ, these designs are predicted to couple 5× to 10× more energy into the hot spot (25 kJ to 40 kJ, depending on laser coupling efficiency; see the red-shaded region in Fig. 145.30) compared to that of indirect drive (4 kJ to 5 kJ; see the blue-shaded region in Fig. 145.30), resulting in 2.5× to 3× lower hot-spot pressures required for ignition (~120 Gbar to 150 Gbar for direct drive versus 350 Gbar to 400 Gbar for indirect drive). The required hot-spot size also becomes smaller with a reduction in E_{hs}. According to Eq. (2) the hot-spot size scales as a square root of the internal energy, leading to a hot-spot size that is a factor of 2.5 to 3 larger in a direct-drive implosion compared to an x-ray-drive implosion.

OMEGA Cryogenic Implosions

To separate 1-D factors limiting the target performance (drive efficiency, adiabat, etc.) from 3-D effects, a series of dedicated experiments was performed on OMEGA with the purpose of improving the accuracy of 1-D code predictions. To identify critical implosion parameters, the 1-D scaling laws for peak pressure, hot-spot energy, and the ignition-pressure parameter are written in terms of implosion velocity v_{imp} (defined as the peak mass-averaged shell velocity), the drive (ablation) pressure p_{abl}, and in-flight shell adiabat α (Ref. 18),

$$p_{\mathrm{hs}}^{\text{1-D}} \sim \frac{p_{\mathrm{abl}}^{1/3}\, v_{\mathrm{imp}}^{10/3}}{\alpha},$$

$$E_{\mathrm{hs}}^{\text{1-D}} \sim E_{\mathrm{kin}} \frac{v_{\mathrm{imp}}^{4/3}}{\alpha^{2/5}\, p_{\mathrm{abl}}^{4/15}},$$

$$\bar{P}_{\text{1-D}} \sim \frac{\sqrt{E_{\mathrm{kin}}}\; v_{\mathrm{imp}}^{4}\; p_{\mathrm{abl}}^{1/5}}{\alpha^{6/5}}. \qquad (3)$$

The implosion velocity and shell kinetic energy E_{kin} are inferred in an experiment by measuring the ablation-front trajectory and mass ablation rate using self-emission imaging.[19] The ablation pressure is inferred from simulations that match the measured ablation-front trajectory, mass ablation rate, bang time,[20] and scattered-light power and spectrum.[21] Finally, the shock-induced adiabat is inferred by measuring shock velocities early in the pulse using VISAR (velocity interferometer system for any reflector).[22] An additional fuel-adiabat increase caused by hot-electron preheat is estimated by measuring the hard x-ray signal[23] and areal density[24,25] in mid- to high-adiabat implosions (the areal density in 1-D, for a given laser energy, depends mainly on the shell adiabat,[26] $\rho R \sim \alpha^{-0.5}$). The estimate of the shell-preheat effect based on the areal-density measurement is valid only for implosions with $\alpha \gtrsim 3.5$ since shell integrity and fuel compression in lower-adiabat implosions are compromised because of the short-scale mix. A detailed comparison of 1-D simulation results using the hydrocode *LILAC*[27] with the data[18] shows good agreement between the two for a variety of target designs and drive conditions. One-dimensional simulations include the nonlocal thermal-transport model,[28] the ray-based cross-beam energy transfer (CBET) model,[29] and first-principle equation-of-state models[30] for both DT ice and the CD ablator.

An analysis of direct-drive implosions on OMEGA has shown that coupling losses caused by CBET[29] significantly reduce the ablation pressure (as much as 40% on OMEGA and up to 60% on the NIF-scale targets), implosion velocity, and shell kinetic energy. Including such losses, a demonstration of the hydrodynamic equivalence of implosions on OMEGA to ignition designs on the NIF requires that the shell's in-flight aspect ratio exceed the current stability threshold level (~22) (Ref. 18). One of the CBET mitigation strategies[31] involves using laser illumination with a laser-beam diameter smaller than the initial shell diameter. This, as demonstrated both theoretically and experimentally, recovers some coupling losses and increases the ablation pressure. Since the effect of CBET is small early in the implosion, when the density scale length and laser intensity are small, beam-zooming schemes[32] can be considered when the beam's focal spot at an early time is at the initial target radius (to maximize the illumination uniformity), then reduced down to 0.6× to 0.7× of the size at the beginning of the main drive.

While the implementation of zooming on OMGEA is still a few years away, a test of the CBET reduction strategy was performed using "static" DPP's, which produces focal spots smaller than the initial target size throughout the entire drive pulse. New distributed phase plates (called SG5, after the super-Gaussian order of the focal-spot profile being close to 5) were designed and installed on OMEGA with the purpose of studying CBET mitigation techniques. These plates have a lower focal-spot nonuniformity level compared to the existing DPP's (so-called SG4). The focal-spot radius was fixed at $R_{\mathrm{b}} = 410\ \mu$m (95% of laser energy is encircled within radius R_{b}). The ratio of R_{b} to target radius (R_{t}) was changed by varying R_{t} from 400 μm to 500 μm. Also, on-target UV energy (available to implode larger targets) was increased by implementing multiple-pulse driver lines (MPD) on OMEGA. In the MPD mode, SSD is turned off during the main pulse, making it possible to increase the UV energy from 26 kJ up to 29 kJ. In this configuration, however, the focal spot becomes slightly elliptical (or more accurately, the 2-D super-Gaussian fit of the focal-spot profile has an azimuthal variation in the super-Gaussian order). The azimuthally averaged focal-spot profile has $n_{SG} = 6.14$ and $R_b = 388\ \mu$m. Using the MPD configuration for larger targets with $R_t = 450\ \mu$m, 480 μm, and 500 μm and the SSD driver for targets with $R_t = 400\ \mu$m, 430 μm, and 450 μm, the ratio R_b/R_t changed from 1.025 to 0.78. According to simulation results (that matched the observables), the smallest target ($R_t = 400\ \mu$m) has a $v_{imp} = 3.5$ to 3.6×10^7 cm/s and hydrodynamic efficiency (the ratio of the shell's kinetic energy to the total laser energy) of $f_{hydro} = 3.5\%$, while the largest target has a similar implosion velocity, $v_{imp} = 3.6$ to 3.7×10^7 cm/s, but more than twice the hydroefficiency, $f_{hydro} = 7.2\%$. Such an increase in hydroefficiency is caused partially by smaller refraction losses experienced by a larger target (smaller R_b/R_t and larger density scale length) and partially by reduced CBET losses. To quantify each effect, a simulation was performed with $R_t = 500\ \mu$m, where R_b was increased to match R_t. In such a simulation, the implosion velocity was dropped by 17% to $v_{imp} = 3 \times 10^7$ cm/s and the shell's hydrodynamic efficiency was reduced by 20% down to $f_{hydro} = 5.8\%$.

Figure 145.31 shows target performance for different target diameters. The hot-spot pressure is inferred[33] by using the measured neutron yield, burn duration Δt_{burn} (using both neutron time-of-flight and framing-camera measurements of x-ray burn duration), neutron-averaged ion temperature $(T_i)_n$, and hot-spot size R_{17} (defined as the radius of 17% of the peak-emission contour for x rays in the 4-keV to 7-keV energy range) at bang time using a time-resolved Kirkpatrick–Baez framing camera.[34] Assuming an isobaric hot spot and fitting the burn history to a Gaussian with full width at half maximum (FWHM) = Δt_{burn}, the maximum burn rate N_{max} relates to neutron yield Y as $N_{max} = 2Y\sqrt{\ln 2/\pi}\big/\Delta t_{burn}$, where $N_{max} = n_T n_D T^2 \int_{V_{hs}} dV\langle\sigma v\rangle/T^2$. Therefore, pressure at bang time can be determined using

$$p_{hs} \simeq \left[8Y\sqrt{\ln 2/\pi}\Big/\left(f_D f_T \Delta t_{burn} \int_{V_{hs}} dV\langle\sigma v\rangle\big/T^2\right)\right]^{1/2}, \quad (4)$$

where $\langle\sigma v\rangle$ is the cross section for D–T reactions, and f_D and f_T are the fractions of D and T in the fuel, respectively. In evaluating the spatial integral in Eq. (4) the following spatial profile for the ion temperature (obtained using simulation results) is assumed:

$$T(r) = T_c\left[1 - (r/R_{hs})^2 \left(1 - 0.15^{3/2}\right)\right]^{2/3},$$

where T_c is the maximum hot-spot temperature, determined by matching

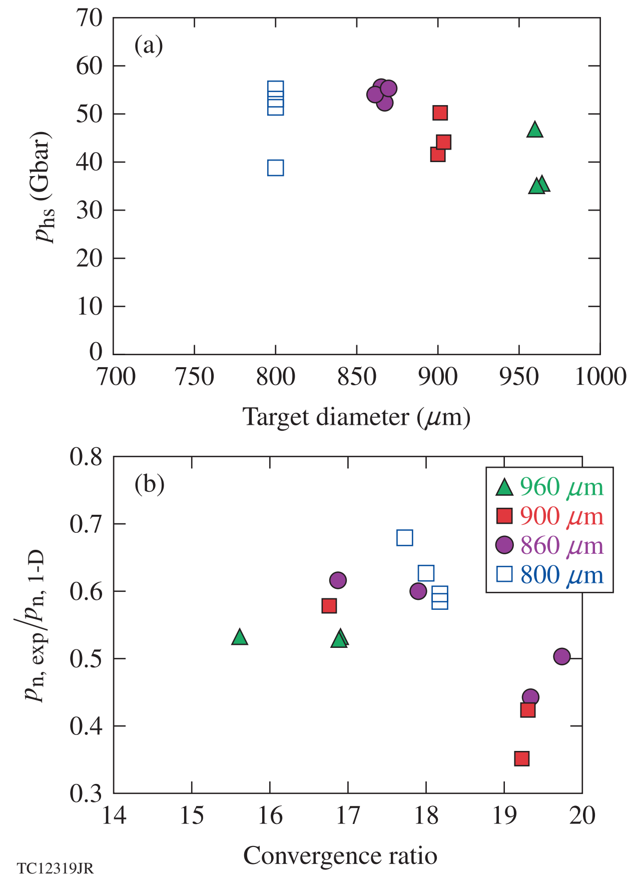

Figure 145.31
(a) Hot-spot pressure, inferred from experimental observables, as a function of target size. (b) Inferred hot-spot pressure normalized to 1-D code predictions versus the predicted shell convergence at 1-D bang time.

$$\left(\int_{V_{hs}} dV\langle\sigma v\rangle\big/T\right)\Big/\left(\int_{V_{hs}} dV\langle\sigma v\rangle\big/T^2\right)$$

with the measured $(T_i)_n$, and, as follows from code predictions, R_{hs} and measured R_{17} are related using $R_{hs} = 1.06\ R_{17}$.

The following two conclusions can be made based on results shown in Fig. 145.31: first, the hot-spot pressure (both absolute and relative to 1-D predictions) degrades with the target size; second, there is a threshold of the shell's convergence ratio, $CR^{1\text{-}D} \simeq 18$, beyond which the hot-spot pressure normalized to the 1-D prediction drops from between 0.5 to 0.7 to between 0.3 to 0.5.

To understand these trends, one must consider the effects of shell nonuniformity. The evolution of long-wavelength nonuniformities seeded by target offset, beam geometry, beam power imbalance, and mispointing is studied using the 3-D hydrocode *ASTER*.[35] This code includes 3-D hydrodynamics, ion and electron thermal conduction (the flux-limited Spitzer model), the CBET model, bremsstrahlung radiation losses, and nuclear reactivities. A simplified 3-D model of laser deposition is used, assuming a spherical symmetry of the plasma corona in the laser-deposition region, when performing ray tracing of individual beams (this approximation is justified because of strong lateral thermal-conduction smoothing in the high-temperature corona in direct-drive implosions). The beam power, timing, and pointing, however, can vary from beam to beam.

Simulations of cryogenic implosions on OMEGA show that the bubbles (areas of low-density material from the central region that protrude into the higher-density shell) developed because of the RT growth of long-wavelength perturbations ($\ell \lesssim 5$) during shell deceleration, increasing the volume of the central region V_{cntr} and reducing the hot-spot pressure $\left(p_{\text{hs}} \sim 1 \big/ V_{\text{cntr}}^{5/3}\right)$ and neutron yield. As the shell converges further, the bubbles eventually break out of the shell, quenching hot-spot confinement and neutron yield. This is shown in Fig. 145.32. Since the burn truncates earlier because of the 3-D effects, the inferred hot-spot pressure reduces as a result of two effects: sampling and an increased volume V_{cntr} of the central region surrounded by the cold shell. Shifting the peak burn to an earlier time because of the nonuniformity growth samples earlier stages of hot-spot formation when shell convergence and the central pressure have not yet reached the peak values. The 3-D effects also increase the central region volume, preventing the fuel material from stagnating and effectively converting the shell kinetic energy into the internal energy of the hot spot. To account for the first effect (early pressure sampling), Fig. 145.33 plots the inferred hot-spot pressure normalized to the predicted pressure at the observed (earlier) bang time as a function of 1-D shell convergence calculated at the experimental bang time. Figure 145.33 shows that implosions with a fuel adiabat $\alpha > 3.5$ proceed close to 1-D predictions up to a shell convergence of CR ~ 17. Further shell convergence does not lead to additional *PdV* work on the hot spot because of the RT growth of low-ℓ modes. An additional limitation on target performance at a lower fuel adiabat is caused by compromised shell integrity resulting from short-wavelength nonuniformity growth during shell acceleration.

In summary, the cryogenic campaign with a reduced beam radius relative to the target radius $\left(R_{\text{b}} \big/ R_{\text{t}} < 1\right)$, performed on OMEGA to reduce CBET losses, demonstrated increased laser coupling and hydrodynamic efficiency. This coupling enhancement, however, did not improve the target performance. Numerical simulations indicate that long-wavelength nonuni-

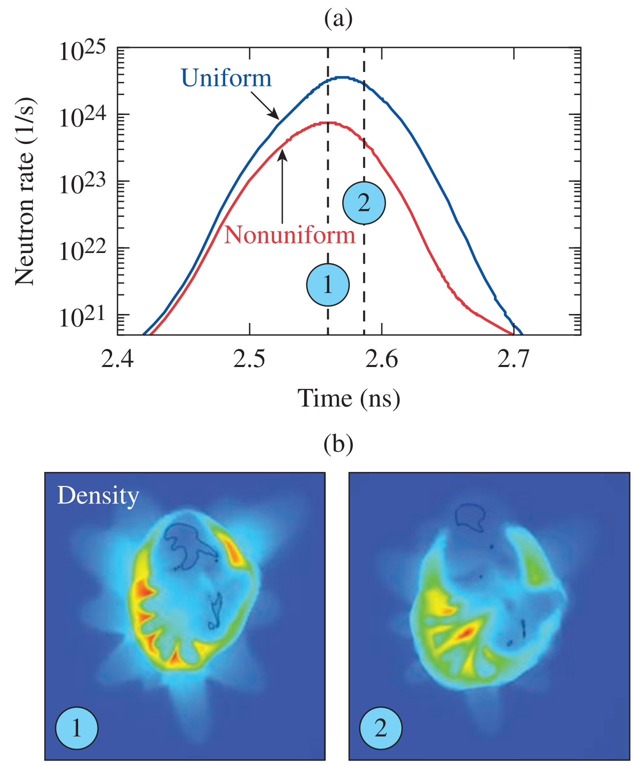

TC12376JR

Figure 145.32
(a) Neutron-production rate calculated using the code *ASTER* without (blue solid line) and with (red solid line) the effects of long-wavelength nonuniformity growth. (b) Simulated shell density maps at times indicated by (1) and (2).

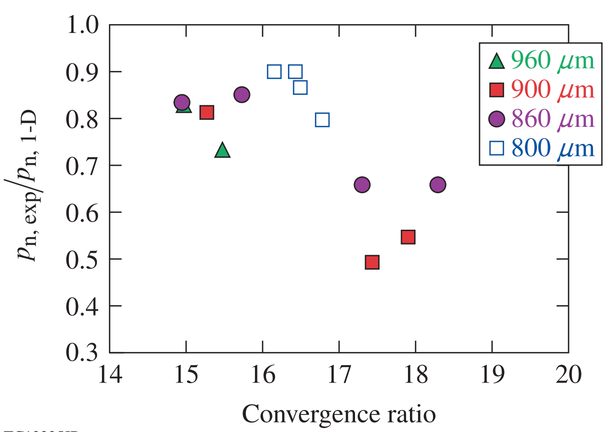

TC12325JR

Figure 145.33
Inferred hot-spot pressure normalized to the 1-D predictions calculated at the experimental bang time versus 1-D shell convergence at the experimental bang time.

formities caused by target offset and power imbalance lead to an increased target central volume and early burn truncation. This effect is exacerbated by reduction in beam overlap when target size increases relative to beam size. Demonstrating hydrodynamic equivalence on OMEGA will require minimizing large-wavelength uniformities seeded by power imbalance and target offset and reusing target debris accumulated during cryogenic target production.

ACKNOWLEDGMENT

This material is based upon work supported by the Department of Energy National Nuclear Security Administration under Award Number DE-NA0001944, the University of Rochester, and the New York State Energy Research and Development Authority. The support of DOE does not constitute an endorsement by DOE of the views expressed in this article.

REFERENCES

1. J. D. Lindl, *Inertial Confinement Fusion: The Quest for Ignition and Energy Gain Using Indirect Drive* (Springer-Verlag, New York, 1998).
2. S. Atzeni and J. Meyer-ter-Vehn, *The Physics of Inertial Fusion: Beam Plasma Interaction, Hydrodynamics, Hot Dense Matter*, International Series of Monographs on Physics (Clarendon Press, Oxford, 2004).
3. J. Paisner *et al*., Laser Focus World **30**, 75 (1994).
4. T. R. Boehly, D. L. Brown, R. S. Craxton, R. L. Keck, J. P. Knauer, J. H. Kelly, T. J. Kessler, S. A. Kumpan, S. J. Loucks, S. A. Letzring, F. J. Marshall, R. L. McCrory, S. F. B. Morse, W. Seka, J. M. Soures, and C. P. Verdon, Opt. Commun. **133**, 495 (1997).
5. S. P. Obenschain *et al*., Phys. Plasmas **3**, 2098 (1996).
6. T. J. Kessler, Y. Lin, J. J. Armstrong, and B. Velazquez, Proc. SPIE **1870**, 95 (1993).
7. T. R. Boehly, V. A. Smalyuk, D. D. Meyerhofer, J. P. Knauer, D. K. Bradley, R. S. Craxton, M. J. Guardalben, S. Skupsky, and T. J. Kessler, J. Appl. Phys. **85**, 3444 (1999).
8. S. Skupsky, R. W. Short, T. Kessler, R. S. Craxton, S. Letzring, and J. M. Soures, J. Appl. Phys. **66**, 3456 (1989).
9. R. H. Lehmberg and J. Goldhar, Fusion Technol. **11**, 532 (1987).
10. V. N. Goncharov, J. P. Knauer, P. W. McKenty, P. B. Radha, T. C. Sangster, S. Skupsky, R. Betti, R. L. McCrory, and D. D. Meyerhofer, Phys. Plasmas **10**, 1906 (2003).
11. V. N. Goncharov, T. C. Sangster, T. R. Boehly, S. X. Hu, I. V. Igumenshchev, F. J. Marshall, R. L. McCrory, D. D. Meyerhofer, P. B. Radha, W. Seka, S. Skupsky, C. Stoeckl, D. T. Casey, J. A. Frenje, and R. D. Petrasso, Phys. Rev. Lett. **104**, 165001 (2010).
12. S. Chandrasekhar, in *Hydrodynamic and Hydromagnetic Stability*, International Series of Monographs on Physics (Clarendon Press, Oxford, 1961), p. 428.
13. J. Sanz, Phys. Rev. Lett. **73**, 2700 (1994); V. N. Goncharov, R. Betti, R. L. McCrory, P. Sorotokin, and C. P. Verdon, Phys. Plasmas **3**, 1402 (1996).
14. S. X. Hu, G. Fiksel, V. N. Goncharov, S. Skupsky, D. D. Meyerhofer, and V. A. Smalyuk, Phys. Rev. Lett. **108**, 195003 (2012).
15. S. P. Obenschain *et al*., Phys. Plasmas **9**, 2234 (2002).
16. R. Betti, P. Y. Chang, B. K. Spears, K. S. Anderson, J. Edwards, M. Fatenejad, J. D. Lindl, R. L. McCrory, R. Nora, and D. Shvarts, Phys. Plasmas **17**, 058102 (2010).
17. R. Betti, K. Anderson, V. N. Goncharov, R. L. McCrory, D. D. Meyerhofer, S. Skupsky, and R. P. J. Town, Phys. Plasmas **9**, 2277 (2002).
18. V. N. Goncharov, T. C. Sangster, R. Betti, T. R. Boehly, M. J. Bonino, T. J. B. Collins, R. S. Craxton, J. A. Delettrez, D. H. Edgell, R. Epstein, R. K. Follet, C. J. Forrest, D. H. Froula, V. Yu. Glebov, D. R. Harding, R. J. Henchen, S. X. Hu, I. V. Igumenshchev, R. Janezic, J. H. Kelly, T. J. Kessler, T. Z. Kosc, S. J. Loucks, J. A. Marozas, F. J. Marshall, A. V. Maximov, R. L. McCrory, P. W. McKenty, D. D. Meyerhofer, D. T. Michel, J. F. Myatt, R. Nora, P. B. Radha, S. P. Regan, W. Seka, W. T. Shmayda, R. W. Short, A. Shvydky, S. Skupsky, C. Stoeckl, B. Yaakobi, J. A. Frenje, M. Gatu-Johnson, R. D. Petrasso, and D. T. Casey, Phys. Plasmas **21**, 056315 (2014).
19. D. T. Michel, C. Sorce, R. Epstein, N. Whiting, I. V. Igumenshchev, R. Jungquist, and D. H. Froula, Rev. Sci. Instrum. **83**, 10E530 (2012).
20. C. Stoeckl, V. Yu. Glebov, S. Roberts, T. C. Sangster, R. A. Lerche, R. L. Griffith, and C. Sorce, Rev. Sci. Instrum. **74**, 1713 (2003).
21. W. Seka, D. H. Edgell, J. P. Knauer, J. F. Myatt, A. V. Maximov, R. W. Short, T. C. Sangster, C. Stoeckl, R. E. Bahr, R. S. Craxton, J. A. Delettrez, V. N. Goncharov, I. V. Igumenshchev, and D. Shvarts, Phys. Plasmas **15**, 056312 (2008).
22. L. M. Barker and R. E. Hollenbach, J. Appl. Phys. **43**, 4669 (1972).
23. C. Stoeckl, V. Yu. Glebov, D. D. Meyerhofer, W. Seka, B. Yaakobi, R. P. J. Town, and J. D. Zuegel, Rev. Sci. Instrum. **72**, 1197 (2001).
24. J. A. Frenje, C. K. Li, F. H. Séguin, D. T. Casey, R. D. Petrasso, T. C. Sangster, R. Betti, V. Yu. Glebov, and D. D. Meyerhofer, Phys. Plasmas **16**, 042704 (2009).
25. C. J. Forrest, P. B. Radha, V. Yu. Glebov, V. N. Goncharov, J. P. Knauer, A. Pruyne, M. Romanofsky, T. C. Sangster, M. J. Shoup III, C. Stoeckl, D. T. Casey, M. Gatu-Johnson, and S. Gardner, Rev. Sci. Instrum. **83**, 10D919 (2012).
26. R. Betti and C. Zhou, Phys. Plasmas **12**, 110702 (2005).
27. J. Delettrez, R. Epstein, M. C. Richardson, P. A. Jaanimagi, and B. L. Henke, Phys. Rev. A **36**, 3926 (1987).
28. V. N. Goncharov, T. C. Sangster, P. B. Radha, R. Betti, T. R. Boehly, T. J. B. Collins, R. S. Craxton, J. A. Delettrez, R. Epstein, V. Yu. Glebov, S. X. Hu, I. V. Igumenshchev, J. P. Knauer, S. J. Loucks, J. A. Marozas, F. J. Marshall, R. L. McCrory, P. W. McKenty, D. D.

Meyerhofer, S. P. Regan, W. Seka, S. Skupsky, V. A. Smalyuk, J. M. Soures, C. Stoeckl, D. Shvarts, J. A. Frenje, R. D. Petrasso, C. K. Li, F. Séguin, W. Manheimer, and D. G. Colombant, Phys. Plasmas **15**, 056310 (2008).

29. I. V. Igumenshchev, D. H. Edgell, V. N. Goncharov, J. A. Delettrez, A. V. Maximov, J. F. Myatt, W. Seka, A. Shvydky, S. Skupsky, and C. Stoeckl, Phys. Plasmas **17**, 122708 (2010).

30. S. X. Hu, B. Militzer, V. N. Goncharov, and S. Skupsky, Phys. Rev. Lett. **104**, 235003 (2010); S. X. Hu, L. A. Collins, V. N. Goncharov, J. D. Kress, R. L. McCrory, and S. Skupsky, Phys. Rev. E **92**, 043104 (2015).

31. I. V. Igumenshchev, D. H. Froula, D. H. Edgell, V. N. Goncharov, T. J. Kessler, F. J. Marshall, R. L. McCrory, P. W. McKenty, D. D. Meyerhofer, D. T. Michel, T. C. Sangster, W. Seka, and S. Skupsky, Phys. Rev. Lett. **110**, 145001 (2013).

32. D. H. Froula, T. J. Kessler, I. V. Igumenshchev, R. Betti, V. N. Goncharov, H. Huang, S. X. Hu, E. Hill, J. H. Kelly, D. D. Meyerhofer, A. Shvydky, and J. D. Zuegel, Phys. Plasmas **20**, 082704 (2013).

33. C. Cerjan, P. T. Springer, and S. M. Sepke, Phys. Plasmas **20**, 056319 (2013).

34. F. J. Marshall, V. N. Goncharov, V. Yu. Glebov, S. P. Regan, T. C. Sangster, and C. Stoeckl, the Ninth International Conference on Inertial Fusion Sciences and Applications (IFSA 2015), Seattle, WA, 20–25 September 2015 (Paper Th.Po.17).

35. I. V. Igumenshchev, V. N. Goncharov, F. J. Marshall, J. P. Knauer, D. H. Froula, and S. P. Regan, "Three-Dimensional Modeling of Direct-Drive Cryogenic Implosions," submitted to Physics of Plasmas.

A Neutron Temporal Diagnostic for High-Yield DT Cryogenic Implosions on OMEGA

Introduction

The temporal history of the neutron production in inertial confinement fusion (ICF) experiments[1] is an important diagnostic signature. In ICF experiments, shells filled with deuterium (D_2) or a deuterium–tritium (DT) mixture are compressed by either direct laser illumination,[2] soft x-ray radiation in a laser-heated hohlraum,[3] or strong magnetic fields[4] to conditions under which thermonuclear fusion occurs. The temporal width of the neutron signal is usually of the order of 100 ps. Experimental signatures from the temporal history of the neutron production are the rising edge of the measured neutron rate, which is influenced by the shock transit through the capsule;[5] the peak of the neutron rate (bang time),[6] a measure of the energy absorbed in the imploding shell; and the trailing edge of the neutron rate that encodes information about material mixing during the stagnation phase of the implosion.[7]

Time-resolved neutron measurements on ICF experiments generally use either a scintillator to convert the neutron energy into visible light[8] or chemical-vapor–deposition (CVD) diamond detectors,[9] which convert the neutron energy directly into an electrical charge. The light from the scintillator is either converted into an electrical signal using a fast photomultiplier tube (PMT) or recorded on a fast optical streak camera.[10,11] The PMT or CVD-based neutron bang-time diagnostics[12–16] do not have the temporal resolution to resolve the details of the neutron pulse; they measure solely the neutron bang time. Only the streak-camera–based neutron temporal diagnostics (NTD's)[10,11] are capable of resolving the details of the neutron temporal history.

High-performance, layered cryogenic DT implosions[17] on the OMEGA laser[18] at the Laboratory for Laser Energetics (LLE) present a particular challenge in measuring the neutron history because of the high-DT neutron yields ($\sim 5 \times 10^{13}$) and a short neutron-production width (of the order of ~50 ps). The size of the cryogenic target shroud system[11] prevents the placement of the scintillator of the NTD system sufficiently close to the target to minimize Doppler broadening of the neutron pulse, which severely compromises the time resolution of the NTD.[10] A dedicated cryogenic-compatible neutron temporal diagnostic (cryoNTD) was developed at LLE to provide high-resolution neutron-emission measurements for D_2-filled cryogenic implosions,[11] but the placement of the streak camera close to the target chamber prevents recording data at high-DT yields because of the excessive neutron background. This article describes the setup of a new NTD system at LLE designed for high-performance, layered DT cryogenic implosions mounted in port P11 of the OMEGA target chamber (P11-NTD). The next section presents the setup of this system. The scintillator can be inserted as close as 9 cm from the target in cryogenic experiments without interfering with the cryogenic target systems. The streak camera is placed in a well-shielded location >10 m from the target, with an ~16-m-long optical relay system transporting the optical signal from the scintillator to the streak camera. The remaining sections report on the performance of the shielding setup, present the temporal impulse-response calibration procedure of the P11-NTD system, and analyze the first experimental results.

Setup of the Detector System

A CAD drawing of the P11-NTD system setup is shown in Fig. 145.34. The front-end scintillator insertion mechanism is a re-entrant into the OMEGA target chamber. A 6-mm-diam, 1-mm-thick plastic scintillator (Bicron BC422) (Ref. 19) is placed in a tungsten-alloy–shielded nose cone,[10] which can be inserted between 2 cm and 25 cm from the target. The first section of the optical relay system is housed inside the front end. The second section of the optical relay, the Target Bay wall periscope, is mounted to the OMEGA Target Bay shield wall. The optical path then leads from the OMEGA building into the OMEGA EP plenum, where the Rochester Optical Streak System (ROSS)[20] camera is mounted on an optical table.

1. Neutron Shielding

Historically, the streak camera of an NTD system has been placed close to the target chamber to minimize the length of the optical relay system.[10,11] This approach works very well for moderate yields ($<1 \times 10^{13}$ neutrons) but does not provide enough shielding to suppress the backgrounds for the high-DT neutron yields (up to 5×10^{13}) produced in cryogenic DT

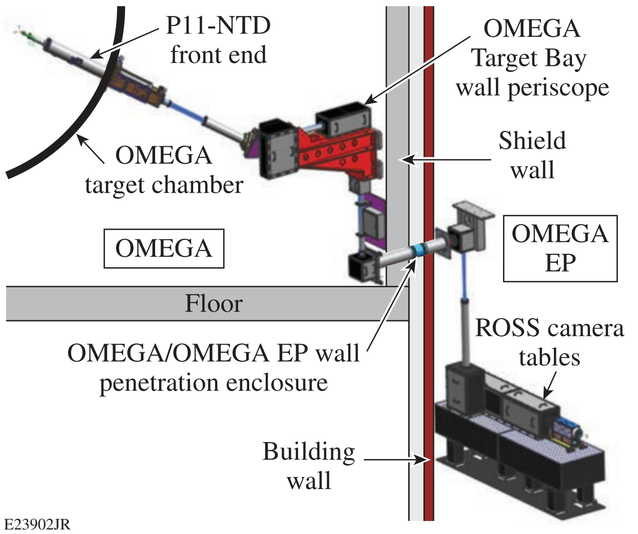

Figure 145.34
A CAD drawing of the P11-NTD (neutron-temporal-diagnostic) detector system integrated into the Omega Laser Facility. A front-end system re-entrant into the target chamber positions the scintillator distances between 2 to 25 cm from the target. An optical relay partially housed in the Target Bay wall periscope structure transports the scintillator light through a penetration in the OMEGA shield wall to a ROSS streak camera in the OMEGA EP plenum.

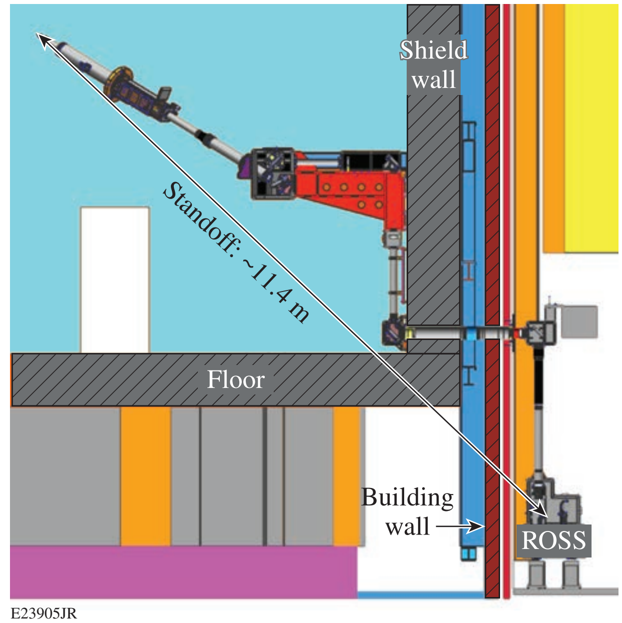

Figure 145.35
A CAD drawing of the P11-NTD shielding setup. The ROSS streak camera is placed 11.4 m from the target. The 60-cm-thick OMEGA target area floor and 80-cm-thick Target Bay shield wall provide most of the neutron shielding.

implosions on OMEGA.[17] To improve the shielding, the streak camera for the P11-NTD was placed behind the primary shield wall of the OMEGA target area in the OMEGA EP plenum (see Fig. 145.35). This location provides a standoff distance to the target of ~11.4 m, with ~1.7 m of concrete in the direct line of sight, which penetrates the OMEGA Target Bay floor, the OMEGA Target Bay retaining wall, and a brick facing wall. It is well known that the performance of a neutron shielding system depends not only on the shielding thickness in the direct line of sight, but also on the number and area of openings such as doors and holes in the shielded volume, which allow scattered neutrons to escape the target area.[21] Since there is a large ~1-m-diam hole under the target chamber, an ~1-m-diam beam tube that carries the OMEGA EP laser pulse from OMEGA EP to OMEGA for joint experiments,[22] and a number of doors into the room under the target area, the performance of this shielding will be worse than a simple estimate using the thickness of the direct line of sight would indicate.

2. Optical System

With the location of the streak camera in a separate building, a relatively complex 16.2-m-long optical path had to be designed. The light collection and transfer system (Fig. 145.36) transports the light from the scintillator to the input plane of ROSS. A fast three-element *f*/2 lens system collects the light from the scintillator with high efficiency. An optical system using a movable

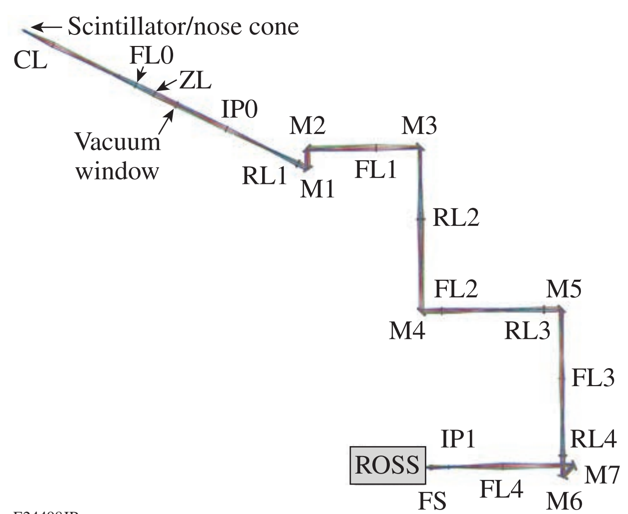

Figure 145.36
A drawing of the optical layout of the relay optics. A fast three-element *f*/2 lens system collects (CL) the light from the scintillator. A zoom (ZL) and field lens (FL0) relay the light through the vacuum window to an intermediate image plane (IP0). A four-stage optical relay, each consisting of an achromatic relay lens (RL1–4) and a field lens (FL1–4), transports the light from the first intermediate image using seven mirrors (M1–M7) to a second image plane (IP1). A three-element focus lens system (FS) focuses the light onto the slit of the streak camera.

zoom lens and a field lens relays the light from the scintillator to an intermediate image plane outside the target chamber. The location of the zoom lens is adjusted to keep the location of the intermediate image plane fixed. A four-stage optical relay, each consisting of an achromatic relay lens and a field lens, transports the light from the first intermediate image plane to an image plane close to the ROSS camera on the optical table in the OMEGA EP building. A three-element achromatic *f*/4 lens system focuses the light from the last image plane onto the photocathode of the ROSS. Since the optical path is not a straight line, seven turning mirrors were required to relay the light from the target chamber through the OMEGA shield wall into the OMEGA EP building. High-quality broadband antireflective (AR) coatings were used on the lenses with a typical loss of ~0.3% per surface, at normal incidence and dielectric high-reflective (HR) coatings were used on the mirrors with a reflectivity of >98.5% over the full spectral width of the scintillator emission from ~350 nm to 450 nm (Ref. 19). The total transmission of the system was estimated to be ~55%, with ~20% losses in the lens material, ~25% in the AR coatings as a result of the incident angular range, and ~10% in the HR coatings.

Even though the optical system is corrected for chromatic aberrations, the chromatic velocity dispersion caused by the change in index of refraction with wavelength will introduce a broadening of the impulse response. Using published values for the index of refraction[23] of the glasses used in the optical system, this effect was estimated for the optical ray passing through the center of all optics to broaden the full width at half maximum (FWHM) of the instrument response by ~8 ps given the spectrum of the scintillator light emission. This value should be considered an upper limit since most of the light passes through thinner glass than the center ray and consequently experiences less chromatic velocity dispersion.

In addition to the signal from the scintillator, light from the OMEGA fiducial system is delivered via an optical fiber and imaged onto the streak camera using an optical system internal to the ROSS camera. The OMEGA fiducial consists of a series of eight pulses spaced 548 ps apart and is amplified separately from the main laser pulse, split, and distributed to various diagnostic instruments for precision timing. This fiducial is also recorded on the P510 ultraviolet streak camera,[24] which measures the laser pulse shape. The common optical fiducial serves as a reference for both the neutron signal and the laser pulse, thereby enabling accurate timing of the NTD signal.

A similar system to the one that images the OMEGA fiducial on the photocathode is used to image the light from a 2-GHz comb generator onto the ROSS photocathode. The signal from this comb generator can be used to linearize the sweep speed of the streak camera.

Shielding Performance

Figure 145.37(a) shows the charge-coupled–device (CCD) image recorded by the P11-NTD diagnostics from a high-yield DT cryo shot (2.6×10^{13} neutrons). Four of the eight fiducial pulses are visible at the top of the image and six of the pulses from the 2-GHz comb generator are seen at the bottom. The CCD image shows very little background compared to the CCD image recorded with the previous-generation NTD system, called H5-NTD [see Fig. 145.38(a)], at the same yield level. The H5-NTD diagnostic also uses a ROSS streak camera, which is mounted ~3 m from the target in the Target Bay, shielded by 50 cm of CH in the direct line of sight and 10 cm of CH in all other directions. Figures 145.37(b) and 145.38(b) show the respective horizontal lineouts through the signals summed over the whole vertical width. Since the scintillator has a very fast rise time of <20 ps and a decay time of ~1.2 ns, the neutron-

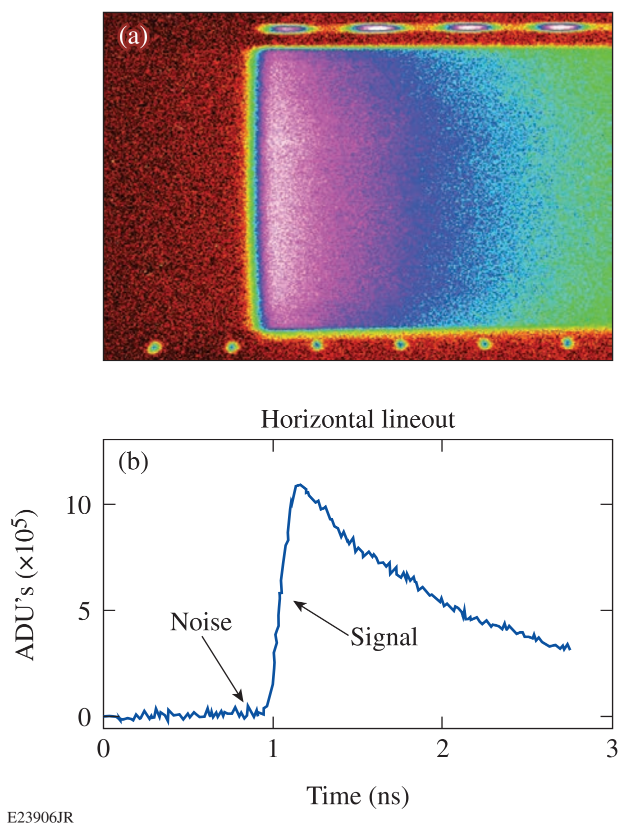

Figure 145.37
(a) A charge-coupled–device (CCD) image from P11-NTD from a high-yield DT cryo shot (2.6×10^{13} neutrons) and (b) a horizontal lineout through the signal summed over the whole vertical width in analog digital units (ADU's).

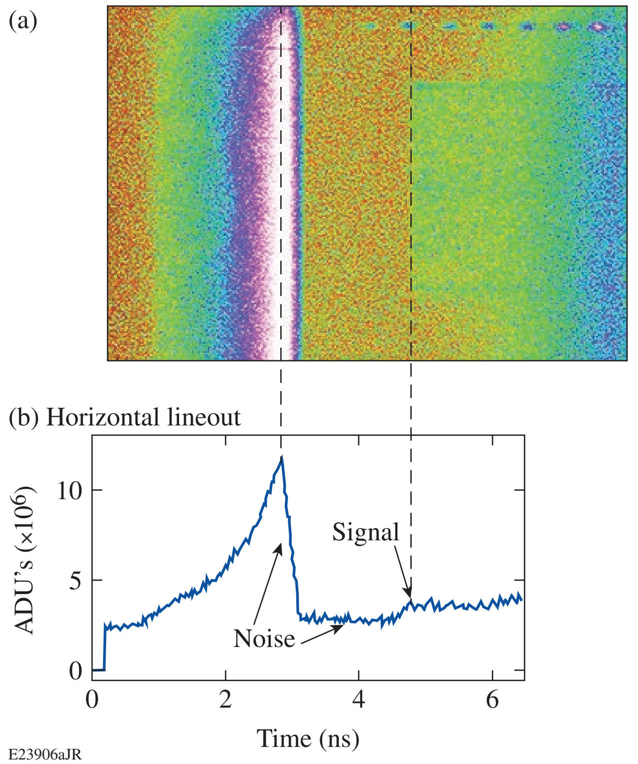

Figure 145.38
(a) A CCD image from H5-NTD from a high-yield DT cryo shot (2.6×10^{13} neutrons) and (b) horizontal lineout through the signal summed over the entire vertical width.

production history information is encoded in the leading edge of the pulse. The most-prominent feature of the background on the H5-NTD signal is a spike at ~2.5 ns, which is most likely caused by scattered neutron background present during the retrace of the streak, which starts a few microseconds after the sweep. The signal-to-noise on the P11-NTD system is ~50, which is an ~200× improvement over H5-NTD with a signal-to-noise ratio of ~0.25 at this yield level. As expected, this improvement is less than the difference the line-of-sight shielding and solid angle (10× improvement resulting from distance) would indicate.

Impulse-Response Calibration

The impulse response of the full P11-NTD including the scintillator, optical transport, and streak camera was measured using x rays from a target illuminated by a short laser pulse (10 ps) from OMEGA EP (see Fig. 145.39). The shielding from the 2-mm-thick tungsten alloy nose cone allows only hard x rays (>200 keV) to interact with the scintillator. Hard x rays are a reasonable substitute for neutrons to generate light in the scintillator because they interact mostly via Compton scattering in the CH scintillator substrate, which generates fast electrons.

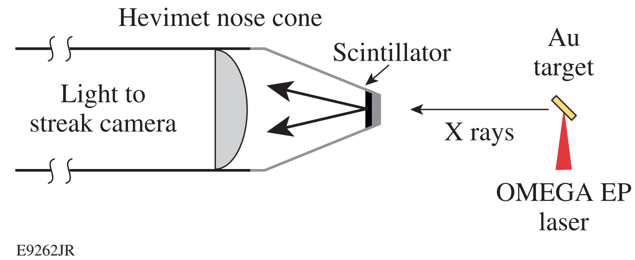

Figure 145.39
Setup of the calibration of the P11-NTD impulse response using x rays from an Au target illuminated by a short OMEGA EP laser pulse (10 ps). The 2-mm-thick Hevimet nose cone allows only hard x rays (>200 keV) to interact with the scintillator.

These >100-keV electrons generate electron-hole pairs similar to the MeV protons produced by the elastic scattering from an incident neutron. Even though the electron-hole pair density for the fast electron is significantly lower than that for a proton because of the difference in stopping power, it is a better substitute for neutron interaction relative to the excitation of the scintillator by UV irradiation, which interacts mostly with the dyes in the scintillator.[25]

For calibration, the OMEGA EP laser was defocused to spot sizes between 150 and 175 μm and the pulse energy was reduced to ~400 J to optimize the signal on the P11-NTD streak camera. The target was an Au foil of $500 \times 500 \times 10$-μm size. Figure 145.40(a) shows the temporal history of the signal from four laser shots with different focal-spot conditions for a 3-ns streak-camera sweep window. This signal is obtained by removing the effect of the long scintillator decay from the recorded signal using a "physical-modeling" approach for the deconvolution.[11] The signal n_i at the pixel location i is given as the recorded signal s_i minus the sum of all earlier neutron signals, which decay exponentially at the scintillator fall time τ, with Δt_p as the time separation of two pixels:

$$n_i = s_i - \sum_{j=0}^{i-1} n_j \exp\left[\frac{(i-j) \times \Delta t_p}{\tau}\right]. \qquad (1)$$

The signals from the x-ray calibration show a stable center section of approximately Gaussian shape with a FWHM of ~50±2 ps, as well as a shoulder (at the start of the signal) and a tail, which both vary with focus condition [see Fig. 145.40(a)]. The shoulder ahead of the main pulse is most likely caused by Cherenkov radiation from MeV Compton-scattered electrons in the *f*/2 collection system since a MeV electron gains ~20 ps/cm on light in glass. The tail after the pulse could be from subrela-

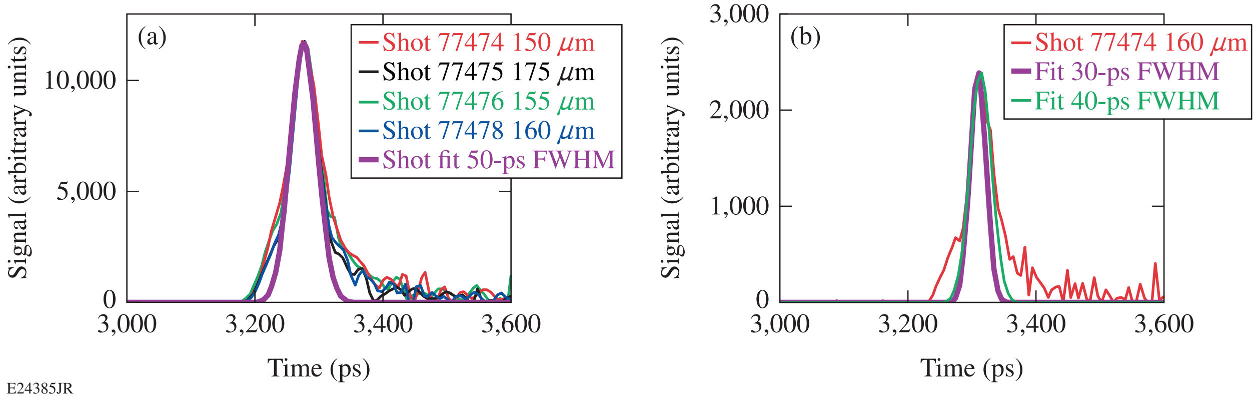

Figure 145.40
(a) Unfolded P11-NTD signals from the impulse response calibrations with a 3-ns sweep window at different focus conditions of the short-pulse laser. A 50-ps FWHM Gaussian fit matches the central part of the signal well. (b) Unfolded P11-NTD signals from the impulse response calibrations with a 1.5-ns sweep window; both a 30-ps and a 40-ps Gaussian are shown.

tivistic electrons generated in the laser–target interaction hitting the high-Z nose cone, generating hard x-ray bremsstrahlung. Both of these effects should scale with laser intensity since the slope of the electron energy distribution should be steeper for a lower laser intensity, which corresponds to a lower number of high- and medium-energy electrons.

A single shot was taken with a faster sweep speed corresponding to a 1.5-ns sweep window [see Fig. 145.40(b)]. Because of the degraded signal-to-noise, a stable fit of a Gaussian to the peak of the signal is no longer possible; several different fits with 30- to 40-ps FHWM are consistent with the data.

To infer the impulse response of the P11-NTD system, the width of the x-ray pulse must be subtracted. Since there is no independent measurement of the x-ray pulse duration, simple estimates must be used. A good estimate of the minimum x-ray pulse duration is ~15 ps because the laser pulse is ~10 ps long and the hot electrons generated in the laser–target interaction typically have a lifetime of a few picoseconds.[26] The maximum pulse duration cannot be longer than the shortest measured pulse duration with the 1.5-ns sweep of ~35 ps. Consequently, a reasonable estimate of the x-ray pulse duration is 25±10 ps. Subtracting the x-ray pulse in quadrature from the measured FWHM of the signal yields an impulse response of ~40±10 ps for the 3-ns sweep window and ~25±10 ps for the 1.5-ns sweep window, respectively.

Data Analysis

Figure 145.41 shows the inferred neutron rate from the deconvolved P11-NTD signal recorded on a recent DT cryogenic implosion on OMEGA with a neutron yield of ~4×10^{13}. The measured neutron temporal history is broadened by several

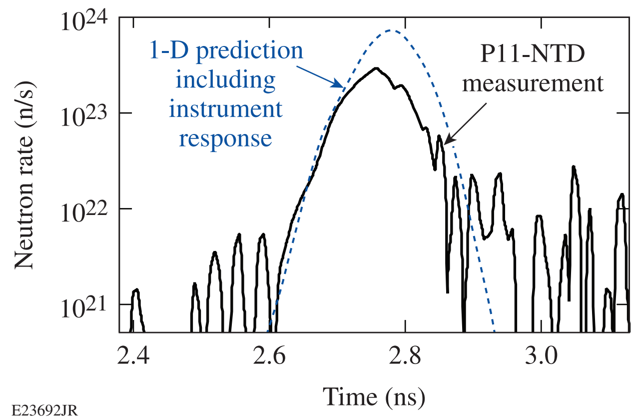

Figure 145.41
Unfolded P11-NTD signal from a high-yield cryo shot (neutron yield of ~4×10^{13}), compared to results from 1-D *LILAC* hydro simulations.

different mechanisms, which must be subtracted to measure the actual width of the neutron pulse from the target. Broadening the neutron energy spectrum caused by the high temperature of the thermonuclear plasma leads to an arrival time spread in the scintillator for DT neutrons:[10]

$$\Delta t_T^{\mathrm{DT}} = 122\sqrt{T} \times d\,, \tag{2}$$

where Δt_T^{DT} is the FWHM of the spread in picoseconds, d is the target-to-detector distance in meters, and T is the neutron-averaged ion temperature in keV. For a 10-cm distance of the P11-NTD scintillator to the target, this effect broadens the signal by ~25 ps at a 4-keV ion temperature, which is typical for most of the high-yield cryo implosions on OMEGA. Additionally, the finite neutron transit time through the scintillator $\Delta t_s = \Delta x / v_n$ broadens the signal by Δt_s^{DT} = 20 ps for a scintillator thickness of Δx = 1 mm and a DT neutron speed of v_n = 5.12 cm/ns. Since the shape of the neutron rate is not far from a Gaussian, the impulse response of the instrument, the thermal broadening, and the transit time spread can be subtracted from the measured FWHM of the signal in quadrature to infer the actual neutron pulse width. For a measured FWHM of the neutron signal of 82±2 ps, the resultant neutron pulse width is calculated to be 65±6 ps.

An alternative method of interpreting the experimental data is to convolve the calculated neutron rate from a simulation with the experimental broadening and compare it to the measured signal. Figure 145.41 compares the results of a 1-D *LILAC* simulation of the cryogenic implosion[17] convolved with the experimental broadening and the P11-NTD data. Since the absolute timing of the NTD instruments is typically of the order of 50 ps (Ref. 11), the simulation data were shifted by ~20 ps to better align with the rising edge of the experimental data. The simulation matches the experimental data very well on the rising edge over more than one order of magnitude in neutron rate. The experimental and simulated neutron rates start to deviate from each other close to the peak of the neutron pulse, with the experimental rate significantly lower than the simulation. This deviation is believed to be caused by 3-D effects, which mix cold material into the hot core plasma, quenching the neutron-production rate earlier than expected in the 1-D simulations.[7]

Summary and Outlook

A new neutron temporal diagnostic (P11-NTD) has been developed to measure the temporal history of the neutron production in high-yield, high-performance cryogenic DT implosions on OMEGA. The ROSS streak camera recording system was placed ~11 m from target chamber center behind the primary shield wall, which reduced the neutron background by a factor of ~200. The remote location of the streak camera required the construction of a complex 16.2-m-long image relay to transport the light from the scintillator to the streak camera. The impulse response of the P11-NTD system was measured using hard x rays generated from the interaction of the 10-ps OMEGA EP laser pulse with an Au target. With the standard 3-ns sweep window an impulse response of ~40±10 ps was inferred, which makes it possible to measure ~65-ps FWHM neutron pulses with an accuracy of ~10%. Preliminary measurements of the impulse response of the system using a 1.5-ns sweep window showed an improved impulse response of ~25±10 ps, which would enable the P11-NTD to measure ~50-ps FWHM neutron pulses with ~10% accuracy once this mode of operation is fully validated.

The technique of placing the streak camera of a NTD system outside the bioshield could be relatively easily adapted to larger ICF facilities like the National Ignition Facility (NIF)[27] or Laser Mégajoule (LMJ).[28] With a typical distance of the shield wall of ~15 m from the target, an NTD on these facilities would need an ~20-m-long optical relay, which could be designed without compromising the temporal resolution. Given the much-higher neutron yields at the NIF or LMJ, the constraints on the optical transmission of the relay system are significantly relaxed and a narrowband (2- to 10-nm) optical filter at the peak of the scintillator emission spectrum could be used to minimize the chromatic group velocity dispersion.

ACKNOWLEDGMENT

This material is based upon work supported by the Department of Energy National Nuclear Security Administration under Award Number DE-NA0001944, the University of Rochester, and the New York State Energy Research and Development Authority. The support of DOE does not constitute an endorsement by DOE of the views expressed in this article.

REFERENCES:

1. J. H. Nuckolls, Phys. Today **35**, 24 (1982).

2. R. S. Craxton, K. S. Anderson, T. R. Boehly, V. N. Goncharov, D. R. Harding, J. P. Knauer, R. L. McCrory, P. W. McKenty, D. D. Meyerhofer, J. F. Myatt, A. J. Schmitt, J. D. Sethian, R. W. Short, S. Skupsky, W. Theobald, W. L. Kruer, K. Tanaka, R. Betti, T. J. B. Collins, J. A. Delettrez, S. X. Hu, J. A. Marozas, A. V. Maximov, D. T. Michel, P. B. Radha, S. P. Regan, T. C. Sangster, W. Seka, A. A. Solodov, J. M. Soures, C. Stoeckl, and J. D. Zuegel, Phys. Plasmas **22**, 110501 (2015).

3 O. A. Hurricane, D. A. Callahan, D. T. Casey, E. L. Dewald, T. R. Dittrich, T. Döppner, M. A. Barrios Garcia, D. E. Hinkel, L. F. Berzak Hopkins, P. Kervin, J. L. Kline, S. Le Pape, T. Ma, A. G. MacPhee, J. L. Milovich, J. Moody, A. E. Pak, P. K. Patel, H.-S. Park, B. A. Remington, H. F. Robey, J. D. Salmonson, P. T. Springer, R. Tommasini, L. R. Benedetti, J. A. Caggiano, P. Celliers, C. Cerjan, R. Dylla-Spears, D. Edgell, M. J. Edwards, D. Fittinghoff, G. P. Grim, N. Guler, N. Izumi, J. A. Frenje, M. Gatu Johnson, S. Haan, R. Hatarik, H. Herrmann, S. Khan, J. Knauer, B. J. Kozioziemski, A. L. Kritcher, G. Kyrala, S. A. Maclaren, F. E. Merrill, P. Michel, J. Ralph, J. S. Ross, J. R. Rygg, M. B. Schneider, B. K. Spears, K. Widmann, and C. B. Yeamans, Phys. Plasmas **21**, 056314 (2014).

4. M. R. Gomez *et al*., Phys. Plasmas **22**, 056306 (2015).

5. J. A. Frenje, C. K. Li, F. H. Séguin, J. Deciantis, S. Kurebayashi, J. R. Rygg, R. D. Petrasso, J. Delettrez, V. Yu. Glebov, C. Stoeckl, F. J. Marshall, D. D. Meyerhofer, T. C. Sangster, V. A. Smalyuk, and J. M. Soures, Phys. Plasmas **11**, 2798 (2004).

6. I. V. Igumenshchev, W. Seka, D. H. Edgell, D. T. Michel, D. H. Froula, V. N. Goncharov, R. S. Craxton, L. Divol, R. Epstein, R. Follett, J. H. Kelly, T. Z. Kosc, A. V. Maximov, R. L. McCrory, D. D. Meyerhofer, P. Michel, J. F. Myatt, T. C. Sangster, A. Shvydky, S. Skupsky, and C. Stoeckl, Phys. Plasmas **19**, 056314 (2012).

7. P. B. Radha, T. J. B. Collins, J. A. Delettrez, Y. Elbaz, R. Epstein, V. Yu. Glebov, V. N. Goncharov, R. L. Keck, J. P. Knauer, J. A. Marozas, F. J. Marshall, R. L. McCrory, P. W. McKenty, D. D. Meyerhofer, S. P. Regan, T. C. Sangster, W. Seka, D. Shvarts, S. Skupsky, Y. Srebro, and C. Stoeckl, Phys. Plasmas **12**, 056307 (2005).

8. G. F. Knoll, *Radiation Detection and Measurement*, 4th ed. (John Wiley, Hoboken, NJ, 2010).

9. G. J. Schmid, R. L. Griffith, N. Izumi, J. A. Koch, R. A. Lerche, M. J. Moran, T. W. Phillips, R. E. Turner, V. Yu. Glebov, T. C. Sangster, and C. Stoeckl, Rev. Sci. Instrum. **74**, 1828 (2003).

10. R. A. Lerche, D. W. Phillion, and G. L. Tietbohl, Rev. Sci. Instrum. **66**, 933 (1995).

11. C. Stoeckl, V. Yu. Glebov, S. Roberts, T. C. Sangster, R. A. Lerche, R. L. Griffith, and C. Sorce, Rev. Sci. Instrum. **74**, 1713 (2003).

12. R. A. Lerche *et al*., Rev. Sci. Instrum. **59**, 1697 (1988).

13. J-P. Garçonnet *et al*., Rev. Sci. Instrum. **63**, 4871 (1992).

14. C. Stoeckl, V. Yu. Glebov, J. D. Zuegel, D. D. Meyerhofer, and R. A. Lerche, Rev. Sci. Instrum. **73**, 3796 (2002).

15. V. Yu. Glebov, D. D. Meyerhofer, T. C. Sangster, C. Stoeckl, S. Roberts, C. A. Barrera, J. R. Celeste, C. J. Cerjan, L. S. Dauffy, D. C. Eder, R. L. Griffith, S. W. Haan, B. A. Hammel, S. P. Hatchett, N. Izumi, J. R. Kimbrough, J. A. Koch, O. L. Landen, R. A. Lerche, B. J. MacGowan, M. J. Moran, E. W. Ng, T. W. Phillips, P. M. Song, R. Tommasini, B. K. Young, S. E. Caldwell, G. P. Grim, S. C. Evans, J. M. Mack, T. Sedillo, M. D. Wilke, D. C. Wilson, C. S. Young, D. Casey, J. A. Frenje, C. K. Li, R. D. Petrasso, F. H. Séguin, J. L. Bourgade, L. Disdier, M. Houry, I. Lantuejoul, O. Landoas, G. A. Chandler, G. W. Cooper, R. J. Lepeer, R. E. Olson, C. L. Ruiz, M. A. Sweeney, S. P. Padalino, C. Horsfield, and B. A. Davis, Rev. Sci. Instrum. **77**, 10E715 (2006).

16. Q. Tang *et al*., Rev. Sci. Instrum. **85**, 046108 (2014).

17. V. N. Goncharov, T. C. Sangster, R. Betti, T. R. Boehly, M. J. Bonino, T. J. B. Collins, R. S. Craxton, J. A. Delettrez, D. H. Edgell, R. Epstein, R. K. Follet, C. J. Forrest, D. H. Froula, V. Yu. Glebov, D. R. Harding, R. J. Henchen, S. X. Hu, I. V. Igumenshchev, R. Janezic, J. H. Kelly, T. J. Kessler, T. Z. Kosc, S. J. Loucks, J. A. Marozas, F. J. Marshall, A. V. Maximov, R. L. McCrory, P. W. McKenty, D. D. Meyerhofer, D. T. Michel, J. F. Myatt, R. Nora, P. B. Radha, S. P. Regan, W. Seka, W. T. Shmayda, R. W. Short, A. Shvydky, S. Skupsky, C. Stoeckl, B. Yaakobi, J. A. Frenje, M. Gatu-Johnson, R. D. Petrasso, and D. T. Casey, Phys. Plasmas **21**, 056315 (2014).

18. T. R. Boehly, D. L. Brown, R. S. Craxton, R. L. Keck, J. P. Knauer, J. H. Kelly, T. J. Kessler, S. A. Kumpan, S. J. Loucks, S. A. Letzring, F. J. Marshall, R. L. McCrory, S. F. B. Morse, W. Seka, J. M. Soures, and C. P. Verdon, Opt. Commun. **133**, 495 (1997).

19. Saint-Gobain Crystals, Newbury, OH 44065 (see http://www.crystals.saint-gobain.com/).

20. R. A. Lerche *et al*., Rev. Sci. Instrum. **75**, 4042 (2004).

21. C. Stoeckl, M. Cruz, V. Yu. Glebov, J. P. Knauer, R. Lauck, K. Marshall, C. Mileham, T. C. Sangster, and W. Theobald, Rev. Sci. Instrum. **81**, 10D302 (2010).

22. C. Stoeckl, J. A. Delettrez, J. H. Kelly, T. J. Kessler, B. E. Kruschwitz, S. J. Loucks, R. L. McCrory, D. D. Meyerhofer, D. N. Maywar, S. F. B. Morse, J. Myatt, A. L. Rigatti, L. J. Waxer, J. D. Zuegel, and R. B. Stephens, Fusion Sci. Technol. **49**, 367 (2006).

23. Schott North America, Inc., Elmsford, NY 10523 (see http://www.us.schott.com).

24. W. R. Donaldson, R. Boni, R. L. Keck, and P. A. Jaanimagi, Rev. Sci. Instrum. **73**, 2606 (2002).

25. Y. Arikawa *et al*., *2007 Annual Progress Report*, 47, Institute for Laser Engineering, Osaka University, Osaka, Japan (February 2008).

26. W. Theobald, A. A. Solodov, C Stoeckl, K. S. Anderson, F. N. Beg, R. Epstein, G. Fiksel, E. M. Giraldez, V. Yu. Glebov, H. Habara, S. Ivancic, L. C. Jarrott, F. J. Marshall, G. McKiernan, H. S. McLean, C. Mileham, P. M. Nilson, P. K. Patel, F. Pérez, T. C. Sangster, J. J. Santos, H. Sawada, A. Shvydky, R. B. Stephens, and M. S. Wei, Nat. Commun. **5**, 5785 (2014).

27. J. D. Lindl and E. I. Moses, Phys. Plasmas **18**, 050901 (2011).

28. D. Besnard, J. Phys.: Conf. Ser. **112**, 012004 (2008).

The Role of HfO_2/SiO_2 Thin-Film Interfaces in Near-Ultraviolet Absorption and Pulsed-Laser Damage

Introduction

It has been well established that nanosecond-pulse laser damage of multilayer coatings comprised of HfO_2/SiO_2 pairs in the near-ultraviolet (near-UV) spectral range is initiated in the high-index HfO_2 component of the coating. Still, very limited information about optical and structural properties of interfacial areas between layers renders interfaces as a probable source of enhanced absorption and damage. The reduced E-field design,[1] which moves intensity peaks away from interfaces into the more-damage–resistant SiO_2 layer, frequently improves damage threshold[2] but does not clarify the role of interfaces in laser damage. The only (to our knowledge) study[3] directly addressing interface absorption and its role in pulsed laser damage used a 1064-nm laser wavelength, with e-beam–deposited metal oxides (including HfO_2) and SiO_2 as high- and low-index materials, respectively. In that study, based on comparative absorption and damage-threshold measurements for half-wave stacks with numerous interfaces and a single-layer high-index material, HfO_2/SiO_2 interfaces made a significant contribution to total absorption and produced lower damage thresholds compared to a single HfO_2 layer. In this work a similar approach is used, but with different coatings designs, to study the contribution of HfO_2/SiO_2 interfaces to absorption in the near-UV and their role in the nanosecond-pulse damage initiation. One of the study goals is to explore how interfaces perform in coatings with different porosity and packing density. For this purpose the coatings were deposited using two techniques: (1) conventional electron-beam evaporation, typically producing rather porous films, and (2) ion-beam sputtering, which creates very densely packed films with sharp interfaces.[4] Despite the difference in thin-film structure, we found that in both cases the interfaces contribute insignificantly to total absorption and are not the main source of damage initiation.

Experimental

The coatings containing HfO_2 and SiO_2 materials were manufactured using either e-beam evaporation with a rate of 1.2 Å/s and 4.6 Å/s for HfO_2 and SiO_2, respectively, and an oxygen backfill pressure of 2×10^{-4} Torr, or reactive ion-beam sputtering, with no assist ion gun, and post-deposition annealing at 300°C for 8 h. The two types of coating samples—single HfO_2 layer and HfO_2/SiO_2 multilayer—were manufactured using a design shown schematically in Fig. 145.42. In the case of e-beam deposition, both samples were prepared in a single vacuum cycle run using shutters beneath the single-layer sample during thin SiO_2 layer deposition. This approach ensured that exactly the same HfO_2 material and deposition conditions were used for either film formation. The ion-beam–sputtered

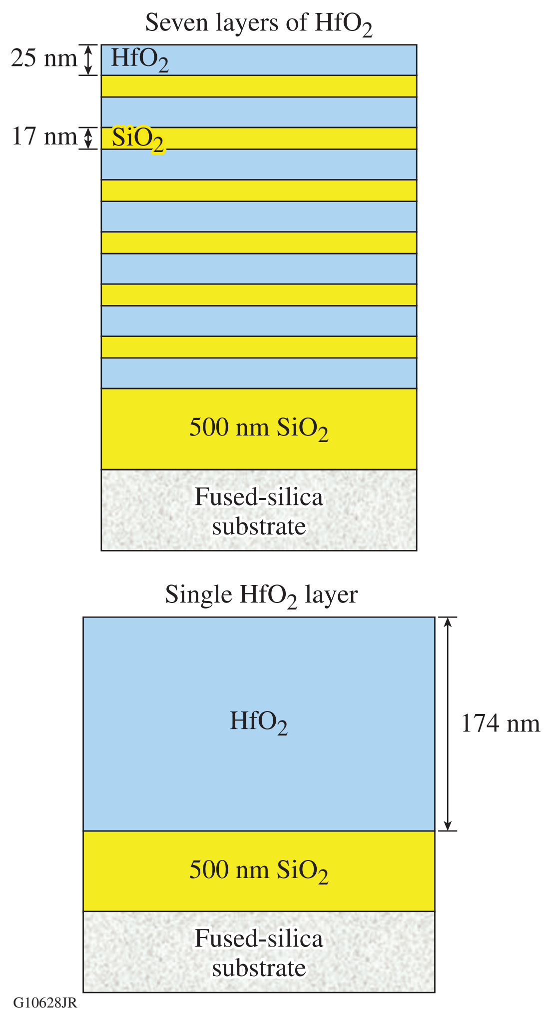

Figure 145.42
Schematic of the film containing seven HfO_2 layers separated by narrow SiO_2 layers and a single layer of HfO_2 film.

coatings were prepared in two separate coating depositions because of hardware limitations. Based on the high reproducibility of the sputtered-coating optical parameters measured for a number of runs, we anticipate that it should not affect the outcome of the experiment.

It is important to note here that a comparative laser-damage study imposes a few stringent requirements on the thin-film design and the resulting laser intensities inside the films. The thin-film structure should not change with the increasing HfO_2 layer thickness (the deposition conditions described above were selected to accomplish this goal); the total integrated HfO_2 layer thickness should be the same for single-layer and multilayer films, and E-field intensities inside both types of film samples must be comparable (preferably very close in value). To fulfill these requirements, HfO_2 single-layer films and HfO_2/SiO_2 multilayer films were manufactured with a total HfO_2 material optical thickness equal to one wave at 355 nm, which corresponds to a physical thickness of 174 nm. The multilayer film was comprised of seven HfO_2 layers, each 25 nm thick, separated by 17-nm-thick SiO_2 layers (see Figs. 145.42 and 145.43).

The thickness of the SiO_2 layers in the multilayer film (seven-layer film for future reference) was optimized to produce an E-field peak and average intensity as close as possible to the E-field intensity in the single-layer film (see Fig. 145.44). High-resolution transmission electron microscopy (TEM) along with x-ray diffraction (XRD) analysis (depicted in Fig. 145.45) reveals a fully amorphous, highly homogeneous film structure for both the seven-layer and single-layer sputtered films. The seven-layer film's interfaces [Fig. 145.45(a)] are sharp, have a roughly estimated width of 2 nm to 4 nm, and indicate no locally increased defect density. The e-beam–evaporated films were also mostly amorphous, but interfaces were not as clearly defined compared to the sputtered films [(see Fig. 145.43(c)].

The coatings were deposited on polished fused-silica substrates with a 500-nm-thick SiO_2 layer that served as an

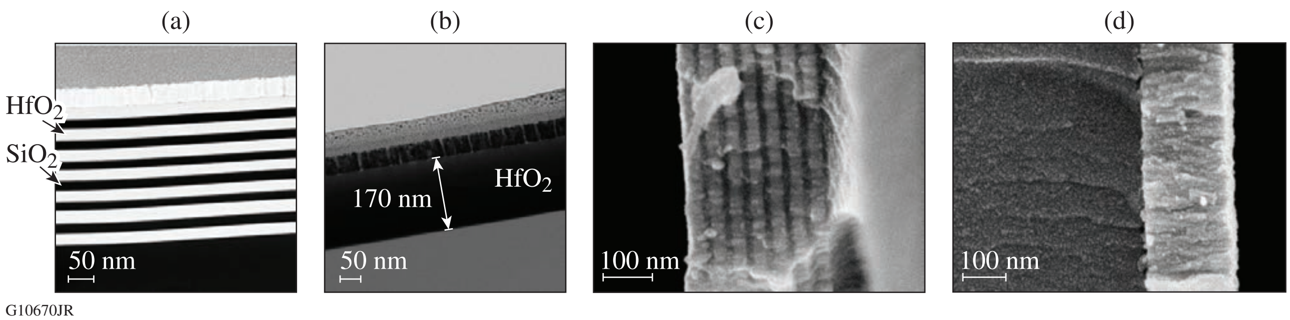

Figure 145.43
Transmission electron microscopy (TEM) images of sputtered HfO_2 films: (a) seven layer and (b) single layer. The top-most conductive layer in (a) and (b) is for TEM imaging purposes only. Electron microscopy images of electron-beam–deposited HfO_2 films: (c) seven layer and (d) single layer.

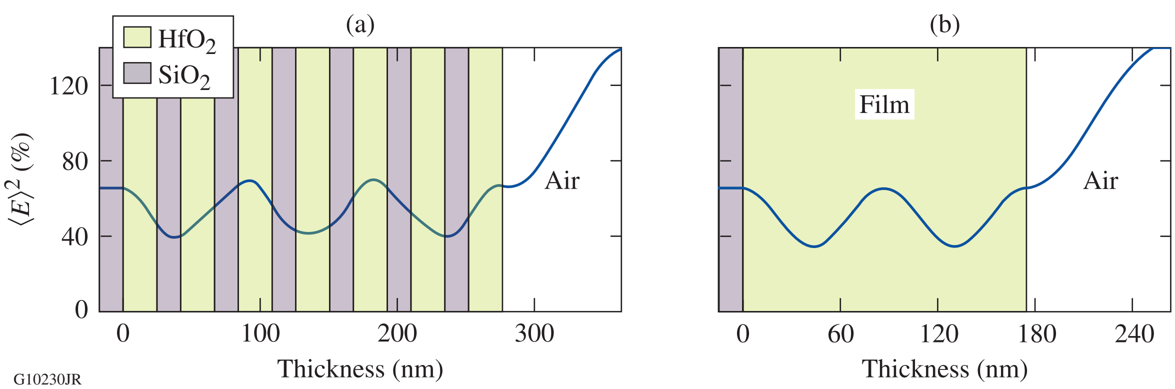

Figure 145.44
E-field intensity distribution in (a) seven-layer and (b) single-layer films.

(a) (b)

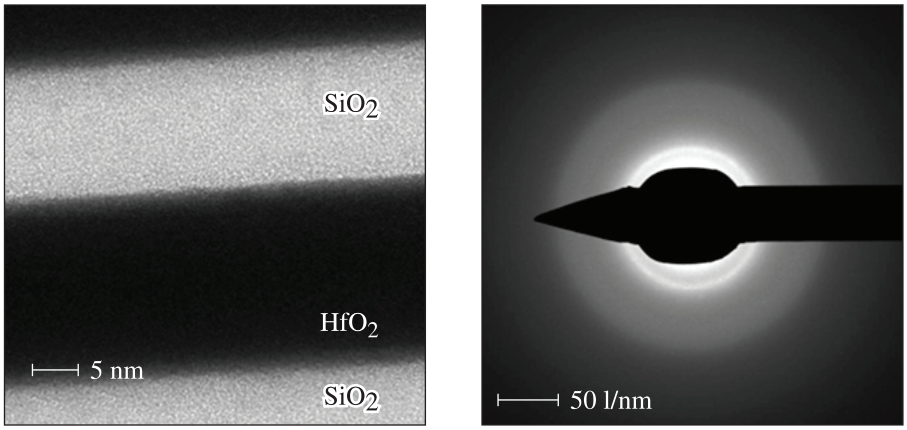

G10632JR

Figure 145.45
(a) A high-resolution TEM image of a seven-layer sputtered film shows a homogeneous structure with sharp interfaces and no evidence of local increased defect density. (b) X-ray diffraction (XRD) analysis confirmed a fully amorphous structure in both types of sputtered film.

insulator from defects introduced into the substrate during the finishing process. While not fully suppressing damage initiation by these defects, introducing such an additional SiO_2 layer leads to distinct substrate defect-driven damage morphology, which could be easily separated from damage initiated inside the HfO_2 film or interfaces (see **Damage Thresholds**, p. 46).

The absorption of the samples was characterized using a continuous-wave, 355-nm laser along with the following two methods: laser calorimetry (LC) and photothermal heterodyne imaging (PHI). The LC method detects heat generated through absorption of laser light and conducted by the film to the calibrated detector located on the front sample surface.[5,6] This method delivers absolute absorption values with good accuracy. The PHI method is a pump–probe laser technique based on the scattering of the probe light caused by local heating of the material by a tightly focused modulated pump beam.[7,8] The PHI method has high sensitivity and submicron spatial resolution but is more suitable for relative measurements because it is very difficult to achieve absolute calibration. Also, since this method is based on modulation of the refractive index of the material, it might be sensitive to the presence of different materials in the multilayer film. For that reason, we will consider LC as the main method of absorption characterization and PHI only as a complementary method.

Laser irradiation of samples was conducted mostly in a 1-on-1 regime (single-pulse irradiation of each sample site) using either 351-nm, 1-ns pulses [at the Laboratory for Laser Energetics (LLE)] or 355-nm, 5-ns pulses [at the Laser Zentrum Hannover (LZH) facility]. The 5-ns pulses were also used with 100-Hz frequency for the multipulse irradiation testing (10,000 pulses in this case) of each site at a fixed laser fluence. In addition, to probe changes in the interfacial structure as compared to the HfO_2 film structure (see **Femtosecond Damage Behavior as a Sensitive Tool to Detect Structural Changes and Its Application to HfO_2/SiO_2 Interfaces**, p. 49), single-pulse irradiation with 1053-nm, 600-fs pulses was conducted for both types of samples in vacuum (to avoid the self-focusing effects in air). Damage was detected using 110×-magnification dark-field microscopy or 150×-magnification Nomarsky microscopy. Laser-damage morphology was further investigated using atomic force microscopy (AFM) and scanning laser microscopy (SLM) as high-resolution tools. The high-spatial-resolution study of damage morphology was essential for separating the contribution to damage from film defects and defects residing in a subsurface layer of the substrate. The latter defects gave rise to large damage craters of up to ~10 μm in diameter, which, after high-resolution mapping, were excluded from damage statistics.

Results and Discussion

1. Absorption Measurements

Absorption-measurement data may provide guidance for anticipated optical losses in the laser system and, in some cases, for nanosecond-pulse damage performance of HfO_2 films.[8] For this study, the total contribution to near-UV absorption in the seven-layer film can come from two sources: structural defects in HfO_2 layers of the film and defects residing within the interfacial structure (absorption inside SiO_2 layers is negligibly small).

Considering additivity, total absorption A_{total} may be presented as follows: $A^7_{total} = A_{HfO_2} + A_{interface}$ for the seven-layer film, and $A^1_{total} = A_{HfO_2}$ for the single-layer film, where the superscripts 7 and 1 represent seven-layer and single-layer films, respectively.

Consequently, since the total thickness of seven hafnia layers is equal to the thickness of the single-layer film, a large-enough contribution from interfaces should result in a larger total absorption for the seven-layer film as compared to the single-layer film. Absorption-measurement results are summarized in Table 145.V.

LC measurement results show, within a margin of error, nearly equal absorption in both seven-layer and single-layer film samples and almost two times higher absorption in the single-layer e-beam film as compared to seven-layer film. This result points to an insignificant contribution to absorption from interfaces.

The PHI method shows an even smaller relative absorption for a seven-layer film containing numerous interfaces that might be partially attributed (as discussed in **Experimental**, p. 43) to different conditions for signal formation (not just absorption) in single-layer and seven-layer films. Still, a 50% difference in the case of sputtered films and an even higher ratio for e-beam films indicates a small contribution from interfaces.

2. Damage Thresholds

The transparent nature of the coatings involved in this study required the careful separation of damage originating from film volume (seven-layer film or single-layer film) and from substrate–subsurface defects introduced during the substrate-finishing process. The presence of an isolating 500-nm-thick SiO_2 layer (see Fig. 145.42) leads to much deeper and larger damage craters initiated by substrate defects, compared to craters formed by absorption inside the HfO_2 layers. AFM mapping clearly reveals this difference (see Figs. 145.46 and 145.47) and allows one to exclude craters initiated by substrate defects from damage statistics.

To find the 351-nm, 1-ns damage threshold, ten sample sites were irradiated with a different laser fluence, and subsequent AFM mapping enabled us to acquire the damage-crater statistics depicted in Fig. 145.48. The thresholds were obtained by

Table 145.V: The 355-nm absorptance of seven-layer and single-layer films measured by laser calorimetry (LC) and photothermal heterodyne imaging (PHI) signals produced with a 355-nm pump laser.

Film type	LC (%)		PHI signal (μV)	
	Ion beam	e-beam	Ion beam	e-beam
Seven layers	0.14±0.01	0.015±0.001	31.5±0.5	0.24±0.10
Single layer	0.13±0.01	0.027±0.002	47.0±0.5	1.28±0.16

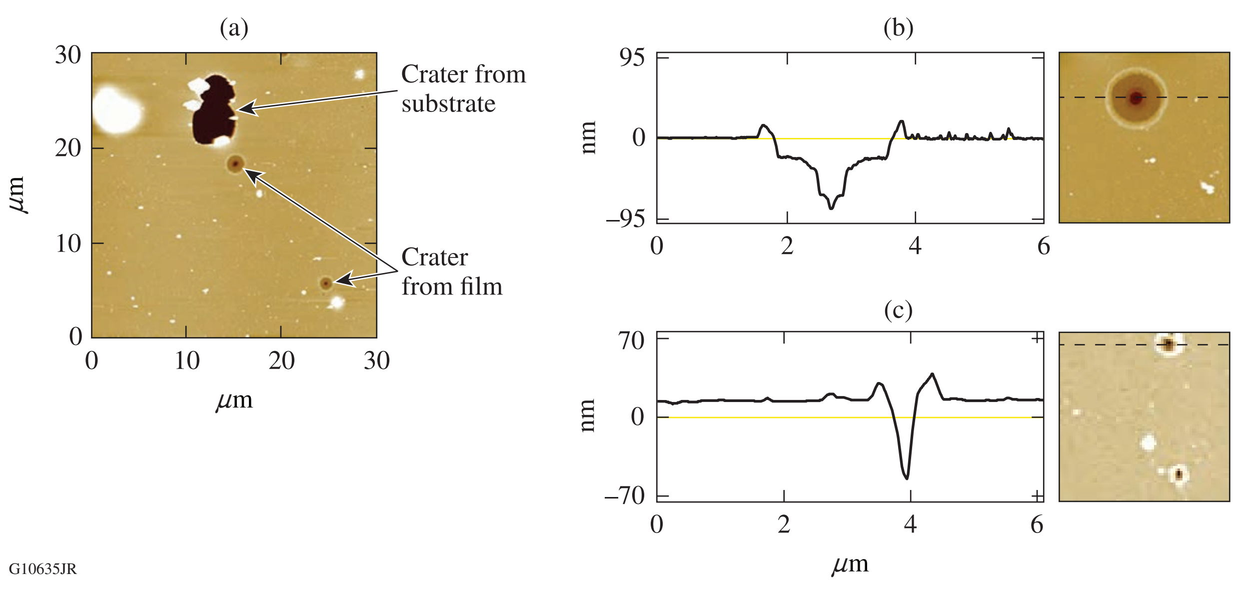

Figure 145.46
Atomic force microscopy mapping of damage morphology in sputtered films: (a) 30 × 30-μm image of the seven-layer film. Large (~10-μm-diam) craters originate from a location corresponding to substrate–subsurface defects and much smaller (≤2-μm-diam) craters originate from the film volume; (b) cross-sectional profile through a crater originating inside the seven-layer film; (c) cross-sectional profile through a crater originating inside the single-layer film.

linear fitting and extrapolation of the trend line to the fluence at which the number of craters is equal to zero. It should be noted that in the case of the e-beam–deposited, seven-layer film, only the upper limit of the threshold value was estimated because of collateral damage caused by substrate defects at laser fluences exceeding 8 J/cm^2. Below this fluence level no craters originating from the film volume were found using AFM mapping.

In the case of 355-nm, 5-ns pulse irradiation, damage morphology was analyzed using 150×-magnification optical microscopy and, for crater profiling, SLM (see Fig. 145.49). Similar to AFM mapping, SLM analysis made it possible to separate the damage originating within the film volume from the substrate-defect–driven damage. Damage thresholds were obtained from the damage probability curves shown in Fig. 145.50. The threshold measurement results are summarized in Table 145.VI.

The thresholds increase only marginally with the pulse-length increase (practically no scaling), which might be explained by different methodology used to derive the thresholds at the two

Table 145.VI: Damage thresholds of ion-beam–sputtered and e-beam–evaporated films.

Film type	Thresholds (J/cm^2)		
	351 nm, 1 ns		355 nm, 5 ns
	Ion beam	e-beam	Ion beam
Single layer	5.5±0.3	4.5±0.3	6.2±0.5
Seven layer	6.5±0.3	≥8	7.5±0.5

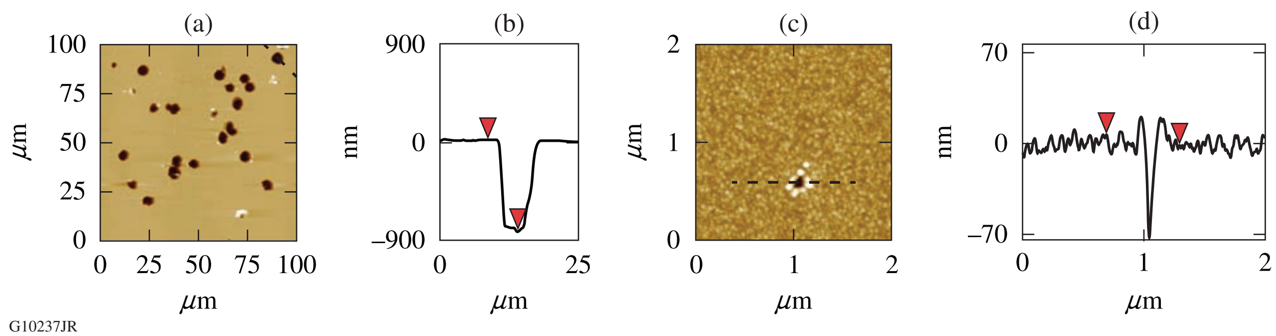

Figure 145.47
Atomic force microscopy mapping of damage morphology in e-beam–deposited films: (a) 100 × 100-μm image of the seven-layer film irradiated with a 5.9-J/cm^2 fluence. Damage morphology is dominated by craters initiated by substrate defects; (b) cross-sectional profile through a typical crater showing depth corresponding to substrate–subsurface absorbing-layer location (~800 nm); (c) 2 × 2-μm image of the single-layer film irradiated with a 4.6-J/cm^2 fluence, which shows a crater originating from within the HfO_2 film volume; and (d) cross-sectional profile through the crater shown in (c).

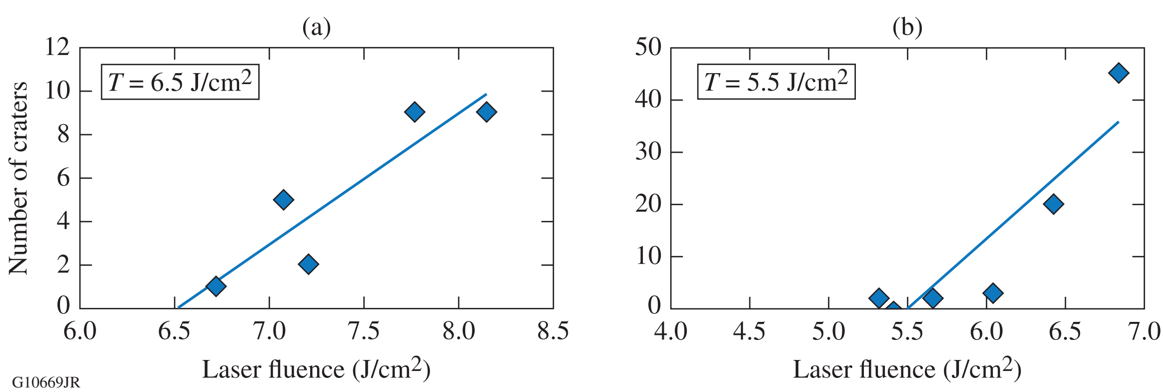

Figure 145.48
The number of damage craters originating from sputtered HfO_2 films as a function of 351-nm, 1-ns laser fluence for (a) seven-layer and (b) single-layer films. The thresholds are obtained by linear extrapolation to the fluence at which the number of craters is equal to zero.

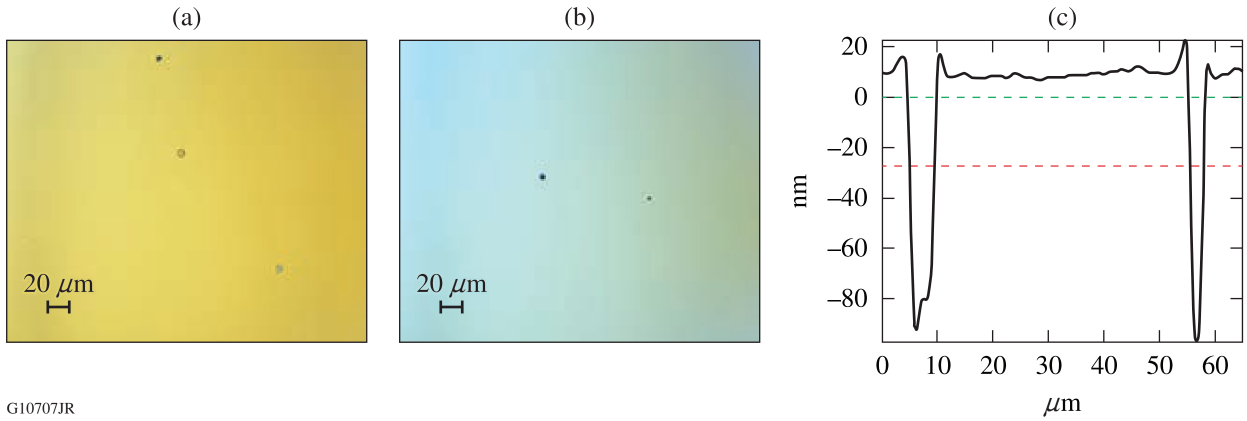

Figure 145.49
Optical microscope images of damage morphology of sputtered films irradiated at close-to-threshold conditions: (a) seven-layer film irradiated at 7.7 J/cm^2 and (b) single-layer film irradiated at 6.3 J/cm^2. (c) An example of crater cross-sectional analysis using scanning laser microscopy (SLM).

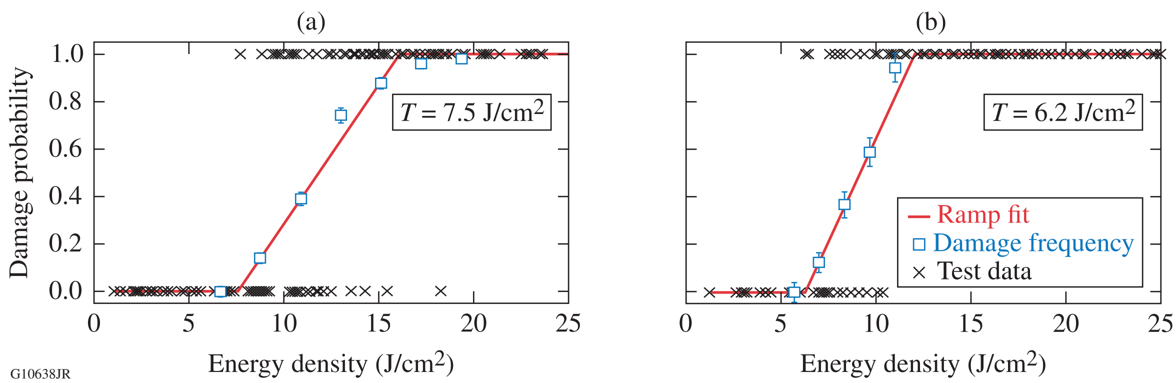

Figure 145.50
Damage-probability curves resulting from 355-nm, 5-ns irradiation of sputtered films: (a) seven-layer and (b) single-layer film. The thresholds are obtained by a linear extrapolation to zero probability.

different facilities (LLE and LZH). More importantly, these results obtained for thin films with distinctly different morphology—densely packed ion-beam–deposited films and highly porous e-beam films—demonstrate higher nanosecond-pulse damage resistance for the film containing numerous HfO_2/SiO_2 interfaces as compared to a single-layer HfO_2 film. Note that the E-field peak intensity in the seven-layer film is slightly (~7%) higher than that in the single-layer film, which means that the threshold ratio normalized by internal intensity would be even higher. Also, at close-to-threshold conditions, only a few damage sites (craters) are initiated in the sputtered seven-layer film [(see Fig. 145.48(a)], and at the same laser fluence of 6.5 J/cm^2 the number of craters initiated in the single-layer film exceeds 20 [(see Fig. 145.48(b)], therefore pointing to lower damage resistance of the single-layer film. All of these facts lead to the conclusion that HfO_2/SiO_2 interfaces are not a source of enhanced near-UV localized absorption and laser damage. One possible explanation for these findings comes from the hypothesis that the interfacial structure is similar to the film structure formed during co-deposition of HfO_2 and SiO_2. It was convincingly demonstrated that in co-deposited films, near-UV absorption is reduced and damage resistance becomes higher in HfO_2 films with an increased SiO_2 content.[9]

3. E-Field Intensity Distribution and Damage Morphology

A correlation between E-field intensity inside a coating and damage initiation is well established. One example is damage originating in nodular-coating defects where a large E-field may be generated.[10] To test the presence of such a link in this study, crater-depth distributions obtained at ~70% above threshold conditions using SLM (see Fig. 145.51) were compared to the E-field intensity distributions depicted in Fig. 145.44. One

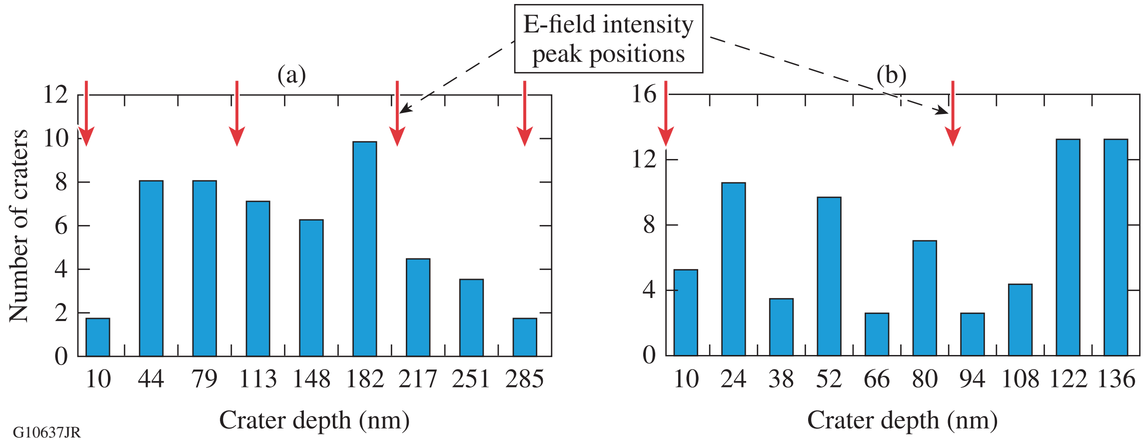

Figure 145.51
Crater-depth distributions obtained from SLM analysis for (a) seven-layer and (b) single-layer films.

can see that crater-depth distributions show no correlation with E-field peak positions; this observation does not change even when the depth bin size used to calculate the distribution is varied.

There are several reasons why a correlation was not observed: First, the intensity variation from the minimum to maximum value was not high for both types of film; the normalized intensity $\left(|E|^2\right)$ varied from 40% to 70% and from 34% to 65% in the seven-layer and single-layer films, respectively. For comparison, in standard quarter-wave reflectors, $|E|^2$ might vary from 0% to 100% (Ref. 11). Second, crater depth depends not only on the location of the localized absorber but also on the amount of energy locally deposited,[12] which leads to a distribution in the crater-depth values.

4. Femtosecond Damage Behavior as a Sensitive Tool to Detect Structural Changes and Its Application to HfO_2/SiO_2 Interfaces

The key to understanding the role of interfaces in pulsed laser damage is a knowledge of how the electronic structure changes during the spatial transition from HfO_2 to SiO_2 and vice versa. An important parameter here is a band gap of E_g and characteristics of the electronic defect states,[13,14] such as location in a gap (see Fig. 145.52), densities, and absorption coefficients. In the absence of structural data for interfaces, an alternative empirical approach is to study the interaction of subpicosecond laser pulses with optical materials—in this particular case, with a film containing numerous HfO_2/SiO_2 interfaces and a single-layer HfO_2 film. Femtosecond-pulse laser damage in dielectrics typically starts with the multiphoton ionization (MPI) process, which is very sensitive to band-gap and defect-state characteristics.[15,16] The sensitivity is linked to a possible change in the number of absorbed photons required to promote an electron into the conduction band, which leads to a dramatic change in the multiphoton absorption coefficient.[17] Since the same defect states might participate in multiphoton absorption of infrared light and single-photon absorption of UV light (see Fig. 145.52), a femtosecond damage study may indicate whether an interfacial structure is more or less damage resistant than an HfO_2 structure in the case of UV light and nanosecond pulses. In this study, the existence of such a correlation was tested by 1053-nm, 600-fs pulse irradiation (1-on-1 test) of single-layer and seven-layer samples. The damage thresholds T, normalized by internal E-field intensity

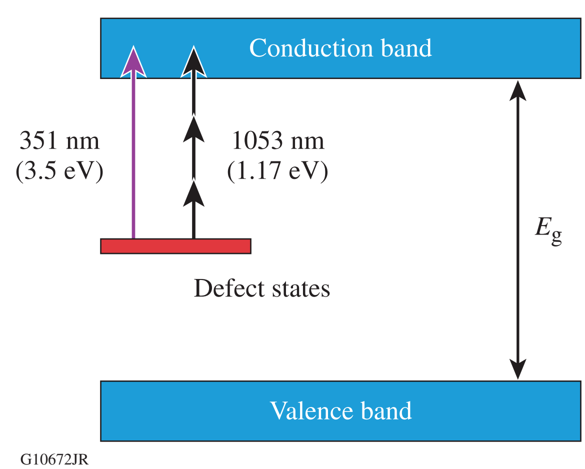

Figure 145.52
Schematic of the dielectric band structure with electronic defect states taking part in single-photon and multiphoton absorption promoting an electron into the conduction band.

[(average intensity was used for normalization because of slow changes across the film (see Fig.145.53)] showed a ratio of $T_{\text{seven layer}}/T_{\text{single layer}} \geq 1.1$ for both ion-beam–sputtered and e-beam–evaporated films.

This result points to a low contribution of interfaces to the MPI process and correlates well with higher near-UV, nanosecond-pulse damage resistance of the interfacial structure as compared to the HfO_2 film, in agreement with the 351-/355-nm threshold measurement results presented in **Damage Thresholds** (p. 46). This result also strongly supports the possibility that initial absorption—single photon for nanosecond pulses and multiphoton for femtosecond pulses—is initiated by the same structural defects.

5. Multipulse Irradiation

From a practical point of view, it is of interest to know how interfaces respond to multipulse, fixed-fluence irradiation. The typical behavior of coatings is characterized by the fatigue effect manifested by a lower threshold and increased scale of damage.[18] For this purpose, 10,000-pulse (355-nm, 5-ns) irradiation at a fixed laser fluence and a 100-Hz repetition rate was performed for seven-layer and single-layer films. The density of produced damage sites (craters) was calculated and compared with damage-site density produced using single-shot irradiation at a fluence slightly above the single-shot threshold. The fatigue effect was observed for both types of films but with a less-pronounced effect for the film with numerous interfaces. The seven-layer film showed a seven-fold increase in damage-site density compared to a 12-fold increase for a single-layer film. This result points to an interfacial structure that is less susceptible to absorbing-defect formation under near-UV light irradiation, as compared to the pure-HfO_2 material.

Conclusions

The role of ion-beam–sputtered and e-beam–evaporated HfO_2/SiO_2 film interfaces in near-UV absorption and nanosecond-pulse damage was investigated by comparing the damage performance of a film with numerous interfaces (seven HfO_2 layers) and a monolayer HfO_2 film. The films were characterized by an overall equal HfO_2 material thickness, comparable E-field intensity, and fully amorphous material structure.

The study revealed a low contribution of interfaces to near-UV absorption and higher nanosecond-pulse damage thresholds for a film with numerous interfaces as compared to a single-layer HfO_2 film. These results indicate that HfO_2/SiO_2 interfacial structures have a higher laser-damage resistance than a structure of a pure HfO_2 film.

The similarity of an interfacial HfO_2/SiO_2 structure to a structure formed during co-deposition of HfO_2 and SiO_2 materials, which is documented to have higher pulsed-laser-damage resistance as compared to a pure HfO_2 film material, may offer a possible explanation for these findings. A correlation found between near-UV, nanosecond-pulse and 1053-nm, 600-fs pulse damage of HfO_2 coatings used for this study allows one to suggest that the initial absorption (single photon for nanosecond pulses and multiphoton for femtosecond pulses) involves the same electronic defect states. The relevance of these results to other high-/low-index film material pairs requires additional studies.

ACKNOWLEDGMENT

This material is based upon work supported by the Department of Energy National Nuclear Security Administration under Award Number DE-NA0001944, the University of Rochester, and the New York State Energy Research and Development Authority. This work is also supported by the

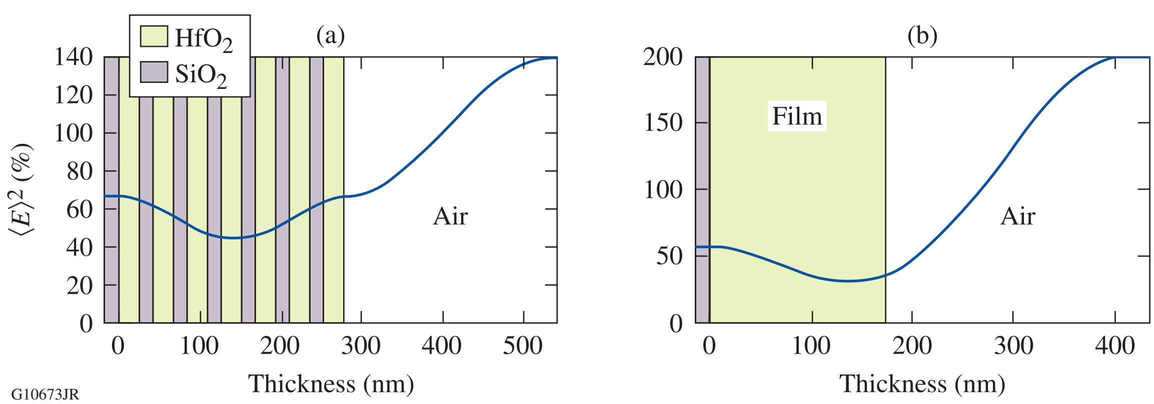

Figure 145.53
The distribution of 1053-nm E-field intensity in (a) seven-layer and (b) single-layer films.

German Federal Ministry of Education and Research within Ultra-Life project under contract #13N11558. The support of DOE does not constitute an endorsement by DOE of the views expressed in this article.

REFERENCES

1. J. H. Apfel, Appl. Opt. **16**, 1880 (1977).
2. D. H. Gill, B. E. Newnam, and J. McLeod, in *Laser Induced Damage in Optical Materials: 1977*, edited by A. J. Glass and A. H. Guenther, Nat. Bur. Stand. (U.S.), Spec. Publ. 509 (U.S. Government Printing Office, Washington, DC, 1977), pp. 260–270.
3. D. Ristau, X. C. Dang, and J. Ebert, in *Laser Induced Damage in Optical Materials: 1984*, edited by H. E. Bennett *et al*., Natl. Bur. Stand. (U.S.), Spec. Publ. 727 (U.S. Government Printing Office, Washington, DC, 1986), pp. 298–306.
4. H. K. Pulker, in *Optical Interference Coatings*, edited by N. Kaiser and H. K. Pulker, Springer Series in Optical Sciences, edited by A. Adibi *et al*. (Springer-Verlag, Berlin, 2003), pp. 131–154.
5. U. Willamowski, D. Ristau, and E. Welsch, Appl. Opt. **37**, 8362 (1998).
6. I. Balasa, L. Jensen, and D. Ristau, Proc. SPIE **8885**, 88851L (2013).
7. S. Berciaud *et al*., Phys. Rev. B **73**, 045424 (2006).
8. S. Papernov, A. Tait, W. Bittle, A. W. Schmid, J. B. Oliver, and P. Kupinski, J. Appl. Phys. **109**, 113106 (2011).
9. L. O. Jensen *et al*., Proc. SPIE **7842**, 784207 (2010).
10. X. Cheng *et al*., Appl. Opt. **53**, A62 (2014).
11. P. Baumeister, *Optical Coating Technology* (SPIE Optical Engineering Press, Bellingham, WA, 2004), pp. 9-56–9-57.
12. S. Papernov, in *Laser-Induced Damage in Optical Materials*, edited by D. Ristau (CRC Press/Taylor & Francis, Boca Raton, FL, 2014), Sec. I, Chap. 3, pp. 25–74.
13. A. S. Foster *et al*., Phys. Rev. B **65**, 174117 (2002).
14. T.-J. Chen and C.-L. Kuoa, J. Appl. Phys. **110**, 064105 (2011).
15. L. Gallais *et al*., Proc. SPIE **8530**, 85300K (2012).
16. W. Rudolph *et al*., Proc. SPIE **8885**, 888516 (2013).
17. L. V. Keldysh, Sov. Phys.-JETP **20**, 1307 (1965).
18. A. Hervy *et al*., Proc. SPIE **9237**, 92370J (2014).

A Chromatic-Aberration Diagnostic Based on a Spectrally Resolved Lateral-Shearing Interferometer

Spatiotemporal coupling in an ultrashort-pulse beam is an important feature that must be characterized for laser–matter interactions and focal-spot improvement. Pulse-front tilt (PFT) arising from a misaligned compressor-grating pair or a simple prism disperses the spatial and spectral envelope of the pulse at focus with respect to wavelength, thereby lowering the available peak power density.[1] Radial-group delay (RGD) arising in a circularly symmetric, refractive-image relay similarly smears the focal spot transversely and longitudinally.[2] Compensation schemes for PFT and RGD based on diffraction and refraction were proposed in Refs. 3 and 4. Space–time coupling can be beneficial in some experimental configurations. Spatial chirp in the beam obtains maximum spatial and spectral overlap at focus, creating a "temporal-focusing effect," which has been useful in the area of micromachining[5] and microscopy.[6] The wavefront-rotation effect introduced by focusing a pulse with PFT creates an angularly separated burst of attosecond pulses reflecting off the laser-induced plasma.[7]

A diagnostic is needed to compensate for and control the spatiotemporal effects, not only from well-defined optical systems but also from nonuniform optical properties such as in dielectric optical coatings. A second-harmonic, single-shot autocorrelator can be used to measure the pulse-front tilt angle[8] or the effect of pulse broadening caused by RGD.[9] Linear autocorrelation methods infer the angle or the curvature of the pulse-front delay by examining, in multiple steps, the fringes between two beams.[2] Other linear techniques are based on spectrally resolving spatial interference. These methods analyze the spectrum of the interference between two laterally sheared fields of the same test beam[10] or between the test and reference fields,[11] where the carrier terms are introduced by either temporal delay or relative tilt; direct fringe analysis can be employed for certain referenced schemes.[12] All these spectral interference methods require a separate system of beam splitters and combiners external to the spectrometer. Scanning the spectral interferogram with a fiber tip[13] or using phase diversity on a cylindrically symmetric beam[14]—both require multiple measurement steps and have been demonstrated. A rather unique scheme called STRIPED FISH[15] provides discrete samples of spectral slices with full two-dimensional (2-D) intensity and phase mapping at each slice by interfering each slice with a reference beam; however, spatial and spectral resolution of this method is poor.

A simpler, spectrally resolved lateral-shearing interferometer is proposed in this work. The separate preconditioning system introducing delay or tilt is replaced by a single Ronchi grating located in front of the entrance slit of a spectrometer. No moving parts are involved; therefore, calibration is performed only once. Full one-dimensional (1-D) chromatic aberrations can be characterized in a single-shot measurement.

The side and top views of the setup are schematically shown in Fig. 145.54, with the spectrometer system laid out linearly.

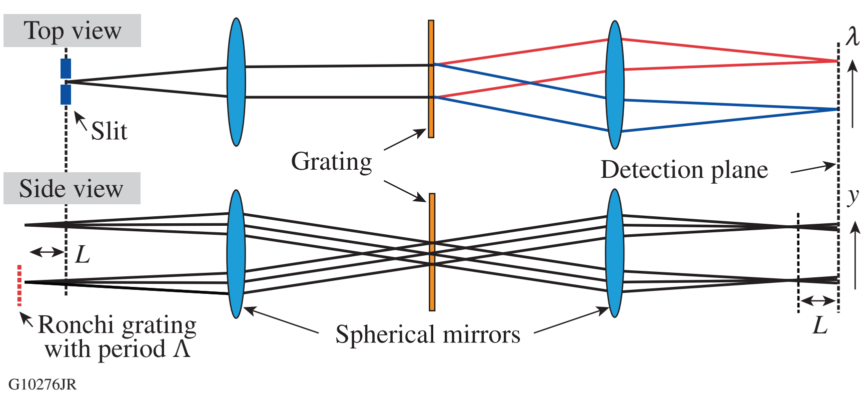

Figure 145.54
A schematic of a spectrally resolved lateral-shearing interferometer. The entrance slit is spectrally resolved in a tangential plane, whereas the sagittal image of the slit is interfered to create a sheared interferogram from which spatial phase can be extracted. Only zeroth- and first-order diffractions are shown in the side view. For convenience, the rays reflected by the spherical mirrors and the spectrometer grating are shown on the other side of the mirror as if they are passing through.

The top view representing the beam diffracting in the horizontal plane corresponds to a normal spectrometer system. The side view shows the beam diffracting through the Ronchi grating in the vertical plane. The detector images the spectrometer slit. The Ronchi plane is imaged before the detector plane; therefore, the first-order diffraction beams are sheared at the detector plane. If the beam is sampled at a fixed horizontal coordinate x_0 by the spectrometer slit, the field at the detector plane going through a Ronchi grating of periodicity Λ is represented by[16]

$$E(x_0, y, \omega) = \sum_{m=0,\pm 1,\ldots} \eta_m A\left(x_0, y + m\frac{2\pi cL}{\omega\Lambda}\right) \times \exp\left(i\frac{2\pi m}{\Lambda} y + i|m|\omega\tau\right), \tag{1}$$

where $A(x_0,y,\omega)$ is the spectral envelope and phase at position y at the entrance slit. The index m is the diffraction order and η_m is the diffraction efficiency at the mth order. The spatial coordinate x_0, hereafter, will not be shown. L is the distance from the Ronchi grating to the entrance slit and τ is the arrival time difference between the first- and zeroth-order diffraction beams; τ is sufficiently small that spectral fringes are not observed. The 1-D Fourier-domain analysis of the interferogram along the spatial axis can separate out the first harmonic H_1 (i.e., the interaction between fields at $m = 0$ and $m = \pm 1$) from dc and higher-order terms. With the phase of $A(y,\omega)$ defined as $\varphi(y,\omega)$, the first harmonic is

$$H_1 \sim \left|A(y,\omega)\right|^2 \exp\left(i\frac{2\pi cL}{\omega\Lambda}\frac{\partial\varphi}{\partial y}\right)\cos(\omega\tau)\exp\left(i\frac{2\pi}{\Lambda}y\right). \tag{2}$$

The phase of H_1, except for the carrier term, contains a phase derivative from which spectrally coupled 1-D spatial phase can be integrated. Purely spectral phase without spatial dependence cancels out in the derivative so it is not measurable in this approach.

Pulse-front delay (PFD) and RGD are linear and quadratic-phase components whose magnitudes vary linearly with the spectral deviation. The phase can be decomposed into chromatic and achromatic components, denoted as $g(y)$ and $f(y)$, respectively:

$$\varphi(y,\omega) = (\omega - \omega_0)\, g(y) + \frac{\omega}{c} f(y), \tag{3}$$

where $f(y)$ is an optical-path difference function in units of distance and $g(y)$ is a relative group delay in units of time; $f(y)$ can be represented as

$$f(y) = \theta_y\, y + y^2/(2R_y) + f_{HO}(y), \tag{4}$$

where θ_y and R_y are the tilt and radius of curvature in the y dimension, respectively, and $f_{HO}(y)$ is the remaining higher-order term. Likewise, $g(y)$ is the sum of linear, quadratic, and higher-order terms [$g_{HO}(y)$]:

$$g(y) = \alpha\left(\frac{y}{r}\right) + \beta\left(\frac{y}{r}\right)^2 + g_{HO}(y), \tag{5}$$

where r is the radius of the beam and α = PFD(r)–PFD(0) and β = RGD(r)–RGD(0). Equations (3) and (5) suggest that the PFD shifts the carrier-phase offset linearly with respect to frequency change, and RGD modifies the carrier frequency linearly with respect to frequency change. The fringe patterns with PFD or RGD dominant cases are illustrated in Fig. 145.55.

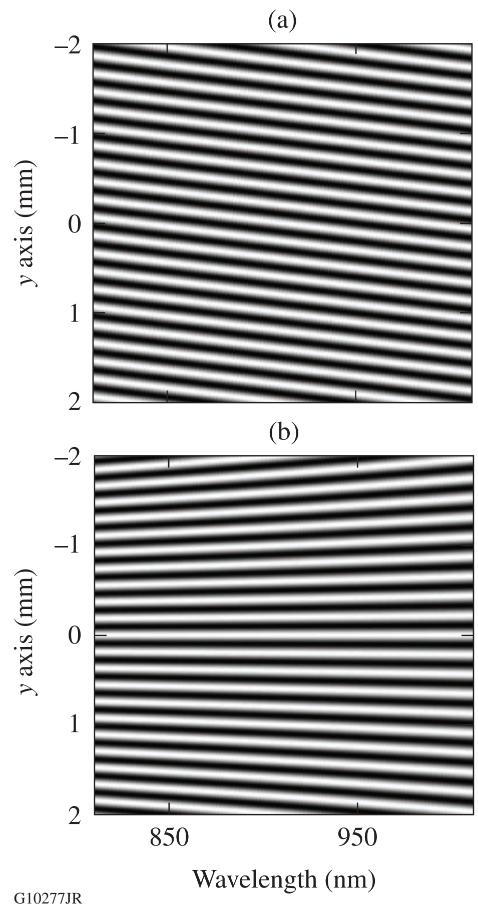

Figure 145.55
Examples of fringe patterns. (a) The tilted fringe indicates pulse-front tilt and (b) the fanning-out fringe indicates radial-group delay.

The algebraic form of $(2\pi cL)/(\omega\Lambda) \cdot \partial\varphi/\partial y$, consistent with Eqs. (3)–(5), is

$$\frac{2\pi cL}{\omega\Lambda}\frac{\partial\varphi}{\partial y} \triangleq \Delta\varphi = c_1 + c_2 y + \left(c_3 + c_4 y\right)\left(\lambda - \lambda_0\right). \tag{6}$$

Comparing Eqs. (4) and (5), the coefficients of Eq. (6) are determined as

$$c_1 = 2\pi \frac{L}{\Lambda}\theta_y, \tag{7}$$

$$c_2 = 2\pi \frac{L}{R_y \Lambda}, \tag{8}$$

$$c_3 = -\frac{2\pi c}{\lambda_0}\frac{L\alpha}{\Lambda r}, \tag{9}$$

$$c_4 = -\frac{4\pi c}{\lambda_0}\frac{L\beta}{\Lambda r^2}. \tag{10}$$

Extracting RGD and PFD information directly from the low-order polynomial fit of $\Delta\varphi$ is less ambiguous than fitting Eq. (3) to the numerically integrated data of $\Delta\varphi$ because of the arbitrary integration constant.

A test bed was set up to measure RGD in a simple refractive system, as shown in Fig. 145.56. The broadband source is a spectrally incoherent, superluminescent light-emitting diode (SLED) with spectral density from 968 to 1076 nm. An actual ultrashort pulse was not required for the demonstration because only relative phases are required to characterize space–time coupling. The SLED is coupled to a single-mode fiber whose tip is used as a point source. A 200-mm-focal-length concave mirror collimates the diverging beam from the fiber tip. The off-axis configuration of the concave mirror introduces astigmatism, but it is not important since the wavefront must be collimated only in the sagittal plane parallel to the spectrometer slit. The collimated beam is sent to the test telescope (L3 and L4) through a 5-mm input aperture. The aperture plane is imaged to M2 and to the slit. The imaging requirement minimizes the chromatic effect on the beam size. The focal lengths of L3 and L4 are 71.6 mm (fused silica) and 378.9 mm (BK7) at 1037 nm, respectively. The calculated RGD of the test telescope in a double-pass configuration is 50.6 fs over a 5-mm aperture. The input aperture is re-imaged through the beam splitter (BS) to the spectrometer slit by an imaging telescope (L1, L2). L1 and L2 have the same 61.0-mm focal length. The single-pass RGD in the imaging telescope is 0.9 fs over 5 mm. The spectrometer is a Czerny–Turner type with a grating groove density of 150 lines/mm (SP-2556, Princeton Instruments). The chromatic aberrations in the imaging telescope are calibrated using a reference interferogram by inserting a retroreflective mirror (M1) behind the aperture. The reference phase is always subtracted from the measured phase.

The distance between the spherical mirrors is shorter than 2*f*, so the collimated input beam slightly diverges at the detector plane in the side view. This is because the commercial spectrometer is required to image only the horizontal dimension while keeping its size compact. The beam sizes at the entrance slit and at the detector plane are, however, the same. The period of the Ronchi grating is separately calibrated using an independently collimated source. The period is found to be 201.1 μm by analyzing the projected image of the Ronchi grating in the Fourier domain.

The measured interferogram and the reconstructed phase are shown in Fig. 145.57. The fringe spacing in Fig. 145.57(a) increases slightly from left to right, indicating the presence of RGD. The reconstructed phase in Fig. 145.57(b) shows the wavelength-dependent quadratic phase, where the curves are spaced out by arbitrary integration constants for visualization purposes. The top curve corresponds to 1068 nm and the bottom to 970 nm. The distance from the Ronchi to the slit, *L*, is 30.08 mm. To maximize the fringe contrast, *L* is approximately set to a multiple of the Talbot distance. The measured RGD is

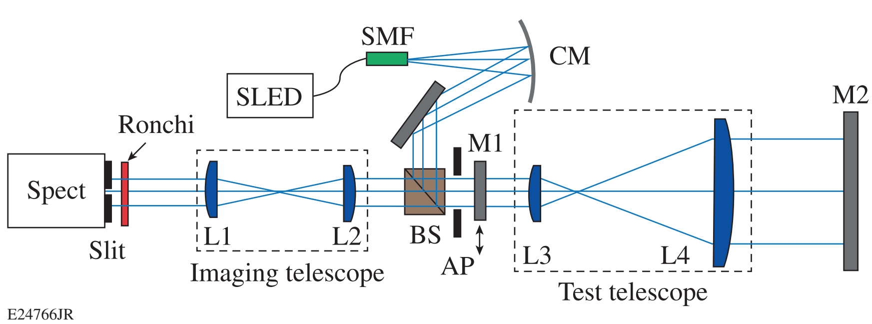

Figure 145.56
Experimental setup. SLED: superluminescent light-emitting diode; SMF: single-mode fiber; CM: concave mirror; BS: beam splitter; AP: aperture; M1 and M2: mirrors; L1–L4: lenses; Spect: spectrometer.

51.1 fs using Eq. (10), which is within 1% of the direct calculation based on dispersion and lens curvature.[17] Figure 145.57(c) shows the sum of both chromatic and achromatic higher-order terms, which is mainly the spherical aberration (i.e., fourth-order phase) in the system.

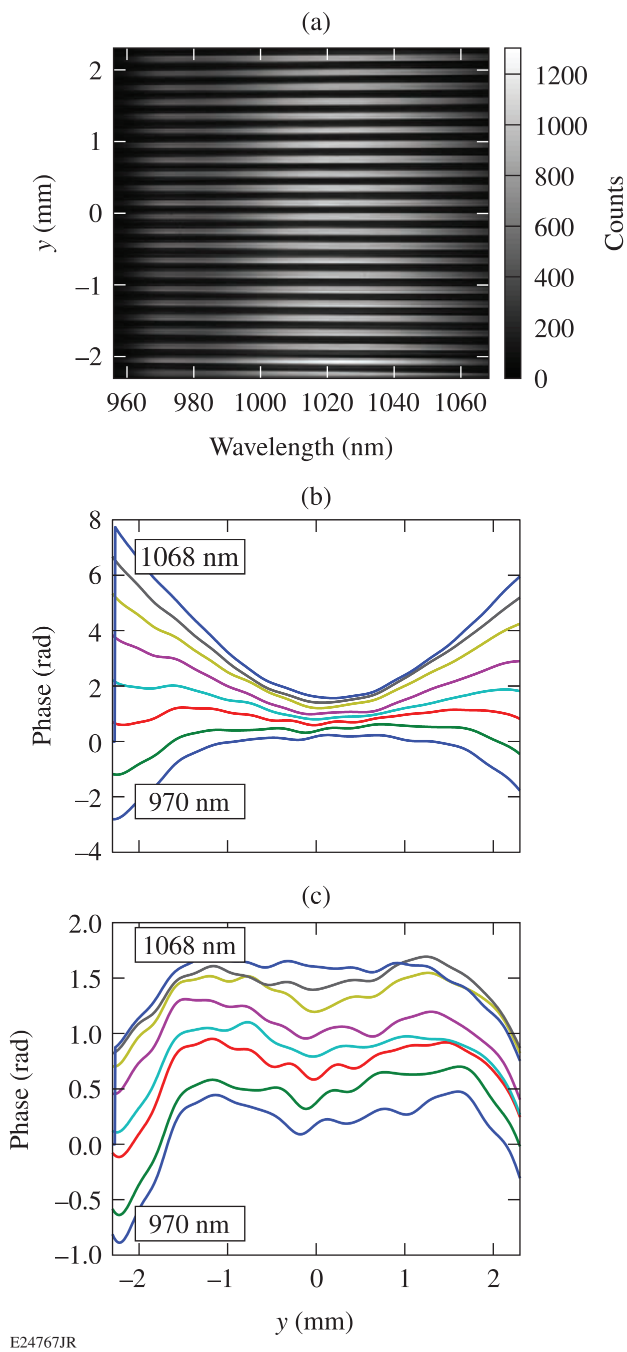

Figure 145.57
Experimental results. (a) Interferogram image, (b) the lineouts of the reconstructed phase at different wavelengths, and (c) the higher-order phase.

A PFD measurement was demonstrated using a BK7 prism (wedge angle of 11°20′) mounted on a rotation stage and placed in front of the Ronchi grating. Since PFD is measured only in the vertical direction (y axis) in this setup, the PFD along the y axis can be varied according to the in-plane rotation angle. Because of the beam deviation and pointing error on insertion of the wedge, the beam centering and pointing must be restored. A flipper mirror was installed between the wedge and the Ronchi grating to send the beam to the pointing and centering diagnostic cameras. The two mirrors between the wedge and L1 were adjusted to restore the alignment. The beam position was aligned within $\pm50~\mu$m and the pointing within $\pm150~\mu$rad, with respect to the reference positions recorded without the wedge. The rather large pointing inaccuracy comes mainly from the mechanical instability of the flipper mirror. The simulation suggests this level of fluctuation introduces only a ±0.5-fs error in PFD. The centering camera images the beam at the equivalent imaging plane of the spectrometer slit. The exact centering alignment becomes important in proportion to the amount of RGD, because any centering shift mixed with RGD [i.e., c_4 of Eq. (10)] will result in additional c_3 as calculated by Eq. (9), which is used to estimate PFD. The insertion of retro-mirror M1 redirects the beam through only the imaging telescope (L1 and L2). The aperture diameter was set to 6 mm. The relative PFD with the wedge is shown in Fig. 145.58. The PFD as measured at seven different angles shows good agreement compared with the calculated PFD. The error bar is the standard deviation of the measured fluctuation in five independent sets of measurements. The PFD at 90° rotation

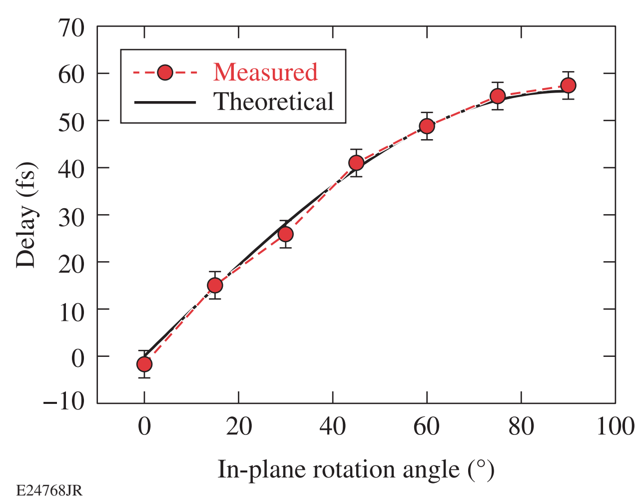

Figure 145.58
Experimental results of measuring the variable pulse-front tilt using an 11° prism.

(wedge parallel to the slit) is 56.2 fs. The standard deviation of the measured PFD with respect to theoretical values is 1.4 fs.

Both RGD and PFD are dependent on beam size; an exact beam size must be specified for given RGD and PFD values. The angle of pulse-front tilt ($\theta_{\Delta T}$) and the temporal radius of curvature in the radial-group delay ($R_{\Delta T}$) could be useful alternatives that are independent of beam size. From the definition of group delay ($\partial\varphi/\partial\omega$), $\theta_{\Delta T}$ is found to be $c\alpha/r$ and $R_{\Delta T}$ is $r^2/(2\beta c^2)$; $R_{\Delta T}$ is 682 ps in the above experiment.

A slightly different arrangement of the system could provide greater flexibility. The Ronchi grating, for example, can be placed directly in front of the detector rather than in front of the entrance slit. Additionally, the input beam rotated by 90° can provide the PFD and RGD information in the orthogonal direction. The rotated beam can also be stacked on top of the original beam to provide 2-D information in a single shot.

The form of Eqs. (6), (9), and (10) suggests that the absolute calibration of the wavelength axis is not necessary for estimating chromatic aberrations (i.e., PFD and RGD) as long as the center wavelength λ_0 is known. The error in the estimation of the absolute wavelength will result in the estimation of the achromatic term [$f(y)$ in Eq. (3)] but not in the chromatic terms. A compact setup made of a non-imaging, dispersive element and a Ronchi or a similar grating might be able to provide the same information.

Regarding the measurements of low-order chromatic aberrations, the full spectrum may not be required. A combination of separate measurements using only narrow-bandwidth sources can also provide the RGD. Reprocessing the data using 2-nm-bandwidth, numerically cropped segments of the measured interferogram at three points (970 nm, 1000 nm and 1030 nm) still results in an RGD within a 1% error. The effect of noise between separate measurements, however, has not yet been evaluated.

A simple, spectrally resolved, 1-D lateral-shearing interferometer that can be used to characterize spatiotemporal coupling in a single shot has been demonstrated. The setup requires only a single Ronchi grating attached in front of a spectrometer. The calibration is done only once, and it can be easily transported. Its accuracy was experimentally demonstrated in the measurements of RGD and PFD. Suggestions have been made on different ways of implementing the basic idea and on the possibility of improving and simplifying the system.

ACKNOWLEDGMENT

This material is based upon work supported by the Department of Energy National Nuclear Security Administration under Award Number DE-NA0001944, the University of Rochester, and the New York State Energy Research and Development Authority. The support of DOE does not constitute an endorsement by DOE of the views expressed in this article.

REFERENCES

1. G. Pretzler, A. Kasper, and K. J. Witte, Appl. Phys. B **70**, 1 (2000).
2. H.-M. Heuck *et al*., Appl. Phys. B **84**, 421 (2006).
3. J. Néauport, Appl. Opt. **46**, 1568 (2007).
4. S.-W. Bahk, J. Bromage, and J. D. Zuegel, Opt. Lett. **39**, 1081 (2014).
5. D. N. Vitek *et al*., Opt. Express **18**, 18,086 (2010).
6. G. Zhu *et al*., Opt. Express **13**, 2153 (2005).
7. H. Vincenti and F. Quéré, Phys. Rev. Lett. **108**, 113904 (2012).
8. Z. Sacks, G. Mourou, and R. Danielius, Opt. Lett. **26**, 462 (2001).
9. T. A. Planchon *et al*., Opt. Lett. **29**, 2300 (2004).
10. C. Dorrer and I. A. Walmsley, Opt. Lett. **27**, 1947 (2002).
11. J. Jasapara and W. Rudolph, Opt. Lett. **24**, 777 (1999).
12. A. P. Kovács *et al*., Appl. Phys. B **80**, 165 (2005).
13. P. Bowlan *et al*., Opt. Express **14**, 11,892 (2006).
14. P. Bowlan and R. Trebino, J. Opt. Soc. Am. B **29**, 244 (2012).
15. P. Gabolde and R. Trebino, Opt. Express **14**, 11,460 (2006).
16. J. Primot and N. Guérineau, Appl. Opt. **39**, 5715 (2000).
17. Z. Bor, J. Mod. Opt. **35**, 1907 (1988).

Isolating and Quantifying Cross-Beam Energy Transfer in Direct-Drive Implosions on OMEGA and the National Ignition Facility

Introduction

In direct-drive inertial confinement fusion (ICF) experiments, laser beams directly illuminate a spherical capsule to drive an implosion. The capsule compression transfers the kinetic energy of the converging shell into the internal energy of the fuel, triggering fusion reactions in the hot dense core.[1] The laser energy that drives the implosion is absorbed in the plasma corona and conducted to the ablation front of the target by electron thermal transport, resulting into ablation of the shell and its corresponding acceleration caused by the rocket effect.[2]

Laser beams crossing in the coronal plasma can drive the stimulated Brillouin scattering (SBS) instability, which can redirect a significant fraction of the incident energy out of the plasma.[3] Cross-beam energy transfer (CBET) is seeded SBS facilitated by ion-acoustic waves driven by the beating of two electromagnetic waves in a plasma.[4] Depending on the amplitude of the driven ion-acoustic wave, energy is transferred from one electromagnetic (pump) wave to another (seed) wave. In direct-drive fusion experiments, outgoing rays that have refracted around the target beat with incoming rays from other beams to transfer significant energy out of the plasma before it can be absorbed. In simulations of direct-drive implosions, where individual beam intensities remain low ($I < 10^{14}$ W/cm^2), the amplitudes of the ion-acoustic waves are small. Nevertheless, significant energy transfer results from the net effect of many beam crossings throughout the coronal plasma.[5–7]

The existence of CBET was first demonstrated by experiments using planar targets.[8,9] In indirect-drive ICF experiments, this mechanism was used to transfer kilojoules of laser energy from the polar to the equatorial drive of an imploding target to improve capsule symmetry,[10–12] but uncertain plasma conditions and the large amplitude of the ion-acoustic waves driven by high single-beam intensities ($I \sim 10^{15}$ W/cm^2) have challenged the ability to obtain an accurate predictive model.[11–13] These experiments additionally identified the ability of CBET to rotate the polarization of the beams, suggesting that polarization rotation should be included when modeling systems with multiple CBET regions.[14,15] Direct-drive experiments used scattered-light spectra and shell-trajectory measurements to demonstrate the existence of CBET[5] and estimate its level.[6,16,17]

This article presents measurements of CBET's effect on coupling laser energy to the ablation front of a target by comparing its effect on the mass ablation rate and ablation-front trajectory in low- and high-CBET regions in the same implosion. A polar-direct-drive configuration[18] was used, in which a ring of beams encircling the equator was dropped and the remaining beams were repointed toward the equator, reducing detrimental CBET at the poles while enhancing it at the equator.[19,20] This combination of low- and high-CBET conditions in the same target implosion made it possible to determine the effects of CBET on hydrodynamic coupling (Fig. 146.1). The simultaneous measurements of the angularly resolved mass ablation rates and shell trajectories determine the kinetic energy of the implosion by providing the instantaneous mass of the target and the ablation-front velocity.

Two-dimensional *DRACO*[21] hydrodynamic simulations performed with an implicit Schurtz–Nicolai–Busquet (iSNB)

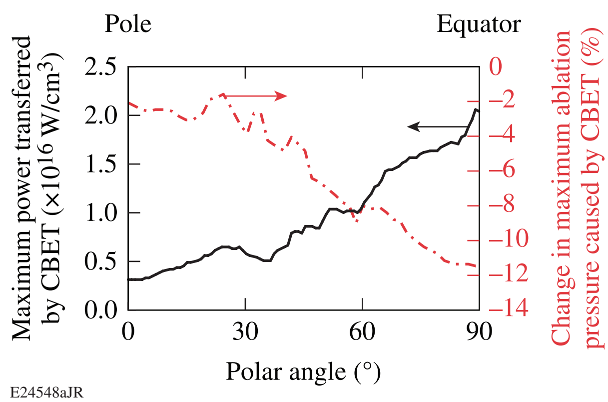

Figure 146.1
The polar-direct-drive laser configuration results in greater power transferred by cross-beam energy transfer (CBET) at the target equator compared to the pole (black curve). The consequent difference in ablation pressure (red dashed–dotted curve) was calculated from 2-D *DRACO* simulations with and without the CBET model for the highest-intensity polar-direct-drive OMEGA experiments (t = 0.8 ns).

thermal-transport model,[22] but without a CBET model, reproduced the measured trajectories at the pole of the target, verifying that the coupling physics is well modeled when CBET effects are negligible. These simulations, however, overpredicted the velocity of the shell and ablation rate at the equator. By including a 3-D ray-based CBET model adapted from 1-D plane-wave equations developed by Randall[4] in the hydrodynamic simulations, the simulated equatorial trajectories agreed better with measurements, while having a minimal impact on the polar trajectory. However, the simulations still overpredicted the drive at the equator.

The geometric ray-propagation model used in *DRACO* transports energy while neglecting diffraction effects that produce small-scale structures (temporal and spatial). The CBET model requires knowledge of the cumulative background pump intensity distributed over the propagation angle and wavelength, which is computed by accumulating the ray-energy path-length product and weighting the sum by the cell volume to capture the relevant hydrodynamic scale.[23] Diffraction may vary the energy transfer above or below the average value computed using this ray model if there is a nonlinear CBET response, but the net effect is uncertain given the small spatial and temporal interaction scales involved. *DRACO*'s ray model does not currently track polarization, but the net effect should be captured by assuming an even mixture, given the even distribution of polarization states generated by the polarization smoothing[24] processes on OMEGA.The correct formulation of the net response of polarization, which depends on the ray-interaction angles, is under investigation and may partially account for the overestimated shell kinetic energy. When a multiplier on the CBET gain was added to the model, excellent agreement between the measured and simulated mass ablation rates and shell trajectories was obtained at all angles. These measurements were performed on OMEGA[25] and at the National Ignition Facility (NIF)[26] to access a wide range of laser intensities, plasma conditions, and laser-beam geometries. The need for the CBET multiplier in all the tested configurations suggests that additional physics effects, such as diffraction, polarization effects, or shortcomings of extending the Randall model to 3-D, should be explored to explain the difference in observed and predicted drives.

Experimental Setup

1. Target and Laser Configuration

a. Isolating CBET. Experiments were performed on OMEGA[25] using forty 351-nm laser beams with equal energies, arranged in the polar-direct-drive configuration, with three rings of beams around each pole of the target chamber. The beams were repointed toward the target equator by 5° for the two inner rings of beams and 20° for the outer ring at each pole, using the angle definitions and pointing description from Ref. 27. The beam profiles were shaped with distributed phase plates[28] that provided second-order super-Gaussian laser spots on target (1/*e* radius of 183 μm). Two-dimensional smoothing by spectral dispersion (SSD)[29] and polarization smoothing[24] were used to treat the laser-intensity profiles. The laser pulses consisted of a 0.7-ns foot, ramping up to a 0.6-ns square pulse that drove the target to its final velocity (Fig. 146.2). The total energy on target was varied among 8.1±0.2 kJ ($I \approx 7 \times 10^{14}$ W/cm^2, where I is the peak overlapped intensity defined as the maximum power during the laser pulse divided by the initial surface area of the target), 11.8±0.1 kJ ($I \approx 10 \times 10^{14}$ W/cm^2), and 16.0±0.1 kJ ($I \approx 14 \times 10^{14}$ W/cm^2). The targets were 19.6±0.3-μm-thick spherical CH shells. They were coated with 2.4±0.2, 1.6±0.2, and 0.6±0.2-μm layers of Si, with outer diameters of 639 μm, known to ±1 μm with a variation between experiments of ±4 μm. The density of the Si coating was 2.1±0.2 g/cm^3 but had a significantly smaller variation (<0.2 g/cm^3) within a particular target batch. Each experimental configuration discussed here used targets from a single batch, so the density variation for a particular configuration was negligible.

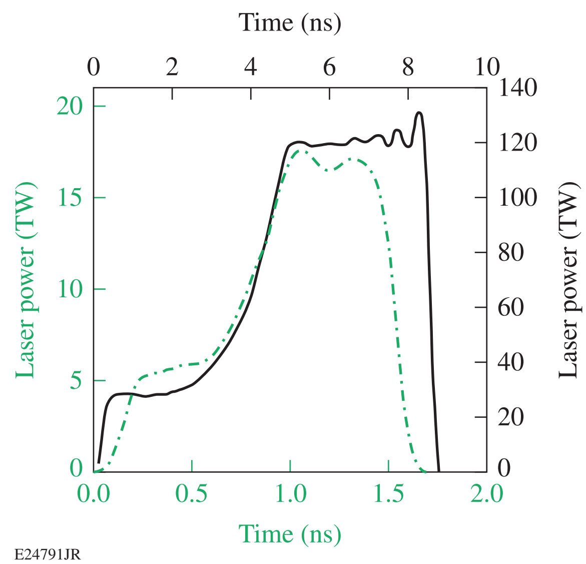

Figure 146.2
The laser pulse shapes are shown for the OMEGA (green dashed–dotted curve) and NIF (black solid curve) experiments.

b. Scaling to ignition conditions. Experiments were performed on the NIF using 192 laser beams (with one beam missing on the 2.5-μm Si experiment) in the indirect-drive configuration, with the polar-direct-drive beam-pointing design and ring energies described in Ref. 30. This pointing design produced a round CH implosion in simulations when CBET was considered without a gain multiplier. The total laser energy was 660 kJ, giving a peak overlapped intensity on target of ~8×10^{14} W/cm^2.

The laser pulse was similar in shape to the OMEGA pulse but extended over 8 ns (Fig. 146.2). Targets were 90±2-μm-thick CH shells with Si coatings of 2.5±0.1 μm and 5±0.1 μm and outer diameters of 2314±2 μm. The density of the Si coating was reported as 2.1±0.2 g/cm^3.

c. Symmetric direct drive on OMEGA. Symmetric direct-drive experiments were performed on OMEGA using all 60 laser beams centered on the target. The same beam-smoothing methods, phase plates, pulse shape, total energies, and intensities were used as in the polar-direct-drive experiments. The targets were also similar to those used in the polar-direct-drive experiments, with 20.1±0.3-μm-thick CH shells having a variation between targets of ±0.8 μm and Si thicknesses of 2.4±0.2, 1.4±0.2, and 0.7±0.2 μm. Outer diameters had an average value of 637 μm, measured to ±2 μm, and a variation between targets of ±11 μm. The density of the Si coating was reported as 2.1±0.2 g/cm^3.

2. Self-Emission Diagnostic

a. Configuration of the x-ray framing camera. The x-ray self-emission was measured using four-strip x-ray framing cameras.[31,32] Two-dimensional images of the coronal x rays were formed using arrays of pinholes (8-μm diameter for OMEGA, 25-μm diameter for the NIF), placed to give 6× magnifications on OMEGA and 2× on the NIF. The ~50-ps time-gated images (~100 ps for the NIF) were taken throughout the implosion, with absolute timing known to ±10 ps and the interstrip timing of ~250 ps known to ±3 ps (Ref. 33). Five filters were used for the images throughout the course of the experiments: (1) 25 μm of Be, (2) 250 μm of Be, (3) 25 μm of Be with 23 μm of Saran, (4) 25 μm of Be with 50 μm of Kapton, and (5) 25 μm of Be with 75 μm of Kapton. Different filters were used to optimize imaging of the ablation front and the interface between the Si and CH in the corona. The 25-μm Be filter (blocking x rays <1 keV) was found to optimally image the CH ablation front late in time because of the lower ablation-front temperature. The 250-μm Be filter (blocking x rays <2 keV) was optimized to image the Si/CH interface as it expanded away from the ablation front because of the higher temperature in the corona. The combination of Be and Saran (blocking x rays <1.6 keV) provided a good compromise between the two. The Be and Kapton filters (blocking x rays <2 keV) were used on the NIF for the first three strips on each camera. Only 25 μm of Be was used for the last strip in each camera to measure the CH ablation-front position. Images were taken from the equator and pole for all of the polar-direct-drive experiments, so that both the variation in ablation rate and ablation-front trajectory with polar angle and the azimuthal symmetry of the implosion could be observed. Both configurations on OMEGA experiments had two equatorial cameras offset by 11° in polar angle from the equator and one camera on the pole to measure the azimuthal symmetry. The NIF experiments had one camera on the equator and one on the pole.

b. Trajectory measurements. X-ray self-emission images of Si-coated CH target implosions were used to determine the mass ablation rate of Si and the ablation-front trajectory of the target.[34,35] While the laser is on, the coronal plasma around the target is continually heated and emits soft x rays. The x-ray intensity that is line integrated through the target is imaged through a pinhole onto a time-gating diagnostic plane. Figure 146.3 shows the x-ray self-emission technique at a time shortly after the laser burned through the Si layer of the target, when the corona consists of an outer Si plasma and an inner CH plasma surrounding the unablated target.

Figure 146.3(b) shows the simulated x-ray intensity profile at the diagnostic plane when two distinct features are observed. Moving from the outside of the plasma toward the target center, an increase in x-ray intensity is observed as the line-integrated distance through the Si plasma increases. A rapid drop in intensity occurs at the interface between the Si and CH as the lower-emitting CH quickly dominates the integrated x-ray emission region (outer feature). The intensity again increases with further progress toward the center of the target until the ablation front is reached. At the ablation front, the emission quickly drops because the shell is optically thick (inner feature). These two features observed in the radial intensity at the diagnostic plane are used to track the positions of the Si/CH interface and ablation front.[35]

Figure 146.4 shows measured x-ray self-emission images and their respective intensity profiles at three different times for a symmetrically illuminated implosion. In the symmetric images, these profiles are angularly averaged around 360° of the image to obtain a measurement accurate to <1 μm for both the inner gradient (ablation-front radius) and outer peak locations (Si/CH interface position). In angularly resolved images, the profiles at the pole and equator are each averaged over 40° (20° at each pole or each side of the equator). The instrument function of the x-ray diagnostic (defined predominantly by the pinhole size) introduced a small systematic shift (~2 μm) between the position of the inner gradient and the actual position of the ablation front.[35] This shift was determined by post-processing simulations with *Spect3D*[36] and convolving with the instrument function to calculate self-emission images. The shifts are known to ±1 μm for the ablation front and ±2 μm for the Si/CH interface.

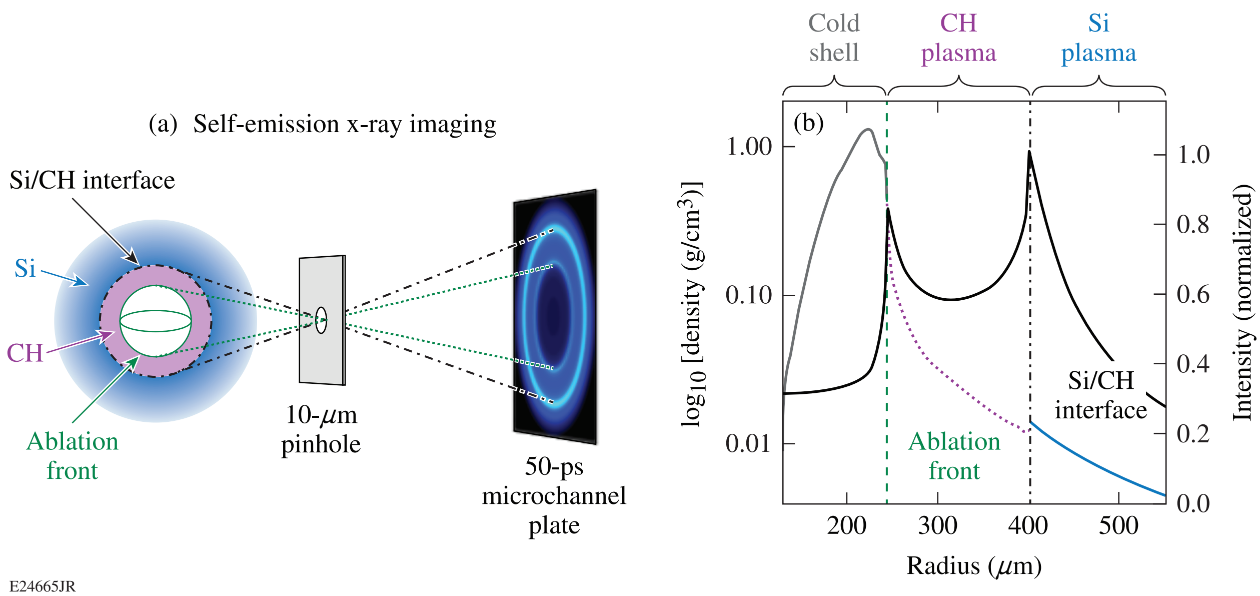

Figure 146.3
(a) Line-integrated x-ray self-emission from the target is imaged through a pinhole and filter (transmits >1 keV) onto an ~50-ps time-gated microchannel plate. (b) Comparison of the calculated radial x-ray intensity profile measured at the diagnostic plane (black solid curve) with the simulated target-density profile in the cold shell (gray solid curve), in the CH plasma (purple dotted curve), and in the Si plasma (blue solid curve). Two peaks in the emission correspond to the positions of the Si/CH interface in the coronal plasma (black dashed–dotted line) and the ablation front of the imploding shell (green dashed line). No instrument function is included in the x-ray intensity profile calculation to illustrate the steep gradients at the ablation surface and Si/CH interface.

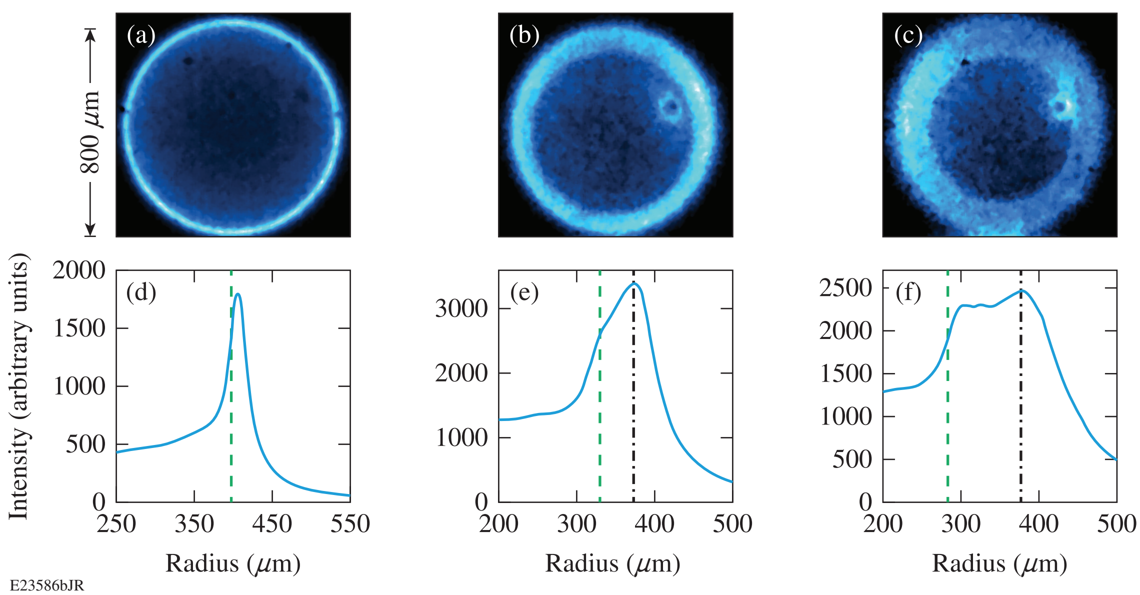

Figure 146.4
Self-emission x-ray images, taken (a) before and [(b),(c)] at two different times shortly after the laser burns through the Si layer, are shown with their corresponding averaged radial profiles. The positions of the measured ablation front (green dashed line) and the Si/CH interface (black dashed–dotted line) are included.

c. Measurements of mass ablation rate. The average mass ablation rate of the Si from the start of the laser pulse to the Si burnthrough time is determined by dividing the total ablated mass (calculated from the initial Si mass) by the time it took the laser to burn through the Si layer. The time-resolved mass ablation rate was determined by varying the thickness of the Si outer layer to determine the time-averaged mass ablation rate at different times during the implosion.

To determine the burnthrough time in each experiment, the measured Si/CH interface and ablation-front positions from the series of images taken for a particular implosion were plotted to generate the ablation-front and Si/CH interface trajectories. The burnthrough time of the Si layer corresponds to the time when the Si/CH interface trajectory separates from the ablation-front trajectory. To accurately determine the burnthrough time, a range of simulations was performed, varying the CBET multiplier. The simulation that simultaneously reproduced both measured trajectories was used to determine the Si burnthrough times around the target. The accuracy of the measurement corresponds to the variation in the burnthrough time for the simulated trajectories that are within the error bars of the experimental measurements.

The Si/CH interface trajectory is sensitive to the initial Si mass. For all experiments in a given target batch, the optimum Si density used in the simulations was determined by finding the density that minimized the differences between the simulated and measured interface trajectories at the pole. The density was varied within the measurement uncertainties (see **Isolating CBET**, below). The absolute error in the mass largely results from the uncertainty in density. This inaccuracy in the calculated mass could mask uncertainties in the equation of state, opacity, and thermal-transport models, but tests show that these effects primarily act symmetrically. Any changes in the models that affect the trajectories symmetrically must be offset by changes in another symmetric coupling model—not the CBET model—to maintain agreement with the measured polar trajectories.

Experiments

1. Isolating CBET

To measure the effects of CBET in direct-drive experiments on OMEGA, a laser configuration was used in which a ring of beams around the equator was turned off and the remaining beams were repointed toward the equator. This configuration limits the intensity of the refracted outgoing light that interacts with incoming polar beams, significantly reducing CBET at the pole. The repointing increases the flux of unabsorbed light propagating through the equatorial coronal plasma, which enhances CBET at the equator (Fig. 146.1). The implosions were designed to have nearly uniform drive around the target when CBET was not taken into consideration, so differences in measured drive between the pole and equator are attributed to CBET.

Figure 146.5 shows x-ray self-emission images taken from the equator after the laser burns through the Si layer. The intensity features visible in the images show the positions of the ablation front and Si/CH interface, which form two concentric ellipses with opposite ellipticity. The ablation-front ellipses show larger shell radii at the equator compared to the pole, demonstrating that the ablation pressure is lower at the equator compared to the pole. The smaller separations between the Si/CH interface and ablation-front ellipses at the equator,

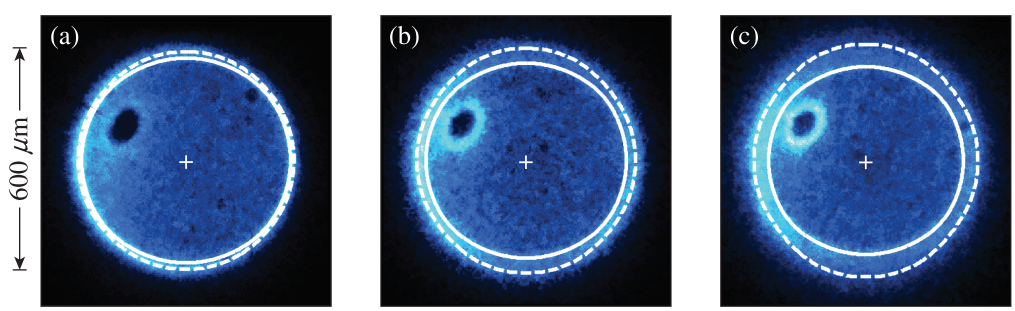

Figure 146.5
X-ray images taken after the burnthrough of a thin Si layer at (a) $t = 0.7$, (b) 0.8, and (c) 0.9 ns in an experiment having the highest intensity (14×10^{14} W/cm^2) are shown. The images indicate earlier burnthrough at the poles of the target (top and bottom of images) than at the equator. The increased separation of the Si/CH interface (dotted line) and ablation front (solid line) at the poles implies a greater time of expansion for the Si from the ablation front. This increased drive results in a smaller ablation-front radius measured at the pole than at the equator.

compared to the pole, indicate that the laser burned through the Si later at the equator. The expansion of the Si/CH interface away from the target and compression of the ablation front as a function of time can be seen through the series of images.

Figure 146.6 shows the ablation-front and interface trajectories used to determine the Si burnthrough times, i.e., the time that each trajectory pair separated with values of 0.59±0.04 ns for the equator and 0.52±0.04 ns for the pole. The later burnthrough time at the equator, compared to the pole, agrees with the lower mass ablation rate at the equator suggested by the individual images. The measured ablation-front radii of 140±2 μm for the equator and 111±2 μm for the pole at 1.49±0.01 ns indicate a lower average ablation pressure at the equator compared to the pole, which leads to a slower velocity.

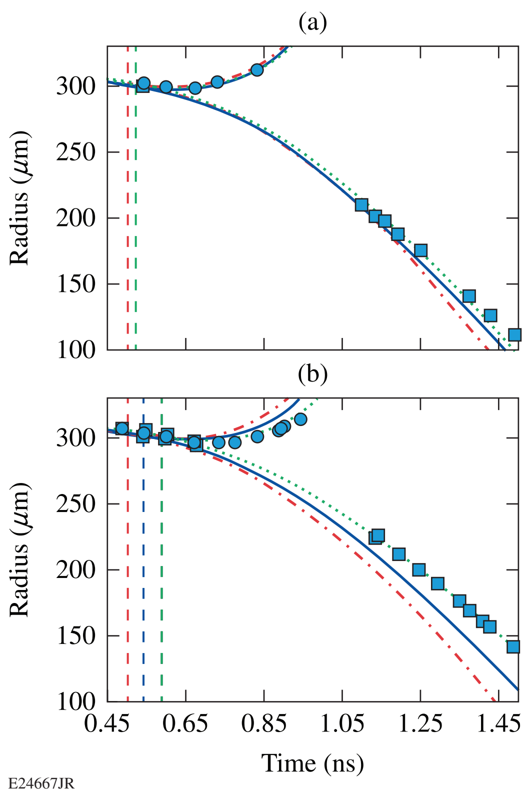

Figure 146.6
Measured Si/CH interface (blue circles) and ablation-front (blue squares) trajectories from three cameras are plotted for the (a) pole and (b) equator for the highest-intensity OMEGA polar-drive experiment with a 2.4-μm layer of Si. Error bars for the radius measurements are smaller than the data points (±2 μm for the ablation-front measurements and ±4 μm for the Si/CH interface measurements). Simulations performed with no CBET model (red dashed–dotted curve), the standard CBET model (blue solid curve), and the CBET model with the best-fitting gain multiplier (green dotted curve; $f_{\text{CBET}} = 2.7$) are shown. The time that the laser burned through the Si in each simulation is marked with a dashed line of the corresponding color. Good agreement between the measurements and all models was obtained at the pole where CBET was minimal.

a. Comparison with hydrodynamic simulations. Figure 146.6 shows good agreement between the trajectory measurements at the pole and polar trajectories taken from *DRACO*[21] simulations that did not include CBET. This agreement at the pole suggests that the coupling physics is well modeled when CBET effects are small. Calculated trajectories at the equator are very similar to those calculated at the pole, which suggests that without CBET, the implosion would be symmetric. However, the measured equatorial trajectories show later burnthrough and a larger final radius than were calculated, indicating that the CBET significantly reduced the drive at this location.

A 3-D ray-based model[23] adapted from the 1-D Randall plane-wave equations[4] was implemented in *DRACO*. Figure 146.6 shows that simulations run with this model calculate a preferential decrease in drive at the equator, bringing simulations into better agreement with measurements. The addition of this CBET model results in small changes in the calculated polar trajectories at early times, verifying that CBET is negligible at the pole until the target radius is $\lesssim$250 μm (~0.9 ns). An increased effect of CBET at the pole is observed at this point because of an increase in the SBS seeds from rays that were previously shadowed by the target and an increase in the incident laser power (Fig. 146.2). Even late in time, however, the ablation-front trajectories calculated without CBET are in reasonable agreement with the measurements.

The trajectories at the equator are slowed to a greater degree than at the poles, indicating that CBET has a stronger effect at this location. The simulated Si burnthrough time is still too early and the ablation-front trajectory still too fast, however, to agree with the measurements. To estimate the CBET modification required to bring simulations into agreement with measurements, a multiplier (f_{CBET}) was incorporated into the CBET gain length:

$$L_{\text{s}}^{-1} = f_{\text{CBET}} \frac{k_0}{4} \frac{n_0}{\epsilon n_{\text{c}}} \left(\frac{m v_q^2}{T_{\text{e}}} \right) \times \left[\left(1 + \frac{3\,T_{\text{i}}}{Z T_{\text{e}}} \right) \left(\frac{\nu_{\text{i}}}{\omega_{\text{s}}} \right) \right]^{-1} P(\eta), \quad (1)$$

given by Eq. (18) in Ref. 4, where all other parameters are defined within the reference.

Figure 146.6 shows that excellent agreement with the measurements was obtained when a multiplier of 2.6±0.3 was used. To determine the optimal multiplier, a χ^2 analysis was used to minimize the differences between measured and simulated trajectories (Fig. 146.7), where

$$\chi^2 = \sum_{i=1}^{N} \frac{1}{N} \frac{\left[r_i - x(t_i)\right]^2}{\sigma_{r_i}^2}, \tag{2}$$

and r_i is the measured position, $x(t_i)$ is the simulated radius, σ_{r_i} is the uncertainty in the experimental measurement (±2 μm for the ablation-front location and ±4 μm for the Si/CH interface position), and N is the total number of points measured. The error bar on the multiplier was determined from the uncertainty in absolute timing (±10 ps)—shifting the experimental image timing relative to the simulation gives an error bar on the multiplier of ±0.4 ps for high intensities to ±0.6 ps for each low-intensity experiment.

All of the simulations described here were performed using the code *DRACO* with the iSNB nonlocal thermal-transport model,[22] *SESAME* equation-of-state tables,[37] and collisional-radiative opacity tables.[38] The polar angle's dependence on the laser energy deposition, hydrodynamic efficiency, and thermal conduction is generated by the polar-direct-drive configuration, which invokes lateral thermal transport.

<u>b. Intensity and Si-thickness scalings.</u> Figure 146.7 shows measurements of the polar and equatorial trajectories for the 2.4-μm Si experiment at three intensities. For each intensity, simulations without CBET agreed well with experimental measurements at the pole, showing that the simulations reproduce

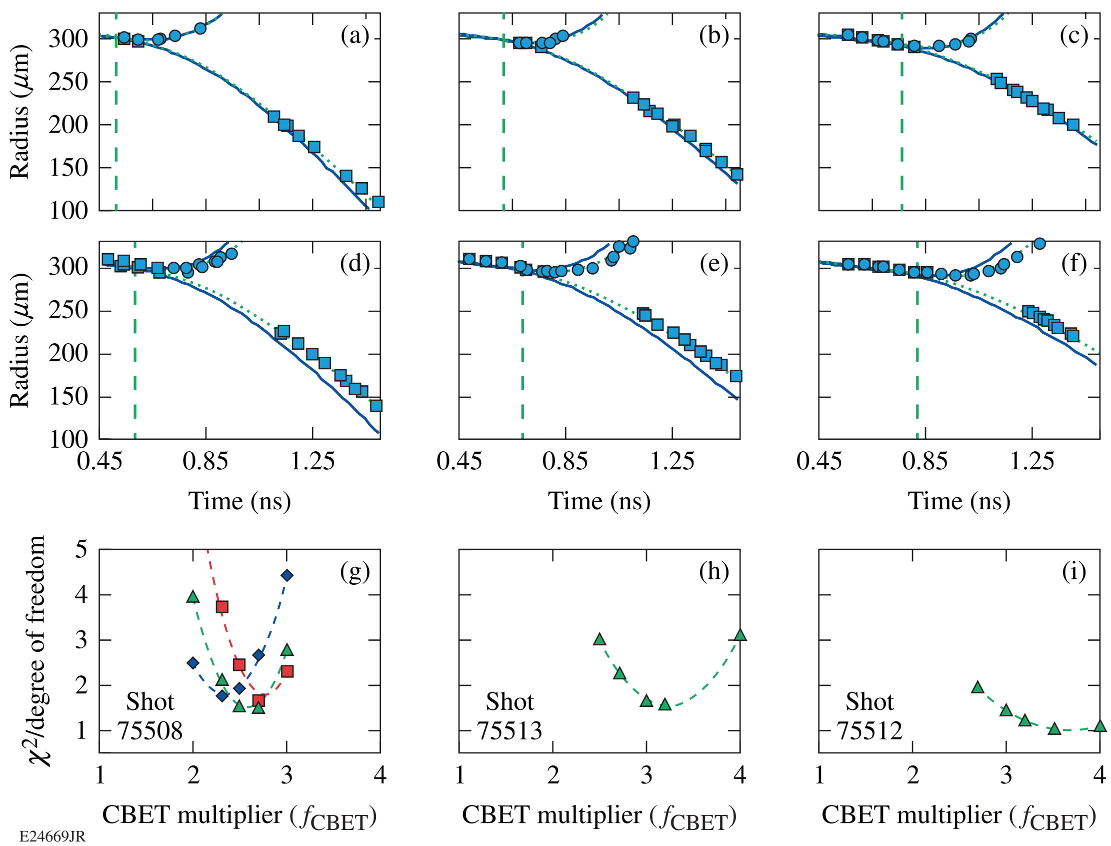

Figure 146.7
Comparison of the measured ablation front (blue squares) and Si/CH interface (blue circles) with simulated trajectories generated by *DRACO* with CBET using no multiplier (blue solid curves) and CBET with the best-fit multiplier (green dotted curves) for targets with 2.5 μm of Si. Included are trajectories for [(a)–(c)] the pole and [(d)–(f)] equator for $I = 14 \times 10^{14}$ W/cm^2 (left column), 10×10^{14} W/cm^2 (middle column), and 7×10^{14} W/cm^2 (right column). The Si burnthrough times are plotted (green dashed lines). The χ^2 minimization analyses are plotted for (g) $I = 14 \times 10^{14}$ W/cm^2, (h) 10×10^{14} W/cm^2, and (i) 7×10^{14} W/cm^2 to determine the optimal multiplier and error bars. For the highest intensity, the χ^2 values are shown for the optimal timing (green triangles), –10 ps (blue diamonds), and +10 ps (red squares). The possible error in the CBET multiplier is determined from the shift in the location of the minimum χ^2 with the uncertainty in the timing.

the hydrodynamic coupling when CBET is negligible, but the ablation rate and ablation-front velocity are overpredicted at the equator. With the introduction of the CBET model using the optimized multiplier, excellent agreement at both the pole and equator was found for each intensity. The optimized values of 2.8±0.5, 3.1±0.5, and 3.9±1.0 were determined for this configuration with overlap intensities of I = 14 × 10^{14} W/cm^2, 10 × 10^{14} W/cm^2, and 7 × 10^{14} W/cm^2, respectively. As the intensity decreases, the χ^2 curve broadens because of the smaller effect of CBET at lower intensities.

Figure 146.8 shows the mass-ablation-rate measurements at the pole and the equator for the highest laser-intensity experiments. The experiments were performed using three different thicknesses of the Si outer layer (0.6, 1.6, and 2.4 μm) to evaluate the average mass ablation rate of the Si at different times during the implosion. For three intensities, good agreement between simulated and experimental burnthrough times verifies the simulated time-resolved mass ablation rates taken when the optimal intensity multiplier was used.

2. Scaling to Ignition Conditions

Figure 146.9 shows the trajectory results from direct-drive experiments performed on the NIF to access ignition-relevant conditions (Table 146.I). The images taken during the NIF experiments were used to measure the ablation-front trajectories at the pole and the equator. Measured ablation-front trajectories agree well with simulations that used a CBET multiplier

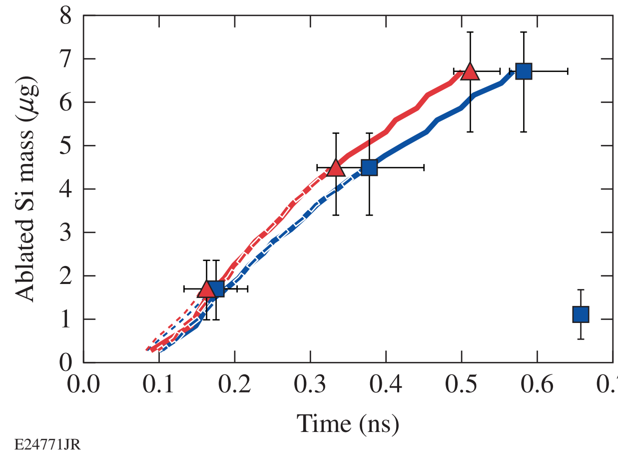

Figure 146.8
Ablated Si mass as a function of the measured burnthrough time at the pole (red triangles) and equator (blue squares) for a laser intensity of 14 × 10^{14} W/cm^2 is compared with simulations (dotted curve: 0.6 μm; dashed curve: 1.6 μm; and solid curve: 2.4 μm) using the optimal multipliers. The small shot-to-shot variations in the simulated ablation rate result from minor variations in the laser pulse and target size. Absolute error bars are shown for the Si mass. The relative error in mass (shown on the sample point in the lower right corner) is reduced because the density can be considered to be the same for all targets in a given batch.

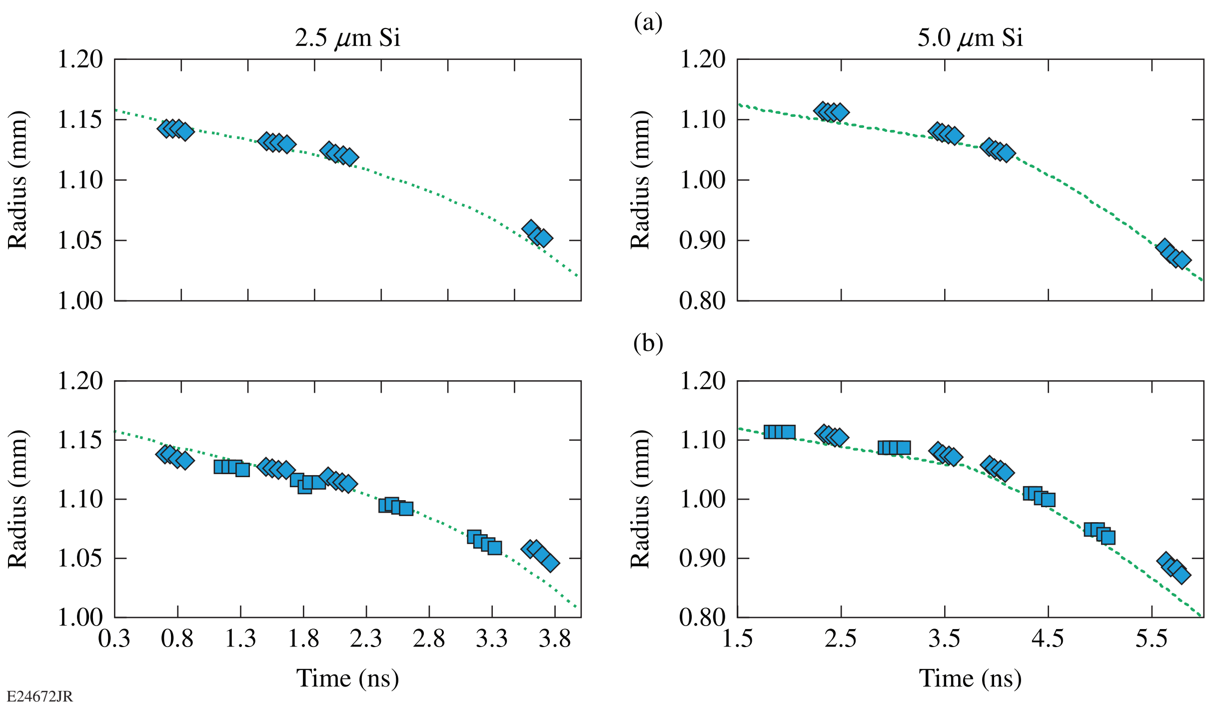

Figure 146.9
The measured ablation-front positions (blue squares) are compared with simulations (green dotted curves) for targets with [(a),(b)] 2.5 μm and [(c),(d)] 5 μm of Si at the [(a),(c)] pole and [(b),(d)] equator.

of 2, which has been shown for similar NIF experiments that used CH shells.[39] To mitigate the effects of shell decompression on the ablation-front trajectories, the experiments were limited to early times. Large perturbations at the ablation front can expand the ablation-front surface away from the shell's center of mass.[39] In the OMEGA experiments, the 2-D SSD limits the imprint, and perturbations were shown to have minimal impact on the trajectories.[35] At both facilities the radiation from the Si layer reduced the Rayleigh–Taylor (RT) growth, but on the NIF, the RT growth caused by high levels of laser imprint occurred in spite of the smoothing effects; this mixed the Si and CH at the interface, reducing the contrast of the outer interface peak in the x-ray images. As a result, the ability to measure the Si/CH interface trajectory on the NIF was limited.

Table 146.I: Comparison of the laser energy (E_L), electron temperature at the quarter-critical surface (T_e), density scale length (L_n), and overlap intensity at the quarter-critical surface (I_{qc}) near the end of the laser pulse for OMEGA and NIF polar-direct-drive experiments.

Parameter	OMEGA	NIF	Ignition
E_L	24 kJ	660 kJ	1500 kJ
T_e	2.7 keV	2.9 keV	4 keV
L_n	150 μm	350 μm	500 μm
I_{qc}	5×10^{14} W/cm^2	3×10^{14} W/cm^2	10^{15} W/cm^2

3. Symmetric Direct Drive on OMEGA

Figure 146.10 shows the trajectory results for symmetric direct-drive experiments on OMEGA. A CBET gain multiplier

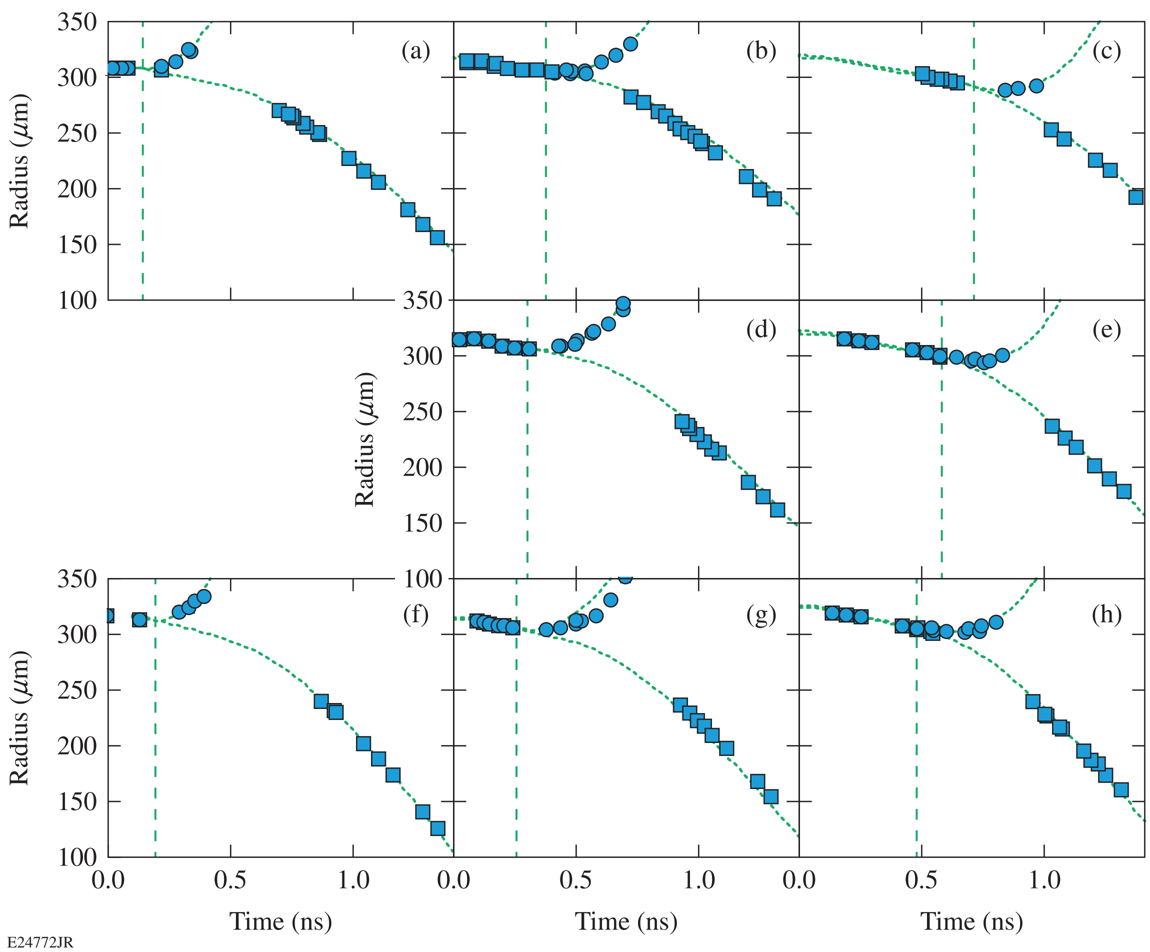

Figure 146.10
Comparison of the measured ablation-front (blue squares) and Si/CH interface (blue circles) positions with simulated trajectories (green dotted curve) for [(a)–(c)] $I = 7 \times 10^{14}$ W/cm^2; [(d),(e)] 10×10^{14} W/cm^2; and [(f)–(h)] 14×10^{14} W/cm^2 for targets with Si thicknesses of [(a),(f)] 0.7 μm; [(b),(d),(g)] 1.6 μm; and [(c),(e),(h)] 2.6 μm. The Si burnthrough times are plotted in the figure (green dashed lines).

of 2 was found to reproduce the trajectories and burnthrough times (mass ablation rates) for all combinations of laser intensity and Si thickness tested.

Conclusions

The CBET physics in direct-drive implosions was analyzed using simultaneous 2-D Si mass-ablation-rate and ablation-front-trajectory measurements. A polar-direct-drive configuration was employed, where beams were removed from the equator of a symmetrically illuminated target and the remaining beams were repointed toward the equator. This configuration suppressed CBET at the pole, while enhancing its effects at the equator. Implosion trajectories simulated without CBET were in good agreement with the measured polar trajectories for all conditions tested. This suggests that the other coupling physics is well modeled at the pole when CBET is small. The calculated mass ablation rates and ablation-front trajectories are in excellent agreement with the measurements at the pole and the equator when a 3-D ray-based CBET model is included in the simulations with a CBET gain multiplier. These measurements were performed on both OMEGA and the NIF to access a wide range of laser intensities, plasma conditions, and laser-beam geometries. The multiplier was necessary for all laser conditions, and the optimal multiplier for each configuration is shown in Fig. 146.11. The multiplier is constant for symmetric OMEGA experiments and decreases with increasing intensity in OMEGA polar-direct-drive implosions. The presence of the CBET gain multiplier required to match the data in all of the configurations tested suggests that additional physics effects should be explored, such as intensity variations caused by diffraction, polarization effects, or shortcomings of extending the 1-D Randall model to 3-D. The variation in the CBET multiplier in the polar-drive configuration, while it is constant in the symmetric configuration, suggests that additional physics may be affecting the polar-drive implosions. For example, the beams pointed toward the equator may experience increased CBET because of their increased interaction length. This increased transfer may saturate at high laser intensities, resulting in a decreasing CBET multiplier. Another candidate for further exploration is the effect of lateral thermal transport on the plasma conditions since the polar-drive configuration experiences lateral temperature gradients that do not exist in a symmetric configuration and the plasma conditions affect the level of energy transfer.

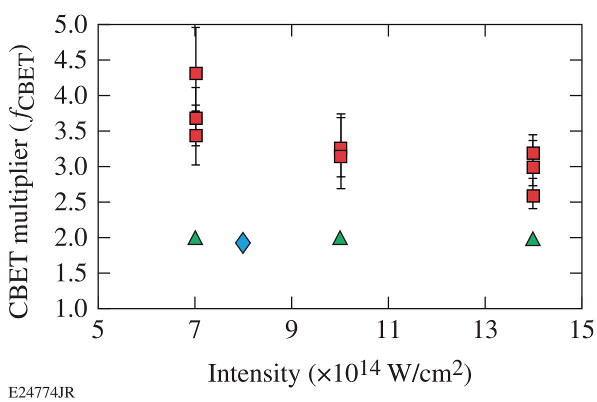

Figure 146.11
CBET multipliers that minimize the χ^2 difference between simulations and measurements are shown as a function of peak laser intensity for OMEGA symmetric direct-drive (green triangles) and polar-direct-drive (red squares) experiments and NIF experiments (blue diamond).

ACKNOWLEDGMENT

The authors thank the operations teams at both the Omega Laser Facility and the National Ignition Facility for their outstanding work. This work was supported by the U.S. Department of Energy Office of Inertial Confinement Fusion under Award Number DE-NA0001944, the University of Rochester, and the New York State Energy Research and Development Authority. The support of DOE does not constitute an endorsement by DOE of the views expressed in this article.

REFERENCES

1. J. Nuckolls *et al.*, Nature **239**, 139 (1972).
2. S. Atzeni and J. Meyer-ter-Vehn, *The Physics of Inertial Fusion: Beam Plasma Interaction, Hydrodynamics, Hot Dense Matter*, International Series of Monographs on Physics (Clarendon Press, Oxford, 2004).
3. W. L. Kruer *et al.*, Phys. Plasmas **3**, 382 (1996).
4. C. J. Randall, J. R. Albritton, and J. J. Thomson, Phys. Fluids **24**, 1474 (1981).
5. W. Seka, D. H. Edgell, J. P. Knauer, J. F. Myatt, A. V. Maximov, R. W. Short, T. C. Sangster, C. Stoeckl, R. E. Bahr, R. S. Craxton, J. A. Delettrez, V. N. Goncharov, I. V. Igumenshchev, and D. Shvarts, Phys. Plasmas **15**, 056312 (2008).
6. I. V. Igumenshchev, W. Seka, D. H. Edgell, D. T. Michel, D. H. Froula, V. N. Goncharov, R. S. Craxton, L. Divol, R. Epstein, R. Follett, J. H. Kelly, T. Z. Kosc, A. V. Maximov, R. L. McCrory, D. D. Meyerhofer, P. Michel, J. F. Myatt, T. C. Sangster, A. Shvydky, S. Skupsky, and C. Stoeckl, Phys. Plasmas **19**, 056314 (2012).
7. D. H. Froula, I. V. Igumenshchev, D. T. Michel, D. H. Edgell, R. Follett, V. Yu. Glebov, V. N. Goncharov, J. Kwiatkowski, F. J. Marshall, P. B. Radha, W. Seka, C. Sorce, S. Stagnitto, C. Stoeckl, and T. C. Sangster, Phys. Rev. Lett. **108**, 125003 (2012).
8. R. K. Kirkwood *et al.*, Phys. Rev. Lett. **76**, 2065 (1996).
9. W. Seka, H. A. Baldis, J. Fuchs, S. P. Regan, D. D. Meyerhofer, C. Stoeckl, B. Yaakobi, R. S. Craxton, and R. W. Short, Phys. Rev. Lett. **89**, 175002 (2002).
10. S. H. Glenzer *et al.*, Science **327**, 1228 (2010).

11. N. B. Meezan *et al*., Phys. Plasmas **17**, 056304 (2010).

12. P. Michel *et al*., Phys. Plasmas **17**, 056305 (2010).

13. P. Michel *et al*., Phys. Plasmas **20**, 056308 (2013).

14. D. T. Michel, S. Depierreux, C. Stenz, V. Tassin, and C. Labaune, Phys. Rev. Lett. **104**, 255001 (2010).

15. D. Turnbull *et al*., Phys. Rev. Lett. **114**, 125001 (2015).

16. I. V. Igumenshchev, D. H. Edgell, V. N. Goncharov, J. A. Delettrez, A. V. Maximov, J. F. Myatt, W. Seka, A. Shvydky, S. Skupsky, and C. Stoeckl, Phys. Plasmas **17**, 122708 (2010).

17. D. T. Michel, V. N. Goncharov, I. V. Igumenshchev, R. Epstein, and D. H. Froula, Phys. Rev. Lett. **111**, 245005 (2013).

18. S. Skupsky, J. A. Marozas, R. S. Craxton, R. Betti, T. J. B. Collins, J. A. Delettrez, V. N. Goncharov, P. W. McKenty, P. B. Radha, T. R. Boehly, J. P. Knauer, F. J. Marshall, D. R. Harding, J. D. Kilkenny, D. D. Meyerhofer, T. C. Sangster, and R. L. McCrory, Phys. Plasmas **11**, 2763 (2004).

19. D. H. Edgell, P. B. Radha, D. H. Froula, V. N. Goncharov, I. V. Igumenshchev, J. F. Myatt, and W. Seka, presented at the 42nd Annual Anomalous Conference, Key West, FL, 25–29 June 2012.

20. J. A. Marozas, T. J. B. Collins, P. W. McKenty, and J. D. Zuegel, presented at the 57th Annual Meeting of the APS Division of Plasma Physics, Savannah, GA, 16–20 November 2015.

21. P. B. Radha, T. J. B. Collins, J. A. Delettrez, Y. Elbaz, R. Epstein, V. Yu. Glebov, V. N. Goncharov, R. L. Keck, J. P. Knauer, J. A. Marozas, F. J. Marshall, R. L. McCrory, P. W. McKenty, D. D. Meyerhofer, S. P. Regan, T. C. Sangster, W. Seka, D. Shvarts, S. Skupsky, Y. Srebro, and C. Stoeckl, Phys. Plasmas **12**, 056307 (2005).

22. D. Cao, G. Moses, and J. Delettrez, Phys. Plasmas **22**, 082308 (2015).

23. J. A. Marozas, T. J. B. Collins, J. D. Zuegel, P. B. Radha, F. J. Marshall, and W. Seka, presented at the 44th Annual Anomalous Absorption Conference, Estes Park, CO, 8–13 June 2014.

24. T. R. Boehly, V. A. Smalyuk, D. D. Meyerhofer, J. P. Knauer, D. K. Bradley, R. S. Craxton, M. J. Guardalben, S. Skupsky, and T. J. Kessler, J. Appl. Phys. **85**, 3444 (1999).

25. T. R. Boehly, D. L. Brown, R. S. Craxton, R. L. Keck, J. P. Knauer, J. H. Kelly, T. J. Kessler, S. A. Kumpan, S. J. Loucks, S. A. Letzring, F. J. Marshall, R. L. McCrory, S. F. B. Morse, W. Seka, J. M. Soures, and C. P. Verdon, Opt. Commun. **133**, 495 (1997).

26. E. M. Campbell and W. J. Hogan, Plasma Phys. Control. Fusion **41**, B39 (1999).

27. P. B. Radha, J. A. Marozas, F. J. Marshall, A. Shvydky, T. J. B. Collins, V. N. Goncharov, R. L. McCrory, P. W. McKenty, D. D. Meyerhofer, T. C. Sangster, and S. Skupsky, Phys. Plasmas **19**, 082704 (2012).

28. Y. Lin, T. J. Kessler, and G. N. Lawrence, Opt. Lett. **21**, 1703 (1996).

29. S. Skupsky, R. W. Short, T. Kessler, R. S. Craxton, S. Letzring, and J. M. Soures, J. Appl. Phys. **66**, 3456 (1989).

30. M. Hohenberger, P. B. Radha, J. F. Myatt, S. LePape, J. A. Marozas, F. J. Marshall, D. T. Michel, S. P. Regan, W. Seka, A. Shvydky, T. C. Sangster, J. W. Bates, R. Betti, T. R. Boehly, M. J. Bonino, D. T. Casey, T. J. B. Collins, R. S. Craxton, J. A. Delettrez, D. H. Edgell, R. Epstein, G. Fiksel, P. Fitzsimmons, J. A. Frenje, D. H. Froula, V. N. Goncharov, D. R. Harding, D. H. Kalantar, M. Karasik, T. J. Kessler, J. D. Kilkenny, J. P. Knauer, C. Kurz, M. Lafon, K. N. LaFortune, B. J. MacGowan, A. J. Mackinnon, A. G. MacPhee, R. L. McCrory, P. W. McKenty, J. F. Meeker, D. D. Meyerhofer, S. R. Nagel, A. Nikroo, S. Obenschain, R. D. Petrasso, J. E. Ralph, H. G. Rinderknecht, M. J. Rosenberg, A. J. Schmitt, R. J. Wallace, J. Weaver, C. Widmayer, S. Skupsky, A. A. Solodov, C. Stoeckl, B. Yaakobi, and J. D. Zuegel, Phys. Plasmas **22**, 056308 (2015).

31. D. K. Bradley, P. M. Bell, J. D. Kilkenny, R. Hanks, O. Landen, P. A. Jaanimagi, P. W. McKenty, and C. P. Verdon, Rev. Sci. Instrum. **63**, 4813 (1992).

32. D. K. Bradley *et al*., Rev. Sci. Instrum. **66**, 716 (1995).

33. D. T. Michel, A. K. Davis, W. Armstrong, R. Bahr, R. Epstein, V. N. Goncharov, M. Hohenberger, I. V. Igumenshchev, R. Jungquist, D. D. Meyerhofer, P. B. Radha, T. C. Sangster, C. Sorce, and D. H. Froula, High Power Laser Science and Engineering **3**, e19 (2015).

34. D. T. Michel, C. Sorce, R. Epstein, N. Whiting, I. V. Igumenshchev, R. Jungquist, and D. H. Froula, Rev. Sci. Instrum. **83**, 10E530 (2012).

35. A. K. Davis, D. T. Michel, S. X. Hu, R. S. Craxton, R. Epstein, V. N. Goncharov, I. V. Igumenshchev, T. C. Sangster, and D. H. Froula, Rev. Sci. Instrum. **85**, 11D616 (2014).

36. J. J. MacFarlane *et al*., High Energy Density Phys. **3**, 181 (2007).

37. B. I. Bennett, J. D. Johnson, G. I. Kerley, and G. T. Rood, Los Alamos National Laboratory, Los Alamos, NM, Report LA-7130 (1978).

38. H. Takabe and T. Nishikawa, J. Quant. Spectrosc. Radiat. Transf. **51**, 379 (1994).

39. P. B. Radha, M. Hohenberger, D. H. Edgell, J. A. Marozas, F. J. Marshall, D. T. Michel, M. J. Rosenberg, W. Seka, A. Shvydky, T. R. Boehly, T. J. B. Collins, E. M. Campbell, R. S. Craxton, J. A. Delettrez, S. N. Dixit, J. A. Frenje, D. H. Froula, V. N. Goncharov, S. X. Hu, J. P. Knauer, R. L. McCrory, P. W. McKenty, D. D. Meyerhofer, J. F. Myatt, R. D. Petrasso, S. P. Regan, T. C. Sangster, H. Sio, S. Skupsky, and A. Zylstra, Phys. Plasmas **23**, 056305 (2015).

Time-Multiplexed Pulse Shaping

Introduction

Optical pulses are used to transmit information, perform remote sensing and metrology, and study physical processes in matter. These optics and photonics applications require the generation of pulses with control of their temporal characteristics, i.e., instantaneous power, timing, phase, and frequency variations over the pulse shape. Numerous techniques can be used to generate high-bandwidth optical waveforms.[1–8] Direct time-domain generation using high-bandwidth modulators is common in telecommunication applications and has benefited from the progress of high-bandwidth, direct-digital-signal synthesis and amplification. Commercial arbitrary waveform generators (AWG's) with an analog bandwidth higher than 10 GHz, sampling rates up to 65 GS/s, and a sampling depth of 8 bits can be used to drive electro-optic modulators and generate high-resolution optical waveforms.[9,10]

The precise generation of shaped optical waveforms is paramount to high-energy lasers that must deliver on-target pulse shapes optimized for laser–matter interaction. The front end of these facilities must generate optical pulses with low relative jitter and high-bandwidth pulse-shape control. The National Ignition Facility (NIF) (192 high-energy beams) uses 48 AWG's to precisely shape 48 seed pulses sent along distinct optical paths that include optical amplification, frequency conversion, beam smoothing, and focusing.[11,12] Full deployment of the Laser Mégajoule Facility (240 high-energy beams) will require 60 pulse-shaping units to precisely shape 60 seed pulses.[13]

This article presents a time-multiplexed pulse-shaping (TMPS) system generating up to eight synchronized optical waveforms that can be sent to eight distinct optical systems, e.g., sequences of optical amplifiers. A single pulse-shaping unit composed of an AWG and an electro-optic modulator generates a waveform composed of the shaped optical waveforms in different time slots. These waveforms are demultiplexed by a precisely calibrated $LiNbO_3$ 1×8 demultiplexer and then retimed. The use of a common pulse-shaping system significantly decreases the relative jitter between output waveforms, resulting in a significant cost reduction. The OMEGA Laser System now uses a single high-bandwidth AWG and a TMPS system to generate three high-resolution shaped pulses that can be propagated in different amplification systems.[14] The OMEGA EP Laser System will significantly benefit from the implementing a similar pulse-shaping system; in particular, higher-resolution waveforms with lower relative jitter will be generated to seed the four beamlines. A tentative layout for a redesigned fiber front end supporting direct drive on the NIF includes six eight-channel TMPS systems to generate 48 high-resolution shaped waveforms. The following sections describe the principle and implementation of the TMPS system and present experimental results focusing on the performance of the demultiplexer.

Principle and Implementation

1. General System Description

The purpose of time-multiplexed pulse shaping is to generate a plurality of shaped optical waveforms on physically distinct optical paths; for example, optical fibers, using a single high-performance pulse-shaping system [Fig. 146.12(a)]. The pulse-shaping unit generates a composite optical waveform composed of the shaped waveforms in their respective time slots. The composite waveform is sent to an optical demultiplexer configured to route different temporal slices to different outputs. In this work, the demultiplexer is configured to maximize the transmission of time slot j from demultiplexer input to output j while minimizing the transmission of other time slots to the same output. Optical fibers after each demultiplexer output relatively delay the demultiplexed waveforms; for example, when synchronized waveforms must propagate in different sections of a laser system and arrive on target with a predefined relative timing.

TMPS allows for significant performance improvement and cost reduction compared to the implementation of multiple pulse-shaping systems. The relative jitter between the generated waveforms is limited only by the short-term variations of the pulse-shaping system's time base, without any impact from the jitter between the pulse-shaping system and an external trigger. Lowering the relative jitter between waveforms is an important

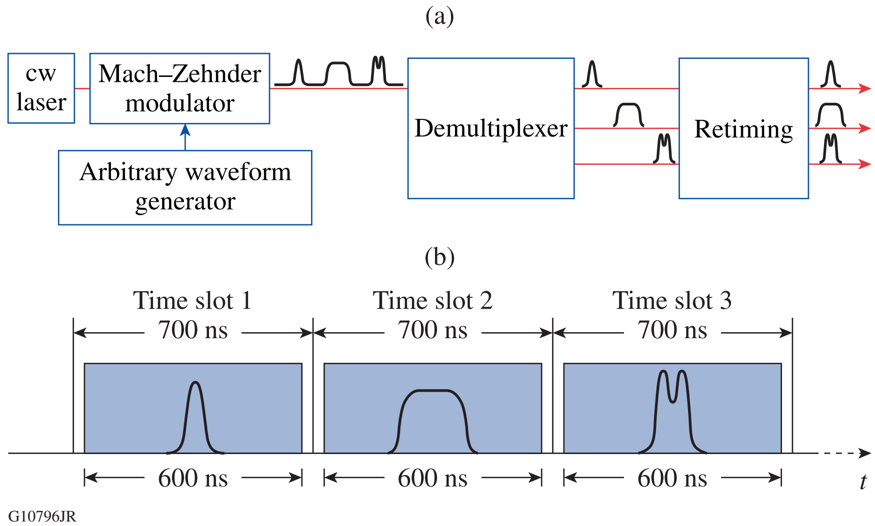

Figure 146.12
(a) Schematic of a time-multiplexed pulse-shaping (TMPS) system. Shaped optical waveforms are generated by modulating a continuous-wave (cw) laser using a Mach–Zehnder modulator driven by an arbitrary waveform generator, demultiplexed, and retimed relative to one another. (b) Timing diagram for the shaped waveforms in the composite waveform generated by the pulse-shaping unit.

consideration when the shaped pulses must be recombined into a single optical waveform later in the system or arrive on target with well-controlled relative timing. Generating multiple shaped optical waveforms with a single pulse-shaping unit instead of several units can significantly reduce the overall cost.

2. Typical Parameters

The required TMPS performance is application dependent. The application we focus on is the seeding of multiple high-energy laser systems. For the seed of each laser system, we allocate a time slot in which the seed pulse can be arbitrarily timed [Fig. 146.12(b)]. This ensures sufficient flexibility to modify the relative timing between seed pulses without reconfiguration or recalibration. In this work, consecutive 700-ns time slots are used because of an operation requirement for OMEGA,[14] where sub-10-ns seed pulses must be temporally tunable by as much as ±300 ns relative to their average timing. The 700-ns slots allow one to tune the seed pulses in a 600-ns range while leaving a 100-ns buffer window for transitioning the demultiplexer between different demultiplexing states.

For an N-channel system (N outputs, N time slots), the demultiplexer performance can be described by the $N \times N$ transmission matrix (T_{ij}), where T_{ij} is the transmission of time slot j from input to output i. Ideally, the diagonal elements are equal to 1 (no loss) and nondiagonal elements are equal to 0 (infinite extinction ratio). In practical conditions (i.e., with insertion losses, demultiplexer and driver imperfections), optimal demultiplexer operation corresponds to maximizing the diagonal elements while minimizing the nondiagonal elements.

3. Demultiplexer Technology

A custom lithium niobate ($LiNbO_3$) waveguide structure composed of fifteen 1×2 $\Delta\beta$ phase-reversal switches[15,16] has been procured from EOSPACE[17] to demonstrate an eight-channel TMPS (Fig. 146.13). In the absence of propagation

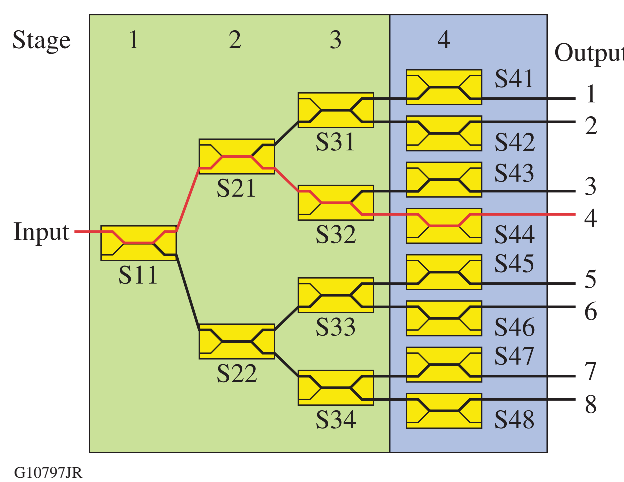

Figure 146.13
Layout of the 1×8 demultiplexer with three demultiplexing stages and one extinction-enhancement stage. Possible optical paths are traced with thick lines. The routing from input to output 4 is traced in red.

losses, the coupling ratio between two adjacent waveguides of length L is described by

$$T_{12} = T_{21} = \frac{1}{1+\left(\Delta\beta L_{\mathrm{c}}/\pi\right)^2}\sin^2\left[\frac{\pi L}{2L_{\mathrm{c}}}\sqrt{1+\left(\Delta\beta L/\pi\right)^2}\right], \quad (1)$$

where $\Delta\beta$ is the difference in propagation constant and L_{c} is the coupling length. The difference $\Delta\beta$ is controlled by applying a voltage that modifies the local refractive index via the electro-optic effect. Figure 146.14 shows an example of the measured transmission characteristics versus applied voltage for a 1053-nm monochromatic source propagating in a packaged $LiNbO_3$ 1×2 $\Delta\beta$ phase-reversal switch. Two voltages corresponding to the bar (no coupling between waveguides, i.e., $T_{12} = 0$) configuration and cross (all light from each waveguide is coupled to the other waveguide, i.e., $T_{12} \sim 1$) configurations of each 1×2 switch must be identified for optimal routing.

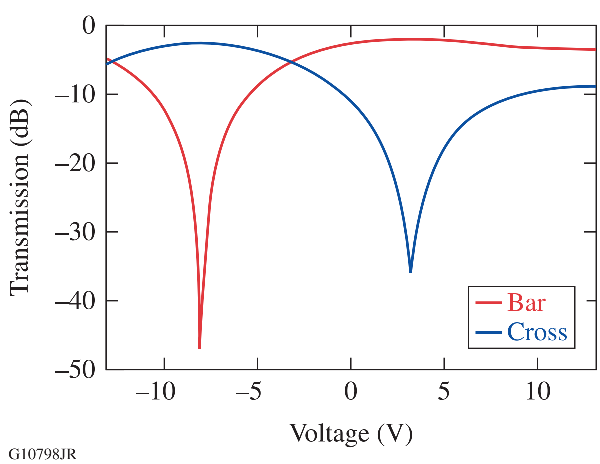

Figure 146.14
Measured transmission from the input to the cross and bar outputs versus voltage for a 1×2 $\Delta\beta$ phase-reversal switch.

The 1×8 demultiplexer designed and fabricated by EOSPACE[17] is organized in four stages (Fig. 146.13):

- Each 1×2 switch in the first three stages (switches S11, S21, S22, S31, S32, S33, and S34) can route its input to either of its outputs for demultiplexing.

- Each switch in the fourth stage (S41 to S48) can route its input to either an output connected to an optical fiber or an unconnected output to enhance the demultiplexer extinction ratio.

4. Driver Technology

To operate the demultiplexer, one must apply control voltages to each of the fifteen 1×2 switches. The most-general driver implementation consists of 15 AWG's that provide a time-dependent voltage to each switch, but this solution is complex, expensive, and cumbersome to integrate. Because demultiplexing requires operating each 1×2 switch in either the bar or cross configuration, a custom driver that produces two independent voltages and switches between them has been designed (Fig. 146.15). The bar and cross voltages are generated by two 12-bit digital-to-analog converters (DAC's) with output voltage between 0 and 5 V, followed by a fast analog switch. An operational amplifier level-shifts and amplifies the analog-switch output to the [–13-V, +13-V] range. A field-programmable gate array (FPGA) drives the fast analog switches. The FPGA uses a 200-MHz clock to specify the state of each analog switch in any 5-ns time window.

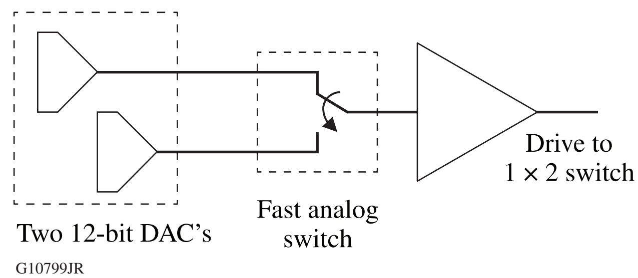

Figure 146.15
Elementary block diagram of the driver for each of the fifteen 1×2 switches in the 1×8 demultiplexer. The field-programmable gate array (FPGA) drives the fast analog switch to produce the voltage value generated by either of the 12-bit digital-to-analog converters (DAC's) and drive the 1×2 switch after amplification.

The state of the 15 analog switches, i.e., the state of each 1×2 switch in the demultiplexer, is defined in a routing table for each output. For example, routing from input to output 4 requires that switch S11 be in the bar configuration, switch S21 in the bar configuration, switch S32 in the cross configuration, and switch S44 in the bar configuration (red path in Fig. 146.13). All other fourth-stage switches are set to the cross configuration to route unwanted light to their unconnected output and enhance the extinction. The FPGA allows for arbitrary demultiplexing patterns, but the switch is sequentially driven for our application, i.e., time slot j is sent to output port j for a given number of cycles of the 200-MHz clock. When externally triggered, the FPGA runs through the defined sequence and waits until the next trigger. The driver and demultiplexer have been successfully operated at trigger rates up to 1 MHz. All results presented here have been obtained at much lower rates (1 kHz and lower), which are more representative of the operating repetition rates of fiber front ends for high-energy laser systems (300 Hz at LLE and 960 Hz on the NIF).

Experimental Results

1. General Information

The experimental results focus on the performance of the 1×8 demultiplexer supporting the TMPS system at 1053 nm. A trigger and 76-MHz reference signals were provided to the FPGA by a digital-delay generator (Stanford Research DG645) and a waveform generator (Agilent 33250A), respectively. The eight demultiplexer output fibers were connected to fiber-coupled DSC30 photodiodes (Discovery Semiconductors) connected to the two sets of four measurement channels of two 12-GHz oscilloscopes (Agilent). The oscilloscopes record the temporally resolved transmission of the demultiplexer between its input and each of its eight outputs.

In static operation, the voltages applied to the fifteen 1×2 switches are constant and the time-independent transmission between the demultiplexer and its eight outputs is characterized by an 8×8 matrix T_{ij}. This matrix has diagonal elements T_{ii} and nondiagonal elements T_{ij} corresponding to the transmission to output i when the demultiplexer is set to route the input light to output i and to other outputs j, respectively. In dynamic operation, the drives applied to the fifteen 1×2 switches change between their two binary voltage values set by the respective DAC's following a pattern determined by the FPGA. The FPGA keeps the drive voltages constant over time slots of specified duration. When 700-ns time slots are used, the transmission between input and each of the eight outputs is averaged over 600-ns intervals at the center of the eight time slots to quantify the demultiplexing performance because no significant transmission variation was observed in these intervals. This allows one to characterize the demultiplexer performance with an 8×8 matrix for specific dynamic conditions (demultiplexing sequence and time-slot duration). Because of details of the experimental implementation, each line of the transmission matrix in dynamic conditions is scaled to the transmission observed for the diagonal element; therefore, the extinction ratios are defined relative to the outputs.

2. Eight-Channel Static Operation

The demultiplexer is first calibrated with static voltages applied to all fifteen 1×2 switches. The static voltage applied to a specific switch is varied and the transmission between the input and one particular output is measured. The path between input and the chosen output must contain the switch being calibrated (e.g., one can choose output 4 to calibrate switches S11, S21, S32, and S44). This yields 15 transmission curves similar to one of the curves plotted in Fig. 146.14. Each of these curves is fitted with a second-order polynomial around its respective minimum and maximum to identify the optimal operation voltages. This calibration leads to the 30 optimal DAC voltages for static routing between input and outputs by the 15 switches.

The static transmission properties of the calibrated demultiplexer were characterized using a high-dynamic-range power meter. With the power meter connected to output i, the driver was sequentially configured to send light to each output j, therefore leading to a measurement of the transmission T_{ij} after normalization by the input power. The measured transmission matrix T_{ij} (Fig. 146.16) has diagonal elements, i.e., insertion losses, ranging from –4.6 to –5 dB and nondiagonal elements ranging from –55 dB to –70 dB, the latter being the measurement detection limit.

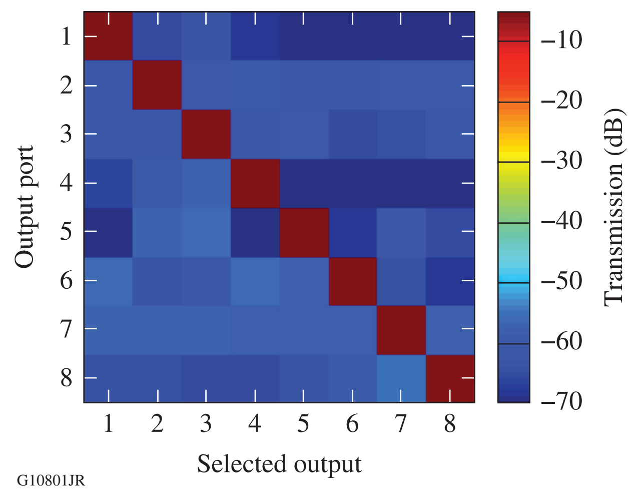

Figure 146.16
Transmission matrix on a logarithmic scale for eight-channel static operation. The transmission is measured at the eight output ports (vertical axis) when the multiplexer is driven to route light to each of the eight ports (horizontal axis).

3. Eight-Channel Dynamic Operation

When the voltage driving a 1×2 switch quickly changes between two different values, e.g., the values corresponding to the bar and cross configurations, the time-resolved switch transmission has a fast component and a slow component. The fast component measured on our system is of the order of 5 ns, including the response time of the custom driver. The slow component is, in comparison, extremely slow (hundreds of microseconds). The existence of these two components implies that drive voltages optimized for static routing are not optimal for dynamic demultiplexing. Non-optimal voltages increase the insertion losses and decrease the extinction ratios. Drive voltages must be calibrated in dynamic operation, i.e., when driving the demultiplexer to route different time slots (with ~μs duration) of the input signal to different outputs. A general formalism has been developed to ensure that the calibration process is computationally efficient and exhaustive. For a particular switch, the temporally resolved demultiplexer outputs are measured and processed to identify the two drive voltages that optimize the switch transmission in dynamic operation. Optimization consists in maximizing transmission for combinations of time slots and output ports where it must be high and minimizing transmission for combinations of time slots and output ports where it must be low.

The demultiplexer was optimized for dynamic operation with eight output channels. The optimal voltages for dynamic operation were found to be significantly different from the optimal static voltages. The 8×8 transmission matrix with these voltages is shown in Fig. 146.17(a). The lowest observed extinction is –46 dB, and all but five out of the 56 nondiagonal elements of the extinction matrix are lower than –50 dB. For comparison, the eight-channel TMPS system has been characterized when using the drive voltages optimized for static routing [Fig. 146.17(b)]. The observed performance degradation confirms that adequate operation in dynamic operation can be obtained only by calibration in dynamic conditions. The transmission properties of the demultiplexer driven with the optimized static voltages are clearly seen in the resulting time-resolved signals measured on the eight output ports (Fig. 146.18).

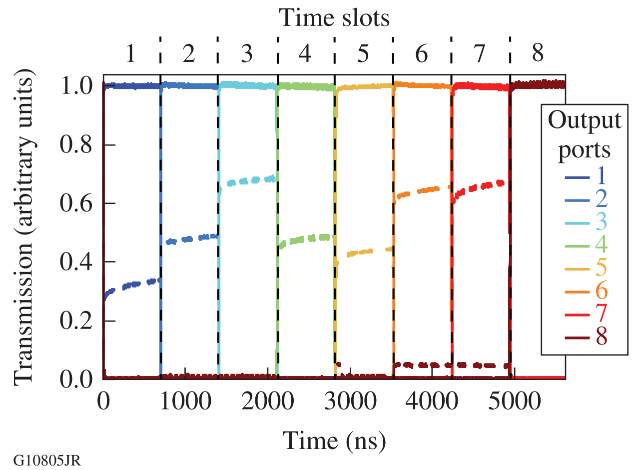

Figure 146.18
Time-resolved transmission measured on the eight output ports in dynamic operation. The continuous and dashed lines correspond to the transmission measured with voltages optimized in dynamic operation and static operation, respectively.

Conclusions

A system architecture to efficiently extend the performance of a single pulse-shaping unit by high-performance demultiplexing has been described. The time-multiplexed pulse-shaping concept generates multiple waveforms in different time slots that are demultiplexed and retimed relative to one another. An experimental implementation of the demultiplexing subsystem based on a 1×8 $LiNbO_3$ demultiplexer based on four stages of 1×2 $\Delta\beta$ phase-reversal switches has been described

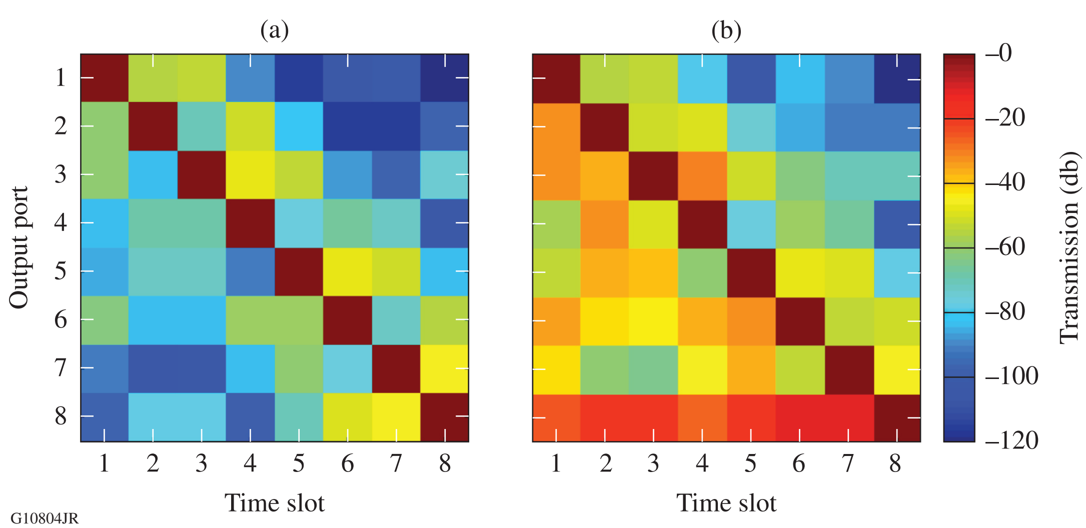

Figure 146.17
Transmission matrix on a logarithmic scale for eight-channel dynamic operation with voltages optimized for (a) dynamic operation and (b) static operation.

and characterized. High-performance demultiplexing has been demonstrated for an eight-channel system (50-dB extinction ratio) by determining optimal values of the drive voltages for each 1×2 switch for dynamic routing.

The demultiplexer was optimized for four-channel operation to support its deployment on OMEGA and OMEGA EP. When demultiplexing of the input waveform to only four output ports is required, the third-stage switches can be used to enhance the extinction ratio of the demultiplexed waveforms. This has led to a measured contrast of the order of 70 dB in dynamic conditions. Operation of the demultiplexer on signals generated at 1064 nm with drive voltages optimized for operation at 1053 nm has led to no significant performance degradation, indicating that the demultiplexer can operate with tunable signals and signals with an optical spectrum broadened by phase modulation.

ACKNOWLEDGMENT

The authors thank G. Kick, R. Hopf, and D. Hassett (Laboratory for Laser Energetics) for their work on the switch driver, and G. Abbas and S. Thaniyavarn (EOSPACE) for fruitful discussion about the demultiplexer. This material is based upon work supported by the Department of Energy National Nuclear Security Administration under Award Number DE-NA0001944, the University of Rochester, and the New York State Energy Research and Development Authority. The support of DOE does not constitute an endorsement by DOE of the views expressed in this article.

REFERENCES

1. A. M. Weiner, Rev. Sci. Instrum. **71**, 1929 (2000).
2. T. Yilmaz *et al*., IEEE Photonics Technol. Lett. **14**, 1608 (2002).
3. P. K. Kondratko *et al*., IEEE Photonics Technol. Lett. **17**, 2727 (2005).
4. A. Monsterleet *et al*., Electron. Lett. **41**, 332 (2005).
5. J. Yao, F. Zeng, and Q. Wang, J. Lightwave Technol. **25**, 3219 (2007).
6. Z. Jiang *et al*., IEEE J. Quantum Electron. **43**, 1163 (2007).
7. Y. Dai and J. Yao, J. Lightwave Technol. **26**, 3329 (2008).
8. M. Bolea *et al*., IEEE Photonics Technol. Lett. **23**, 618 (2011).
9. Arbitrary Waveform Generation Model No. AWG70001A, Tektronix, Inc., Beaverton, OR 97077, http:/www.tek.com (24 May 2016).
10. Keysight Technologies, Inc., Santa Rosa, CA 95403-1738, http://www.keysight.com/main/home.jspx?cc=US&lc=eng (21 April 2016).
11. P. J. Wisoff *et al*., Proc. SPIE **5341**, 146 (2004).
12. C. A. Haynam *et al*., Appl. Opt. **46**, 3276 (2007).
13. J.-F. Gleyze *et al*., Proc. SPIE **7916**, 79160I (2011).
14. T. Z. Kosc, J. H. Kelly, E. M. Hill, C. Dorrer, L. J. Waxer, and W. R. Donaldson, Proc. SPIE **9345**, 93450H (2015).
15. H. Kogelnik and R. Schmidt, IEEE J. Quantum Electron. **12**, 396 (1976).
16. S. Thaniyavarn, Proc. SPIE **578**, 192 (1985).
17. EOSPACE, Inc., Redmond, WA 98052, http://www.eospace.com (17 May 2016).

Continuous Distributed Phase-Plate Advances for High-Energy Laser Systems

Introduction

The symmetric-direct-drive (SDD) and polar-direct-drive (PDD) configurations utilized in inertial confinement fusion[1,2] (ICF) driven by high-power lasers require target illumination that conforms to the design shape or objective with a high degree of fidelity. Nonuniformity in the lower spherical-harmonic ℓ modes can have a significant impact on ICF target performance since these modes imprint for the longest period of time and are the most difficult to smooth.

Continuous phase plates are used in SDD and PDD ICF applications because they offer control of the far-field intensity envelope in the presence of typical laser system phase aberrations. The resultant time-averaged, far-field spot intensity has a well-controlled shape. The goal is to design phase-dislocation–free continuous phase plates that produce a speckled far field whose envelope and spectrum are controlled, unaffected by system aberrations and speckle that can be smoothed.

This article describes a novel distributed phase plate (DPP) design process that achieves higher fidelity to the design objectives relative to existing methods. The novel DPP design code is called *Zhizhoo*' and is capable of producing a continuous phase-dislocation–free DPP with low near-field modulation that achieves a <1% to 2% weighted $\sigma_{\rm rms}$ error of the far-field spot shape in a few minutes using a multicored personal computer with optional GPU accelerations.

The versatility of the *Zhizhoo*' design technique is evident in its ability to craft far-field envelopes from simple super-Gaussian to rather arbitrary shapes.[3] The phase-plate design techniques presented here can be applied to phase plates with or without constraining the far-field power spectrum to lower spectral power in the long-wavelength band. The ability of this technique to calculate phase-dislocation–free continuous phase plates is closely linked to maintaining a correlation with the speckle pattern and minimizing the phase gradient.[3] Various phase-plate designs will be presented for a few high-power laser systems that highlight the various capabilities of *Zhizhoo*'.

Zhizhoo' DPP Design Tool

The *MATLAB*-based tool *Zhizhoo*'[3,4] crafts continuous DPP's; the salient features of *Zhizhoo*' are as follows:

(a) Employs a feedback loop: Unlike other methods currently in use, *Zhizhoo*' employs a novel feedback technique as a fundamental tool to generate DPP profiles with tight control of the resultant far-field spot shape and phase plate; e.g., far-field shape, arbitrary azimuthal and radial variations, DPP phase gradient, DPP phase spectral control, and phase anomaly-free designs.[3] The algorithm employs a highly modified Fienup-type algorithm as part of the whole feedback loop.[5,6] The overall technique is novel in its approach and is very fast because of the feedback (which distinguishes *Zhizhoo*' as it hastens convergence via augmentation) and the *FFTW*-based methods.[7] In addition, a robust phase-unwrapping algorithm is employed that solves Poisson's equation in the least squares sense (algorithm adapted from Ref. 8).

(b) Designs far-field envelopes from simple super-Gaussian to rather arbitrary shapes: Simple or exotic far-field envelope shapes are effortlessly handled with *Zhizhoo*'. Wide design objectives and/or steep profiles will require correspondingly higher surface or phase gradients in the DPP. *Zhizhoo*' can maintain envelope control, even down to the ~1% $\sigma_{\rm rms}$ level.

(c) Uses an optimal filter: An important aspect of the *Zhizhoo*' feedback loop is the Wiener or optimal filter.[3] The Wiener filter employs the well-known speckle statistics from Goodman[9,10] to model the speckle "noise" to create an optimal filter that accurately extracts the true envelope shape.

Zhizhoo' Intermediate NIF Polar-Direct-Drive Distributed Phase Plate Designs

The National Ignition Facility's (NIF's) PDD asymmetric far-field spot design objective is an ideal candidate to test the shape control capabilities of *Zhizhoo*'. The NIF PDD asymmetric spot shape is a composite spot consisting of a primary super-Gaussian plus an offset secondary ellipse that is modulated by an offset aperturing function referred to as "spot-masking apodization" (SMA). The asymmetric far-field spot objective for NIF PDD cannot be considered an ellipse nor can it be accurately represented as a distorted ellipse. The 43×43-cm-sq–aperture intermediate NIF PDD design for one of the equatorial spots is shown in Fig. 146.19(a) along with the resultant speckled spot in Fig. 146.19(b). The effect of SMA is clearly observed in Fig. 146.19(b), where the over-the-horizon portion of the spot is occluded.

It is crucial to the success of NIF PDD experiments that the DPP design prepared for the manufacturing process be as close as possible to the design objective. Otherwise, the far-field spot's integrity severely degrades in the presence of both manufacturing phase error (MPE) and near-field wavefront error (WFE). A DPP design that initially has the highest integrity level will remain more intact, relative to an insufficient design. NIF's WFE was measured and imposed upon the DPP's for a worst-case analysis via *DRACO* hydrodynamic simulations. The strongest NIF beamline WFE was a weaker aberration than a 25-μm-rms (root-mean-square) MPE, setting the acceptable MPE tolerance to 25-μm rms.

During the NIF's PDD (intermediate and ignition-scale) DPP design process, a potential manufacturing problem surfaced. The issue was the result of a combination of interferometric measurements and the machine's internal phase-unwrapping algorithms. The resulting unwrapped phase would produce areas of phase dropouts and occasionally large regions of π discontinuities. However, the phase-unwrapping procedure incorporated within *Zhizhoo*' is designed to be immune to areas of noise and regions of π discontinuities. It was demonstrated that the phase-unwrapping algorithm was more than capable of removing and correcting the corrupted phase data from the instrument.[11] Utilizing the phase-unwrapping algorithm from *Zhizhoo*' is a cost-effective alternative to procuring expensive interferometers. The algorithm is able to correct the phase errors from the intermediate energy scale up to the ignition-scale designs.

Steep-Profile, Low-Ripple, Flattoped Round Spots

Low-ripple, flattopped spots with steep profiles are additional design objectives compatible with the *Zhizhoo*' DPP design method. Traditionally, DPP's have had difficulty designing low-ripple, flattopped spots because the designs tended to ring as the spot shape rolls off to zero. In contrast, *Zhizhoo*'-crafted DPP's tend not to suffer the same fate because of the feedback control with augmentation of the design profile.

The OMEGA EP laser required a redesign for its 1.8-mm-wide spot because of damage that the turning mirror suffered from high-level modulation caused by a retroreflection back through the focusing lens. The close proximity of the turning mirror posed a design challenge for *Zhizhoo*' by mandating wavelength control of the DPP's feature size. The design for the far-field envelope demanded a large flat area with a fast roll-off.

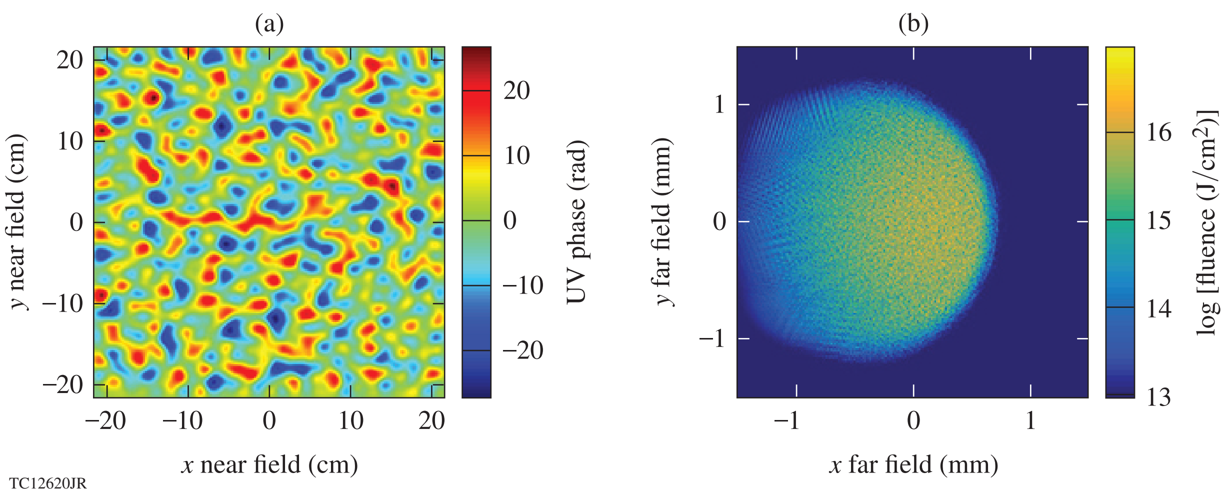

Figure 146.19
The intermediate NIF polar-direct-drive (PDD) distributed phase plate (DPP) design crafted for (a) an equatorial beam profile and (b) the resultant speckled spot. The speckled image on the log scale demonstrates the remarkable speckle rejection and smooth profile at low intensity not obtainable using other methods. Note that the design objective function and the extracted envelope are nearly indistinguishable at a <1% rms (root-mean-square) error.

The low-ripple (2.5%) resultant extracted envelope is shown in Fig. 146.20(a). The equivalent free-space back-propagation was determined to be 6 m, which drove the DPP design to use large feature sizes to minimize near-field modulations [see Fig. 146.20(b)]. The larger feature sizes had the side effect of driving up the peak-to-peak phase depth of the DPP because of the smaller bandwidth distribution of the phase, which also increased local phase gradients.

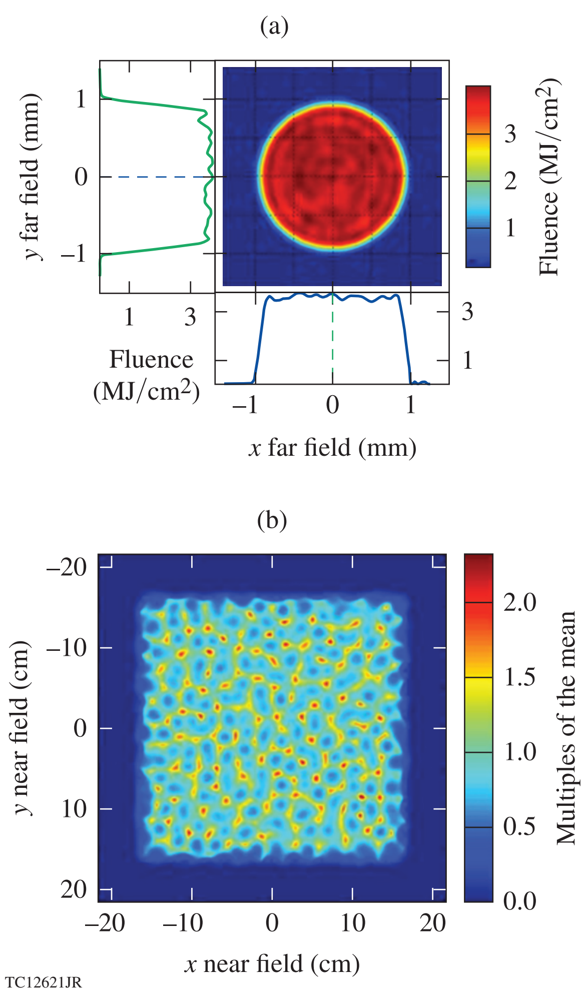

Figure 146.20
(a) The OMEGA EP low-ripple, 1.8-mm-wide far-field extracted envelope. (b) The resulting near-field low-level modulation from a retroreflection is indicative of the large DPP feature sizes.

The Dynamic Compression Sector (DCS) laser also required a low-ripple, flattopped spot but with two additional attributes: decreased mid-range spectrum (high pass) and a flexible spot shape via dispersion control. The high-pass DPP design procedure, similar to the method reported in Ref. 3, successfully reduced the power in the long- to mid-wavelength modes, even in the presence of predicted DCS WFE (see Fig. 146.21). The DCS DPP design provides a trade-off among several smoothing attributes, including spot shape and intensity on target, by adjusting a differential grating that changes the dispersion experienced by the 1-D, multi-FM smoothing by spectral dispersion system.[12]

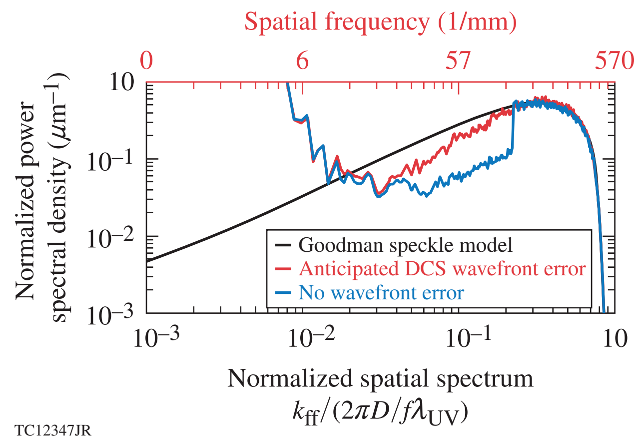

Figure 146.21
The far-field speckled spot spectrum for the DCS Laser System. The Goodman speckle model is shown as a reference to indicate the ability of the high-pass DPP design to modify the far-field spot's spectrum (blue curve). In the presence of predicted DCS laser WFE, the high-pass DPP design still maintains a decreased spectrum over the spectral band (red curve). DCS: Dynamic Compression Sector; WFE: wavefront error.

Conclusion

The continuous phase-plate design code *Zhizhoo*' is capable of crafting DPP's for a variety of high-power laser systems, each having different design constraints. *Zhizhoo*' designs continuous DPP's with simple envelope shapes or exotic shapes with asymmetry. The code *Zhizhoo*' crafts DPP's with a high degree of fidelity to the design objective. A higher-fidelity DPP design results in a more-faithful representation of the desired objective function when the DPP is subjected to WFE and MPE. The flexibility of the *Zhizhoo*' design code makes it easy to create multiple designs, even when the design requirements change because *Zhizhoo*' can respond in a short period of time or produce multiple realizations to improve beam-overlap nonuniformity reduction.

ACKNOWLEDGMENT

This material is based upon work supported by the Department of Energy National Nuclear Security Administration under Award Number DE-NA0001944, the University of Rochester, and the New York State Energy Research and Development Authority. The support of DOE does not constitute an endorsement by DOE of the views expressed in this article.

REFERENCES

1. C. P. Verdon, Bull. Am. Phys. Soc. **38**, 2010 (1993).
2. S. E. Bodner, D. G. Colombant, J. H. Gardner, R. H. Lehmberg, S. P. Obenschain, L. Phillips, A. J. Schmitt, J. D. Sethian, R. L. McCrory, W. Seka, C. P. Verdon, J. P. Knauer, B. B. Afeyan, and H. T. Powell, Phys. Plasmas **5**, 1901 (1998).
3. J. A. Marozas, J. Opt. Soc. Am. A **24**, 74 (2007).
4. Inspired by Anishinaabe words *Zhizhoo'*, meaning "spreads someone using something," and *zhizhoo'an*, meaning "spreads something using something," just as the phase plate spreads out the diffraction-limited, far-field spot to match the far-field objective. J. D. Nichols and E. Nyholm, *A Concise Dictionary of Minnesota Ojibwe* (University of Minnesota Press, Minneapolis, 1995).
5. R. W. Gerchberg and W. O. Saxton, Optik **35**, 237 (1972).
6. J. R. Fienup, Appl. Opt. **21**, 2758 (1982).
7. M. Frigo and S. G. Johnson, Proc. IEEE **93**, 216 (2005).
8. D. C. Ghiglia and L. A. Romero, J. Opt. Soc. Am. A **11**, 107 (1994).
9. J. W. Goodman, *Introduction to Fourier Optics* (McGraw-Hill, New York, 1988).
10. J. W. Goodman, in *Laser Speckle and Related Phenomena*, edited by J. C. Dainty, Topics in Applied Physics (Springer-Verlag, Berlin, 1984), Vol. 9, Chap. 2, pp. 9–75.
11. LLNL kindly fabricated *Zhizhoo'*-crafted DPP prototypes and measured them using their interferometers, which provided the data for this analysis.
12. J. A. Marozas, J. D. Zuegel, and T. J. B. Collins, Bull. Am. Phys. Soc. **52**, 145 (2007); *ibid*. **53**, 249 (2008); *ibid*. **54**, 306 (2009); *ibid*. **55**, 294 (2010).

Nanomechanics and Laser-Induced Damage in Optical Multilayer Dielectric Gratings

Introduction

Multilayer dielectric (MLD) pulse-compressor gratings are critical components used in a high-peak-power laser system's amplification system and have been a focus of recent research and development efforts because of their low damage thresholds.[1,2] At LLE, the peak-power capability—and, therefore, the overall performance of the petawatt-class OMEGA EP Laser System—is limited by the laser-damage resistance of diffraction gratings in the chirped-pulse–amplification (CPA) pulse compressors for each beamline.[3–6] Increasing the damage thresholds of these components is, therefore, an important objective.

A low-temperature chemical cleaning approach developed by Howard *et al.*[7] to improve the performance of these MLD gratings has demonstrated that grating coupons that were cleaned using the optimized method consistently met OMEGA EP requirements on diffraction efficiency (>97%) and 1053-nm laser-damage resistance at 10 ps (>2.7 J/cm^2). They also observed that, for samples with the highest damage threshold, there were minimal laser-conditioning effects, suggesting a transition from a contamination-driven laser-damage mechanism to defect-driven damage for well-cleaned components. Hereafter, this metric—laser-induced–damage threshold (LIDT)—will be referred to as optical testing. Such optical testing is the most common way to characterize the performance and, therefore, the quality of an MLD grating that has been cleaned for use in a high-power laser system.

There is some concern that cleaning procedures and/or fabrication techniques for gratings can mechanically weaken the fragile grating pillars, possibly affecting the grating's resistance to laser damage and, therefore, warrant mechanical characterization. The development of a methodology to monitor a grating's mechanical properties will enable one to better understand the fabrication and cleaning processes and will point to appropriate modifications that will preserve or enhance the grating's integrity.

Nano-indentation of MLD gratings[8] is our adopted approach, and the indents that invoke fracture of the silica walls are treated in detail. Nano-indentation and/or uniaxial compression of patterned surfaces manufactured by techniques such as focused ion-beam (FIB) milling and lithography[9] have shown tremendous potential in isolating the ductile response of the material from its brittle response. These studies prominently feature the uniaxial compression of metallic high-aspect-ratio micro- and nanopillars,[10–13] produced by FIB milling, with diameters ranging from 75 nm to 7.5 μm. Such structures are used to study the ductile deformation of metals, specifically size effects and their dependence on properties such as yield strength.

Experiments on micropillars of amorphous silica subjected to uniaxial compression have recently been reported by Lacroix *et al.*[14,15] Their findings indicate that silicate glasses are very suitable for micropillar compression because the ratio of the yield stress to Young's modulus is comparatively high compared to a typical metal. They also demonstrated the experimental conditions under which plastic flow can be obtained in compression of these pillars without catastrophic failure and accompanied only by minor, well-defined radial crack patterns.

The LIDT of amorphous silica gratings for ultrahigh intensity laser systems has been studied extensively in literature.[16,17] The electric field is known to be maximum at the top area of the grating walls. It is in this region of local enhancement that damage initiates, defining the ultimate damage threshold.

Both tests (laser-induced damage and nano-indentation), although vastly different in nature and implementation, inherently measure the performance of the grating (optical versus mechanical). Fracture, caused by a concentration of mechanical stresses, is an integral part of these measurements. Therefore, it is imperative and almost intuitive to explore mechanical testing (nano-indentation) as a means to complement and even precede optical testing to establish the "quality" and performance of an MLD grating sample. We are guided by the observation that both optical fields (electric and magnetic) and mechanical fields (stress and strain), when interacting with the grating geometrical features and with defects and inhomogeneities, will show significant concentrations.

Materials and Methods

1. Fabrication of MLD Gratings

The process of manufacturing MLD gratings has been detailed extensively in published literature[7,8,18] and is summarized here for completeness.

The first step is to deposit the MLD coating on the glass substrate (fused silica or BK7) by reactive evaporation at 200°C as a thick, modified-quarter-wave thin-film stack[19] with hafnia (HfO_2) and silica (SiO_2) used as the high- and low-index materials, respectively. Next, a bottom antireflective coating (BARC) layer (organic polymer) may be applied to the multilayer mirror, followed by a layer of photoresist coating. Interference lithography is used to pattern the grating (grooves, 1740 lines per mm). Once patterned, etching is performed to remove the BARC and a portion of the top MLD layer, leaving the silica wall geometry.

Finally, organic (BARC, photoresist layers, etch products, and environmental contamination) and inorganic residues (metallic contaminants) are stripped away in a final cleaning process. For the grating samples used in this work, the silica walls were ~440 nm high with a slightly tapered geometry (~250 nm wide at the base and ~150 nm wide at the top).[8]

2. An Optimized Procedure for Cleaning MLD Gratings to Maximize Laser-Damage Thresholds

For this study, cleaning experiments were performed on small-scale MLD grating coupons. Round hafnia/silica MLD gratings (100 mm in diameter, 3 mm thick) were broken into eight equally sized, wedge-shaped coupons. All cleaning experiments described in this section were performed on uncleaned gratings with BARC and photoresist still intact (that is, they were not subjected to any photoresist stripping or cleaning operations other than those described here). Uncleaned gratings can be easily distinguished by their characteristic brown and hazy appearance (which disappears when a grating is well cleaned), attributed to the residual organic materials.

Acid piranha, the most widely used chemical cleaning agent at higher temperatures,[18] was insufficient for our low-temperature (40°C) process; a multistep technique is warranted to ensure a wide-range removal of performance-limiting contaminants. This cleaning methodology—discussed in Howard's work[2,7,8,18–20] and adapted by improvising on existing literature for cleaning gratings (such as Refs. 18 and 21) and semiconductor wafer processing—was split into two parts: a partial clean consisting of six steps and a final clean that included a plasma step. The cleaning process is summarized in Table 146.II.

The final clean, which is a third plasma treatment, can be either an air plasma[7] or an oxygen plasma (conventionally used

Table 146.II: Cleaning process for the MLD gratings used in this work.

Cleaning Process				Process Steps	
	Step	Temperature (°C)	Time (min)	Chemical	Purpose
Partial clean	1	40	15	5:1 piranha spray	Strip photoresist and etch residues
	2	40	15	2:1 piranha spray	Strip photoresist and etch residues
	3	23	10	Air plasma (6.8-W power)	Completely remove BARC
	4	40	10	1:1:6 SC-2 no-stir soak	Remove metallic contamination
	5	23	10	Air plasma (6.8-W power)	Remove light organic matter
	6	23	5	2800:1 BOE* soak	Reduce grating duty cycle
Final step	7	23	15	Air plasma (6.8-W power) OR Oxygen plasma (6.8-W power)	Remove organics from grating surface

*buffer oxide etch

in grating cleaning procedures). As shown later, this choice can have a decisive effect on the laser-damage threshold attained by a grating sample.

3. Laser-Damage Testing

Damage testing was carried out at LLE's damage-testing facility on the short-pulse (10-ps) system with operating capabilities in both air and high vacuum (4×10^{-7} Torr). The MLD grating samples studied here were tested in air using *s*-polarized light at 1053 nm at an incident beam angle of 61° with an irradiation spot size of 370 μm (e^{-1} in intensity) in the far field. Beam analysis and fluence calculations were performed using the Ophir–Spiricon commercial laser-beam profiler. Laser damage was assessed *in situ* using a white-light imaging system (~100× magnification). Damage was defined as a feature on the sample's surface that was not observed before laser irradiation.[20,22] Damage thresholds are reported as beam-normal fluences. An example of a damage site on grating 566-5 is shown in Fig. 146.22.

Our damage tests employed the *N*-on-1 testing regime performed in air. Particulars of this testing protocol and others, such as 1-on-1, can be found in literature.[23] *N*-on-1 (stepwise ramped fluence) testing is conducted by irradiating the sample site at a fluence that is well below the 1-on-1 threshold for ten shots. If no damage is detected, the same site is irradiated with five more shots at a slightly increased fluence. This is continued until damage is observed in white light, at which point the damage onset fluence is recorded as the *N*-on-1 threshold for that site. The *N*-on-1 test is repeated for five sites on each MLD grating sample to generate an average and a standard deviation, which are reported as the *N*-on-1 threshold and measurement error, respectively.

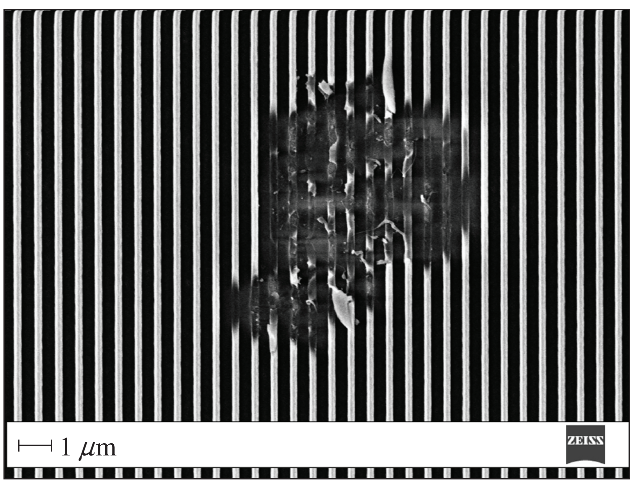

G10719JR

Figure 146.22
A scanning electron microscope (SEM) image of an *N*-on-1 laser-induced–damage site on the multilayer dielectric (MLD) grating structure.

4. Nano-Indentation of MLD Gratings

An MTS Nanoindenter XP fitted with a conical tip (60° included angle, 1-μm tip radius) was used in this work. The system was calibrated by performing nano-indentation on fused silica. Because of the limited imaging capabilities of the instrument and given the submicron scale of the pillar structures, it was not possible to resolve the impressions made by the indenter using the nano-indenter's built-in microscopy; instead, the sample had to be transferred to a scanning electron microscope (SEM) to observe the indents and "wall" damage. Loads in the 0.1- to 0.5-mN range were used and three types of indents could be produced by simply displacing the location of the indentation tip on the grating: centered, partially off-centered, and mostly off-centered indents.

Experimental Results

1. LIDT Results for Gratings and Cleaning Processes

In this study, the fabrication method of gratings was the same across the three samples: 13P-11-56/#566-3, 13P-11-56/#566-5, and 5P-12-56/#644-1. The cleaning procedures detailed earlier were used to prepare these gratings before they were subjected to laser-damage testing. The details of the cleaning methods for our samples are included in Table 146.III. Hereafter, for purposes of brevity, the grating samples will be addressed as #566-3, #566-5, and #644-1.

Two of the gratings (#566-3 and #566-5) that originated from the same coating run were processed together until the cleaning step. The third grating specimen (#644-1) was fabricated a year later using an identical coating process (5P-12-56).

Table 146.III: Summary of LIDT results for gratings and specific cleaning methods used.

Grating	Cleaning Process	Diffraction Efficiency Results (%)	*N*-on-1 LIDT (J/cm^2); air
13P-11-56/#566-3	Partial + air plasma	97.3±0.2	3.66±0.51
13P-11-56/#566-5	Partial + O_2 plasma	97.3±0.5	4.30±0.25
5P-12-56/#644-1	Partial + O_2 plasma	97.9±0.5	1.82±0.08

2. Nano-Indentation Data and Grating Brittleness

Nano-indentation tests were performed on all three grating samples at loads of 0.1, 0.2, 0.3, 0.4, and 0.5 mN. For each sample and at each load, nine indents were made at locations several microns apart. The aim here was to make as many decentered indents as possible. As mentioned in detail elsewhere,[8,24] the centered indents are useful in measuring the yield strength of silica at nanoscale corresponding to this unique geometry. Conversely, off-centered indents are inherently related to fracture of the grating walls, which can now be used to explore a connection with LIDT (associated with fracture as well). This is shown in Fig. 146.23.

Therefore, after performing indentations on the samples, we analyzed each corresponding load-displacement curve to separate the off-centered indents from the centered ones. An example for #566-5 indented at a load of 0.2 mN is shown in Fig. 146.24. The load-displacement curves make a clear distinction between centered and off-centered indents. The centered indent looks similar to an indent in a bulk material[8,24] and has no wall fracture associated with it. The difference, however, from bulk nano-indentation is that in bulk nano-indentation the surrounding material laterally constrains the material deformation. In grating ("wall") nano-indentation, such lateral constraint is reduced because of the small thickness of the silica wall. The other two curves, showing the off-centered indents, include fracture that is seen by the sudden break in the curve (leading to a "plateau") followed by additional loading.

For the purpose of extracting a metric that can be useful in analyzing the mechanical performance of gratings, which can then be compared to their optical performance (LIDT), we located the point of fracture initiation for each of the load-displacement curves. This is illustrated in Fig. 146.25 for grating #566-3 at a load of 0.2 mN. The location of the fracture initiation point (penetration depth Δ) for each indent depends on the amount of decentering; naturally, this is different for each indent (see Fig. 146.25). To evaluate the grating as a whole at

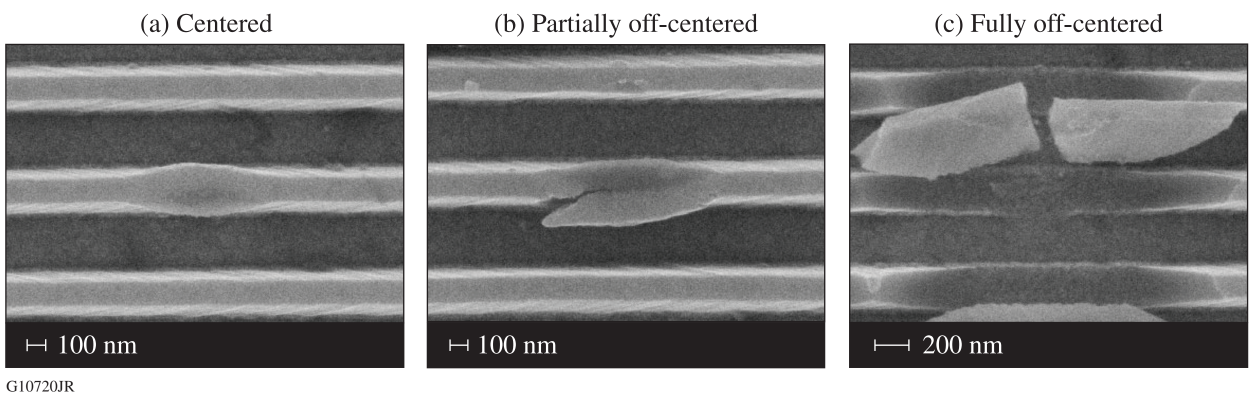

Figure 146.23
Three distinct nano-indentation responses are seen in MLD gratings.

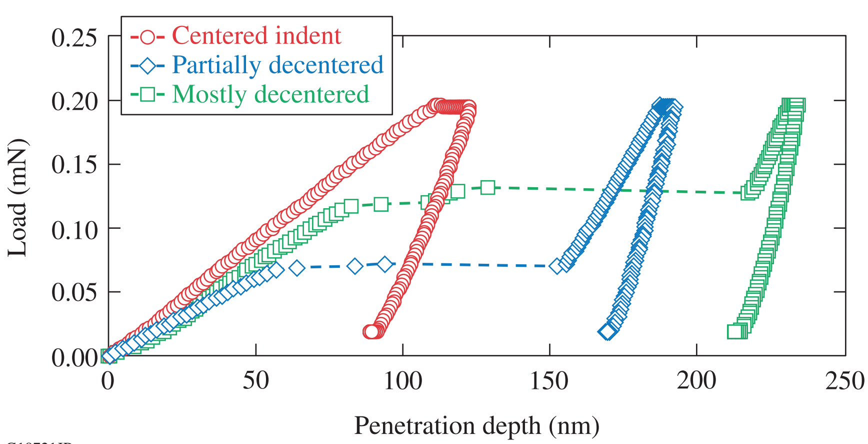

Figure 146.24
Load-displacement curves of nano-indentation for grating #566-5 with a 0.2-mN load.

that particular load, however, we chose the smallest penetration depth across all indents to represent the value at which fracture is initiated. In this example (Fig. 146.25), a penetration depth of 81 nm is the weakest site for failure under a nanomechanical load of 0.2 mN and will be designated as Δ_{min}. Similarly, data can be collected across all three grating samples for a load range of 0.2 to 0.5 mN.

We considered only those indents made at loads varying from 0.2 to 0.5 mN since indentations made at the 0.1-mN load did not yield any discernible instances of fracture.

3. Brittleness, Deformation, and LIDT

The penetration depths corresponding to the weakest sites for fracture initiation (Δ_{min}) at each load and sample are plotted against the measured values of LIDT in Fig. 146.26.

Using the methodology discussed in literature[8] based on the geometry of the grating walls (width at the top of the wall, $w \sim$ 150 nm) and contact area a (function of radius of indenter R and load applied P) defined at the time of initiation of fracture corresponding to Δ_{min}, we can determine the yield "strength" of the grating and plot it against measurements of LIDT. The yield strength is a stress found for the maximum load and the impression area. The contact area radius a is found by

$$a = \sqrt{2R\Delta_{min}} \tag{1}$$

and the corresponding uniaxial yield strength by

$$\sigma_Y = \frac{P}{2aw}. \tag{2}$$

The extracted yield stress is correlated to the LIDT in Fig. 146.27.

4. Geometrical Discontinuities and Surface Heterogeneities

The MLD gratings, after cleaning treatments, are observed to have a distinctive type of surface defect as seen in SEM images—disfiguration along the top of the wall (also referred to as "undulations").

Observations from several SEM images such as the ones shown in Fig. 146.28 reveal a direct correlation between the

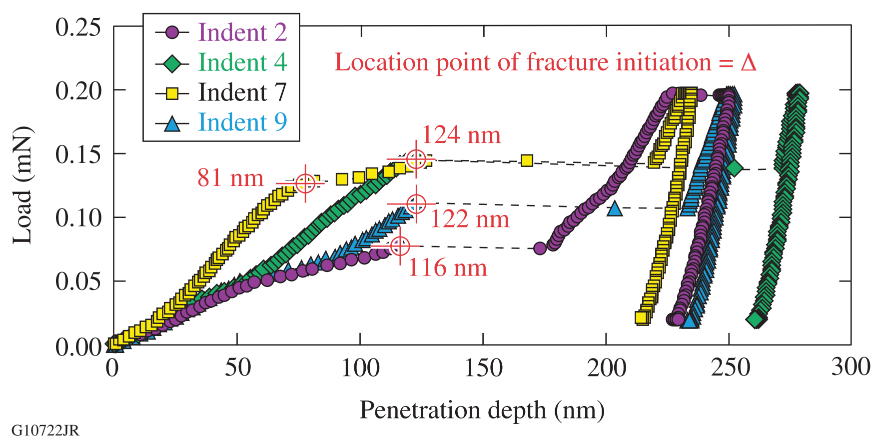

Figure 146.25
The location of fracture initiation is measured using the load-displacement curves for off-centered indents made on MLD grating #566-3 with a 0.2-mN load.

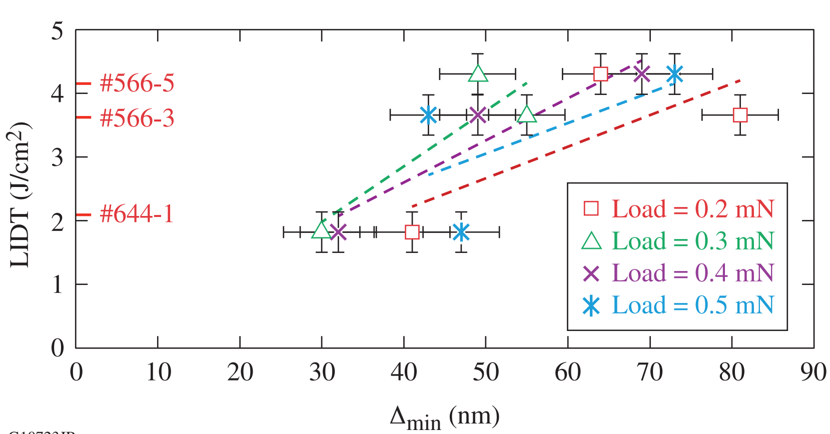

Figure 146.26
Relationship of laser-induced–damage threshold (LIDT) and the minimum depth of penetration into the MLD grating needed to initiate fracture.

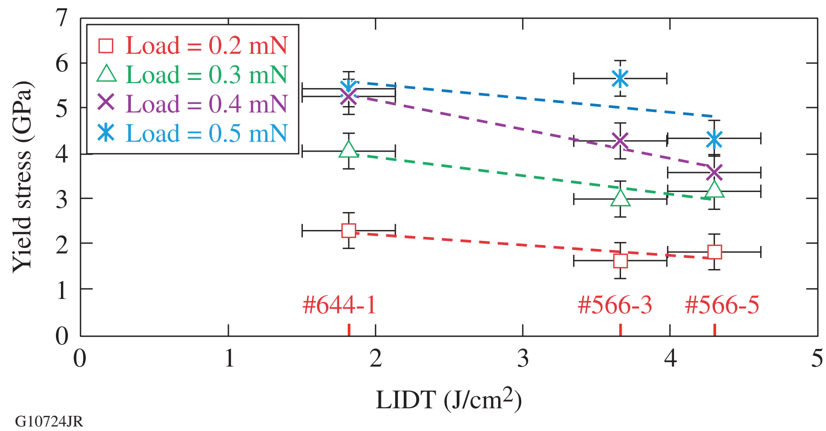

Figure 146.27
Relationship of LIDT and the extracted yield stress.

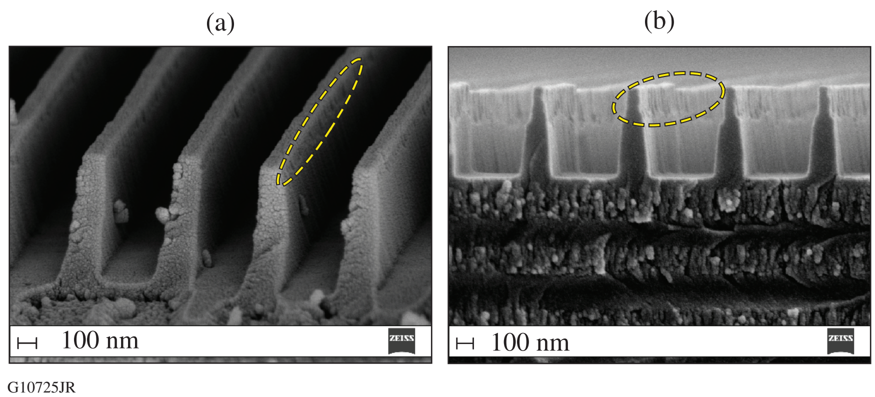

Figure 146.28
Severity of the undulations on the grating walls are related to the measured LIDT.

sizes of the undulations, seen as disfigurement at the top of the grating walls [circled in Figs. 146.28(a) and 146.28(b)], and the measured LIDT. Stronger undulations are associated with gratings that performed poorly in the optical testing, yielding lower values of laser-damage thresholds. Such surface defects (numerically modeled in the next section) are expected to play an important role in determining the quality of a particular grating since they would concentrate electric fields and mechanical stresses associated with nano-indentation. Therefore, they are an important consideration to our experiments.

These defects are thought to be regions of concentration of both mechanical and optical fields and are, therefore, important features to be included in our numerical modeling.

Numerical Simulations

For the numerical simulations, we used the commercial finite element package ABAQUS® (version 6.14-1). Guided by 2-D finite element analysis (FEA) performed previously,[8,25] the nano-indentation experiment was modeled as a 3-D problem using hexagonal, eight-node linear brick elements for the grating structure. The indentation region was significantly smaller than the size of the sample modeled; therefore, this area of large deformation was modeled using a highly refined mesh as compared to regions surrounding it.

The grating structure is defined as an elastic–plastic material composed of silica with an underlying layer of hafnia (~130 nm). The elastic modulus of silica was selected as 95 GPa (Ref. 26) and a Poisson ratio of 0.17. Isotropic hardening was implemented to model plasticity in the material corresponding to a yield stress of 2.8 GPa (based on the work described in Chap. 4 of Ref. 25). Hafnia was modeled as an elastic material with a Young's modulus of 130 GPa and a Poisson ratio of 0.25 (Ref. 26). The indenter tip (~1400-GPa diamond, elastic modulus) was modeled as an analytical rigid body since we did not expect it to deform during the experiment.

The nano-indentation problem was set up for simulation in four different ways as seen in Fig. 146.29. Since the purpose of this work is to correlate optical and mechanical damage fields in grating testing, we will mainly consider simulations of off-centered indents—namely the 25%, 50%, and fully decentered models (details of the centered model are discussed elsewhere[8,25]). Our goal is to simulate the nano-indentation testing. These analyses can then be used

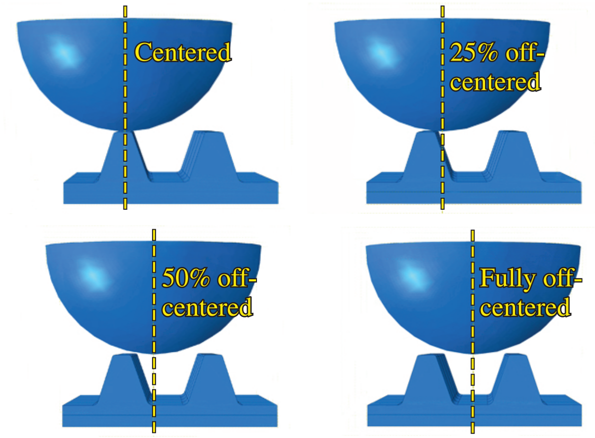

Figure 146.29
The ABAQUS® simulations were run using four setups to represent "centered" and "off-centered" indents.

to evaluate the different regions in a grating structure where stresses are concentrated.

1. Simulation of Off-Centered Nano-Indentation

We have observed (Sec. 4.3.1 of Ref. 25) that a high degree of indenter tip off-center coupled with a relatively deep penetration depth (≳150 nm) of indenter tip corresponds to catastrophic indents on the grating structure. Such "slightly"-to-"mostly" off-centered indents include effects of both ductility and brittle deformation.

Figures 146.30(a)–146.30(d) show the evolution of localized deformation and damage for a 50% decentered indent as the depth of penetration of the indenter tip is increased from 50 nm to 250 nm. The regions of highest concentration of maximum principal stress are seen in the regions of the grating wall that are "stretched" at lower penetration depths. As greater penetration depths of 170 nm and 250 nm are reached, the highest concentrations of maximum principal stress also extend to the adjacent wall since it is also now in significant contact with the indenter tip. This not only causes both the walls to stretch excessively but also affects the "foot" of the wall, which is found to concentrate maximum principal stress. It should be noted here that we have not modeled crack growth in this simulation; therefore, it is highly likely that excessive stretching seen in off-centered indents corresponding to high depths of penetration would indeed fracture the silica walls. In summary, the sequence of events in off-centered indentation consists of mechanical stretching of the grating top, followed by load shearing with neighboring pillars and load transmission to the base of the grating.

2. Simulation of Geometric Discontinuities

The 3-D simulations discussed previously assume that the shape of the grating is rectilinear. We now take into account some of the inhomogeneities that are encountered with gratings that can potentially act as regions to concentrate mechanical stresses in a nano-indentation test and have a direct impact on its laser-damage threshold.

The off-centered nano-indentation experiment is now modeled as a plane-strain simulation in 2-D and is meshed using four-node bilinear plane-strain quadrilateral elements. Highly refined meshing is used near the area of contact with a progressively coarser mesh away from the zone of maximum deformation (grating walls and the top few layers of the grating). The grating structure is modified to include the effects of thickness

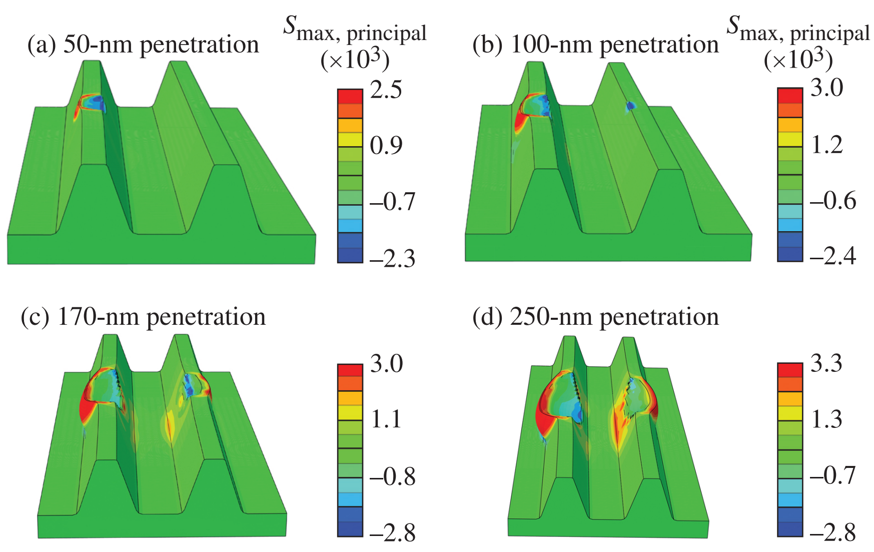

Figure 146.30
Damage is restricted to a single wall for penetration of 50 nm but extends to the adjacent wall as the penetration increases, eventually leading to fracture (stress is given in MPa).

discontinuity evident as disfigurement of the grating walls (undulations shown in SEM images in an earlier section). The results from the simulation are compared to those from an ideal grating structure and illustrated in Figs. 146.31(a) and 146.31(b).

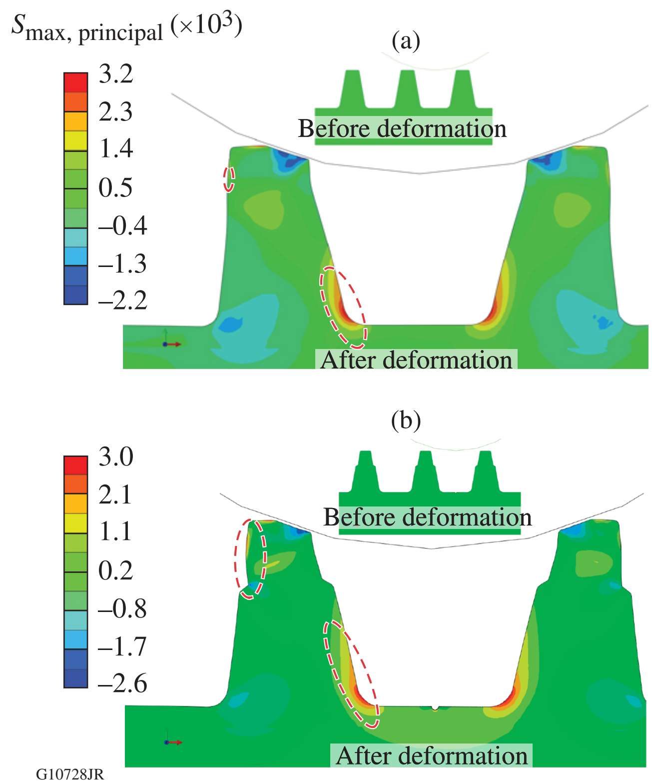

Figure 146.31
Comparison of (a) an ideal grating (no defects) with (b) a disfigured grating simulated for a penetration depth of 50 nm.

It is evident that, for a penetration depth of only 50 nm, the "disfigured" grating concentrates maximum principal stresses at the foot of the grating wall as well as along the undulation (peak stress ~3 GPa), whereas there is no significant accumulation of stresses along the wall of the ideal grating shape.

In addition to the stress concentration along the foot of the grating, the thickness discontinuity includes an additional effect, reminiscent of concentrated plastic shear deformation (shear banding).

The plastic strain (maximum principal component) for ideal and disfigured gratings at a penetration depth of 50 nm is plotted in Figs. 146.32(a) and 146.32(b), respectively. This helps to further assess the areas of the grating structure that are exposed to stress concentration in a nano-indentation test. It is seen that there is a "banding" effect in the upper region of the grating wall where it makes contact with the indenter tip. This "band," or the region under plastic strain, is significantly evolved in the disfigured grating as compared to the ideal grating structure.

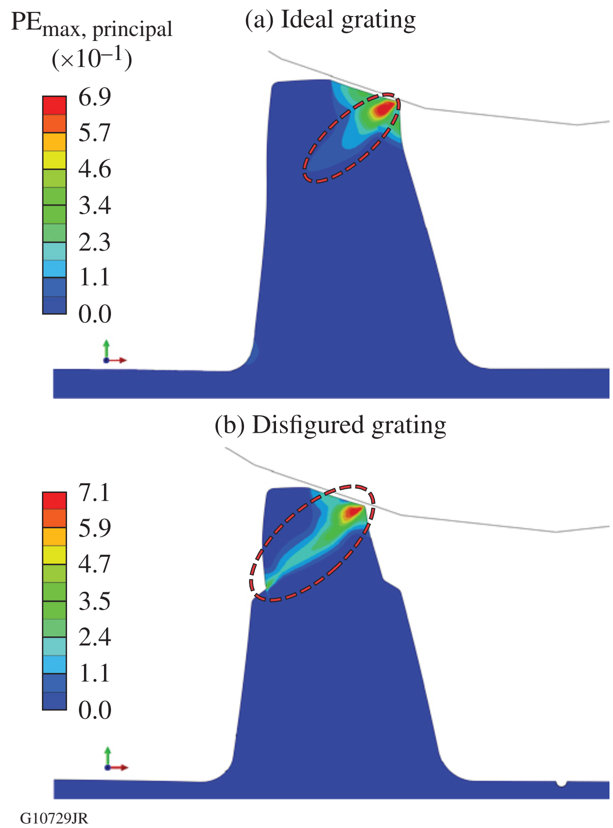

Figure 146.32
(a) A shear band caused by the plastic strain is prominent only in the area of contact with the indenter tip. (b) The shear band for the ideal shape is prominent in the disfigured grating and extends across the top width of the grating wall.

We have also modeled nanometer-sized porosity at the grating "floor." A 100-nm pore is shown in Figs. 146.30(b) and 146.31(b). Such pores also concentrate tensile mechanical stresses, exactly as they concentrate electrical fields[27–30] by enhancing localized absorption effects.[31]

Discussion

1. Effect of Cleaning Procedures on LIDT

The cleaning procedure is widely reported to have a significant impact on the damage threshold of these pulse-compression gratings.[18,20] Extensive research dedicated to studying the effects of various cleaning processes (Piranha at different temperatures, Nano-Strip)[9,32–36] on the threshold at 10 ps, 1053 nm shows that the efficiency of the process (measured by reduction in traces of photopolymers and organic contaminants after cleaning) is linked to the LIDT measured for the grating.

For our purposes, subtle differences in the cleaning processes (shown in Table 146.III), such as using air plasma over oxygen plasma, cause significant changes in the measured LIDT for the respective gratings. Specifically, this is the only difference between gratings #566-3 and #566-5 (which were processed identically until this point), and yet the latter performed much better in optical testing (LIDT 4.3±0.25 J/cm^2). The same is true in comparing #566-3 and #644-1. Therefore, it must be emphasized that, although these differences in cleaning procedures might seem insignificant, they lead to critically different optical performances.

It must also be noted that although we have shown that changes in cleaning methods have led to vastly different values of measured LIDT, this is not the main purpose of this study, and they are discussed elsewhere.[2,7,20]

2. Thickness Undulation and Concentration of Mechanical Fields

Guided by SEM images (in Fig. 146.28) and LIDT data, an apparent relationship between the shape of the top of the grating wall and the optical performance of the grating can be summarized as follows:

- Undulations can amplify electric-field intensification in those regions, leading to higher damage probability.
- Two-dimensional finite element analysis shows higher stress concentrations and shear band development in a disfigured grating for the same ~50-nm penetration depths.

The primary purpose of the 3-D simulation was to identify the regions of the grating structure that are affected in a nano-indentation test and then use these regions to compare nano-indentation to the results from a laser-damage–threshold test. Specifically, for a 50% off-centered indent, Fig. 146.30 shows that the highest levels of maximum principal stress are concentrated in the stretched part of the wall at lower levels of penetration depth. This region can be thought of as the site of fracture initiation in the nano-indentation experiment.

The indentation depth at which the maximum principal stress exceeds the fracture stress of silica corresponds to the location of the point of fracture initiation (compare to Δ_{min} indicated in load-displacement curves; see Fig. 146.25). The numerical simulations (Fig. 146.30) indicate that this indentation depth is in the 50-nm to 100-nm range, which corresponds well with experimental data. As indentation depths increase, fracture becomes imminent and is suggested by the spatial increase in stretched regions of the grating wall (near the top) as well as adjoining areas where stress is concentrated—the stretched region in the adjacent grating wall and foot of the grating.

It is widely reported in literature[16,17,19,37,38] that in a laser-damage–threshold test, the damage to the MLD grating appears to start at the upper edge of the silica walls—where the modulus of the square of the electric field is highest.[16,17] SEM images of our gratings (Fig. 146.28) after cleaning show distinctive disfigured regions at the top of the grating wall, which in some cases have thinned the gratings to a great extent. Guided by these SEM images and LIDT data, there is an apparent relation between the shape of the top of the grating (or, severity of undulations created) and the respective values of damage threshold measured in optical testing. Gratings with smaller degrees of thickness disfigurement are associated with higher values of laser-damage thresholds. Any inhomogeneity along the top of the grating wall will amplify the catastrophic effects of the laser energy used to irradiate these gratings.

Having established that analyzing these undulations is an important aspect of understanding why gratings behave differently in LIDT, we can now discuss how nanomechanical testing of these silica walls can be used to understand their performance. For a penetration depth of 50 nm, it is observed in the 2-D finite element model that the two highlighted regions in the figure for the ideal [Fig. 146.31(a)] and disfigured [Fig. 146.31(b)] grating concentrate the highest levels of (tensile) maximum principal stress. Based on the area around the top of the grating wall, it is clear that for a given penetration depth, the disfigured grating experiences much higher levels of stress (~2.5 GPa) as compared to an ideal grating in the same region (<1 GPa). This shows that mechanical stresses are amplified greatly for a disfigured grating, and, as the severity of undulations increases, it can be expected that stresses would also increase, ultimately leading to a mechanical failure of the grating wall.

Plastic strains are also useful in understanding deformation of these gratings, and it is seen that during the nano-indentation test, a “shear band” develops as contact proceeds. Figures 146.32(a) and 146.32(b) compare the shear bands of ideal and disfigured grating structures, respectively. Clearly, the banding effect is more severe in the case of the grating with an undulation and extends across the width of the wall along the region where it is disfigured. Strains as high as 45% are seen in regions away from the contact area and are highlighted in the figure. The shear band in the ideally shaped grating is contained mostly within the area that is in contact with the indenter tip.

It must also be noted that the penetration depth chosen here (50 nm) to model the nano-indentation stresses in the grating is similar to the values of $\Delta_{\min}$, from the load-displacement curves, which represents the point of fracture initiation. Therefore, it can be inferred that under nanomechanical testing, the gratings with more-severe undulations will fracture before gratings that are relatively free of these features. This result is critical in explaining why gratings with a lower $\Delta_{\min}$ have a lower LIDT (shown in Fig. 146.26). We also note that these simulations highlight that a nanomechanical test exposes regions of the grating structure that are impervious to its laser-threshold performance statistics.

3. Correlation of Optical and Mechanical Tests (LIDT and $\Delta_{\min}$)

Figure 146.26 shows LIDT for the three differently cleaned gratings against $\Delta_{\min}$ at various loads used to measure the nano-indentation. It is apparent that there is a strong linear dependence of $\Delta_{\min}$ on the measured LIDT (J/cm^2). LIDT increases with increasing values of $\Delta_{\min}$; that is, the more "brittle" a grating, the lower its damage threshold. This correlation is novel and important for two different reasons. First, it provides us with a quantitative metric that can be used to predict optical performance of gratings based on nanomechanical tests alone. Simply put, a grating that shows an earlier initiation of fracture in an off-centered nano-indentation test (tracked using load-displacement curves) has a greater likelihood to be associated with a lower LIDT value as compared to a grating that could absorb more mechanical stress before fracture initiation. Second, this result can also be extended to correlate yield stress in these gratings (at the time of first fracture) to their respective laser-damage thresholds. The relation of LIDT and yield stress in Fig. 146.27 indicates that a grating with a higher LIDT will have a lower value of yield stress. This means that for decreasing yield strength, the grating is more ductile or can absorb more mechanical energy before it fractures. In summary, gratings with higher ductility demonstrate higher LIDT.

It is also worth noting from Fig. 146.26 that the correlating lines, when extended, have intercepts near zero. Of course, all gratings have a nonzero LIDT; however, this observation indicates that, if the deflection $\Delta_{\min}$ to fracture is practically nil, the resulting LIDT also vanishes. Such a correlation of fracture and LIDT is in agreement with the discussion in this section.

We will now discuss first-principles–based dimensionless metrics for correlating our results between nano-indentation and optical performance. Our goal is to cast our results in a way that may extend their range of validity to experimental conditions, other than the ones we have used here. In essence, we are seeking appropriate ways to cast our experimental results in a dimensionless form.

Higher ductility in grating structures can be considered in terms of stretched zones as indicated in finite-element simulations [Fig. 146.30(c)]. This stretching before fracture initiation in an off-centered indent is attributed to the (tangential) stress (hoop) exerted by the indenter. This phenomenon is broadly analogous to an internally pressurized cylinder. The pressure causes the cylinder to expand or stretch and we can calculate a hoop strain ($\varepsilon_{\theta\theta}$) associated with it. The fracture strain is calculated for the penetration depth ($\Delta_{\min}$) at which stretching leads to fracture initiation and also depends on the indenter's radius and the grating pitch.[25] We can now normalize $\Delta_{\min}$ by the hoop strain ($\varepsilon_{\theta\theta}$).

We also need to normalize LIDT's to some nominal threshold fluence. It is reported in Ref. 39 that the damage in the optical material is established once the temperature of the defect-surrounding material reaches its melting point. Therefore, threshold fluence as a function of this critical temperature (melting point of the optical material, which, in our case, is silica) can be now estimated as

$$F_0 = \frac{3.1\,T_c K_h \sqrt{\tau}}{\gamma\sqrt{D}} = 2.8\ \text{J/cm}^2, \tag{3}$$

where F_0 is the threshold damage fluence, T_c is the critical temperature or the melting point of silica ≈1900 K, K_h is the thermal conductivity = 1.4 W/(mK), τ is the pulse duration = 10 ps, D is the thermal diffusivity (for silica) = 0.0075 cm^2/s, and γ is the absorptivity at 1053 nm = 10^{-3}.

Therefore, the LIDT of the gratings can be normalized to F_0. The dimensional plot shown earlier in Fig. 146.26 is replotted in Fig. 146.33 by using dimensionless quantities. This plot may be used to ascertain the trend that, for increasing fracture strains, the normalized laser-induced–damage fluence will also increase. As the correlating lines pass through the origin, the implication is that high brittleness would lead to very low LIDT.

Conclusions

A novel analysis has been presented to show that nano-indentation testing, supported by SEM images and finite-element simulations, can be effectively used to interpret the quality of a grating post-cleaning. The most widely accepted metrics to rate the performance of MLD gratings used in

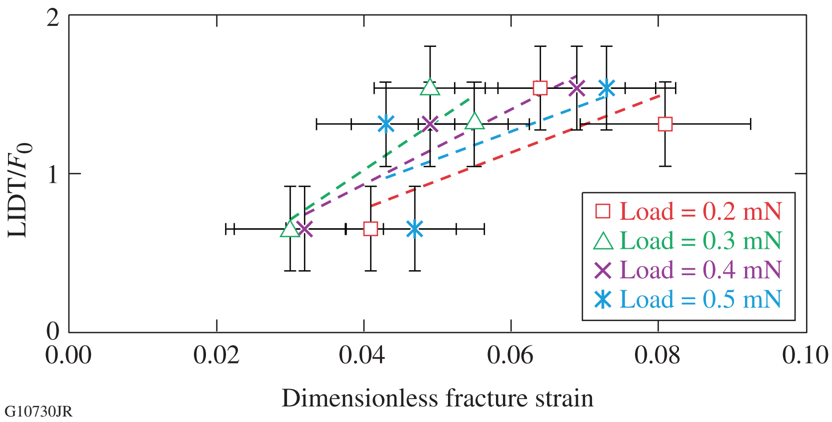

Figure 146.33
Normalized plot showing the dependence of damage thresholds on fracture strain developed in gratings during nano-indentation testing.

high-powered laser systems are expressed through optical tests in the form of LIDT's. Not only do nanomechanical tests naturally complement laser-damage testing by providing a fracture-derived metric (Δ_{min}) that distinguishes between grating samples based on their propensity to fracture, but they also expose identical regions of the grating structure to stresses as in a laser-damage test. The analogy is illustrated in Fig. 146.34. Therefore, we have argued that nanomechanical testing carried out in the proposed way (that is, identifying the weakest mode of the grating deformation) can be implemented as a rapid first test to predict how MLD gratings will perform when subjected to more-rigorous and specialized optical tests such as laser-damage testing.

In Fig. 146.34, we summarize schematically the analogy between stress/strain field concentration and electromagnetic-field concentration.

The main conclusions from this study are as follows: (1) Subtle changes in grating cleaning techniques lead to significant changes in the measured LIDT. (2) Our work shows a strong correlation between the nanomechanical fracture-based metric Δ_{min} and LIDT measured through optical testing for the grating samples evaluated. It is observed that a smaller value of LIDT is associated with a smaller Δ_{min} or, simply, a grating that has a tendency to fracture easily in a nano-indentation test will most likely have the lowest laser-damage threshold. (3) LIDT decreases as the measured yield stress for the grating samples increases. In other words, the less-deformable gratings lead to reduced LIDT. (4) The presence and size of undulations, or surface heterogeneities, on the grating structure have a direct impact on how the grating performs in both mechanical and optical tests. A grating with severe disfigurement at the top of the wall is more likely to have a low value of LIDT, as compared to a grating that was relatively free of this artifact. (5) Off-centered nano-indentation and LIDT measurements expose the same regions of the structure of the MLD grating and, therefore, can be seen as complementary tests.

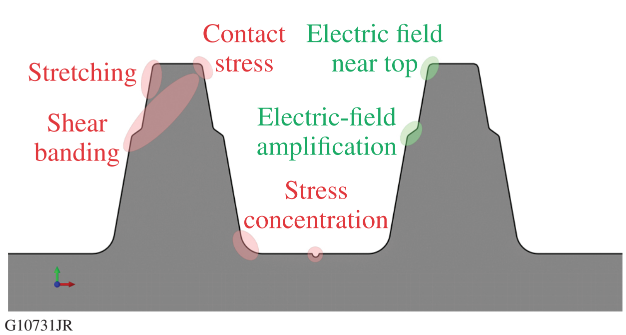

Figure 146.34
Nano-indentation exposes the same areas of the grating structure as an optical test by concentrating mechanical fields (stress, strain) in the regions normally associated with amplified electric fields.

In summary, we have presented a novel way of using nano-indentation testing, electron microscopy, and finite-element simulations to interpret the LIDT's of amorphous silica optical gratings.

ACKNOWLEDGMENT

The authors express their appreciation to the University of Rochester's Laboratory for Laser Energetics (LLE) for continuing support. One of the authors (K. Mehrotra) is supported by an LLE Horton Fellowship. This material is based upon work supported by the Department of Energy National Nuclear Security Administration under Award Number DE-NA0001944, the University of Rochester, and the New York State Energy Research and Development Authority. The support of DOE does not constitute an endorsement by DOE of the views expressed in this article.

The authors thank the late Dr. S. D. Jacobs for useful discussions that helped in conceiving this work. We also thank B. Patterson for her help in numerical simulations.

REFERENCES

1. F. Kong *et al*., Opt. Laser Technol. **73**, 39 (2015).
2. H. P. H. Liddell, "Enhancing the Performance of Multilayer-Dielectric Diffraction Gratings Through Cleaning Process Modifications and Defect Mitigation," Ph.D. thesis, University of Rochester, 2013.
3. D. Strickland and G. Mourou, Opt. Commun. **56**, 219 (1985).
4. G. A. Mourou, in *Encyclopedia of Modern Optics*, edited by R. D. Guenther, D. G. Steel, and L. P. Bayvel (Elsevier Academic Press, Amsterdam, 2005), pp. 83–84.
5. L. J. Waxer, D. N. Maywar, J. H. Kelly, T. J. Kessler, B. E. Kruschwitz, S. J. Loucks, R. L. McCrory, D. D. Meyerhofer, S. F. B. Morse, C. Stoeckl, and J. D. Zuegel, Opt. Photonics News **16**, 30 (2005).
6. J. A. Britten *et al*., Proc. SPIE **2714**, 511 (1996).
7. H. P. Howard, A. F. Aiello, J. G. Dressler, N. R. Edwards, T. J. Kessler, A. A. Kozlov, I. R. T. Manwaring, K. L. Marshall, J. B. Oliver, S. Papernov, A. L. Rigatti, A. N. Roux, A. W. Schmid, N. P. Slaney, C. C. Smith, B. N. Taylor, and S. D. Jacobs, Appl. Opt. **52**, 1682 (2013).
8. K. Mehrotra, H. P. Howard, S. D. Jacobs, and J. C. Lambropoulos, AIP Adv. **1**, 042179 (2011).
9. M. L. Schattenburg *et al*., the International Symposium on Nanomanufacturing (ISNM 2006), Cambridge, MA, 1–3 November 2006 (Paper TS3C-44).
10. J. R. Greer, W. C. Oliver, and W. D. Nix, Acta Mater. **53**, 1821 (2005).
11. J.-Y. Kim and J. R. Greer, Acta Mater. **57**, 5245 (2009).
12. J.-Y. Kim, D. Jang, and J. R. Greer, Acta Mater. **58**, 2355 (2010).
13. W. D. Nix *et al*., Thin Solid Films **515**, 3152 (2007).
14. R. Lacroix *et al*., International Journal of Applied Glass Science **3**, 36 (2012).
15. R. Lacroix *et al*., Acta Mater. **60**, 5555 (2012).
16. J. Neauport *et al*., Opt. Express **15**, 12508 (2007).
17. S. Hocquet, J. Neauport, and N. Bonod, Appl. Phys. Lett. **99**, 061101 (2011).
18. *LLE Review Quarterly Report* **112**, 228, Laboratory for Laser Energetics, University of Rochester, Rochester, NY, LLE Document No. DOE/SF/19460-790 (2007).
19. J. B. Oliver, T. J. Kessler, H. Huang, J. Keck, A. L. Rigatti, A. W. Schmid, A. Kozlov, and T. Z. Kosc, Proc. SPIE **5991**, 59911A (2005).
20. *LLE Review Quarterly Report* **131**, 149, Laboratory for Laser Energetics, University of Rochester, Rochester, NY, LLE Document No. DOE/NA/28302-1034 (2012).
21. H. T. Nguyen, C. C. Larson, and J. A. Britten, Proc. SPIE **7842**, 78421H (2010).
22. J. Keck, J. B. Oliver, T. J. Kessler, H. Huang, J. Barone, J. Hettrick, A. L. Rigatti, T. Hoover, K. L. Marshall, A. W. Schmid, A. Kozlov, and T. Z. Kosc, Proc. SPIE **5991**, 59911G (2005).
23. C. R. Wolfe *et al*., in *Laser Induced Damage in Optical Materials: 1989*, edited by H. E. Bennett *et al*., Natl. Inst. Stand. Technol. (U.S.), Spec. Publ. 801 (U.S. Government Printing Office, Washington, DC, 1990), pp. 360–375.
24. K. Mehrotra, H. P. Howard, S. D. Jacobs, and J. C. Lambropoulos, in *Local Probing Techniques and* In-Situ *Measurements in Materials Science*, edited by N. Balke *et al*., Mater. Res. Soc. Symp. Proc. Vol. 1474, mrss12-1474-ccc08-13 (Materials Research Society, Pittsburgh, PA, 2012).
25. K. Mehrotra, "Nano-Mechanics of Optical Structures for High Laser-Damage Threshold Applications," Ph.D. thesis, University of Rochester, 2016.
26. K. Mehrotra, J. B. Oliver, and J. C. Lambropoulos, Appl. Opt. **54**, 2435 (2015).
27. N. Bloembergen, Appl. Opt. **12**, 661 (1973).
28. Y. Jee, M. F. Becker, and R. M. Walser, J. Opt. Soc. Am. B **5**, 648 (1988).
29. A. Salleo *et al*., Proc. SPIE **3244**, 341–347 (1998).
30. F. Y. Génin *et al*., J. Opt. Soc. Am. A **18**, 2607 (2001).
31. S. Papernov and A. W. Schmid, J. Appl. Phys. **82**, 5422 (1997).
32. D. J. Smith *et al*., in *International Conference on Ultrahigh Intensity Lasers: Development, Science and Emerging Applications (ICUIL 2008)* (ICUIL, Tongli, China, 2008), pp. 78–79.
33. B. Ashe *et al*., Proc. SPIE **6720**, 67200N (2007).
34. B. Ashe, K. L. Marshall, C. Giacofei, A. L. Rigatti, T. J. Kessler, A. W. Schmid, J. B. Oliver, J. Keck, and A. Kozlov, Proc. SPIE **6403**, 64030O (2007).
35. S. Chen *et al*., Proc. SPIE **7655**, 765522 (2010).
36. S. Chen *et al*., High Power Laser Part. Beams **23**, 2106 (2011).
37. J. A. Britten *et al*., Proc. SPIE **5273**, 1 (2004).
38. B. C. Stuart *et al*., Proc. SPIE **2714**, 616–629 (1996).
39. S. Papernov, in *Laser-Induced Damage in Optical Materials*, edited by D. Ristau (CRC Press/Taylor & Francis, Boca Raton, FL, 2014), Sec. I, Chap. 3, pp. 25–74.

Permeation Fill-Tube Design for Inertial Confinement Fusion Target Capsules

Introduction

In inertial confinement fusion (ICF)[1] a target capsule containing a cryogenic deuterium–tritium (DT) ice layer and low-density DT gases is imploded directly by intense laser pulses[2] or indirectly by x rays in a hohlraum.[3] During a typical implosion, intense illumination of the target rapidly heats and ablates the outer capsule material. Conservation of momentum drives the remaining capsule material and fuel toward the center of the target sphere, where the initially gaseous fuel forms a "hot spot" that ignites fusion reactions, which propagate radially outward through the main fuel layer.[3] The ultimate goal of ICF is to ignite the imploding target capsule, producing net energy gain; however, during an implosion, hydrodynamic instabilities in the ablation front can reduce the energy yield by distorting the hot spot or dispersing the main fuel layer.

Currently, two main methods are being used to fill the ICF target capsule with DT fuel—fill-tube filling[4] and permeation filling.[5] In fill-tube filling, a small fill tube provides a connection between the empty target capsule and a reservoir of gaseous DT. A valve downstream of the supply is opened, and DT flows into the target capsule. Once the desired amount of DT is inside the target capsule, the supply is shut off.

Permeation filling has no fill-tube connection between the empty target capsule and a reservoir of gaseous DT. Instead, this method relies on the target capsule being permeable to DT at the filling temperature and nonpermeable at some lower temperature. A valve downstream of the supply is opened and, at a controlled pressure ramp rate, DT flows into a heated pressure vessel containing an empty target capsule. The buckling strength and permeability of the target capsule shell limit the rate of DT pressure rise.[6] Once the desired amount of DT has entered the target capsule, corresponding to the maximum DT fill pressure, the supply valve is closed. The pressure vessel and target capsule are then cooled to a temperature at which the internal pressure will not cause the target capsule to rupture or leak extensively when DT in the chamber surrounding the target capsule is evacuated.

One common capsule material (i.e., ablator) used in permeation filling is made by using the glow-discharge polymerization (GDP) process.[7] Alternate ablators such as beryllium, silicon, and high-density carbon are of interest in ICF experiments that study hydrodynamic instabilities.[8] Unfortunately, target capsules made of these materials are not sufficiently permeable to DT to be used in permeation filling. The current infrastructure at LLE is based on permeation filling. To study alternate ablator materials, a new cryostat design based on a fill-tube fill system is required—a multiyear, multimillion dollar project. A novel design combining the attributes of permeation and fill-tube filling is described next. This design requires no changes to LLE's current infrastructure, which will allow the study of alternate ablator materials in cryogenic experiments to begin immediately.

Description of the Permeation Fill-Tube Design

The permeation fill-tube (PFT) target assembly is shown in Fig. 146.35, while a more detailed image of the upper portion of the assembly is shown in Fig. 146.36. The gravity vector points down in these images. The geometry of the target support is driven by the requirement that the target capsule must be at the same elevation or lower than the permeation cell, and the support structure must not interfere with the laser beams.

Figure 146.37 shows a typical PFT assembly. The permeation cell is connected to the target capsule by a fill tube with adhesive joints. The fill tube itself is made of two separate tubes that are also glued together. The larger-diameter tube is fused silica with an outer polymeric coating and has an outer diameter (OD) of 0.15 mm and inner diameter (ID) of 0.10 mm. The smaller-diameter tube is borosilicate glass and is tapered from an OD of 0.1 mm and ID of 0.080 mm to an OD of 0.030 mm and ID of 0.022 mm. Smaller diameters for fill tubes will be investigated in the future. The initial geometry was chosen because of its high rigidity and strength for initial filling and layering experiments.

The PFT method combines attributes of fill-tube filling[4] and permeation filling.[6] Here the target capsule is nonpermeable to

DT while the permeation cell is permeable to DT at the filling temperature and nonpermeable at some lower temperature. A valve downstream of the supply is opened and, at a controlled pressure ramp rate, DT flows into a heated pressure vessel containing an empty PFT target assembly (shown in Fig. 146.35). The buckling strength and permeability of the target capsule shell limit the rate of DT pressure rise.[6] DT flows through the permeation cell's shell through the fill tube and into the target capsule. At a steady state the gas pressure is equal in both capsules. Once the desired amount of DT has entered the PFT assembly, corresponding to the maximum DT fill pressure, the supply valve is closed. The pressure vessel and the PFT target assembly are then cooled to a temperature at which the internal assembly's pressure will not cause the target capsule or the permeation cell to rupture or leak appreciably when DT in the chamber surrounding the PFT assembly is finally evacuated.

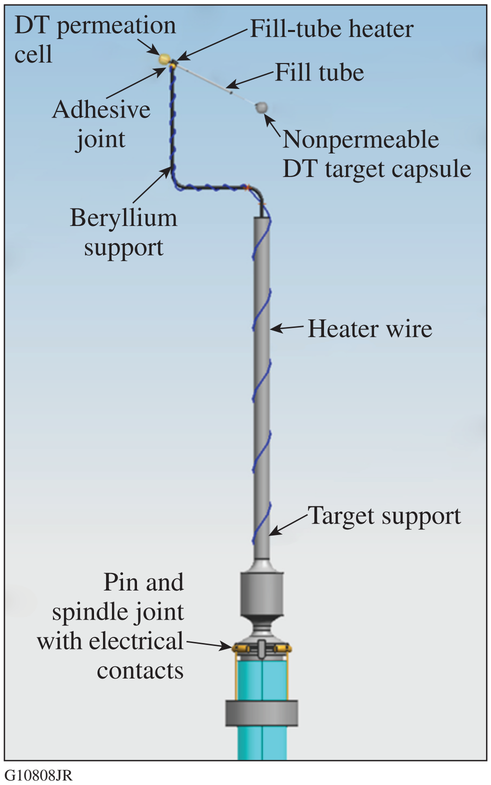

Figure 146.35
Permeation fill-tube target assembly. DT: deuterium–tritium.

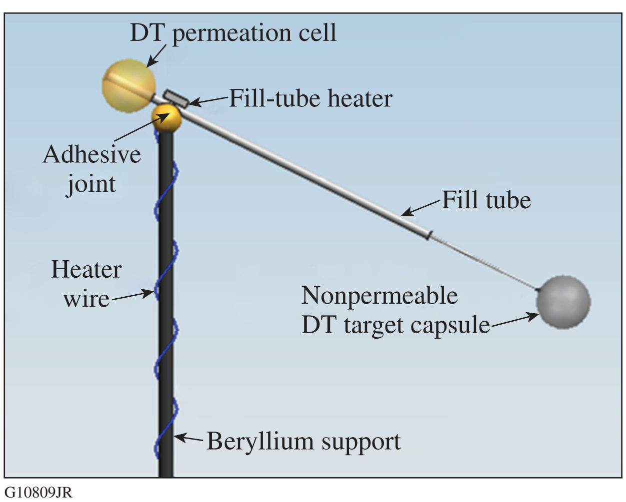

Figure 146.36
Detailed view of the upper portion of a permeation fill-tube target assembly.

The heater glued to the fill tube (shown in Figs. 146.35 and 146.36) is a microchip resistor (ERJ-XGNF1–1Y) capable of delivering up to ~1 mW. The heater creates a pressure delta to drive more fuel into the target capsule than the permeation cell during the layering process. Without this heater, the pressures in the target capsule and the permeation cell would be equal.

The initial PFT prototype did not use nonpermeable ablators, such as beryllium, silicon, and high-density carbon (HDC), since, because of their opacity to visible light, the ice layers would not have been visible. LLE uses optical backlit shadowgraphic characterization of cryogenic target ice layers with submicron resolution.[9] The initial PFT assembly with a HDC target capsule, used for our manufacturing studies, is shown in Fig. 146.38(a). The PFT assembly in our layering studies used GDP capsules for both the permeation cell and the

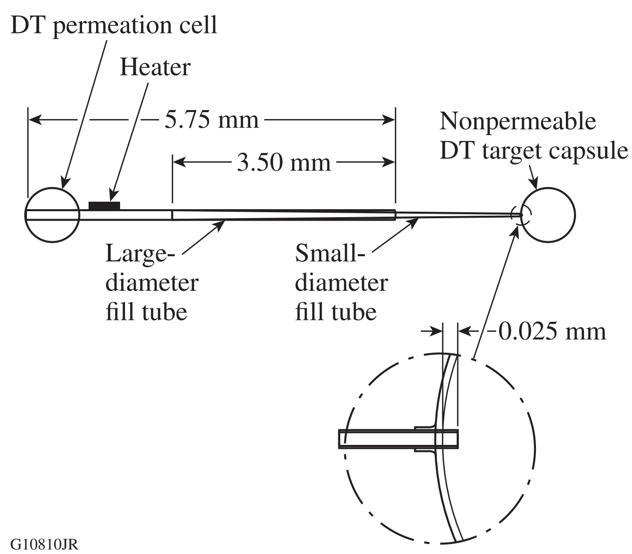

Figure 146.37
Permeation fill-tube assembly. (All dimensions are in millimeters.)

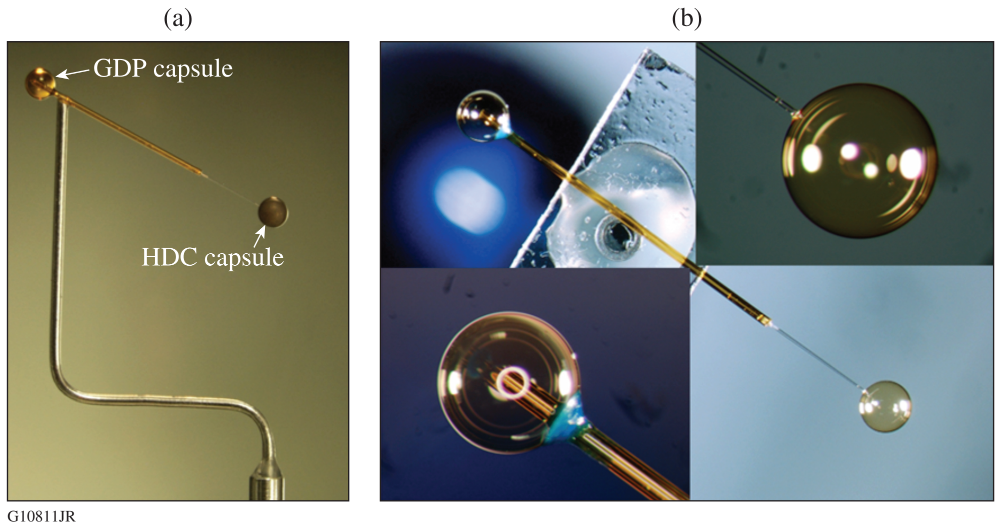

Figure 146.38
(a) Image of a PFT target assembly with a glow-discharge polymerization (GDP) permeation cell and high-density carbon (HDC) nonpermeable target capsule; (b) image of a PFT assembly with a GDP permeation cell and GDP target capsule.

target capsule [see Fig. 146.38(b)]. The target capsule was made from GDP so the ice layer would be visible for layering studies. Both capsules had an OD of 0.430 mm, with wall thicknesses of 0.022 and 0.008 mm for the permeation cell and the target capsule, respectively. A future fill will use a nonpermeable multilayer (GDP/Si/GDP) target capsule shell.

PFT Layering Process

The PFT assembly is located inside a copper layering sphere filled with helium (see Fig. 146.39). Initially DT in the PFT assembly is rapidly cooled (~1 K/s) to several degrees below its triple point. Next, the temperature of the copper layering sphere is gradually raised until all of the solid DT in the target capsule is gone and the solid DT in the fill-tube section nearest the target capsule begins to melt. At this point the temperature of the layering sphere is dropped ~0.001 mK every 15 min. This causes the DT to solidify and an ice crystal "seed" to grow out of the fill tube into the target capsule. The initial growth of a single ring (shown in Fig. 146.40) indicates that, as the temperature continues to drop, the final ice layer will contain a single hexagonal close-packed (hcp) crystal, as required for high-yield ICF implosions.[10]

Layering experiments were successful using the same layering protocol as existing stalk-mounted (non-fill-tube)

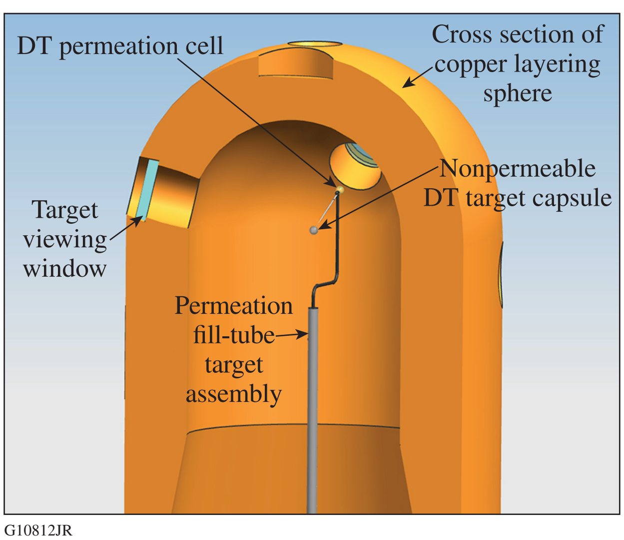

Figure 146.39
PFT assembly located inside a copper layering sphere.

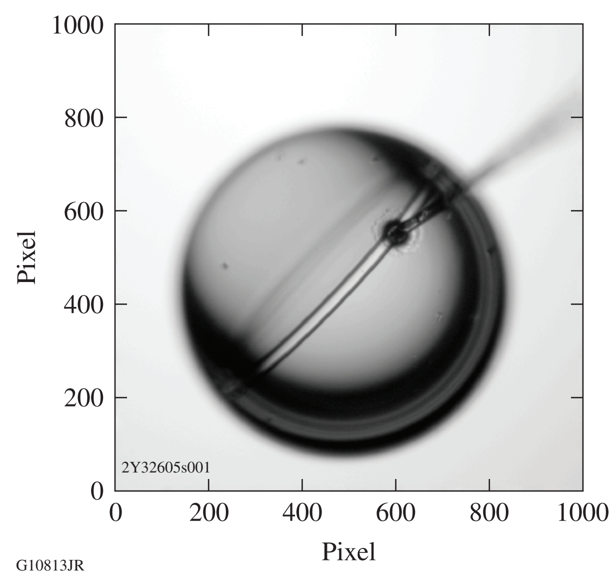

Figure 146.40
Image of single crystal seed that grows out of the fill tube. The initial growth of a single ring is indicative of a final ice layer that will be composed of a single hexagonal close-packed (hcp) crystal, which is required for high-yield ICF implosions.[10]

targets. An image of the resulting single-hcp-crystal ice layer characterized by optical backlit shadowgraphy is shown in Fig. 146.41(a). The inner ice surface roughness is 0.98-μm rms (root mean square) and the average ice thickness is 61 μm. Figure 146.41(b) shows the inner ice surface radius in red and outer ice surface radius in blue. The difference between the blue curve and the red curve is the ice thickness. (A smaller radius of the inner ice surface, shown in red, corresponds to a thicker ice layer.) The image is unwrapped with the zero position referring to the 3:00 position in Fig. 146.41(a). The stalk position is ~50°, leading to thick ice near the fill tube (highlighted). The test ice layer is significantly thicker near the fill tube because of the higher (~6×) thermal conductivity of borosilicate glass compared to helium. From Fig. 146.41(b) it appears that the maximum variation in ice thickness near the fill tube is ~7 μm, but it is actually larger because the fill tube obscures the shadowgraph data, causing the image analysis to fail in this area. From Fig. 146.41(b), the effect of the fill tube is seen over ~±23° on either side of the fill tube. The thick spot will be discussed further in the next section.

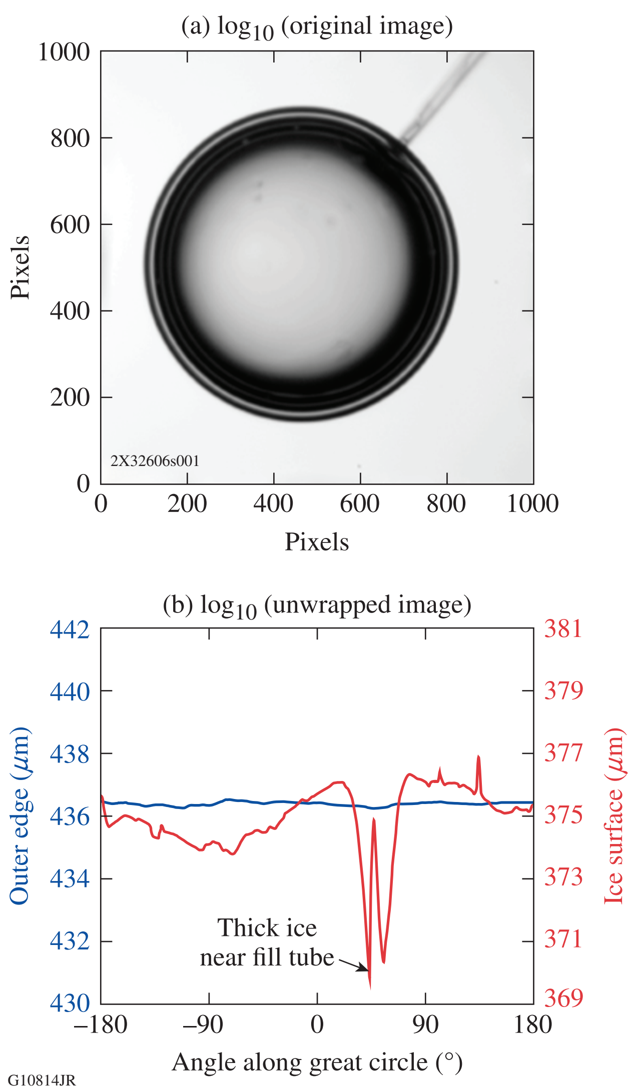

Figure 146.41
(a) An image of a final single hcp crystal ice layer characterized by optical backlit shadowgraphy; (b) the inner ice surface radius is shown in red and the outer ice surface radius in blue.

It is possible to control the relative pressure of DT in the two capsules by using the PFT heater located near the permeation cell shown in Fig. 146.36. With the heater turned on (~1 mW) and the layering-sphere temperature above the critical point of DT, ~40 K, gas is preferentially driven toward the target capsule. Next, the DT in the layering sphere is rapidly cooled (~1 K/s) several degrees below DT's triple point, causing the DT in the target capsule and the fill tube's end attached to the target capsule to freeze. At this point the PFT heater is turned off and the layering process described previously can begin. As long as the ice plug remains in the fill tube during the subsequent layering process, the amount of DT in the target capsule will remain constant.

Heat-Transfer Model

It is preferable to use a heat-transfer model to investigate the effects of the fill tube, glue spot, target capsule geometry, and material properties on layer-thickness uniformity for PFT ICF targets. If the layer-thickness uniformity of the current design can be accurately modeled, we are confident that we will be able to numerically evaluate future ICF target designs. Using models to design targets is more efficient than building physical prototypes.

The DT solid/gas phase boundary is represented by an isotherm at DT's triple point of ~19.7 K. The PFT temperature profile was modeled by a finite volume method (FVM) using ANSYS *FLUENT* v16. A two-dimensional axisymmetric model of the PFT target assembly inside a 1-in.-diam copper layering sphere filled with ~2 Torr of helium was constructed. The model includes both capsules, the fill tube, the glue spot connecting the target capsule to the fill tube, DT decay heating, and sublimation/deposition of DT in the permeation cell, fill tube, and target capsule. The layering sphere was treated as a complete surface and is represented by a uniform-temperature boundary condition. Holes in the layering sphere were ignored so a computationally efficient axisymmetric model can be used.

Decay heating of DT causes the target to be hotter than its surroundings. Helium was used to conduct the heat generated by DT to the surrounding copper sphere. In the model, DT can exist in only one of two phases—solid or gaseous. The sublimation/deposition temperature used for DT was 19.7 K. Initial models used *FLUENT*'s two-phase routines. Since only steady-state results were of interest, a more-efficient solution procedure was developed. Using user-defined DT material properties (density and conductivity) that were a function of temperature yielded identical steady-state results as *FLUENT*'s two-phase routine and were more efficient to run. Both solution procedures model only heat transfer by conduction, and mass conservation is not automatically taken into account. In either modeling method, conservation of DT mass is controlled by a manual iterative process. Knowing the actual total mass of DT in the PFT assembly, the layering sphere's fixed-temperature boundary condition can be adjusted until the desired mass of DT contained in the PFT assembly is obtained.

Figure 146.42 shows the model geometry. The outer portion of the DT physically touching the target capsule shell uses a cell size of 1×1 μm to resolve the gas/ice-phase boundary (shown in Fig. 146.43). Other areas of the model use a coarser mesh for a more-efficient solution. Based on a mesh refinement study, the results presented are mesh independent. Thermal conductivities at ~20 K are 0.0255, 0.009, 0.35, 0.05, 0.333, 0.15, 0.15, and 59 W/m/K for He (Ref. 11), DT gas,[12] DT solid,[12] GDP plastic shell,[13] Stycast 1266 (Ref. 14), fused silica,[15] borosilicate glass,[15] and beryllium,[16] respectively. Densities are 0.0065, 0.7, 260, 1420, 1120, 2640, 2640, and 1851 kg/m^3 for He, DT gas, DT solid, GDP plastic shell, Stycast 1266, fused silica, borosilicate glass, and beryllium, respectively. A user-defined function (UDF) was used for the 200-W/kg decay heat of DT (Ref. 13). (Note: Borosilicate glass conductivity was used for fused silica and polyimide conductivity was used for the GDP capsule because of the lack of cryogenic material property data.)

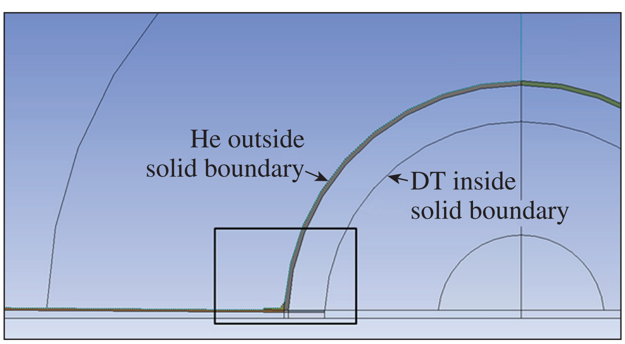

Figure 146.42
Model geometry near the target capsule.

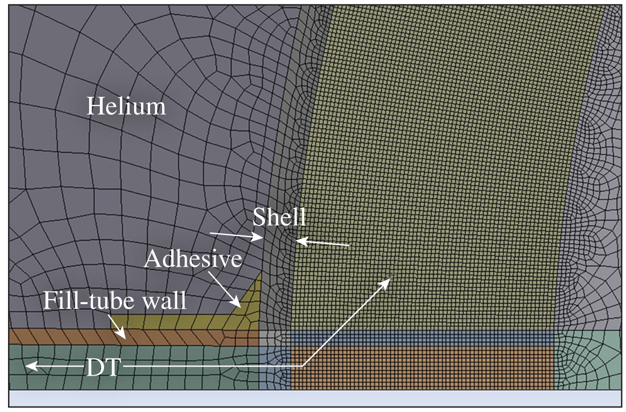

Figure 146.43
Image of the fine mesh required to resolve the solid/gas phase boundary near the target capsule.

Figure 146.44 shows temperature contours predicted by the model. The temperature is hottest at the center of the target (radioactive decay) and coldest at the isothermal boundary condition representing the copper layering sphere. Figure 146.45 illustrates the resulting solid/gas phase boundary predicted by the model (DT ice is shown in red). Figure 146.46 is an unwrapped image of the model ice thickness overlaid on the measured ice thickness of the layer in the experimental PFT target; the fill tube is located at ~50°. The model thickness profile is very similar to experimental results. One difference is that the actual ice layer shows a thick spot in the ice above the hole in the layering sphere (required to insert the target

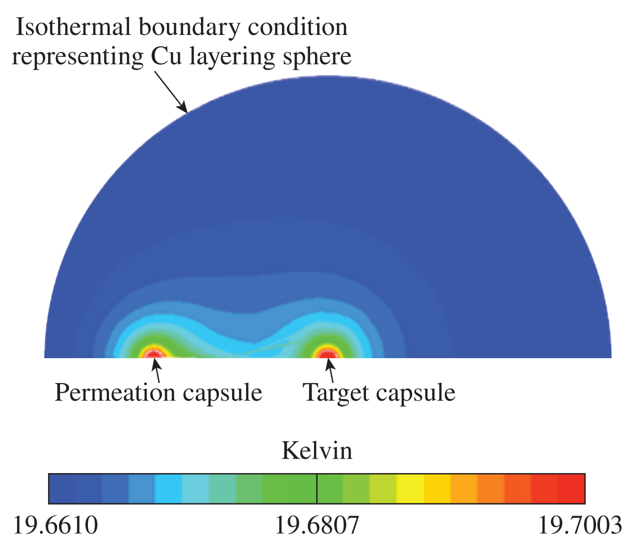

Figure 146.44
Modeled temperature contours of the target and copper layering sphere.

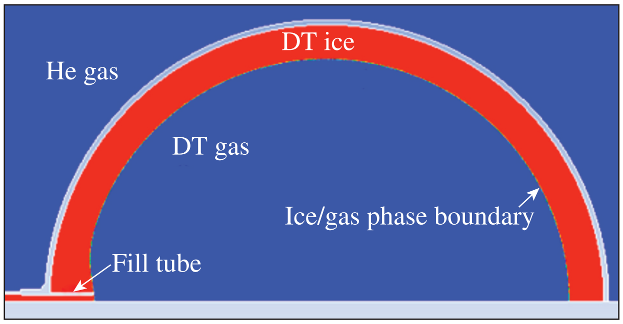

Figure 146.45
The ice/gas phase boundary predicted by the model (DT ice is shown in red).

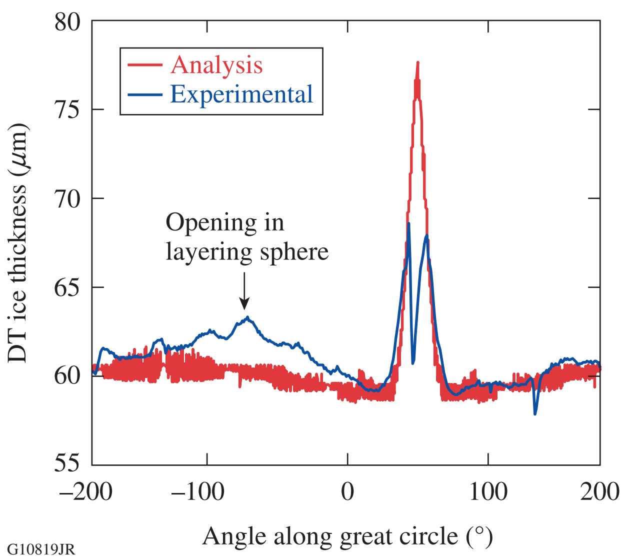

Figure 146.46
Unwrapped image of the model prediction of ice thickness overlaid on actual ice thickness; the fill tube is located at ~50°.

into the layering sphere). The hole cannot be modeled since the axis for the axisymmetric model is aligned with the fill tube. The thermal model estimates the peak thickness variation to be ~17 μm near the fill tube, and the effect of the fill tube is apparent ~±20° on either side. The model accurately predicts the uniformity of the actual ice-layer thickness. This verifies the modeling methodology so good estimates of ice uniformity for other ICF target designs can be made numerically.

The nonuniformity in the ice thickness near the fill tube for the target design discussed above is too large for high-yield ICF implosions. Three critical design parameters affecting this nonuniformity are (1) the fill tube's size, (2) the target shell's thermal conductivity, and (3) the fill tube's thermal conductivity. The decay heat from the target is conducted (radially) away from the target shell. Nonuniformities in this conduction path distort the isotherms, resulting in ice-thickness nonuniformity. If the isotherms were perfectly concentric about the target shell, the ice thickness would be uniform. The thermal conductivity of borosilicate glass is ~6× higher than helium, causing a cold spot near the fill tube that results in locally thicker ice. Minimizing the borosilicate glass cross-sectional area or its thermal conductivity will minimize this effect. Less obvious is the effect of shell conductivity on ice-thickness uniformity. The fill-tube causes temperature variations in the θ direction in the axisymmetric model, resulting in nonconcentric isotherms. When the shell has high thermal conductivity, it "short circuits" the θ temperature variations, resulting in more-concentric isotherms.

Here we use the model to quantify the effect of alternate target designs on ice-layer nonuniformities near the fill tube. First we investigate the effect of a fill tube's cross-sectional area on the ice-thickness uniformity near the fill tube. The effect of borosilicate fill-tube size on ice-thickness uniformity with a GDP (low thermal conductivity of 0.05 W/m/K) shell is shown in Fig. 146.47. The fill-tube size has a significant effect on variations in ice-layer thickness near the fill tube. The variation decreases from ~30% for the 30-μm-OD fill tube to ~10% for the 10-μm-OD fill tube.

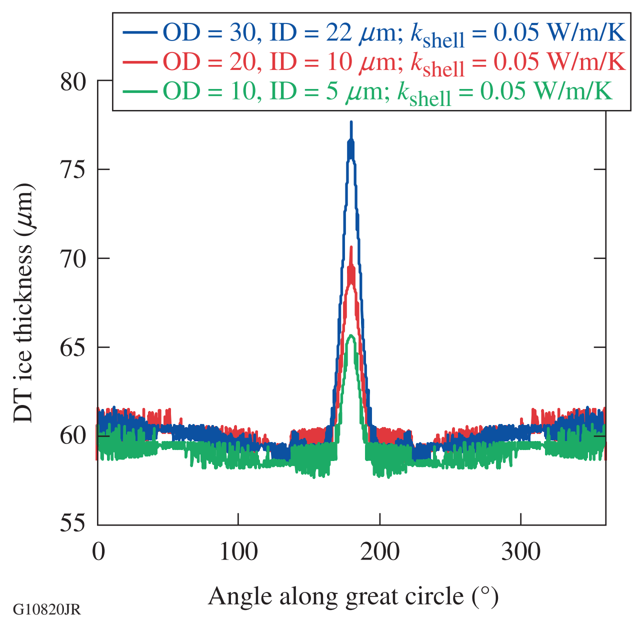

Figure 146.47
Unwrapped image of the model prediction of ice thickness for three different fill-tube cross sections with a GDP shell having a thermal conductivity of 0.05 W/m/K.

The effect of the shell's thermal conductivity for a 20-μm-OD, 10-μm-ID borosilicate fill tube with 20 μm of penetration into the shell is shown in Fig. 146.48. The shell's thermal conductivity has a significant effect on variations in ice-layer thickness near the fill tube. Bulk beryllium at ~20 K has a thermal conductivity of ~59 W/m/K. If a target shell has a thermal conductivity approaching that of bulk beryllium, it would almost completely negate the ice-thickness variations near the fill tube.

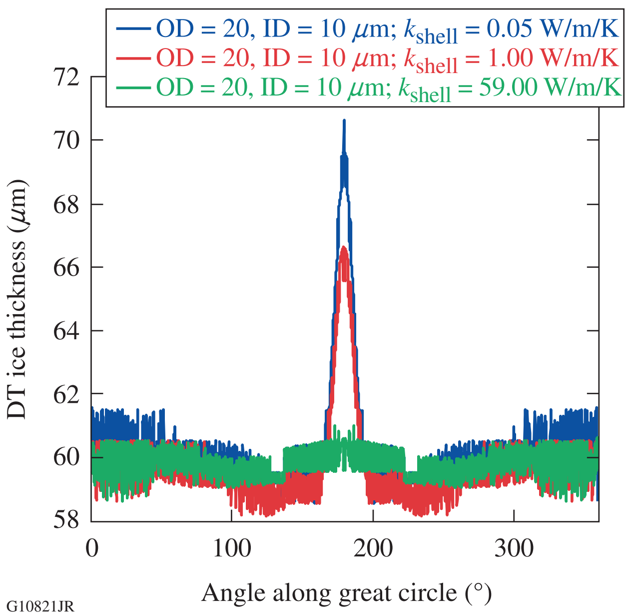

Figure 146.48
Unwrapped image of the model prediction of ice thickness for three different shell thermal conductivities with a 20-μm OD, 10-μm ID borosilicate fill tube.

Conclusions

An ICF target has been successfully filled and a <1-μm-rms DT ice layer has been developed using a novel fill design that combines attributes of permeation and fill-tube filling. This new filling method allows LLE to immediately begin the study of nonpermeable cryogenic target capsules with their current infrastructure. A numerical model has been presented that accurately predicts the ice nonuniformities near the fill tube as seen in empirical data. Using this model, target designs with better ice-thickness uniformity have been proposed. One key but less obvious factor that improves ice uniformity is the target shell's conductivity. Numerical simulations show that high-conductivity shells (e.g., shells with the conductivity of bulk beryllium at ~20 K, 59 W/m/K) completely negate the fill-tube–induced ice nonuniformities.

ACKNOWLEDGMENT

This material is based upon work supported by the Department of Energy National Nuclear Security Administration under Award Number DE-NA0001944, the University of Rochester, and the New York State Energy Research and Development Authority. The support of DOE does not constitute an endorsement by DOE of the views expressed in this article.

REFERENCES

1. J. Nuckolls *et al*., Nature **239**, 139 (1972).
2. R. L. McCrory, D. D. Meyerhofer, R. Betti, R. S. Craxton, J. A. Delettrez, D. H. Edgell, V. Yu. Glebov, V. N. Goncharov, D. R. Harding, D. W. Jacobs-Perkins, J. P. Knauer, F. J. Marshall, P. W. McKenty, P. B. Radha, S. P. Regan, T. C. Sangster, W. Seka, R. W. Short, S. Skupsky, V. A. Smalyuk, J. M. Soures, C. Stoeckl, B. Yaakobi, D. Shvarts, J. A. Frenje, C. K. Li, R. D. Petrasso, and F. H. Séguin, Phys. Plasmas **15**, 055503 (2008).
3. J. D. Lindl, Phys. Plasmas **2**, 3933 (1995).
4. D. E. Solomon and T. M. Henderson, J. Phys. D: Appl. Phys. **8**, L85 (1975).
5. S. O. Kucheyev and A. V. Hamza, J. Appl. Phys. **108**, 091101 (2010).
6. *LLE Review Quarterly Report* **81**, 6, Laboratory for Laser Energetics, University of Rochester, Rochester, NY, LLE Document No. DOE/SF/19460-335 (1999).
7. A. Nikroo *et al*., General Atomics, San Diego, CA, Report GA–A23881 (2002).
8. A. J. MacKinnon, N. B. Meezan, J. S. Ross, S. Le Pape, L. Berzak Hopkins, L. Divol, D. Ho, J. Milovich, A. Pak, J. Ralph, T. Döppner, P. K. Patel, C. Thomas, R. Tommasini, S. Haan, A. G. MacPhee, J. McNaney, J. Caggiano, R. Hatarik, R. Bionta, T. Ma, B. Spears, J. R. Rygg, L. R. Benedetti, R. P. J. Town, D. K. Bradley, E. L. Dewald, D. Fittinghoff, O. S. Jones, H. R. Robey, J. D. Moody, S. Khan, D. A. Callahan, A. Hamza, J. Biener, P. M. Celliers, D. G. Braun, D. J. Erskine, S. T. Prisbrey, R. J. Wallace, B. Kozioziemski, R. Dylla-Spears, J. Sater, G. Collins, E. Storm, W. Hsing, O. Landen, J. L. Atherton, J. D. Lindl, M. J. Edwards, J. A. Frenje, M. Gatu-Johnson, C. K. Li, R. Petrasso, H. Rinderknecht, M. Rosenberg, F. H. Séguin, A. Zylstra, J. P. Knauer, G. Grim, N. Guler, F. Merrill, R. Olson, G. A. Kyrala, J. D. Kilkenny, A. Nikroo, K. Moreno, D. E. Hoover, C. Wild, and E. Werner, Phys. Plasmas **21**, 056318 (2014).
9. D. H. Edgell, W. Seka, R. S. Craxton, L. M. Elasky, D. R. Harding, R. L. Keck, M. Pandina, M. D. Wittman, and A. Warrick, presented at the 46th Annual Meeting of the Division of Plasma Physics, Savannah, GA, 15–19 November 2004.
10. T. C. Sangster, R. Betti, R. S. Craxton, J. A. Delettrez, D. H. Edgell, L. M. Elasky, V. Yu. Glebov, V. N. Goncharov, D. R. Harding, D. Jacobs-Perkins, R. Janezic, R. L. Keck, J. P. Knauer, S. J. Loucks, L. D. Lund, F. J. Marshall, R. L. McCrory, P. W. McKenty, D. D. Meyerhofer, P. B. Radha, S. P. Regan, W. Seka, W. T. Shmayda, S. Skupsky, V. A. Smalyuk, J. M. Soures, C. Stoeckl, B. Yaakobi, J. A. Frenje, C. K. Li, R. D. Petrasso, F. H. Séguin, J. D. Moody, J. A. Atherton, B. D. MacGowan, J. D. Kilkenny, T. P. Bernat, and D. S. Montgomery, Phys. Plasmas **14**, 058101 (2007).

11. N. B. Vargaftik *et al*., *Handbook of Thermal Conductivity of Liquid Gases* (CRC Press, Boca Raton, FL, 1994)
12. P. C. Souers, *Hydrogen Properties for Fusion Energy* (University of California Press, Berkeley, CA, 1986).
13. Material Properties: Polyimide (Kapton), http://cryogenics.nist.gov/MPropsMAY/Polyimide%20Kapton/PolyimideKapton_rev.htm (24 May 2016).
14. S. Laumann *et al*., J. Mater. Res. **26**, 1861 (2011).
15. Thermal and Mechanical Properties of Glass (Quartz, Pyrex, Borosilicate), http://www.yutopian.com/Yuan/prop/Glass.html (24 May 2016).
16. Be Properties, https://www.bnl.gov/magnets/staff/gupta/cryogenic-data-handbook/Section7.pdf (24 May 2016).

Acidic Magnetorheological Finishing of Infrared Polycrystalline Materials

Introduction

Magnetorheological finishing (MRF) is a polishing technique used to produce high-precision optics. It is known for its relatively high material-removal rate (mrr);[1] subnanometer surface roughness on various materials, especially glass;[2–4] good figure/shape accuracy;[5] deterministic nature;[1] and the ability to polish complex shapes at a large size range.[6] For some materials, however, the conventional alkaline water-based magnetorheological (MR) fluid tends to leave noticeable artifacts and a relatively high roughness on the surface;[7–10] e.g., Jacobs *et al*.[7] talked about the difficulties in using a conventional MR fluid to polish calcium fluoride (CaF_2) and potassium dihydrogen phosphate (KDP). It was shown that since CaF_2 is a soft material [H_V = 1.65 GPa (Ref. 11)], it is easily chipped and tends to experience a large number of fine scratches. On the other hand, KDP is particularly soluble in water; therefore, any water-based MR fluid is not recommended when polishing this material. The alternative MR fluid for finishing CaF_2 was based on a lubricant component (PEG 200) instead of water to soften the MR fluid and prevent fine scratches. The magnetic-field strength on the MRF machine was also reduced to further soften the MR fluid. The results showed a root-mean-square (rms) surface roughness of ~1 nm for this material. For KDP, the water component was replaced with dicarboxylic acid ester. Surface-roughness results (when using nanodiamond as a polishing abrasive) were as low as ~20-nm peak-to-valley (p–v) and ~1.6-nm rms. Similarly, Menapace *et al*.[12] [Lawrence Livermore National Laboratory (LLNL)] successfully polished a 50 × 50-mm^2 KDP substrate using an optimized nonaqueous MR fluid. The surface microroughness achieved was in the mid-angstrom level, along with a 5× improvement in the surface figure. More recently, Pattanaik *et al*.[13] described the use of an MRF setup for polishing a nonmagnetic copper substrate using an oil-based MR fluid. By modifying both the MR fluid composition [mainly the concentration of carbonyl iron (CI), a polishing abrasive, and an oil-based medium] and the experimental setup (relative rotational movement between the workpiece and MR fluid), they found the optimal conditions at which a smooth surface roughness is achieved.

Another group of materials that is relatively challenging to finish by using MRF [and other techniques (see Refs. 14–16)] consists of crystalline[8,17] and polycrystalline materials.[9,10,18] The difficulty arises because of the material anisotropy in the unit cell regime (mostly found at the less-symmetric lattice systems, such as hexagonal) and/or in the grain-array regime.[19–21] Kozhinova *et al*.[9] (and later Hallock *et al*.[10]) demonstrated the use of an altered MR fluid to finish an infrared (IR) polycrystalline material—chemical-vapor–deposited (CVD) ZnS. They showed that when this material is processed with a conventional alkaline MR fluid, surface-artifact phenomena known as “pebbles”[9,22] (in the mesostructured regime) and “orange peel” (in the grain-structure regime)[23] are raised on the finished surface; furthermore, the more material removed by MRF, the rougher the surface. They experimented with the MRF process by using a modified MR fluid in which the CI particles were replaced with a “soft” CI type and the carrier medium was modified from alkaline to acidic. When using this type of modified MR fluid, the surface artifacts and roughness can be minimized.

In our ongoing research, we investigate the role of chemical and mechanical effects on the mrr during MRF of IR polycrystalline materials, with considerable focus on CVD ZnS. Seeking an explanation to Kozhinova’s findings, we investigated[19] the anisotropy of ZnS during MRF using four dominant single-crystal orientations of ZnS (100, 110, 111, and 311). The relative mrr’s between the different orientations were examined during MRF, using three chemomechanically modified MR fluids: pH 6 with viscosity (η) of ~197 cP, pH 5 with $\eta \approx$ 117 cP, and pH 4 with $\eta \approx$ 47 cP. We used unique CI particles coated with a thin layer of zirconia to protect the iron particles from rapid corrosion in acidic conditions.[24–26] We found that the minimal variation in the removal rate between the four crystalline orientations was obtained with a pH 4 and low-viscosity (~47-cP) MR fluid. This suggested that during MRF, most of the grains within the polycrystalline material are polished at relatively the same rate (uniformly), leaving a few surface artifacts (pebbles) and a relatively low surface roughness. When this formulation was tested on several CVD ZnS substrates, we found that pebble artifacts were minimal with this composition; however, surface microroughness was relatively high at ~44-mm rms. The missing part in our previous work[19] was lacking polishing abrasive in the acidic MR fluid. In this article we describe our efforts to further reduce the appearance of pebbles and improve surface roughness on several CVD ZnS substrates and other important IR polycrystalline materials using an acidic, low-viscosity MR fluid. A modified version of zirconia-coated CI particles to further increase the acidic MR fluid's lifespan at pH 4.5 (Refs. 27 and 28) is used. We first examine the effect of two polishing abrasives—alumina and nanodiamond—on the removal-rate uniformity of single-crystal orientations of ZnS and then examine the surface finish of several IR polycrystalline materials that were polished with two acidic, low-viscosity MR fluids containing these two polishing abrasives.

Experimental Details

1. IR Optical Substrates

The crystalline materials and their relevant properties are listed in Table 146.IV. All single-crystal ZnS samples were grown, cut, and supplied by the same supplier.[29] Polycrystalline CVD ZnS materials were obtained from different suppliers, each providing one sample (samples A, B, C, and D in Table 146.IV). Technically the material is listed as CVD ZnS; however, differences are anticipated because of variations in detailed manufacturing conditions with each supplier.[20,30] Also, samples A–C are forward-looking IR (FLIR) ZnS, while sample D is elemental ZnS.

Hot isostatic pressed (HIP) ZnS, CVD ZnSe, and MgF_2 were also provided from different suppliers. All materials were ground and pre-polished in-house, as described in Ref. 9, to a flatness of 1 to 2 λ, a p–v roughness of <40 nm, and an rms of <4 nm.

2. Acidic MR Fluids

The MR fluids we used are based on the "advanced zirconia-coated CI particles." The particles' synthesis and characterization are widely described in Refs. 27 and 28. The use of the coated particles in an acidic suspension greatly improves the MR fluid's lifespan by suppressing oxidation of the carbonyl iron particles. The primary formulation of the acidic MR

Table 146.IV: Characteristics and properties of IR crystalline materials.

Sample ID	Sample Type	Crystal Structure	H_V (GPa)*	Grain Size (μm)
ZnS (100)	Single crystal	Cubic	1.89±0.03 (Ref. 19)	N/A
ZnS (110)	Single crystal	Cubic	1.71±0.04 (Ref. 19)	N/A
ZnS (111)	Single crystal	Cubic	2.93±0.04 (Ref. 19)	N/A
ZnS (311)	Single crystal	Cubic	2.17±0.12 (Ref. 19)	N/A
ZnS A†	Polycrystalline; CVD; FLIR	Cubic	1.86±0.02 (Ref. 28)	1.18±0.34**
ZnS B†	Polycrystalline; CVD; FLIR	Cubic	1.72±0.02 (Ref. 28)	2.03±0.64**
ZnS C‡	Polycrystalline; CVD; FLIR	Cubic	1.61±0.14 (Ref. 28)	—
ZnS D‡	Polycrystalline; CVD; elemental	Cubic	2.00±0.03 (Ref. 28)	1.94±0.46**
HIP ZnS	Polycrystalline; CVD; HIP	Cubic	1.33±0.05 (Ref. 28)	75 to 150 (Ref. 22)
ZnSe	Polycrystalline; CVD	Cubic	0.90±0.06 (Ref. 28)	43±9.00 (Ref. 31)
MgF_2	Polycrystalline	Tetragonal	2.29±0.05 (Ref. 28)	~0.45*** (Ref. 32)

*Taken with a Tukon 300 BM Micro-Indenter at 100-g force for single-crystal samples and 400-g force for all other samples.
**The lineal-intercept method for determining average grain size was used.
***An image-analyzing software was used.
†From U.S. vendors
‡From Chinese vendors

fluid, given in Table 146.V, was blended off-line using a shaft mixer. Small portions of powder were incrementally added to a mixture of water and a particle-dispersant agent [polyethylene-imine (PEI), Sigma Aldrich] to form a slurry. The acid (glacial acetic acid, Sigma Aldrich) was added last. Polishing abrasives—alumina and diamond (see Table 146.VI for more details)—were added (to separate fluids) at a different stage of the experiment, when the fluids were circulating on the MRF machine. This had no effect on the fluids' viscosity or pH value. For the alumina-based MR fluid, the abrasive concentrations evaluated, in volume percent (vol %), were 0 vol %, 1 vol %, 2 vol %, and 3 vol %. For the nanodiamond-based MR fluid, the abrasive concentrations evaluated were 0 vol %, 0.06 vol %, 0.12 vol %, and 0.18 vol %. Note that the diamond-abrasive concentration is one order of magnitude lower than that of alumina because the nanodiamond abrasive is more aggressive than alumina. The acidic MR fluids had an off-line viscosity of ~45 cP. The pH of the fluids throughout the experiments was 4.53±0.09 and 4.54±0.11 for the alumina and diamond-based fluids, respectively. One liter from each fluid was prepared and loaded on the MRF machine.

Table 146.V: Acidic MR-fluid formulation showing the different components, their original form of supply, and their relative portion in the fluid (in volume percent).

Component	Form of Supply	MR Fluid (vol %)
Advanced zirconia-coated CI particles	Powder	27.97
DI (de-ionized) water	Liquid	49.30
Polyethylene-imine	50 wt% in water	20.71
Acetic acid	~16-M solution	2.02

3. MRF Spotting Experiment

An MRF spotting experiment was conducted on a research MRF machine, referred to as the "spot-taking machine" (STM).[7] The STM has features similar to a conventional MRF machine; however, it is not designed to perform a full run of polishing. It is capable of taking single spots at a time because of a lack of part movement. An example of an MRF spot and the removal function is shown in Fig. 146.49. The acidic MR fluids (containing different abrasive types and concentrations) were used in a screening spotting experiment on single-crystal orientations of ZnS. Each single-crystal substrate was spotted twice with a given acidic fluid for 1 min. The peak removal rate (prr) was then measured. Following the screening experiment with single-crystal ZnS, the fluids with the highest abrasive concentration (i.e., 3 vol% alumina and 0.18 vol% diamond) were used in the second spotting stage of polycrystalline IR materials. Each polycrystalline substrate was spotted once for 15 min to remove between 0.7 to 1.0 μm of material at the deepest depth of penetration (ddp). The spotting time was chosen

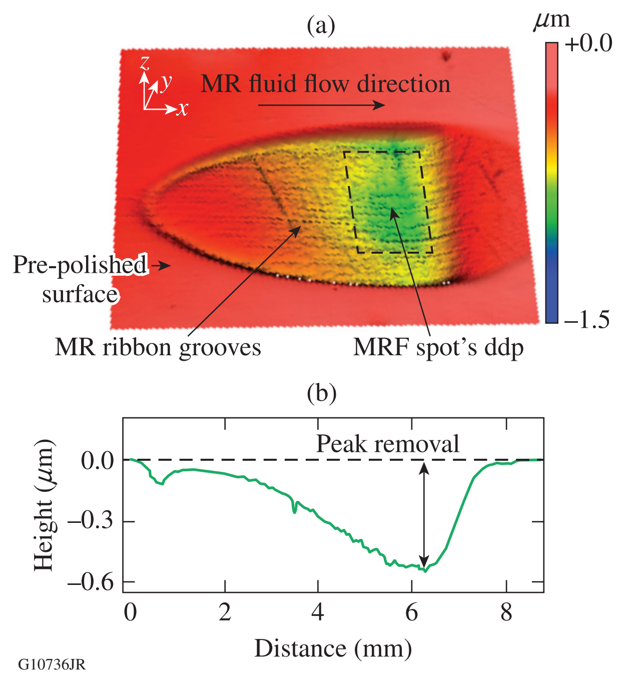

Figure 146.49
(a) A 3-D white-light interferometer image (12×8 mm^2) of a magnetorheological finishing (MRF) spot taken on a pre-polished chemical-vapor–deposited (CVD) ZnS substrate (sample A) designating the spot's depth of deepest penetration (ddp), MR ribbon grooves, and MR fluid-flow direction. (b) The MRF removal function shows the peak removal around the spot's ddp.

Table 146.VI: Polishing abrasives, their source, and characteristics.

Polishing Abrasive	Source	Form of Supply	Particle Size* (nm)
Alumina (alpha)	NanoTek	Dry powder	d_{15} = 19; d_{50} = 52; d_{80} = 169
DIANAN® nanodiamond	Straus Chemical	Dry powder	d_{15} = 13; d_{50} = 28; d_{80} = 143

*Particle-sized data were obtained with the AcoustoSizer IIS-Particle size and zeta potential analyzer.[33] Samples contained 0.5 wt% of abrasive in DI water. All suspensions were dispersed using a sonication bath for 20 min prior to measurement.

based on Ref. 9, which states that pebbles on a pre-polished CVD ZnS surface are exposed after ~0.5 μm of material has been removed. Machine settings were 1.3-mm ribbon height, 0.2-mm (for single crystals) and 0.3-mm (for polycrystalline) penetration depth, 220-rpm wheel speed, 110-rpm pump speed, and a 15-A electric current.

4. Metrology

a. Material removal rate of single-crystal ZnS substrates. Peak removal rates for all spots taken on the single-crystal substrates were obtained with a Zygo Mark IV laser interferometer[34] by subtracting the spotted area from the original surface and dividing the difference by the spotting time, i.e., 1 min. The peak removal is measured as the deepest vertical depth of material removed by MRF (see Fig.146.49).

b. Surface artifacts and microroughness of polycrystalline materials. The submillimeter- and millimeter-sized pebbles on the spotted polycrystalline materials, which are a direct result of the CVD growth technique,[9,22,35,36] were evaluated using a Zygo white-light, non-contact interferometer—the NewView™ 100 (Ref. 37). A 5× objective (with a 1.39 × 1.04-mm^2 field of view) was used to capture two areal-roughness measurements at the ddp of the spots. These measurements were analyzed, using a low-pass filter option in MetroPro, to screen out the roughness and leave only the surface waviness.[38] An example of a low-pass filtered measurement is given in Figs. 146.50(a)–146.50(c), where (a) the original measurement is decomposed to (b) a waviness plot and (c) a roughness plot. The waviness data provide an indication on the pebbles' severity on the surface. Surface microroughness, which captures submicron- and micron-sized features, such as pits, scratches, and grain boundaries (known as orange peel[23]), was measured using the NewView 100™ with a 20× objective (a 0.35 × 0.26-mm^2 field of view). Four areal measurements were taken at the ddp of each spot. Within each areal measurement, five lineout scans were collected in the direction of the MR fluid flow. This helps to avoid the grooves created by the MR ribbon during MRF (see Fig. 146.49), which are a direct result of the workpiece being stationary and not rotating on the STM. We believe that the lineout data better reflect the roughness one would obtain if a conventional MRF machine with a full run would have been used. All p–v and rms-roughness data were averaged and are presented in Tables 146.VII and 146.VIII for CVD ZnS and Tables 146.IX and 146.X for the other IR materials.

Results

1. Material Removal Rate of Single-Crystal ZnS

The average prr for all four single-crystal ZnS substrates finished with various amounts of alumina and diamond abrasives in the acidic MR fluids is given in Table 146.VII and Figs. 146.51(a) and 146.51(b). Both sources indicate that the addition of abrasives increased the overall prr of the acidic fluids. When alumina was first added to the acidic fluid, the average prr of all four orientations increased by ~59%—from ~0.029 μm/min to ~0.046 μm/min (see the highlighted line in Table 146.VII); when diamonds were first added to the acidic fluid, the average increased by ~46%—from ~0.026 μm/min to ~0.038 μm/min. For the acidic fluids with alumina, an additional amount of abrasive has no real effect on the prr. Observation of the data within the standard deviation shows little change in the average prr with increased abrasive concentration after the first dose is added [Fig. 146.51(a)]. For the acidic fluid containing the diamonds, however, an additional amount of abrasive linearly increases the average prr of the fluid [Fig. 146.51(b)]. The highest average prr of the fluid is achieved when 3× the amount of diamond abrasive is used—i.e., 0.18 vol %.

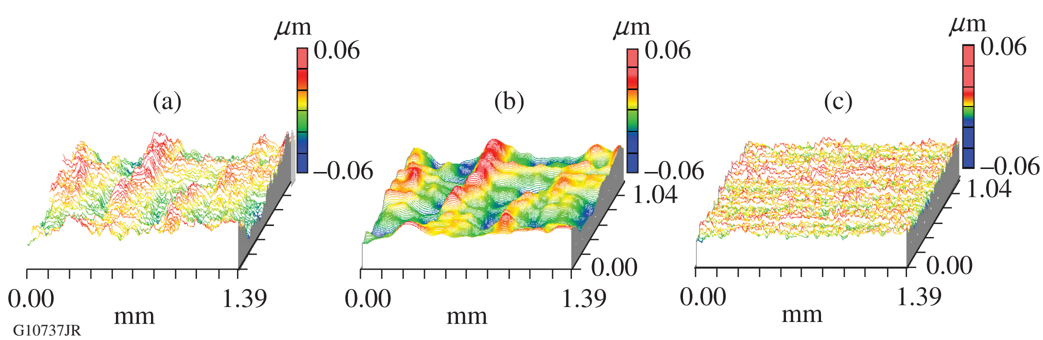

Figure 146.50
A set of 3-D white-light interferometer images (1.39 × 1.04 mm^2) of a CVD ZnS (sample A) substrate finished with a conventional alkaline MR fluid. (a) Original measurement showing both surface waviness and roughness, (b) low-pass filter analysis showing surface waviness (indication of pebbles), and (c) screened-out high-frequency roughness.

Table 146.VII: Average peak removal rate (μm/min) for single-crystal substrates of ZnS finished with acidic MR fluids that contain various amounts of alumina and nanodiamond abrasives. Note that the alumina-abrasive concentration is an order of magnitude higher than the nanodiamond.

Single-Crystal Orientation	Acidic MR Fluid with Alumina Abrasive				Acidic MR Fluid with Nanodiamond Abrasive			
	0 vol %	1 vol %	2 vol %	3 vol %	0 vol %	0.06 vol %	0.12 vol %	0.18 vol%
100	0.030±0.002	0.045±0.001	0.040±0.001	0.041±0.000	0.029±0.000	0.035±0.000	0.046±0.007	0.053±0.001
110	0.028±0.000	0.046±0.004	0.048±0.002	0.039±0.000	0.029±0.002	0.043±0.003	0.050±0.003	0.056±0.004
111	0.032±0.003	0.045±0.000	0.049±0.003	0.041±0.002	0.020±0.002	0.036±0.008	0.046±0.003	0.051±0.005
311	0.028±0.001	0.048±0.002	0.040±0.003	0.045±0.002	0.025±0.001	0.037±0.001	0.040±0.007	0.053±0.000
Average	0.029±0.002	0.046±0.001	0.044±0.005	0.042±0.002	0.026±0.004	0.038±0.004	0.046±0.004	0.053±0.002

Table 146.VIII: Surface waviness as p–v and rms collected with a 5× objective at the spots' ddp of four polycrystalline, CVD ZnS substrates provided by different suppliers. Data were obtained using a low-pass filter.

CVD ZnS Sample ID	Acidic MR Fluid with Alumina Abrasive			Acidic MR Fluid with Nanodiamond Abrasive		
	ddp (μm); removal rate (μm/min)	p–v (nm)	rms (nm)	ddp (μm); removal rate (μm/min)	p–v (nm)	rms (nm)
Sample A	0.76; 0.051	62.26±33.02	7.06±1.76	0.95; 0.063	64.51±1.31	9.24±0.86
Sample B	0.77; 0.051	54.83±13.33	7.22±1.34	0.84; 0.056	47.29±0.48	5.51±0.22
Sample C	0.69; 0.046	194.67±42.24	24.14±0.82	1.10; 0.073	55.47±.91	7.35±1.76
Sample D	0.79; 0.053	147.85±1.91	16.43±0.72	0.94; 0.063	71.46±12.43	7.81±2.34

Table 146.IX: Surface microroughness as areal and lineout p–v and rms collected with a 20× objective at the spots' ddp of four polycrystalline, CVD ZnS substrates provided by different suppliers.

Sample	Acidic MR Fluid with Alumina Abrasive				Acidic MR Fluid with Nanodiamond Abrasive			
	Areal		Lineouts		Areal		Lineouts	
	p–v (nm)	rms (nm)	p–v (nm)	rms (nm)	p–v (nm)	rms (nm)	p–v (nm)	rms (nm)
A	694.23±8.10	18.53±1.58	75.70±7.88	14.22±1.35	1361.11±147.15	14.33±1.01	28.46±4.54	6.10±1.24
B	694.68±25.87	20.38±1.79	79.39±15.19	15.58±2.75	775.50±285.04	10.32±2.54	27.66±4.38	5.93±0.76
C	903.72±110.06	39.48±1.80	111.67±52.06	29.83±4.47	1364.06±53.33	26.94±1.70	32.87±7.58	7.79±1.98
D	1160.39±343.47	36.08±4.74	136.03±20.64	28.39±4.32	1215.28±138.67	18.35±2.91	30.08±4.26	6.94±0.85

Table 146.X: Surface waviness as p–v and rms, collected with a 5× objective at the spots' ddp of three polycrystalline IR substrates. Data were obtained using a low-pass filter.

Sample	Acidic MR Fluid with Alumina Abrasive		Acidic MR Fluid with Nanodiamond Abrasive	
	p–v (nm)	rms (nm)	p–v (nm)	rms (nm)
HIP ZnS	331.37±84.21	58.52±14.01	379.21±13.35	58.35±3.04
ZnSe	377.94±21.65	53.06±0.71	236.33±83.42	29.31±6.67
MgF_2	45.69±8.01	5.76±1.33	9.81±0.75	4.84±4.15

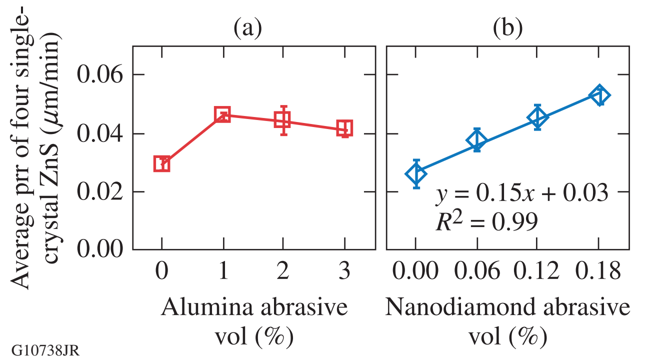

Figure 146.51
Average peak removal rate (prr) of all four single-crystal orientations versus abrasive concentration in the acidic MR fluid. (a) Alumina-based acidic MR fluid and (b) nanodiamond-based acidic MR fluid. Note that the alumina-abrasive concentration is ~10× higher than that of the nanodiamond abrasive.

For the next stage of the experiment—MRF of polycrystalline IR substrates—acidic formulations that contained the maximum amount of alumina and nanodiamond abrasives were used (i.e., a concentration of 3 vol % of alumina and 0.18 vol % of nanodiamonds).

2. Surface Finish of Polycrystalline CVD ZnS

The surface finish at the spots' ddp for all CVD ZnS samples (A–D) measured with 5× and 20× objectives is shown in Tables 146.VIII and 146.IX, respectively. Pebbles were studied using data from Table 146.VIII representing surface waviness (original roughness data are provided in **Appendix A**, p. 107). Surface microroughness was studied using data from Table 146.IX. Table 146.VIII indicates that the alumina-based acidic MR fluid produced less waviness on the surface of samples A and B than on samples C and D, in which the waviness was ~50% higher. When the samples were finished with a nanodiamond-based acidic MR fluid, similar surface waviness was observed for samples A and B. For samples C and D, however, the level of waviness is closer in value to that of samples A and B. Surface microroughness data in Table 146.IX show a similar trend to what was seen with surface waviness. When finished with an alumina-based acidic MR fluid, the microroughness of samples A and B was similar; the microroughness of samples C and D was similar, but ~40% higher than that of samples A and B. When the samples were finished with a nanodiamond-based acidic MR fluid, all samples showed a remarkable surface microroughness as a lineout of ~30-nm p–v and ~6-nm rms, and the large difference in roughness among samples A–D was diminished. A power spectral density (PSD) analysis of samples A–D, given in Fig. 146.52, also shows that MRF using the nanodiamond-based acidic MR fluid resulted in less pebbles on the surface and improved surface microroughness. At a spatial frequency below 100 mm^{-1} (corresponding to a lateral distance of 0.1 mm and higher), all CVD ZnS samples show a flatter and lower power density (PD) trend line. This indicates a reduction in pebbles on the surfaces that are finished with an acidic MR fluid containing nanodiamonds. At a spatial frequency above 100 mm^{-1} (a range that represents microroughness), samples A and B reach the lowest PD value, indicating that their microroughness is lower compared to samples C and D. Overall, the PSD results support the waviness and roughness analyses presented in Tables 146.VIII and 146.IX.

White-light interferometer micrographs taken with a 20× objective (given in Figs. 146.53 and 146.54) show the different

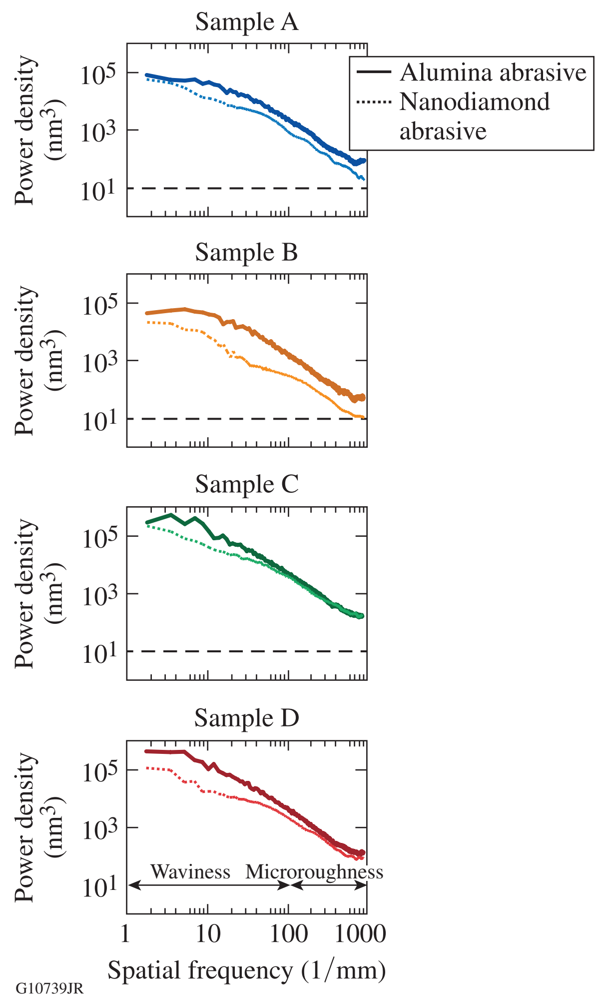

Figure 146.52
Power spectral density (PSD) for CVD ZnS samples A–D. The solid curves designate an acidic MR fluid with an alumina abrasive; the dotted curves designate acidic MR fluid with a nanodiamond abrasive.

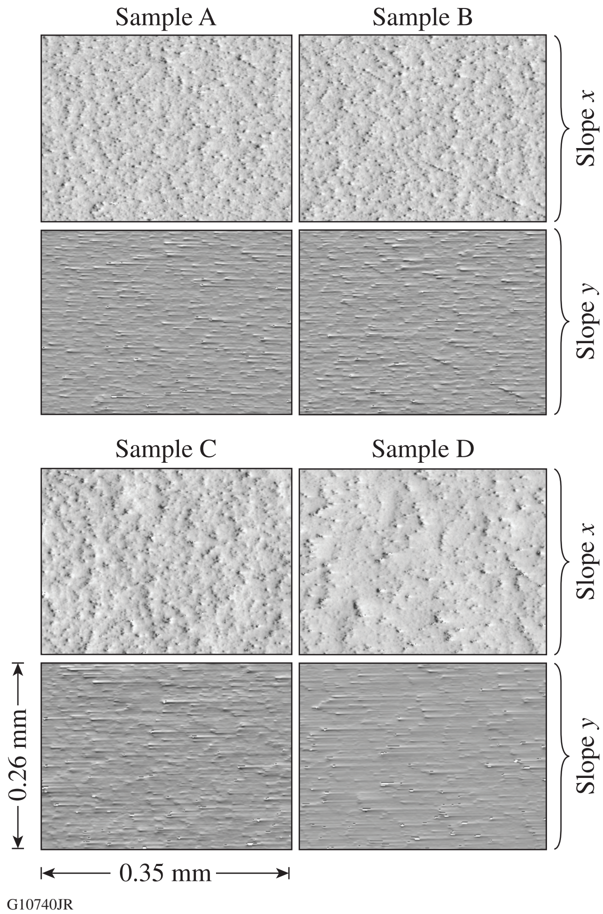

Figure 146.53
White-light interferometer (Zygo NewView™ 100) micrographs (20× objective; 0.35 × 0.26 mm^2) at the ddp of CVD ZnS samples A–D finished with an acidic MR fluid containing an alumina abrasive. The top micrographs designate "slope *x* surface maps;" the bottom micrographs designate "slope *y* surface maps." Pits on the surface (seen in the *x* slope maps) correspond to MR ribbon grooves (seen in the *y* slope maps) in the direction of the MR fluid flow.

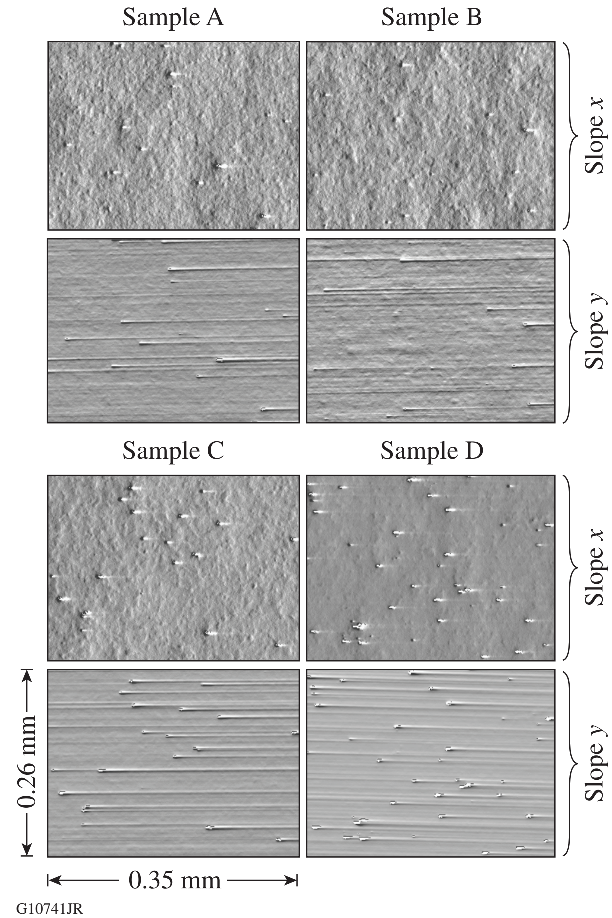

Figure 146.54
White-light interferometer (Zygo NewView™ 100) micrographs (20× objective; 0.35 × 0.26 mm^2) at the ddp of CVD ZnS samples A–D finished with an acidic MR fluid containing a nanodiamond abrasive. The top micrographs designate "slope *x* surface maps;" the bottom micrographs designate "slope *y* surface maps." Pits on the surface (seen in the *x* slope maps) correspond to MR ribbon grooves (seen in the *y* slope maps) in the direction of the MR fluid flow.

textures on surfaces finished with the two acidic MR fluids. For the alumina-based MR fluid (Fig. 146.53), a pitted pattern appears on all CVD ZnS samples (A–D). These pits seem to be a result of the grooves created by the MR ribbon in the direction of the MR fluid flow ("slope *y* surface map" micrographs in Fig. 146.53). A similar observation was found when nanodiamonds were used in the acidic MR fluid. In this case, however, the amount of pits and grooves is significantly lower, especially for samples A and B.

3. Surface Finish of Other Polycrystalline IR Optical Materials

The two acidic MR fluids used with polycrystalline, CVD ZnS substrates A–D, described in **Surface Finish of Polycrystalline CVD ZnS** (p. 103), were also used on CVD HIP ZnS, CVD ZnS, and MgF_2—which is not a CVD-grown material. Tables 146.X and 146.XI show the surface waviness and surface microroughness, respectively, of these materials (original data collected with a 5× objective are given in **Appendix A**, p. 107). Table 146.X indicates that CVD HIP ZnS and CVD ZnSe share similar values of waviness when finished with alumina-based acidic MR fluid. The pebbles on the surfaces are of the same order of magnitude. No change is seen in the emergence and size of pebbles on the CVD HIP ZnS surface when using nanodiamond abrasives instead of alumina in the acidic fluid. The surface waviness of CVD ZnSe, however, improves by ~40% when using a nanodiamond abrasive in the acidic MR fluid, indicating a reduction in the appearance of pebbles on the sur-

Table 146.XI: Surface microroughness as areal and lineout p–v and rms collected with a 20× objective at the spots' ddp of three polycrystalline IR substrates.

Sample	Acidic MR Fluid with Alumina Abrasive				Acidic MR Fluid with Nanodiamond Abrasive			
	Areal		Lineout		Areal		Lineout	
	p–v (nm)	rms (nm)	p–v (nm)	rms (nm)	p–v (nm)	rms (nm)	p–v (nm)	rms (nm)
HIP ZnS	1180.68±158.00	47.48±8.72	160.62±31.7	36.39±9.56	1476.20±251.10	58.80±15.90	191.30±57.67	54.30±20.60
ZnSe	1734.16±230.39	81.49±9.57	193.55±38.2	46.37±9.77	2270.10±351.85	66.80±8.31	87.39±26.31	21.20±5.72
MgF_2	554.91±142.89	7.72±0.72	38.81±5.881	6.68±0.75	43.54±12.72	1.32±0.13	6.06±0.92	1.09±0.18

face. Magnesium fluoride does not experience the pebble-like structure seen in CVD-grown materials. However, an ~80% improvement is seen in p–v and rms values of this material when using the acidic MR fluid with nanodiamond abrasives.

Surface microroughness results seen in Table 146.XI show that better surface roughness for the CVD HIP ZnS surface was obtained when an alumina abrasive was used in the acidic MR fluid. This is also seen in Figs. 146.55 and 146.56, in which the substrate's roughness is somewhat less pronounced and defined in Fig. 146.55 than in Fig. 146.56. When avoiding the MR ribbon grooves by taking roughness measurements as lineouts (see "Lineout" columns in Table 146.XI), a remarkable reduction in the p–v and rms values is observed. Overall, the alumina-based MR fluid provided better surface roughness for HIP CVD ZnS than the nanodiamond-based fluid.

The microroughness of CVD ZnSe finished with the acidic MR fluid and alumina abrasive is relatively high. A significant reduction in surface roughness, however, was found when this material was finished with nanodiamonds in the MR fluid.

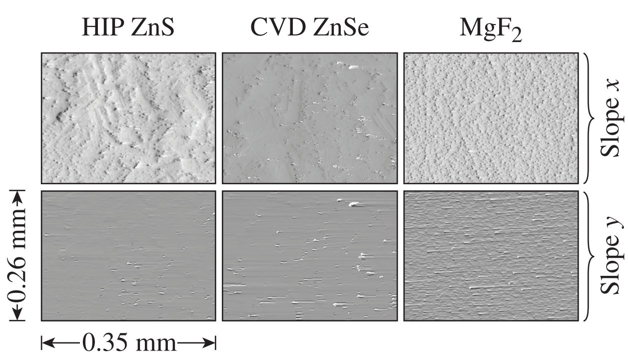

Figure 146.55
White-light interferometer (Zygo NewView™ 100) micrographs (20× objective; 0.35 × 0.26 mm^2) at the ddp of CVD HIP ZnS, CVD ZnSe, and MgF_2 finished with an acidic MR fluid containing an alumina abrasive. Pits on the surface (seen in the *x* slope maps) correspond to MR ribbon grooves (seen in the *y* slope maps) in the direction of the MR fluid flow.

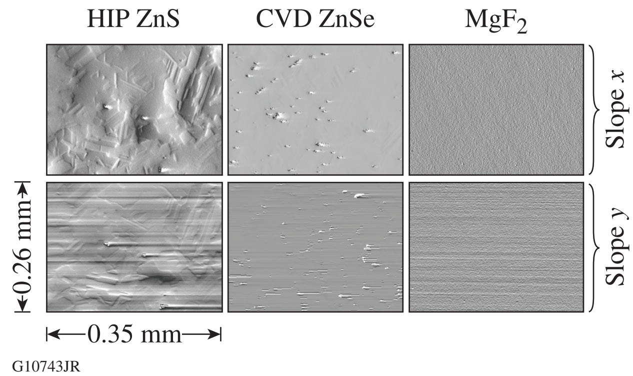

Figure 146.56
White-light interferometer (Zygo NewView™ 100) micrographs (20× objective; 0.35 × 0.26 mm^2) at the ddp of CVD HIP ZnS, CVD ZnSe, and MgF_2 finished with an acidic MR fluid containing a nanodiamond abrasive. Pits on the surface (seen in the *x* slope maps) correspond to MR ribbon grooves (seen in the *y* slope maps) in the direction of the MR fluid flow.

Figure 146.56 demonstrates the diminished small-scale pebbles on the surface of a CVD ZnSe substrate finished with an acidic MR fluid containing nanodiamonds. PSD data (Fig. 146.57) show similar observations. The power-density versus spatial-density plot of the surface finished with nanodiamonds shows significantly lower values than the alumina abrasive, indicating a reduction in the surface roughness (and pebbles) on the surface. For the MgF_2 substrate, finishing this material with an acidic MR fluid containing alumina provided a relatively good surface roughness (~38-nm p–v and ~7-nm rms as lineout). Roughness was significantly improved by more than 80% when using fluid containing nanodiamonds (~7-nm p–v and ~1-nm rms as lineout), with similar improvements in PSD results for this material obtained with the acidic MR fluid containing nanodiamonds being substantially better than that of an alumina-based MR fluid.

Discussion

Adding polishing abrasives to the acidic MR fluid increased the overall material removal rate of the fluid, while maintaining relatively good uniformity among the different single-crystal orientations of ZnS. Adding an alumina abrasive to the fluid

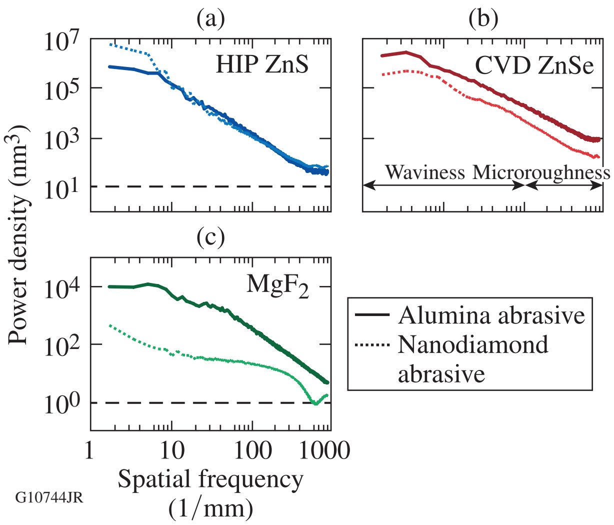

Figure 146.57
Power spectral density (PSD) for (a) CVD HIP ZnS, (b) CVD ZnSe, and (c) MgF_2 samples. The solid curves designate an acidic MR fluid with an alumina abrasive; the dotted curves designate an acidic MR fluid with nanodiamond abrasive.

caused saturation in the material removal rate with the first addition of a 1-vol % abrasive. With a nanodiamond abrasive, a constant increase in the material removal rate of ~18% was seen with any additional portion of abrasive. Surface waviness and PSD results show a significant reduction in the emergence of pebbles on the surface of several CVD ZnS substrates (samples A–D) finished with an acidic MR fluid containing nanodiamonds. The surface microroughness achieved was as low as ~30-nm p–v and ~6-nm rms. Furthermore, the variation in surface artifacts and roughness among the different CVD ZnS substrates, which is known to result from differences in detailed manufactory conditions of different suppliers,[30] was also resolved when a nanodiamond abrasive was used in the acidic MR fluid. The pronounced pits and MR grooves on the finished surfaces are believed to contribute to the overall roughness data collected and presented in this work. Since these grooves result from parts being stationary and not rotating during the process, we assume that lower roughness data, especially p–v, could be obtained if these surfaces were polished on a commercial MRF machine. The nanodiamond-based acidic MR fluid seemed to reduce the surface artifacts and microroughness of CVD ZnSe and MgF_2, but not those of CVD HIP ZnS. This finding was unexpected since CVD HIP ZnS is most similar to CVD ZnS; therefore, we would expect it to show similar surface waviness and roughness findings. This led us to the conclusion that the ceramic's crystallite (grain) size might have an effect on the resultant finish of the samples. Among the four types of polycrystalline evaluated here, CVD ZnS and MgF_2 have a smaller grain size. For these two materials, a good surface roughness and a minimal level of surface artifacts and pebbles were observed. The CVD ZnSe has an intermediate grain size (~45 μm) among the four evaluated materials. For this material some degree of surface artifacts and a surface microroughness of ~87-nm p–v and 21-nm rms were observed. The CVD HIP ZnS has the highest grain size of all four materials (~75 μm) because of the high temperature (~1000°C) reached during the HIP process, where recrystallization of the grains occurs.[22] With this material, a high degree of surface artifacts and pebbles was found on the MR-finished surface with both acidic fluids containing alumina and nanodiamonds. The surface microroughness was fairly high as well (>160-nm p–v and >36-nm rms). Further investigation of this assumption is required.

Conclusion

The addition of a polishing abrasive to the low-pH, low-viscosity MR fluid did not seem to affect the relative mrr among the different single-crystal orientations of ZnS. The overall mrr of the single-crystal orientations increased with an increasing nanodiamond concentration in the fluid but remained more or less the same when the concentration of alumina abrasives was increased. Surface-waviness and PSD results have shown that the emergence of pebbles on the surface of several CVD ZnS substrates (samples A–D) finished with the acidic MR fluid containing nanodiamonds was significantly reduced and the surface microroughness achieved was as low as ~30-nm p–v and ~6-nm rms. Furthermore, the variation in surface artifacts and microroughness among the different CVD ZnS substrates was also resolved with this type of abrasive in the acidic MR fluid. The pronounced pits and MR grooves observed on the finished surfaces contributed to the overall roughness data we collected; we believe that lower roughness data, particularly p–v, can be obtained if these surfaces were to go through a complete finishing run on a commercial MRF machine. The acidic MR fluid with nanodiamonds seemed to reduce the surface artifacts and microroughness of CVD ZnSe and MgF_2 but not that of CVD HIP ZnS. We speculate that the ceramic's grain size might have some influence in this matter. Further investigation is clearly required.

ACKNOWLEDGMENT

We thank Dr. S. Gorodkin and QED Technologies for their help and guidance with the surface waviness analysis using MetroPro software. This material is based upon work supported by the Department of Energy National Nuclear Security Administration under Award Number DE-NA0001944, the University of Rochester, and the New York State Energy Research and Development Authority. The support of DOE does not constitute an endorsement by DOE of the views expressed in this article. This work is synergistic with the NSF I/UCRC Center for Freedom Optics (IIP-1338877 and IIP-1338898).

Appendix A: White-Light Interferometer Roughness Data Collected with a 5× Objective

The data in Tables 146.XII and 146.XIII were used to perform the waviness analysis described in **Results** (p. 101).

Table 146.XII: Surface roughness (areal and lineout) collected with a 5× objective at the spots' ddp of four CVD ZnS substrates.

CVD ZnS Sample ID	Acidic MR Fluid with Alumina Abrasive				Acidic MR Fluid with Nanodiamond Abrasive			
	Areal		Lineouts		Areal		Lineouts	
	p–v (nm)	rms (nm)	p–v (nm)	rms (nm)	p–v (nm)	rms (nm)	p–v (nm)	rms (nm)
Sample A	287.56±180.42	13.42±2.00	72.93±12.18	12.56±1.16	525.96±177.97	12.53±0.91	55.78±12.35	10.64±2.53
Sample B	737.48±486.54	15.12±2.32	76.91±13.84	13.60±1.46	360.24±10.53	8.21±0.45	36.27±7.01	7.08±0.94
Sample C	1292.91±1241.49	29.37±0.94	146.63±19.77	26.98±2.10	379.23±27.48	10.46±2.13	39.90±5.40	7.99±1.08
Sample D	918.48±599.05	36.52±0.76	184.47±27.50	32.05±5.13	529.31±155.43	11.85±3.54	50.42±9.49	9.19±1.74

Table 146.XIII: Surface roughness (areal and lineout) collected with a 5× objective at the spots' ddp of CVD HIP ZnS, CVD ZnSe, and MgF_2.

Sample	Acidic MR Fluid with Alumina Abrasive				Acidic MR Fluid with Nanodiamond Abrasive			
	Areal		Lineouts		Areal		Lineouts	
	p–v (nm)	rms (nm)	p–v (nm)	rms (nm)	p–v (nm)	rms (nm)	p–v (nm)	rms (nm)
HIP ZnS	1254.13±641.29	72.67±14.50	290.56±60.10	65.26±18.10	868.02±47.76	71.70±2.95	262.40±53.54	62.90±10.40
ZnSe	1528.77±784.67	74.25±1.96	308.96±43.77	68.19±10.90	1714.70±0.76	46.70±5.98	178.90±31.38	36.00±7.02
MgF_2	237.10±1.55	8.33±1.55	46.06±8.35	7.81±1.31	37.89±4.85	2.16±0.15	7.19±1.59	1.22±0.29

REFERENCES

1. S. D. Jacobs, D. Golini, Y. Hsu, B. E. Puchebner, D. Strafford, Wm. I. Kordonski, I. V. Prokhorov, E. Fess, D. Pietrowski, and V. W. Kordonski, Proc. SPIE **2576**, 372 (1995).
2. S. D. Jacobs, S. R. Arrasmith, I. A. Kozhinova, L. L. Gregg, A. B. Shorey, H. J. Romanofsky, D. Golini, Kordonski. W. I., P. Dumas, and S. Hogan, in *Finishing of Advanced Ceramics and Glasses*, edited by R. Sabia, V. A. Greenhut, and C. G. Pantano, Ceramic Transactions, Vol. 102 (The American Ceramic Society, Westerville, OH, 1999), pp. 185–199.
3. J. E. DeGroote, H. J. Romanofsky, I. A. Kozhinova, J. M. Schoen, and S. D. Jacobs, Proc. SPIE **5180**, 123 (2003).
4. S. N. Shafrir, J. C. Lambropoulos, and S. D. Jacobs, J. Manuf. Sci. Eng. **129**, 961 (2007).
5. D. Golini, in *Precision Science and Technology for Perfect Surfaces*, edited by Y. Furukawa, Y. Mori, and T. Kataoka, JSPE Publication Series No. 3 (The Japan Society for Precision Engineering, Tokyo, Japan, 1999), pp. 132–137.
6. M. Beier *et al*., Proc. SPIE **8884**, 88840S (2013).
7. *LLE Review Quarterly Report* **80**, 213, Laboratory for Laser Energetics, University of Rochester, Rochester, NY, LLE Document No. DOE/SF/19460-321, NTIS Order No. DE00761211 (1999).
8. S. D. Jacobs, F. Yang, E. M. Fess, J. B. Feingold, B. E. Gillman, W. I. Kordonski, H. Edwards, and D. Golini, Proc. SPIE **3134**, 258 (1997).
9. I. A. Kozhinova, H. J. Romanofsky, A. Maltsev, S. D. Jacobs, W. I. Kordonski, and S. R. Gorodkin, Appl. Opt. **44**, 4671 (2005).
10. B. Hallock *et al*., in *Frontiers in Optics 2008/Laser Science XXIV/Plasmonics and Metamaterials/Optical Fabrication and Testing*, OSA Technical Digest (CD) (Optical Society of America, Washington, DC, 2008), Paper OThB2.
11. "Calcium Fluoride Properties (CaF_2)," ISP Optics, Irvington, NY, 10533, http://www.janis.com/Libraries/Window_Transmissions/CalciumFluoride_CaF2_TransmissionCurveDataSheet.sflb.ashx.
12. J. A. Menapace, P. R. Ehrmann, and R. C. Bickel, Proc. SPIE **7504**, 750414 (2009).
13. L. N. Pattanaik and H. Agarwal, Int. J. Adv. Mech. Eng. **4**, 611 (2014).
14. L. L. Gregg, A. E. Marino, J. C. Hayes, and S. D. Jacobs, Proc. SPIE **5180**, 47 (2004).
15. J. D. Nelson *et al*., Proc. SPIE **8708**, 870815 (2013).
16. M. Brophy, J. D. Nelson, and T. Hordin, in *Classical Optics 2014*, OSA Technical Digest (online) (Optical Society of America, Kohala Coast, Hawaii, 2014), Paper OW3B.3.
17. I. Kozhinova, S. R. Arrasmith, J. C. Lambropoulos, S. D. Jacobs, and H. J. Romanofsky, Proc. SPIE **4451**, 277 (2001).
18. C. Supranowitz *et al*., Proc. SPIE **6545**, 65450S (2007).
19. S. Salzman, H. J. Romanofsky, Y. I. Clara, L. J. Giannechini, G. West, J. C. Lambropoulos, and S. D. Jacobs, Proc. SPIE **8884**, 888407 (2013).
20. J. McCloy *et al*., Proc. SPIE **8016**, 80160I (2011).
21. W. D. Callister, *Materials Science and Engineering*, 2nd ed. (Wiley, New York, 1991), pp. 131–141.

22. J. S. McCloy and R. W. Tustison, *Chemical Vapor Deposited Zinc Sulfide*, Vol. PM237 (SPIE, Bellingham, WA, 2013).

23. E. M. Gavrishchuk *et al*., Inorg. Mater. **43**, 579 (2007).

24. R. Shen, H. Yang, S. N. Shafrir, C. Miao, M. Wang, J. Mici, J. C. Lambropoulos, and S. D. Jacobs, U.S. Patent No. 8,808,568 B2 (19 August 2014).

25. S. N. Shafrir, H. J. Romanofsky, M. Skarlinski, M. Wang, C. Miao, S. Salzman, T. Chartier, J. Mici, J. C. Lambropoulos, R. Shen, H. Yang, and S. D. Jacobs, Appl. Opt. **48**, 6797 (2009).

26. R. Shen, S. N. Shafrir, C. Miao, M. Wang, J. C. Lambropoulos, S. D. Jacobs, and H. Yang, J. Colloid Interface Sci. **342**, 49 (2010).

27. L. J. Giannechini, "Design and Quantification of Highly Corrosion-Resistant Magnetorheological Finishing Powder," M.S. thesis, University of Rochester, 2015.

28. S. Salzman, L. J. Giannechini, H. J. Romanofsky, N. Golini, B. Taylor, S. D. Jacobs, and J. C. Lambropoulos, Proc. SPIE **9633**, 963307 (2015).

29. SurfaceNet GmbH, Landersumer Weg 40, D-48431 Rheine, Germany.

30. S. Salzman, H. J. Romanofsky, S. D. Jacobs, and J. C. Lambropoulos, Prec. Eng. **43**, 257 (2016).

31. J. A. Salem, National Aeronautics and Space Administration, Glenn Research Center, Cleveland, OH, Report NASA/TM—2006-214100 (2006).

32. T.-C. Wen and D. K. Shetty, Proc. SPIE **7302**, 73020Z (2009).

33. Colloidal Dynamics, Ponte Vedra Beach, FL 32082.

34. Zygo Mark IVxp™, Zygo Corporation, Middlefield, CT 06455-1291, http://www.zygo.com (25 May 2016).

35. J. S. Goela and R. L. Taylor, J. Mater. Sci. **23**, 4331 (1988).

36. K. L. Lewis *et al*., in *Proceedings of the Ninth International Conference on Chemical Vapor Deposition 1984*, edited by Mc. D. Robinson *et al*. (Electrochemical Society, Pennington, NJ, 1984), pp. 530–545.

37. NewView™ 100, White Light Optical Profiler (areal over 0.26 mm × 0.35 mm with a 20× Mirau objective, no filter) by Zygo Corporation, Middlefield, CT 06455-1270, http://www.zygo.com (25 May 2016).

38. G. West, "Measuring Surface Texture in MRF Spots on Polycrystalline Material," LLE Internal Memorandum, Laboratory for Laser Energetics, University of Rochester, Rochester, NY (3 August 2011).

Publications and Conference Presentations

Publications

S.-W. Bahk, C. Dorrer, R. G. Roides, and J. Bromage, "Chromatic-Aberration Diagnostic Based on a Spectrally Resolved Lateral-Shearing Interferometer," Appl. Opt. **55**, 2413 (2016).

E. L. Dewald, F. Hartemann, P. Michel, J. Milovich, M. Hohenberger, A. Pak, O. L. Landen, L. Divol, H. F. Robey, O. A. Hurricane, T. Döppner, F. Albert, B. Bachmann, N. B. Meezan, A. J. MacKinnon, D. Callahan, and M. J. Edwards, "Generation and Beaming of Early Hot Electrons onto the Capsule in Laser-Driven Ignition Hohlraums," Phys. Rev. Lett. **116**, 075003 (2016).

T. Döppner, D. A. Callahan, O. A. Hurricane, D. E. Hinkel, T. Ma, H.-S. Park, L. F. Berzak Hopkins, D. T. Casey, P. Celliers, E. L. Dewald, T. R. Dittrich, S. W. Haan, A. L. Kritcher, A. MacPhee, S. Le Pape, A. Pak, P. K. Patel, P. T. Springer, J. D. Salmonson, R. Tommasini, L. R. Benedetti, E. Bond, D. K. Bradley, J. Caggiano, J. Church, S. Dixit, D. Edgell, M. J. Edwards, D. N. Fittinghoff, J. Frenje, M. Gatu Johnson, G. Grim, R. Hatarik, M. Havre, H. Herrmann, N. Izumi, S. F. Khan, J. L. Kline, J. Knauer, G. A. Kyrala, O. L. Landen, F. E. Merrill, J. Moody, A. S. Moore, A. Nikroo, J. E. Ralph, B. A. Remington, H. F. Robey, D. Sayre, M. Schneider, H. Streckert, R. Town, D. Turnbull, P. L. Volegov, A. Wan, K. Widmann, C. H. Wilde, and C. Yeamans, "Demonstration of High Performance in Layered Deuterium-Tritium Capsule Implosions in Uranium Hohlraums at the National Ignition Facility," Phys. Rev. Lett. **115**, 055001 (2015).

C. Dorrer, L. J. Waxer, A. Kalb, E. M. Hill, and J. Bromage, "Single-Shot, High-Resolution, Fiber-Based Phase-Diversity Photodetection of Optical Pulses," Proc. SPIE **9732**, 97320P (2016).

A. J. Harvey-Thompson, A. B. Sefkow, T. N. Nagayama, M. S. Wei, E. M. Campbell, G. Fiksel, P.-Y. Chang, J. R. Davies, D. H. Barnak, V. Y. Glebov, P. Fitzsimmons, J. Fooks, and B. E. Blue, "Diagnosing Laser-Preheated Magnetized Plasmas Relevant to Magnetized Liner Inertial Fusion," Phys. Plasmas **22**, 122708 (2015).

V. V. Ivanov, A. A. Anderson, and I. A. Begishev, "Four-Color Laser Diagnostics for Z-Pinch and Laser-Produced Plasma," Appl. Opt. **55**, 498 (2016).

L. C. Jarrott, M. S. Wei, C. McGuffey, A. A. Solodov, W. Theobald, B. Qiao, C. Stoeckl, R. Betti, H. Chen, J. Delettrez, T. Döppner, E. M. Giraldez, V. Y. Glebov, H. Habara, T. Iwawaki, M. H. Key, R. W. Luo, F. J. Marshall, H. S. McLean, C. Mileham, P. K. Patel, J. J. Santos, H. Sawada, R. B. Stephens, T. Yabuuchi, and F. N. Beg, "Visualizing Fast Electron Energy Transport into Laser-Compressed High-Density Fast-Ignition Targets," Nat. Phys. **12**, 499 (2016).

H. M. Johns, R. C. Mancini, T. Nagayama, D. C. Mayes, R. Tommasini, V. A. Smalyuk, S. P. Regan, and J. A. Delettrez, "Shell Stability and Conditions Analyzed Using a New Method of Extracting Shell Areal Density Maps from Spectrally Resolved Images of Direct-Drive Inertial Confinement Fusion Implosions," Phys. Plasmas **23**, 012709 (2016).

J. D. Kilkenny, P. M. Bell, D. K. Bradley, D. L. Bleuel, J. A. Caggiano, E. L. Dewald, W. W. Hsing, D. H. Kalantar, R. L. Kauffman, D. J. Larson, J. D. Moody, D. H. Schneider, M. B. Schneider, D. A. Shaughnessy, R. T. Shelton, W. Stoeffl, K. Widmann, C. B. Yeamans, S. H. Batha, G. P. Grim, H. W. Herrmann, F. E. Merrill, R. J. Leeper, J. A. Oertel, T. C. Sangster, D. H. Edgell, M. Hohenberger, V. Yu. Glebov, S. P. Regan, J. A. Frenje, M. Gatu-Johnson, R. D. Petrasso, H. G. Rinderknecht, A. B. Zylstra, G. W. Cooper, and C. Ruiz, "The National Ignition Facility Diagnostic Set at the Completion of the National Ignition Campaign, September 2012," Fusion Sci. Technol. **69**, 420 (2016).

F. J. Marshall, P. B. Radha, M. J. Bonino, J. A. Delettrez, R. Epstein, V. Yu. Glebov, D. R. Harding, C. Stoeckl, J. A. Frenje, M. Gatu Johnson, F. H. Séguin, H. Sio, A. Zylstra, and E. Giraldez, "Polar-Direct-Drive Experiments with Contoured-Shell Targets on OMEGA," Phys. Plasmas **23**, 012711 (2016).

P. E. Masson-Laborde, M. C. Monteil, V. Tassin, F. Philippe, P. Gauthier, A. Casner, S. Depierreux, C. Neuville, B. Villette, S. Laffite, P. Seytor, P. Fremerye, W. Seka, D. Teychenné, A. Debayle, D. Marion, P. Loiseau, and M. Casanova, "Laser Plasma Interaction on Rugby Hohlraum on the Omega Laser Facility: Comparisons Between Cylinder, Rugby, and Elliptical Hohlraums," Phys. Plasmas **23**, 022703 (2016).

Y. Ping, A. Fernandez-Panella, H. Sio, A. Correa, R. Shepherd, O. Landen, R. A. London, P. A. Sterne, H. D. Whitley, D. Fratanduono, T. R. Boehly, and G. W. Collins, "Differential Heating: A Versatile Method for Thermal Conductivity Measurements in High-Energy-Density Matter," Phys. Plasmas **22**, 092701 (2015).

M. J. Rosenberg, A. B. Zylstra, F. H. Séguin, H. G. Rinderknecht, J. A. Frenje, M. Gatu Johnson, H. Sio, C. J. Waugh, N. Sinenian, C. K. Li, R. D. Petrasso, S. LePape, T. Ma, A. J. Mackinnon, J. R. Rygg, P. A. Amendt, C. Bellei, L. R. Benedetti, L. Berzak Hopkins, R. M. Bionta, D. T. Casey, L. Divol, M. J. Edwards, S. Glenn, S. H. Glenzer, D. G. Hicks, J. R. Kimbrough, O. L. Landen, J. D. Lindl, A. MacPhee, J. M. McNaney, N. B. Meezan, J. D. Moody, M. J. Moran, H.-S. Park, J. Pino, B. A. Remington, H. Robey, M. D. Rosen, S. C. Wilks, R. A. Zacharias, P. W. McKenty, M. Hohenberger, P. B. Radha, D. Edgell, F. J. Marshall, J. A. Delettrez, V. Yu. Glebov, R. Betti, V. N. Goncharov, J. P. Knauer, T. C. Sangster, H. W. Herrmann, N. M. Hoffman, G. A. Kyrala, R. J. Leeper, R. E. Olson, J. D. Kilkenny, and A. Nikroo, "A Direct-Drive Exploding-Pusher Implosion as the First Step in Development of a Monoenergetic Charged-Particle Backlighting Platform at the National Ignition Facility," High Energy Density Phys. **18**, 38 (2016).

M. Rutkauskas, C. Farrell, C. Dorrer, K. L. Marshall, T. R. Lundquist, P. Vedagarbha, and D. T. Reid, "High-Resolution Subsurface Microscopy of CMOS Integrated Circuits Using Radially Polarized Light," Opt. Lett. **40**, 5502 (2015).

S. Salzman, H. J. Romanofsky, L. J. Giannechini, S. D. Jacobs, and J. C. Lambropoulus, "Magnetorheological Finishing of Chemical-Vapor Deposited Zinc Sulfide via Chemically and Mechanically Modified Fluids," Appl. Opt. **55**, 1481 (2016).

S. Salzman, H. J. Romanofsky, S. D. Jacobs, and J. C. Lambropoulos, "Surface–Texture Evolution of Different Chemical-Vapor-Deposited Zinc Sulfide Flats Polished with Various Magnetorheological Fluids," Prec. Eng. **43**, 257 (2016).

J. Serafini, Y. Akbas, L. Crandall, R. Bellman, C. K. Williams, and R. Sobolewski, "Time-Resolved, Nonequilibrium Carrier Dynamics in Si-on-Glass Thin Films for Photovoltaic Cells," Semicond. Sci. Technol. **31**, 045006 (2016).

W. Shang, J. Yang, W. Zhang, Z. Li, B. Deng, Y. Dong, T. Zhu, C. Huang, X. Zhan, Y. Mei, L. Guo, R. Yu, S. Li, S. Jiang, S. Liu, F. Wang, Y. Ding, B. Zhang, and R. Betti, "Experimental Demonstration of Laser to X-Ray Conversion Enhancements with Low Density Gold Targets," Appl. Phys. Lett. **108**, 064102 (2016).

S. A. Slutz, W. A. Stygar, M. R. Gomez, K. J. Peterson, A. B. Sefkow, D. B. Sinars, R. A. Vesey, E. M. Campbell, and R. Betti, "Scaling Magnetized Liner Inertial Fusion on Z and Future Pulsed-Power Accelerators," Phys. Plasmas **23**, 022702 (2016).

J. Wang, F. Coppari, R. F. Smith, J. H. Eggert, A. E. Lazicki, D. E. Frantanduono, J. R. Rygg, T. R. Boehly, G. W. Collins, and T. S. Duffy, "X-Ray Diffraction of Molybdenum Under Shock Compression to 450 GPa," Phys. Rev. B **92**, 174114 (2015).

R. Yan, R. Betti, J. Sanz, H. Aluie, B. Liu, and A. Frank, "Three-Dimensional Single-Mode Nonlinear Ablative Rayleigh–Taylor Instability," Phys. Plasmas **23**, 022701 (2016).

Forthcoming Publications

B. P. Chock, T. B. Jones, and D. R. Harding, "Effect of a Surfactant on the Electric-Field Assembly of Oil/Water Emulsions for Making Foam Targets," to be published in Fusion Science and Technology.

T. J. B. Collins, J. A. Marozas, S. Skupsky, D. Cao, P. W. McKenty, J. A. Delettrez, and G. Moses, "Design Options for Polar-Direct-Drive Targets—From Alpha Heating to Ignition," to be published in the Journal of Physics: Conference Series.

A. K. Davis, D. Cao, D. T. Michel, M. Hohenberger, R. Epstein, V. N. Goncharov, S. X. Hu, I. V. Igumenshchev, J. A. Marozas, A. V. Maximov, J. F. Myatt, P. B. Radha, S. P. Regan, T. C. Sangster, and D. H. Froula, "Isolating and Quantifying Cross-Beam Energy Transfer in Direct-Drive Implosions," to be published in Physics of Plasmas (invited).

B. Delorme, M. Olzazbal-Loumé, A. Casner, Ph. Nicolaï, D. T. Michel, G. Riazuelo, N. Borisenko, J. Breil, S. Fujioka, M. Grech, A. Orekhov, W. Seka, A. Sunahara, D. H. Froula, V. Goncharov, and V. T. Tikhonchuk, "Experimental Demonstration of Laser Imprint Reduction Using Underdense Foams," to be published in Physics of Plasmas.

W. R. Donaldson, J. Katz, R. Huff, E. M. Hill, J. H. Kelly, J. Kwiatkowski, R. Brannon, and R. Boni, "Picosecond Beam-Timing System for the OMEGA Laser," submitted to Review of Scientific Instruments.

R. Epstein, S. P. Regan, B. A. Hammel, L. J. Suter, H. A. Scott, M. A. Barrios, D. K. Bradley, D. A. Callahan, C. Cerjan, G. W. Collins, S. N. Dixit, T. Döppner, M. J. Edwards, D. R. Farley, K. B. Fournier, S. Glenn, S. H. Glenzer, I. E. Golovkin, A. Hamza, D. G. Hicks, N. Izumi, O. S. Jones, M. H. Key, J. D. Kilkenny, J. L. Kline, G. A. Kyrala, O. L. Landen, T. Ma, J. J. MacFarlane, A. J. Mackinnon, R. C. Mancini, R. L. McCrory, D. D. Meyerhofer, N. B. Meezan, A. Nikroo, H.-S. Park, P. K. Patel, J. E. Ralph, B. A. Remington, T. C. Sangster, V. A. Smalyuk, P. T. Springer, R. P. J. Town, and J. L. Tucker, "Applications and Results of X-Ray Spectroscopy in Implosion Experiments at the National Ignition Facility," to be published in Proceedings of Atomic Processes in Plasmas (invited).

R. K. Follett, J. A. Delettrez, D. H. Edgell, V. N. Goncharov, R. J. Henchen, J. Katz, D. T. Michel, J. F. Myatt, J. G. Shaw, A. A. Solodov, C. Stoeckl, B. Yaakobi, and D. H. Froula, "Two-Plasmon–Decay Mitigation in Direct-Drive Inertial Confinement Fusion Experiments Using Multilayer Targets," to be published in Physical Review Letters.

D. R. Harding, D. C. Whitaker, and C. Fella, "Growth of a Solid DT Crystal from the Liquid Inside Inertial Confinement Fusion Targets," to be published in Fusion Science and Technology.

S. X. Hu, L. A. Collins, V. N. Goncharov, J. D. Kress, T. R. Boehly, R. Epstein, R. L. McCrory, and S. Skupsky, "First-Principles Studies on the Equation-of-State, Thermal-Conductivity, and Opacity of Deuterium–Tritium and Polystyrene (CH) for Inertial Confinement Fusion Applications," to be published in the Journal of Physics: Conference Series.

S. X. Hu, L. A. Collins, V. N. Goncharov, J. D. Kress, R. L. McCrory, and S. Skupsky, "First-Principles Investigations on Ionization and Thermal Conductivity of Polystyrene (CH) for Inertial Confinement Fusion Applications," to be published in Physics of Plasmas.

I. V. Igumenshchev, V. N. Goncharov, F. J. Marshall, J. P. Knauer, E. M. Campbell, D. H. Froula, R. L. McCrory, S. P. Regan, T. C. Sangster, and S. Skupsky, "Three-Dimensional Modeling of Direct-Drive Cryogenic Implosions on OMEGA," to be published in Physics of Plasmas.

J. D. Kilkenny, J. A. Caggiano, R. Hatarik, J. P. Knauer, D. B. Sayre, B. K. Spears, S. V. Weber, C. B. Yeamans, C. J. Cerjan, L. Divol, M. J. Eckart, V. Yu. Glebov, H. W. Herrmann, S. Le. Pape, D. H. Munro, G. P. Grim, O. S. Jones, L. Berzak-Hopkins, M. Gatu-Johnson, A. J. Mackinnon, N. B. Meezan, D. T. Casey, J. A. Frenje, J. M. Mcnaney, R. Petrasso, H. Rinderknecht, W. Stoeffl, and A. B. Zylstra, "Understanding the Stagnation and Burn of Implosions on NIF," to be published in the Journal of Physics: Conference Series.

J. A. Marozas, T. J. B. Collins, J. D. Zuegel, P. W. McKenty, D. Cao, S. Fochs, and P. B. Radha, "Continuous Distributed Phase Plate Design Advances for High-Energy Laser Systems," to be published in the Journal of Physics: Conference Series.

J. F. Myatt, J. G. Shaw, V. N. Goncharov, J. Zhang, A. V. Maximov, R. W. Short, R. K. Follett, W. Seka, D. H. Edgell, and D. H. Froula, "Laser–Plasma Interaction in Direct-Drive Inertial Confinement Fusion," to be published in the Journal of Physics: Conference Series.

B. W. Plansinis, W. R. Donaldson, and G. P. Agrawal, "Temporal Waveguides for Optical Pulses," to be published in the Journal of the Optical Society of America B.

P. B. Radha, V. N. Goncharov, M. Hohenberger, T. C. Sangster, R. Betti, R. S. Craxton, D. H. Edgell, R. Epstein, D. H. Froula, J. A. Marozas, F. J. Marshall, R. L. McCrory, P. W. McKenty, D. D. Meyerhofer, D. T. Michel, S. X. Hu, W. Seka, A. Shvydky, S. Skupsky, J. A. Frenje, M. Gatu Johnson, R. D. Petrasso, T. Ma, S. Le Pape, and A. J. Mackinnon, "Direct-Drive-Implosion Physics: Results from OMEGA and the National Ignition Facility," to be published in the Journal of Physics: Conference Series.

P. B. Radha, M. Hohenberger, D. H. Edgell, J. A. Marozas, F. J. Marshall, D. T. Michel, M. J. Rosenberg, W. Seka, A. Shvydky, J. W. Bates, T. R. Boehly, T. J. B. Collins, E. M. Campbell, R. S. Craxton, J. A. Delettrez, S. N. Dixit, J. A. Frenje, D. H. Froula, V. N. Goncharov, S. X. Hu, M. Karasik, J. P. Knauer, S. Le Pape, R. L. McCrory, P. W. McKenty, D. D. Meyerhofer, J. F. Myatt, S. P. Obenschain, R. D. Petrasso, S. P. Regan, T. C. Sangster, H. Sio, S. Skupsky, and A. B. Zylstra, "Direct Drive: Simulations and Results from the National Ignition Facility," to be published in Physics of Plasmas (invited).

P. B. Radha, M. Hohenberger, F. J. Marshall, D. T. Michel, J. W. Bates, T. R. Boehly, T. J. B. Collins, R. S. Craxton, J. A. Delettrez, S. N. Dixit, D. H. Edgell, J. A. Frenje, D. H. Froula, V. N. Goncharov, S. X. Hu, M. Karasik, J. P. Knauer, S. Le Pape, J. A. Marozas, R. L. McCrory, P. W. McKenty, D. D. Meyerhofer, J. F. Myatt, S. P. Obenschein, R. D. Petrasso, S. P. Regan, M. J. Rosenberg, T. C. Sangster, W. Seka, A. Shvydky, H. Sio, S. Skupsky, and A. B. Zylstra, "Polar-Direct-Drive Experiments at the National Ignition Facility," to be published in the Journal of Physics: Conference Series.

M. Sharpe, W. T. Shmayda, and W. U. Schröder, "Tritium Migration to the Surfaces of Stainless-Steel 316, Aluminum 6061, and Oxygen-Free, High-Conductivity Copper," to be published in Fusion Science and Technology.

W. T. Shmayda, M. D. Wittman, R. F. Earley, J. L. Reid, and N. P. Redden, "The Laboratory for Laser Energetics' Hydrogen Isotope Separation System," to be published in Fusion Engineering and Design (invited).

C. Stoeckl, R. Boni, F. Ehrne, C. J. Forrest, V. Yu. Glebov, J. Katz, D. J. Lonobile, J. Magoon, S. P. Regan, M. J. Shoup III, A. Sorce, T. C. Sangster, and D. Weiner, "A Neutron Temporal Diagnostic for High-Yield DT Cryogenic Implosions on OMEGA," to be published in Review of Scientific Instruments.

N. D. Viza, M. H. Romanofsky, M. J. Moynihan, and D. R. Harding, "The Effect of a Surfactant on the Operation of T-Junctions for Mass-Producing Foam Targets," to be published in Fusion Science and Technology.

Conference Presentations

M. J. Rosenberg, A. A. Solodov, W. Seka, R. Epstein, J. F. Myatt, S. P. Regan, M. Hohenberger, T. J. B. Collins, P. Michel, D. P. Turnbull, J. D. Moody, J. E. Ralph, M. A. Barrios, and J. W. Bates, "Planar Laser–Plasma Interaction Experiments at Direct-Drive Ignition-Relevant Scale Lengths at the National Ignition Facility," NIF User Group Meeting, Livermore, CA, 1–3 February 2016.

J. D. Zuegel, A. Agliata, S.-W. Bahk, I. A. Begishev, W. A. Bittle, T. Buczek, J. Bunkenburg, D. Canning, A. Consentino, D. Coppenbarger, R. Cuffney, C. Dorrer, J. Fini, D. H. Froula, G. Gates, M. J. Guardalben, D. Haberberger, S. Hadrich, C. Hall, H. Huang, R. K. Jungquist, C. Kellogg, T. J. Kessler, G. Kick, E. Kowaluk, B. E. Kruschwitz, T. Lewis, J. Magoon, J. Marciante, D. D. Meyerhofer, C. Mileham, M. Millecchia, S. F. B. Morse, P. M. Nilson, A. Okishev, J. B. Oliver, R. G. Peck, C. Rees, B. S. Rice, E. Riedle, A. L. Rigatti, C. Robillard, R. G. Roides, M. H. Romanofsky, J. Rothhardt, M. J. Shoup III, C. Smith, C. Stoeckl, R. Taylor, L. J. Waxer, and D. Weiner, "Technology Development and Prospects for 100-PW-Class Optical Parametric Chirped-Pulse Amplification Pumped by OMEGA EP," the 2nd International Symposium on High Power Laser Science and Engineering, Suzhou, China, 15–18 March 2016.

The following presentations were made at Industrial Associates, Rochester, NY, 21–22 March 2016:

L. E. McIntire, M. Divoky, W. H. Knox, S.-W. Bahk, and J. D. Zuegel, "High-Contrast, Closed-Loop Control of Continuous-Wave Laser Beam Profiles."

B. W. Plansinis, W. R. Donaldson, and G. P. Agrawal, "Controlling the Optical Pulse Spectrum with an Electro-Optic Phase Modulator."

B. W. Plansinis, W. R. Donaldson, and G. P. Agrawal, "Temporal Waveguiding Caused by Time Reflection and Refraction."

R. Betti, A. R. Christopherson, A. Bose, K. M. Woo, J. Howard, K. S. Anderson, E. M. Campbell, J. A. Delettrez, V. N. Goncharov, F. J. Marshall, R. L. McCrory, S. P. Regan, T. C. Sangster, C. Stoeckl, W. Theobald, M. J. Edwards, R. Nora, B. K. Spears, and J. Sanz, "The Most Unsolved Problem in Plasma Physics: Demonstrating a Burning Plasma in the Laboratory," Solved and Unsolved Problems in Plasma Physics, Princeton, NJ, 28–30 March 2016 (invited).

Measurements of the Effect of Adiabat on Shell Decompression in Direct-Drive Implosions on OMEGA

In inertial confinement fusion (ICF), laser beams are used to implode a spherical shell of deuterium and tritium. To reach maximum compression and achieve fusion conditions, the fuel entropy must be minimized (close to the Fermi-degenerated limit).[1,2] This requires accurate control of the shocks and compression waves launched during the implosion.[3] The entropy in ICF is commonly characterized by the shell's adiabat (α) defined as the mass-averaged ratio of the shell's pressure to the Fermi-degenerated pressure.[4,5] One-dimensional (1-D) simulations suggest that reducing the adiabat increases the shell density and reduces shell thickness. At a low adiabat, however, short-scale nonuniformities amplified by the Rayleigh–Taylor (RT) instability lead to shell decompression, which increases its effective adiabat.[5–9] Therefore, optimizing the implosion performance requires a balance between minimizing the adiabat and reducing the RT growth to maintain a compressible shell.

The effect of the adiabat on shell compression has typically been studied by measuring its effect on integrated performance parameters (e.g., neutron yield and areal density). Recently, several studies have shown that increasing the adiabat of the shell improved the neutron yield in both direct-[10,11] and indirect-drive[12,13] configurations. For low-adiabat implosions, the nonuniformities were shown to result in the ablator mixing into the hot spot, which cooled the hot spot and reduced the fusion performance.[14,15] A threshold was observed in the calculated adiabat where, above the threshold, the measured areal density was recovered by 1-D simulations.[16] Previous research aimed at studying integrated implosions has used flux-limiter models,[11,17–19] but these models did not reproduce the mass ablation rate and the conduction-zone length correctly, which led to errors in the calculation of the laser imprint and the RT growth.[20]

This article presents the first measurements of the effect of adiabat on the shell decompression and the first hydrodynamic simulations[21] that reproduce the detailed experimental observables by including laser imprint[17] and cross-beam energy transfer (CBET)[22] models. The maximum in-flight shell thickness was obtained using a novel technique where the outer and inner surfaces of the shell were simultaneously measured using self-emission images of the imploding target. When the calculated adiabat of the shell was decreased from $\alpha = 6$ to $\alpha = 4.5$, the shell thickness was measured to decrease from 75±2 μm to 60±2 μm, but when the adiabat was decreased further to $\alpha = 1.8$, the shell thickness was measured to increase to 75±2 μm. Over this adiabat range, the measured minimum core size continued to decrease, demonstrating that the decompression of the shell measured for low adiabats was not caused by errors in the adiabat calculations, but a result of the increase in the RT growth. The optimum performance (minimum shell thickness and maximum neutron yield) was obtained for $\alpha = 3$. In simulations that did not include laser imprint, the simulated thicknesses were close to measurements for $\alpha > 3$, but they significantly underestimated the shell thickness for $\alpha \leq 3$, which confirmed that the decompression measured for low adiabats was a result of laser imprint. The simulations that included state-of-the-art models reproduce the measured outer-shell trajectory, maximum in-flight shell thicknesses, inner-shell deceleration, minimum core size, and neutron yields and show that the increased shell thickness for $\alpha \leq 3$ is caused by laser imprint.

The experiments employed 60 ultraviolet ($\lambda_0 = 351$ nm) laser beams on the OMEGA laser.[23] The laser beams uniformly illuminated the target and were smoothed by polarization smoothing,[24] smoothing by spectral dispersion (SSD),[25] and distributed phase plates (fourth-order super-Gaussian with 95% of the energy contained within the initial target diameter).[26] On some shots, the laser imprint was increased by turning off SSD. A 100-ps-long picket and a $1.7\pm0.2 \times 10^{14}$-W/cm^2 foot on the rise of the drive pulse were used to set the adiabat of the shell.[9] They were followed by a 2-ns-long drive pulse that accelerated the target to its final velocity of ~200 km/s. The picket intensity was varied between 0.85×10^{14} W/cm^2 and 5.5×10^{14} W/cm^2 to vary the adiabat of the shell between 1.8 and 6. The total laser energy was 21±0.3 kJ, which resulted in a maximum on-target overlapped intensity of $4.7\pm0.06 \times 10^{14}$ W/cm^2. The shells were made of 26.5±0.2-μm-thick glow-discharge polymer (CH with a density of 1.03 g/cm^3) with an outer radius of 433±4 μm and filled with 11±0.5 atm of deuterium.

The recently developed self-emission x-ray imaging technique[27] was adapted to simultaneously measure the outer- and inner-shell trajectories (Fig. 147.1). The soft x rays emitted by the imploding target were imaged with an array of 10-μm-diam pinholes onto a four-strip, fast x-ray framing camera[28] using a magnification of 6. With this setup, the point-spread function (PSF) of the diagnostic had a diameter at full width at half maximum of d_{PSF} = 12 μm. The images were integrated over 40 ps. A 25.4-μm-thick Be filter was used to select the soft x rays above ~1 keV. The absolute timing between the laser pulse and the images was known to an accuracy of 20 ps and the interstrip timing was determined within 5 ps (Refs. 29 and 30).

Figure 147.1(c) shows the x-ray self-emission profile at the beginning of the deceleration of the shell calculated by post-processing the hydrodynamic simulations [Fig. 147.1(b)] with *Spect3D*.[31] The inner edge of the outer peak generated by the coronal plasma was used to determine the position of the outer surface of the shell, while the outer edge of the central emission (hot spot) was used to determine the position of the inner surface of the shell. The emission of the coronal plasma is maximum near the outer surface of the shell because the plasma has a larger density and the integration distance to the detector is maximum. Just inside the outer surface of the shell, the emission drops by a factor of 2 over a few microns as the emission from the back of the target is absorbed into the cold shell. When the shell begins to decelerate, the pressure of the hot spot rapidly increases ($P_{hs} \propto 1/R^5$), resulting in an increase in the electron temperature and a rapid start of the emission of x rays from the hot spot with energies above 1 keV. The maximum emission occurs close to the inner edge of the shell, where the shell is ablated and the plasma has a high density. To account for the PSF of the diagnostic, the edge position is measured using the 10% intensity point [$0.1 \times (I_{max} - I_{min}) + I_{min}$, where I_{max} and I_{min} are the maximum and minimum emissions inside the coronal emission]. During the deceleration phase, this outer edge corresponds to the inner side of the cold shell where the temperature drops below 400 eV.

Figure 147.2 shows the self-emission images measured at the end of the laser pulse and at maximum compression. Accurate measurements of the positions of the outer- and inner-shell radii were obtained by averaging the positions of the inner edge of the outer peak and the outer edge of the hot-spot emission determined at each angle. To reduce the noise, self-emission images were angularly averaged over the spatial resolution of the diagnostic ($\theta_{avg} = d_{PSF}/R \approx 20°$, where R is either the outer- or inner-shell radius). With this method, the standard deviation in the variation (as a function of the angle) of the position of the outer edge (inner edge) of the shell was σ_{outer} = ±2 μm (σ_{inner} = ±3 μm), resulting in an error in the 360° averaged radius of $\delta R_{outer} = \sigma_{outer}/\sqrt{N_p} \approx 0.2$ μm (Ref. 30) ($\delta R_{inner} \approx \pm 0.5$ μm), where $N_p = 2\pi R/d_{PSF}$ is the number of independent measurements and R is the averaged radius. To measure the inner-shell radius, an additional error was introduced by the difference between the 10% intensity point and the inner radius. A maximum error of ~2 μm was determined

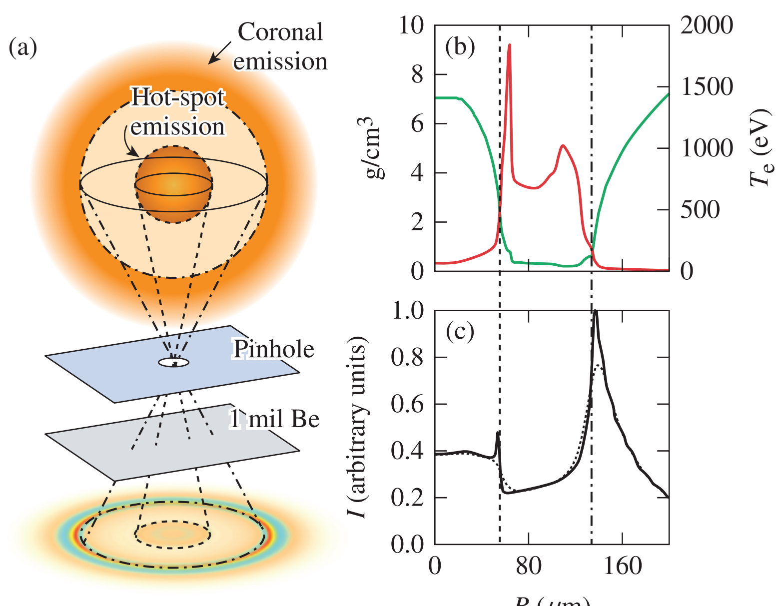

Figure 147.1
(a) The x-ray emission above 1 keV from the coronal plasma and the hot spot was imaged by a pinhole through a Be filter and measured by an x-ray framing camera. A synthetic image calculated for an implosion with an adiabat of 6 is shown. (b) The temperature (green curve) and density profiles (red curve) of the target are compared with the (c) self-emission profiles measured at the diagnostic plane with (dotted curve) and without (solid curve) convolving with the point-spread function (PSF) of the diagnostic. The positions of the outer (dashed–dotted vertical lines) and inner shell (dashed vertical lines) are indicated.

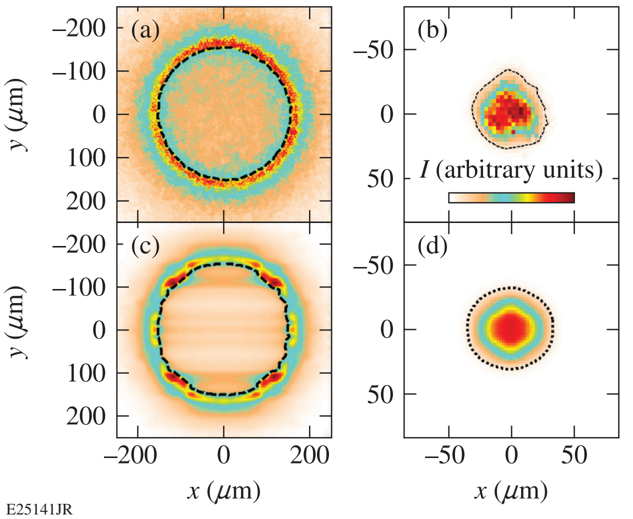

Figure 147.2
Comparisons of the [(a),(b)] measured and [(c),(d)] calculated self-emission images at the end of the laser pulse (2.6 ns) and at the maximum compression (3 ns), respectively. The positions of the [(a),(c)] outer and [(b),(d)] inner shell are shown as dashed black lines and dotted black lines, respectively.

by comparing those two quantities in hydrodynamic simulations performed with and without nonuniformities (Fig. 147.3).

Figure 147.3 shows the simultaneous measurement of the outer and inner surfaces of the shell, which determined the maximum in-flight shell thickness, the deceleration of the shell, and the minimum core size. Once the laser turned off, the position of the outer surface was determined by extrapolating the measured outer-shell trajectory along a free-fall line. During this time (up to 70 ps), the target was not accelerated by the laser and it imploded with a constant velocity (simulations show that at this time convergence effects are negligible). The 4% error in the measurement of the velocity of the outer shell[30] resulted in a maximum error of ±1 μm in the inferred outer-shell radius at the beginning of the core emission.

Figure 147.4(a) shows that when SSD was used, the maximum in-flight shell thickness was measured to decrease from 75 μm to 60 μm when the adiabat was decreased from $\alpha = 6$ to $\alpha = 4.5$, but when the adiabat was reduced to $\alpha = 1.8$, the thickness of the shell increased to 75 μm. This is not consistent with the reduction of the shell's adiabat. For each experiment, the measured outer-shell trajectory was nearly identical, indicating that the ablation pressure was similar among these shots. This increase in shell thickness is not explained by an error in the adiabat calculation because the measured minimum core size continued to decrease as the adiabat was reduced [Fig. 147.4(b)] and the neutron yield was up to 5× larger for the lower-adiabat ($\alpha = 1.8$ to $\alpha = 3$) implosions compared with the higher-adiabat ($\alpha = 4.5$ to $\alpha = 6$) implosions [Fig. 147.4(c)]. This is consistent with previous observations that showed a mild reduction in the areal density measured at maximum neutron yield compared to 1-D simulations at low adiabat.[11] The measured increase in

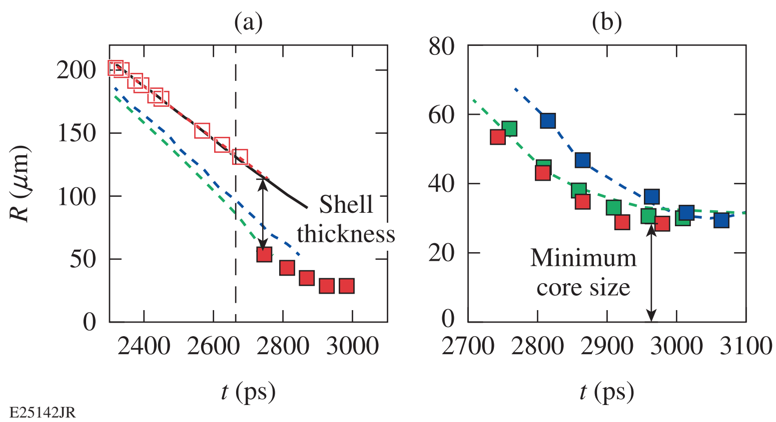

Figure 147.3
(a) The thickness of the shell was determined by the distance between the outer-shell radius (open squares) extrapolated with a constant velocity (short dashed red line) and the inner-shell radius (solid squares) at the time when the hot spot first emits x rays. Once the laser turned off (long black dashed line), the position of the outer surface was determined by extrapolating the measured outer-shell trajectory along a free-fall line. The inner surface trajectory at $1/e$ of the maximum density was calculated from a simulation without laser imprint (dashed blue curve) and with laser imprint (dashed green curve). For the two simulations, the outer-shell trajectories at 0.2 of the maximum are the same (black curve) and are in excellent agreement with measurements. (b) The measured inner-surface trajectories (red squares) are compared with a 2-D simulations with (green squares) and without (blue squares) laser imprint. The trajectories of the surface where the hot-spot electron temperature drops below 400 eV is plotted for both simulations (dashed curves). The laser beams were smoothed by smoothing by spectral dispersion (SSD) and drove the implosion with $\alpha = 3$, which is slightly larger than the adiabat in the simulation (+2.5) because of the experimental reproducibility.

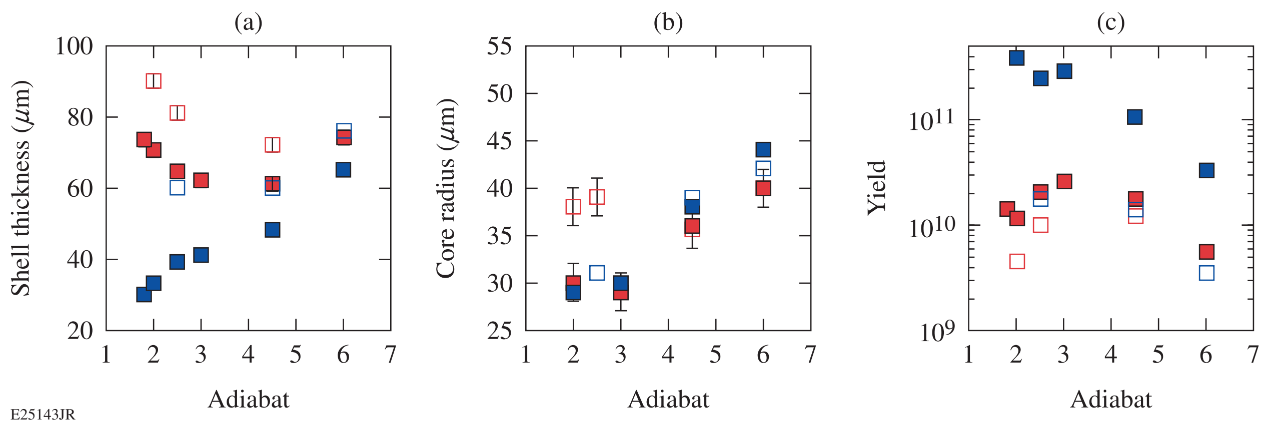

Figure 147.4
(a) The measured shell thicknesses at the beginning of the core emission, (b) core radii at maximum compression, and (c) neutron yields were compared for the different adiabats with (solid red points) and without (open red points) SSD. The corresponding simulations with (open blue squares) and without imprint (solid blue squares) are shown.

the shell thickness for low-adiabat implosions was consistent with an increase in the RT growth that resulted in larger shell nonuniformities, which decompressed the shell.

To understand the shell decompression measured for low-adiabat implosions, hydrodynamic simulations were performed with the 2-D hydrodynamic code *DRACO*[17] using the current state-of-the-art models for nonlocal thermal transport,[32,33] CBET, first-principles equation of state,[34] and laser imprint (including modes between 2 and 200). To resolve both CBET and laser imprint, each simulation required approximately three months of computational time on ~300 cores. Only the shell nonuniformities caused by laser imprint were simulated because the RT growth is dominant for large modes (>100) and the perturbations caused by target roughness are smaller by about a factor of 10 than those imposed by imprint. For all simulations, the trajectory of the outer surface of the shell was well reproduced, indicating that the hydrodynamic efficiency was correctly modeled.[29] Simulations were able to reproduce the maximum in-flight shell thickness, inner-shell deceleration, minimum core size, and neutron yield (Figs. 147.3 and 147.4). This excellent agreement for $\alpha \le 3$ suggests that the shell decompression measured for low-adiabat implosions was caused by laser imprint. For larger-adiabat implosions, the excellent agreement shows that the reduction in the RT growth with the shell adiabat was correctly modeled. For the lowest-adiabat ($\alpha \le 2$) implosions, the simulated shell was broken in-flight, which produced a nonphysical hole (i.e., ring) in the shell as a result of the 2-D symmetry. This resulted in a large increase in the final core size and a strong reduction in neutron yield.

The fact that the final core size was significantly smaller for lower-adiabat implosions, even when the maximum in-flight shell thickness was similar, is a result of the laser imprint primarily decompressing the outer surface of the shell. The inner-shell density, and therefore the inner-shell pressure, remained large, leading to a small final core radius.[10] Furthermore, the core pressure was reduced slightly by the RT-induced mix of the CH into the D_2 core, allowing the shell to converge further. For the larger-adiabat implosions, the shell thickness increased because of increased shock heating, resulting in a smaller convergence.

Figure 147.4 shows that hydrodynamic simulations performed without laser imprint (1-D–like) are in better agreement with measurements for high-adiabat shots, but they significantly underestimate the shell thickness for low-adiabat implosions. For $\alpha \le 3$, these simulations predict that the shell thickness continues to decrease contrary to the experiments. This confirms that the laser imprint causes the decompression of the shell. This increased decompression resulted in an increasing difference between the measured and calculated neutron yields [Fig. 147.4(c)].

When the laser imprint was increased by turning SSD off, the thickness of the shell was increased by ~25%, leading to a reduced neutron yield for each adiabat tested (Fig. 147.4). Compared to SSD-on shots, a weaker degradation of the implosion performances (smaller increase of the core size and smaller reduction in neutron yield) was obtained for a larger adiabat (α = 4.5) than for a lower adiabat (α = 2.5 and α = 2). This is a result of the larger laser imprint that required a stronger mitigation of the RT growth to keep the shell compressible.

In summary, the decompression of an imploding shell was studied by measuring the maximum in-flight shell thicknesses for adiabats ranging from 1.8 to 6 and comparing the results with the first 2-D hydrodynamic simulations, which included laser imprint, nonlocal thermal transport, CBET, and first-principles equation-of-state models. When the adiabat of the shell was decreased, the shell thickness was initially measured to decrease. Reducing the adiabat below 3 resulted in an increasing shell thickness. Over this adiabat scan, the measured minimum core size continued to decrease, showing that the decompression of the shell measured for low adiabats was not caused by errors in the adiabat calculations but by an increase in the RT growth. Hydrodynamic simulations reproduced the measured outer-shell trajectory, maximum in-flight shell thicknesses, inner-shell deceleration, minimum core size, and neutron yields. Simulations that did not include laser imprint were in good agreement with measurements for $\alpha > 3$, but they significantly underestimated the shell thickness for $\alpha \leq 3$, which confirmed that the decompression measured for low adiabats was a result of laser imprint.

ACKNOWLEDGMENT

This work was supported by the U.S. Department of Energy Office of Inertial Confinement Fusion under Award Number DE-NA0001944, the University of Rochester, and the New York State Energy Research and Development Authority. The support of DOE does not constitute an endorsement by DOE of the views expressed in this article.

REFERENCES

1. M. C. Herrmann, M. Tabak, and J. D. Lindl, Phys. Plasmas **8**, 2296 (2001).

2. R. Betti, K. Anderson, V. N. Goncharov, R. L. McCrory, D. D. Meyerhofer, S. Skupsky, and R. P. J. Town, Phys. Plasmas **9**, 2277 (2002)

3. J. Nuckolls *et al*., Nature **239**, 139 (1972).

4. J. D. Lindl, *Inertial Confinement Fusion: The Quest for Ignition and Energy Gain Using Indirect Drive* (Springer-Verlag, New York, 1998).

5. S. E. Bodner, D. G. Colombant, J. H. Gardner, R. H. Lehmberg, S. P. Obenschain, L. Phillips, A. J. Schmitt, J. D. Sethian, R. L. McCrory, W. Seka, C. P. Verdon, J. P. Knauer, B. B. Afeyan, and H. T. Powell, Phys. Plasmas **5**, 1901 (1998).

6. S. E. Bodner, Phys. Rev. Lett. **33**, 761 (1974).

7. V. N. Goncharov, R. Betti, R. L. McCrory, P. Sorotokin, and C. P. Verdon, Phys. Plasmas **3**, 1402 (1996).

8. V. N. Goncharov, J. P. Knauer, P. W. McKenty, P. B. Radha, T. C. Sangster, S. Skupsky, R. Betti, R. L. McCrory, and D. D. Meyerhofer, Phys. Plasmas **10**, 1906 (2003).

9. V. N. Goncharov, T. C. Sangster, T. R. Boehly, S. X. Hu, I. V. Igumenshchev, F. J. Marshall, R. L. McCrory, D. D. Meyerhofer, P. B. Radha, W. Seka, S. Skupsky, C. Stoeckl, D. T. Casey, J. A. Frenje, and R. D. Petrasso, Phys. Rev. Lett. **104**, 165001 (2010).

10. V. N. Goncharov, T. C. Sangster, R. Betti, T. R. Boehly, M. J. Bonino, T. J. B. Collins, R. S. Craxton, J. A. Delettrez, D. H. Edgell, R. Epstein, R. K. Follet, C. J. Forrest, D. H. Froula, V. Yu. Glebov, D. R. Harding, R. J. Henchen, S. X. Hu, I. V. Igumenshchev, R. Janezic, J. H. Kelly, T. J. Kessler, T. Z. Kosc, S. J. Loucks, J. A. Marozas, F. J. Marshall, A. V. Maximov, R. L. McCrory, P. W. McKenty, D. D. Meyerhofer, D. T. Michel, J. F. Myatt, R. Nora, P. B. Radha, S. P. Regan, W. Seka, W. T. Shmayda, R. W. Short, A. Shvydky, S. Skupsky, C. Stoeckl, B. Yaakobi, J. A. Frenje, M. Gatu-Johnson, R. D. Petrasso, and D. T. Casey, Phys. Plasmas **21**, 056315 (2014).

11. P. B. Radha, C. Stoeckl, V. N. Goncharov, J. A. Delettrez, D. H. Edgell, J. A. Frenje, I. V. Igumenshchev, J. P. Knauer, J. A. Marozas, R. L. McCrory, D. D. Meyerhofer, R. D. Petrasso, S. P. Regan, T. C. Sangster, W. Seka, and S. Skupsky, Phys. Plasmas **18**, 012705 (2011).

12. O. A. Hurricane *et al*., Nature **506**, 343 (2014).

13. H. S. Park *et al*., Phys. Rev. Lett. **112**, 055001 (2014).

14. S. P. Regan, R. Epstein, B. A. Hammel, L. J. Suter, J. Ralph, H. Scott, M. A. Barrios, D. K. Bradley, D. A. Callahan, C. Cerjan, G. W. Collins, S. N. Dixit, T. Doeppner, M. J. Edwards, D. R. Farley, S. Glenn, S. H. Glenzer, I. E. Golovkin, S. W. Haan, A. Hamza, D. G. Hicks, N. Izumi, J. D. Kilkenny, J. L. Kline, G. A. Kyrala, O. L. Landen, T. Ma, J. J. MacFarlane, R. C. Mancini, R. L. McCrory, N. B. Meezan, D. D. Meyerhofer, A. Nikroo, K. J. Peterson, T. C. Sangster, P. Springer, and R. P. J. Town, Phys. Plasmas **19**, 056307 (2012).

15. T. Ma, P. K. Patel, N. Izumi, P. T. Springer, M. H. Key, L. J. Atherton, L. R. Benedetti, D. K. Bradley, D. A. Callahan, P. M. Celliers, C. J. Cerjan, D. S. Clark, E. L. Dewald, S. N. Dixit, T. Döppner, D. H. Edgell, R. Epstein, S. Glenn, G. Grim, S. W. Haan, B. A. Hammel, D. Hicks, W. W. Hsing, O. S. Jones, S. F. Khan, J. D. Kilkenny, J. L. Kline, G. A. Kyrala, O. L. Landen, S. Le Pape, B. J. MacGowan, A. J. Mackinnon, A. G. MacPhee, N. B. Meezan, J. D. Moody, A. Pak, T. Parham, H.-S. Park, J. E. Ralph, S. P. Regan, B. A. Remington, H. F. Robey, J. S. Ross, B. K. Spears, V. Smalyuk, L. J. Suter, R. Tommasini, R. P. Town, S. V. Weber, J. D. Lindl, M. J. Edwards, S. H. Glenzer, and E. I. Moses, Phys. Rev. Lett. **111**, 085004 (2013).

16. T. C. Sangster, V. N. Goncharov, R. Betti, P. B. Radha, T. R. Boehly, D. T. Casey, T. J. B. Collins, R. S. Craxton, J. A. Delettrez, D. H. Edgell, R. Epstein, C. J. Forrest, J. A. Frenje, D. H. Froula, M. Gatu-Johnson, V. Yu. Glebov, D. R. Harding, M. Hohenberger, S. X. Hu, I. V. Igumenshchev, R. Janezic, J. H. Kelly, T. J. Kessler, C. Kingsley, T. Z. Kosc, J. P. Knauer, S. J. Loucks, J. A. Marozas, F. J. Marshall, A. V. Maximov, R. L. McCrory, P. W. McKenty, D. D. Meyerhofer, D. T. Michel, J. F. Myatt, R. D. Petrasso, S. P. Regan, W. Seka, W. T. Shmayda, R. W. Short, A. Shvydky, S. Skupsky, J. M. Soures, C. Stoeckl, W. Theobald, V. Versteeg, B. Yaakobi, and J. D. Zuegel, Phys. Plasmas **20**, 056317 (2013).

17. P. B. Radha, T. J. B. Collins, J. A. Delettrez, Y. Elbaz, R. Epstein, V. Yu. Glebov, V. N. Goncharov, R. L. Keck, J. P. Knauer, J. A. Marozas, F. J. Marshall, R. L. McCrory, P. W. McKenty, D. D. Meyerhofer, S. P. Regan, T. C. Sangster, W. Seka, D. Shvarts, S. Skupsky, Y. Srebro, and C. Stoeckl, Phys. Plasmas **12**, 056307 (2005).

18. S. X. Hu, P. B. Radha, J. A. Marozas, R. Betti, T. J. B. Collins, R. S. Craxton, J. A. Delettrez, D. H. Edgell, R. Epstein, V. N. Goncharov, I. V. Igumenshchev, F. J. Marshall, R. L. McCrory, D. D. Meyerhofer, S. P. Regan, T. C. Sangster, S. Skupsky, V. A. Smalyuk, Y. Elbaz, and D. Shvarts, Phys. Plasmas **16**, 112706 (2009).

19. S. X. Hu, V. N. Goncharov, P. B. Radha, J. A. Marozas, S. Skupsky, T. R. Boehly, T. C. Sangster, D. D. Meyerhofer, and R. L. McCrory, Phys. Plasmas **17**, 102706 (2010).

20. D. T. Michel, A. K. Davis, V. N. Goncharov, T. C. Sangster, S. X. Hu, I. V. Igumenshchev, D. D. Meyerhofer, W. Seka, and D. H. Froula, Phys. Rev. Lett. **114**, 155002 (2015).

21. S. X. Hu, D. T. Michel, A. K. Davis, R. Betti, P. B. Radha, E. M. Campbell, D. H. Froula, and C. Stoeckl, "Understanding the Effects of Laser Imprint on Plastic-Target Implosions on OMEGA," to be published in Physics of Plasmas.

22. J. A. Marozas and T. J. B. Collins, Bull. Am. Phys. Soc. **57**, 344 (2012).

23. T. R. Boehly, D. L. Brown, R. S. Craxton, R. L. Keck, J. P. Knauer, J. H. Kelly, T. J. Kessler, S. A. Kumpan, S. J. Loucks, S. A. Letzring, F. J. Marshall, R. L. McCrory, S. F. B. Morse, W. Seka, J. M. Soures, and C. P. Verdon, Opt. Commun. **133**, 495 (1997).

24. T. R. Boehly, V. A. Smalyuk, D. D. Meyerhofer, J. P. Knauer, D. K. Bradley, R. S. Craxton, M. J. Guardalben, S. Skupsky, and T. J. Kessler, J. Appl. Phys. **85**, 3444 (1999).

25. S. Skupsky, R. W. Short, T. Kessler, R. S. Craxton, S. Letzring, and J. M. Soures, J. Appl. Phys. **66**, 3456 (1989).

26. T. J. Kessler, Y. Lin, J. J. Armstrong, and B. Velazquez, Proc. SPIE **1870**, 95 (1993).

27. D. T. Michel, C. Sorce, R. Epstein, N. Whiting, I. V. Igumenshchev, R. Jungquist, and D. H. Froula, Rev. Sci. Instrum. **83**, 10E530 (2012).

28. D. K. Bradley, P. M. Bell, J. D. Kilkenny, R. Hanks, O. Landen, P. A. Jaanimagi, P. W. McKenty, and C. P. Verdon, Rev. Sci. Instrum. **63**, 4813 (1992).

29. D. T. Michel, V. N. Goncharov, I. V. Igumenshchev, R. Epstein, and D. H. Froula, Phys. Rev. Lett. **111**, 245005 (2013).

30. D. T. Michel, A. K. Davis, W. Armstrong, R. Bahr, R. Epstein, V. N. Goncharov, M. Hohenberger, I. V. Igumenshchev, R. Jungquist, D. D. Meyerhofer, P. B. Radha, T. C. Sangster, C. Sorce, and D. H. Froula, High Power Laser Science and Engineering **3**, e19 (2015).

31. J. J. MacFarlane *et al*., High Energy Density Phys. **3**, 181 (2007).

32. G. P. Schurtz, Ph. D. Nicolaï, and M. Busquet, Phys. Plasmas **7**, 4238 (2000).

33. D. Cao, G. Moses, and J. Delettrez, Phys. Plasmas **22**, 082308 (2015).

34. S. X. Hu, L. A. Collins, V. N. Goncharov, J. D. Kress, R. L. McCrory, and S. Skupsky, Phys. Rev. E **92**, 043104 (2015).

Optical Smoothing of Laser Imprinting in Planar-Target Experiments on OMEGA EP Using One-Dimensional Multi-FM Smoothing by Spectral Dispersion

Introduction

One of the primary missions of the National Ignition Facility (NIF)[1] is to experimentally demonstrate ignition with inertial confinement fusion (ICF),[2–4] either by the indirect-drive (or x-ray–drive) approach, where laser beams heat the inside of a high-*Z* enclosure ("hohlraum") in which an implosion capsule is placed,[4] or by the direct-drive approach, where a capsule is illuminated directly by the laser beams to launch the capsule implosion.[5] In ICF the stability of the shell that encases the fusion fuel during the implosion is a key determinant of achieving ignition. Achieving sufficient irradiation uniformity for a successful direct-drive–ignition experiment necessitates the use of single-beam smoothing. Typical requirements for direct-drive illumination are in excess of what is required for indirect-drive illumination since direct drive lacks the inherent smoothing of the radiation field as it flows from the hohlraum wall to the capsule.[6–8]

Shell stability is primarily degraded by the growth of hydrodynamic instabilities that cause both short- and long-wavelength modulations of the shell's areal density. These modulations can result in shell breakup during the acceleration phase of the implosion or lead to a mixing of the cold shell material with the hot fuel,[9] quenching the fusion reactions and reducing target performance during the implosion's deceleration phase. The dominant hydrodynamic instability is the Rayleigh–Taylor (RT) instability.[10,11] It develops during the acceleration phase of the fusion target as the cold dense shell material is accelerated by the hot, low-density blowoff plasma.

In direct-drive targets, initial perturbations that lead to RT growth are primarily seeded by target-surface roughness and nonuniformities of the incident laser intensity ("imprint"). Laser imprinting occurs because spatial variations in the laser intensity drive pressure variations into the target. This distorts the shock and ablation front and creates lateral mass flow in the shock-compressed material, resulting in mass modulations at the ablation surface of the driven target.[12] Various laser-smoothing techniques have been developed to reduce the level of imprinting. These include distributed phase plates (DPP's),[13] continuous-contour phase plates (CPP's),[14] polarization smoothing,[15] induced spatial incoherence (ISI),[16] and smoothing by spectral dispersion (SSD).[17]

SSD varies the interference speckle pattern of a DPP- or CPP-focused laser beam on a shorter time scale than the characteristic hydrodynamic response time of the target, i.e., the imprinting time. This is achieved by adding bandwidth, typically of a few angstroms, to the fundamental laser frequency using an electro-optical modulator. Introducing spectral dispersion to the broadened-bandwidth light, which is focused by including a phase plate, causes the interference structure from beamlets originating at different phase-plate elements to vary in time. At any given moment, the intensity profile is highly modulated because of the interference pattern from the phase-plate–modulated wavefront, but the time-averaged intensity is smoothed.[17]

Some instability mitigation is provided by the SSD system currently installed on the NIF,[18,19] although the level of smoothing is less than that required for direct-drive–ignition experiments.[8] There are two potential paths to implementing SSD beam smoothing for direct-drive ignition on the NIF: (1) Two-dimensional (2-D) SSD, as currently used on the OMEGA laser,[20] has been shown to reduce single-beam irradiation nonuniformities to the few-percent level[21] and to efficiently suppress instability seeds.[22] Adding a comparable 2-D SSD system to the NIF would necessitate major modifications to the preamplifier modules (PAM's) and require additional tripler crystals to convert the extra bandwidth.[8,23] (2) One-dimensional smoothing by spectral dispersion with multiple phase-modulation frequencies (1-D multi-FM SSD)[24,25] was developed at LLE as a more cost-effective and labor-efficient solution to providing the smoothing level required for the current NIF polar-direct-drive–ignition point design. It is compatible with the existing NIF Laser System, and modifications that are necessary to implement 1-D multi-FM SSD on the NIF are limited to fiber-based systems in the Master Oscillator Room, in addition to a new diffraction grating in the PAM.[8] Both 2-D SSD and 1-D multi-FM SSD are predicted to provide the smoothing required by the ignition design.

A prototype multi-FM seed source has been implemented in Beamline 4 of the OMEGA EP laser[26] to validate the predicted multi-FM performance. Amplifying and angularly dispersing the phase-modulated beam in a NIF PAM before injection into Beamline 4 ensures the compatibility of the multi-FM system with the NIF's front end.

The multi-FM performance qualification consists of two parts: (1) measurement of equivalent-target-plane modulations of the laser intensity and (2) validation of the numerical treatment of 1-D multi-FM SSD to predict imprint levels and instability growth with dedicated on-target shots. The remaining sections briefly describe the multi-FM SSD system and its implementation on OMEGA EP; discuss the equivalent-target-plane measurements to characterize modulations in the focal-spot intensity using different SSD methods; describe the experiments that characterize laser-imprint levels by measuring the RT instability growth, including 2-D hydrodynamic simulations of the data; and present our conclusions.

One-Dimensional Multi-FM SSD on OMEGA EP

The implementation of 1-D multi-FM SSD into the front end of Beamline 4 on OMEGA EP is shown schematically in Fig. 147.5. Two separate pulse-shaping systems provide different levels of SSD bandwidth to the laser pulse by transforming the incident electric field $E(t) \propto \exp(i\omega_\mathrm{L} t)$ to

$$E(t) \propto \exp\left[i\omega_\mathrm{L} t + i\sum_n \delta_n \cos(\omega_n t + \varphi_n)\right]. \tag{1}$$

Here, ω_L is the incident laser frequency; t is the time; and δ_n, ω_n, and φ_n are the modulation depth, frequency, and phase of modulator n, respectively, with the sum being calculated over the number of modulators in the system. The OMEGA EP main-pulse front end introduces bandwidth to the fundamental laser frequency to suppress stimulated Brillouin scattering (SBSS SSD) in the laser system optics. It operates with a modulation frequency of 3 GHz and a modulation depth of 5.5 in the infrared (IR), resulting in a ultraviolet (UV) bandwidth of 0.1 THz. In parallel, a picket-pulse channel provides the bandwidth for the 1-D multi-FM SSD. It comprises three modulators with incommensurate frequencies of 21.2 GHz, 22.8 GHz, and 31.9 GHz and corresponding modulation depths of 0.45, 1.04, and 2.07, respectively. This results in a combined bandwidth in the UV of ~0.5 THz. Multi-FM SSD is typically applied to the early part of the laser pulse during which laser imprint dominates, with SBSS SSD bandwidth applied to the main portion. The two parts are then optically combined to form the desired pulse shape and SSD bandwidth profile. This dynamic bandwidth reduction ensures that the increased bandwidth of multi-FM SSD is not applied during the high-intensity portion of the laser pulse, where it can potentially damage the laser optics.[27] After optical combination, the beam is passed through a diffraction grating, resulting in

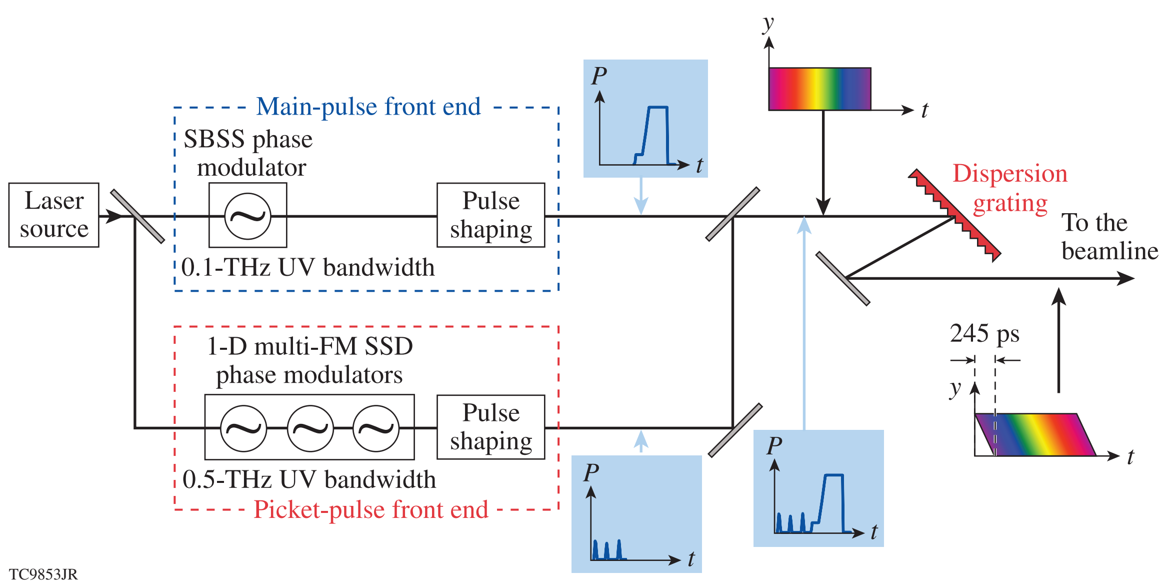

Figure 147.5
One-dimensional multi-FM setup of Beamline 4 on OMEGA EP. Two separate front ends provide bandwidth for either stimulated Brillouin scattering suppression (SBSS) or multi-FM smoothing by spectral dispersion (SSD). The two pulses are then combined optically to form the desired pulse shape and SSD profile. A grating introduces spectral dispersion, resulting in a spatiotemporal shear of 245 ps.

spectral dispersion of the phase-modulated beam and the spatial frequency modulation across the beam necessary for SSD. The grating imposes an uncompensated spatiotemporal shear of Δt = 245 ps to the pulse. Since the NIF laser's front end, for which multi-FM has been designed, is a fiber-based system, it is not possible to place an additional grating in the laser chain before the phase modulators to compensate for this temporal skew. This imposes a minimum rise time of ~250 ps to the portion of the laser pulse to which the multi-FM bandwidth is applied.

For the experiments discussed below, the pulse shapes were generated fully in either the SBSS or the multi-FM SSD front end, without employing dynamic bandwidth reduction.

Equivalent-Target-Plane Measurements

High-resolution, equivalent-target-plane (ETP) measurements of the UV irradiation uniformity of SSD-smoothed laser pulses were performed using the setup shown in Fig. 147.6. The setup is very similar to the UV ETP system on OMEGA, which has been demonstrated to fully resolve individual speckles.[28] After frequency conversion and before focusing into the target chamber, a portion of the Beamline 4 light is picked up using a 4% beam splitter and focused onto a camera with an off-axis parabola. This provides an image of the focal spot equivalent to the on-target conditions with a spatial resolution of ~4 μm. The speckle size w is given by the relationship $w = \lambda f \approx$ 6.5 μm, with λ and f being the laser wavelength and imaging f number, respectively.

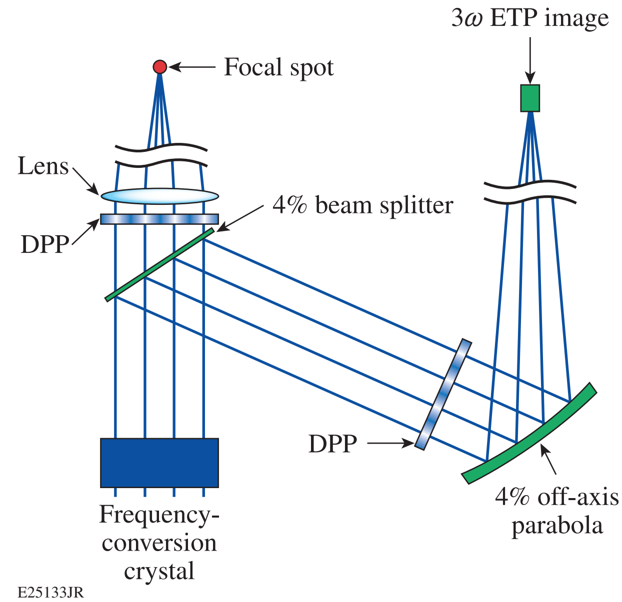

Figure 147.6
The equivalent-target-plane (ETP) diagnostic on OMEGA EP measures the focal-spot profile of a low-power, phase-plate–focused beam with and without SSD bandwidth. DPP: distributed phase plate.

Images of the far-field profile of a wEP-SG8-0800 DPP irradiated with a 2-ns pulse and using different levels of SSD are shown in Fig. 147.7. In addition to the time-integrated far-field data, each image shows central lineouts through the data in the horizontal and vertical directions, below and to the right of the far-field image, respectively. All far-field spots contain the same

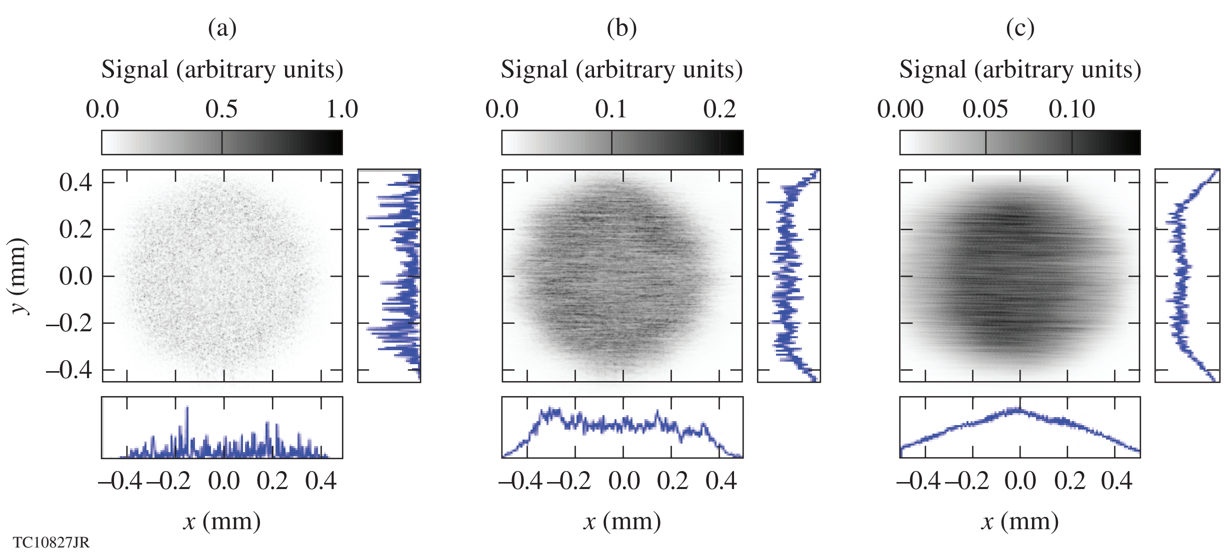

Figure 147.7
Equivalent-target-plane images of the far field of a wEP-SG8-0800 phase plate and central lineouts in the horizontal and vertical directions. (a) With no applied SSD bandwidth, the speckle pattern of the phase-plate–focused far field is well resolved. (b) SBSS SSD and (c) multi-FM SSD applied smoothing in the horizontal direction. The data smoothed by multi-FM SSD are significantly smoother in both the vertical and horizontal directions because of the increased bandwidth.

amount of energy, and the color scales have been adjusted for each image to fully capture the recorded signal range.

The case where no SSD has been applied is shown in Fig. 147.7(a). There is no SSD bandwidth and the speckle pattern is unperturbed and stationary throughout the pulse duration. The speckle pattern is well resolved in the ETP data, and the central lineouts through the data exhibit severe intensity modulations in both the x and y directions. Figure 147.7(b) shows the effect of applying SBSS SSD to the laser pulse. The speckle pattern is displaced in the horizontal direction, smoothing the time-integrated intensity profile. Applying 1-D multi-FM SSD results in the far-field laser spot shown in Fig. 147.7(c)—the smoothest of the three cases shown here—where the intensity modulations in the central lineouts are reduced considerably. Both SBSS SSD and multi-FM SSD apply the angular dispersion in one dimension only, resulting in the smoothing applied predominantly in a single direction (horizontal in Fig. 147.7). As can be seen from the central lineouts, despite the 1-D nature of the applied SSD bandwidth, smoothing is observed in both the x and y directions.

The recorded ETP data agree well with numerical predictions of the smoothing performance. Figure 147.8 shows azimuthally averaged power spectral densities (PSD's) of the far-field data in Fig. 147.7 (blue lines) and the equivalent theoretical predictions (red). The predicted PSD's were calculated by propagating measured near-field phase fronts using the code *Waasikwa'*,[29] which incorporates numerical models of the phase plate and SSD. The experimental data agree well with the predictions up to the ETP system resolution at a frequency of ~0.1 μm^{-1}. While SBSS SSD generates a notably smoother

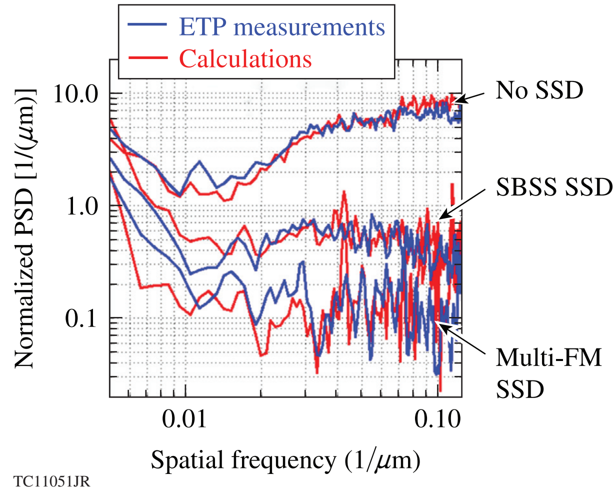

Figure 147.8
The azimuthally averaged power spectral densities of the far-field data in Fig. 147.7 (blue) agree well with the numerical predictions for the different SSD cases (red). Over the plotted frequency range, the power amplitudes are reduced by 50% for multi-FM versus SBSS SSD. PSD: power spectral density.

profile than in the case of no applied SSD, multi-FM SSD reduces the PSD amplitudes further by ~50% to 70% in the range of 0.01 to 0.1 μm^{-1}, corresponding to modes ~100 to 1000 of an ignition-scale target.

Measurements and Simulations of Experimental RT Growth

Experiments were performed to study the effect of multi-FM smoothing on laser imprinting in dedicated OMEGA EP target experiments. The experimental setup shown schematically in Fig. 147.9 is based on similar RT-growth experiments per-

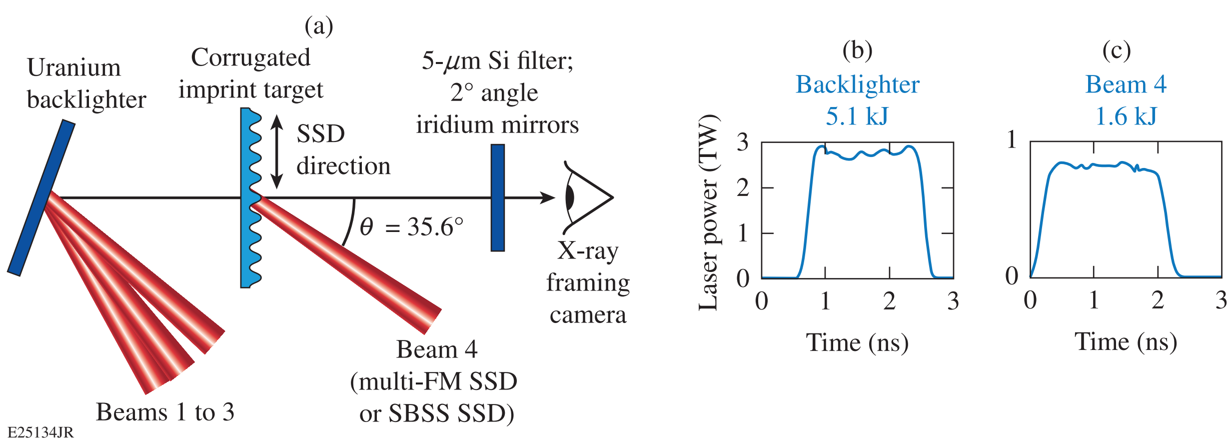

Figure 147.9
Rayleigh–Taylor growth of laser-imprint–seeded modulation and an imposed 30-μm corrugation were tracked by face-on radiography. The spatial variation in the optical depth of the imprint target was recorded using a fast x-ray framing camera giving 100-ps snapshots of the target evolution.

formed on OMEGA.[22,30] A planar, 20-μm-thick CH foil was driven with ~1.6 kJ by Beamline 4 using a 2-ns square pulse with an on-target irradiance of ~10^{14} W/cm^2 and a rise time of ~250 ps, dominated by the temporal skew imposed by the SSD dispersion grating. The imprint target featured a single-mode, sinusoidal surface corrugation with a wavelength of 30 μm and amplitude of 0.1 μm that acts as a reference for the imprint-seeded, broadband RT growth. For a typical ignition-scale direct-drive target, this corresponds to a Legendre mode of ~350 (Ref. 7).

The corrugation was oriented approximately perpendicular to the active SSD direction. The experiments were carried out with either SBSS SSD or multi-FM SSD applied over the full duration of the drive laser. Operation without any SSD bandwidth was not supported because of the potential risk of optics damage in the laser system. The RT-amplified corrugation mode and broadband laser imprint were measured using face-on x-ray radiography of the driven target, providing an optical-depth map of the target at discrete times and highlighting areas of spike and bubble growth. The backlighter was a uranium foil driven with Beamlines 1, 2, and 3 of the OMEGA EP laser with a 2-ns pulse containing a total of ~5 kJ of energy and an on-target irradiance of ~3×10^{14} W/cm^2. An undriven, 3-μm-thick Al foil was placed between the backlighter and the imprint foil. This foil acted as a shield, protecting the imprint target from plasma blowoff generated at the backlighter, as well as from soft x-ray emission that could preheat the imprint target. X rays transmitted through the Al heat shield and the imprint target were imaged with 10-μm pinholes onto a fast x-ray framing camera.[31] A combination of iridium-coated, grazing-incidence mirrors oriented at a 2° angle of incidence and 5-μm-thick Si filtering limited the recorded x-ray energy to ~1.5 keV. The x-ray framing camera recorded multiple snapshots of the target's optical depth over an ~1-ns window, with individual images integrated over the camera gate width of ~100 ps. This radiography technique lacks the sensitivity to measure imprint levels or the preimposed corrugation feature directly and relies on RT growth of the target modulations to produce detectable levels of variation in optical depth.

Unlike previous planar-target imprint experiments performed on OMEGA (see, e.g., Ref. 22), in the experiments discussed here the imprint target was irradiated from the side facing the detector (compare Fig. 147.9). Driving the imprint target from the rear is the preferred option since the CH target itself acts as a filter for its own self-emission. The reverse geometry for the multi-FM measurements, however, is necessitated by the beam and diagnostics layout on OMEGA EP, where all beams originate from the same direction. At an x-ray energy of 1.5 keV, the energy used to probe the optical-depth evolution, a 20-μm-thick plastic foil attenuates the x-ray flux to ~25%. This drops the achievable signal-to-noise ratio in these experiments by approximately a factor of 4 compared to a rear-driven geometry since the backlighter emission competes with higher levels of self-emission.

To extract the evolution of modulation amplitudes, the optical-depth maps are converted into frequency space by Fourier transformation. Examples of experimental optical-depth maps are shown in Fig. 147.10, with Fig. 147.10(a) using SBSS SSD and Fig. 147.10(b) using 1-D multi-FM SSD; Figs. 147.10(c) and 147.10(d) are the equivalent frequency maps, respectively. The optical-depth maps, plotted on the same color scale, were obtained ~1.75 ns after the onset of the laser drive. In these data, the initially imposed corrugation is oriented vertically; i.e., lines of equal amplitude are parallel to the y direction, and the active SSD direction is approximately horizontal. While the corrugation mode is more dominant in the multi-FM–smoothed data, the corrugation is well resolved in both data sets, appear-

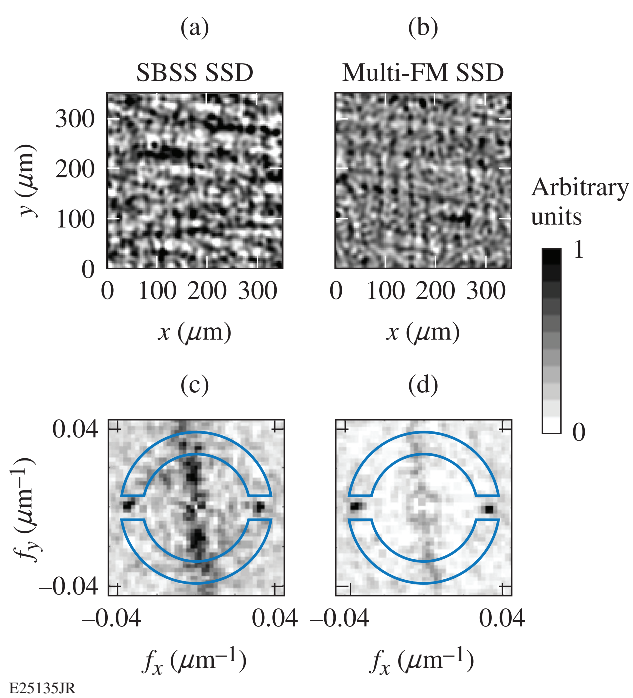

Figure 147.10
[(a),(b)] Optical-depth data with SBSS SSD and multi-FM SSD, respectively. The 30-μm corrugation appears as vertical lines, with SSD acting mainly in the horizontal direction. In frequency space [(c),(d)] the corrugation appears as a single peak at $f_x = 1/30\ \mu\text{m}^{-1}$. Because of the 1-D nature of multi-FM SSD, broadband imprint is predominantly located along f_y for $f_x \sim 0$. The semicircles denote the analysis region for the $f \sim 1/30$-μm broadband mode.

ing as vertical lines in the optical depth, and as a single peak in frequency space for $f_x = 1/30\ \mu\text{m}^{-1}$ and $f_y = 0$. In both cases, broadband imprint and RT growth are predominantly visible in the direction perpendicular to the active SSD smoothing, appearing as irregular structures in the horizontal direction in the optical-depth data and elevated mode amplitudes in the f_y direction for $f_x \sim 0$ in the frequency maps. The data are oriented such that the corrugation feature falls at $f_y = 0$, while a slight target misalignment resulted in the direction of least smoothing (i.e., perpendicular to the active SSD direction) at $\varphi \approx 98°$. The broadband-imprint feature along this direction is noticeably broader in f_x for the SBSS data [Fig. 147.10(c)] than in the multi-FM case [Fig. 147.10(d)], as expected from the improved smoothing of 1-D multi-FM SSD.

To calculate areal density from the measured optical depth, the backlighter emission was characterized by radiographing an undriven sample target in a dedicated experiment. The sample target was made of the same CH material as the imprint target and comprised multiple steps of known CH thickness. This calibration experiment directly relates experimental optical depth and target areal densities and confirms a central backlighter energy of ~1.5 keV.

The experimentally measured evolution of the 30-μm corrugation is shown in Fig. 147.11(a), plotting the areal-density amplitude as a function of time. The circles denote data recorded with 1-D multi-FM SSD applied to the drive laser, while the squares denote data taken with SBSS SSD. Since the corrugation mode is preimposed and not an imprint feature, its growth and absolute amplitude should be independent of the applied SSD bandwidth, as confirmed by the experimental data. The data points in Fig. 147.11(b) show the root-mean-square (rms) amplitude of the broadband 30-μm imprint, corresponding to the azimuthally integrated $f \sim 1/30\text{-}\mu\text{m}^{-1}$ mode in frequency space, but excluding a region of $\Delta f_x = \Delta f_y = 1/250^{-1}\ \mu$m centered around the corrugation peak at $f_x = 1/30\ \mu\text{m}^{-1}$ and $f_y = 0$. The integration range is marked by the region inside the two semicircles overlaid onto the frequency space maps in Figs. 147.10(c) and 147.10(d). These data were recorded on the same shots as the data shown in Fig. 147.11(a). While there is considerable noise in the data, the SBSS-smoothed amplitudes consistently exceed the multi-FM case by a factor of ~2.

Simulation results for the growth of the corrugation mode and the rms amplitude of the $f \sim 1/30\text{-}\mu$m broadband imprint mode are shown as the solid lines in Figs. 147.11(a) and 147.11(b), respectively. The target evolution was simulated using the 2-D radiation–hydrodynamics code *DRACO*,[32] which

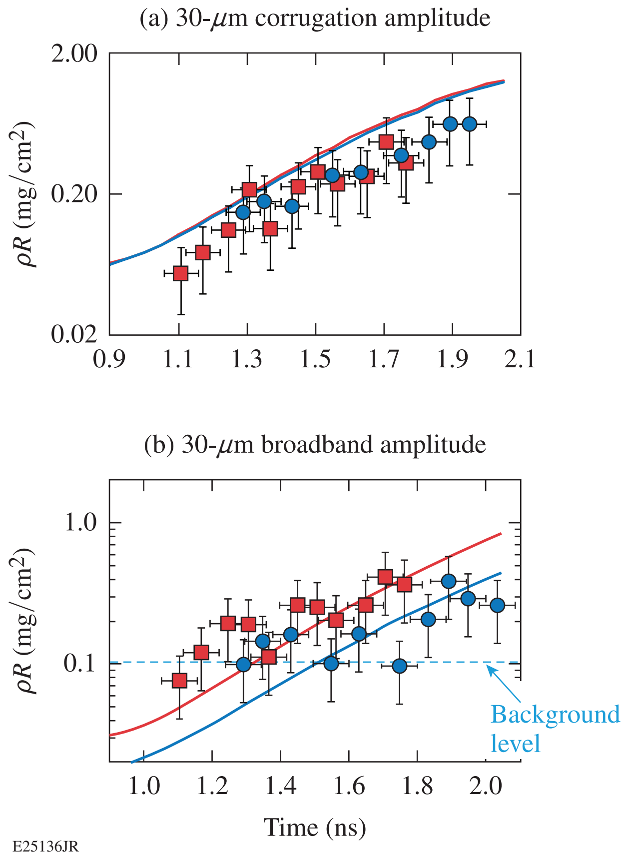

Figure 147.11
(a) Time evolution of the 30-μm experimental (data points) and simulated (lines) corrugation amplitudes. The red squares denote data acquired with SBSS SSD and the blue circles denote data acquired with multi-FM SSD. The corrugated mode is not affected by imprint and exhibits a growth rate independent of the SSD bandwidth. (b) Root-mean-square (rms) amplitude of the experimental (data points) and simulated (lines) broadband 30-μm mode. The dashed horizontal line denotes the background level in the experimental data. The red and blue lines are 2-D *DRACO* simulated growth rates for SBSS and multi-FM, respectively.

includes a 3-D ray-trace package to model the laser absorption. The effect of the SSD bandwidth is taken into account by calculating the far-field laser spots multiple times per picosecond using the code *Waasikwa'*.[29] The code uses the near-field laser intensity and phase, including the SSD bandwidth and its effect, and propagates it through the phase plate and the main lens to obtain an instantaneous far field. Figure 147.12(a) illustrates a laser beam's near-field lineout along the SSD active direction as a function of time, with different colors illustrating the change in light frequency related to the SSD bandwidth. The temporal skew caused by the uncompensated diffraction grating in the SSD chain results in an initially sub-aperture beam incident onto the DPP, which gradually increases in area to full aperture by the end of the 245-ps skew interval. The action of 1-D SSD and an uncompensated diffraction grating result in an asymmetric and time-dependent far-field spot and speckle pattern, as illustrated in Figs. 147.12(b) and 147.12(c), which show calculated far-field profiles at 20 ps and 100 ps, respectively.

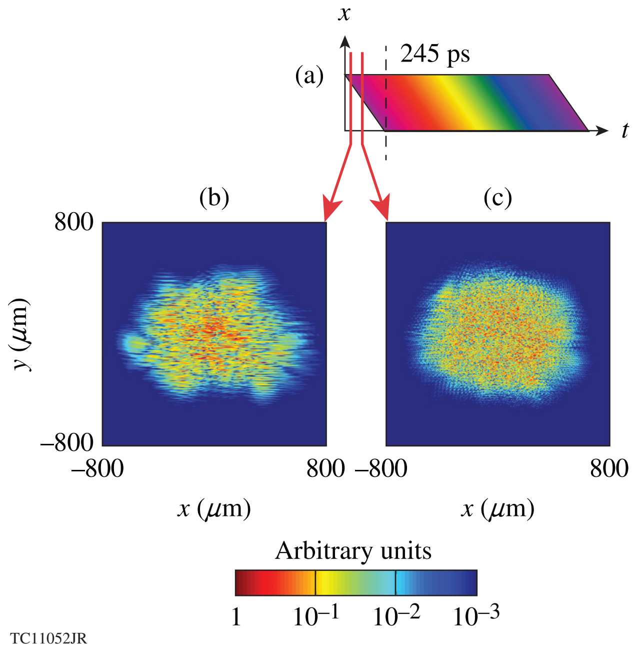

Figure 147.12
(a) Illustration of the laser beam's near field along the SSD active direction versus time. [(b),(c)] Far fields calculated by *Waasikwa*' from instantaneous near fields at times of 20 ps and 100 ps, respectively.

To fully simulate the interaction of the 1-D multi-FM and SBSS SSD-smoothed laser beams with the target requires a 3-D hydrocode and a 3-D ray trace. In such calculations, the instantaneous far fields would be used to assign the energy of rays launched at the outer boundary of the simulation region, which would then be traced through the plasma, depositing their energy in cells of the simulation mesh by the inverse bremsstrahlung process, capturing the asymmetry of the SSD action with respect to the target's x and y coordinates. In 2-D cylindrical hydro simulations with a 3-D ray trace, however, such as used for the simulations presented here, the x and y coordinates are reduced to a single axis by averaging the laser deposition along the azimuthal angle φ. This makes it impossible to capture the effect of SSD with a single 2-D calculation. It is possible to simplify the problem, however, by taking advantage of the fact that at early stages of the laser drive, the nonuniformities are small and the RT growth is in its linear stage. During the linear stage, individual modulation modes do not interact with each other and can be considered independently. This allows one to reproduce the 3-D nature of the experiment with a set of 2-D hydrocode simulations in which each simulation considers only a single frequency slice of the incident far-field spectrum.

As illustrated in Fig. 147.13, the full 3-D target response was calculated by dividing the instantaneous, incident far field [Fig. 147.13(a)] into 120 frequency slices at a 3° separation

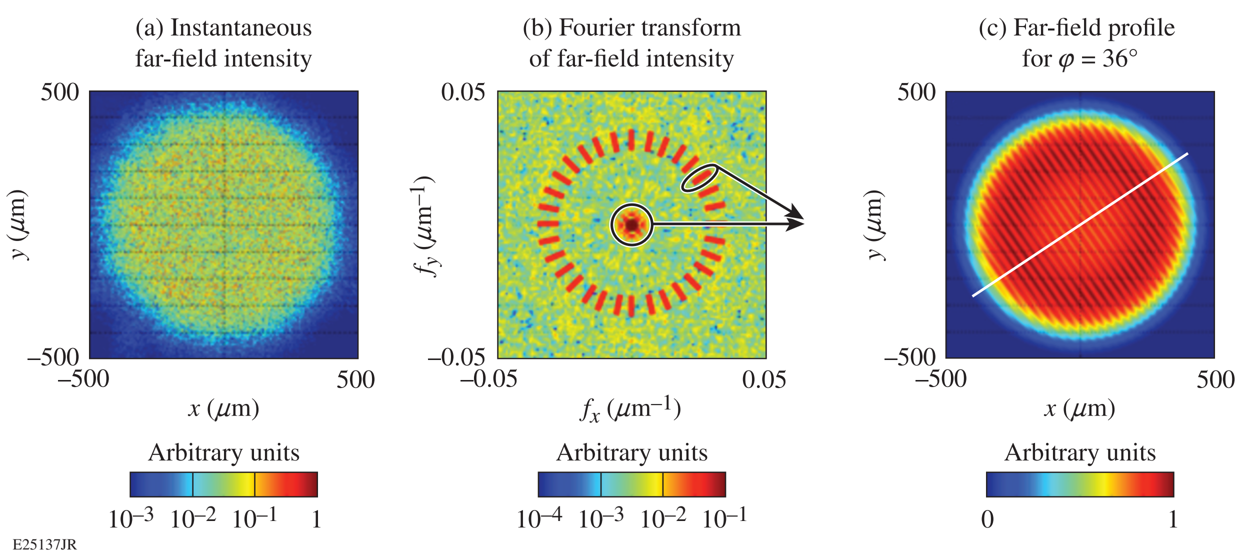

Figure 147.13
Combining multiple 2-D simulations using a reduced far-field spot as the input captured the 3-D experimental imprint. The instantaneous laser far field (a) is converted into frequency space (b) and divided into 120 frequency slices with 3° separation. (c) The reduced far-field spot for $\varphi = 36°$ is constructed by combining the low-spatial-frequency envelope with the 29- to 31-μm wavelength range of the $\varphi = 36°$ frequency slice.

[Fig. 147.13(b)]. Combining the time-varying, low-spatial-frequency envelope at the center of the frequency map with the Fourier modes with the 29- to 31-μm wavelengths contained within each frequency slice gives a "reduced" far-field spot. This reduced far-field spot contains modulations in only a single direction, as determined by the selected frequency slice, and can be used as an input for a 2-D simulation. An example of such a reduced far field [Fig. 147.13(c)] shows the far-field spot for the $\varphi = 36°$ frequency slice. In these 2-D calculations, the initial target corrugation was included in only the frequency slice for $\varphi = 0°$; i.e., along the 1-D multi-FM SSD active direction and the direction of the most-efficient smoothing.

Individual frequency-slice calculations that emulate the effect of 1-D multi-FM SSD are presented in Fig. 147.14. These images show mass-density profiles of the accelerated foil at 1.75 ns. Figure 147.14(a) shows the case for the frequency slice at $\varphi = 90°$ (along the vertical axis and perpendicular to the multi-FM SSD active direction); Fig. 147.14(b) shows the case for the frequency slice at $\varphi = 69°$. The smoothing is least efficient perpendicular to the SSD active direction, and the density profile shown in Fig. 147.14(a) has noticeable RT growth, resulting from far-field–spot modulations and laser imprint. In contrast, the profile in Fig. 147.14(b) exhibits very little growth, emphasizing how 1-D multi-FM SSD efficiently suppresses imprint modes that have a non-negligible component along the active SSD direction.

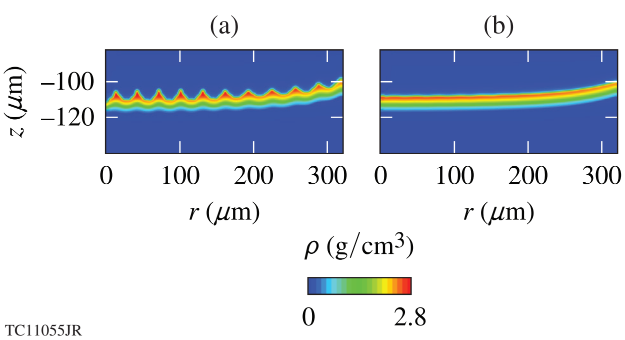

Figure 147.14
Profiles of the calculated foil density at 1.75 ns using 1-D multi-FM SSD for two of the 120 laser far-field frequency slices with wavelengths of 29 to 30 μm. (a) The least amount of imprint mitigation is found for the far-field frequency component perpendicular to the active SSD direction. (b) At 69° off the active SSD direction, imprint is already significantly reduced.

As shown in Fig. 147.15, *DRACO* simulations reproduce imprint and corrugation features seen in the Fourier space of the experimental optical-depth maps, such as the directionality of the SSD observed in frequency space (compare to Fig. 147.10). The broadband imprint is dominated by Fourier modes perpendicular to the active SSD direction and close to $f_x \sim 0$, while the modes with $f_x \neq 0$ are effectively removed by the SSD (more so in the case of multi-FM than SBSS SSD).

The simulated corrugation amplitudes versus time are shown in Fig. 147.11(a) as the solid lines. While the growth rate observed in the experiment is reproduced correctly, the simulation exhibits a 40%-higher amplitude compared to the experimental data. The source of the disagreement between the experimental growth of the preimposed corrugation and its simulation is currently unknown, but it is likely caused by a combination of the background in the data or an uncharacterized level of surface roughness of the imprint foil. The simulated broadband imprint amplitudes of the nonuniformities at a frequency of 1/30 μm^{-1} are shown in Fig. 147.11(b) for the SBSS (red line) and multi-FM SSD case (blue line). The numerical calculations reproduce the experimental data within the error bars once the data exceed the background level. The simulations predict an ~2× reduction of the imprint level for the multi-FM SSD case compared to the SBSS SSD case, consistent with the experimental data. The calculations further reproduce

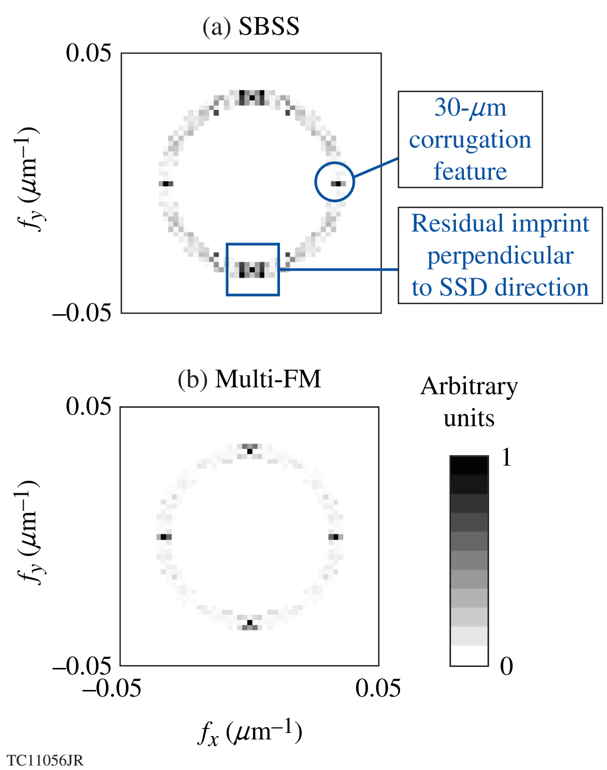

Figure 147.15
Fourier transform of *DRACO*-simulated optical depth at 1.75 ns for $f \sim 1/30$ μm using (a) SBSS SSD and (b) multi-FM SSD.

the directionality of SSD observed in frequency space [compare Fig. 147.15 and Figs. 147.10(c) and 147.10(d)]. The broadband imprint is dominated by Fourier modes perpendicular to the active SSD direction and close to $f_x \sim 0$, while the modes with $f_x \neq 0$ are effectively removed by SSD (more so in the case of multi-FM than SBSS SSD).

Conclusions

In summary, 1-D multi-FM SSD beam smoothing was developed at LLE to provide sufficient far-field uniformity for direct-drive inertial confinement fusion applications at the National Ignition Facility. A prototype of the multi-FM system has been implemented in the NIF-like Beamline 4 on the OMEGA EP laser for verification purposes. Multi-FM SSD beam-smoothing performance was verified with both equivalent-target-plane measurements of the laser's far field and in dedicated planar-target experiments by comparing smoothing rates with SBSS SSD and multi-FM SSD. Numerical calculations using the code *Waasikwa*' agree well with measurements of the multi-FM–smoothed, far-field spatial frequency spectrum. In the planar-target experiments, Rayleigh–Taylor growth rates of laser-imprinted and preimposed surface modulations at $f \sim 1/30\ \mu$m were measured by face-on x-ray radiography. As expected, the growth of the preimposed surface corrugation is independent of the SSD bandwidth, while 1-D multi-FM SSD is observed to reduce imprint levels by ~50% compared to SBSS SSD. The target experiment was simulated using the 2-D hydrodynamics code *DRACO* and realistic, time-dependent, far-field spot intensity calculations that included the effect of SSD. The 3-D nature of the imprint experiment was captured in the 2-D calculations by 120 individual simulations of a reduced far-field spot, containing only broadband modes in a single 2-D frequency slice. Within the error bars, the simulations correctly reproduce the relative and absolute amplitude levels between multi-FM and SBSS-SSD–smoothed broadband data, but they fail to capture the absolute amplitudes of the preimposed corrugation mode. An experimental unknown, such as surface roughness or an unaccounted-for background level, may be the cause of this discrepancy. Despite this discrepancy, the experimental data show a clear enhancement in smoothing performance of multi-FM SSD compared to SBS-suppression SSD, in agreement with simulations.

ACKNOWLEDGMENT

This material is based upon work supported by the Department of Energy National Nuclear Security Administration under Award Number DE-NA0001944, the University of Rochester, and the New York State Energy Research and Development Authority. The support of DOE does not constitute an endorsement by DOE of the views expressed in this article.

REFERENCES

1. G. H. Miller, E. I. Moses, and C. R. Wuest, Opt. Eng. **43**, 2841 (2004).
2. J. Nuckolls *et al.*, Nature **239**, 139 (1972).
3. J. D. Lindl, *Inertial Confinement Fusion: The Quest for Ignition and Energy Gain Using Indirect Drive* (Springer-Verlag, New York, 1998).
4. S. Atzeni and J. Meyer-ter-Vehn, *The Physics of Inertial Fusion: Beam Plasma Interaction, Hydrodynamics, Hot Dense Matter, International Series of Monographs on Physics* (Clarendon Press, Oxford, 2004).
5. R. S. Craxton, K. S. Anderson, T. R. Boehly, V. N. Goncharov, D. R. Harding, J. P. Knauer, R. L. McCrory, P. W. McKenty, D. D. Meyerhofer, J. F. Myatt, A. J. Schmitt, J. D. Sethian, R. W. Short, S. Skupsky, W. Theobald, W. L. Kruer, K. Tanaka, R. Betti, T. J. B. Collins, J. A. Delettrez, S. X. Hu, J. A. Marozas, A. V. Maximov, D. T. Michel, P. B. Radha, S. P. Regan, T. C. Sangster, W. Seka, A. A. Solodov, J. M. Soures, C. Stoeckl, and J. D. Zuegel, Phys. Plasmas **22**, 110501 (2015).
6. P. W. McKenty, V. N. Goncharov, R. P. J. Town, S. Skupsky, R. Betti, and R. L. McCrory, Phys. Plasmas **8**, 2315 (2001).
7. T. J. B. Collins, J. A. Marozas, K. S. Anderson, R. Betti, R. S. Craxton, J. A. Delettrez, V. N. Goncharov, D. R. Harding, F. J. Marshall, R. L. McCrory, D. D. Meyerhofer, P. W. McKenty, P. B. Radha, A. Shvydky, S. Skupsky, and J. D. Zuegel, Phys. Plasmas **19**, 056308 (2012).
8. M. Hohenberger, P. B. Radha, J. F. Myatt, S. LePape, J. A. Marozas, F. J. Marshall, D. T. Michel, S. P. Regan, W. Seka, A. Shvydky, T. C. Sangster, J. W. Bates, R. Betti, T. R. Boehly, M. J. Bonino, D. T. Casey, T. J. B. Collins, R. S. Craxton, J. A. Delettrez, D. H. Edgell, R. Epstein, G. Fiksel, P. Fitzsimmons, J. A. Frenje, D. H. Froula, V. N. Goncharov, D. R. Harding, D. H. Kalantar, M. Karasik, T. J. Kessler, J. D. Kilkenny, J. P. Knauer, C. Kurz, M. Lafon, K. N. LaFortune, B. J. MacGowan, A. J. Mackinnon, A. G. MacPhee, R. L. McCrory, P. W. McKenty, J. F. Meeker, D. D. Meyerhofer, S. R. Nagel, A. Nikroo, S. Obenschain, R. D. Petrasso, J. E. Ralph, H. G. Rinderknecht, M. J. Rosenberg, A. J. Schmitt, R. J. Wallace, J. Weaver, C. Widmayer, S. Skupsky, A. A. Solodov, C. Stoeckl, B. Yaakobi, and J. D. Zuegel, Phys. Plasmas **22**, 056308 (2015).
9. D. K. Bradley, J. A. Delettrez, R. Epstein, R. P. J. Town, C. P. Verdon, B. Yaakobi, S. Regan, F. J. Marshall, T. R. Boehly, J. P. Knauer, D. D. Meyerhofer, V. A. Smalyuk, W. Seka, D. A. Haynes, Jr., M. Gunderson, G. Junkel, C. F. Hooper, Jr., P. M. Bell, T. J. Ognibene, and R. A. Lerche, Phys. Plasmas **5**, 1870 (1998).
10. S. E. Bodner, Phys. Rev. Lett. **33**, 761 (1974).
11. S. Chandrasekhar, in *Hydrodynamic and Hydromagnetic Stability, International Series of Monographs on Physics* (Clarendon Press, Oxford, 1961).
12. V. N. Goncharov, S. Skupsky, T. R. Boehly, J. P. Knauer, P. McKenty, V. A. Smalyuk, R. P. J. Town, O. V. Gotchev, R. Betti, and D. D. Meyerhofer, Phys. Plasmas **7**, 2062 (2000).
13. Y. Lin, T. J. Kessler, and G. N. Lawrence, Opt. Lett. **21**, 1703 (1996).
14. S. N. Dixit *et al.*, Proc. SPIE **2633**, 141 (1995).

15. T. R. Boehly, V. A. Smalyuk, D. D. Meyerhofer, J. P. Knauer, D. K. Bradley, R. S. Craxton, M. J. Guardalben, S. Skupsky, and T. J. Kessler, J. Appl. Phys. **85**, 3444 (1999).

16. R. H. Lehmberg and S. P. Obenschain, Opt. Commun. **46**, 27 (1983).

17. S. Skupsky, R. W. Short, T. Kessler, R. S. Craxton, S. Letzring, and J. M. Soures, J. Appl. Phys. **66**, 3456 (1989).

18. B. J. MacGowan *et al*., Phys. Plasmas **3**, 2029 (1996).

19. C. A. Haynam *et al*., Appl. Opt. **46**, 3276 (2007).

20. T. R. Boehly, D. L. Brown, R. S. Craxton, R. L. Keck, J. P. Knauer, J. H. Kelly, T. J. Kessler, S. A. Kumpan, S. J. Loucks, S. A. Letzring, F. J. Marshall, R. L. McCrory, S. F. B. Morse, W. Seka, J. M. Soures, and C. P. Verdon, Opt. Commun. **133**, 495 (1997).

21. S. P. Regan, J. A. Marozas, R. S. Craxton, J. H. Kelly, W. R. Donaldson, P. A. Jaanimagi, D. Jacobs-Perkins, R. L. Keck, T. J. Kessler, D. D. Meyerhofer, T. C. Sangster, W. Seka, V. A. Smalyuk, S. Skupsky, and J. D. Zuegel, J. Opt. Soc. Am. B **22**, 998 (2005).

22. T. R. Boehly, V. N. Goncharov, O. Gotchev, J. P. Knauer, D. D. Meyerhofer, D. Oron, S. P. Regan, Y. Srebro, W. Seka, D. Shvarts, S. Skupsky, and V. A. Smalyuk, Phys. Plasmas **8**, 2331 (2001).

23. S. Skupsky and R. S. Craxton, Phys. Plasmas **6**, 2157 (1999).

24. *LLE Review Quarterly Report* **114**, 73, Laboratory for Laser Energetics, University of Rochester, Rochester, NY, LLE Document No. DOE/NA/28302-826, NTIS Order No. DE2008935224 (2008).

25. J. A. Marozas, J. D. Zuegel, and T. J. B. Collins, Bull. Am. Phys. Soc. **55**, 294 (2010).

26. L. J. Waxer, M. J. Guardalben, J. H. Kelly, B. E. Kruschwitz, J. Qiao, I. A. Begishev, J. Bromage, C. Dorrer, J. L. Edwards, L. Folnsbee, S. D. Jacobs, R. Jungquist, T. J. Kessler, R. W. Kidder, S. J. Loucks, J. R. Marciante, D. N. Maywar, R. L. McCrory, D. D. Meyerhofer, S. F. B. Morse, A. V. Okishev, J. B. Oliver, G. Pien, J. Puth, and A. L. Rigatti, in *Conference on Lasers and Electro-Optics/Quantum Electronics and Laser Science Conference and Photonic Applications Systems Technologies, OSA Technical Digest* (CD) (Optical Society of America, Washington, DC, 2008), Paper JThB1.

27. *LLE Review Quarterly Report* **85**, 39, Laboratory for Laser Energetics, University of Rochester, Rochester, NY, LLE Document No. DOE/SF/19460-378, PB2006106656 (2000).

28. S. P. Regan, J. A. Marozas, J. H. Kelly, T. R. Boehly, W. R. Donaldson, P. A. Jaanimagi, R. L. Keck, T. J. Kessler, D. D. Meyerhofer, W. Seka, S. Skupsky, and V. A. Smalyuk, J. Opt. Soc. Am. B **17**, 1483 (2000).

29. J. A. Marozas, S. P. Regan, J. H. Kelly, D. D. Meyerhofer, W. Seka, and S. Skupsky, J. Opt. Soc. Am. B **19**, 7 (2002).

30. V. A. Smalyuk, T. R. Boehly, D. K. Bradley, V. N. Goncharov, J. A. Delettrez, J. P. Knauer, D. D. Meyerhofer, D. Oron, D. Shvarts, Y. Srebro, and R. P. J. Town, Phys. Plasmas **6**, 4022 (1999).

31. D. K. Bradley *et al*., Rev. Sci. Instrum. **66**, 716 (1995).

32. P. B. Radha, V. N. Goncharov, T. J. B. Collins, J. A. Delettrez, Y. Elbaz, V. Yu. Glebov, R. L. Keck, D. E. Keller, J. P. Knauer, J. A. Marozas, F. J. Marshall, P. W. McKenty, D. D. Meyerhofer, S. P. Regan, T. C. Sangster, D. Shvarts, S. Skupsky, Y. Srebro, R. P. J. Town, and C. Stoeckl, Phys. Plasmas **12**, 032702 (2005).

Plasma Characterization Using Ultraviolet Thomson Scattering from Ion-Acoustic and Electron Plasma Waves

Introduction

Optical Thomson scattering from collective plasma oscillations is a standard technique for diagnosing underdense plasma conditions in high-energy-density-physics experiments.[1] Thomson scattering is used to make spatially[2] and temporally resolved[3–5] measurements of the electron temperature (T_e), ion temperature (T_i), electron density (n_e), fluid velocity ($\mathbf{u}$), heat flux, ionization state (Z), and ion species fractions (for a multiple ion species plasma). Thomson scattering is used here to diagnose a number of plasma-wave instabilities including stimulated Brillouin scattering,[6–8] stimulated Raman scattering,[9] two-ion decay,[10] and two-plasmon decay.[11,12]

Thomson-scattering diagnostics take a local measurement of the plasma conditions averaged over a small volume (typically ~50 μm^3). The Thomson-scattering volume is created by overlapping the waist of the probe laser with an aperture stop within the collection system [typically a pinhole at the spectrometer's entrance (see Fig. 147.16)]. Light scattered from the Thomson-scattering volume is collected by a telescope and transported to a spectrometer/streak-camera pair to obtain spectral and temporal resolution.[2]

By conserving momentum ($\mathbf{k}_0 = \mathbf{k}_s + \mathbf{k}$), Thomson-scattering probes the plasma waves with wavelengths $\lambda = 2\pi \big/ |\mathbf{k}|$ ($\mathbf{k}_0$, $\mathbf{k}_s$, and $\mathbf{k}$ are the wave vectors of the probe beam, scattered light, and plasma wave, respectively). The normal modes of the plasma are observed in the Thomson-scattering spectra when probing the appropriate wavelengths, and the measured frequencies of these normal modes provide a powerful diagnostic of the plasma conditions. This collective Thomson-scattering regime is typically characterized by comparing the probed wavelength to the Debye length $\left[\lambda_{De} \equiv v_{te} \big/ \omega_{pe}\right.$, where $v_{te} = \sqrt{T_e \big/ m_e}$ is the electron thermal velocity, $\omega_{pe} = \sqrt{4\pi e^2 n_e \big/ m_e}$ is the plasma frequency in centimeter–gram–second (cgs) units, and m_e is the electron mass]. When $k\lambda_{De} < 1$, electron plasma wave (EPW) features are present in the spectrum; when $k\lambda_{De} < \sqrt{ZT_e \big/ T_i}$, ion-acoustic features are observed.

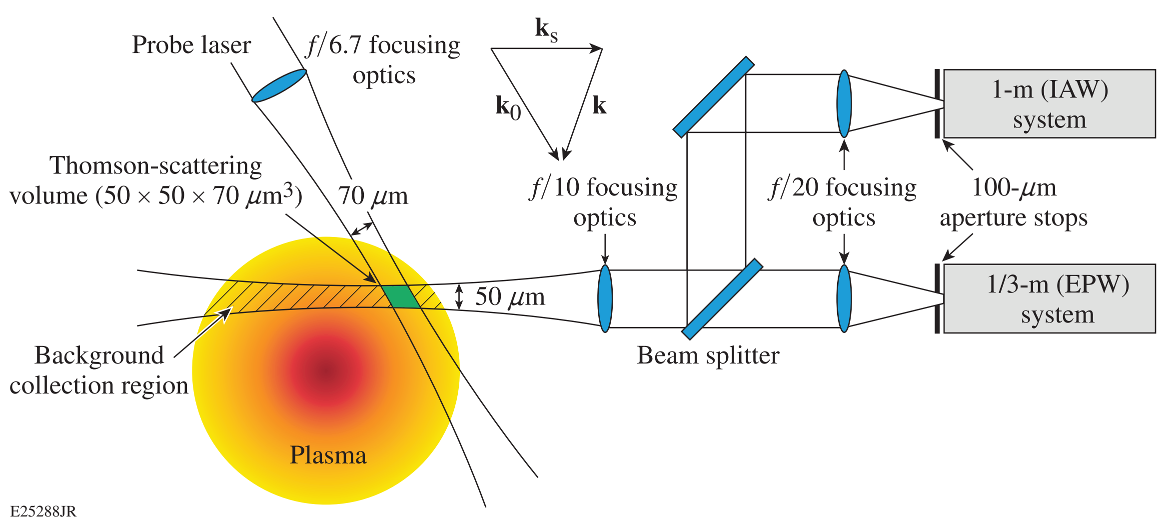

Figure 147.16
Thomson-scattering diagnostic configuration on OMEGA. Note that the schematic shows transmissive optics but the actual focusing/collection optics were reflective. IAW: ion-acoustic wave; EPW: electron plasma wave.

In practice, the complete shape of the Thomson-scattering spectrum is used to determine the plasma conditions by integrating the differential Thomson-scattered power per unit frequency per unit solid angle per unit volume over the Thomson-scattering volume and the solid angle of the collection optic:[1]

$$\frac{\partial^3 P_\mathrm{s}}{\partial\omega\partial\Omega\partial V}=\frac{I_0 n_\mathrm{e} r_0^2}{2\pi}\left|\hat{k}_\mathrm{s}\times\left(\hat{k}_\mathrm{s}\times\hat{E}_0\right)\right|\left(1+\frac{2\omega}{\omega_0}\right)S(k,\omega), \quad (1)$$

where I_0 is the incident probe-beam intensity, $r_0 = e^2/m_\mathrm{e}c^2$ is the classical electron radius, $\hat{E}_0$ is the polarization direction of the probe beam, and $\omega\,(\omega_0)$ is the frequency of the plasma wave (probe beam). The frequency of the scattered light is given by the matching condition

$$\omega_\mathrm{s}=\omega_0-\omega, \quad (2)$$

where $\omega \in \mathbb{R}$ and waves with negative frequency propagate antiparallel to $\mathbf{k}$.

The dynamic form factor (neglecting collisions and in the absence of applied magnetic fields) is derived from the linearized Vlasov equation (and Poisson's equation),

$$S(\mathbf{k},\omega)=\frac{(k\lambda_\mathrm{De})^2}{\pi\omega}\left[\left|1-\frac{\chi_\mathrm{e}}{\varepsilon}\right|^2\mathrm{Im}\{\chi_\mathrm{e}\}\right.$$
$$\left.+\sum_j\frac{Z_j^2 n_{i,j}T_{i,j}}{n_\mathrm{i}T_\mathrm{e}}\left|\frac{\chi_\mathrm{e}}{\varepsilon}\right|^2\mathrm{Im}\{\chi_{i,j}\}\right], \quad (3)$$

where the sum is over ion species, $n_{i,j}$ ($T_{i,j}$) is the number density (temperature) of the j^th ion species, $n_\mathrm{i} = \Sigma_j Z_j n_{i,j}$, and $\varepsilon \equiv 1 + \chi_\mathrm{e} + \Sigma_j\chi_{i,j}$ is the plasma dielectric function. The electron (χ_e) and ion (χ_i) susceptibilities are

$$\chi_\mathrm{s}(\mathbf{k},\omega)=\frac{4\pi q_\mathrm{s}^2 n_\mathrm{s0}}{m_\mathrm{s}k^2}\int_{-\infty}^{\infty}\mathrm{d}v\,\frac{\mathbf{k}\cdot\partial f_\mathrm{s0}/\partial\mathbf{v}}{\omega-\mathbf{k}\cdot\mathbf{v}-i\gamma}, \quad (4)$$

where n_{s0} and f_{s0} are the unperturbed number density and velocity distribution, respectively.

The dominant modes observed in collective Thomson-scattering experiments are given by the real part of the roots of $\varepsilon(\mathbf{k},\omega) = 0$. The difference in frequency between the scattered light and probe beam in the lab frame is determined by substituting the lab frame probe $(\omega_0'+\mathbf{k}_0\cdot\mathbf{u})$ and scattered-light $(\omega_\mathrm{s}'=\omega_\mathrm{s}+\mathbf{k}_\mathrm{s}\cdot\mathbf{u})$ frequencies and the plasma-wave frequency into Eq. (2), which, for scattering from ion-acoustic waves, gives

$$\Delta\omega_\pm=(\omega_\mathrm{s}'-\omega_0')=\pm kc_s-\mathbf{k}\cdot\mathbf{u}, \quad (5)$$

and from EPW's

$$\Delta\omega_\pm=(\omega_\mathrm{s}'-\omega_0')=\pm\sqrt{\omega_\mathrm{pe}^2+3k^2v_\mathrm{te}^2}-\mathbf{k}\cdot\mathbf{u}, \quad (6)$$

where $\Delta\omega_\pm$ corresponds to the frequency shift in the blue- and red-shifted light and $c_s=\sqrt{(ZT_\mathrm{e}+3T_\mathrm{i})/m_\mathrm{i}}$ is the sound speed (m_i is the ion mass).

Equation (5) shows that the frequencies of the two ion-acoustic wave (IAW) spectral peaks are given by the sound speed, fluid velocity, and plasma-wave vector. The frequency of the peaks in the EPW spectrum is dominated by the electron density because the contribution to the frequency shift related to the ω_pe^2 term in Eq. (6) is typically much larger than the contribution from the other terms. To obtain further information from Thomson-scattering spectra, synthetic power spectra generated using the kinetic description [Eq. (1)] are directly compared to measured spectra. In theory, arbitrary moments of the unperturbed velocity distributions (or their projections along $\mathbf{k}$) can be inferred by fitting Eq. (1) to measured spectra, but experimental uncertainties and degeneracy between parameter variations limit practical measurements to the fourth moment (heat flux) and require the shape of the unperturbed velocity distribution (f_{s0}) to be assumed (e.g., Maxwellian or Maxwellian with polynomial corrections).[13,14]

A common challenge in determining accurate plasma conditions from Thomson-scattering spectra is that measured spectra have broader peaks than calculated spectra. This has been attributed to ion–ion collisions,[13,15] plasma gradients, and probing a range of wave vectors.[16] As a first-order approximation, these effects can be accounted for by convolving the calculated spectra with a Gaussian response function. A physically consistent model is required, however, to measure parameters that depend on the detailed shape and not just the frequency of the spectral peaks.

The impact of gradients on Thomson-scattering measurements can be approximated by comparing the derivatives of Eqs. (5) and (6) to the linear Landau-damping rates. Gradient effects can be neglected when the broadening of the spectral peaks related to gradients is much less than the broadening caused by damping. In the weak damping limit, the damping rate is given by the imaginary part of the dielectric function divided by the spectral derivative of its real part evaluated at the normal mode frequency $\left[\omega_\text{i} = -\varepsilon_\text{i} / \left(\partial\varepsilon_\text{r} / \partial\omega\right)\right]$ (Ref. 17). Simplifying to 1-D, the dominant term in broadening of the spectral peaks caused by spatial gradients in Eq. (5) is typically the fluid velocity gradient $\delta\omega_\pm = \delta x k \partial u/\partial x$, and variations in the probed wave vector give $\delta\omega_\pm = \delta k(\pm c_s - u)$. Wave-vector variations are typically negligible in Eq. (6) and the dominant spatial term is $\delta\omega_\pm = \delta x \omega_\text{pe} / L_\text{n}$, where L_n is the density scale length.

Some of the physical effects that should be included when fitting measured Thomson-scattering spectra to calculated spectra are presented in this article. The following sections (1) present experimentally measured Thomson-scattering spectra from IAW's and EPW's from a series of direct-drive inertial confinement fusion implosions[18] on the OMEGA laser[19] and discuss spectral calibration and background radiation; (2) describe the techniques used to analyze the measured spectra; (3) present the methods used to calculate the plasma gradients and compare the results of fitting Thomson-scattering data with and without accounting for gradient effects; (4) discuss error analysis and present the results of applying these techniques to the measured scattering spectra; and (5) summarize our findings.

Thomson-Scattering Measurements

The Thomson-scattering diagnostic on OMEGA consists of a reflective *f*/10 collection system coupled to two spectrometer/streak-camera pairs.[2] The *f*/6.7 probe beam ($\lambda_{4\omega}$ = 263.25 nm) had a best-focus diameter of ~70 μm (Ref. 20). The spectral resolutions of the IAW and EPW systems were 0.05 nm and 0.5 nm, respectively. The scattering volume was ~50 × 50 × 70 μm^3. The angle between the probe beam and collection optic was 120°.

Figure 147.17 shows IAW and EPW Thomson-scattering spectra taken during 60-beam ($\lambda_{3\omega}$ = 351-nm) implosions on the OMEGA laser with the Thomson-scattering diagnostic configured to probe wave vectors perpendicular to the target normal. The targets were 870-μm-diam, 23-μm-thick spherical CH shells filled with 10 atm of D_2 gas. The laser pulse was a 1.2-ns square pulse preceded by three 100-ps picket pulses with a total energy of 12 kJ. Distributed phase plates[21] were used on each beam to define 860-μm full width at 95% flattop laser spots using *f*/6.7 lenses.

1. Spectral Sensitivity

The spectral sensitivity of the Thomson-scattering diagnostic was calculated using

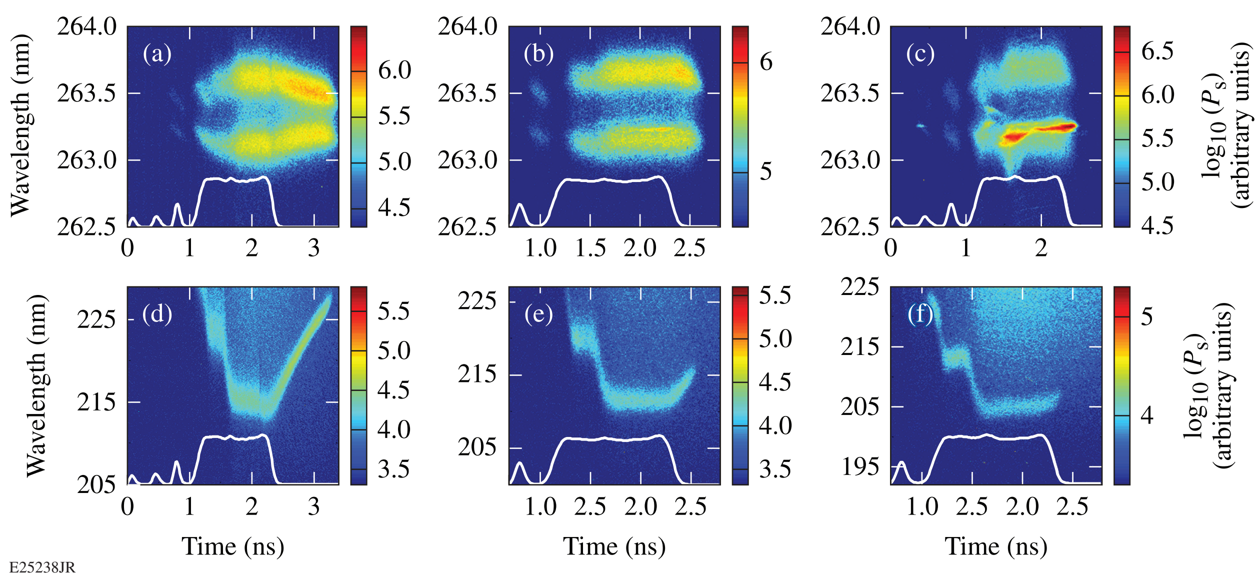

Figure 147.17
Thomson scattering from [(a)–(c)] IAW's and [(d)–(f)] EPW's at [(a),(d)] 400 μm, [(b),(e)] 300 μm, and [(c),(f)] 200 μm from the initial target surface. The drive-laser pulse shape is overlaid. The bright features at ~263.2 nm in the IAW spectra correspond to reflected or refracted light from the probe beam.

$$C(\lambda)=\frac{m\bullet k\bullet G\bullet px}{M}\left(\frac{\lambda}{hc}\right)Q(\lambda)T(\lambda)\frac{\mathrm{CCD}\,e^{-}\bullet\mathrm{nm}}{\mathrm{pixel}\bullet\mathrm{watt}},$$

the system parameters of which are shown in Table 147.I (h = 6.62×10^{-27} erg • s). The number of charge-coupled–device (CCD) counts per pixel is given by the product of the sensitivity with the power scattered $\left[C(\lambda)\int \mathrm{d}\Omega\int \mathrm{d}V\partial^3 P_\mathrm{s}/\partial\lambda\partial\Omega\partial V,\right.$ where $\left.\partial P_\mathrm{s}/\partial\lambda=(\mathrm{d}\omega/\mathrm{d}\lambda)\partial P_\mathrm{s}/\partial\omega\right]$ integrated over the scattering volume and the solid angle of the collection optics.

Figure 147.18 shows the ratio of measured-to-calculated signals for a variety of Thomson-scattering configurations (planar and spherical targets using 2ω and 4ω probe beams). The predictions are within a factor of 2 of the measured values, which is sufficient for determining appropriate probe energies and filtering when designing experiments. Although the fits shown in this article were normalized to minimize χ^2, it was necessary to account for the spectral sensitivity of the detector when fitting the EPW spectra because the sensitivity varied significantly (factor of 2) over the range of wavelengths included in the fits.

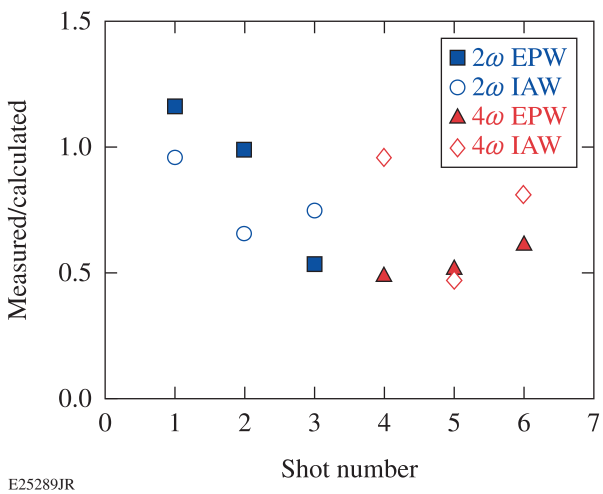

Figure 147.18
The ratio of measured-to-calculated peak scattering signals for the IAW and EPW features using 2ω (526.5-nm) and 4ω (263.25-nm) probe beams.

2. Background Radiation

The two primary sources of background radiation are bremsstrahlung and Thomson scattering from beams other than the Thomson probe. The two types of background radiation can be distinguished by noting that self-Thomson scattering of the drive beams occurs only when the drive lasers are on, while bremsstrahlung radiation can persist beyond the end of the laser pulse. The background radiation from Thomson scattering of other beams can be calculated using Eq. (1). The differential bremsstrahlung power in watts per unit wavelength (λ) per unit volume (V) per unit solid angle (Ω) is[1]

$$\frac{\partial^3 P_\mathrm{Br}}{\partial\lambda\partial\Omega\partial V}=\frac{6.61\times10^{-35}}{4\pi}\frac{gZ_\mathrm{eff}^2 n_\mathrm{e}^2}{\lambda^2 T_\mathrm{e}^{1/2}}e^{-0.124/\lambda T_\mathrm{e}}, \tag{7}$$

where $Z_\mathrm{eff}^2=\langle Z^2\rangle/\langle Z\rangle$, n_e is in cm^{-3}, λ is in cm, T_e is in keV, and the Gaunt factor $g \sim 1$.

Because the background radiation comes from the entire conical volume observed by the Thomson-scattering diagnostic, an accurate calculation of the background radiation requires spatially resolved knowledge of the plasma conditions along the entire line of sight of the Thomson-scattering collection system (Fig. 147.16). For all of the analysis in this article, the bremsstrahlung radiation was calculated by ray tracing simulations from the radiation–hydrodynamics code *LILAC*[22] from the collection optic back through the plasma while integrating Eq. (7) along the rays. The amount of background radiation observed by the diagnostic as a function of the distance from the image plane in the plasma is approximately constant because the col-

Table 147.I: Calibration parameters for the OMEGA Thomson-scattering diagnostic.

Parameter	Symbol	Value	Units
Optical transmission	$T(\lambda)$	~0.01	
Photocathode quantum efficiency	$Q(\lambda)$	~0.1	Photoelectron/photon
Spectrometer dispersion	m	0.002 to 0.03	nm/μm at PC
Sweep rate	k	1.1×10^{-12}	s/μm at CCD
Streak-tube gain	G	150	CCD electron/photoelectron
Pixel size	px	170	μm^2/pixel
Tube magnification	M	1.3	

PC: photocathode; CCD: charge-coupled device.

lection efficiency of the diagnostic falls off at the same rate as the area of the observed conical cross section increases. For practical estimates, a cylinder with the diameter of the optical aperture stop at the plasma image plane and a length sufficient to include the entire plasma along the view of the collection system is a reasonable background-collection volume.

Analysis

The plasma parameters in the Thomson-scattering data shown in Fig. 147.17 were inferred by minimizing $\chi^2 = \int \mathrm{d}\lambda \left[a_\mathrm{s} P_\mathrm{s}(\lambda) + a_\mathrm{B} P_\mathrm{B}(\lambda) - P_\mathrm{M}(\lambda)\right]^2$ for a series of spectral lineouts at different times (P_s, P_B, and P_M are the calculated Thomson-scattered power, the calculated background power, and the measured power, respectively; a_s and a_B are normalization coefficients). Distinct normalization coefficients were used for the Thomson-scattered and background radiation because their relative intensities are sensitive to optical alignment. The coefficients were determined by differentiating χ^2 with respect to a_s and a_B and solving the resulting system of equations:

$$a_\mathrm{s} \equiv \frac{\left(\int \mathrm{d}\lambda P_\mathrm{M} P_\mathrm{s}\right)\left(\int \mathrm{d}\lambda P_\mathrm{B}^2\right) - \left(\int \mathrm{d}\lambda P_\mathrm{M} P_\mathrm{B}\right)\left(\int \mathrm{d}\lambda P_\mathrm{s} P_\mathrm{B}\right)}{\left(\int \mathrm{d}\lambda P_\mathrm{s}^2\right)\left(\int \mathrm{d}\lambda P_\mathrm{B}^2\right) - \left(\int \mathrm{d}\lambda P_\mathrm{s} P_\mathrm{B}\right)},$$

$$a_\mathrm{B} \equiv \frac{\int \mathrm{d}\lambda P_\mathrm{B}^2 (P_\mathrm{M} - a_\mathrm{s} P_\mathrm{s})}{\int \mathrm{d}\lambda P_\mathrm{B}^2}.$$

Figure 147.19 shows spectra (averaged over 50 ps) from Figs. 147.17(a) and 147.17(d) taken at 2.8 ns. The spectra are compared to the best-fit spectra calculated with and without gradients. The IAW fit calculated without gradients is not even qualitatively similar to the measurement, while the EPW spectrum is reasonably well reproduced except in the wings of the spectral peak. The electron temperatures inferred independently from the EPW (1.15-keV) and IAW (0.77-keV) spectra were not self-consistent, and the ion temperature inferred from the IAW (1.62-keV) spectrum was unphysically high for the experimental configuration.

Gradients

1. Plasma Gradients

When gradients are present, the observed scattered light is a superposition of scattering from the various plasma conditions present within the scattering volume (spatially and temporally). The effects of gradients can be included in calculated spectra by taking a weighted sum of spectra calculated at the various plasma conditions.

The typical plasma parameters that are required to account for gradients within the Thomson-scattering volume are the spatial and temporal derivatives of the fluid velocity and electron density. Two methods of approximating the derivatives are ray-tracing hydrodynamic simulations or using mass and momentum conservation to calculate the gradients iteratively using measured spectra.

The fits shown in Fig. 147.19, where gradients were included, are significantly better than those without gradients (without introducing any additional degrees of freedom). Table 147.II compares plasma parameters inferred from the fits with and without gradients and the results of *LILAC* simulations. When

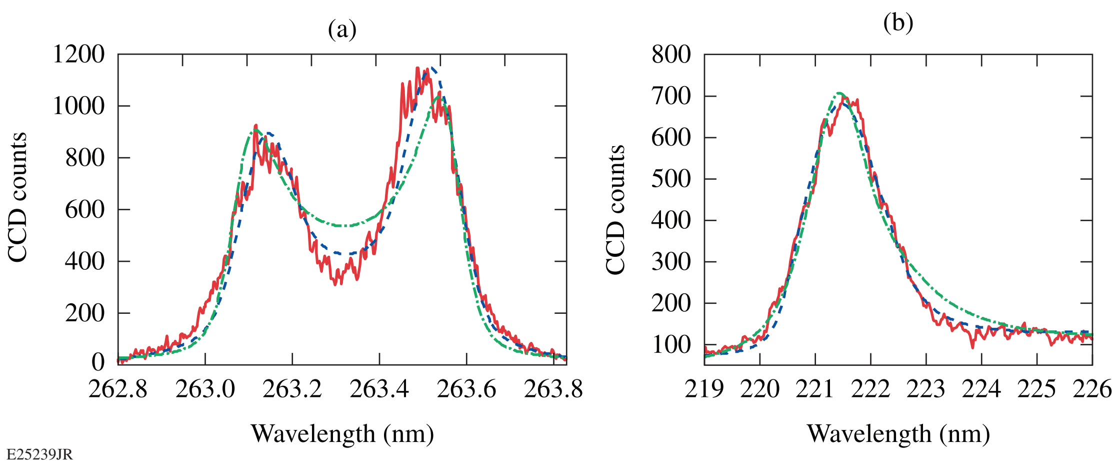

Figure 147.19
Thomson-scattering spectral lineouts at 2.8 ns (400 μm from the target) for scattering from (a) IAW's and (b) EPW's. The solid red curves are the measured spectra, the dashed blue curves are the best fit with gradients included, and the dashed–dotted green curves are the best fit without gradients.

Table 147.II: Comparison of the plasma parameters inferred from the calculated spectra shown in Fig. 147.19. The density is given in 10^{20} cm^{-3} and the temperatures are in keV. The plasma was assumed to be completely ionized. The typical error (see **Error**, p. 131) is ~5% for n_e, ~20% for T_e from the EPW, ~5% for T_e from the IAW, and ~40% for T_i.

	EPW fits		IAW fits	
	n_e	T_e	T_e	T_i
Gradients	4.40	0.93	0.85	0.82
No gradients	4.04	1.15	0.77	1.62
Simulation	4.45	0.78	0.78	0.58

gradients were included in the fits, the electron temperatures inferred from the IAW and EPW spectra were within 10%, and the ion temperature inferred from the IAW spectrum was slightly lower than the electron temperature, consistent with expectations for a laser-ablated plasma a few hundred picoseconds after the end of the laser pulse. The corresponding simulated plasma parameters shown in Table 147.II were also in better agreement with the inferred values when gradients were included in the fits. The electron density inferred from the EPW spectrum and the electron temperature inferred from the IAW spectrum were relatively insensitive to the effects of gradients.

The gradients in plasma parameters used to calculate the spectra in Fig. 147.19 were assumed to be independent and to have a Gaussian distribution of weights. While the gradients in various plasma parameters are not independent in reality, this assumption is valid when the gradient in a single plasma parameter is dominant. The choice of a Gaussian weight distribution was based on the results of ray-trace calculations and is primarily determined by the use of a Gaussian probe beam.

The plasma gradients were calculated by ray tracing density profiles from hydrodynamic simulations. Rays were traced from the probe to the detector and their overlap on a 3-D grid was used to calculate intensity-weighted histograms of the plasma conditions in the Thomson-scattering volume as a function of time. This technique provided a good approximation to the plasma gradients (both temporal and spatial) and implicitly accounts for the effects of refraction. It allowed for self-consistent comparisons between Thomson-scattering measurements and hydrodynamic simulations by comparing the inferred values from the measurement to the intensity-weighted average value in the calculated interaction volume.

An alternative approach to calculating plasma gradients that avoids relying on hydrodynamic predictions is to calculate the gradients iteratively using the measured spectra. This technique relies on the fact that the density and flow velocity can be determined relatively accurately without knowledge of the gradients. The temporal derivatives of the density and fluid velocity can be determined using time-resolved spectra, and the spatial derivatives can be calculated using conservation of mass and momentum. Assuming that the Thomson-scattering volume is small compared to the relevant scale lengths, the electron density and fluid velocity and their spatial and temporal derivatives can be treated as 1-D constants (spatially) over the scattering volume. The continuity and momentum equations for species α are

$$\frac{\partial n_\alpha}{\partial t}+\frac{\partial}{\partial x}n_\alpha u_\alpha=0,$$

$$\frac{\partial u_\alpha}{\partial t}+u_\alpha\frac{\partial u_\alpha}{\partial x}=-\frac{1}{m_\alpha n_\alpha}\frac{\partial}{\partial x}n_\alpha T_\alpha.$$

Defining the mass density ($\rho\equiv\Sigma_\alpha m_\alpha n_\alpha$) and center-of-mass velocity ($u\equiv\rho^{-1}\Sigma_\alpha m_\alpha n_\alpha u_\alpha$), assuming $m_e \ll m_i$, and solving for the spatial derivatives give

$$\frac{\partial\rho}{\partial x}=\frac{\rho}{u^2-\eta}\left(\frac{\partial u}{\partial t}-\frac{u}{\rho}\frac{\partial\rho}{\partial t}+\frac{\partial\eta}{\partial x}\right), \tag{8}$$

$$\frac{\partial u}{\partial x}=\frac{u}{u^2-\eta}\left(\frac{\eta}{\rho u}\frac{\partial\rho}{\partial t}-\frac{\partial u}{\partial t}+\frac{\partial\eta}{\partial x}\right), \tag{9}$$

where $\eta\equiv\left(ZT_e+T_i\right)/m_i$ for a single ion species and $\eta\equiv\left[\left(Z_1R+Z_2\right)T_e+\left(1+R\right)T_i\right]/\left(m_1R+m_2\right)$ for two-ion species $\left(R\equiv n_1/n_2\right)$. These equations are unchanged if the mass density is replaced by the electron density because the constant factor of $\rho=n_e\left(m_1R+m_2\right)/\left(Z_1R+Z_2\right)$ cancels out. Equations (8) and (9) do not allow for an iterative calculation of the terms involving the spatial gradients in temperature, but these are usually negligible.

2. Instrument Effects

Variations in the probed wave vector (because of the finite *f* number of the probe and collection optics) can lead to asymmetry in both the amplitude and width of the two IAW peaks. A wave-vector gradient results in asymmetric IAW peaks when variations in the probed wave vector result in the two scattering peaks being shifted by different magnitudes. The source of this asymmetry is the fact that the term corresponding to the propagation of IAW's in Eq. (5) (the first term on the right-hand side) causes the red- and blue-shifted IAW peaks to shift in opposite directions when the magnitude of the probed wave vector is varied, but the Doppler-shifted term (last term on the right-hand side) shifts both peaks in the same direction. A sufficient condition for wave-vector gradients to cause asymmetry in an IAW spectrum is

$$\left|\frac{\partial \Delta\omega_+}{\partial k}\right| - \left|\frac{\partial \Delta\omega_-}{\partial k}\right| = \left|c_s - u\cos\theta_{\mathrm{f}}\right| - \left|c_s + u\cos\theta_{\mathrm{f}}\right| \neq 0, \quad (10)$$

where θ_{f} is the angle between the flow velocity and the probed wave vector (**k**). This inequality is satisfied whenever $c_s > 0$, $u > 0$, and $\cos\theta_{\mathrm{f}} \neq 0$. This correction has a significant impact when using the IAW feature to infer the relative drift between the ions and electrons.[23]

The range of probed wave vectors was determined by treating the focusing and collection optics as a superposition of point sources and calculating each pairwise interaction. The wave-vector gradients cannot be approximated by 1-D Gaussian distributions because variations in the probed wave vector affect the magnitude of the observed wave vector and its projection along the fluid velocity. Each pairwise interaction was sorted into a bivariate histogram of wave-vector magnitude and projection along the fluid velocity (100 bins were used).

Figure 147.20 shows spectra calculated with and without gradient/wave-vector effects. To show the amount of broadening introduced by the gradients, the "no-gradients" spectra in Fig. 147.20 correspond to the same plasma parameters as the spectra where gradients were included. The IAW spectra [Fig. 147.20(a)], including the effects of gradients results in a nearly constant amount of spectral broadening because probed wave-vector gradients (which do not vary in time), were the dominant source of broadening. Density gradients cause significant broadening of the EPW spectral peaks [Fig. 147.20(b)] only during the rise of the laser pulse and after the laser is turned off because the temporal gradients vanish and the density scale length is relatively long when the plasma is in steady state.

Error

Figure 147.21 shows the electron densities and temperatures inferred from the EPW spectra and the plasma temperatures inferred from the IAW spectra. The plasma parameters predicted by 1-D hydrodynamic simulations (*LILAC*) are shown

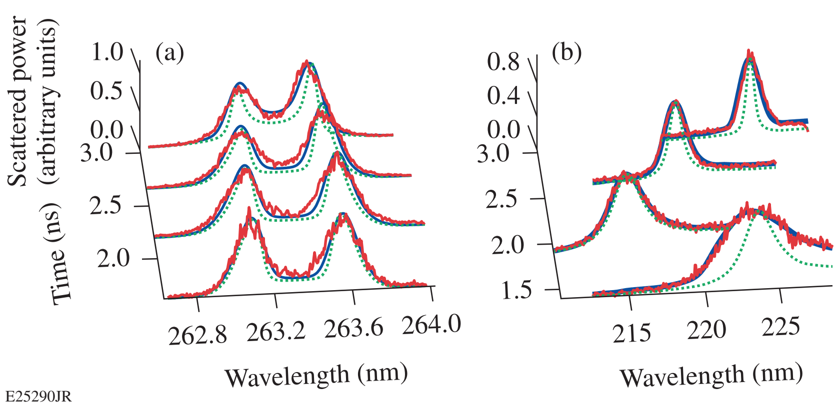

Figure 147.20
Measured spectral lineouts (red) and the corresponding calculated spectra (blue) at several different times for the (a) IAW and (b) EPW collected at 400 μm from the initial target surface. The green dotted curves correspond to calculated spectra using the same plasma parameters as the best-fit curve (blue) but without including gradient/wave-vector effects.

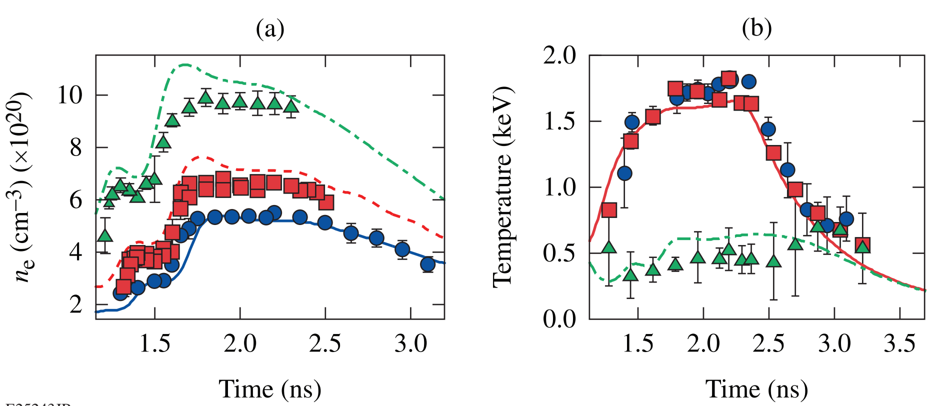

Figure 147.21
(a) Measured (symbols) and simulated (curves) electron density at 400 μm (circles), 300 μm (squares), and 200 μm (triangles) from the initial target surface. (b) Electron temperature inferred from IAW (squares) and EPW (circles) spectra, and ion temperature (triangles) inferred from the IAW spectra at 400 μm. The error in absolute timing is ~100 ps.

as solid curves. Because the error in Thomson-scattering measurements is sensitive to a number of fixed parameters, a Monte Carlo approach was used for the analysis. The inferred plasma parameters and error bars shown in Fig. 147.21 correspond to the mean and standard deviation of 100 fits, where the fixed parameters shown in Table 147.III were varied on each iteration using normally distributed values with variances characteristic to each parameter. The uncertainties shown in Table 147.III are generous estimates because the actual uncertainties (particularly in the gradients, which were the dominant source of error) are not well characterized. The error introduced by noise was accounted for by adding random noise (on each iteration) with variance equal to the variance between the measured spectrum and the initial best fit.

Table 147.III: Uncertainties included in error analysis.

Parameter	Standard deviation
Point-spread function	20%
Spectrometer dispersion	2%
Spectrometer alignment	100 μm
Gradients	20%

Summary

Simultaneous measurements of IAW and EPW Thomson-scattering spectra were obtained using a 263.25-nm probe beam. A fully reflective collection system was used to record light scattered from EPW's at electron densities up to 10^{21} cm^{-3}, which produced scattering peaks near 200 nm. An accurate analysis of the experimental Thomson-scattering spectra required accounting for plasma gradients, instrument sensitivity, optical effects, and background radiation. Two methods for calculating plasma gradients using hydrodynamic simulations or by fitting measured spectra iteratively were presented. Fits to measured Thomson-scattering spectra show the importance of including gradient effects. For example, the electron temperature inferred from the EPW feature was overestimated by ~35% when density gradients were neglected. The ion temperature was overestimated by ~50% when gradients in the flow and finite optical effects were neglected. The finite diameter of the probe focusing and collection optics was shown to introduce an asymmetry in the amplitude and width of the IAW features when a plasma flow was present.

ACKNOWLEDGMENT

This material is based upon work supported by the Department of Energy National Nuclear Security Administration under Award Number DE-NA0001944, the University of Rochester, and the New York State Energy Research and Development Authority.

REFERENCES

1. D. H. Froula, S. H. Glenzer, N. C. Luhmann, and J. Sheffield, *Plasma Scattering of Electromagnetic Radiation: Theory and Measurement Techniques*, 2nd ed. (Academic Press, Burlington, MA, 2011).
2. J. Katz, R. Boni, C. Sorce, R. Follett, M. J. Shoup III, and D. H. Froula, Rev. Sci. Instrum. **83**, 10E349 (2012).
3. S. H. Glenzer *et al*., Phys. Rev. Lett. **82**, 97 (1999).
4. D. S. Montgomery *et al*., Phys. Rev. Lett. **87**, 155001 (2001).
5. D. H. Froula, L. Divol, H. A. Baldis, R. L. Berger, D. G. Braun, B. I. Cohen, R. P. Johnson, D. S. Montgomery, E. A. Williams, and S. H. Glenzer, Phys. Plasmas **9**, 4709 (2002).
6. C. E. Clayton, C. Joshi, and F. F. Chen, Phys. Rev. Lett. **51**, 1656 (1983).
7. S. H. Glenzer *et al*., Phys. Rev. Lett. **86**, 2565 (2001).
8. D. H. Froula, L. Divol, and S. H. Glenzer, Phys. Rev. Lett. **88**, 105003 (2002).
9. K. L. Baker, R. P. Drake, B. S. Bauer, K. G. Estabrook, A. M. Rubenchik, C. Labaune, H. A. Baldis, N. Renard, S. D. Baton, E. Schifano, A. Michard, W. Seka, and R. E. Bahr, Phys. Rev. Lett. **77**, 67 (1996).
10. C. Niemann, R. L. Berger, L. Divol, D. H. Froula, O. Jones, R. K. Kirkwood, N. Meezan, J. D. Moody, J. S. Ross, C. Sorce, L. J. Suter, and S. H. Glenzer, Phys. Rev. Lett. **100**, 045002 (2008).
11. H. A. Baldis and C. J. Walsh, Phys. Fluids **26**, 1364 (1983).
12. R. K. Follett, D. H. Edgell, R. J. Henchen, S. X. Hu, J. Katz, D. T. Michel, J. F. Myatt, J. Shaw, and D. H. Froula, Phys. Rev. E **91**, 031104(R) (2015).
13. J. F. Myatt, W. Rozmus, V. Yu. Bychenkov, and V. T. Tikhonchuk, Phys. Rev. E **57**, 3383 (1998).
14. J. Zheng, C. X. Yu, and Z. J. Zheng, Phys. Plasmas **4**, 2736 (1997).
15. J. Zheng, C. X. Yu, and Z. J. Zheng, Phys. Plasmas **6**, 435 (1999).
16. T. E. Tierney IV *et al*., J. Phys. A, Math. Gen. **36**, 5981 (2003).
17. D. R. Nicholson, *Introduction to Plasma Theory, Wiley Series in Plasma Physics* (Wiley, New York, 1983).

18. V. N. Goncharov, T. C. Sangster, R. Betti, T. R. Boehly, M. J. Bonino, T. J. B. Collins, R. S. Craxton, J. A. Delettrez, D. H. Edgell, R. Epstein, R. K. Follet, C. J. Forrest, D. H. Froula, V. Yu. Glebov, D. R. Harding, R. J. Henchen, S. X. Hu, I. V. Igumenshchev, R. Janezic, J. H. Kelly, T. J. Kessler, T. Z. Kosc, S. J. Loucks, J. A. Marozas, F. J. Marshall, A. V. Maximov, R. L. McCrory, P. W. McKenty, D. D. Meyerhofer, D. T. Michel, J. F. Myatt, R. Nora, P. B. Radha, S. P. Regan, W. Seka, W. T. Shmayda, R. W. Short, A. Shvydky, S. Skupsky, C. Stoeckl, B. Yaakobi, J. A. Frenje, M. Gatu-Johnson, R. D. Petrasso, and D. T. Casey, Phys. Plasmas **21**, 056315 (2014).

19. T. R. Boehly, R. S. Craxton, T. H. Hinterman, J. H. Kelly, T. J. Kessler, S. A. Kumpan, S. A. Letzring, R. L. McCrory, S. F. B. Morse, W. Seka, S. Skupsky, J. M. Soures, and C. P. Verdon, Rev. Sci. Instrum. **66**, 508 (1995).

20. A. J. Mackinnon, S. Shiromizu, G. Antonini, J. Auerbach, K. Haney, D. H. Froula, J. Moody, G. Gregori, C. Constantin, C. Sorce, L. Divol, R. L. Griffith, S. Glenzer, J. Satariano, P. K. Whitman, S. N. Locke, E. L. Miller, R. Huff, K. Thorp, W. Armstrong, W. Bahr, W. Seka, G. Pien, J. Mathers, S. Morse, S. Loucks, and S. Stagnitto, Rev. Sci. Instrum. **75**, 3906 (2004).

21. T. J. Kessler, Y. Lin, J. J. Armstrong, and B. Velazquez, Proc. SPIE **1870**, 95 (1993).

22. J. Delettrez, R. Epstein, M. C. Richardson, P. A. Jaanimagi, and B. L. Henke, Phys. Rev. A **36**, 3926 (1987).

23. J. Hawreliak *et al.*, J. Phys. B: At. Mol. Opt. Phys. **37**, 1541 (2004).

Measurements of Hot-Electron Temperature in Laser-Irradiated Plasmas

Introduction

Recently published work[1–3] has studied the production of hot electrons related to the two-plasmon–decay (TPD) instability caused by laser pulse interaction with solid planar targets at an irradiation of 10^{14} W/cm^2. The hot electrons generated by TPD can preheat the cold compressed core in cryogenic implosions, thereby degrading the final compression and the target performance.[4–6] The first step in evaluating preheat is to determine the hot-electron temperature (T_{hot}). It is required for (a) deducing the total energy in hot electrons from the measured target x-ray radiation (K_α or continuum), and (b) calculating the hot-electron energy deposition in the fuel, i.e., the preheat. In previous work[1–3] we deduced T_{hot} from the measured hard x-ray (HXR) spectrum using a three-channel fluorescence-photomultiplier hard x-ray detector (HXRD).[7] The total energy in hot electrons (E_{hot}) was derived from the Mo K_α line intensity from an embedded Mo target. We extend those measurements here by

a. implementing a new nine-channel hard x-ray image-plate (HXIP) spectrometer to measure the hot-electron temperature more reliably and to derive the total energy in hot electrons. The spectrum is recorded on image plates (IP's) that are absolutely calibrated;[8] this feature makes it possible to derive E_{hot} (which was not the case with the uncalibrated HXRD, where E_{hot} was derived from K_α measurements). T_{hot} is found to be consistently lower (by a factor of 1.5 to 1.7) than the results reported in Ref. 1.

b. performing experiments to measure T_{hot} independently of the x-ray continuum spectrum (using ratios of K_α lines). The results (see **K_α Measurement of T_{hot}**, p. 138) were consistent with those derived from the continuum spectrum measured by HXIP.

c. measuring the thermal (softer) x-ray spectrum from the heated plasma and including it in the derivation of the total energy in hot electrons from the high-energy continuum.

d. demonstrating that the total energy in hot electrons derived from the measurements of K_α and from the high-energy continuum are consistent.

Determining preheat of fusion targets by hot electrons consists of two stages: (1) determining T_{hot} and then the total energy in hot electrons (or the total number of hot electrons) and (2) determining the energy deposited by the hot electrons in the compressed, cold target core. The second stage is target specific and is not discussed in this article. The first stage yields a quasi-universal curve of the fraction $f_{hot} = E_{hot}/E_L$ of laser energy (E_L) converted to hot electrons. As shown in Ref. 1, f_{hot} for planar targets rises steeply from the TPD threshold at a laser intensity of ~1.5×10^{14} W/cm^2 and then saturates at a value of a few percent above ~7×10^{14} W/cm^2. For spherical targets, the value of f_{hot} at a given laser intensity is smaller than it is for planar targets (because the density scale length is smaller in spherical targets). However, when f_{hot} is plotted as a function of the calculated TPD linear gain (or, alternatively, as a function of the measured T_{hot}), the measured f_{hot} points fall on a quasi-universal curve, independent of the target geometry.[2,3] Therefore, the planar-target measurements in this and previous articles[1–3] are relevant to calculating preheat in spherically imploding fusion targets: the fraction f_{hot} (and the concomitant T_{hot}) serves as a source to calculate the transport of hot electrons through the target at hand.

We used two methods to determine the total energy in hot electrons in our planar-target experiments: (1) the emission of K_α lines from an embedded high-Z target layer and (2) from the high-energy bremsstrahlung emission. The targets must be thick enough to capture most of the hot electrons. The targets in these experiments were either 30-μm-thick Mo or 125-μm-thick CH [the targets discussed in **K_α Measurement of T_{hot}** (p. 138) were for measuring T_{hot}, not E_{hot}, and were thicker]. In each case the range of most electrons is smaller than the target thickness, so most of the hot-electron energy is included. The high-Z targets were coated with a 30-μm-thick CH layer;

therefore, in all cases the laser interacted with CH, and the production of hot electrons was the same for the same laser intensity and target geometry. In the cases of high-Z targets, it was evident that the laser did not burn through the outer CH layer because of the absence of high-Z lines, except for the inner-shell K_α transitions, i.e., lines excited by the hot electrons.

Measuring E_{hot} in implosion experiments is difficult because (a) a high-Z layer cannot be incorporated into the target core without modifying the desired implosion characteristics and (b) the electrons (mostly those that miss the compressed core) lose a small fraction of their energy in making one pass through the target; this requires knowledge of the hot-electron divergence and refluxing back into the target. Cryogenic targets present an additional complication: even if E_{hot} is known, the preheat of the compressed fuel is not simple to derive because most of the HXR radiation is emitted by the CH corona, not the compressed fuel.[9] However, measuring the hot-electron source using thick planar targets makes it possible to calculate the transport of hot electrons through the fusion target at the same TPD gain or the same T_{hot}.

High-Z target layers in the previous work served a different purpose than in the present experiments: in the previous experiments, the high-Z K_α lines were used to determine E_{hot} (while the required T_{hot} came from HXRD, which, being uncalibrated, could not yield E_{hot}). Here, T_{hot} comes from HXIP (i.e., from the continuum slope) as well as from K_α line ratios (in the targets discussed in **K_α Measurement of T_{hot}**, p. 138), whereas E_{hot} also comes from the absolutely calibrated HXIP.

The laser configuration here was the same as in Ref. 1: four OMEGA EP[10] beams intersected the target at an angle of 23° with respect to the target normal. The laser pulse had a square temporal shape with a width of 2 ns. The irradiance was varied in the range of ~1 to 7×10^{14} W/cm^2 by increasing the laser energy in the range of ~2 to 9 kJ.

The energy in hot electrons (E_{hot}) was derived from either the K_α emission from the high-Z layers or the HXR bremsstrahlung radiation (using the calibrated readings of the HXIP). The relation between the measurements and E_{hot} was calculated using the *EGSnrc* Monte Carlo code.[11] The code assumes, as input, a Maxwellian hot-electron spectrum that is transported through the planar target. Figure 147.22 shows the calculated ratios of hot-electron energy and radiation yield as well as hot-electron energy and K_α emission. The blue curve uses the photostimulated luminescence unit (PSL) for channel 5 of the HXIP (see the next section). Using the intermediate channel 5 avoids the effect of thermal (or plasma) radiation on the lower channels, as well as the noise effect on the higher channels. Because of the good agreement of simulated and measured channel signals (see **Image-Plate–Based HXR Spectrometer**, p. 136), the same result would have been obtained with any other intermediate channel. The curves fall with increasing electron temperature because the radiation yields increase with T_{hot} [the curves rise at temperatures above ~100 keV (not shown in Fig. 147.22)]. Figure 147.22 can be used to determine E_{hot} (provided T_{hot} is known) because the x-ray yields for both the crystal x-ray spectrometer (XRS),[1] used to measure the Mo K_α line, and the image plates[8] are absolutely calibrated. The sharper fall of the HXIP (blue) curve was shown to be mitigated when the thermal radiation was included in the analysis (see **The Fraction of Laser Energy Converted to Hot Electrons**, p. 140). The blue curve in Fig. 147.22 assumes a 125-μm-thick CH target; the red curve is for a 30-μm-thick CH coating over 30-μm-thick Mo. If the HXIP is used with a target containing a high-Z layer, the HXR is emitted primarily by the high-Z material and the blue curve will be lower by a factor Z since the HXR yield from a

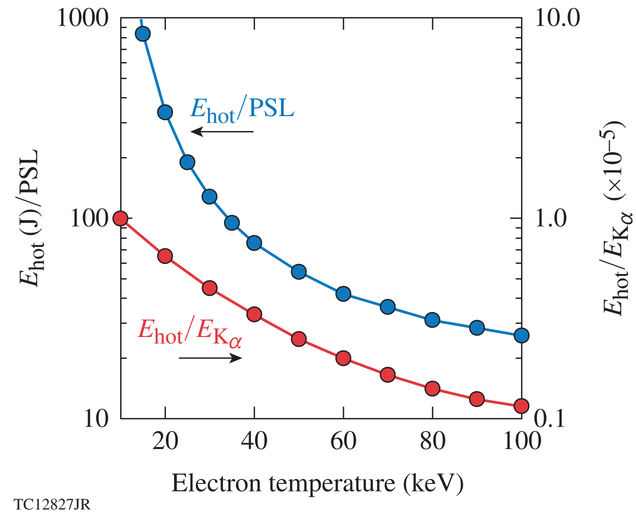

Figure 147.22
Curves used to determine the total energy in hot electrons for the two methods: using K_α and using continuum radiation. Shown are Monte Carlo calculations of the energy in hot electrons (E_{hot}) divided by either the measured Mo K_α energy per unit solid angle in the target normal direction (for targets containing a 30-μm-thick Mo layer) or the photostimulated luminescence (PSL) signal (for thick CH targets) registered by the fifth channel of the hard x-ray image-plate (HXIP) diagnostic. The inverse of these curves is simply the x-ray yield per energy in hot electrons. The x-ray energy is converted to PSL units using the known absolute calibration of the image plates.

thick target is proportional to Z.[12] For low hot-electron temperatures, the thermal plasma emission (which is not calculated by the Monte Carlo code) is not negligible with respect to the hot-electron bremsstrahlung. Therefore, the measured radiation must be corrected before applying the blue curve in Fig. 147.22 (discussed in **The Fraction of Laser Energy Converted to Hot Electrons**, p. 140).

Using planar targets has an advantage over spherical targets: the density scale length $\left[\equiv (1/n\, \mathrm{d}n/\mathrm{d}x)^{-1}\right]$ in these experiments (for the highest intensity) was ~400 μm (from 2-D hydrodynamic simulations of the experiments).[1] For a given laser irradiance, the laser energy required to generate a long-scale-length plasma is smaller for planar targets than for spherical targets.[13,14]

Image-Plate–Based HXR Spectrometer

The hot-electron temperature was measured by a nine-channel instrument (HXIP) using an image plate as a detector. Image plates[8] contain an x-ray–sensitive layer of phosphor $BaF(Br,I){:}Eu^{2+}$. Recorded data are read in the photostimulated luminescence (PSL) process. The sensitivity of image plates was shown to be linear over five orders of magnitude in intensity.[15] The HXIP is contained in a 3/4-in.-thick lead enclosure to reduce background radiation from other radiation sources in the vacuum tank, including scattered target radiation. Additionally, the inside faces of the lead were covered, sequentially, by copper, aluminum, and Mylar layers to attenuate fluorescence from the walls. The spectral decomposition of the target radiation is achieved by an array of nine filters (aluminum and copper of different thicknesses) placed halfway between the target and the image-plate detector, with a total distance between the target and the image plate of 49 cm. Figure 147.23 shows the x-ray transmission curves of the nine filters. Figure 147.24 shows a typical image obtained on the HXIP. A single image plate records the nine projections through the filters (the signals) as well as the background. The background measured outside the nine squares is a result of Compton scattering of target radiation from the components within the HXIP enclosure and fluorescence from these components (primarily the lead walls). An additional background is caused by smearing (or bleeding) from the IP laser scanning. One advantage of using an IP-based system is that the total background is recorded and can be subtracted from the signals. The background is significant for only the last few channels (i.e., highest photon energy). For the first few channels the relative background intensity is <1%, for the intermediate channels it is <5%, and for the last channels it is ~50% of the signals. Therefore, knowing the background is essential to determining a reliable temperature. If the background is not fully subtracted, the inferred temperature will be too high. One indication that the 2-D background subtraction is valid is that the resulting net signals are uniform over the square area of even the last channels.

The wall layers behind and close to the IP are one source of background radiation that requires special attention. Radiation that traverses the IP is absorbed into the back wall and scattered; fluorescent radiation enters the IP from its back. Monte Carlo

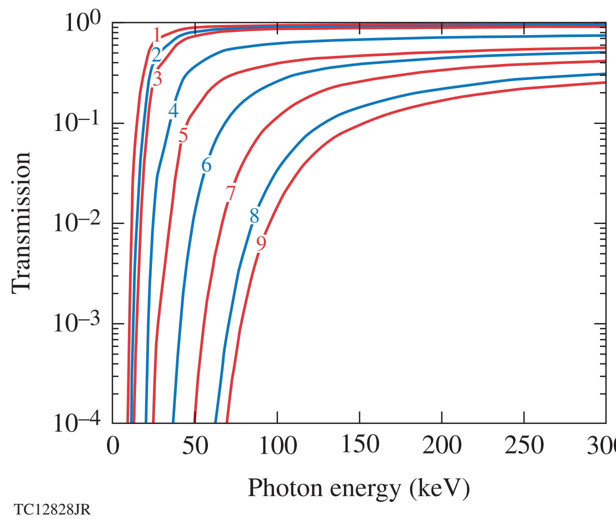

Figure 147.23
X-ray transmission of HXIP channels 1 to 9 (left to right) as a function of the photon energy. Higher-number channels are sensitive to progressively higher photon energies.

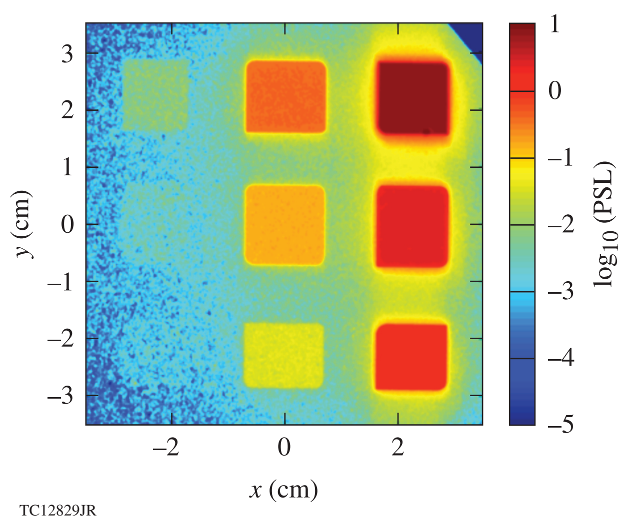

Figure 147.24
A typical image (logarithmic intensity scale) obtained on an HXIP. The signals from nine channels are seen, as well as a background around and between the signals. The ability to subtract the background around each channel image makes it possible to correctly determine the emitted spectrum.

simulations show that the back-wall radiation is not uniform over the scale of the signal size (15 mm × 15 mm) because of the proximity; however, its intensity is about 20× lower than the total signal for any of the channels and is therefore unimportant.

Since the scattered radiation is removed from the net signals, they reflect only the transmission through the filters, which can be calculated without a Monte Carlo simulation. Figure 147.25 shows the calculated response curves for several hot-electron temperatures. The target HXR radiation spectrum is assumed to be a single exponential of the temperature T_{hot}. The measurements at each channel agree well with the best-fit curve, suggesting that the exponential assumption is valid. Therefore, in calculating the energy in hot electrons from Fig. 147.22, any channel (above the first) should give the same result. The signal curve relating to the HXIP in Fig. 147.22 corresponds to channel 5. This channel was chosen because lower channels are burdened by the plasma thermal radiation and by bound-free absorption in high-Z layers; also, higher channels may be too weak for reliable measurement. The filters for channel 5 absorb strongly below ~20 keV; this is the reason for the steep drop in the HXIP curve in Fig. 147.22. A special case is the first channel, which includes the radiation tail from the thermal plasma. This is why we normalized the curves and the data points to the second (rather than the first) channel.

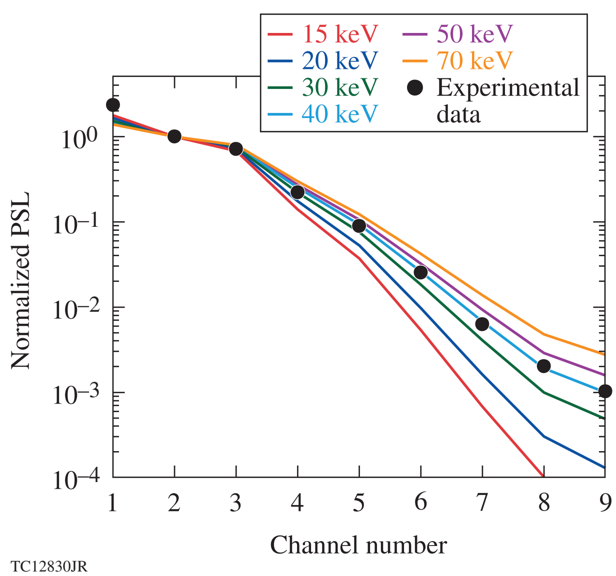

Figure 147.25
A typical example of determining hot-electron temperature using the HXIP data. The curves represent the nine-channel data, calculated by using the filter transmissions and measured image-plate (IP) sensitivity. To determine the hot-electron temperature, the curves of PSL data were normalized to the channel 2 data. Channel 1's excess signal is explained by the plasma thermal emission.

To demonstrate the role of the thermal radiation, Fig. 147.26(a) shows the simultaneous HXR spectrum deduced from the HXIP and the tail of the thermal spectrum measured using XRS. The irradiance for this shot was 6×10^{14} W/cm^2. The HXIP spectrum (which was assumed to be exponential) was obtained using the temperature from Fig. 147.25 and was normalized to the measured channel 5 signal. The target in Fig. 147.26 was CH; for a target with a higher-Z layer, the intensity of the induced component in Fig. 147.26(a) would be higher by about a fac-

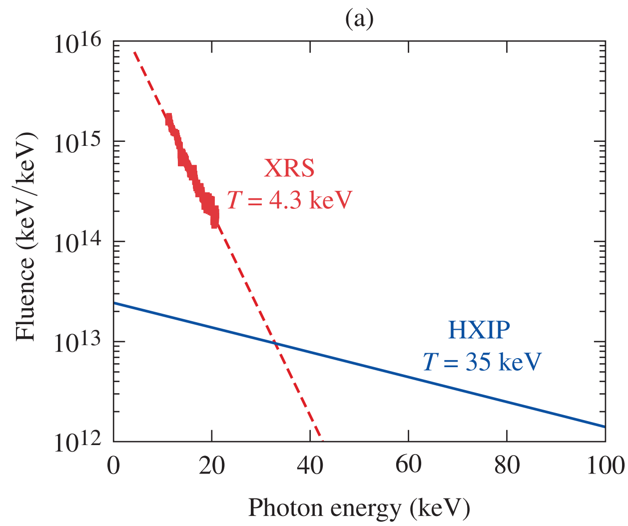

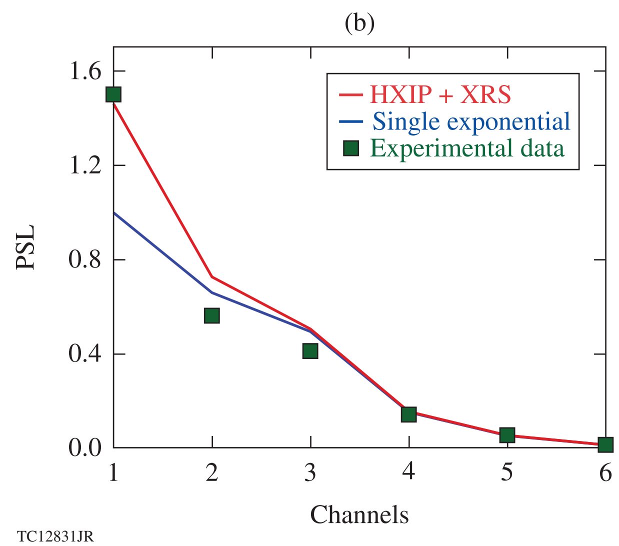

Figure 147.26
(a) The tail of the plasma-emission spectrum measured by the x-ray spectrometer (XRS) diagnostic (red line) and the hard x-ray (HXR) radiation emitted by hot electrons, as deduced from the HXIP measurement (blue line). (b) Using the sum of the two spectra in (a) as the input spectrum, the simulated channel signals (red curve) reproduce the measured HXIP data, including channel 1 (solid green squares), unlike the single-exponential spectrum (blue curve).

tor of Z, while the thermal plasma radiation would not change since the laser interaction in all cases is in the CH coating. Figure 147.26 illustrates that using HXIP alone to deduce the hot-electron temperature is valid if the first channel is excluded from the fitting procedure. Figure 147.26(b) shows the result of replacing the assumed single HXR exponential with the sum of the two exponentials in Fig. 147.26(a). The inclusion of the thermal spectrum with the calculated HXIP data agrees with the measured points for all channels, including channel 1. Figure 147.26(a) also shows that for low T_{hot} (<30 keV), the two spectra must be untangled (discussed in **The Fraction of Laser Energy Converted to Hot Electrons**, p. 140). For most fusion experiments, the relevant temperature is much higher and the low-temperature case is of interest only for exploring the TPD instability threshold. Figure 147.27 shows the compilation of temperature measurements from different shots as a function of the laser intensity. The temperatures inferred using HXIP measurements are represented by the orange squares. The other points in Fig. 147.27 are discussed in the next section.

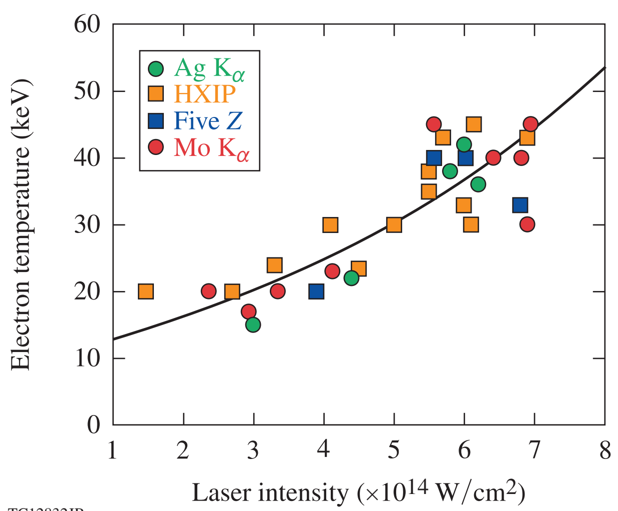

Figure 147.27
Compilation of measured hot-electron temperatures. The curve serves to guide the eye.

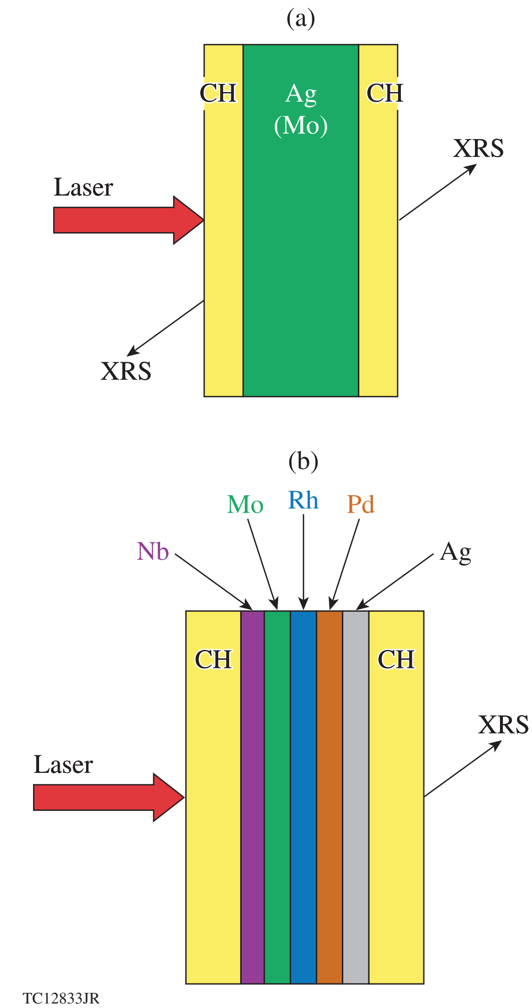

Figure 147.28
Target configurations for three experiments designed to measure the hot-electron temperature using K$_\alpha$ emission from high-Z targets (not drawn to scale): (a) Thick molybdenum and silver targets. The targets consist of 100-μm-thick molybdenum (127-μm-thick silver), coated with 30 μm of CH on both sides. The measured quantities are the ratios of K$_\alpha$ emission from the front and rear of the target. (b) Five-element target. The target consists of five layers (Nb, Mo, Rh, Pd, and Ag), 5 μm thick each, coated with 30 μm of CH on both sides. The measured quantity is the K$_\alpha$ for increasing-Z elements.

K$_\alpha$ Measurement of T_{hot}

Because of the discrepancy in temperature obtained by the HXRD (see Fig. 8 of Ref. 1) and HXIP, we designed three experiments to measure T_{hot} in a way that does not depend on the continuum radiation. Figure 147.28 shows the target configuration for the three experiments.

1. Thick Molybdenum Target

The target in this experiment consisted of 100-μm-thick molybdenum, coated with 30 μm of CH on both sides. The Mo thickness was larger than the range for most hot electrons, so the Mo K$_\alpha$ line was attenuated while traveling to the back of the target. For lower hot-electron temperatures, the K$_\alpha$ is emitted closer to the front surface, consequently being absorbed more when exiting from the back. Therefore, the ratio of the Mo K$_\alpha$ yields from the front and back of the target decreases with increasing T_{hot}. The ratio as a function of T_{hot} is calculated by the Monte Carlo code and shown in Fig. 147.29(a). The directions of the angles are with respect to the target normal. In the experiment, the laser intensity was varied and the calculated

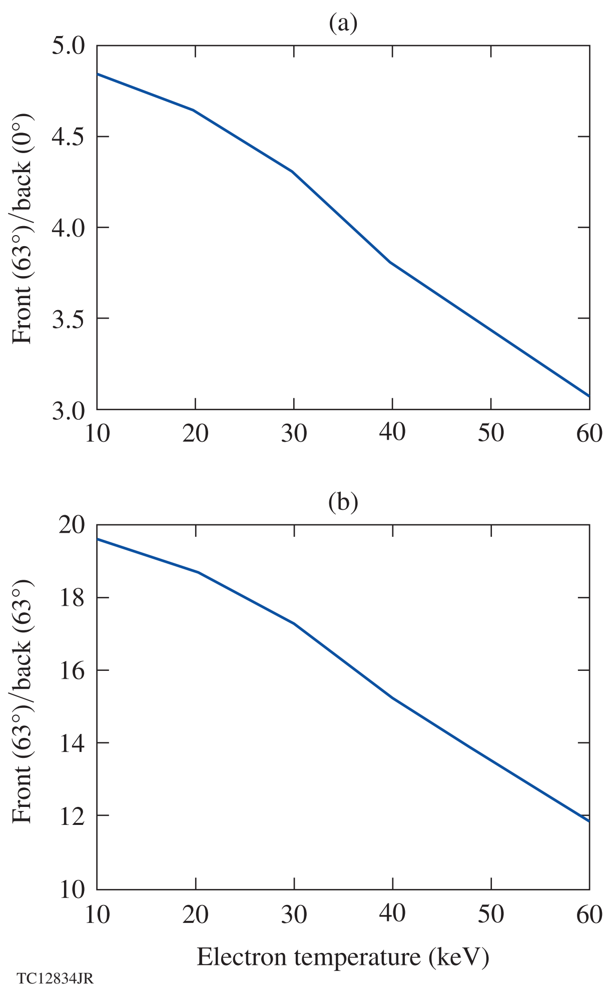

Figure 147.29
The ratios of Mo K_α and Ag K_α yields from the front and of the thick (a) Mo and (b) Ag targets, in the direction toward the detectors, as functions of the hot-electron temperature, calculated by the Monte Carlo code. The direction angles are with respect to target normal.

ratio was used to determine the hot-electron temperature. The resulting temperatures are shown by the solid red circles in Fig. 147.27.

2. Thick Silver Target

A 127-μm-thick silver layer replaced the molybdenum layer in the previous experiment. The Monte Carlo-calculated ratio of the Ag K_α yields from the front and back of the target is shown in Fig. 147.29(b). The higher K edge of Ag (25 keV) as compared with Mo (20 keV) reduces the fraction of coronal radiation available for K_α excitation and, therefore, supports ruling it out as a significant contributor to the observed K_α line (further discussed later in this section). The temperature results obtained are shown by the solid green circles in Fig. 147.27.

3. Five-Element Target

This target consists of five layers (Nb, Mo, Rh, Pd, and Ag), 5 μm thick each, coated with 30 μm CH [Fig. 147.28(b)]. The five corresponding K_α lines are measured using XRS behind the target. The five layers are of increasing Z in the direction of the incident laser (Z = 41, 42, 45, 46, 47). Each K_α line of a given Z can excite the K_α lines of the lower-Z layers but not of the higher-Z layers. The main effect is the decrease in the number of hot electrons as they move in the direction of the laser. Therefore, the XRS at the back of the target measures five K_α lines of decreasing intensity for increasing Z (see Fig. 147.30). This decrease is slower for a higher hot-electron temperature. The Monte Carlo code simulations of hot-election transport through this target are used to derive T_{hot} from the rate of K_α intensity drop as a function of Z (see Fig. 147.31). The resulting temperatures are shown by the solid blue squares in Fig. 147.27.

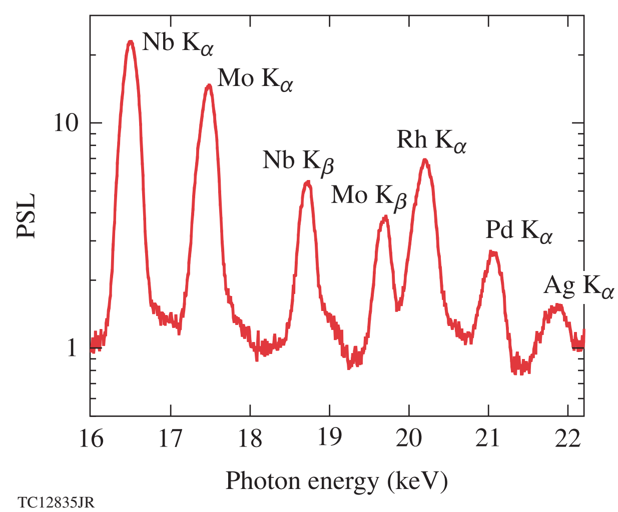

Figure 147.30
An example of the x-ray spectrum from a five-element target, as measured by XRS. The K_α lines are used to determine the hot-electron temperature.

In addition to hot electrons, K_α lines can also be excited by radiation, both thermal radiation from the plasma and bremsstrahlung radiated by the hot electrons. Only the latter, however, is accounted for in the Monte Carlo simulations. Therefore, plasma radiation's contribution to the K_α intensity must be shown to be negligible. A clear indication that the K_α lines in our experiments are excited primarily by hot electrons and their radiation and not by plasma radiation is seen in the laser-intensity dependence of the K_α lines. Figure 6 of Ref. 1 shows that for a rise in the laser intensity by a factor of ~2, the Mo K_α intensity rises by almost a factor of 10^4 (see also the related Fig. 147.34 below). On the other hand, the plasma

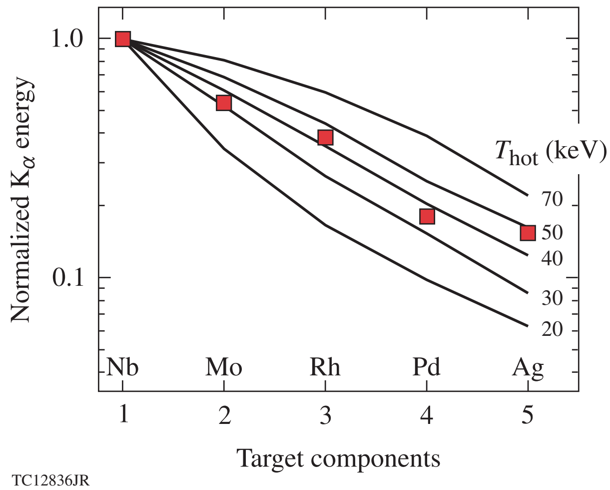

Figure 147.31
Monte Carlo curves of K_α intensity for the five elements in the target, normalized to the first element. The data (for a laser irradiance of 6×10^{14} W/cm^2) indicate $T_{hot} \sim 40$ keV.

continuum intensity increases about linearly with the laser intensity, indicating that its contribution to the K_α excitation is negligible. An additional indication of the ratio between the two radiations in a pure CH target is seen in Fig. 147.26(a). For T_{hot} higher than ~20 keV, the hot-electron curve rises sharply (because of increased hot-electron production at higher intensities) and the continuum above the K edge of, say, Ag (25 keV) will be dominated by the hot-electron bremsstrahlung.

The Fraction of Laser Energy Converted to Hot Electrons

As seen in Fig. 147.26(a), the total measured x-ray yield includes a contribution from the thermal-plasma radiation, which is not included in the Monte Carlo code calculations. Therefore, the measured radiation should be corrected (reduced) before using the blue curve in Fig. 147.22 to deduce the energy in hot electrons. This correction is especially important at low hot-electron temperatures, where the hot-electron bremsstrahlung drops very fast. Figure 147.32 shows the correction factor; i.e., the ratio $R = PSL_{hot}/PSL_{total}$ of hot-electron–induced radiation and total radiation (including the thermal-plasma radiation), measured in channel 5, as a function of T_{hot}. The correction factor R is calculated using the measured composite x-ray spectra, like those of Fig. 147.26(a): the spectrum (with and without the plasma component) is multiplied by channel 5, filters transmission and the IP sensitivity, and then integrated over photon energies. This ratio can be approximated as $R = -0.521 + 4.81 \times 10^{-2} \times T_{hot} - 3.59 \times 10^{-4} \times T_{hot}^2$, where T_{hot} is in keV. The results are shown in Fig. 147.32.

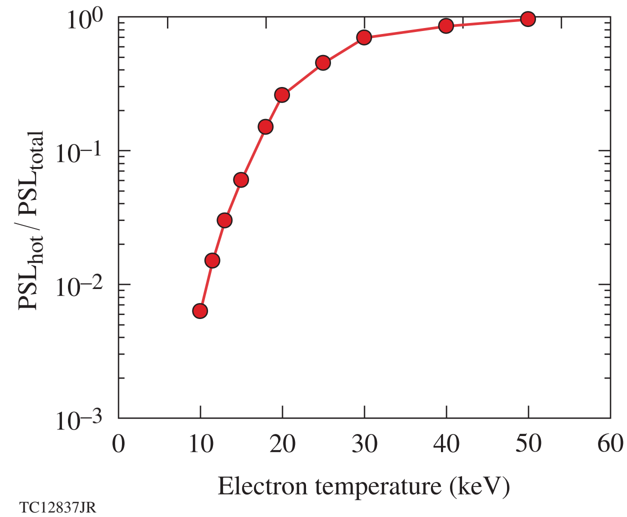

Figure 147.32
Relative contribution of the plasma electrons and the hot electrons to the measured total x-ray spectrum. Experimental curves such as the two curves shown in Fig. 147.26(a), for various laser intensities, are convolved with the HXIP sensitivity of channel 5; plotted is the ratio of the signal caused by hot electrons alone and that caused by the hot electrons plus the plasma radiation. As the hot-electron temperature drops, so does the relative contribution of hot-electron radiation to the total measured x-ray yield.

Using the correction factor R, the HXIP curve in Fig. 147.22 can now be modified to allow for the contribution of the plasma radiation with the results shown in Fig. 147.33. The red curve is the corresponding blue curve from Fig. 147.22, shown as reference. To use this curve, the experimental radiation must be corrected for the plasma radiation. The blue curve in Fig. 147.33 was obtained by multiplying the red curve by the correction factor (Fig. 147.32). When using the blue curve in Fig. 147.33, the total measured channel 5 readings must be used (without subtracting the thermal contribution). The corrected curve indicates that the dependence of the hot-electron yield on hot-electron temperature is weak. Therefore, the discrepancy between the HXRD and HXIP temperature results (see the **Introduction**, p. 134) is not very important when calculating the energy in hot electrons; however, the penetration depth of hot electrons, relevant to preheat calculation, remains important.

To verify the validity of the present derivation of hot-electron energy, Fig. 147.34 compares the fraction of laser energy converted into hot electrons (f_{hot}) using the present HXIP results (blue circles) and previous Mo K_α results[1] (red circles). The HXIP results refer to 125-μm-thick CH targets, whereas the Mo K_α results refer to CH-coated Mo targets. The tempera-

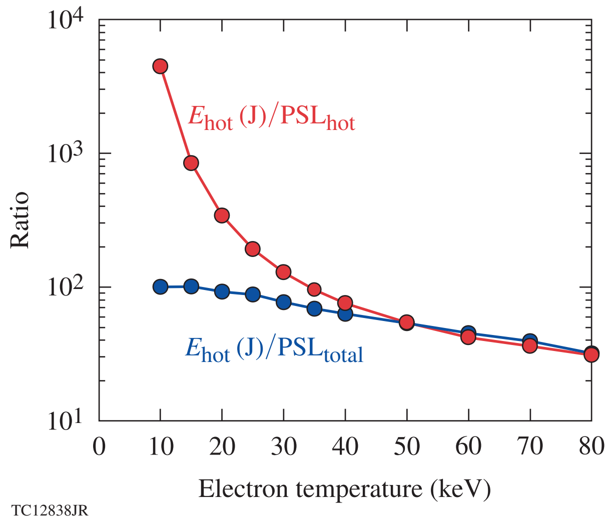

Figure 147.33
The blue curve in Fig. 147.22 is adjusted to include the contribution of the thermal radiation, using the results of Fig. 147.32. The red curve here reproduces the unadjusted Fig. 147.22 curve. Since that curve shows E_{hot}/PSL_{hot} and Fig. 147.32 shows the ratio PSL_{hot}/PSL_{total}, the product of these quantities is E_{hot}/PSL_{total} and is represented here by the blue curve. When the adjusted, measured channel 5 signal is used, the resulting E_{hot} is seen to depend only weakly on T_{hot}.

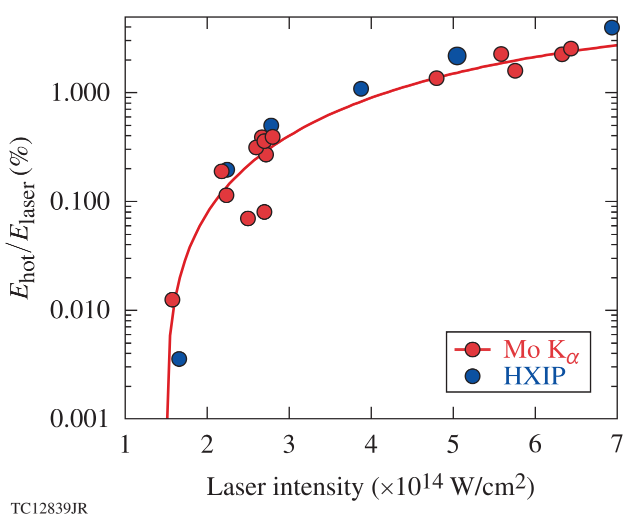

Figure 147.34
The fraction of total laser energy converted to energy in hot electrons. The red circles represent the data from Ref. 1, using the Mo K_α line from a CH-coated Mo target, with T_{hot} corrected based on the laser-intensity scaling found in the present experiments. The blue circles represent data from a 125-μm-thick CH target, using the HXR continuum measured by HXIP. The results indicate that these two methods of deducing E_{hot} are equivalent.

ture values in the older experiment were corrected using the scaling with laser intensity obtained in this experiment. The agreement shows that the method for measuring hot-electron energy using the HXIP (corrected for the thermal radiation) is consistent with the method in Ref. 1 using Mo K_α lines. The agreement also shows that the production of hot electrons in CH-coated Mo is very similar to that in thick CH targets. It should be noted that the large possible error in f_{hot} (because of the thermal contribution) near the threshold can be tolerated because of the steep rise, and that typical fusion implosion experiments correspond to the upper end of the intensity range in Fig. 147.34, where the thermal contribution is negligible.

Conclusion

This article extends our previous measurements[1–3] of the temperature and total energy of laser-generated hot electrons, using 2-ns UV pulses at 10^{14} W/cm^2 on the OMEGA EP laser.[1–3] The three-channel fluorescence-photomultiplier detector (HXRD) was replaced with a nine-channel image-plate–based detector (HXIP). For the same conditions, the measured temperatures are lower than those measured using a HXRD by a factor of ~1.5 to 1.7. This measurement was supplemented with three experiments that measured the hot-electron temperature using K_α emission from high-Z target layers. These experiments gave temperatures that were consistent with those measured using the HXIP. The lower hot-electron temperatures, however, do not significantly impact the deduced total energy in hot electrons when the effect of the thermal plasma radiation on bremsstrahlung measurements is taken into account.

Lower temperatures mean that the simulated preheat in cryogenic spherical implosions, using HXRD temperatures, could be overestimated, however, since lower T_{hot} entails smaller penetration into the target core. In fact, recent cryogenic experiments[16] show that the preheat is smaller than predicted (by measuring the degradation in areal density compared to the one predicted), and even the preheat remains small when the production of hot electrons increases significantly. This could be caused by reduced penetration of hot electrons into the core.

While the fraction of laser energy converted into hot electrons is found to increase up to 1% to 3% with the laser intensity, other factors can contribute to lowering the preheat of the cold dense shell in spherical implosions, such as a large angular divergence of the hot electrons.[17] High-Z ablators are capable of reducing the production of hot electrons because of a shorter scale length and a higher plasma temperature.[18]

ACKNOWLEDGMENT

This material is based upon work supported by the Department of Energy National Nuclear Security Administration under Award Number DE-NA0001944, the University of Rochester, and the New York State Energy Research and Development Authority.

REFERENCES

1. B. Yaakobi, P.-Y. Chang, A. A. Solodov, C. Stoeckl, D. H. Edgell, R. S. Craxton, S. X. Hu, J. F. Myatt, F. J. Marshall, W. Seka, and D. H. Froula, Phys. Plasmas **19**, 012704 (2012).

2. D. H. Froula, B. Yaakobi, S. X. Hu, P.-Y. Chang, R. S. Craxton, D. H. Edgell, R. Follett, D. T. Michel, J. F. Myatt, W. Seka, R. W. Short, A. Solodov, and C. Stoeckl, Phys. Rev. Lett. **108**, 165003 (2012).

3. D. H. Froula, D. T. Michel, I. V. Igumenshchev, S. X. Hu, B. Yaakobi, J. F. Myatt, D. H. Edgell, R. Follett, V. Yu. Glebov, V. N. Goncharov, T. J. Kessler, A. V. Maximov, P. B. Radha, T. C. Sangster, W. Seka, R. W. Short, A. A. Solodov, C. Sorce, and C. Stoeckl, Plasma Phys. Control. Fusion **54**, 124016 (2012).

4. J. D. Lindl, *Inertial Confinement Fusion: The Quest for Ignition and Energy Gain Using Indirect Drive* (Springer-Verlag, New York, 1998), Chap. 11.

5. *LLE Review Quarterly Report* **79**, 121, Laboratory for Laser Energetics, University of Rochester, Rochester, NY, LLE Document No. DOE/SF/19460-317, NTIS Order No. DE2002762802 (1999).

6. V. A. Smalyuk, D. Shvarts, R. Betti, J. A. Delettrez, D. H. Edgell, V. Yu. Glebov, V. N. Goncharov, R. L. McCrory, D. D. Meyerhofer, P. B. Radha, S. P. Regan, T. C. Sangster, W. Seka, S. Skupsky, C. Stoeckl, B. Yaakobi, J. A. Frenje, C. K. Li, R. D. Petrasso, and F. H. Séguin, Phys. Rev. Lett. **100**, 185005 (2008).

7. C. Stoeckl, V. Yu. Glebov, D. D. Meyerhofer, W. Seka, B. Yaakobi, R. P. J. Town, and J. D. Zuegel, Rev. Sci. Instrum. **72**, 1197 (2001).

8. A. L. Meadowcroft, C. D. Bentley, and E. N. Stott, Rev. Sci. Instrum. **79**, 113102 (2008).

9. A. R. Christopherson, R. Betti, W. Theobald, and J. Howard, "Probing Hot Electron Preheat and Hot Spot Asymmetries in ICF Implosions," the Ninth International Conference on Inertial Fusion Sciences and Applications (IFSA 2015), Seattle, WA, 20–25 September 2015 (Paper Th.O.2.2).

10. *LLE Review Quarterly Report* **125**, 37, Laboratory for Laser Energetics, University of Rochester, Rochester, NY, LLE Document No. DOE/NA/28302-993 (2010).

11. I. Kawrakow, Med. Phys. **27**, 485 (2000); I. Kawrakow, E. Mainegra-Hing, D. W. O. Rogers, F. Tessier, and B. R. B. Walters, "The EGSnrc Code System: Monte Carlo Simulation of Electron and Photon Transport," National Research Council Canada, Ottawa, Canada, NRCC Report PIRS-701 (May 2011).

12. K. A. Brueckner, Phys. Rev. Lett. **36**, 677 (1976); R. P. Drake, R. E. Turner, B. F. Lasinski, E. A. Williams, K. Estabrook, W. L. Kruer, E. M. Campbell, and T. W. Johnston, Phys. Rev. A **40**, 3219 (1989); T. Döppner *et al*., Phys. Rev. Lett. **108**, 135006 (2012).

13. D. T. Michel, A. V. Maximov, R. W. Short, J. A. Delettrez, D. Edgell, S. X. Hu, I. V. Igumenshchev, J. F. Myatt, A. A. Solodov, C. Stoeckl, B. Yaakobi, and D. H. Froula, Phys. Plasmas **20**, 055703 (2013).

14. D. T. Michel, A. V. Maximov, R. W. Short, S. X. Hu, J. F. Myatt, W. Seka, A. A. Solodov, B. Yaakobi, and D. H. Froula, Phys. Rev. Lett. **109**, 155007 (2012).

15. J. Miyahara *et al*., Nucl. Instrum. Methods Phys. Res. **A246**, 572 (1986).

16. V. N. Goncharov, T. C. Sangster, R. Betti, T. R. Boehly, M. J. Bonino, T. J. B. Collins, R. S. Craxton, J. A. Delettrez, D. H. Edgell, R. Epstein, R. K. Follet, C. J. Forrest, D. H. Froula, V. Yu. Glebov, D. R. Harding, R. J. Henchen, S. X. Hu, I. V. Igumenshchev, R. Janezic, J. H. Kelly, T. J. Kessler, T. Z. Kosc, S. J. Loucks, J. A. Marozas, F. J. Marshall, A. V. Maximov, R. L. McCrory, P. W. McKenty, D. D. Meyerhofer, D. T. Michel, J. F. Myatt, R. Nora, P. B. Radha, S. P. Regan, W. Seka, W. T. Shmayda, R. W. Short, A. Shvydky, S. Skupsky, C. Stoeckl, B. Yaakobi, J. A. Frenje, M. Gatu-Johnson, R. D. Petrasso, and D. T. Casey, Phys. Plasmas **21**, 056315 (2014).

17. B. Yaakobi, A. A. Solodov, J. F. Myatt, J. A. Delettrez, C. Stoeckl, and D. H. Froula, Phys. Plasmas **20**, 092706 (2013).

18. R. K. Follett, J. A. Delettrez, D. H. Edgell, V. N. Goncharov, R. J. Henchen, J. Katz, D. T. Michel, J. F. Myatt, J. Shaw, A. A. Solodov, C. Stoeckl, B. Yaakobi, and D. H. Froula, Phys. Rev. Lett. **116**, 155002 (2016).

A Pulse-Front-Tilt–Compensated Streaked Optical Spectrometer with High Throughput and Picosecond Time Resolution

Introduction

Time-resolved spectroscopy, using an optical spectrometer coupled to a streak-camera recording system, is a common diagnostic technique in the field of short-pulse laser physics research. Streaked spectrometers analyze a point-source input by aligning the dispersed output of the spectrometer to the input slit of a streak camera. These instruments are particularly effective for single-shot experiments requiring detailed measurements of optical spectra with temporal resolutions of the order of picoseconds to nanoseconds. The overall temporal resolution of such instruments depends on the streak camera's performance and the configuration of the spectrometer used. For many demanding applications, a streaked-spectrometer instrument must have high spectral and temporal resolution while maintaining large optical throughput. These three parameters are intrinsically linked and the ability to simultaneously optimize them is limited. This article presents a novel technique that decouples throughput considerations from the spectral- and temporal-resolution optimization process.

Background of Pulse-Front Tilt

Pulse-front tilt (PFT) is a time-shearing effect inherent to angular dispersion in which the arrival time of light varies linearly with position across the beam in the plane of dispersion.[1,2] PFT can be explained geometrically by examining the path-length difference introduced across the beam at a dispersive interface (Fig. 147.35). In the case where a diffraction grating is used to generate angular dispersion, the total PFT after dispersion is given by

$$\Delta t = Nm\lambda / c, \tag{1}$$

where N is the total number of illuminated grating groves, m is the grating order used, λ is the wavelength of light, and c is the speed of light. An important quantity in spectrometer design is the angular dispersion that relates the change in angle of diffraction β to the change in wavelength and is given by

$$\mathrm{d}\beta / \mathrm{d}\lambda = mG / \cos(\beta). \tag{2}$$

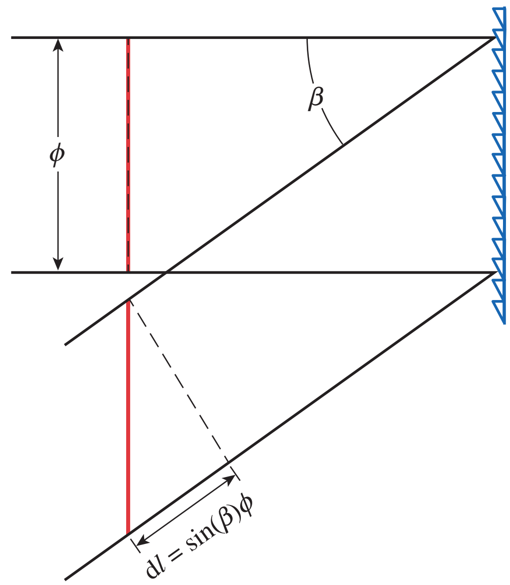

Figure 147.35
Pulse-front tilt (PFT) is introduced by the path-length asymmetries of a beam exiting an angularly dispersive medium. The total PFT increases with beam diameter and angular dispersion.

Combining Eqs. (1) and (2), and relating N to the beam diameter ϕ and groove density G, produces an expression that illustrates the difficulty of designing a spectrometer with high spectral resolution, good temporal resolution, and large throughput:

$$\Delta t = \frac{\phi\lambda\cos(\beta)}{c}\frac{\mathrm{d}\beta}{\mathrm{d}\lambda}. \tag{3}$$

For a given angular dispersion, attempts to improve throughput by increasing the size of the collection optic will result in a loss of temporal resolution.

Spectral- and Temporal-Resolution Limitations

The size of an individual spectral-resolution element can be defined as the product of the instrument's spatial impulse response multiplied by the linear dispersion ($\delta\lambda = \Delta x\ \mathrm{d}\lambda/\mathrm{d}x$). The linear dispersion ($\mathrm{d}\lambda/\mathrm{d}x$) is the product of the angular dispersion and the output image's focal length. The imaging performance of the spectrometer, the point-spread function (PSF_{SC}) of the streak camera, and the size of the input object's image (wM) all contribute to the spatial impulse response. Adding these terms in quadrate gives

$$\Delta x^2 = (wM)^2 + PSF_{geo}^2 + PSF_{dif}^2 + PSF_{SC}^2, \qquad (4)$$

where w is the size of the input object, M is the magnification of the spectrometer along the axis of dispersion, and PSF_{geo} and PSF_{dif} are the geometric and diffractive limitations, respectively, of the spectrometer imaging optics. It is worth noting that, for a fixed collection aperture, attempts to improve spectral resolution by using a longer output focal length will increase M if asymmetric conjugates are used or will increase PFT if symmetric conjugates are used.

Three main mechanisms generally limit the temporal resolution of a streak camera: (1) the line-spread transit (LST) time, (2) electron transit time spread (TTS), and (3) space-charge broadening. LST is defined as the time it takes the sweep to traverse the width of a static cathode image and can be reduced by using a fast sweep rate and a narrowly focused cathode image. TTS arises because electrons generated at the photocathode have a distribution of initial velocity vectors and do not take the same amount of time to reach the phosphor output screen. TTS can be decreased by reducing the overall transit time or narrowing the excess electron energy distribution through judicious choice of photocathode material and/or signal wavelengths. Space-charge broadening is caused by the repulsive force felt from neighboring photoelectrons as they travel down the tube. Space-charge broadening spoils the image of the cathode and effectively increases the achieved LST. This effect can be managed by keeping the total electron-current density below an experimentally determined threshold level.

Segmented Spectrometer Design

Using a rectangular mask to limit the beam size and, therefore, the total number of grooves illumined at the grating surface is a viable technique to decrease total PFT.[3] While simple and effective, this method reduces system throughput and is not suitable for low-signal applications. Additionally, decreasing the beam size increases the imaging f number. When taken to the extreme, the masked aperture generates a large diffraction-limited spot size that spoils the instrument's spectral resolution. This result is consistent with the concept that spectral resolving power is directly proportional to the number of illuminated grating grooves.

A new type of spectrometer layout is proposed that uses the concept of a masked grating aperture to improve temporal resolution but maintains the throughput of an unmasked system. This is accomplished by breaking the full-aperture beam into a series of discrete rectangular segments. Each segment is prescribed an appropriate amount of delay, such that after the beam exits the dispersive medium, the individual segments are temporally aligned. Figure 147.36 shows how a transmission echelon optic is used to generate the required delay profile to compensate the overall PFT. The residual PFT is only what is accumulated across a single segment. The temporal delay between each segment is determined by the step height of the echelon optic and is set to be equal to the total PFT of a single segment. The practical limitations to the minimum echelon step width are the same as for a masked spectrometer. The echelon step width is minimized until the diffraction-limited spot size is comparable to the other contributing terms in the spectrometer's PSF.

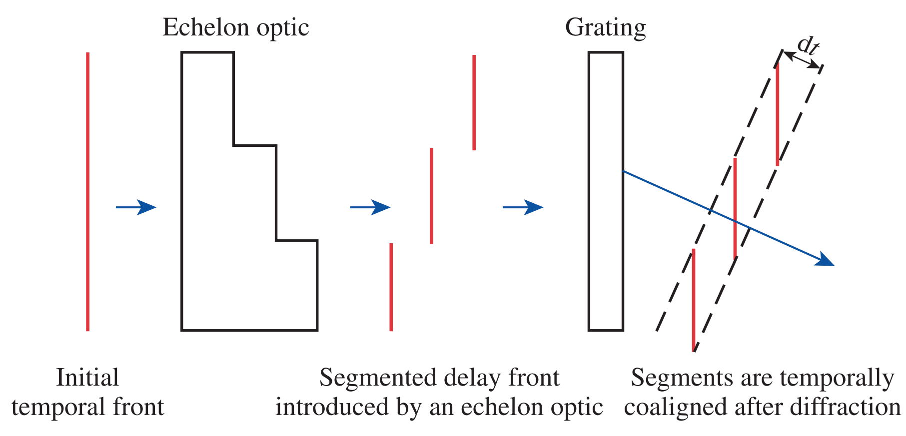

Figure 147.36
PFT can be reduced with no loss to throughput by segmenting the incoming beam into multiple sub-elements that are individually delayed to compensate for the path-length difference introduced by the diffraction grating. The residual PFT is limited to the accumulation across a single segment and the overall temporal resolution is improved by a factor equal to the number of sub-elements used.

Spectrometer Design

A prototype segmented spectrometer (Fig. 147.37) has been designed to support the development of a fiber-optic Thomson-scattering system at LLE. Thomson scattering will be used to characterize the growth of electron plasma waves in pump–probe experiments that last less than 25 ps. The spectrometer was designed to match the 1-ps temporal resolution of the Rochester Optical Streak System 8200 (Ref. 4). The spectrometer provides a 100-nm spectral field of view centered at the 527-nm Thomson-scattering probe wavelength with a 0.8-nm spectral resolution. Light from the plasma-wave experiment will be coupled to the spectrometer using a gradient-index fiber optic. The fiber has a 50-μm core diameter and a 0.2 (*f*/2.5) numerical aperture. The input signal is collimated by a 225-mm-focal-length, color-corrected doublet lens operating at *f*/2.9. Angular dispersion is provided by a 300-g/mm transmission grating that generates 40 ps of pulse-front tilt. A 34-element reflective echelon optic with 2.2-mm step widths and 174-μm step heights is used to improve the achievable temporal resolution to 1.2 ps. Individual spectrometer segments focus to the streak camera at *f*/100, producing diffraction-limited spot sizes of 55-μm full width at half maximum (FWHM). Figure 147.38 shows how the echelon step width was optimized to improve temporal resolution while maintaining spectral resolution close to the performance of the nominal full-aperture system.

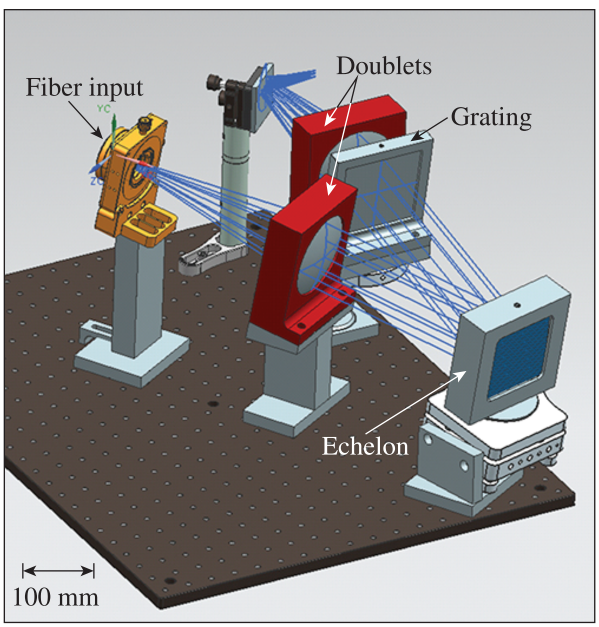

Figure 147.37
CAD model of the spectrometer layout. A pair of *f*/2.9 doublets collimate and focus the dispersed input from a 50-μm-core fiber optic. The PFT from the 300-g/mm transmission grating is reduced by using a 34-element reflective echelon optic.

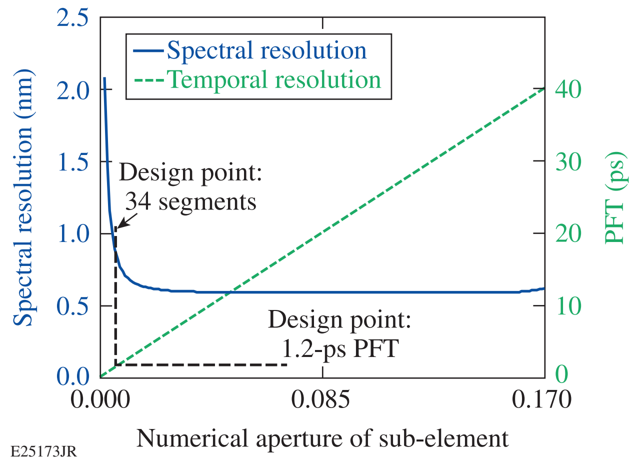

Figure 147.38
Spectral resolution is determined by convolving the modeled imaging-performance parameters and multiplying by linear dispersion. The overall beam size was selected based on the geometric limitations of the imaging optics. Temporal resolution was improved by segmenting the full beam into properly delayed sub-elements. The design point represents a compromise between these factors, resulting in 0.8-nm spectral resolution, 1.2-ps temporal resolution, and *f*/2.9 throughput.

Conclusions

This article presents a novel spectrometer design that decouples the relationship between throughput and pulse-front tilt. An echelon optic is used to segment the aperture of the spectrometer into a series of sub-elements that are optically and temporally co-aligned. This technique makes it possible to optimize the spectral resolution, throughput, and temporal resolution simultaneously.

ACKNOWLEDGMENT

This material is based upon work supported by the Department of Energy National Nuclear Security Administration under Award Number DE-NA0001944, the University of Rochester, and the New York State Energy Research and Development Authority. The support of DOE does not constitute an endorsement by DOE of the views expressed in this article.

REFERENCES

1. J. Hebling, Opt. Quantum Electron. **28**, 1759 (1996).
2. S. Akturk, X. Gu, P. Bowlan, and R. Trebino, J. Opt. **12**, 093001 (2010).
3. A. Visco, R. P. Drake, D. H. Froula, S. H. Glenzer, and B. B. Pollock, Rev. Sci. Instrum. **79**, 10F545 (2008).
4. Sydor Instruments, LLC, Rochester, NY 14624.

Design of an Extreme Ultraviolet Spectrometer Suite to Characterize Rapidly Heated Solid Matter

Introduction

Solid-density hot plasmas can be created by using a high-intensity laser incident on a solid metal foil.[1] Following irradiation by the high-intensity laser, the target heats in a matter of picoseconds. Electrons in the laser's focal spot are rapidly energized and confined to a target volume by a sheath set up around the target. The fast electrons thermalize through collisional and noncollisional processes that occur much faster than the hydrodynamic expansion time scale. This makes it possible to heat the target to high temperatures before the onset of hydrodynamic motion, allowing one to measure the hot plasma in a pre-expanded state. These conditions form a platform for measuring intrinsic material properties such as the equation of state (EOS) of high-energy-density (HED) matter.

X-ray and ultraviolet spectroscopy have been used to extract information about the temperature and density evolution of hot, solid-density targets in a variety of conditions. A new extreme ultraviolet (XUV) spectrometer has been built to make temperature measurements that provide complementary information to higher-energy spectroscopic observations (e.g., K_α-line spectroscopy or thermal-line radiation) of the mass-averaged temperature. The XUV radiation is highly localized to the surface of the promptly heated material before expansion. The early-time heating dynamics of the target are important to understand for future off-Hugioniot EOS measurements.

Spectrometer Layout

Figure 147.39 provides a schematic overview of the spectrometer and camera layout. A high-throughput XUV spectrometer was realized using a grazing-incidence toroidal reflector and a variable line-space grating.[2] A precision-cut 100-mm × 2-mm slit[3] is held close to the target with a re-entrant nose cone. All direct lines of sight between the target interaction and the charge-coupled–device (CCD) detector are shielded by a minimum of 6-mm tungsten to minimize the noise from hard x-ray hits on the camera. Two limited apertures inside the spectrometer serve to limit stray light. The spectrometer consists of a modular front section that can be mounted to a scientific CCD camera (Spectral Instruments SI-800), an image plate, or an x-ray streak camera. Two identical spectrometers have been built for simultaneous time-averaged and time-resolved XUV emission studies.

The spectrometer consists of a 450-lines/mm, variable line space grating[2] and a toroidal mirror,[2] which images the spectrum to a flat-field detector located outside the target chamber. Both the grating and mirror operate at a grazing angle of 7.5°. The mirror and the detector plane are located 190 mm and 570 mm from the laser focus, respectively. The view angle for both spectrometers is 45° with respect to the optical axis of the incident laser. The solid angle of both spectrometers is limited by the toroidal reflector and is 3×10^{-3} sr; the spectrometer

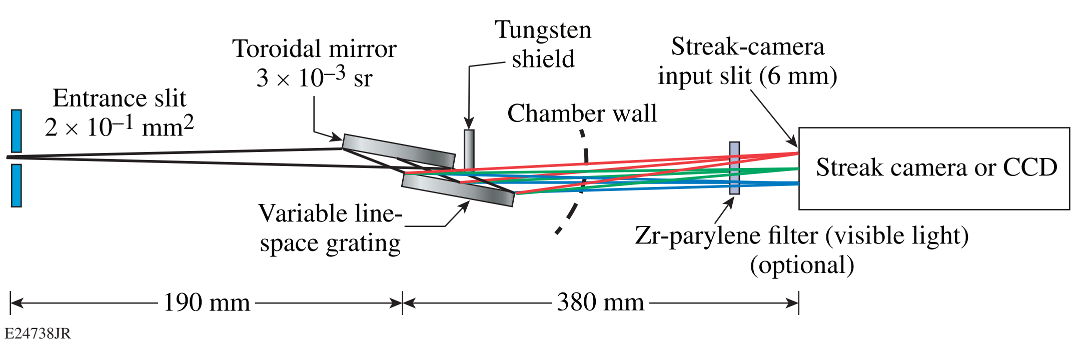

Figure 147.39
Schematic diagram of the extreme ultraviolet (XUV) flat-field spectrometer. CCD: charge-coupled device.

has a magnification of 3, giving a field of view of ~500 μm in the target plane. A ray-trace model of the spectrometer was implemented in the code *FRED* to simulate the optical performance of the spectrometer.[4] The simulation predicts a spectral resolution of 0.1-nm full width at half maximum (FWHM) at 12.5 nm.

Figure 147.40 shows a schematic of the spectrometer with the top sectioned for clarity. The slit aperture is held in place with a threaded cap on the front nose cone. The cap may be removed to replace or inspect the aperture slit between shots. A pointer can be attached to the nose cone to aid in spectrometer alignment on the target chamber's viewing system. The cone-shaped projection on the front of the spectrometer body limits blast material from the experiment from depositing into the spectrometer or onto the fine-adjust knobs of the grating carriage. The toroidal mirror is pinned in place on a custom kinematic mounting. The grating can be rotated ±3° about two axes to allow for pointing and spectral window adjustment. The actuators for the tip/tilt adjustment pass through to the front end to allow for adjustment between shots when the chamber

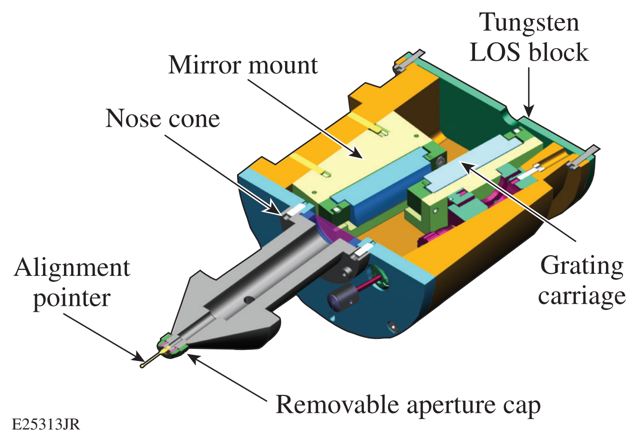

Figure 147.40
Schematic of the re-entrant spectrometer's front end. LOS: line of sight.

is vent cycled. The outer casing of the spectrometer is vented with sintered plugs to allow for venting during pump out. The tungsten line-of-sight (LOS) shield forms the rear panel on the enclosure and provides a limited aperture for the spectrum to pass through to the detector.

Experiment

An experiment to validate the spectrometer performance and to measure short-pulse heating was conducted on LLE's Multi-Terawatt (MTW) Laser System.[5,6] The experimental setup is shown schematically in Fig. 147.41. A 100 × 100 × 3-μm Al foil was irradiated with 7±1 J of 527-nm light in a 1-ps pulse with a contrast ratio of ~10^{14}. The contrast is estimated by measuring the pulse contrast at the fundamental frequency and calculated for the second-harmonic process.[7] The laser delivered a focus with 80% of the energy contained into a 10-μm spot when measured on a low-power shot. The on-target intensity was ~3×10^{18} W/cm^2. The XUV photocathode on the streak camera was a 200-Å gold layer flash coated onto a 0.5-μm parylene base layer. The full photocathode slit measures 60 mm × 200 μm wide but typically only the central 6 mm × 50 μm of the slit is used when the camera is set for best temporal focusing.

Data Analysis

Figure 147.42 shows a time-integrated spectrum taken with the spectrometer onto a FUJI TR image-plate (IP) detector. The spectrum occupies ~1 mm on the IP detector in the direction opposite the spectrum; the values shown are the summed values from the scanned data. The IP was scanned at a resolution of 50 μm and a sensitivity level of 10,000. Several atomic transition lines from Al III, IV, and V ions are visible superimposed on the continuum emission in this time-integrated shot. The strongest lines observed are listed in Table 147.IV; these values were obtained from the National Institute of Standards and Technology (NIST)[8] wavelength database. The Al III transition was observed in absorption

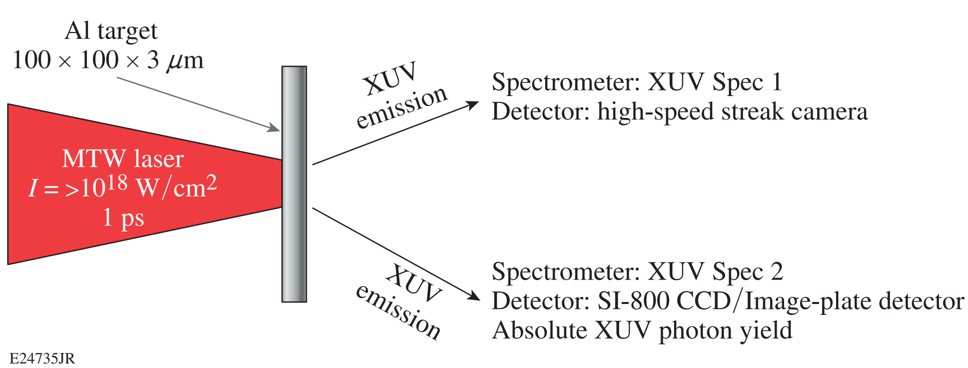

Figure 147.41
Schematic diagram of the experimental setup. MTW: Multi-Terawatt.

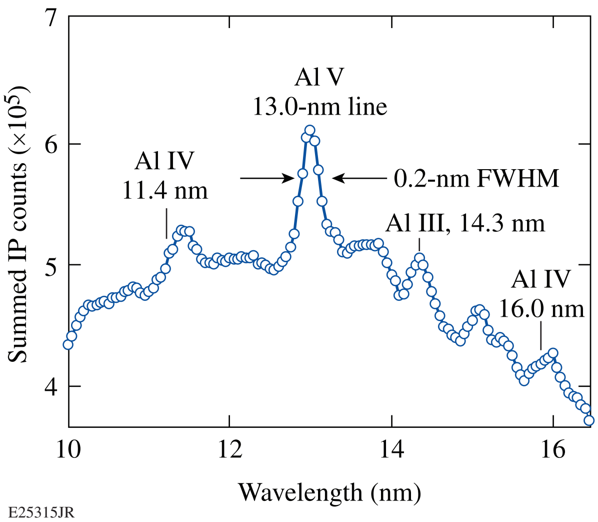

Figure 147.42
Spectrum acquired on a 7-J, 1-ps laser shot onto a $100 \times 100 \times 3$-μm Al target. The spectrometer resolution was measured to be 0.2-nm full width at half maximum (FWHM).

Table 147.IV: Aluminum atomic spectral lines identified in a short-pulse, heated aluminum target.

Ion	Experimental data (nm)	Reference data[8] (nm)	Relative intensity[8]	Oscillator strength[8]
Al IV	11.4±0.2	11.646	250	0.332
Al V	13.0±0.2	13.0847	1000	0.175
Al IV	16.0±0.2	16.169	700	0.017
Al III	14.3±0.2	14.395	—	—

only and no tabular data exist for the line strength or relative intensity. Additionally, the spectrometer resolution at 13.0 nm was measured to be 0.2-nm FWHM. The Al line at 13.0 nm is a doublet (13.0 and 13.1 nm) and some broadening of the peak is expected; however, the resolution at this wavelength is consistent with simulation predictions (0.2 nm versus 0.1 nm). The peak at 15.1 nm is likely O IV ions from an oxide layer on the surface of the target.

Figure 147.43 compares a time-resolved spectrum recorded on an MTW shot and a synthetic spectrum. For this comparison we used the collisional-radiative code *Spect3D* to compute the emergent radiation from the radiation–hydrodynamics simulation.[9] The XUV atomic model in *Spect3D* includes all ionization stages and excited-state energy levels. A radiation–hydrodynamics simulation was run with parameters closely tied to the experiment.[10] In the simulation, a uniform energy density corresponding to the electron deposition was applied to the solid metal target and allowed to freely expand. The target temperature was initialized in the simulation at 100 eV. The emission is assumed to be in local thermodynamic equilibrium. In the time period of interest, the emission is predicted to be dominated by a smooth continuum with all the atomic transitions dissolved into the continuum. Later in time, the strongest emissions from ground-state transitions are observed. Previous inferences of temperature from the emission in this region have shown significant departures between the temperature observed in the continuum and electronic line ratios in time-integrated XUV spectrum measurements.[11,12] The streaked data here show that the continuum and line radiation occur at substantially different times in the expansion. This may explain the discrepancy between the temperature inferred from line emission and continuum emission.

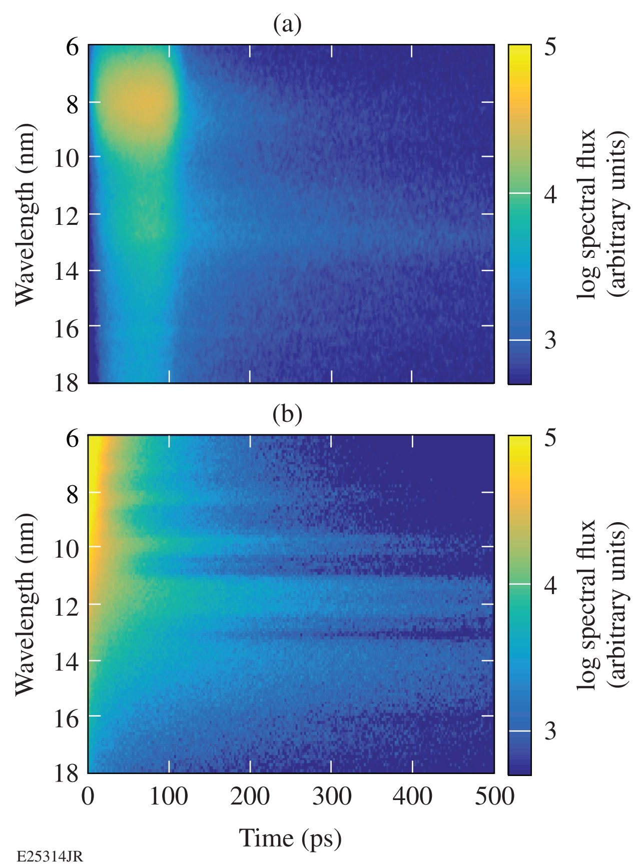

Figure 147.43
Comparison of (a) streaked XUV data and (b) simulation.

The streaked spectra can be corrected for the wavelength-dependent photocathode sensitivity. The first step is to take a photometric calibration of the streaked spectrometer. A method similar to those described in Ref. 13 will be implemented when correcting the raw streak-camera data. During a shot, the streaked and time-integrated spectrometer acquires a spectrum. The spectrum captured, on a calibrated IP detector, is then compared to a streaked spectrum summed in the temporal direction. Grating efficiency as a function of wavelength will be corrected using a rigorous coupled-wave theory code, taking into account the groove shape, depth, and metal reflectivity.[14]

Conclusion

A spectrometer capable of measuring the time-resolved XUV emission of a rapidly heated metal target has been designed and implemented. The spectrometer has a measured resolution of 0.2 nm at a design wavelength of 13 nm. The time-resolved spectra show reasonable agreement with radiation–hydrodynamic simulations. Future experiments will further explore the surface-temperature dynamics of these targets in a variety of metals.

ACKNOWLEDGEMENT

This material is based upon work supported by the Department of Energy National Nuclear Security Administration under Award Number DE-NA0001944, the University of Rochester, and the New York State Energy Research and Development Authority. This work was performed under the auspices of the U.S. Department of Energy, Office of Science, Office of Fusion Energy Sciences Award Number DE-SC-0012317.

REFERENCES

1. R. G. Evans *et al*., Appl. Phys. Lett. **86**, 191505 (2005).
2. HORIBA Scientific, Edison, NJ 08820-3097.
3. National Aperture, Inc. Salem, NH 03079.
4. *FRED*, Photon Engineering, LLC, Tucson, AZ 85711 http://www.photonengr.com/software (1 June 2016).
5. V. Bagnoud, I. A. Begishev, M. J. Guardalben, J. Puth, and J. D. Zuegel, Opt. Lett. **30**, 1843 (2005).
6. C. Dorrer, I. A. Begishev, A. V. Okishev, and J. D. Zuegel, Opt. Lett. **32**, 2143 (2007).
7. I. A. Begishev, C. R. Stillman, S. T. Ivancic, S.-W. Bahk, R. Cuffney, C. Mileham, P. M. Nilson, D. H. Froula, J. D. Zuegel, and J. Bromage, "Efficient Second-Harmonic Generation of Large-Aperture Multi-Terawatt Hybrid Nd:Laser Subpicosecond Pulses for Laser–Matter Interactions," to be submitted to Applied Physics.
8. NIST Atomic Spectra Database, NIST Standard Reference Database #78, Version 5, see http://www.nist.gov/pml/data/asd.cfm (1 June 2016).
9. J. J. MacFarlane *et al*., High Energy Density Phys. **3**, 181 (2007).
10. J. Delettrez, R. Epstein, M. C. Richardson, P. A. Jaanimagi, and B. L. Henke, Phys. Rev. A **36**, 3926 (1987).
11. T. Ma *et al*., Rev. Sci. Instrum. **79**, 10E312 (2008).
12. U. Zastrau *et al*., Phys. Rev. E **78**, 066406 (2008).
13. R. Florido, R. C. Mancini, T. Nagayama, R. Tommasini, J. A. Delettrez, S. P. Regan, V. A. Smalyuk, R. Rodríguez, and J. M. Gil, High Energy Density Phys. **6**, 70 (2010).
14. L. Li *et al*., Appl. Opt. **38**, 304 (1999).

Influence of Surface Modifications on the Adsorption and Absorption of Tritium into Stainless-Steel 316

Introduction

High concentrations of tritium develop on stainless-steel (SS) surfaces exposed to a tritium atmosphere.[1] These high concentrations are attributed to tritium dissolution within the adsorbed water layers present on all metal surfaces.[1–4] Tritium dissolved within these layers contributes ≥20% to the total inventory absorbed by SS.[1] Additionally, these water layers govern the migration of the isotope during an exposure to a tritium atmosphere, as well as during a storage period following the exposure. Because such a large fraction of the tritium inventory resides in the water layers, altering these layers by altering the metal surface can significantly affect the total quantity of tritium absorbed by SS.

In the present study, the effect of altering the metal surface on the migration and total absorption of tritium into SS 316 was investigated by preparing SS samples with a variety of surface modifications, which included mechanical polishing, electropolishing (EP),[5,6] gold plating, nitric-acid treatments, and Fe or Cr oxidation.[7] The migration and total absorption of tritium in the various SS samples was measured using plasma-induced ion sputtering[8] and thermal desorption.[9]

A quantitative tritium migration model (QTRIMM) based on Fickian diffusion through composite media is used to describe the measured total tritium inventories and migration rates. The composite medium treated in this model is the adsorbed water layer(s)/metal-lattice system. This model accounts for the high concentrations of tritium on the surfaces of SS by relating the tritium concentrations on the surface and in the metal lattice at the surface/metal-lattice interface.[8]

Modeling

QTRIMM is based on a numeric solution to the diffusion equation[10] and can be used to calculate the tritium concentration profiles in a metal substrate.[8] The boundary conditions used in this model are based on several fundamental assumptions. The first assumption is that a rapid equilibrium occurs between tritium in the gas phase and tritium dissolved in the adsorbed surface water. The second assumption is that all isotope exchange reactions have equal probability; consequently, there will be equal tritium mole fractions in the gas phase and on the surface. Equal reaction probabilities are not likely because the formation of double-isotope species, such as T_2O, is not as probable as the formation of a single-isotope species, such as HTO. The consequence of making this limiting assumption will be discussed later.

$$\chi_{\text{surf}} = \chi_{\text{gas}}, \tag{1}$$

where χ_{surf} and χ_{gas} are the mole fractions of tritium in the adsorbed water layers and gas phase, respectively. The assumption of equal mole fractions leads to an equation for the quantity of adsorbed tritium (A_{surf}) on a stainless-steel surface during exposure to tritium gas:

$$A_{\text{surf}} = \lambda * \chi_{\text{gas}} * \text{SA} * Q * \frac{\text{2-mol H}}{\text{1-mol H}_2\text{O}}, \tag{2}$$

where λ is the tritium decay constant (Bq), SA is the surface area of the metal (m^2), and Q is the surface concentration of absorbed water (mol H_2O/m^2).

Once tritium adsorbs onto the metal surface, it can diffuse into the metal lattice. To determine the flux of tritium across the surface-water layer/metal-lattice interface, the tritium concentrations at the interface are related through the ratio of the tritium solubilities in the two regions.[8]

The final assumption is that negligible quantities of tritium desorb from the surface during the storage period between charging the sample with tritium and each experiment. Little tritium is expected to desorb during this period because the samples were stored under dry helium at 1 atm. Measurements of the residual tritium in the storage vessels show that less than 5% of the activity is lost to the vessel during the storage period. Tritium concentrations redistribute throughout the sample by diffusing from the water layer into the metal lattice to attain an equilibrium state.

Experimental Setup and Procedures

1. Surface Modifications

The surfaces of each sample underwent various pretreatments intended to modify the metal surface. All samples measured $5.1 \times 1.8 \times 0.3\ cm^3$, and their surfaces were machined away to remove manufacturing defects and to expose the metal lattice. The samples were cleaned first with acetone follwed by de-ionized water, and finally dried with isopropyl alcohol. Samples receiving no additional treatment are referred to as "as received" or AR. The next modification involved mechanically polishing the AR samples to yield finer surface finishes. Several mechanically polished samples were then electroplated with gold to a thickness of 1.7 μm. To bind the gold to the surface, a nickel strike interface was necessary. This interfacial layer had a thickness of 6 μm. Another subset of the mechanically polished samples was treated with methods III and IV described by Boulange-Petermann *et al.* for generating hydrophobic and hydrophilic surfaces.[11] In this technique, the samples were washed with 0.5 M of NaOH and then placed in either a 0.2-M or a 4-M nitric-acid bath. Lower acid concentrations are expected to yield more hydrophobic surfaces, while higher acid concentrations should yield hydrophilic surfaces.

The remaining mechanically polished samples were divided into three sets and each set was electropolished for a different duration. The first set (EP2) was electropolished for 10 min while the second set (EP3) was electropolished for 5 min. The third set (EP) was electropolished for an unknown time, as determined by the polisher. The intent of increasing the duration of electropolishing was to extend the surface chromium concentrations deeper into the metal lattice. Increased chromium concentrations are expected to reduce tritium adsorption.[12]

Several samples from the third set of electropolished samples were subjected to one of two treatments intended to enhance either the Fe or the Cr concentrations in the near-surface region.[7] These treatments were intended to test the impact of surface composition on the tritium absorption into stainless steel.

2. Surface Analysis

The surface roughness of each finish was measured using a Zygo NewView 100 interferometer or a Zygo NEXView interferometer (Table 147.V). No surface roughness data were available for Batch C oxidation treatments.

The near-surface compositions obtained with x-ray photoelectron spectroscopy (XPS) for select samples are shown in Figs. 147.44 and 147.45. The surfaces of samples treated to enhance either the Fe concentrations (oxidation treatment #1) or the Cr concentrations (oxidation treatment #2) exhibited two distinct regions, each with different Fe and Cr concentrations. In the present study, the average surface concentrations of Fe and Cr were used because the experimental methods represent average tritium interactions with the entire sample's surface. The near-surface composition for the EP sample shows an increase in the Cr content compared to AR, polished, and the nitric-acid–treated samples. However, the EP process suppressed the Fe content compared to AR and the acid and oxidation treatments. It is also clear that the 0.2- and 4-M acid treatments increased both the Cr and Fe content of the near surface compared to AR, but the increase in Cr between the two acid treatments is nearly identical.

Comparatively, oxidation treatment #2, and the polished samples have a Cr and Fe composition that falls in between the two acid treatments. Therefore, if the surface composition controls tritium absorption, the total quantity of absorbed tritium in polished samples and samples undergoing oxidation treatment #2 should be between the tritium quantities contained within the samples treated with either concentration of nitric acid.

Figures 147.45–147.47 compare the Fe and Cr $2p_{3/2}$ photoelectron spectra as a function of depth into the metal sample. To collect these data, the surfaces were etched at a rate of 6.7 nm/min and a spectrum collected every 15 s. The resulting collection of spectra for a single sample shows the evolution of the oxidation states of Fe and Cr as a function of depth. In

Table 147.V: Measured surface roughness (R_a) for various surface finishes.

Batch A		Batch B		Batch C	
Finish	R_a (nm)	Finish	R_a (nm)	Finish	R_a (nm)
AR1	434	AR2	351	AR3	535
EP2	110	Polish #12	338	Polished	81
EP3	85	Polish #8	316	EP	92
0.2-M HNO_3	74	Polish #3	46		
4 M	73	Gold	57		

general, the results show a decrease in the oxide concentration and an increase in the elemental composition of each metal with increasing depth. Additionally, each set of spectra indicate that all surfaces (except EP samples and samples that underwent oxidation treatment #1) are dominated by a mix of iron (III) and iron (II) oxides, with a smaller concentration of chromium (III) oxide.

3. Sample Loading

All stainless-steel samples were charged with tritium by exposing the samples to a deuterium–tritium (DT) gas mixture at 25°C for 24 h. After exposure, the samples were stored in separate metal containers under a dry helium atmosphere. Three separate batches of samples were charged with tritium using the pressures and tritium purities given in Table 147.VI.

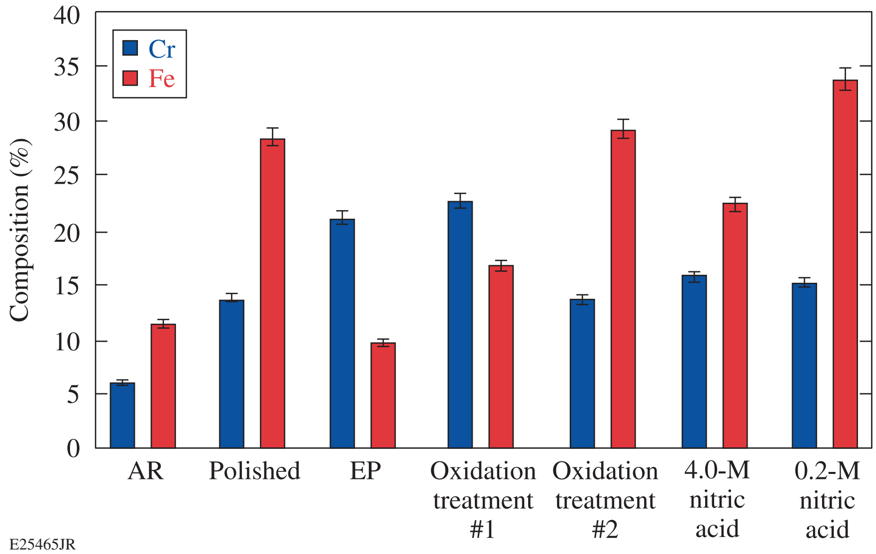

Figure 147.44
Measured Cr and Fe content in select samples using x-ray photoelectron spectroscopy (XPS).

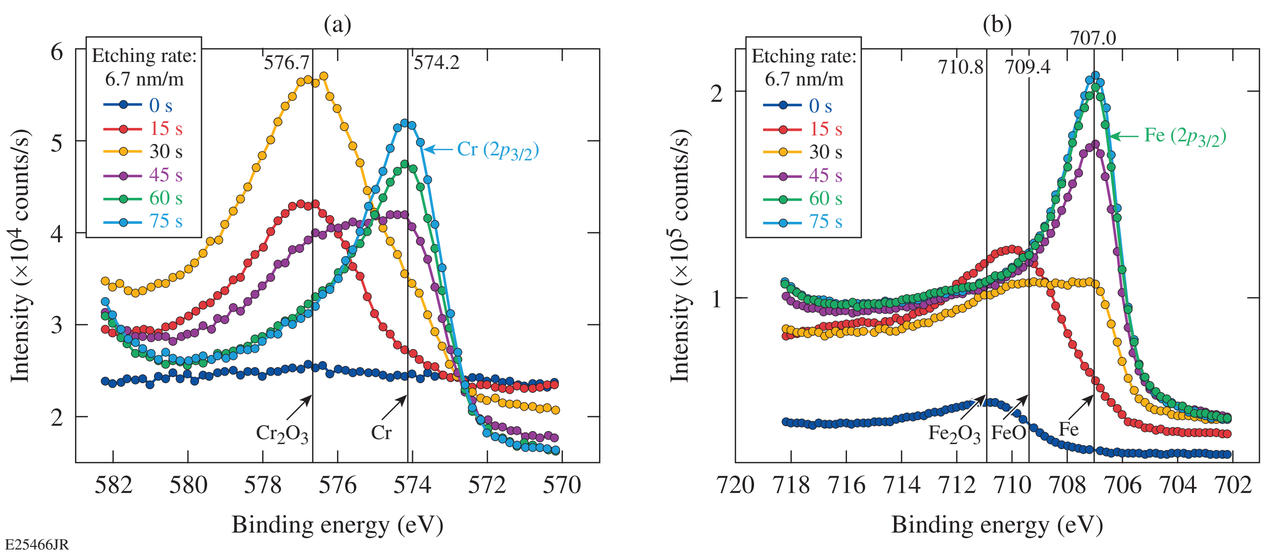

Figure 147.45
XPS photoelectron spectra for (a) Cr and (b) Fe atoms bound to the surface of as-received (AR) samples.

Table 147.VI: Sample loading and storage conditions.

Batch	Pressure (Torr)	Tritium (%)	Storage time (days)
A	550	57	13 to 29
B	530	58	8 to 29
C	550	59	6 to 18

4. Experimental Procedure

Total tritium inventories were measured with temperature-programed desorption (TPD) as described in previous work.[9] Tritium migration in the near-surface region was measured with plasma-induced ion sputtering, also described elsewhere.[8]

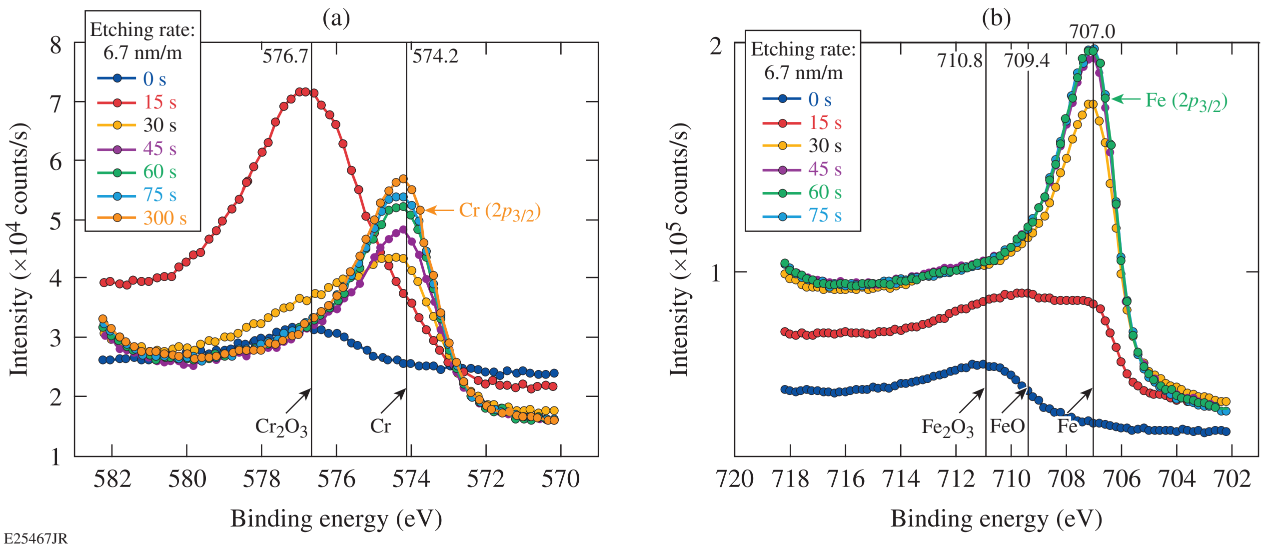

Figure 147.46
XPS photoelectron spectra for (a) Cr and (b) Fe atoms bound to the surface of samples treated with 4 M of HNO_3.

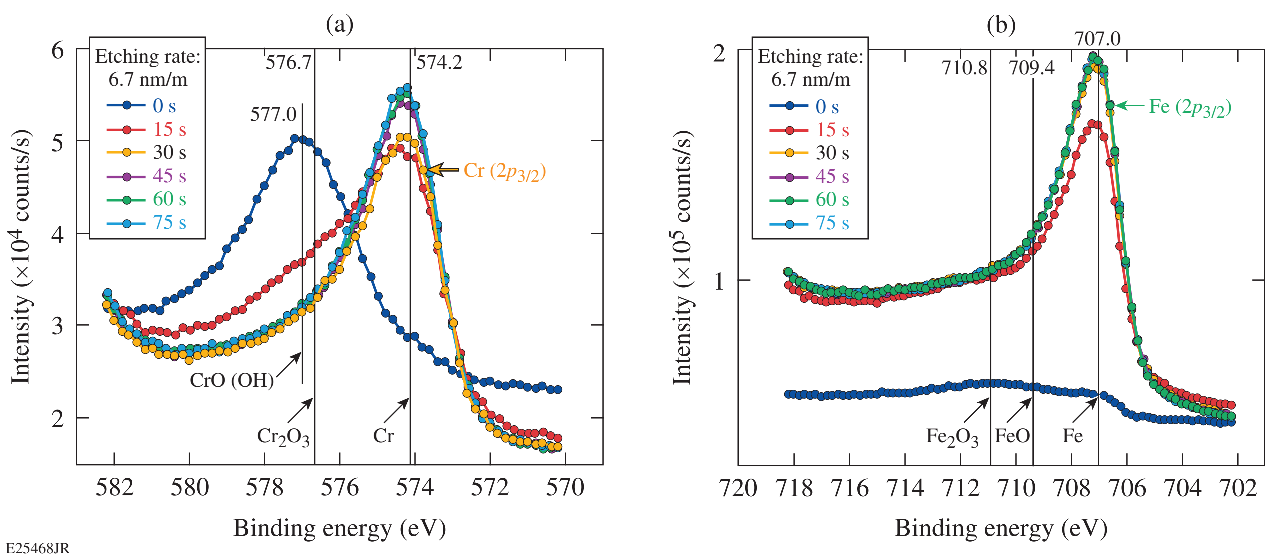

Figure 147.47
XPS photoelectron spectra for (a) Cr and (b) Fe atoms bound to the surface of samples treated with 0.2 M of HNO_3.

Results and Discussion

The total quantity of tritium removed during thermal desorption experiments shows a strong dependence on the surface composition as illustrated in Figs. 147.48 and 147.49. Each thermal desorption experiment was run at least twice, using separate and fresh samples to verify reproducibility. The AR samples were included to gauge how the various surface modifications influence the total tritium inventory and to provide a reference between the different loading batches. The observed variation in the tritium inventories between the different batches has not been resolved yet, but it is likely a result of subtle changes in the loading, storage, and handling procedures.

The data in Fig. 147.48 demonstrate that, relative to AR1 samples, electropolishing reduces the total quantity of tritium absorbed by the metal. However, increasing the electropolishing duration from 5 to 10 min caused no further reduction in the total tritium inventory.

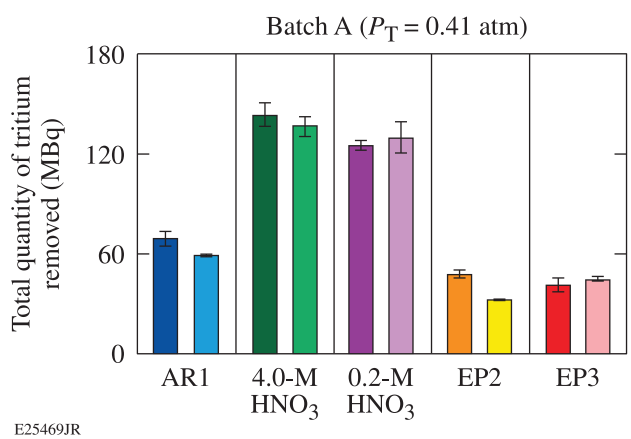

Figure 147.48
Quantities of tritium removed during thermal desorption experiments using samples loaded with tritium in Batch A.

The data in Fig. 147.48 also demonstrate that the nitric-acid treatments result in significantly higher quantities of tritium absorbed into the samples, as compared with AR1 samples. The higher inventories are evident even though the acid treatment increased the Cr content in the near surface (Fig. 147.44). Contrary to expectations, these results suggest that the increased Cr concentration did not reduce tritium adsorption or absorption.

In general, mechanically polishing a SS surface leads to a reduction in the quantity of absorbed tritium (Fig. 147.50). However, this reduction in total tritium inventory is not exclusively caused by smoother surfaces. For example, polish #12 and polish #8 samples from Batch B in Fig. 147.50 had a surface roughness similar to the AR2 samples but retained half the tritium present on AR2 samples. Additional polishing of both samples in Batch C to reduce the surface roughness about eightfold from ~351 nm to 46 nm did not reduce the absorbed tritium content.

The measured total tritium inventories in gold-plated, SS (Au-SS) samples suggest that the electroplated gold layer does not act as a barrier to tritium absorption. The Au-SS samples contain less tritium than the AR2 samples, but comparable inventories to the polish #3 samples (Fig. 147.50). This suggests that the reduction in absorbed tritium, when comparing Au-SS to AR2 samples, is likely a result of polishing the samples, not electroplating them with gold.

The data provided in Fig. 147.49 again suggest that increasing the near-surface Cr concentration does not alter the absorption of tritium into the substrate. First, the EP samples have

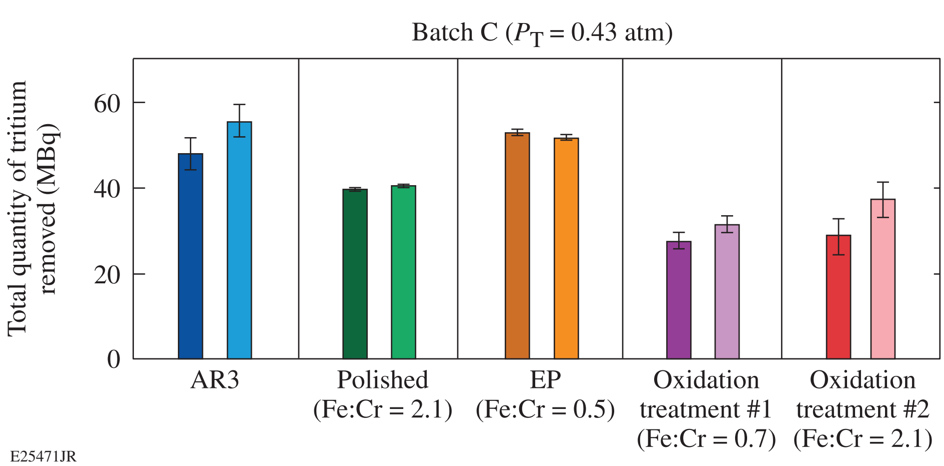

Figure 147.49
Quantities of tritium removed during thermal desorption using samples from Batch C.

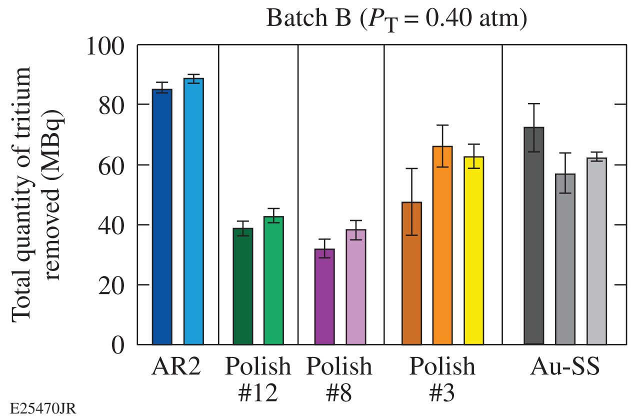

Figure 147.50
Quantities of tritium removed during thermal desorption experiments using samples loaded with tritium in Batch B.

significantly higher Cr concentrations in the near surface, as compared with the AR samples (Fig. 147.44). However, the EP samples show comparable tritium inventories to the AR3 samples. This is, again, contrary to the expectation that increased Cr concentrations in the near surface lead to lower tritium inventories. Furthermore, samples treated with oxidation treatment #1 showed comparable Cr concentrations to the EP samples (Fig. 147.44), but significantly lower total tritium inventories (Fig. 147.49). Finally, samples treated with oxidation treatment #2 show comparable tritium inventories to oxidation treatment #1, even though the Cr and Fe concentrations are significantly different (Fig. 147.44). These results suggest that the chemical composition of the near surface of stainless steel does not influence the absorption of tritium. It should also be noted that an increase in near-surface Fe concentrations does not account for the observed differences in total inventories. Significantly different tritium inventories were recorded for samples that underwent the nitric-acid treatments and the oxidation treatment #2. However, the Fe and Cr concentrations were comparable.

The results shown in Fig. 147.48 also confirm that simply polishing SS surfaces reduces the tritium inventory in SS samples. Furthermore, mechanical polishing a surface does not reduce the tritium inventory to the same degree as oxidizing a surface.

The results in Fig. 147.49 show no correlation with surface roughness (0 to 0.54 μm) to the total activity determined by thermal programmed desorption. Different surface alterations show similar roughness values but drastic variability in the total activity as seen for polish #4 and the nitric-acid treatments. This trend suggests that an increased surface area is not indicative of increased tritium absorption. The data may suggest that the role of the surface area in the absorption of tritium may contribute little compared to the chemical absorption processes.

Using the data shown in Figs. 147.48–147.50, the surface concentration of adsorbed water (Q) can be determined using QTRIMM. These concentrations were determined by varying Q values until the calculated and measured total tritium inventories agreed. Averages of the data shown in Figs. 147.48–147.50 were used in this fitting procedure. The minimization was accomplished using *MATLAB*'s nonlinear least-squares fitting routine. The results of the fits are shown in Table 147.VII for the various surface finishes and loading batches.

The calculated Q values correspond to submonolayer water coverage of the surface, which is on the lower end of the expected values.[13] These low values are likely a result of the limiting assumption of equal isotopic exchange prob-

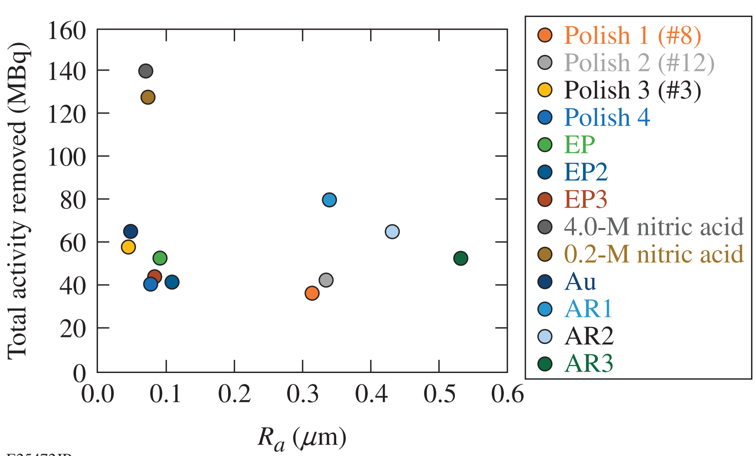

Figure 147.51
Total activity collected from various samples as a function of surface roughness.

Table 147.VII: Results of fitting thermal and pulsed-plasma data using QTRIMM. Q values were determined from thermal-desorption data, while the removal efficiencies were determined from pulsed-plasma experiments.

Batch	Metal finish	Q (μmol/m^2)	Removal efficiency	A_{surf}/A_{total} (%)
A	AR1 (Fe:Cr = 1.8)	22.04	n/a	49
A	4-M HNO_3 (Fe:Cr = 1.3)	55.74	n/a	57
A	0.2-M HNO_3 (Fe:Cr = 2.1)	50.21	n/a	57
A	EP2	11.39	n/a	40
A	EP3	12.66	n/a	42
B	AR2	31.7	0.41	88
B	Polish #12	11.6	0.59	68
B	Polish #8	9.1	0.61	62
B	Polish #3	19.4	0.52	79
C	AR3	15.7	0.34	73
C	Polished	10.7	0.63	65
C	EP (Fe:Cr = 0.5)	16.0	0.75	74
C	Oxidized (Fe:Cr = 0.7)	6.2	0.91	51
C	Oxidized (Fe:Cr = 2.1)	7.7	0.84	56

abilities. Lowering the exchange probability for the formation of double isotope species T_2O on the metal surface will result in an increase in the calculated quantity of adsorbed water. The derived Q values indicate that ≥44% of the total tritium inventory is initially located within the adsorbed water layers (Table 147.VII).

The Q values found from fitting thermal-desorption data agree with data obtained from pulsed-plasma experiments. No plasma data were collected for Batch A. Representative results obtained from samples supporting AR, polished, EP, and Fe-oxidized surfaces from Batch B that were subjected to a pulsed plasma are shown in Fig. 147.52. The data shown have been normalized to the quantity of tritium removed during the first exposure in each respective series to allow for direct comparison of the trends in each data series. These trends indicate that the mechanism for tritium migration to the surface is diffusion from the metal lattice between each plasma exposure.[8]

Figure 147.52 also shows fits to the data using QTRIMM. These fits were calculated by using Q values obtained from thermal-desorption fits and by varying only the removal efficiency (ε) until the data and calculations agreed. To be consistent, only Q values obtained from QTRIMM fitted to thermal desorption data for samples with the same surface finish and charged with tritium in the same batch were used to fit pulsed-plasma data. The resulting fits to data show excellent agreement for all data series, except for samples that underwent selective oxidation pretreatments. Removal efficiencies found for each fit are given in Table 147.VII for each surface modification.

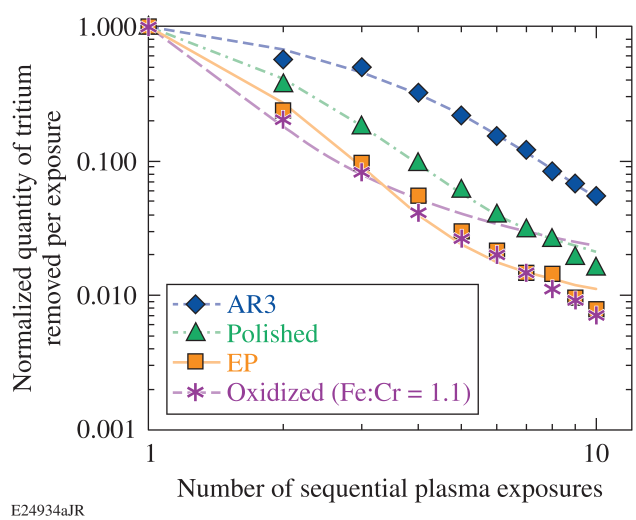

Figure 147.52
Comparison of the results obtained from pulsed-plasma experiments to best fits (calculated using QTRIMM) of various samples charged with tritium in Batch B. The error in each data point is ±5%.

Conclusions

The experimental data show that modifying the near surface (≤40 nm) of a SS surface by polishing, EP, selective oxidation, or nitric-acid treatments can significantly alter the total quantity of absorbed tritium. These results suggest that a significant fraction of the total tritium inventory initially resides on the surface since as these modifications affect only the near surface of the metal substrate (<10 nm).

The nitric-acid treatments of the electropolished SS 316 surfaces increased the total tritium inventory by 200% when compared against untreated (AR) samples and 300% compared to EP samples. These results suggest that nitric-acid treatments created more hydrophilic surfaces when compared to untreated (AR) samples.

The differences in the total tritium inventories for the various surface treatments appear to be related to the quantity of water adsorbed on the surface. Increasing or decreasing the water content appears to increase or decrease the total tritium inventory. Figures 147.48 and 147.49 suggest that a 50% reduction in water concentration results in a 35% reduction in total tritium inventory in the electropolished case. On the other hand, increasing the water content by a factor of ~2.4 increased the total tritium inventory by 200% in the nitric-acid–treatment case. Measuring the water isotherms is necessary to confirm the calculation results.

The absorption and migration of tritium in each SS sample can be described using QTRIMM. Comparing the output of this model to thermal-desorption data allowed us to determine the surface concentration of adsorbed water. Using this surface concentration, the initial contribution of adsorbed tritium to the total inventory was determined to be ≥44%. Additionally, by using the Q values derived from fitting thermal-desorption data, we could accurately describe the migration of tritium to the surface for each sample during pulsed-plasma experiments.

ACKNOWLEDGMENT

This material is based upon work supported by the Department of Energy National Nuclear Security Administration under Award Number DE-NA0001944, the University of Rochester, and the New York State Energy Research and Development Authority. The support of DOE does not constitute an endorsement by DOE of the views expressed in this article.

REFERENCES

1. R.-D. Penzhorn *et al*., J. Nucl. Mater. **353**, 66 (2006).
2. T. Hirabayashi, M. Saeki, and E. Tachikawa, J. Nucl. Mater. **126**, 38 (1984).
3. M. A. Henderson, Surf. Sci. Rep. **46**, 1 (2002).
4. T. Ohmi *et al*., Rev. Sci. Instrum. **64**, 2683 (1993).
5. Y. T. Sasaki, J. Vac. Sci. Technol. A **25**, 1309 (2007).
6. S.-J. Lee and J.-J. Lai, J. Mater. Process. Technol. **140**, 206 (2003).
7. T. Ohmi *et al*., J. Electrochem. Soc. **140**, 1691 (1993).
8. M. Sharpe, W. T. Shmayda, and W. U. Schröder, Fusion Sci. Technol. **70**, 97 (2016).
9. M. J. Quinlan, W. T. Shmayda, S. Lim, S. Salnikov, Z. Chambers, E. Pollock, and W. U. Schröder, Fusion Sci. Technol. **54**, 519 (2008).
10. J. Crank, *The Mathematics of Diffusion* (Oxford University Press, Oxford, 1979), p. 189.
11. L. Boulange-Petermann, B. Baroux, and M.-N. Bellon-Fontaine, J. Adhes. Sci. Technol. **7**, 221 (1993).
12. Y. Ozeki *et al*., Fusion Sci. Technol. **60**, 1499 (2011).
13. M. Nishikawa *et al*., J. Nucl. Mater. **277**, 99 (2000).

Hugoniot and Release Measurements in Diamond Shocked up to 26 Mbar

Introduction

The behavior of carbon at millions to billions of atmospheres of pressure is integral to evolution models for many solar and extrasolar planets (Uranus, Neptune, 55 Cancri E)[1,2] and white dwarf stars.[3,4] In Uranus and Neptune, carbon exists in the form of methane (CH_4) ice at the surface but may be in its elemental form near the core, where pressures and temperatures reach ~8 Mbar and ~8000 K, respectively.[5,6] Theoretical predictions suggest that the interiors of Uranus, Neptune, or Neptune-like exoplanets might contain diamond or even liquid oceans of carbon.[1,5] This strongly motivates studies of carbon's high-pressure response in both its solid and liquid phases.[7–9]

Carbon's equation of state (EOS) is also important to developing predictive models for inertial confinement fusion (ICF) experiments, where diamond shells are used to contain and compress the hydrogen fuel.[10] An ICF implosion uses a series of finely tuned shock waves to precompress the shell (ablator) and fuel. This initiates near isentropic compression while adding the desired amount of entropy needed to hydrodynamically stabilize the main implosion. An optimal target design is a delicate balance between these two effects. The diamond used in ICF targets is polycrystalline with grain sizes of ~10 nm (Refs. 11 and 12). The low surface roughness and isotropic character of this nanocrystalline diamond (NCD) compared to single-crystal diamond (SCD) makes NCD less susceptible to hydrodynamic instabilities seeded by crystal anisotropy at the ablator/fuel interface. Current implosion designs melt the NCD with the first shock to further limit instability growth. Modeling an ICF implosion requires accurate knowledge of NCD's response to multimegabar shocks and its behavior when it releases from these extreme pressures into the low-density fuel.

To date, data for carbon above the diamond melt boundary are limited to shock-compression measurements.[13–15] None of these data include NCD; high-precision measurements (relative density error < 1.5%) for SCD exist up to only 18 Mbar (Ref. 15). Shock Hugoniot data in solid diamond[16–18] and the solid–liquid coexistence region[7,8,15] are supplemented by ramp-compression measurements,[19,20] which are used to explore matter at temperatures significantly lower than temperatures on the Hugoniot. Ramp-compression data exist up to 8 Mbar in solid SCD[20] and 50 Mbar for solid NCD,[19] but theories describing liquid carbon above 18 Mbar are unconstrained by high-precision experiments. The experiments presented here provide high-pressure (up to 26 Mbar) shock-compression and release data for both full-density SCD (ρ_0 = 3.515 g/cm^3) and the lower-density NCD (ρ_0 ~ 3.36 g/cm^3) used in ICF capsules. The Hugoniot data provide a clear constraint on the pressure, density, and internal energy of liquid carbon, while the release data constrain the isentropes from these high-pressure, high-temperature shock states to a several-fold drop in pressure.[21,22]

Single-shock Hugoniot data for diamond (both SCD and NCD) were collected to 26 Mbar using impedance-matching (IM) techniques with quartz as a reference material. These new SCD data agree with density-functional theory molecular dynamics (DFT-MD) calculations for liquid carbon.[23] The data for NCD, which are expected to be at a slightly higher temperature, exhibit a compressibility that is even stiffer than shock-compressed SCD measurements and DFT-MD predictions. The NCD data suggest that, in addition to carbon's anomalously stiff fluid state, either its thermal properties are inadequately understood or the shock compression of NCD undergoes an additional (frictional) heating explained by its slightly lower density.

The release data were collected by releasing shock-compressed diamond into several lower-impedance materials with known shock Hugoniots including quartz,[24,25] CH,[26] silica foam,[25,27] and liquid D_2 (Refs. 28 and 29). This technique was previously used by Knudson, Desjarlais, and Pribram-Jones to benchmark the release of shocked quartz[25] and aluminum.[29] Data were acquired for diamond releasing from 8 to 20 Mbar, so release paths originated from both the coexistence region and liquid phase. The release data mostly agree with predictions using existing EOS models that do not include strength effects, indicating that strength does not largely affect the diamond release physics at these pressures. The release measurements into the low-density liquid D_2 are particularly valuable for constraining ICF models since liquid D_2 is a good surrogate for the deuterium–tritium fuel in an ICF target.

The following sections describe the experimental design, targets, and diagnostics used in the laser-driven shock experiments; show the IM technique used to measure Hugoniot and release states; and present the NCD data analysis techniques followed by the results.

Experimental Technique

The experiments were performed at the Omega Laser Facility, a Nd:glass laser that is frequency tripled to a wavelength of 351 nm (Ref. 30). The experiments used 6 to 12 beams having temporally square pulses with durations of 2, 3, or 3.7 ns with total energies between 1.1 and 3.7 kJ. The beams with an 876-μm-diam laser focal spot were smoothed by spectral dispersion[31] and distributed phase plates.[32] On-target laser intensities of 0.66 to 3.3×10^{14} W/cm^2 were achieved, producing shock pressures up to 26 Mbar in the diamond targets.

The NCD targets were designed to provide both Hugoniot and release measurements on each shot. The targets [Fig. 148.1(a)] comprised a CH ablator, a Z-cut α-quartz standard (pusher), and an NCD sample glued to the pusher's rear surface. IM data were obtained at this interface for NCD Hugoniot measurements. A standard material [quartz, polystyrene (CH), SiO_2 foam, or liquid D_2] was in contact with the rear side of the NCD sample to determine its release behavior. Adjacent to the NCD sample, a quartz witness provided a reference for the temporal history of the shock velocity. The witness was required because internal scattering attributed to the nanometer-sized diamond grains and their random orientations make NCD opaque to visible light.[12] For this reason, shock velocities in the NCD were measured from transit times. To facilitate these measurements, the NCD sample and rear standard were positioned to provide an unobstructed view of ~100 μm of the rear quartz pusher and NCD faces as shown in Figs. 148.1(a) and 148.1(b).

Examples of planar cryogenic and warm SCD target designs are shown in Fig. 148.2. SCD is transparent, obviating the need for the quartz witness, which allowed us to use one to three rear standards to obtain multiple release measurements on a single shot. Hugoniot measurements were made at the quartz/SCD interface and release measurements were made at the SCD/rear-standard interfaces. A thin (0.3- or 2-μm) gold layer was deposited on the rear of the CH ablator in some targets to help prevent preheat in the SCD and standards. A quartz baseplate (30 to 50 μm thick) was attached to the front side of the diamond whenever a gold layer was not used.

The NCD targets used nanocrystalline diamond (fabricated by Diamond Materials GmbH) identical to those used in ICF targets at the National Ignition Facility (NIF).[33] The density of the NCD samples was determined to be 3.360±0.002 g/cm^3 using an Archimedes' measurement of a larger reference

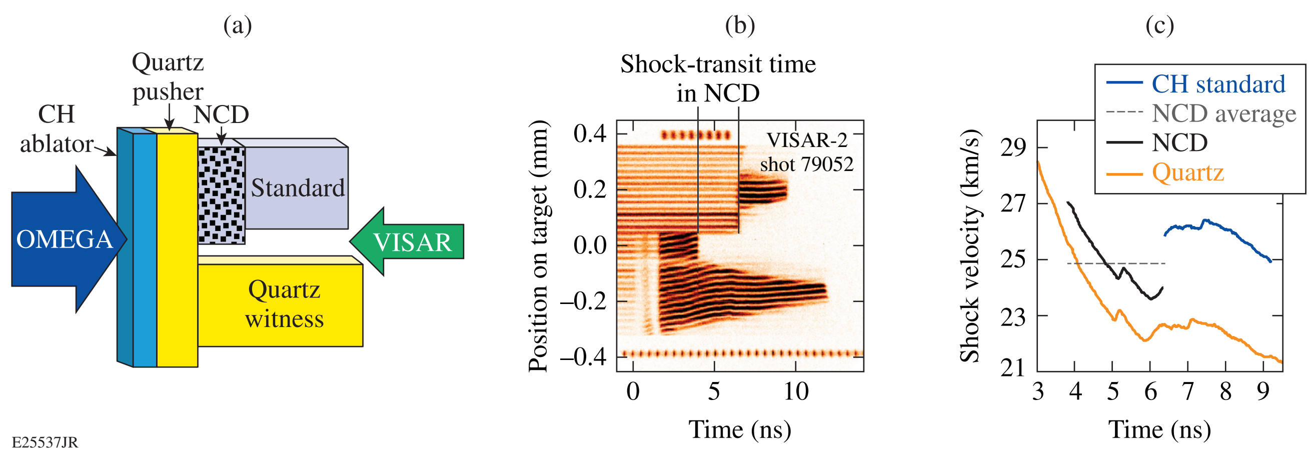

Figure 148.1
(a) The nanocrystalline diamond (NCD) target design comprising a CH ablator, a quartz pusher and witness, an NCD sample, and a standard positioned to facilitate measurements of transit times. (b) Raw VISAR (velocity interferometer system for any reflector) data from an experiment using the target design in (a). (c) Extracted shock velocities from (b). The shock-velocity profile in NCD (black line) was inferred from the average shock velocity (dashed line) and the observed shock-velocity profile in the adjacent quartz witness (orange line) using the nonsteady waves correction.[34] The shock-velocity profile in the CH standard (solid blue line) is observed once the shock breaks out of the NCD.

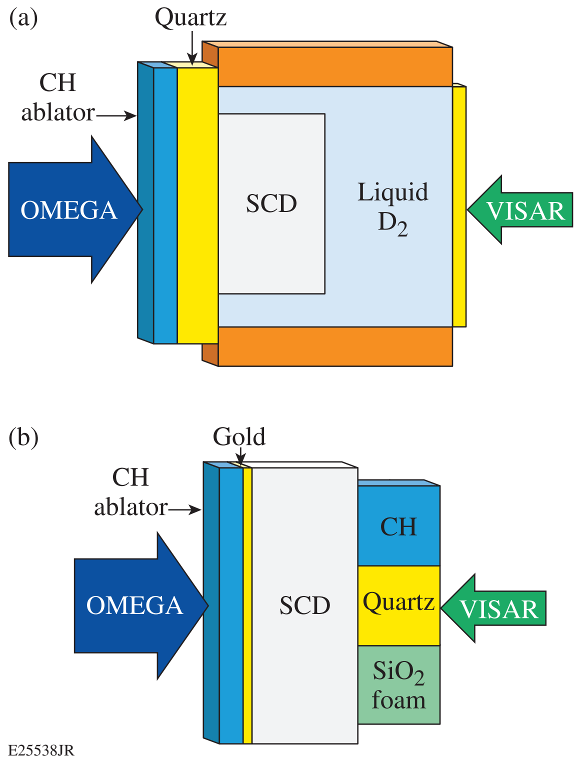

Figure 148.2
Schematics of (a) planar cryogenic and (b) warm targets used in single-crystal diamond (SCD) Hugoniot and release experiments. Targets had a CH ablator and one to three standards (liquid D_2, CH, quartz, or SiO_2 foam) on the rear side of the SCD.

sample from the same batch.[12] The SCD foils obtained from Applied Diamond had a density of $\rho_0 = 3.515$ g/cm^3 and were natural with a $\langle 110 \rangle$ orientation or fabricated with chemical vapor deposition (CVD) with a $\langle 100 \rangle$ orientation. The quartz (ρ_0 = 2.65 g/cm^3), CH (ρ_0 = 1.05 g/cm^3), and SiO_2-foam ($\rho_0 \sim 0.2$g/cm^3) pieces (see Table 148.I for exact values) were obtained from Schafer Corporation. The planar cryogenic targets [Fig. 148.2(a)] comprised a liquid D_2–filled, cylindrical copper cell sealed with quartz on both faces. The initial D_2 density was determined from the temperature in the cryogenic cell and varied between 0.170 and 0.174 g/cm^3 on a shot-to-shot basis.[35] The uncertainty in the SiO_2 foam density was estimated to be ~2%, and uncertainties in the SCD, quartz, CH, and liquid D_2 densities were assumed to be negligible.

The shock velocities for impedance matching were measured using the line-imaging velocity interferometer system for any reflector (VISAR) described in Ref. 36. Opposite the drive beams, the VISAR probe beam is incident on the rear side of the target and the reflected signal is relayed to a pair of interferometers. A delay etalon is inserted into one leg of each interferometer so that changes in Doppler shifts of the reflected probe beam, corresponding to moving reflective interfaces, are registered as fringe shifts in the interference pattern. The fringe shifts are proportional to the velocity of the moving interface through the velocity per fringe (VPF), which depends inversely on the etalon thickness and the index of refraction of the target medium at the 532-nm probe wavelength. The indices of refraction for the target materials at 532 nm were 2.42 (SCD), 1.55 (quartz), 1.59 (CH), 1.04 (0.2-g/cm^3 SiO_2 foam),[27] and 1.14 (0.174-g/cm^3 liquid D_2) (Ref. 28).

The two interferograms, which are recorded on separate streak cameras, provide time histories of the velocity of moving interfaces with ~10-ps resolution.[36] Fringe jumps or 2π phase ambiguities between the two records are resolved by using etalons of different thicknesses. The velocities presented here for the NCD Hugoniot and all release measurements are those measured using the more-sensitive VISAR leg. Measurements using the less-sensitive VISAR leg are presented for some SCD Hugoniot measurements because it provided better-resolved fringe shifts of the rapidly decaying shock at the quartz/SCD interface. Errors were estimated to be the larger of 5% of a fringe using the more-sensitive leg or the difference between the velocity from the more-sensitive leg and the weighted velocity average from both legs. An example of raw VISAR data and the extracted shock velocities from an NCD experiment using the target design in Fig. 148.1(a) are shown in Figs. 148.1(b) and 148.1(c). The VISAR diagnostic provides 1-D spatial resolution along the slit of the streak camera so that shock velocities are observed over an ~800-μm slice of the target.

The targets were shock compressed to a metallic fluid state producing a reflective shock front. VISAR recorded the shock velocity as a function of time in the transparent materials.[36] In opaque materials, the VISAR probe beam cannot reach the shock front within the target. Instead, VISAR registers the time that the shock breaks out of the opaque material. For example, the shock transit time in the NCD sample is given by the time between the two vertical lines in Fig. 148.1(b). The first time is registered by the arrival of the shock at the rear of the quartz pusher. The second time is registered from its arrival at the rear NCD interface. For transparent materials, higher-precision, *in-situ*, time-varying shock-velocity profiles were measured. A streaked optical pyrometer[37] (SOP) with an ~5-ps temporal resolution provided additional measurements of shock transit times. Average velocities in NCD were corrected using the nonsteady waves model discussed below.

Table 148.I: Diamond release data. All the single-crystal diamond (SCD) samples had a ⟨110⟩ orientation except for the SCD in shot 73733, which had a ⟨100⟩ orientation. U_s^C and U_s^{Stan} are the shock velocities at the interface between the diamond and the lower-impedance standard (quartz, CH, silica foam, or liquid D_2). U_s^{Stan} was corrected to account for the glue layer (when necessary) by linearly fitting to the measured shock velocity in the standard over a small time interval and extrapolating the fit backward across the glue layer. The initial densities of the liquid D_2 and foam samples are given in mg/cm^3 in column 3.

Shot	Diamond Type	Standard	U_s^C (km/s)	U_s^{Stan} (km/s)
77003	SCD	D_2 (174)	29.47±0.06	38.60±0.27
77848	SCD	D_2 (170)	28.56±0.06	36.86±0.12
77851	SCD	D_2 (170)	27.39±0.09	34.49±0.12
77856	SCD	D_2 (170)	29.10±0.06	37.83±0.13
79050	SCD	D_2 (174)	25.03±0.10	30.14±0.33
79053	SCD	D_2 (172)	24.62±0.10	29.29±0.22
73733	SCD	quartz	25.88±0.06	24.52±0.09
75397	SCD	quartz	23.67±0.07	21.63±0.15
75399	SCD	quartz	23.87±0.07	21.92±0.11
75400	SCD	quartz	23.20±0.11	21.05±0.16
75402	SCD	quartz	23.93±0.07	21.77±0.11
75404	SCD	quartz	29.05±0.7	27.61±0.11
77857	SCD	quartz	31.60±0.06	30.17±0.09
77859	SCD	quartz	31.57±0.06	30.05±0.09
77860	SCD	quartz	29.33±0.06	28.29±0.09
75397	SCD	CH	23.48±0.07	24.00±0.10
75399	SCD	CH	23.84±0.13	24.94±0.12
75400	SCD	CH	23.20±0.07	23.36±0.15
75404	SCD	CH	28.77±0.07	32.00±0.11
77857	SCD	CH	31.64±0.06	35.37±0.09
77859	SCD	CH	31.46±0.06	35.08±0.10
77860	SCD	CH	29.20±0.06	32.46±0.09
75397	SCD	foam (191)	23.63±0.07	25.01±0.16
75400	SCD	foam (191)	23.10±0.07	24.83±0.16
77004	NCD	D_2 (173)	26.68±0.82	33.29±0.12
77006	NCD	D_2 (172)	30.81±0.96	40.19±0.12
77002	NCD	quartz	31.21±0.45	30.11±0.09
77007	NCD	quartz	28.09±0.32	26.48±0.09
79048	NCD	quartz	22.16±0.18	20.44±0.16
77005	NCD	CH	28.09±0.33	31.90±0.09
77861	NCD	CH	25.76±0.31	27.92±0.10
77862	NCD	CH	24.48±0.26	26.25±0.09
79052	NCD	CH	23.94±0.16	25.87±0.16
79056	NCD	CH	26.57±0.28	28.93±0.16
79060	NCD	CH	22.93±0.20	24.87±0.25
79051	NCD	foam (198)	23.51±0.25	26.22±0.24

NCD: nanocrystalline diamond

Impedance-Matching Technique

Both Hugoniot and release states in diamond were measured using impedance matching (IM). The IM technique closes the Rankine–Hugoniot equations[22] to solve for pressure (P), density (ρ), and specific internal energy (E) in a shock-compressed material:

$$\rho_0 U_\mathrm{s} = \rho\left(U_\mathrm{s} - u_\mathrm{p}\right), \tag{1}$$

$$P = P_0 + \rho_0 U_\mathrm{s} u_\mathrm{p}, \tag{2}$$

$$E = E_0 + \frac{1}{2}\left(P + P_0\right)\left(\frac{1}{\rho_0} - \frac{1}{\rho}\right). \tag{3}$$

These equations describe the jump conditions across a shock front, where U_s is the shock velocity, u_p is the particle velocity, and states upstream of the shock are characterized by the subscript 0 (Ref. 22). By measuring U_s and u_p, the kinematic EOS parameters P, ρ, and E can be determined. In these experiments, U_s is measured using VISAR and u_p is determined using the IM technique, which relies on the equilibration of P and u_p at the interface between the material of interest (diamond) and a material with a known EOS. This method for measuring the Hugoniot and release behavior is described in the following two sections.

1. Hugoniot Measurements

The Hugoniot of an uncharacterized sample is measured with knowledge of the standard's EOS and the shock velocities about the standard/sample interface. In this work, the diamond Hugoniot data were measured using a quartz standard.[24,25] The pressure and particle velocity in the shocked quartz at the quartz pusher/diamond interface are given by the intersection of the Rayleigh line [Eq. (2)] and the quartz Hugoniot (cubic form taken from Ref. 25). When the shock crosses into the diamond, the pressure and particle velocity are continuous at the contact interface to maintain equilibrium. Since diamond has higher impedance ($\rho_0 U_\mathrm{s}$), the quartz is re-shocked to a higher pressure, off its principal Hugoniot, to reach this new (P, u_p) state. This state, given by the intersection in the P–u_p plane of the quartz re-shock and the diamond Rayleigh line, marks a state on the diamond's Hugoniot.

The quartz re-shock was modeled using a Mie–Grüneisen EOS of the form

$$P = P_\mathrm{H} + \Gamma\rho\left(E - E_\mathrm{H}\right) \tag{4}$$

with

$$E - E_\mathrm{H} = \frac{1}{2}\left(P + P_\mathrm{H}\right)\left(\frac{1}{\rho_1} - \frac{1}{\rho}\right), \tag{5}$$

where P_H and E_H are the pressure and specific internal energy, respectively, on the quartz principal Hugoniot, ρ_1 is the density in the singly shocked quartz upstream of the re-shock, and ρ, P, and E are the density, pressure, and specific internal energy, respectively, in the re-shocked quartz. This re-shock model used the same reference Hugoniot P_H and effective Grüneisen parameter $\Gamma = \Gamma_\mathrm{eff}$ as the quartz release model described in Ref. 25. It should be noted that P_H and Γ_eff are not necessarily physical; they were optimized such that the quartz release model matched experimental data and first-principles molecular dynamics (FPMD) simulations. This same construct should be accurate for modeling the re-shock since the quartz compresses only 20% to 30%. Indeed, the diamond P–u_p data determined by this model are only 1% to 2% higher than those obtained using the simple reflected Hugoniot approximation.

2. Release Measurements

The release behavior of shocked diamond was measured by impedance matching between diamond and several lower-impedance standards. The initial and final states of the diamond release are determined using the known Hugoniots of the diamond materials (measured previously or in this study) and those of the standards. By using various lower-impedance standards, the diamond release is measured at incrementally lower end-state pressures, mapping the release path in P–u_p space.

The release standards used in these experiments have been suitably characterized: quartz,[24,25] CH,[26] silica foam,[25,27] and liquid D_2 (Refs. 28 and 29). The diamond–D_2 IM data are particularly valuable to ensuring that the initial stages of an ICF implosion set the fuel on the correct adiabat for an optimal implosion.

The CH and liquid-D_2 Hugoniot fits used in this work were re-analyzed using new data for the standards used in those IM studies. The CH Hugoniot data from Barrios,[26] which used a quartz standard, were re-analyzed using the updated quartz Hugoniot and release model from Knudson and Desjarlais.[25] Similarly the liquid-D_2 Hugoniot data from Hicks,[28] which used an aluminum standard, were re-analyzed by Knudson *et al.* and presented in Ref. 29. The liquid-D_2 Hugoniot from the Hicks experiments was used in this analysis because both works were performed on the OMEGA laser and had the same initial densities to within 2.5%. Because the Hicks Hugoniot fit was determined for $\rho_0 = 0.174$ g/cm^3, the $U_\mathrm{s}^{D_2}$ data plotted here were normalized to that initial density using the corrective term $2.29\left(1-\rho_0 / \rho_0^{\text{Hicks}}\right)$. This offset was determined in Ref. 28 by comparing the effect of ρ_0 on the Hugoniots that were modeled using the stiffest and softest D_2 EOS tables; it affected this data set by only <0.2%.

Shock velocities in diamond and the standards were measured at the IM interface and are presented in Table 148.I. The shock velocity in diamond at the point of breakout into the standard was measured directly from the VISAR data in SCD and inferred from the nonsteady wave correction in NCD. The shock velocity in the standard was extrapolated backward across the glue layer to this same point. The extrapolation was done by linearly fitting to the measured shock velocity over a 150- to 500-ps time interval when the shock first entered the standard. *HYDRA* simulations for a different shock experiment involving a quartz/LiH interface with a 0-, 2-, and 4-μm-thick oil layer between them showed that extrapolating the shock velocity backward across the entire oil (or glue) layer (as opposed to midway) most accurately represented shock behavior at the interface when the two materials were in direct contact.[38] Only data with steady or smoothly decaying shocks over 150 ps on both sides of the interface were used in the release analysis.

NCD Data Analysis

EOS data obtained from impedance matching require accurate measurements of shock velocities and error propagation to provide high-confidence data. Modern VISAR systems can provide <1% velocity measurements in transparent samples,[36] yielding precise EOS data.[26] Opaque or translucent samples like NCD present a considerably different challenge. The methods used to obtain average shock velocities (i.e., transit times) and to correct those velocities for unsteadiness are described below.

1. Measurements of Shock Transit Times

Average shock velocities in the NCD samples were determined using the measured thicknesses and shock transit times presented in Table 148.II. VISAR and SOP were used to measure the times that the shock exited the quartz pusher (t_1) and the NCD (t_2). This defined the total time ($\Delta t_{\text{total}} = t_2 - t_1$) that the shock spent in the NCD sample and the glue layer preceding it. The transit time across the NCD sample alone is calculated by

$$\Delta t_{\text{NCD}} = \Delta t_{\text{total}} - \Delta x_{\text{glue}} / U_{\text{s}}^{\text{glue}},$$

where Δx_{glue} is the estimated glue thickness (described in **Measurements of Thickness**, below) and $U_{\text{s}}^{\text{glue}}$ is the shock velocity in the glue estimated using the *SESAME* 7603 table for epoxy and the known pressure and particle velocity at the quartz pusher/glue interface.

For targets with an uncovered NCD step, as shown in Fig. 148.1(a), shock breakout times were measured using the drop in the VISAR reflectivity across the step/vacuum interface seen in Fig. 148.1(b). The peak in the derivative of the reflectivity, denoting the steepest slope in the drop in signal, defined the shock breakout time. This method yielded the most-consistent and most-precise transit times since the peaks were measured to ~5 ps. For targets without the steps, breakout times were defined by the rapid change in thermal emission recorded by the SOP at the quartz pusher/glue/witness interface (t_1) and the NCD/glue/standard interface (t_2). The steepest slope of the SOP signal was used to define t_1 and t_2. An additional uncertainty up to 50 ps was applied to these measurements because the location of the peak defining t_1 or t_2 was not as consistent since it varied with the thickness of the glue layer. The SOP signal does not drop to zero at the glue (or liquid D_2) interface, as was observed in the VISAR reflectivity at the step/vacuum interface. As the shock approached the rear surface of the NCD sample, the VISAR reflectivity and the SOP signal increased exponentially because of reduced volumetric scattering. This contributed to the uncertainty in t_2 because the emission continuously increased across the NCD/glue/standard (or liquid D_2) interface.

2. Measurements of Thickness

The step heights of the NCD samples glued to the quartz pushers (Δx_{total}) were measured using white-light interferometry with a Zygo NexView 3-D optical surface profiler. The average NCD step height was referenced to the quartz pusher in the areas where the breakout times were measured. The glue thicknesses were estimated by combining these measurements with the thickness profiles of the individual samples (Δx_{NCD}), measured using a dual confocal microscope. Glue layers were kept to ~1 μm and are defined by $\Delta x_{\text{glue}} = \Delta x_{\text{total}} - \Delta x_{\text{NCD}}$. For some targets, Δx_{glue} was set to 0 μm because a negative glue thickness was inferred; the uncertainty always permitted a positive glue thickness. The average shock velocity in NCD alone was determined using $\left\langle U_{\text{s}}^{\text{NCD}}\right\rangle = \left(\Delta x_{\text{total}} - \Delta x_{\text{glue}}\right) / \Delta t_{\text{NCD}}$.

3. Nonsteady Wave Correction

In laser-driven experiments, steady shocks are difficult to attain because of the expanding ablation plasma. A technique for correcting the average shock velocity to account for nonsteadiness was developed for use in laser-driven experiments.[34] For a large planar drive, the shock-velocity history in an opaque sample is related to and corrected by the observed history in

Table 148.II: NCD transit time data and Hugoniot data from impedance matching (IM) with a quartz standard. The shock transit times (Δt_{total}) and thicknesses (Δx_{total} and Δx_{NCD}), where "total" denotes the combined NCD sample and preceding glue layer, were used to determine the average shock velocity in NCD $\left(\langle U_{\text{s}}^{\text{NCD}}\rangle\right)$. $\langle U_{\text{s}}^{\text{NCD}}\rangle$ was corrected using the method described in **Nonsteady Wave Correction** (p. 164) to determine $U_{\text{s}}^{\text{NCD}}(t_1)$ at the IM interface. The shock velocity in quartz $\left[U_{\text{s}}^{Q}(t_1)\right]$ and $U_{\text{s}}^{\text{NCD}}(t_1)$ were used in the IM analysis to determine the particle velocity $\left(u_{\text{p}}^{\text{NCD}}\right)$, pressure ($P^{\text{NCD}}$), and density ($\rho_{\text{NCD}}$) on the NCD Hugoniot.

Shot	Δt_{total} (ns)	Δx_{total} (μm)	Δx_{NCD} (μm)	$\langle U_{\text{s}}^{\text{NCD}}\rangle$	$U_{\text{s}}^{Q}(t_1)$	$U_{\text{s}}^{\text{NCD}}(t_1)$	$u_{\text{p}}^{\text{NCD}}$	P^{NCD} (Mbar)	ρ^{NCD} (g/cm^3)
77001	2.035±0.020	64.24±0.44	63.29±0.45	31.10±0.36	29.54±0.09	31.25±0.36	17.62±0.13	18.50±0.17	7.71±0.17
77002	1.890±0.023	62.27±0.38	61.89±0.29	32.75±0.45	31.59±0.09	33.03±0.42	19.29±0.16	21.40±0.22	8.08±0.22
77004*	2.384±0.069	64.80±0.54	64.97±0.50	27.19±0.82	25.94±0.09	27.79±0.80	14.86±0.18	13.87±0.26	7.25±0.34
77005	2.082±0.020	63.03±0.31	62.69±0.28	30.10±0.33	30.17±0.09	31.26±0.31	18.25±0.13	19.17±0.16	8.07±0.17
77006*	2.051±0.063	64.19±0.23	63.31±0.50	30.89±0.96	29.27±0.09	31.20±0.96	17.36±0.23	18.19±0.36	7.61±0.41
77007	2.109±0.019	63.44±0.39	63.71±0.33	30.08±0.32	29.81±0.09	31.28±0.31	17.88±0.12	18.80±0.16	7.85±0.14
77861	2.263±0.021	63.06±0.43	62.61±0.30	27.67±0.31	27.44±0.09	28.89±0.29	16.11±0.11	15.63±0.13	7.60±0.14
77862	2.319±0.019	61.72±0.30	61.43±0.27	26.49±0.25	26.51±0.09	27.66±0.24	15.44±0.10	14.35±0.11	7.61±0.13
79048	2.704±0.011	62.18±0.41	62.14±0.27	22.97±0.17	23.57±0.17	24.52±0.17	13.29±0.16	10.95±0.15	7.34±0.12
79049	1.951±0.008	62.07±0.48	62.17±0.26	31.79±0.26	33.87±0.16	35.10±0.26	20.98±0.21	24.74±0.27	8.36±0.17
79051	2.502±0.011	62.65±0.58	63.00±0.25	25.04±0.25	26.06±0.16	27.57±0.24	15.02±0.16	13.92±0.17	7.39±0.14
79052	2.517±0.011	63.58±0.30	62.45±0.34	24.81±0.15	25.61±0.16	27.06±0.15	14.69±0.15	13.36±0.15	7.35±0.11
79054	2.481±0.011	61.31±0.73	61.83±0.28	24.70±0.30	26.80±0.16	27.15±0.30	15.82±0.17	14.43±0.18	8.06±0.21
79055	2.263±0.010	61.54±0.68	61.39±0.25	27.11±0.30	28.22±016	29.70±0.31	16.67±0.17	16.63±0.19	7.66±0.17
79056	2.315±0.008	65.17±0.66	62.45±0.30	26.98±0.26	28.02±0.16	29.52±0.28	16.51±0.17	16.38±0.18	7.63±0.16
79057	2.196±0.010	61.60±0.44	61.22±0.25	27.87±0.22	28.56±0.16	29.93±0.22	16.97±0.17	17.07±0.18	7.76±0.15
79058	2.142±0.015	62.72±0.36	62.87±0.25	29.28±0.26	31.00±0.16	32.42±0.25	18.81±0.18	20.49±0.21	8.01±0.16
79059	2.398±0.010	61.66±0.46	61.84±0.25	25.70±0.21	26.91±0.16	28.40±0.21	15.65±0.16	14.94±0.16	7.49±0.13
79060	2.571±0.015	61.89±0.32	62.16±0.42	24.07±0.18	25.49±0.16	26.77±0.21	14.64±0.17	13.16±0.13	7.42±0.16
21233 (EP)	1.917±0.011	61.95±0.41	61.40±0.33	32.03±0.26	33.95±0.16	35.29±0.25	21.04±0.22	24.94±0.28	8.32±0.17
21237 (EP)	2.079±0.010	63.02±0.48	62.63±0.26	30.12±0.25	31.82±0.16	33.41±0.25	19.37±0.19	21.75±0.23	8.00±0.15

*Shots 77004 and 77006, which used liquid D_2–filled targets, were not included in the NCD Hugoniot fit because of the large uncertainty in measuring Δt_{total} from the lack of step/vacuum interfaces and contractions of the glue layers in the cryogenic cell.

an adjacent transparent witness.[34] This requires that the EOS of the witness and witness be known.

The amplitudes and temporal spacing of perturbations originating at the laser drive and arriving at the shock fronts in NCD and the adjacent quartz witness depend on their relative equations of state. Deviations from $\langle U_s^{NCD} \rangle$ are correlated to the observed velocity profile in the witness by $\delta U_s^{NCD}(t-t_1) = G\delta U_s^Q\left[(t-t_1)/F\right]$, where G and F are linear scaling factors that describe the relative amplitude and time history, respectively, of the shock-velocity profiles; δU_s^Q is the deviation from the average shock velocity in the quartz witness over the time period $\Delta t_{NCD}/F$, which corresponds to the same set of temporal perturbations experienced by the NCD; F is determined by the relative sound speeds and Hugoniots in the two materials; and G is additionally affected by the Grüneisen parameters. The quartz Hugoniot and $\Gamma = \Gamma_{eff}(U_s)$ were taken from Ref. 25, and quartz sound speeds were determined from the derivatives of the release paths calculated using that construct. Since the intention of this work was to measure the NCD Hugoniot, an iterative process was used where initial estimates for the Hugoniot, Γ's, and sound speeds were taken from a tabular EOS (LEOS 9061) (Ref. 23). This EOS model was chosen because the high-pressure SCD Hugoniot data best agree with LEOS 9061 predictions. The NCD velocity histories for the entire data set were first determined using the correction with these initial estimates. Then, impedance matching was done using the measured U_s^Q and inferred U_s^{NCD} at the IM interface to produce a linear U_s–u_p relation in NCD. The process was repeated using the updated Hugoniot fit so that the NCD velocity profiles were iteratively corrected until the linear U_s–u_p relation converged. An example of an NCD velocity history determined using this method is shown by the black curve in Fig. 148.1(c).

Velocity extrapolation across the glue layer at the quartz/NCD interface was treated differently to take advantage of the quartz witness. A continuous velocity profile was inferred across the glue layer at the quartz pusher/witness interface. Using this interpolation, the velocity profile in the witness beginning at the time the shock enters the NCD,

$$\left(t_1 + \Delta x_{glue}/U_s^{glue}\right),$$

was used in the nonsteady wave correction to determine F and G. With knowledge of F and G,

$$U_s^{NCD}(t) = \langle U_s^{NCD} \rangle + G\delta U_s^Q\left[(t-t_1)/F\right]$$

was used to calculate the NCD shock velocities at times t_1 and t_2 needed for impedance matching.

Results

1. Hugoniot Data

<u>*a. SCD:*</u> The SCD Hugoniot data are listed in Table 148.III and plotted in Fig. 148.3 with existing diamond data by Knudson *et al.*[8] and Hicks *et al.*[15] The Knudson *et al.* experiments primarily used full-density (3.515-g/cm^3) microcrystalline diamond and were performed using magnetically driven flyer-plate techniques. The Hicks experiments and this work, both IM experiments carried out using the OMEGA laser, used ⟨110⟩-oriented SCD and a quartz standard. The existing data in Fig. 148.3 suggest that *SESAME* 7830 best models the Hugoniot across the coexistence region (6 to 10.5 Mbar) and beyond the melt (>10.5 Mbar). This work measured less compressibility, however, than *SESAME* 7830 above 15 Mbar; this stiffer behavior is predicted by a DFT-MD EOS model (LEOS 9061).[23]

The Hicks data plotted in Fig. 148.3 are not the same as presented in the original publication; the data were re-analyzed using the updated quartz Hugoniot and the same re-shock formulation presented here. For a given pressure, this re-analysis decreased the density by ~3%. For $P^C > 20$ Mbar (corresponding to $P^Q > 16$ Mbar at the IM point), the quartz Hugoniot fit used in impedance matching was extrapolated to higher pressures than given in the quartz data set.[24,25] If the extrapolation of the quartz Hugoniot is not valid at higher pressure, this could contribute to the apparent stiffening of the Hugoniot data that relied on a quartz standard.

<u>*b. NCD:*</u> The NCD Hugoniot was measured between 10 and 25 Mbar. The data are presented in Table 148.II and plotted in the U_s–u_p and P–ρ planes in Fig. 148.4. The Hugoniot curves derived from the EOS tables in Fig. 148.4 were modeled using the appropriate lower initial density $\left(\rho_0^{NCD} = 3.36\ \mathrm{g/cm^3}\right)$. The NCD U_s–u_p Hugoniot data are approximately linear and were fit to $U_s = a_0 + a_1(u_p - \beta)$, where the coefficients and their standard deviations are listed in Table 148.IV. An orthogonally weighted least-squares linear fit was taken about the centroid of the data (β) so that the uncertainties in a_0 and a_1 are uncorrelated.[39] The standard deviation in the fit is given by[39]

$$\sigma_{U_s}(u_p) = \left[\sigma_{a_0}^2 + \sigma_{a_1}^2 (u_p - \beta)^2\right]^{1/2}.$$

The NCD data are slightly stiffer than predictions using LEOS 9061 [Fig. 148.4(b)], which well-represented the SCD

Table 148.III: ⟨110⟩ SCD Hugoniot data from impedance matching with a quartz standard.

Shot	U_s^Q	U_s^{SCD}	P^{SC} (Mbar)	U_p^{SCD}	ρ^{SCD} (g/cm^3)
79050	27.54±0.16	28.47±0.10	16.00±0.16	15.98±0.16	8.02±0.11
79053	28.68±0.16	29.56±0.10	17.51±0.17	16.85±0.16	8.17±0.12
77848	32.94±0.11	33.84±0.06	23.79±0.19	20.00±0.16	8.59±0.10
77858	33.17±0.09	34.07±0.06	24.15±0.18	20.16±0.15	8.61±0.10
77860	33.77±0.10	34.24±0.06	24.92±0.20	20.70±0.17	8.89±0.12
77851	34.62±0.09	35.06±0.06	26.27±0.24	21.32±0.19	8.97±0.13
77856	34.82±0.09	35.29±0.07	26.62±0.25	21.46±0.20	8.97±0.14

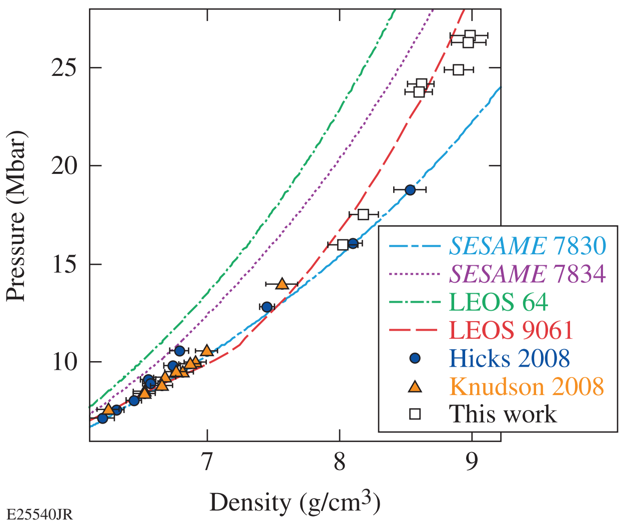

Figure 148.3
Full-density (ρ_0 = 3.515 g/cm^3) diamond Hugoniot data from this work (open squares), Knudson[8] (orange triangles), and Hicks[15] re-analyzed using the updated quartz equation of state (EOS)[25] (blue circles). The data are compared to Hugoniots modeled using diamond EOS tables.

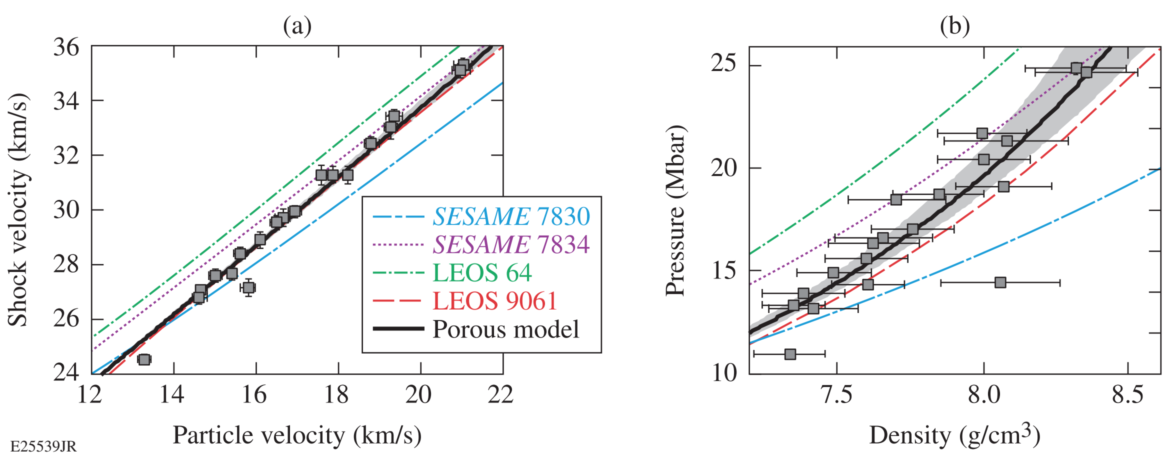

Figure 148.4
NCD (ρ_0 = 3.36 g/cm^3) Hugoniot data (gray squares) from impedance matching with a quartz standard. (a) The shock velocity versus particle velocity data and (b) the pressure versus density data are compared to Hugoniots modeled using diamond EOS tables and a porous model (solid black line) modeled using Eq. (6) with Γ = 1.03. The porous model using Γ = 1.03±0.1 is shown by the gray-shaded areas.

Table 148.IV: Coefficients and uncertainties to the orthogonally weighted least-squares fit to the NCD U_s–u_p data of the form $U_s = a_0 + a_1 (u_p - \beta)$.

a_0 (km/s)	a_1	β (km/s)	σ_{a_0}	σ_{a_1}
29.424	1.361	16.62	0.077	0.037

Hugoniot in the same pressure range (Fig. 148.3). NCD's lower initial density and reduced compressibility compared to SCD are consistent with that of a porous sample:

$$\left(m = \rho_0^{\text{SCD}} \Big/ \rho_0^{\text{NCD}} = 1.046\right).$$

Porous samples exhibit stiffer and even "reverse" Hugoniots as a result of added entropy during the pore-collapse phase of compression.[22]

We find that NCD's Hugoniot can be described using a simple porosity model from McQueen[21] (black line in Fig. 148.4), given by

$$P_{\text{H}}^{\text{NCD}}(\rho) = P_{\text{H}}^{\text{SCD}}(\rho) \frac{1 - \frac{\Gamma}{2}\left(\frac{\rho}{\rho_0^{\text{SCD}}} - 1\right)}{1 - \frac{\Gamma}{2}\left(\frac{\rho}{\rho_0^{\text{NCD}}} - 1\right)}, \tag{6}$$

where $P_{\text{H}}^{\text{SCD}}$ is the SCD Hugoniot, ρ_0^{SCD} = 3.515 g/cm^3, ρ_0^{NCD} = 3.36 g/cm^3, and Γ = 1.03. This model is derived from the definition of the Grüneisen parameter, such that the Hugoniots of the porous and crystal-density materials are related through Γ. The reference Hugoniot $\left(P_{\text{H}}^{\text{SCD}}\right)$ was established by fitting the SCD U_s–u_p Hugoniot data in the same high-pressure fluid region (>11 Mbar) as where the NCD data were obtained. This orthogonally weighted linear fit is given by U_s = (30.018±0.057) + (1.208±0.020) (u_p–17.12). For simplicity, Γ was assumed to be constant and was optimized at 1.03. The range of the porous model using Γ = 1.03±0.1 is represented by the gray-shaded area in Fig. 148.4. Γ ~ 1 is ~20% higher than predicted by the DFT-MD model, which predicts Γ ~ 0.8 over the same density range as the data. This suggests that compared to the DFT-MD model, more energy goes into ΔP than other degrees of freedom for a given ΔE. This difference is related to the discrepancy between the DFT-MD Hugoniot (using ρ_0^{NCD}) and the NCD data despite agreement with the SCD Hugoniot data.

c. Error analysis: The values and errors in the Hugoniot data (Tables 148.II and 148.III) represent the mean and standard deviation of each parameter determined using a Monte Carlo error analysis with 10,000 runs for NCD and 100,000 runs for SCD. For each run, the observable parameters $\left(U_s^Q\right.$ and U_s^{SCD} for SCD, or U_s^Q Δx_{NCD}, Δx_{total}, Δt_{total}, and ρ_0^{NCD} for NCD) were varied within their error estimates. The cubic quartz U_s–u_p coefficients and Γ_{eff} used in impedance matching were varied once per run using the co-variance matrices listed in Ref. 25. For NCD, the nonsteady wave correction and impedance matching were done each time until convergence was met, yielding 10,000 possible sets of Hugoniot data. The total error bars in ρ^{NCD} are between 1.5% and 3%, with the dominating error caused by the uncertainty in target metrology and transit times.

2. Release Data

The diamond release data (Table 148.I) are plotted in Fig. 148.5 in terms of the observables, i.e., shock velocities on either side of the IM interface. The U_s^{C} and U_s^{Stan} data are shown for the release of diamond into liquid D_2, SiO_2 foam, CH, and quartz (the blue triangles, green diamonds, red squares, and orange circles, and respectively). The data are compared to the velocities predicted at the IM interface (lines) using the diamond EOS models. These lines were created using states on the diamond Hugoniot (abscissa) from which release paths were calculated. The intersections of release paths with the Hugoniot of the known standard provided the final states (ordinate).

The SCD release data in Fig. 148.5(a) show that *SESAME* 7830 (black lines) and LEOS 9061 (colored lines) are best for modeling the overall behavior of the diamond release at the pressures where their respective Hugoniots are most valid, i.e., *SESAME* 7830 below $U_s^{\text{C}} < 28$ km/s and LEOS 9061 above that velocity. The SCD data with $U_s^{\text{C}} < 24.4$ km/s, which corresponds to the completion of melt along the Hugoniot,[7] should be in the coexistence region upon release. The data do not deviate from the *SESAME* 7830 predictions, which do not include strength effects, indicating that strength does not play a significant role in the release from >8 Mbar. Shock-wave splitting into an elastic precursor and an inelastic wave should not occur until U_s^{C} decays below ~22.3 km/s in the ⟨110⟩ SCD and ~21.6 km/s in polycrystalline diamond,[16] and therefore should not affect the SCD or NCD data sets.

For the NCD [Fig. 148.5(b)], the data are well represented using a Mie–Grüneisen release model referencing the porous Hugoniot shown in Fig. 148.4 with a constant Γ = 1.03 along the

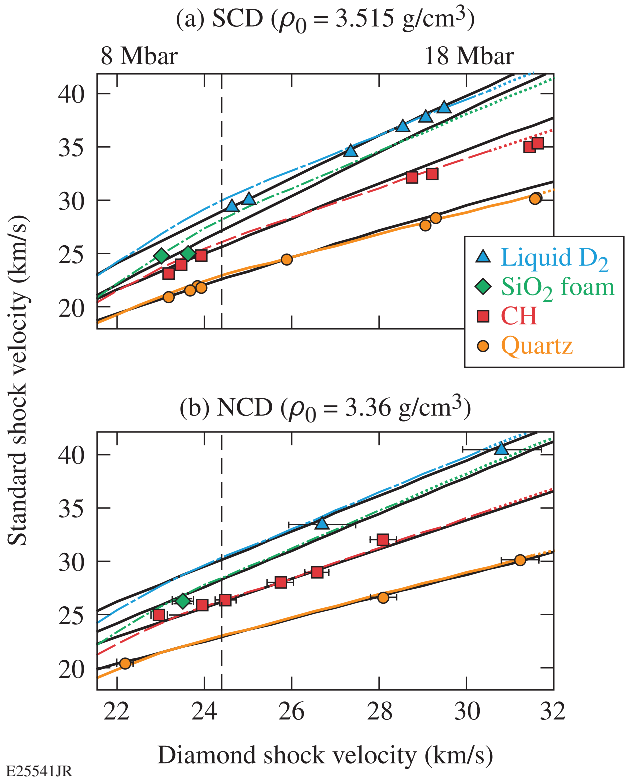

Figure 148.5
(a) SCD and (b) NCD release data compared to predictions using diamond EOS models and existing Hugoniot fits for the standards. Data points are shock velocities for diamond releasing into liquid D_2 (blue triangles), SiO_2 foam (green diamonds), CH (red squares), and quartz (orange circles). Predicted $U_s^C-U_s^{Stan}$ relationships using LEOS 9061 (colored lines) to model the diamond Hugoniot and release paths and existing Hugoniot fits for the standards: liquid D_2 (Refs. 28 ad 29) (dashed–dotted blue line), SiO_2 foam[27] (dashed–dotted green line), CH (Ref. 26) (dashed red line), and quartz[24,25] (solid orange line). Dotted portions of lines indicate that an extrapolation of the Hugoniot fit outside the standard's data range was used. The black lines in (a) are predicted $U_s^C-U_s^{Stan}$ relationships using *SESAME* 7830 to model the diamond Hugoniot and release paths. The black lines in (b) are predicted $U_s^C-U_s^{Stan}$ relationships using a Mie–Grüneisen model for the diamond Hugoniot and release paths with the same Γ = 1.03. The dashed vertical lines in (a) and (b) indicate the completion of melt on the diamond Hugoniot at 24.4(±0.4) km/s (Ref. 7). For data to the left of the line, diamond released from the coexistence region. For data to the right of the line, diamond released from the liquid phase.

release path (black lines). This is consistent with the Γ = 1.03 used in the porous model that fits the Hugoniot data. LEOS 9061 (colored lines) is also adequate for predicting the release data, despite a slight 1% to 2% offset in inferred density for a given pressure on the initial Hugoniot state. The NCD data in the range $24 < U_s^{NCD} < 32$ km/s (~12 < P^{NCD} < ~20 Mbar) release from an initial state where LEOS 9061 is within the error of the NCD Hugoniot measurements. While LEOS 9061 does not fully capture the NCD Hugoniot, it does represent the release data. This indicates that LEOS 9061 correctly models the NCD ablator's release into surrogate liquid D_2 fuel when the experimental liquid D_2 Hugoniot (Hicks[28] re-analyzed by Knudson[29]) is used. For comparison, the Kerley deuterium model[40] predicts faster shock velocities at the IM interface than the Hicks Hugoniot fit.

The NCD was most likely shocked into the liquid phase at the front NCD surface where the Hugoniot was measured. In the shots to the left of the melt line in Fig. 148.5(b), the shock decayed sufficiently enough during its transit that the NCD was at least partially solid upon release at its rear surface. This was apparent from the VISAR data of the unobstructed NCD step, which showed finite reflectivity at the NCD free surface after shock breakout, indicating a solid rather than a liquid state. The U_s^{Stan} data still follow the LEOS 9061 predictions, whereas when SCD released from the solid phase, the U_s^{Stan} data were slower than the LEOS 9061 predictions. Thermal effects from NCD's porosity could be contributing to the different response when NCD releases from the coexistence region.

Conclusions

The Hugoniot and release behavior of diamond were measured at multimegabar pressures and the Grüneisen parameter for high-pressure fluid carbon was extracted from the experimental data sets. These measurements are important to constrain models used in planetary astrophysics and to design ICF targets with NCD ablators. The SCD Hugoniot above 15 Mbar agrees with DFT-MD calculations (LEOS 9061) in liquid carbon. NCD's response to shock compression is slightly stiffer than that of SCD and the DFT-MD predictions, even when taking into account its lower initial density. This behavior can be described using a standard porosity model,[21] indicating that thermal effects from the initial pore collapse affect NCD's high-pressure Hugoniot. This effect must be included when using the EOS tables to model NCD. The stiffer NCD response compared to the DFT-MD EOS model (LEOS 9061) has implications for ICF target designs because additional heating raises the adiabat of the implosion. A Grüneisen parameter of ~1 in the liquid phase (11 to 26 Mbar) was derived from the experimental NCD and SCD Hugoniot fits. This value is consistent with a Mie–Grüneisen EOS that accurately models the NCD release data.

We measured two data points of NCD releasing into liquid D_2 and six SCD/liquid D_2 data points, which are especially valuable for constraining ICF models that describe the NCD ablator release into the hydrogen fuel.[41,42] The diamond–liquid

D_2 IM data can be reproduced when using the appropriate diamond EOS model (*SESAME* 7830 or LEOS 9061 based on the diamond type and U_s^C) and the experimental liquid D_2 Hugoniot.[28,29] Overall, the release response of both types of diamond are adequately modeled using existing EOS tables, which do not include strength effects. Strength may affect the diamond release behavior at lower pressure when the elastic precursor is separated from the main shock wave. Some difference in behavior exists between SCD and NCD when releasing from the coexistence region. Thermal effects from NCD's porosity could be the source of this difference.

ACKNOWLEDGMENT

This material is based upon work supported by the Department of Energy National Nuclear Security Administration under Award No. DE-NA0001944, the University of Rochester, and the New York State Energy Research and Development Authority. The support of DOE does not constitute an endorsement by DOE of the views expressed in this article.

REFERENCES

1. M. Ross, Nature **292**, 435 (1981).
2. N. Madhusudhan, K. K. M. Lee, and O. Mousis, Astrophys. J. Lett. **759**, L40 (2012).
3. H. M. Van Horn, *Unlocking the Secrets of White Dwarf Stars* (Springer International Publishing, Switzerland, 2015).
4. T. S. Metcalfe, M. H. Montgomery, and A. Kanaan, Astrophys. J. **605**, L133 (2004).
5. F. Ancilotto *et al*., Science **275**, 1288 (1997).
6. T. Guillot, Annu. Rev. Earth Planet. Sci. **33**, 493 (2005).
7. J. H. Eggert, D. G. Hicks, P. M. Celliers, D. K. Bradley, R. S. McWilliams, R. Jeanloz, J. E. Miller, T. R. Boehly, and G. W. Collins, Nat. Phys. **6**, 40 (2010).
8. M. D. Knudson, M. P. Desjarlais, and D. H. Dolan, Science **322**, 1822 (2008).
9. A. A. Correa *et al*., Phys. Rev. B **78**, 024101 (2008).
10. A. J. MacKinnon, N. B. Meezan, J. S. Ross, S. Le Pape, L. Berzak Hopkins, L. Divol, D. Ho, J. Milovich, A. Pak, J. Ralph, T. Döppner, P. K. Patel, C. Thomas, R. Tommasini, S. Haan, A. G. MacPhee, J. McNaney, J. Caggiano, R. Hatarik, R. Bionta, T. Ma, B. Spears, J. R. Rygg, L. R. Benedetti, R. P. J. Town, D. K. Bradley, E. L. Dewald, D. Fittinghoff, O. S. Jones, H. R. Robey, J. D. Moody, S. Khan, D. A. Callahan, A. Hamza, J. Biener, P. M. Celliers, D. G. Braun, D. J. Erskine, S. T. Prisbrey, R. J. Wallace, B. Kozioziemski, R. Dylla-Spears, J. Sater, G. Collins, E. Storm, W. Hsing, O. Landen, J. L. Atherton, J. D. Lindl, M. J. Edwards, J. A. Frenje, M. Gatu-Johnson, C. K. Li, R. Petrasso, H. Rinderknecht, M. Rosenberg, F. H. Séguin, A. Zylstra, J. P. Knauer, G. Grim, N. Guler, F. Merrill, R. Olson, G. A. Kyrala, J. D. Kilkenny, A. Nikroo, K. Moreno, D. E. Hoover, C. Wild, and E. Werner, Phys. Plasmas **21**, 056318 (2014).
11. J. Biener, D. D. Ho, C. Wild, E. Woerner, M. M. Biener, B. S. El-dasher, D. G. Hicks, J. H. Eggert, P. M. Celliers, G. W. Collins, and N. E. Teslich, Jr., Nucl. Fusion **49**, 112001 (2009).
12. C. Dawedeit *et al*., Diam. Relat. Mater. **40**, 75 (2013).
13. H. Nagao *et al*., Phys. Plasmas **13**, 052705 (2006).
14. S. Brygoo *et al*., Nature Materials **6**, 274 (2007).
15. D. G. Hicks, T. R. Boehly, P. M. Celliers, D. K. Bradley, J. H. Eggert, R. S. McWilliams, R. Jeanloz, and G. W. Collins, Phys. Rev. B **78**, 174102 (2008).
16. R. S. McWilliams, J. H. Eggert, D. G. Hicks, D. K. Bradley, P. M. Celliers, D. K. Spaulding, T. R. Boehly, G. W. Collins, and R. Jeanloz, Phys. Rev. B **81**, 014111 (2010).
17. K. Kondo and T. J. Ahrens, Geophys. Res. Lett. **10**, 281 (1983).
18. M. N. Pavlovskii, Sov. Phys.-Solid State **13**, 741 (1971).
19. R. F. Smith, J. H. Eggert, R. Jeanloz, T. S. Duffy, D. G. Braun, J. R. Patterson, R. E. Rudd, J. Biener, A. E. Lazicki, A. V. Hamza, J. Wang, T. Braun, L. X. Benedict, P. M. Celliers, and G. W. Collins, Nature **511**, 330 (2014).
20. D. K. Bradley, J. H. Eggert, R. F. Smith, S. T. Prisbrey, D. G. Hicks, D. G. Braun, J. Biener, A. V. Hamza, R. E. Rudd, and G. W. Collins, Phys. Rev. Lett. **102**, 075503 (2009).
21. R. G. McQueen *et al*., in *High-Velocity Impact Phenomena*, edited by R. Kinslow (Academic Press, New York, 1970).
22. Ya. B. Zel'dovich and Yu. P. Raĭzer, in *Physics of Shock Waves and High-Temperature Hydrodynamic Phenomena*, edited by W. D. Hayes and R. F. Probstein (Academic Press, New York, 1966).
23. L. X. Benedict *et al*., Phys. Rev. B **89**, 224109 (2014).
24. M. D. Knudson and M. P. Desjarlais, Phys. Rev. Lett. **103**, 225501 (2009).
25. M. D. Knudson and M. P. Desjarlais, Phys. Rev. B **88**, 184107 (2013).
26. M. A. Barrios, D. G. Hicks, T. R. Boehly, D. E. Fratanduono, J. H. Eggert, P. M. Celliers, G. W. Collins, and D. D. Meyerhofer, Phys. Plasmas **17**, 056307 (2010).
27. M. D. Knudson and R. W. Lemke, J. Appl. Phys. **114**, 053510 (2013).
28. D. G. Hicks, T. R. Boehly, P. M. Celliers, J. H. Eggert, S. J. Moon, D. D. Meyerhofer, and G. W. Collins, Phys. Rev. B **79**, 014112 (2009).
29. M. D. Knudson, M. P. Desjarlais, and A. Pribram-Jones, Phys. Rev. B **91**, 224105 (2015).
30. T. R. Boehly, D. L. Brown, R. S. Craxton, R. L. Keck, J. P. Knauer, J. H. Kelly, T. J. Kessler, S. A. Kumpan, S. J. Loucks, S. A. Letzring, F. J. Marshall, R. L. McCrory, S. F. B. Morse, W. Seka, J. M. Soures, and C. P. Verdon, Opt. Commun. **133**, 495 (1997).

31. S. Skupsky, R. W. Short, T. Kessler, R. S. Craxton, S. Letzring, and J. M. Soures, J. Appl. Phys. **66**, 3456 (1989).

32. Y. Lin, T. J. Kessler, and G. N. Lawrence, Opt. Lett. **20**, 764 (1995).

33. E. I. Moses *et al*., Phys. Plasmas **16**, 041006 (2009).

34. D. E. Fratanduono, D. H. Munro, P. M. Celliers, and G. W. Collins, J. Appl. Phys. **116**, 033517 (2014).

35. P. C. Souers, *Hydrogen Properties for Fusion Energy* (University of California Press, Berkeley, CA, 1986).

36. P. M. Celliers, D. K. Bradley, G. W. Collins, D. G. Hicks, T. R. Boehly, and W. J. Armstrong, Rev. Sci. Instrum. **75**, 4916 (2004).

37. M. C. Gregor, R. Boni, A. Sorce, J. Kendrick, C. A. McCoy, D. N. Polsin, T. R. Boehly, P. M. Celliers, G. W. Collins, D. E. Fratanduono, J. H. Eggert, and M. Millot, Rev. Sci. Instrum. **87**, 114903 (2016).

38. A. Lazicki, R. A. London, F. Coppari, D. Erskine, J. Hawreliak, D. Fratanduono, P. Celliers, J. Eggert, M. Millot, D. Swift, G. Collins, M. Morales, K. Capersen, S. Kucheyev, H. Whitley, J. Caster, and J. Nilsen, "Shock Equation of State of LiH to 1100 GPa," submitted to Physical Review E.

39. P. M. Celliers, G. W. Collins, D. G. Hicks, and J. H. Eggert, J. Appl. Phys. **98**, 113529 (2005).

40. G. I. Kerley, Sandia National Laboratory, Albuquerque, NM, Report SAND2003-3613 (2003).

41. H. F. Robey, T. R. Boehly, P. M. Celliers, J. H. Eggert, D. Hicks, R. F. Smith, R. Collins, M. W. Bowers, K. G. Krauter, P. S. Datte, D. H. Munro, J. L. Milovich, O. S. Jones, P. A. Michel, C. A. Thomas, R. E. Olson, S. Pollaine, R. P. J. Town, S. Haan, D. Callahan, D. Clark, J. Edwards, J. L. Kline, S. Dixit, M. B. Schneider, E. L. Dewald, K. Widmann, J. D. Moody, T. Döppner, H. B. Radousky, A. Throop, D. Kalantar, P. DiNicola, A. Nikroo, J. J. Kroll, A. V. Hamza, J. B. Horner, S. D. Bhandarkar, E. Dzenitis, E. Alger, E. Giraldez, C. Castro, K. Moreno, C. Haynam, K. N. LaFortune, C. Widmayer, M. Shaw, K. Jancaitis, T. Parham, D. M. Holungal, C. F. Walters, B. Haid, E. R. Mapoles, J. Sater, C. R. Gibson, T. Malsbury, J. Fair, D. Trummer, K. R. Coffee, B. Burr, L. V. Berzins, C. Choate, S. J. Brereton, S. Azevedo, H. Chandrasekaran, D. C. Eder, N. D. Masters, A. C. Fisher, P. A. Sterne, B. K. Young, O. L. Landen, B. M. Van Wonterghem, B. J. MacGowan, J. Atherton, J. D. Lindl, D. D. Meyerhofer, and E. Moses, Phys. Plasmas **19**, 042706 (2012).

42. S. Hamel, L. X. Benedict, P. M. Celliers, M. A. Barrios, T. R. Boehly, G. W. Collins, T. Döppner, J. H. Eggert, D. R. Farley, D. G. Hicks, J. L. Kline, A. Lazicki, S. LePape, A. J. Mackinnon, J. D. Moody, H. F. Robey, E. Schwegler, and P. A. Sterne, Phys. Rev. B **86**, 094113 (2012).

The National Direct-Drive Program on OMEGA and at the National Ignition Facility

Introduction

The main approach to ignition by means of laser-driven inertial confinement fusion (ICF)[1] currently pursued at the National Ignition Facility (NIF)[2] is x-ray (or indirect) drive (ID), where the laser energy absorbed in a high-Z hohlraum is re-emitted in the form of x rays that drive the fuel capsule. In the other mainline ICF laser approach, direct drive (DD),[3] the target is driven by laser irradiation directly coupled to the plasma ablated from the imploding capsule. The main advantage of ID is reduced sensitivity of implosions to short-scale beam nonuniformities. The main advantage of DD is higher coupling efficiency (by a factor of 3 to 5) of the laser energy into kinetic energy of the shell (hydrodynamic efficiency) compared to that of ID. The OMEGA Laser System[4] and the KrF laser NIKE at the Naval Research laboratory (NRL)[5] have been the principal facilities for DD experiments in the U.S. When the decision to pursue ID as the main ICF approach was made by the U.S. ICF program back in 1976, single-beam laser quality was a major concern for achieving high compression in DD implosions without the shell breaking apart from the Rayleigh–Taylor (RT) instability[1] seeded by laser imprint. Early challenges in improving beam uniformity have been resolved over the last several decades by introducing several beam-smoothing techniques. These include distributed phase plates (DPP's),[6] polarization smoothing with birefringent wedges,[7] and smoothing by spectral dispersion (SSD).[8] In addition, implementing adiabat-shaping techniques[9,10] significantly reduced the impact of RT instability growth during shell acceleration. Also, imprint reduction was demonstrated by using mid-Z–doped ablators[11] and high-Z target overcoats.[12] Such progress along with the challenges in achieving ignition on the NIF using ID[13] suggests considering direct drive as a viable alternative for developing a burning-plasma platform in a laboratory. In addition to the conventional "hot-spot" ignition designs, several alternative direct-drive–ignition schemes have been proposed in the past. Shock ignition,[14] the most-promising approach, is currently being considered as an alternative symmetric direct-drive–ignition design for the NIF.

Compared to x-ray drive, direct-drive targets couple a larger fraction of laser energy into shell kinetic energy and internal energy of the neutron-producing central region of the target (hot spot) at peak fuel compression. This relaxes the requirement on shell convergence and hot-spot pressure in an igniting target. The ignition condition follows from Lawson criterion,[15,16] which can be written in a form commonly used in the ICF community as[1]

$$(\rho R)_{\text{hs}} \times T \gtrsim 0.3\ \text{g}/\text{cm}^3 \times 5\ \text{keV}, \tag{1}$$

where ρ, R_{hs}, and T are the hot-spot density, radius, and ion temperature, respectively. The requirement shown in Eq. (1) is intuitively simple: the hot-spot temperature must be ~5 keV for PdV work of the incoming shell to overcome radiation losses and have an alpha-particle production rate sufficient to create bootstrap heating; an areal density of ~0.3 g/cm^2 is required to stop alpha particles inside the hot spot at these temperatures. A product of these two quantities enters into the ignition condition since ignition at lower temperatures and higher areal densities is still possible because the cold shell becomes more opaque to radiation at higher shell areal densities (assuming that larger hot-spot areal density leads to larger shell areal densities), limiting radiation losses from the hot spot.[16] Substituting expressions for the pressure $p_{\text{hs}} = (1 + Z)\rho T/m_{\text{i}}$ (Z is the average ion charge and m_{i} is the average ion mass) and internal energy $E_{\text{hs}} = 3/2\, p_{\text{hs}} V_{\text{hs}}$ (V_{hs} is the neutron-averaged hot-spot volume) into Eq. (1) gives a minimum pressure requirement (threshold) for ignition:

$$p_{\text{hs}} > p_{\text{thr}} \equiv 250\ \text{Gbar}\left(\frac{E_{\text{hs}}}{10\ \text{kJ}}\right)^{-1/2},$$

or (2)

$$\overline{P} \equiv \frac{p_{\text{hs}}}{p_{\text{thr}}} = \left(\frac{p_{\text{hs}}}{250\ \text{Gbar}}\right)\sqrt{\frac{E_{\text{hs}}}{10\ \text{kJ}}} > 1,$$

where $\overline{P}$ is the ignition pressure parameter. Equation (2) also sets the limit on the hot-spot volume in an igniting target:

$$V_{\text{hs}} < V_{40}\left(\frac{E_{\text{hs}}}{10\text{ kJ}}\right)^{3/2}, \text{ or } \max\left(R_{\text{hs}}\right) \sim \sqrt{E_{\text{hs}}}, \qquad (3)$$

where $V_{40} = 4\pi/3\ (40\ \mu\text{m})^3$ is the volume of a 40-μm sphere. Figure 148.6 plots the alpha-amplification factor ($Y_\alpha / Y_{\text{no}\,\alpha} - 1$, where Y_α and $Y_{\text{no}\,\alpha}$ are the target yields with and without alpha-particle deposition and fuel heating, respectively) as a function of ignition pressure parameter $\overline{P}$. The plot is obtained using 1-D *LILAC*[17] simulations of cryogenic targets at different laser drive energies (from OMEGA- to the NIF-scale designs). The solid line in the figure shows a fit to the simulation results at $\overline{P} < 1$, $\delta Y / Y = \overline{P} \exp\left(1.7\,\overline{P}^{\,2/3}\right)$. $\overline{P} \sim 1$ defines the ignition threshold. When $\overline{P} > 1$ and the fuel areal density at peak compression is large enough [$(\rho R)_{\text{fuel}} > 1$ g/cm^2] to burn a significant fraction of the main fuel, the target gain greatly exceeds unity ($G > 10$). In simulations where the main fuel areal density is low, the shell burnup fraction is not significant and the yield amplification continues to follow the fit even for $\overline{P} > 1$.

Spherically symmetric DD cryogenic designs on OMEGA presently couple up to 0.44 kJ (out of 26-kJ incident laser energy) into the hot-spot internal energy.[18] When hydrodynamically scaled to the NIF-size laser energy (1.5 MJ to 1.8 MJ), these designs are predicted to couple 5× to 10× more energy into the hot spot [25 kJ to 40 kJ for DD designs, depending on the laser-coupling efficiency] compared to that of ID (4 kJ to 5 kJ is inferred in the current best-performing ID implosions on the NIF), resulting in 2.5× to 3× lower hot-spot pressures required for DD ignition. The hot-spot size also gets larger with E_{hs} [see Eq. (3)], leading to smaller shell convergence ratio (CR ~ 22 compared to 35 to 40 in the ID ignition designs) and resulting in less-demanding long-wavelength drive-uniformity requirements.

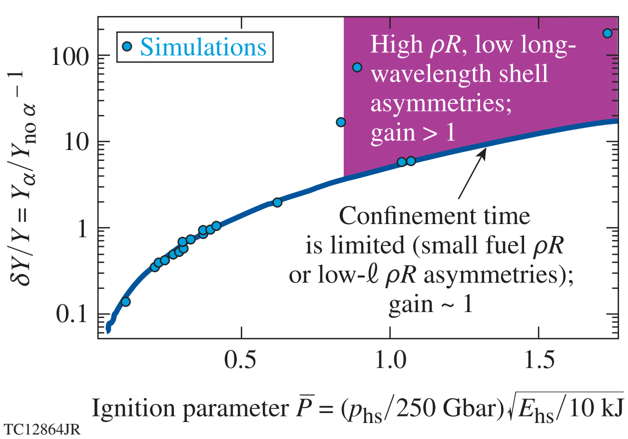

Figure 148.6
Alpha-amplification factor $\delta Y/Y$ as function of the ignition pressure parameter $\overline{P}$. The points represent the results of 1-D *LILAC* simulations of designs at different laser energies in the range of OMEGA to National Ignition Facility (NIF) scale. The solid line shows a fit to the simulation results at $\overline{P} < 1$, $\delta Y / Y = \overline{P} \exp\left(1.7\,\overline{P}^{\,2/3}\right)$.

With the goal of a successful ignition demonstration using direct drive, the recently established national DD strategy has several elements and involves the following facilities and institutions: Omega (a leading facility for DD research); NRL [which leads the effort on laser imprint reduction and plays a major role in the mitigation of coupling losses caused by laser–plasma interaction (LPI)]; Lawrence Livermore National Laboratory (which recently established a DD working group concentrating its effort on understanding LPI at ignition-relevant scales, developing DD target designs with yields in the range from 100 kJ to a few MJ, and developing 3-D computational capability for DD applications); and Los Alamos National Laboratory (which leads the effort in simulating high-Z overcoats, experimental study of long-wavelength drive asymmetry, and developing platforms to study material properties in the warm-dense-matter regime). The elements of DD strategy include experimentally demonstrating on OMEGA the hot-spot conditions ($p_{\text{hs}} > 100$ Gbar) relevant for ignition at MJ-scale laser energies available on the NIF and developing an understanding of LPI and laser coupling using DD experiments on the NIF in the current indirect-drive configuration.

OMEGA Cryogenic Implosions

The target performance depends on both the drive and uniformity conditions. We begin this section with a discussion on the one-dimensional (1-D) physics.

1. One-Dimensional Physics

To emphasize the importance of drive conditions in designing ignition targets, the 1-D scaling laws (which exclude multidimensional effects) for peak pressure and hot-spot energy are written in terms of implosion parameters: implosion velocity v_{imp} (the peak mass-averaged shell velocity), peak drive (ablation) pressure p_{abl}, adiabat α of the unablated fuel mass (ratio of the shell pressure to Fermi pressure at shell density), and peak in shell kinetic energy E_{kin} (Ref. 19):

$$p_{\mathrm{hs}}^{1\text{-D}} \sim \frac{p_{\mathrm{abl}}^{1/3}\, v_{\mathrm{imp}}^{10/3}}{\alpha},$$

$$E_{\mathrm{hs}}^{1\text{-D}} \sim E_{\mathrm{kin}} \frac{v_{\mathrm{imp}}^{4/3}}{\alpha^{2/5}\, p_{\mathrm{abl}}^{4/15}},$$

$$\overline{P}_{1\text{-D}} \sim \frac{\sqrt{E_{\mathrm{kin}}}\, v_{\mathrm{imp}}^{4}\, p_{\mathrm{abl}}^{1/5}}{\alpha^{6/5}}. \tag{4}$$

Modeling these critical implosion parameters must be experimentally validated before an assessment of the importance of multidimensional effects on the target performance can be made. The implosion velocity and shell kinetic energy are inferred in an experiment by measuring ablation-front trajectory and mass ablation rate using self-emission imaging.[20] The ablation pressure is inferred from simulations that match the measured ablation-front trajectory, mass ablation rate, bang time,[21] and scattered-light power and spectrum.[19,22] Finally, the shock-induced adiabat is inferred by measuring shock velocities early in the pulse using the velocity interferometer system for any reflector (VISAR).[23] An additional increase in the fuel adiabat caused by hot-electron preheat is estimated by measuring the hard x-ray signal[24] and areal density[25,26] in mid- to high-adiabat implosions (the areal density in 1-D, for a given laser energy, depends mainly on shell adiabat,[27] $\rho R \sim \alpha^{-0.5}$). A detailed comparison of 1-D simulation results using *LILAC* with the data shows good agreement between the two for a variety of target designs and drive conditions.[19] One-dimensional simulations include a nonlocal thermal-transport model,[28] a ray-based cross-beam energy transfer (CBET) model[29] (see discussion on CBET in **Laser Coupling and CBET**, p. 177), and first-principles equation-of-state (FPEOS) models[30] for both the DT ice and CD ablator.

2. Multidimensional Effects

The stability properties of indirect- and direct-drive designs are different. In direct drive, a thin CH layer is ablated from the shell early in the pulse to take advantage of the higher hydrodynamic efficiency of DT.[19] Since the shell consists mainly of DT during acceleration, the fuel adiabat α [which enters into the ignition scaling laws shown in Eqs. (4)] and the average in-flight shell adiabat α_{shell} (which determines shell stability property) are approximately equal, $\alpha \sim \alpha_{\mathrm{shell}}$ ($\alpha_{\mathrm{shell}} \gtrsim \alpha$ in adiabat-shaped designs[10]). Then, the shell's in-flight aspect ratio (IFAR, defined as ratio of the target radius to the shell thickness) can be written as[31]

$$\mathrm{IFAR}_{\mathrm{DD}} \sim \frac{v_{\mathrm{imp}}^{2}}{\left(p_{\mathrm{abl}}^{2/5}\, \alpha_{\mathrm{shell}}^{3/5}\right)} \sim \frac{v_{\mathrm{imp}}^{2}}{\left(p_{\mathrm{abl}}^{2/5}\, \alpha^{3/5}\right)}. \tag{5}$$

While the in-flight shell adiabat in DD designs is determined primarily by the strength of initial shocks (the radiation preheat in DD cryogenic implosions raises the fuel adiabat by ~20%), the shell adiabat and IFAR in ID designs are determined mainly by the radiation transport, ablator opacity, and x-ray drive spectrum (the majority of shell mass during acceleration in indirect drive consists of the ablator material; ablator and main fuel masses become approximately equal at the end of acceleration). As a result,

$$\mathrm{IFAR}_{\mathrm{ID}} \nsim \frac{v_{\mathrm{imp}}^{2}}{\left(p_{\mathrm{abl}}^{2/5}\, \alpha_{\mathrm{shell}}^{3/5}\right)}. \tag{6}$$

Note that even though IFAR and the ablation-front RT growth in ID are determined by the x-ray heating of the ablator and not by the strength of initial shocks, the initial condition for RT instability is set during the shock propagation through the shell early in the drive, the so-called Richtmyer–Meshkov (RM) phase of perturbation evolution.[32] Therefore, the difference in the stability properties of indirectly driven shells for $\alpha = 1.4$ and "high-foot" $\alpha = 2.5$ designs[13] is caused mainly by differences in nonuniformity growth during the RM phase.[33]

Substituting Eq. (5) into Eq. (4) gives the following hot-spot scaling laws for DD implosions:

$$p_{\mathrm{hs}}^{1\text{-D}} \sim p_{\mathrm{abl}} \mathrm{IFAR}^{5/3},$$

$$V_{\mathrm{hs}}^{1\text{-D}} \sim \frac{E_{\mathrm{kin}}}{p_{\mathrm{abl}} \mathrm{IFAR}},$$

$$E_{\mathrm{hs}}^{1\text{-}D} \sim E_{\mathrm{kin}} \mathrm{IFAR}^{2/3},$$

$$\overline{P}_{1\text{-D}} \sim p_{\mathrm{abl}} \sqrt{E_{\mathrm{kin}}}\, \mathrm{IFAR}^{2}. \tag{7}$$

Equations (7) shows that the hot-spot pressure and the ignition pressure parameter $\overline{P}$ can be increased in 1-D mainly by raising the shell IFAR (by reducing the shell mass, for example) and by making the laser drive more efficient (by increasing the ablation pressure and shell kinetic energy). The maximum value of IFAR in a design is set by the target stability properties and the level of nonuniformity seeds: the short-scale modes (which satisfy $k\Delta < 1$, where k is the perturbation wave number and Δ is the in-flight shell thickness) disrupt the shell during the implosion if IFAR is too large [current cryogenic implosions on OMEGA are unstable if IFAR > 20 $(\alpha/3)^{1.1}$ (Ref. 19)]. The long-wavelength perturbations ($k\Delta > 1$) seeded by the laser power imbalance, laser mispointing, and target misalignment can prevent the hot spot from reaching the 1-D stagnation pressures if the RT instability and Bell–Plesset (BP)[1] nonuniformity growth are excessively large during deceleration. The design IFAR can be increased, nevertheless, if (1) the short-scale nonuniformities seeded by target imperfections and imprint are reduced and (2) the source of the long-wavelength perturbations (beam imbalance, target offset, and beam mispointing) is minimized.

3. Target Performance

Figure 148.7 shows the scaled ignition pressure parameter $\overline{P}$ inferred in OMEGA cryogenic implosions. Since v_{imp}, p_{abl}, and α are invariants with respect to laser energy E_{L} and E_{kin} is proportional to E_{L} (assuming constant laser-coupling efficiency for different E_{L}), $\overline{P}$ scales as $\sqrt{E_{\text{kin}}}$ [see Eq. (2)]. Therefore, extrapolating the OMEGA results to the NIF-scale laser energy leads to $\overline{P}_{\text{scaled}} = \overline{P}_{\text{OMEGA}} \left(E_{\text{L}}^{\text{NIF}} / E_{\text{L}}^{\text{OMEGA}}\right)^{1/2}$.

The latter quantity is plotted in Fig. 148.7 for OMEGA cryogenic implosions driven at different values of the fuel adiabat (calculated using *LILAC* simulations). The hot-spot pressure and internal energy are inferred[18,34] by using the measured neutron yield, the burn duration Δt_{burn} (Ref. 21), the neutron-averaged ion temperature $\langle T_{\text{i}} \rangle_{\text{n}}$, and the hot-spot size. Diamonds represent the experimentally inferred $\overline{P}_{\text{scaled}}$ and squares represent the 1-D *LILAC* predictions. The trend lines represent the best linear fit to the simulation data. The highest hot-spot pressure inferred in these experiments is 56±7 Gbar (Ref. 18). According to Fig. 148.7, when scaled to the laser energy available on the NIF, the current OMEGA implosions reach up to ~40% of the pressure required for ignition. Then, using the alpha amplification scaling shown in Fig. 148.6, these implosions would yield a 2× yield amplification because of alpha heating. Similar conclusions were reached using an independent calculation recently performed based on the $P\tau$ analysis.[35]

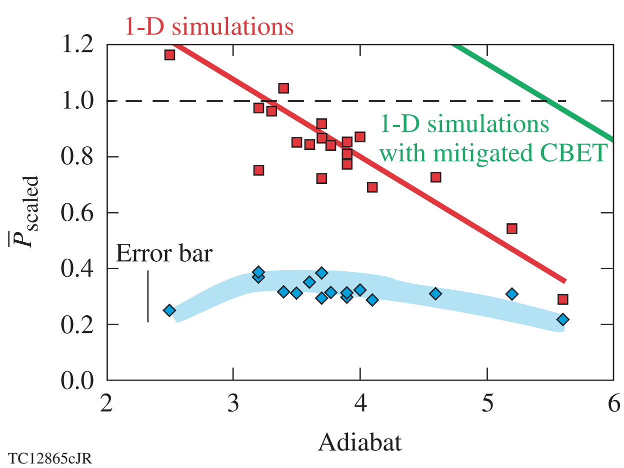

Figure 148.7
Ignition pressure parameter scaled to 1.8-MJ laser energy. Diamonds represent values inferred from the experimental data, squares show the 1-D simulation results with the full cross-beam energy transfer (CBET) effect, and the solid green line represents a linear fit through simulations with CBET fully mitigated. The short vertical line shows a typical error bar for the inferred values of $\overline{P}$. To ignite, $\overline{P}_{\text{scaled}}$ in a design must exceed unity (dashed line).

To understand the trends shown in Fig. 148.7, the effects of shell nonuniformity must be considered. As the shell adiabat increases, the target performance becomes less sensitive to the nonuniformity growth and the inferred $\overline{P}$ approaches the 1-D–predicted values. For lower values of shell adiabat, however, the deviation of the observed $\overline{P}$ from the predictions increases. Since the 1-D value of $\overline{P}$ decreases with the adiabat [see Eq. (4)], the inferred value has a maximum at $\alpha \sim 3.5$, which is a consequence of the interplay between a 1-D reduction in $\overline{P}$ and a shell stability improvement as the adiabat increases.

The performance-degradation mechanisms in cryogenic DD implosions include both the long-wavelength modes and the short-scale growth (which breaks up the shell during acceleration and introduces mix between the ablator and the hot spot as well as between the cold, denser part of the fuel and the hot spot). The long-wavelength modes increase the volume of a central, lower-density region (which forms the hot spot when the effects of asymmetry growth are negligible but might contain colder regions excluded from the hot spot in a perturbed implosion) as well as create thin spots in the cold shell during deceleration, producing expanding bubbles that reduce pusher efficiency and limit hot-spot confinement.[18,36]

4. Three-Dimensional Results

The evolution of long-wavelength nonuniformities seeded by the target offset, beam geometry, beam-power imbalance, and mispointing is studied using the 3-D hydrocode *ASTER*.[36] These simulations show that such nonuniformities form bubbles (regions of low-density material that protrude from the central region into the higher-density shell) that develop because of the deceleration in RT and BP growth. As the shell continues to converge, the bubbles eventually break out of the shell, prematurely quenching the hot-spot confinement and neutron yield.[34,36] Because nonuniformities cause the peak burn to occur earlier, our observations based on the fusion products sample the implosion conditions when the shell convergence has not yet reached the peak value. This effect and nonradial flows caused by the 3-D effects prevent the fuel from reaching stagnation, limiting conversion efficiency of shell kinetic energy into internal energy of the hot spot at peak burn.

The experimental evidence of low-mode asymmetries includes the x-ray self-emission imaging from a tracer Ti layer embedded into the CH shell.[37] This technique shows that significant low-mode nonuniformities developed during deceleration. Another self-emission imaging technique that maps the implosion shape during the acceleration indicates the growth of low-ℓ modes while the target is being driven by laser illumination.[38] In addition, significant variations in the measured ion temperature along different lines of sight (LOS's) in cryogenic implosions are also indicative of asymmetry flows. The ion temperature is inferred in an experiment by measuring the spectral width of neutrons created as a result of fusing D and T. The spectral broadening, however, is caused not only by the thermal effects but also by the bulk motion with velocity distribution not aligned in a single direction. This results in higher temperature inferred from the fit $\langle T\rangle_{\mathrm{fit}}$ compared to the true thermal ion temperature T (Refs. 31 and 39): $\langle T\rangle_{\mathrm{fit}} \simeq T + 2/3\, m_{\mathrm{i}} V_{\mathrm{f}}^2$, where m_{i} is the average mass of fusion-reaction products and V_{f} is the bulk velocity. Since asymmetry growth creates different V_{f} along different LOS's, different values of ion temperature are inferred along multiple LOS's in a highly distorted implosion. The maximum measured temperature difference along three LOS's in OMEGA cryogenic implosions is shown in Fig. 148.8(a). The inferred temperature differences, up to 1 keV, correspond to nonradial flow velocities of $V_{\mathrm{f}} \sim 2.5 \times 10^7$ cm/s. This is consistent with the results of 3-D *ASTER* simulations that include the effect of power imbalance and target offset. The plot in Fig. 148.8(b) shows the calculated neutron spectra at three perpendicular views (solid lines) together with neutron spectrum calculated without the effect of bulk motion (dashed line). Figure 148.8(a) also shows that the measured temperature variation strongly correlates with the yield degradation relative to the 1-D predictions, suggesting that the residual kinetic energy plays a detrimental role in reducing the target performance.

The performance degradation in lower-adiabat implosions ($\alpha < 2.5$) is caused by both the long wavelengths (as described above) and the short-scale nonuniformities. The latter are seeded mainly by laser imprint, nonuniformities caused by target fabrication, and debris accumulated during cryogenic target production. Simulations indicate that the surface defects are the most damaging since they quickly evolve into nonlinear bubbles (modulations that produce local depressions in shell density) at the ablation front that are not stabilized by ablation[40] and grow at a rate exceeding the classical limit. Such growth leads to the ablator mixing into the main fuel and the vapor region.[41] These effects are directly observed in experiments. The ablator/cold shell mix is inferred from the backlit images obtained using a monochromatic x-ray imager.[42] The observed enhancement in x-ray attenuation by the main fuel in the low-adiabat implosion, not predicted by 1-D calculations,

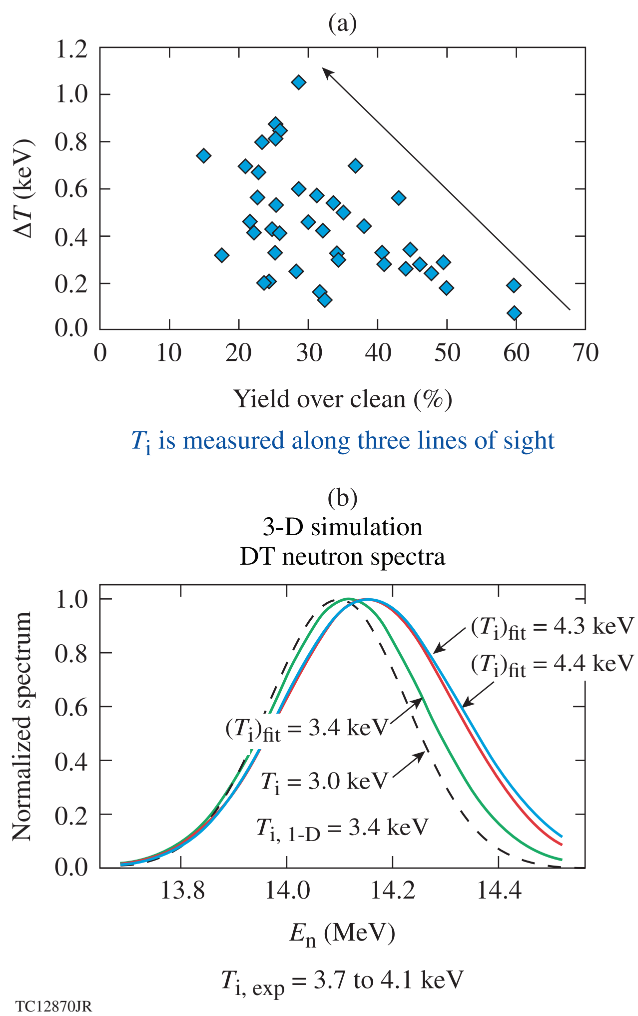

Figure 148.8
(a) The measured variation in ion temperature ΔT (keV) among three lines of sight in cryogenic implosions on OMEGA as a function of yield-over-predictions. (b) Neutron spectra along three perpendicular views (solid lines) as calculated using *ASTER* simulations of an OMEGA cryogenic implosion assuming ~20-μm target offset and 15%-root-mean-square (rms) power imbalance. The dashed line shows the neutron spectrum without the effects of the bulk fuel motion.

is consistent with 0.1% to 0.2% atomic mixing of C into DT. No mixing is required to explain the observed fuel opacity in higher-adiabat implosions ($\alpha > 3.5$). In addition, the x-ray core emission at peak compression is also enhanced when the fuel adiabat is reduced to $\alpha < 2.5$, indicating that ablator carbon penetrates all the way into the hot spot during the implosion.[43] The plastic ablator in direct-drive designs is thin and gets ablated in the middle of the drive pulse. The presence of the ablator in the hot spot suggests therefore a significant growth in local surface features that produce jet-like structures in the shell early in the implosion and bring the ablator material into the hot spot.[41]

5. Laser Coupling and CBET

The shell's stability properties can be significantly improved by increasing laser coupling and making the shell thicker. This can be accomplished by increasing the drive hydroefficiency. An analysis of direct-drive implosions on OMEGA has shown that coupling losses related to CBET[29] significantly limit the ablation pressure (as much as 40% on OMEGA and up to 60% on NIF-scale targets), implosion velocity, and shell kinetic energy. CBET results from the scattering of incoming laser light caused by stimulated Brillouin scatter. The reduction in the ablation pressure caused by CBET is shown in Fig. 148.9, where the ablation pressure, calculated at the time when the ablation surface had converged by a factor of 2.5, is plotted for OMEGA and NIF-scale symmetric designs at different drive intensities. Considering such losses, demonstrating the hydrodynamic equivalence of implosions on OMEGA to ignition designs on the NIF requires the shell IFAR to exceed the current stability threshold level (~22) (Ref. 19).

One of the CBET mitigation strategies[44] involves reducing the laser beam size relative to the initial target size. This strategy, as demonstrated both theoretically and experimentally, recovers some coupling losses and increases the ablation pressure.[29,34,45] The benefit of reducing beam size to enhance laser coupling is illustrated in Fig. 148.10, where the predicted time-dependent ablation pressure (plotted as a function of shell convergence) is shown for different ratios of R_b/R_t (R_b is defined as the radius of a 95% beam-energy contour). Figure 148.10 shows that the largest increase in coupling occurs early in the implosion when the critical surface is at a larger radius and the refraction effects prevent beams from intersecting in regions where CBET is effective (Mach ~ 1 surface in plasma corona). Later in the implosion when the critical surface has moved inward a sufficient distance, beams start to intersect in the CBET-resonant regions and exchange their energy, increasing CBET losses. When CBET is fully mitigated, the shell's kinetic and hot-spot internal energies increase, allowing implosions to reach ignition condition at a higher adiabat. This is illustrated in Fig. 148.7, where the green trend line shows the ignition pressure parameter with the enhanced laser

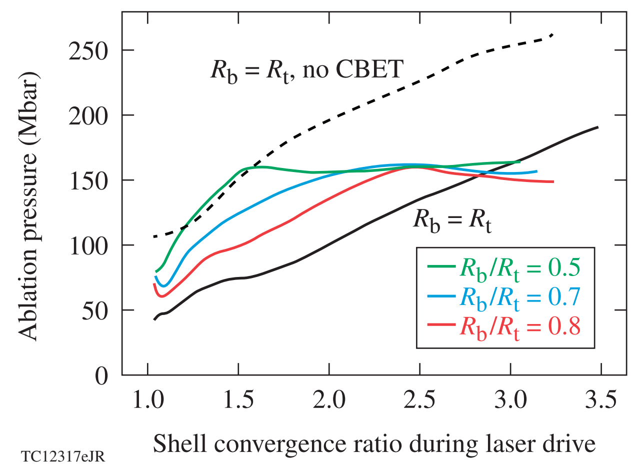

Figure 148.10
Time-dependent ablation pressure as a function of shell convergence for designs driven at $I = 9 \times 10^{14}$ W/cm^2.

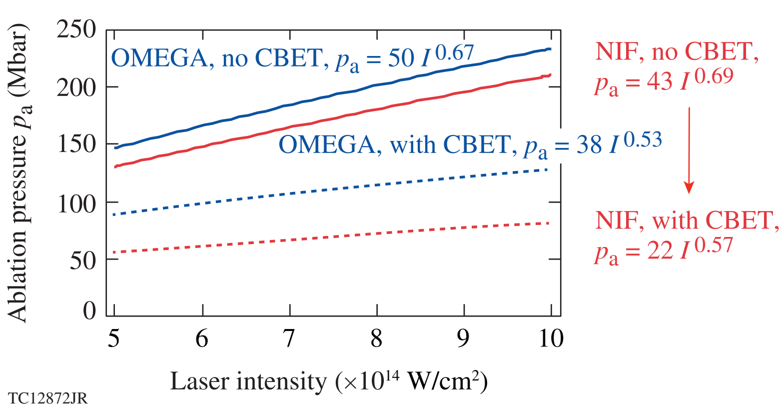

Figure 148.9
Ablation pressure as a function of incident laser intensity for OMEGA and NIF-scale designs. Solid lines show the calculation results without the effect of CBET; dashed lines include the effect of CBET. The ablation pressure was calculated when the ablation front had converged by a factor of 2.5 from its initial radius.

coupling. The adiabat in the ignition designs can be increased in this case up to $\alpha \sim 5.5$, significantly improving the shell's stability properties.

Experimental campaigns performed on OMEGA with the reduced R_b / R_t have demonstrated increased hydrodynamic efficiency.[34] The target performance in such implosions, however, was degraded. This was explained, based on the results of 3-D *ASTER* simulations,[36] by asymmetries caused by power imbalance, enhanced in these implosions because of reduced beam overlap.

Conclusions

The direct-drive approach to ignition, when compared to indirect-drive designs, offers a significant increase (by a factor of 3 to 5) in laser coupling to the shell kinetic energy. Cryogenic implosions on OMEGA have reached hot-spot pressures of 56 Gbar, which is ~40% of what is required for ignition. Extrapolating these results to NIF-scale laser energy is predicted to enhance the yield caused by alpha heating by a factor of 2. The cryogenic campaigns with reduced beam size relative to the target size $\left(R_b / R_t < 1\right)$, performed on OMEGA to reduce CBET losses, demonstrated increased laser coupling and hydrodynamic efficiency; however, this coupling enhancement did not improve the target performance. Numerical simulations indicate that long-wavelength nonuniformities caused by target offset and power imbalance lead to an increased target central volume and early burn truncation. Reaching the goal of demonstrating hydrodynamic equivalence on OMEGA must include improving laser power balance, target position, and target quality at shot time. CBET must also be reduced to increase the fuel mass and improve shell stability. CBET mitigation strategies include reduction in the beam size relative to the target size and laser wavelength separation.[46]

ACKNOWLEDGMENT

This material is based upon work supported by the Department of Energy National Nuclear Security Administration under Award Number DE-NA0001944, the University of Rochester, and the New York State Energy Research and Development Authority. The support of DOE does not constitute an endorsement by DOE of the views expressed in this article.

REFERENCES

1. S. Atzeni and J. Meyer-ter-Vehn, *The Physics of Inertial Fusion: Beam Plasma Interaction, Hydrodynamics, Hot Dense Matter*, International Series of Monographs on Physics (Clarendon Press, Oxford, 2004).
2. J. Paisner *et al*., Laser Focus World **30**, 75 (1994).
3. R. S. Craxton, K. S. Anderson, T. R. Boehly, V. N. Goncharov, D. R. Harding, J. P. Knauer, R. L. McCrory, P. W. McKenty, D. D. Meyerhofer, J. F. Myatt, A. J. Schmitt, J. D. Sethian, R. W. Short, S. Skupsky, W. Theobald, W. L. Kruer, K. Tanaka, R. Betti, T. J. B. Collins, J. A. Delettrez, S. X. Hu, J. A. Marozas, A. V. Maximov, D. T. Michel, P. B. Radha, S. P. Regan, T. C. Sangster, W. Seka, A. A. Solodov, J. M. Soures, C. Stoeckl, and J. D. Zuegel, Phys. Plasmas **22**, 110501 (2015).
4. T. R. Boehly, D. L. Brown, R. S. Craxton, R. L. Keck, J. P. Knauer, J. H. Kelly, T. J. Kessler, S. A. Kumpan, S. J. Loucks, S. A. Letzring, F. J. Marshall, R. L. McCrory, S. F. B. Morse, W. Seka, J. M. Soures, and C. P. Verdon, Opt. Commun. **133**, 495 (1997).
5. S. P. Obenschain *et al*., Phys. Plasmas **3**, 2098 (1996).
6. T. J. Kessler, Y. Lin, J. J. Armstrong, and B. Velazquez, Proc. SPIE **1870**, 95 (1993).
7. T. R. Boehly, V. A. Smalyuk, D. D. Meyerhofer, J. P. Knauer, D. K. Bradley, R. S. Craxton, M. J. Guardalben, S. Skupsky, and T. J. Kessler, J. Appl. Phys. **85**, 3444 (1999).
8. S. Skupsky, R. W. Short, T. Kessler, R. S. Craxton, S. Letzring, and J. M. Soures, J. Appl. Phys. **66**, 3456 (1989).
9. V. N. Goncharov, J. P. Knauer, P. W. McKenty, P. B. Radha, T. C. Sangster, S. Skupsky, R. Betti, R. L. McCrory, and D. D. Meyerhofer, Phys. Plasmas **10**, 1906 (2003).
10. V. N. Goncharov, T. C. Sangster, T. R. Boehly, S. X. Hu, I. V. Igumenshchev, F. J. Marshall, R. L. McCrory, D. D. Meyerhofer, P. B. Radha, W. Seka, S. Skupsky, C. Stoeckl, D. T. Casey, J. A. Frenje, and R. D. Petrasso, Phys. Rev. Lett. **104**, 165001 (2010).
11. S. X. Hu, G. Fiksel, V. N. Goncharov, S. Skupsky, D. D. Meyerhofer, and V. A. Smalyuk, Phys. Rev. Lett. **108**, 195003 (2012).
12. S. P. Obenschain *et al*., Phys. Plasmas **9**, 2234 (2002).
13. O. A. Hurricane *et al*., Nature **506**, 343 (2014).
14. R. Betti, C. D. Zhou, K. S. Anderson, L. J. Perkins, W. Theobald, and A. A. Solodov, Phys. Rev. Lett. **98**, 155001 (2007).
15. J. D. Lawson, Proc. Phys. Soc. Lond. B **70**, 6 (1957).
16. R. Betti, P. Y. Chang, B. K. Spears, K. S. Anderson, J. Edwards, M. Fatenejad, J. D. Lindl, R. L. McCrory, R. Nora, and D. Shvarts, Phys. Plasmas **17**, 058102 (2010).
17. J. Delettrez, R. Epstein, M. C. Richardson, P. A. Jaanimagi, and B. L. Henke, Phys. Rev. A **36**, 3926 (1987).
18. S. P. Regan, V. N. Goncharov, I. V. Igumenshchev, T. C. Sangster, R. Betti, A. Bose, T. R. Boehly, M. J. Bonino, E. M. Campbell, D. Cao, T. J. B. Collins, R. S. Craxton, A. K. Davis, J. A. Delettrez, D. H. Edgell, R. Epstein, C. J. Forrest, J. A. Frenje, D. H. Froula, M. Gatu Johnson, V. Yu. Glebov, D. R. Harding, M. Hohenberger, S. X. Hu, D. Jacobs-Perkins, R. T. Janezic, M. Karasik, R. L. Keck, J. H. Kelly, T. J. Kessler,

J. P. Knauer, T. Z. Kosc, S. J. Loucks, J. A. Marozas, F. J. Marshall, R. L. McCrory, P. W. McKenty, D. D. Meyerhofer, D. T. Michel, J. F. Myatt, S. P. Obenschain, R. D. Petrasso, R. B. Radha, B. Rice, M. Rosenberg, A. J. Schmitt, M. J. Schmitt, W. Seka, W. T. Shmayda, M. J. Shoup III, A. Shvydky, S. Skupsky, S. Solodov, C. Stoeckl, W. Theobald, J. Ulreich, M. D. Wittman, K. M. Woo, B. Yaakobi, and J. D. Zuegel, Phys. Rev. Lett. **117**, 025001 (2016).

19. V. N. Goncharov, T. C. Sangster, R. Betti, T. R. Boehly, M. J. Bonino, T. J. B. Collins, R. S. Craxton, J. A. Delettrez, D. H. Edgell, R. Epstein, R. K. Follet, C. J. Forrest, D. H. Froula, V. Yu. Glebov, D. R. Harding, R. J. Henchen, S. X. Hu, I. V. Igumenshchev, R. Janezic, J. H. Kelly, T. J. Kessler, T. Z. Kosc, S. J. Loucks, J. A. Marozas, F. J. Marshall, A. V. Maximov, R. L. McCrory, P. W. McKenty, D. D. Meyerhofer, D. T. Michel, J. F. Myatt, R. Nora, P. B. Radha, S. P. Regan, W. Seka, W. T. Shmayda, R. W. Short, A. Shvydky, S. Skupsky, C. Stoeckl, B. Yaakobi, J. A. Frenje, M. Gatu-Johnson, R. D. Petrasso, and D. T. Casey, Phys. Plasmas **21**, 056315 (2014).

20. D. T. Michel, C. Sorce, R. Epstein, N. Whiting, I. V. Igumenshchev, R. Jungquist, and D. H. Froula, Rev. Sci. Instrum. **83**, 10E530 (2012).

21. C. Stoeckl, V. Yu. Glebov, S. Roberts, T. C. Sangster, R. A. Lerche, R. L. Griffith, and C. Sorce, Rev. Sci. Instrum. **74**, 1713 (2003).

22. W. Seka, D. H. Edgell, J. P. Knauer, J. F. Myatt, A. V. Maximov, R. W. Short, T. C. Sangster, C. Stoeckl, R. E. Bahr, R. S. Craxton, J. A. Delettrez, V. N. Goncharov, I. V. Igumenshchev, and D. Shvarts, Phys. Plasmas **15**, 056312 (2008).

23. L. M. Barker and R. E. Hollenbach, J. Appl. Phys. **43**, 4669 (1972).

24. C. Stoeckl, V. Yu. Glebov, D. D. Meyerhofer, W. Seka, B. Yaakobi, R. P. J. Town, and J. D. Zuegel, Rev. Sci. Instrum. **72**, 1197 (2001).

25. J. A. Frenje, C. K. Li, F. H. Séguin, D. T. Casey, R. D. Petrasso, T. C. Sangster, R. Betti, V. Yu. Glebov, and D. D. Meyerhofer, Phys. Plasmas **16**, 042704 (2009).

26. C. J. Forrest, P. B. Radha, V. Yu. Glebov, V. N. Goncharov, J. P. Knauer, A. Pruyne, M. Romanofsky, T. C. Sangster, M. J. Shoup III, C. Stoeckl, D. T. Casey, M. Gatu-Johnson, and S. Gardner, Rev. Sci. Instrum. **83**, 10D919 (2012).

27. R. Betti and C. Zhou, Phys. Plasmas **12**, 110702 (2005).

28. V. N. Goncharov, T. C. Sangster, P. B. Radha, R. Betti, T. R. Boehly, T. J. B. Collins, R. S. Craxton, J. A. Delettrez, R. Epstein, V. Yu. Glebov, S. X. Hu, I. V. Igumenshchev, J. P. Knauer, S. J. Loucks, J. A. Marozas, F. J. Marshall, R. L. McCrory, P. W. McKenty, D. D. Meyerhofer, S. P. Regan, W. Seka, S. Skupsky, V. A. Smalyuk, J. M. Soures, C. Stoeckl, D. Shvarts, J. A. Frenje, R. D. Petrasso, C. K. Li, F. Séguin, W. Manheimer, and D. G. Colombant, Phys. Plasmas **15**, 056310 (2008).

29. I. V. Igumenshchev, D. H. Edgell, V. N. Goncharov, J. A. Delettrez, A. V. Maximov, J. F. Myatt, W. Seka, A. Shvydky, S. Skupsky, and C. Stoeckl, Phys. Plasmas **17**, 122708 (2010).

30. S. X. Hu, B. Militzer, V. N. Goncharov, and S. Skupsky, Phys. Rev. Lett. **104**, 235003 (2010); S. X. Hu, L. A. Collins, V. N. Goncharov, J. D. Kress, R. L. McCrory, and S. Skupsky, Phys. Rev. E **92**, 043104 (2015).

31. V. N. Goncharov, in *Laser-Plasma Interactions and Applications*, edited by P. McKenna, D. Neely, R. Bingham, and D. A. Jaroszynski, Scottish Graduate Series (Springer, Switzerland, 2013), Chap. 7, pp. 135–183.

32. V. N. Goncharov, O. V. Gotchev, E. Vianello, T. R. Boehly, J. P. Knauer, P. W. McKenty, P. B. Radha, S. P. Regan, T. C. Sangster, S. Skupsky, V. A. Smalyuk, R. Betti, R. L. McCrory, D. D. Meyerhofer, and C. Cherfils-Clérouin, Phys. Plasmas **13**, 012702 (2006).

33. D. S. Clark *et al*., Phys. Plasmas **21**, 112705 (2014).

34. V. N. Goncharov, S. P. Regan, T. C. Sangster, R. Betti, T. R. Boehly, E. M. Campbell, J. A. Delettrez, D. H. Edgell, R. Epstein, C. J. Forrest, D. H. Froula, V. Yu. Glebov, D. R. Harding, S. X. Hu, I. V. Igumenshchev, F. J. Marshall, R. L. McCrory, D. T. Michel, J. F. Myatt, P. B. Radha, W. Seka, A. Shvydky, C. Stoeckl, W. Theobald, B. Yaakobi, and M. Gatu-Johnson, J. Phys.: Conf. Ser. **717**, 012008 (2016).

35. A. Bose, K. M. Woo, R. Betti, E. M. Campbell, D. Mangino, A. R. Christopherson, R. L. McCrory, R. Nora, S. P. Regan, V. N. Goncharov, T. C. Sangster, C. J. Forrest, J. Frenje, M. Gatu Johnson, V. Yu. Glebov, J. P. Knauer, F. J. Marshall, C. Stoeckl, and W. Theobald, Phys. Rev. E **94**, 011201(R) (2016).

36. I. V. Igumenshchev, V. N. Goncharov, F. J. Marshall, J. P. Knauer, E. M. Campbell, C. J. Forrest, D. H. Froula, V. Yu. Glebov, R. L. McCrory, S. P. Regan, T. C. Sangster, S. Skupsky, and C. Stoeckl, Phys. Plasmas **23**, 052702 (2016).

37. R. C. Shah, B. M. Haines, F. J. Wysocki, J. F. Benage, J. Fooks, V. Glebov, P. Hakel, M. Hoppe, I. V. Igumenshchev, G. Kagan, R. C. Mancini, F. J. Marshall, D. T. Michel, T. J. Murphy, M. E. Schoff, C. Stoeckl, and B. Yaakobi, "Systematic Fuel Cavity Asymmetries in Directly Driven ICF Implosions," submitted to Physical Review Letters.

38. D. T. Michel, A. K. Davis, W. Armstrong, R. Bahr, R. Epstein, V. N. Goncharov, M. Hohenberger, I. V. Igumenshchev, R. Jungquist, D. D. Meyerhofer, P. B. Radha, T. C. Sangster, C. Sorce, and D. H. Froula, High Power Laser Science and Engineering **3**, e19 (2015).

39. T. J. Murphy, Phys. Plasmas **21**, 072701 (2014).

40. R. Betti and J. Sanz, Phys. Rev. Lett. **97**, 205002 (2006).

41. I. V. Igumenshchev, V. N. Goncharov, W. T. Shmayda, D. R. Harding, T. C. Sangster, and D. D. Meyerhofer, Phys. Plasmas **20**, 082703 (2013).

42. C. Stoeckl, M. Bedzyk, G. Brent, R. Epstein, G. Fiksel, D. Guy, V. N. Goncharov, S. X. Hu, S. Ingraham, D. W. Jacobs-Perkins, R. K. Jungquist, F. J. Marshall, C. Mileham, P. M. Nilson, T. C. Sangster, M. J. Shoup III, and W. Theobald, Rev. Sci. Instrum. **85**, 11E501 (2014).

43. T. C. Sangster, V. N. Goncharov, R. Betti, P. B. Radha, T. R. Boehly, D. T. Casey, T. J. B. Collins, R. S. Craxton, J. A. Delettrez, D. H.

Edgell, R. Epstein, C. J. Forrest, J. A. Frenje, D. H. Froula, M. Gatu-Johnson, V. Yu. Glebov, D. R. Harding, M. Hohenberger, S. X. Hu, I. V. Igumenshchev, R. Janezic, J. H. Kelly, T. J. Kessler, C. Kingsley, T. Z. Kosc, J. P. Knauer, S. J. Loucks, J. A. Marozas, F. J. Marshall, A. V. Maximov, R. L. McCrory, P. W. McKenty, D. D. Meyerhofer, D. T. Michel, J. F. Myatt, R. D. Petrasso, S. P. Regan, W. Seka, W. T. Shmayda, R. W. Short, A. Shvydky, S. Skupsky, J. M. Soures, C. Stoeckl, W. Theobald, V. Versteeg, B. Yaakobi, and J. D. Zuegel, Phys. Plasmas **20**, 056317 (2013).

44. I. V. Igumenshchev, D. H. Froula, D. H. Edgell, V. N. Goncharov, T. J. Kessler, F. J. Marshall, R. L. McCrory, P. W. McKenty, D. D. Meyerhofer, D. T. Michel, T. C. Sangster, W. Seka, and S. Skupsky, Phys. Rev. Lett. **110**, 145001 (2013).

45. D. H. Froula, T. J. Kessler, I. V. Igumenshchev, R. Betti, V. N. Goncharov, H. Huang, S. X. Hu, E. Hill, J. H. Kelly, D. D. Meyerhofer, A. Shvydky, and J. D. Zuegel, Phys. Plasmas **20**, 082704 (2013).

46. I. V. Igumenshchev, W. Seka, D. H. Edgell, D. T. Michel, D. H. Froula, V. N. Goncharov, R. S. Craxton, L. Divol, R. Epstein, R. Follett, J. H. Kelly, T. Z. Kosc, A. V. Maximov, R. L. McCrory, D. D. Meyerhofer, P. Michel, J. F. Myatt, T. C. Sangster, A. Shvydky, S. Skupsky, and C. Stoeckl, Phys. Plasmas **19**, 056314 (2012).

Measuring the Refractive Index of a Laser-Plasma Optical System

Using laser-plasma optical systems to manipulate the basic properties of light waves has caused a recent surge of interest.[1–4] Plasma-based photonic devices are attractive because they can be ultrafast, damage resistant, and easily tunable. Alleviating concerns about optic damage by replacing conventional optics with plasma-based components could lead to the next generation of high-power, large-scale laser facilities. Plasma gratings in particular have received a great deal of attention because they are routinely used to mediate cross-beam energy transfer in indirect-drive inertial confinement fusion (ICF) experiments at the National Ignition Facility (NIF).[5–7] Multiple experiments[8,9]—including ICF experiments at the NIF[10,11]—have consistently failed, however, to observe the level of energy transfer expected on the basis of linear theory.

Recently, that theory was revisited when it was recognized that plasma gratings could also be used to dynamically control the polarization of light waves.[1] The effect of a laser-plasma system on an independent probe laser beam can be described by a complex refractive-index perturbation that is a function of the wavelength shift between the interacting beams; the system can consequently (anisotropically) modify both the phase and the amplitude of the probe and therefore act as a wave plate and/or a polarizer.[1] Turnbull *et al.* recently presented the first demonstration of a laser-plasma wave plate utilizing the system's nonzero real refractive-index perturbation that exists even in the absence of a wavelength shift between the beams. This article reports on our use of wavelength tuning to more fully map out the complete refractive-index perturbation. For the first time the real component is measured as a function of the wavelength shift. The imaginary component, which underlies cross-beam energy transfer (CBET) experiments at the NIF, is measured with sufficient accuracy to resolve both nonresonant and resonant energy transfer and is found to be in excellent agreement with linear theory (both for the first time), yielding implications for ICF experiments. The data also include the first demonstration of a laser-plasma polarizer with 85% to 87% extinction, further complementing the existing suite of plasma-based photonic devices.

Our laser-plasma optical system consists of a plasma with electron density n_e, electron temperature T_e, and ion temperature T_i, as well as a "pump" laser beam with electric field E_0 and frequency ω_0. A probe laser beam with E_1 and ω_1 will encounter resonances if $\omega_1 - \omega_0 = \pm\omega_{IAW}$; i.e., the frequency difference between the two beams is equal to the frequency of an ion-acoustic wave (IAW) with wave number $k_b = \left|\mathbf{k}_0 - \mathbf{k}_1\right|$. The driven ion-acoustic wave mediates energy transfer between the two beams, thereby modifying the probe's amplitude. As described by the Kramers–Kronig relations, any frequency-dependent variation of the probe's amplitude in the vicinity of an optical resonance must be accompanied by variation in the real refractive index seen by the probe. The net impact of the pump on the probe beam can be described as a complex refractive-index perturbation $\delta\eta$ such that $E_1' = E_1 \exp\left(ik_1 \delta\eta L / \eta_0\right)$ after interacting with the laser-plasma system, where L is the interaction length and η_0 is the unperturbed plasma refractive index. The full expression for the refractive-index perturbation was derived in Michel *et al.*[1] using a kinetic plasma model. Critically, it was also shown in that work that the perturbation is seen only by the component of the probe's electric field that is parallel to the projection of the pump's electric field in the probe's plane of polarization (cf., Fig. 148.11). The ability to induce anisotropy via the relative orientation of the pump and probe polarizations can be exploited for precise manipulation of the probe's polarization.[1,2] Here we present measurements that show excellent agreement with linear theory for both the real and imaginary components of the refractive-index perturbation as a function of the wavelength shift between the pump and probe. Previously, the real component had been measured only at zero-wavelength shift,[2] and measurements of the imaginary component were not found to agree with linear theory.[8]

The experiment was conducted at Lawrence Livermore National Laboratory's Jupiter Laser Facility. A gas jet equipped with a 3-mm-outlet-diam supersonic nozzle released methane gas prior to the arrival of the pump and probe, which were focused over the nozzle with a relative crossing angle of 27°. Two different phase plates were used to give the pump and

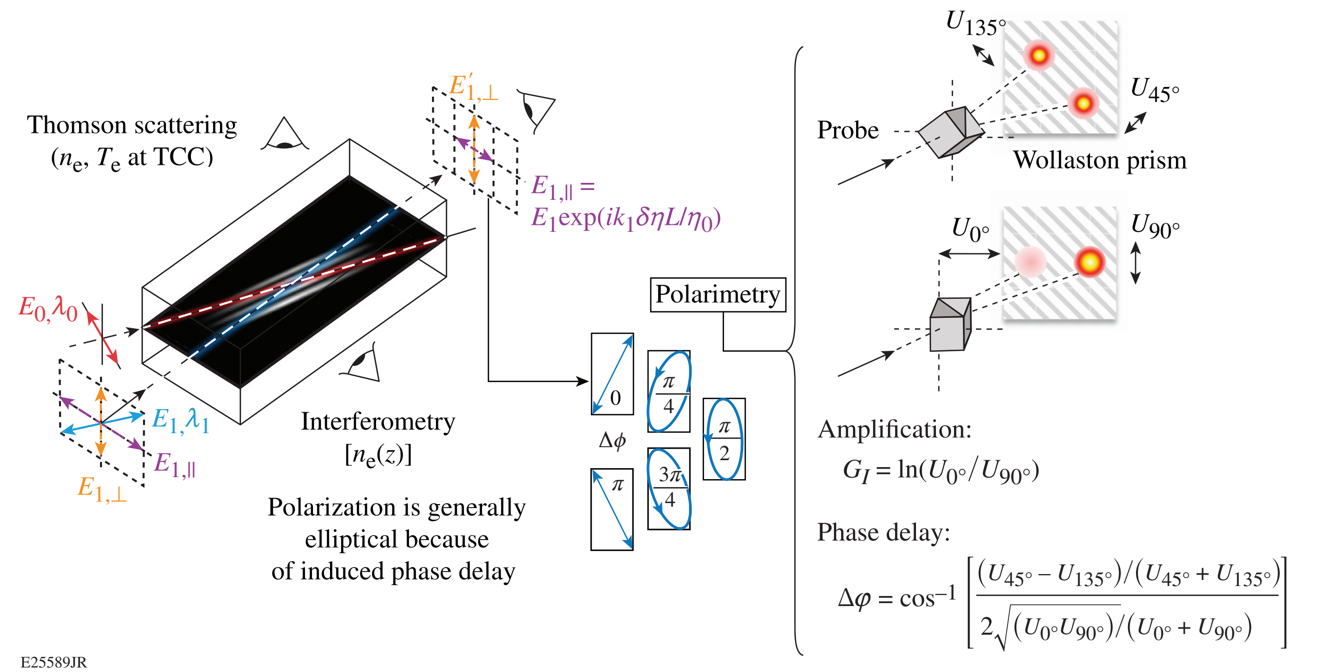

Figure 148.11
The presence of the pump introduces anisotropy to the plasma as seen by an independent probe beam. Only the component of the probe's polarization that is aligned with the pump polarization will have its amplitude and/or phase modified by the interaction, both of which can be measured using polarimetry. TCC: target chamber center.

probe speckled but roughly flattop (in an average sense) intensity distributions with 600-μm and 200-μm diameters at best focus, respectively. The pump had an ≈3-ns square pulse shape and established the plasma conditions prior to the arrival of the probe, which had an ≈250-ps Gaussian pulse shape with the peak delayed ≈1.3 ns from the rise of the pump. Using the nominal pump energies (292±8 J), fast-diode–based, pulse-shape measurements, and an assumed spot size based on the phase-plate properties, the pump intensity was expected to be in the range of $I_0 = (3.6\pm0.2) \times 10^{13}$ W/cm^2 averaged over the interaction region. The initial probe energy and intensity were ≈27 mJ and 3.4×10^{11} W/cm^2, respectively. Both beams used the fundamental frequency of an Nd:YLF laser ($\lambda \approx 1053$ nm), but different front ends allowed wavelength tuning within the bandwidth of the gain medium; here, a range of $-3 \le \Delta\lambda \le +3$ Å was used, where $\Delta\lambda$ is the wavelength difference between pump and probe. A polarizer was used before the last turning mirror to orient the probe polarization close to 45° relative to the horizontal pump polarization. This provides a convenient and novel method of diagnosing probe amplitude changes induced by the laser-plasma system; exploiting the anisotropic nature of the interaction, only the horizontal component of the probe's polarization will either grow or decay under the influence of the pump, and the orthogonal vertical polarization provides a baseline that factors in shot-to-shot variation of the incident probe-beam energy as well as inverse bremsstrahlung absorption in the plasma, as shown in Fig. 148.11. Separating the polarizations with a Wollaston prism subsequent to the interaction and taking their ratio provides a direct measure of the amplification. To compare with linear theory, the plasma electron density and temperature were measured with Thomson scattering. The scattered light was dominated by the high-energy pump beam, collected at a scattering angle of 90°, and directed to a streaked spectrometer measuring the blue-shifted electron plasma wave feature. To obtain additional information about density gradients in the plasma, optical interferometry was used, employing a dedicated diagnostic beam that was incident on the plasma orthogonal to the pump beam. Both diagnostics were analyzed at the time of the pump–probe interaction. The experimental setup is shown in Fig. 148.11.

The effect of the refractive-index perturbation's imaginary component can be expressed as a gain exponent G, where $E'_{1,\parallel} = E_1\exp(G)$ and $G = k_1\Im[\delta\eta]L/\eta_0$. Intensity being proportional to the square of the electric field, the intensity gain exponent is $G_I = 2G$ and is related to amplification, the ratio of intensity in each polarization subsequent to the interaction, by $G_I = \ln(A)$. Figure 148.12 shows the experimental data plotted with a calculation using the linear theory developed to compute CBET in indirect-drive ICF experiments on the NIF.[5] The electron density and temperature inputs used in the calculation were $n_e / n_c = 0.0104$ and T_e = 220 eV, where n_c is the critical density, consistent with the experimentally measured values of $n_e / n_c = 0.011 \pm 0.001$, and T_e = 224±24 eV. Since several necessary inputs were not directly measured, three-dimensional radiation–hydrodynamic simulations using *HYDRA*[12] were performed to obtain estimates for ion temperature and flow velocity. The pump-beam energy, spatial profile, and pulse shape used in the simulation closely reproduced the experimental conditions, and the initial methane gas density and the flux limiter were then adjusted to match the measured electron density and temperature. The simulations predicted an ion temperature of $T_i / T_e \approx 0.09$, whereas $T_i / T_e \approx 0.12$ is used in the linear theory best fit. The small difference is comparable to the level of ion heating expected from thermalizing the energy in the driven ion-acoustic waves, which is not included in the simulations. *HYDRA* also predicts an outwardly directed radial flow resulting from the expansion of the plasma channel formed by the pump beam, which broadens the ion-acoustic resonance by shifting the peak in different portions of the interaction region; this was directly imported into the linear theory calculation because of the lack of a flow velocity measurement. The effective pump intensity was also reduced 20% from the expected value (to $I_0 = 2.9 \times 10^{13}$ W/cm^2), which we attribute to unmeasured transport losses through the final optics, inverse bremsstrahlung absorption in the plasma, pump depletion effects, and/or imperfect focusing of the pump beam. In specifying the crossing angle, the calculation takes into account the finite spread given by the *f*/6.7 and *f*/10 pump and probe beams, respectively, which also broadens the ion-acoustic resonance. Finally, the peak location of the ion-acoustic resonance was most easily matched by specifying the ion species fractions as f_C = 0.4 and f_H = 0.6, whereas f_C = 0.2 and f_H = 0.8 were expected based on the initial methane-gas composition. This implies that species separation is occurring in this system. In principle, hydrogen—being lighter and having a higher charge-to-mass ratio—is expected to lead the plasma channel expansion, leaving a higher concentration of carbon in the interaction region. This effect has been observed previously using simultaneous electron and ion feature Thomson scattering in an expanding CH plasma.[13,14] Assessing this effect quantitatively requires multi-ion-fluid simulations, however, and is considered outside the scope of this study. Species separation is an increasingly active field of research in the ICF community.[15–19]

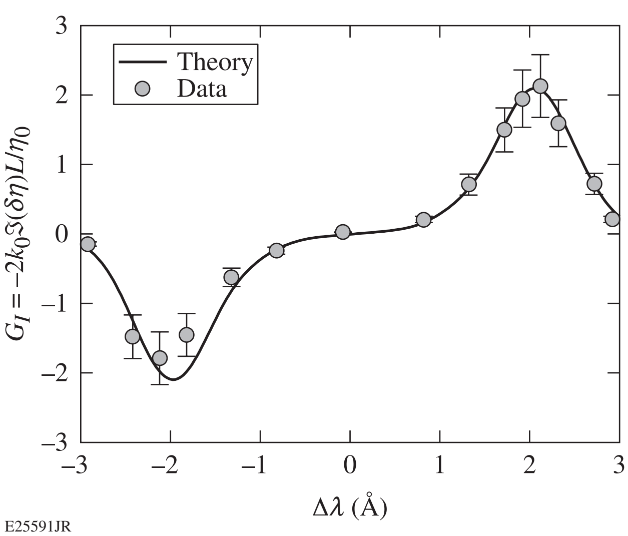

Figure 148.12
The intensity gain exponent is plotted as a function of the relative wavelength shift between the probe and pump. The parameters used in the linear theory calculation are listed in the text and are quite consistent with measured values (where available) and three-dimensional *HYDRA* simulations.

It is evident that the linear theory accurately reproduces the data both near the resonance peaks and in the off-resonant region between the Stokes and anti-Stokes peaks. Previous work utilizing a simple geometry had determined that CBET was maximized near the ion-acoustic resonance, but the peak location was not predicted accurately; the data lacked the precision to measure off-resonant transfer. It was also determined that the gain was lower than expected from the linear theory by a factor of 20 (Ref. 8). ICF hohlraums have also provided evidence that the amount of energy transfer is less than expected from linear theory.[10,11] In both previous examples, the linear theory calculations used plasma conditions taken entirely from radiation–hydrodynamic simulations. The agreement found in this better-characterized experiment suggests that inaccuracies in the assumed density and temperature may be one source of discrepancy. Weak turbulence effects associated with having many of these coupled-beam interactions in the same region of plasma may also be a factor in indirect-drive ICF.[10] Note that while the conditions of this experiment are very different from an ICF environment in terms of wavelength, intensity, density, and temperature, it can still be considered a good surrogate by several metrics. Gain was larger in this experiment than even the most resonant of interactions in an ICF hohlraum, so this can be considered an upper bound on the parameter space relevant to ICF. Furthermore, the normalized ion-acoustic–wave damping is $\nu/\omega_{IAW} \approx$ 0.1 to 0.2 (i.e., strongly damped) in both cases; achieving this in the present experiment motivated the use of the multispecies methane gas.[20]

As mentioned, the imaginary refractive-index perturbation component is accompanied by a real refractive-index change, which introduces a phase delay between the probe's vertical (noninteracting) and horizontal (interacting) components. While amplification was determined by separating the vertical and horizontal components and taking their ratio (which is insensitive to the phase delay), inferring the phase delay $\Delta\phi$ requires a second measurement in which the Wollaston prism is rotated 45° in order to separate the 45° and 135° polarization components. With each signal's energy in arbitrary units given by U_j, where j is the polarization angle, the phase delay for each pair of measurements (assuming polarized light and perfect shot-to-shot reproducibility) is given by

$$\Delta\phi = \cos^{-1}\left[\frac{\left(U_{45^\circ} - U_{135^\circ}\right)\Big/\left(U_{45^\circ} + U_{135^\circ}\right)}{2\sqrt{U_{0^\circ}U_{90^\circ}}\Big/\left(U_{0^\circ} + U_{90^\circ}\right)}\right]. \quad (1)$$

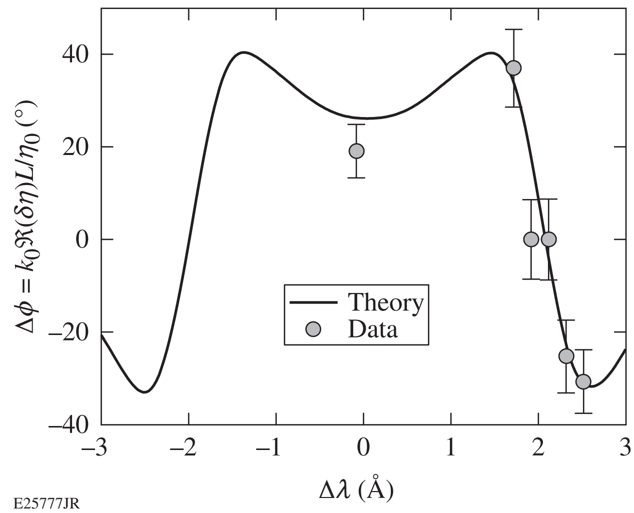

Figure 148.13
The phase delay induced by the real refractive-index perturbation is plotted as a function of the wavelength shift between the pump and probe. The linear theory is once again in good agreement with the experimental data.

Unlike the imaginary component, the real component of the refractive-index perturbation is nonzero even in the absence of a wavelength shift between the pump and probe. Turnbull *et al.* exploited this property previously in the first demonstration of a laser-plasma wave plate, converting an initially elliptical polarization into a nearly ideal circular polarization.[2] Here, wavelength tuning capability allows us to validate other points along the real refractive-index perturbation curve, as shown in Fig. 148.13. Again, the linear theory provides a good match to the experimental data using the same parameters that were used to fit the amplification data, with key features—nonzero phase delay at zero wavelength shift, larger dephasing on either side of the resonance, and zero dephasing at the peak—evident in the data. Note that the measurement does not actually discriminate between positive and negative phase delay, but since the data are consistent with the shape of the curve as predicted by linear theory, we assume that those points to the left of the peak are positive and points to the right of the peak are negative. This is the first (to our knowledge) measurement of a laser-plasma optical system's real refractive-index perturbation as a function of wavelength tuning.

The experiment was designed in such a way to test the concept of a "plasma polarizer," which was proposed by Michel *et al.*[1] When $\lambda_1 - \lambda_0 < 0$, the probe transfers energy to the pump but only out of its horizontal component (which is aligned with the pump polarization) resulting from the anisotropy of the laser-plasma system, so the system is effectively a linear polarizer. The data point at the negative peak of Fig. 148.12 represents an extinction of 85%. The data are shown in Fig. 148.14; the incident polarization was oriented in order to have nearly equal horizontal and vertical components, but after propagating through the system, the horizontal polarization is significantly attenuated. Additional shots were conducted in which the incident probe intensity was increased up to $I_1 \approx 3 \times 10^{12}$ W/cm^2, and the extinction stayed in the range of 85% to 87%. Note that the probe is otherwise minimally affected by the system because the phase delay induced between the vertical polarization and what is left of the horizontal polarization is close to zero near the resonance peak, absorption in this fairly tenuous plasma is calculated to be modest, and the probe is not degraded by other laser–plasma instabilities. Maintaining similar plasma conditions, the extinction could be increased or decreased by changing the pump intensity. This demonstrates another ultrafast, damage-resistant, and tunable laser-plasma photonic device. Having now achieved both a wave plate and a polarizer, it is possible to design a laser Q switch using only laser-plasma systems.

In summary, a laser-plasma optical system's complete refractive index—both its imaginary and real components—was mapped out for the first time, using a consistent set of laser and plasma parameters. It was found to be in excellent agreement with the linear theory for coupled beams in a plasma that is used to compute cross-beam energy transfer in indirect-drive ICF experiments. The ability to correctly predict energy transfer in this well-characterized context, but not in ICF experiments,[10,11] points to possible errors in the hydrodynamic inputs to the ICF

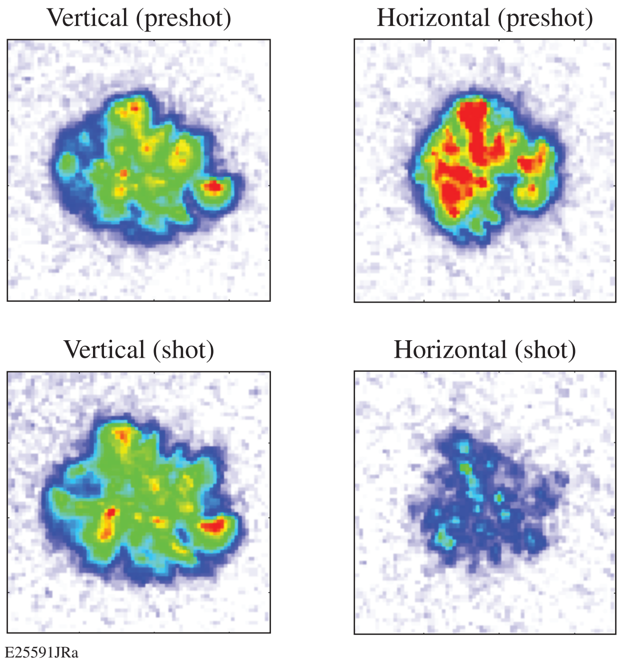

Figure 148.14
The anisotropic laser-plasma system acts like a pure linear polarizer at the negative resonance peak, depleting the probe's horizontal polarization component. The color scale for each pair is normalized to the vertical polarization. The vertical and horizontal spots appear to be different because the Wollaston prism slightly affects the imaging. The pre-shot images were obtained without any plasma, and the horizontal polarization was brighter than the vertical polarization because the polarizer setting the incident polarization was not quite oriented at 45°; 85% to 87% of the horizontal polarization was then extinguished by the laser-plasma polarizer, whereas the vertical polarization was minimally perturbed by the system.

calculations and/or weak turbulence effects from having many such coupled beam interactions in the same volume of plasma. We also achieved the first demonstration of a laser-plasma polarizer, which extinguished 85% to 87% of an independent probe beam's horizontal polarization.

ACKNOWLEDGMENT

This work was performed under the auspices of the U.S. Department of Energy by Lawrence Livermore National Laboratory under Contract DE-AC52-07NA27344. This work was supported by the LLNL-LDRD Program under Project No. 42074. We thank the staff of the Jupiter Laser Facility and Suzanne Ali for enabling a successful experimental campaign. DT also acknowledges useful discussions regarding species separation with C. Bellei, P. Amendt, and G. Kagan.

REFERENCES

1. P. Michel, L. Divol, D. Turnbull, and J. D Moody, Phys. Rev. Lett. **113**, 205001 (2014).
2. D. Turnbull, P. Michel, T. Chapman, E. Tubman, B. B Pollock, C. Y. Chen, C. Goyon, J. S Ross, L. Divol, N. Woolsey, and J. D Moody, Phys. Rev. Lett. **116**, 205001 (2016).
3. D. J. Stark *et al*., Phys. Rev. Lett. **115**, 025002 (2015).
4. G. Lehmann and K. H. Spatschek, Phys. Rev. Lett. **116**, 225002 (2016).
5. P. Michel *et al*., Phys. Rev. Lett. **102**, 025004 (2009).
6. S. H. Glenzer *et al*., Science **327**, 1228 (2010).
7. J. D. Moody *et al*., Nat. Phys. **8**, 344 (2012).
8. R. K. Kirkwood *et al*., Phys. Rev. Lett. **76**, 2065 (1996).
9. R. K. Kirkwood, J. D. Moody, A. B. Langdon, B. I. Cohen, E. A. Williams, M. R. Dorr, J. A. Hittinger, R. Berger, P. E. Young, L. J. Suter, L. Divol, S. H. Glenzer, O. L. Landen, and W. Seka, Phys. Rev. Lett. **89**, 215003 (2002).
10. P. Michel *et al*., Phys. Rev. Lett. **109**, 195004 (2012).
11. R. P. J. Town *et al*., Phys. Plasmas **18**, 056302 (2011).
12. M. M. Marinak *et al*., Phys. Plasmas **8**, 2275 (2001).
13. J. S. Ross *et al*., Rev. Sci. Instrum. **83**, 10E323 (2012).
14. P. Amendt *et al*., Phys. Rev. E **91**, 023103 (2015).
15. J. R. Rygg, J. A. Frenje, C. K. Li, F. H. Séguin, R. D. Petrasso, J. A. Delettrez, V. Yu. Glebov, V. N. Goncharov, D. D. Meyerhofer, S. P. Regan, T. C. Sangster, and C. Stoeckl, Phys. Plasmas **13**, 052702 (2006).
16. G. Kagan and X.-Z. Tang, Phys. Plasmas **19**, 082709 (2012).
17. C. Bellei and P. A. Amendt, Phys. Rev. E **90**, 013101 (2014).
18. M. J. Rosenberg, A. B. Zylstra, F. H. Séguin, H. G. Rinderknecht, J. A. Frenje, M. Gatu Johnson, H. Sio, C. J. Waugh, N. Sinenian, C. K. Li, R. D. Petrasso, P. W. McKenty, M. Hohenberger, P. B. Radha, J. A. Delettrez, V. Yu. Glebov, R. Betti, V. N. Goncharov, J. P. Knauer, T. C. Sangster, S. LePape, A. J. Mackinnon, J. Pino, J. M. McNaney, J. R. Rygg, P. A. Amendt, C. Bellei, L. R. Benedetti, L. Berzak Hopkins, R. M. Bionta, D. T. Casey, L. Divol, M. J. Edwards, S. Glenn, S. H. Glenzer, D. G. Hicks, J. R. Kimbrough, O. L. Landen, J. D. Lindl, T. Ma, A. MacPhee, N. B. Meezan, J. D. Moody, M. J. Moran, H.-S. Park, B. A. Remington, H. Robey, M. D. Rosen, S. C. Wilks, R. A. Zacharias, H. W. Herrmann, N. M. Hoffman, G. A. Kyrala, R. J. Leeper, R. E. Olson, J. D. Kilkenny, and A. Nikroo, Phys. Plasmas **21**, 122712 (2014).
19. H. G. Rinderknecht, M. J. Rosenberg, C. K. Li, N. M. Hoffman, G. Kagan, A. B. Zylstra, H. Sio, J. A. Frenje, M. Gatu Johnson, F. H. Séguin, R. D. Petrasso, P. Amendt, C. Bellei, S. Wilks, J. Delettrez, V. Yu. Glebov, C. Stoeckl, T. C. Sangster, D. D. Meyerhofer, and A. Nikroo, Phys. Rev. Lett. **114**, 025001 (2014).
20. E. A. Williams *et al*., Phys. Plasmas **2**, 129 (1995).

Commissioning an X-Ray Detector System for Spectral Analysis of Tritium-Filled Targets

Introduction

Both glass and plastic targets filled with deuterium–tritium mixtures (DT) are used at LLE for research into inertial confinement fusion experiments. These targets are imploded with the 60-beam OMEGA Laser System. The permeation-filling process can take up to a week since the targets must be pressurized to tens of atmospheres without crushing the fragile, thin-wall shells. The overall time required to fill targets depends on the permeation time constant. Typically five or six permeation time constants are used to fill targets to the desired pressure. Although the fill pressure and DT ratio are known precisely, a nondestructive method to verify that the targets actually contain the expected fill pressure at shot time is currently unavailable. Two factors can lead to underfilling a target: (1) The permeation time constant is underestimated so sufficient time is not allowed for the charging pressure to equilibrate with the gas pressure inside the target, or (2) a defect develops in the shell, causing the target to depressurize more rapidly than predicted by the permeation time constant.

An x-ray detection system (XDS) originally developed to measure bremsstrahlung of tritium β decay from the surface of metals[1–3] has been modified and developed with the capability of measuring the pressure of DT fuel inside a target just prior to the shot. This system permits rapid, nondestructive identification of underpressurized targets. This article details the design of the system, discusses preliminary measurements of x-ray emission from glass and plastic targets, and demonstrates that the method can achieve accurate, repeatable measurements.

Equipment Design Features

The XDS comprises three primary components: a high-resolution, dual-axes imaging system for repeatable, accurate target positioning; a helium enclosure with triple-axes micrometer positioning; and an Amptek silicon drift detector (SDD). The SDD was fit with a silicon nitrate (Si_3N_4) window to measure x-ray energies from 200 eV to 40 keV. The detector features a 25-mm^2 silicon drift diode with a measured 130-eV full-width-at-half-maximum resolution at 5.9 keV.

The arrangement of the equipment is illustrated in Fig. 148.15. The origin of the optical axes was defined by centering the window of the detector on the x, y origin in one camera's field of view (FOV) and the side view of the detector window in the z origin of the other camera. The detector was then retracted 25.4 mm in the z direction so that targets placed in the center of both cameras' FOV would be positioned 25.4 mm in front of the detector with a repeatable precision of 10 μm. During all measurement campaigns, the environment was purged with helium at a flow rate of 4 L/min to provide a

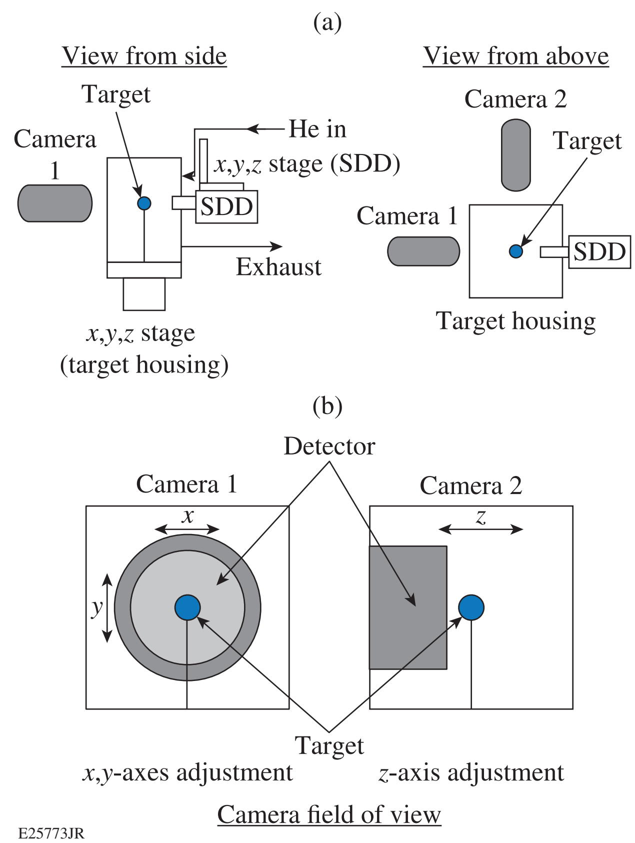

Figure 148.15
Layout of the x-ray detection system. SDD: silicon drift detector.

tenfold volume exchange per minute within the enclosure to minimize air contamination of the chamber and to purge any tritium that permeated from plastic targets.

The response of the SDD was calibrated in air and helium using an ^{55}Fe source. The resulting spectrum is shown in Fig. 148.16. Calibration in air shows the suppression of lower-energy K_α lines such as aluminum and the presence of the argon K_α, as expected. K_α lines from manganese, the ^{55}Fe decay product, are also clearly visible in both the air and helium cover gases. A ^{109}Cd source was used to calibrate the detector over the full energy range of the tritium spectrum.

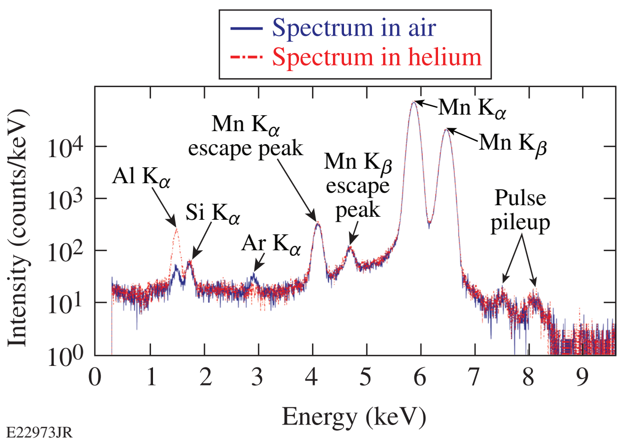

Figure 148.16
The response of the silicon drift detector to an ^{55}Fe source in air and helium.

Spectral Analysis of SiO_2, CH, and CD Targets

Decay betas in tritium-filled targets generate both fluorescent and bremsstrahlung x rays as they interact with the shell material. These interactions are illustrated in Fig. 148.17 for both glass (SiO_2) and plastic targets. The permeability of tritium through glass is very low at room temperature and very little tritium is present in the enclosure. Additionally, the solubility of tritium in glass is very low and very little tritium resides inside the glass wall of the shell. Almost all decay betas originate in the DT gas and interact with the glass to generate x rays. These electrons have insufficient energy to penetrate the glass wall. By contrast, plastic is highly soluble and permeable to tritium. A 100-nm Al permeation barrier is applied to the shell's exterior to reduce tritium losses from the targets to manageable levels. The plastic contains a significant amount of tritium, and measureable amounts of tritium escape into the enclosure. In this case, decay betas originate in the gas and the plastic and can penetrate the aluminum overcoat together with x rays and tritium molecules.

The emission spectra of glass targets are dominated by the fluorescence from silicon and oxygen atoms in the shell's wall. Two spectra from a glass target filled with 10 atm of 38.3% tritium in DT are shown in Fig. 148.18: one for a 5-min measurement time and one for a 15-h measurement time. The longer measurement time yielded a higher-resolution spectrum with more-discernible features, notably the Al K_α line from the housing of the detector itself. Figure 148.19 illustrates that once the DT gas has leaked out of the glass target, the emission spectrum drops to background levels, demonstrating that the amount of tritium dissolved into the glass is negligible.

Three glass-target silicon K_α lines were measured for 5 min and compared. Two of these targets were imploded on OMEGA later on the same day. As shown in Fig. 148.20, the two silica targets had a Si K_α count rate within 5% of each other and produced neutron yields within 10% of each other on OMEGA.

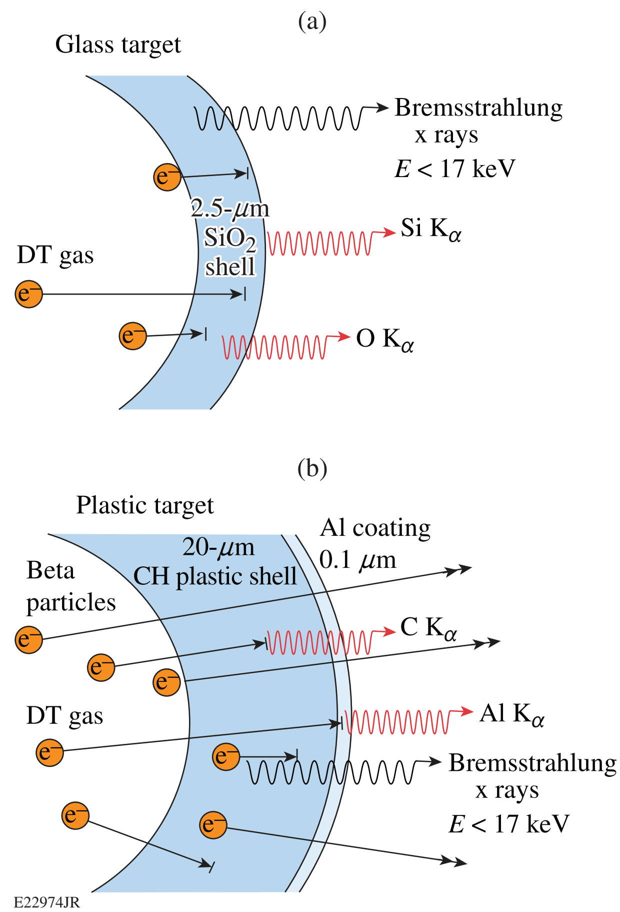

Figure 148.17
Illustration of the interactions decay betas undergo in glass and plastic targets.

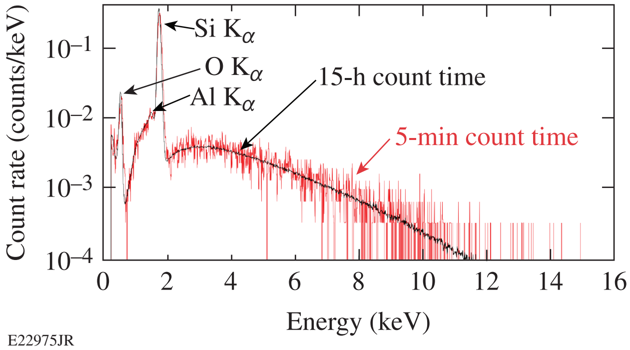

E22975JR

Figure 148.18
Comparison of a 5-min emission spectrum and a 15-h emission spectrum collected from a glass target containing 3.83 atm of T.

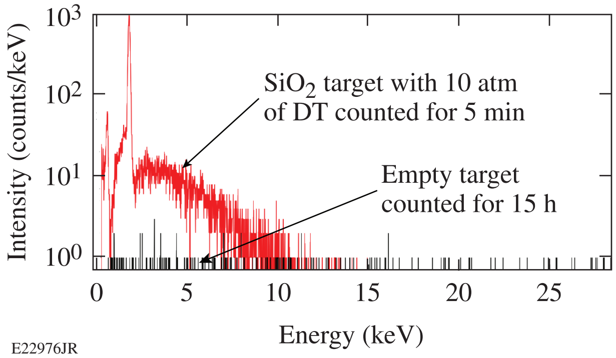

E22976JR

Figure 148.19
A 5-min spectrum collected from a glass target containing 10 atm of DT compared to a 15-h spectrum collected from glass target that has lost its DT.

Fluorescence does not dominate emission spectra from plastic targets. Figure 148.21 compares two plastic targets in the energy range from 2.5 keV to 12 keV. One target was filled with 4.2 atm of T_2 at Lawrence Livermore National Laboratory (LLNL) and then shipped to LLE at liquid nitrogen temperature for attachment to a stalk. The second target was filled at LLE with 16.7 atm of 38.3% tritium in DT, or an equivalence of 3.2 atm of T_2 gas. This target was attached to its support stalk using ~80 ng of epoxy prior to filling with DT. Both targets exhibited strong bremsstrahlung emission with fluorescence K_α peaks for aluminum and oxygen. Additionally, the target filled at LLE presented silicon and sulfur K_α lines. Tritium soaked into the silicon stalk and the epoxy while the target was filled with tritium at LLE and subsequently fluoresced the silicon and the sulfur present in the epoxy. The larger amplitude of the aluminum K_α line found in the emission spectrum of the LLNL target may be attributed to the higher tritium pressure and thinner shell wall in that target by comparison to the LLE target.

Target number	Target ID	Si K_α rate	Neutron yield ($\times 10^{13}$)
SiO_2–1	ISE-3Q14-01-8	31.9	3.02
SiO_2–2	ISE-3Q14-01-5	31.3	n/a
SiO_2–3	ISE-3Q14-01-27	33.5	3.42

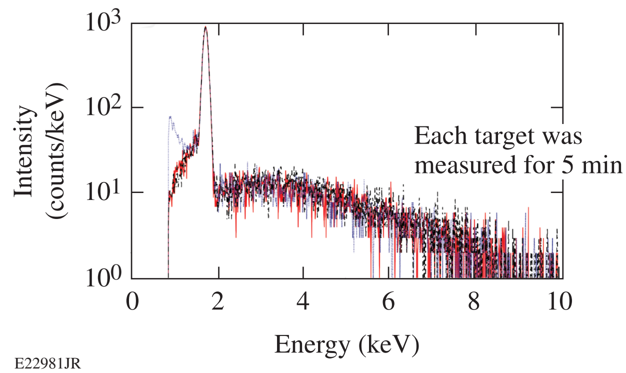

E22981JR

Figure 148.20
Five-minute spectra of the three glass targets listed in the table. These targets were fielded on OMEGA.

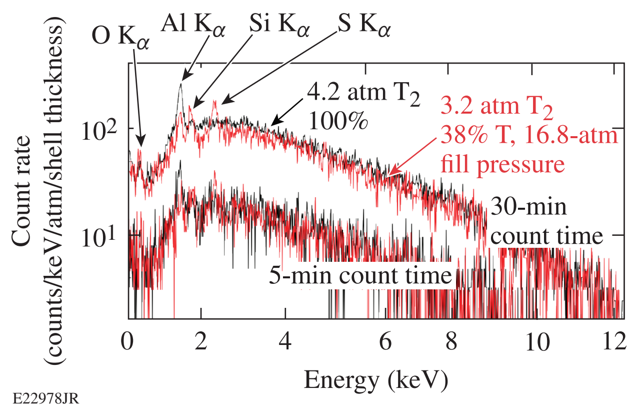

E22978JR

Figure 148.21
Five-minute spectra collected from two plastic targets: one filled to 3.2 atm of T_2; the other filled with 4.2 atm of T_2.

Beta particles that emerge from the plastic targets can interact with the detector window if the detector is within the beta range. This effect is demonstrated in Fig. 148.22, where emission spectra from plastic and silica targets are compared at 2.54 cm and 1.27 cm from the detector. The silica target exhibits the same bremsstrahlung spectrum at 1.27 cm as it does at 2.54 cm since no betas escape the shell. On the other hand, the emission spectrum from the plastic target develops a more-pronounced bremsstrahlung signature than the silica target at 1.27 cm when the target is close enough to the detector for escape betas to interact with the detector window.

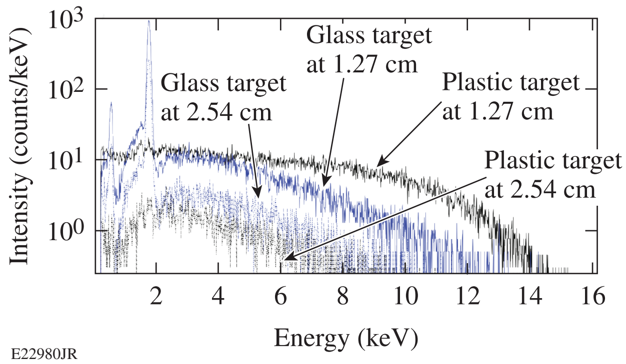

Figure 148.22
Comparison of spectra collected from glass and plastic targets at two distances from the detector to illustrate how decay betas escape from plastic targets interacting with the detector.

Correlation Between Plastic Target Activity and Pressure

Gas loss from plastic targets is approximately exponential. The permeation time constant is measured for each target using D_2 gas at General Atomics after fabrication. These time constants are then used to guide the tritium-filling rate. Once charged to the desired pressure with tritium gas, the targets are placed in cold storage to reduce permeant losses. Targets at LLNL are stored at 77 K, increasing the permeation time constant by a factor of about 1100, while targets at LLE are stored at 150 K, increasing the permeation time constant by a factor of about 800.

The x-ray spectra of five plastic targets were taken continuously while they were outgassing at room temperature to correlate the tritium activity against the gas pressure. All targets were measured at 2.54 cm from the detector face to suppress bremsstrahlung from the detector membrane. The environment was purged with helium at a flow rate of 4 L/min during measurements to prevent a buildup of tritium in the housing as targets outgassed. Two targets (A1 and B1) were measured immediately after removal from cold storage during the diagnostic development campaign and then again after five days of outgassing at 24-h intervals for an additional five days. Three targets (A2, B2, and B3) were measured continuously upon removal from cold storage for a period of six days to obtain the energy/time spectrum. The targets in Group A were filled at LLE with 16.7 atm of DT (38.3% tritium) or an equivalent T_2 fill pressure of 3.2 atm while the targets in Group B were filled at LLNL with T_2. Estimates of tritium content in the targets at the time of the initial x-ray emission measurement and the shell composition are provided in Table 148.V.

All targets were mounted at LLE. For the ease of comparison, DT-filled targets are from here on reported in their equivalent T_2 concentrations.

The time evolution of the spatially integrated count rate of the targets takes on the shape of a double-exponential function as seen in Fig. 148.23. Decay betas from two sources are most likely responsible for the shape of the activity–time curve: decay betas from tritium gas inside the shell and decay betas from tritium dissolved in the target shell. The decay in activity is the result of losing tritium through diffusion through the shell or the dissolution of tritium out of the shell into the helium gas flow away from the detector. The two sources are referred to as the "gas activity" and the "shell activity" to differentiate between the two sources and their effect on the time evolution of the spectrum. The time constant for the gas activity component is expected to be short and dependent on the gas pressure in the target. The shell activity is expected to have a very long time constant since the tritons are most likely chemically bound in the plastic. A 40-h measurement of the change in the baseline activity suggests the time constant for the shell activity is of the order of 3.6 years.

Table 148.V: Tritium-fill pressure and the estimated tritium pressure in each target at the time of the x-ray measurement.

Target ID	Tritium-fill pressure (atm)	Estimated target pressure at time of x-ray measurement (atm)	Shell composition
A1	3.2*	2.9	CD
A2	3.2*	2.4	CH
B1	5.0	3.6	CH
B2	5.1	3.2	CD
B3	12.2	12.2	CD

*Actual fill pressure of 16.7 atm using 38.3% T in DT.

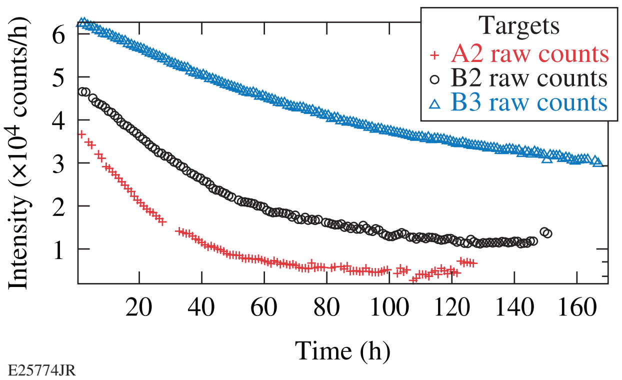

Figure 148.23
The time evolution of the spectrally integrated count rate of three plastic targets outgassing at room temperature.

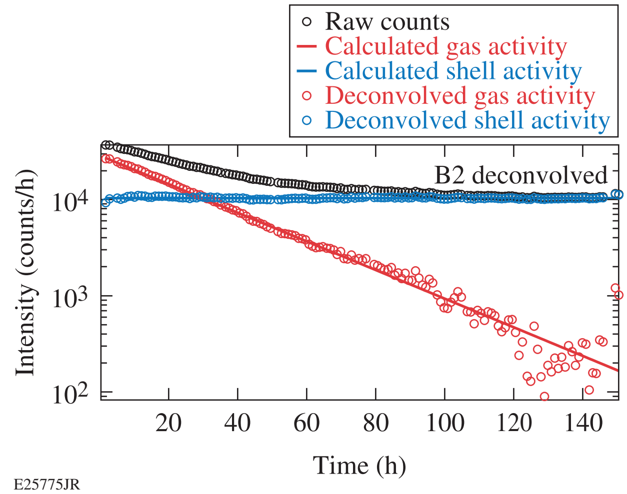

Figure 148.24
The continuous x-ray spectrum from a plastic target deconvoluted to show the contributions from the DT gas inside the target and from DT gas dissolved in the plastic.

The spectra were fit with weighted double-exponential functions after reaching the baseline shell activity and using 3.6 years as the half-life for the shell's exponential function. Using the measured coefficients, the gas and shell activity were deconvolved from the spectra by subtracting each from the raw data as shown in Fig. 148.24. The measured permeation time constants for the gas activity source are provided in Table 148.VI and compared against the values provided by General Atomics. In each case the DT time constants are longer by at least 50% than the reported time constants determined with D_2 gas.

The pressure of the targets at each measurement interval was calculated using the reported soak time and fill pressures and the measured DT time constant, assuming the tritium loss rate from the target to be exponential. Table 148.VII compares the soak and fill pressures. The calculated target pressure evolution was plotted against the deconvolved gas activity evolution and is shown in Fig. 148.25. Pressure correlates linearly with activity as expected. The slopes of the pressure–activity curves

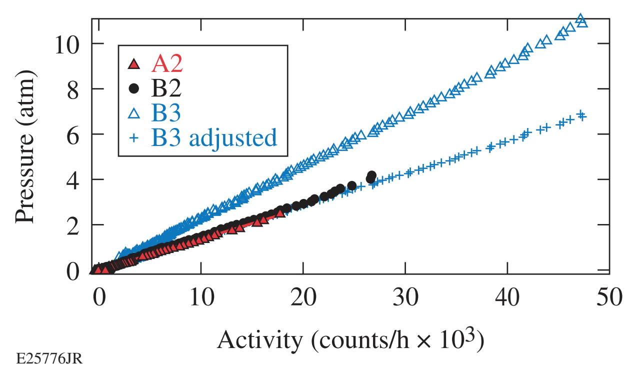

Figure 148.25
The calculated DT pressure loss from a plastic target compared against the x-ray emission from the residual DT inside the plastic target.

Table 148.VI: Comparison of the D_2 reported time constant with the measured time constant using DT.

Target ID	D_2 reported time constant (h)	Mass-adjusted time constant (h)*	DT time constant (h)	Ratio of measured/reported
A2	5.1	5.7	12.8	2.3
B2	11.3	13.8	20.2	1.5
B3	23.7	26.5	39.0	1.5

*GA reported half-lives converted to a DT-equivalent time constant using a root-mass difference of the hydrogen isotopologues: D_2, DT, and T_2, i.e., $\sqrt{5/4}$ and T_2 by $\sqrt{3/2}$.

for targets A2 and B2 lie within 8% of one another, while the slope for target B3 is 1.6× greater than the average slopes of the other two targets. Taking the measured tritium activity to be accurate with <1% error in the counting statistics, the initial fill pressure of B3 should be closer to 7.6 atm of T_2 as opposed to the reported 12.2 atm. The pressure–activity curve for B3 using a fill pressure of 7.6 atm of T_2 (shown in Fig. 148.25) is observed to fall in line with the curves for the other two targets. The reduced fill pressure is being determined under the assumption that targets A2 and B2 had more accurately reported fill pressures since their slopes were within 8% of each other.

The shell activity of each target was measured independently using liquid scintillation counting at the end of each measurement campaign. Each target was crushed in liquid scintillation fluid to capture any residual tritium. Each crushed shell was soaked in the liquid scintillation fluid for several days to leach tritium from the plastic. A 1-mL aliquot was extracted from the leachate and measured in the liquid scintillation counter. These activities are also summarized in Table 148.VII. The shell activity was found to be linearly proportionate to the fill pressure of the target, or the initial total activity. Additionally, the plastic walls retained ~30% of the initial target activity.

Conclusions

An XDS has been developed and successfully commissioned with an intended application of nondestructively measuring the activity in tritium-filled targets. The XDS allows for an expedient verification of tritium content in a target prior to it being loaded into the OMEGA target chamber. The measured activities of two of the glass targets have been measured to have a Si K_α activity rate within 5% of each other, which corresponded to neutron yields within 10% after being imploded by the 60-beam OMEGA Laser System. This activity in glass targets is believed to provide a suitable initial baseline for comparison with future glass targets, allowing targets to be screened for low, or vacant, tritium content.

The T_2 permeation half-life has been measured for three plastic targets by continuously measuring the decrease in activity over a period of six days each. The measured half-lives were observed to be between 1.5× and 2.3× longer than the corresponding D_2 half-life values measured by the manufacturer, after taking into account the root–mass difference for DT and T_2. The activity of the tritium bound to the shell was observed to be proportionate to the initial fill pressure. The shell activity was ~30% of the total activity in the target.

The target fill pressure at the time of x-ray measurement was calculated taking into account the different half-lives, fill pressures, and storage times of the targets. Based on the target fill pressure, the activity of A2 was calculated to be 17% lower than A1. The measured activity of A2 was 16% less than A1 for a +1% difference. The targets from Group B exhibited significant deviation from their expected activities. The difference between the expected and measured activities is attributed to an underestimate in the permeation time constant. Adjusting for the longer time constant in the activity of B3 reconciles the apparent discrepancy in the pressure–activity curve when the B3 curve is compared against the curves measured for A2 and B2. The fill pressure of B2 at the time of measurement was calculated to be 7% less than B1, with an expected similar difference in activity. The actual measured activity for B2 was 11% greater than B1 for a difference of +18%. The actual fill pressure of B3 was calculated to be ~33% less than the value reported by General Atomic, based on the slope of the pressure versus activity over time when compared with targets A2 and B2.

The XDS is a robust, nondestructive technique for confirming the actual tritium fill pressure in either glass or plastic targets.

Table 148.VII: Comparison of the shell activity to fill pressure and total target activity.

Target ID	Soak pressure (atm)	Target pressure (atm)	Fill-to-destruction duration	Shell activity (kBq)	Shell activity/ target pressure (kBq/atm)	Shell/total activity (%)
A2	3.2*	2.4	48	926	386	31
B2	5.1	3.2	46	950	297	28
B3	12.2	7.6**	53	1259	166	29

*Adjusted for the actual T_2 content.
**Fill pressure based on known soak time and DT measured time constant.

ACKNOWLEDGEMENT

This material is based upon work supported by the Department of Energy National Nuclear Security Administration under Award Number DE-NA0001944, the University of Rochester, and the New York State Energy Research and Development Authority. The support of DOE does not constitute an endorsement by DOE of the views expressed in this article.

REFERENCES

1. L. Mao *et al*., Nucl. Instrum. Methods Phys. Res. B **269**, 105 (2011).
2. M. Matsuyama, K. Watanabe, and K. Hasegawa, Fusion Eng. Des. **39–40**, 929 (1998).
3. M. Matsuyama, H. Nakatani, and K. Watanabe, Fusion Eng. Des. **10**, 405 (1989).

The Eighth Omega Laser Facility Users Group Workshop

Introduction

The Eighth Omega Laser Facility Users Group (OLUG) Workshop was held at the Laboratory for Laser Energetics (LLE) on 27–29 April 2016. More than 110 scientists, postdoctoral fellows (postdocs), and students from institutions in the U.S. and abroad attended the workshop. As has been the case in previous workshops, postdocs and students received travel support for the workshop from the Department of Energy's (DOE's) National Nuclear Security Administration (NNSA).

The Workshop Program

The workshop program included an overview on the National Inertial Confinement Fusion (ICF) Program presented by Keith LeChien from NNSA; four review and science talks by Craig Sangster (National ICF Direct-Drive Program), Carlo Graziani (Inferring Morphology and Strength of Magnetic Fields from Proton Radiographs), Philip Nilson (High-Resolving-Power, Ultrafast Streaked X-Ray Spectroscopy on OMEGA EP), and Jonathan Davies (An Overview on Laser-Driven Magnetized Liner Inertial Fusion on OMEGA); one Omega Laser Facility talk given Samuel Morse (Progress on Recommendations and Items of General Interest); three poster sessions including a total

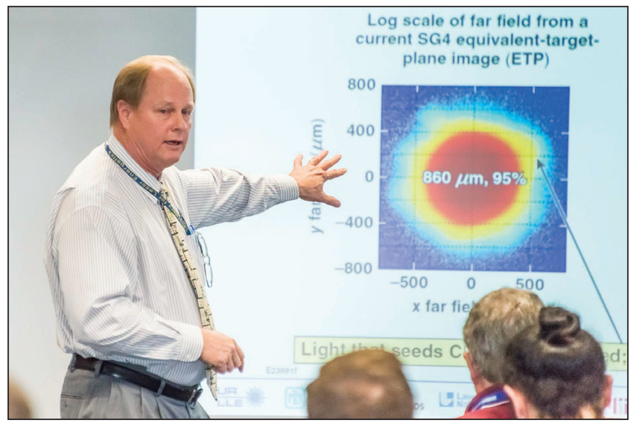

U2046JR

Figure 148.26
Craig Sangster (LLE) discussed the National ICF Direct-Drive Program.

U2045JR

Figure 148.27
Attendees at the Eighth Omega Laser Facility Users Group Workshop.

of 76 research posters and 15 Omega Laser Facility posters (the majority of the contributed posters were presented by postdocs and students) two mini-workshop sessions dedicated to streak cameras (organized by Charles Sorce) and magneto-inertial fusion electrical discharge system (MIFEDS) (organized by Gennady Fiksel); a students and postdocs panel discussion; a discussion and presentation of the **Findings and Recommendations** (p. 197); and research and career opportunity talks by representatives from Lawrence Livermore National Laboratory (LLNL) (Robert Heeter), Los Alamos National Laboratory (LANL) (S. Batha), Sandia National Laboratories (SNL) (P. Knapp), and LLE (Michael Campbell).

Student and Postdoctoral Poster Awards

In an effort to motivate and reward excellence in young researchers, the posters presented at the OLUG Workshop by students and postdocs are reviewed and ranked by a committee of scientists. As a result, prizes and honorable mentions are given to those posters at the top of the ranking. The following are the awards granted at this OLUG Workshop:

Student Awards

1st prize: Scott Feister, Ohio State University, "Acquisition and Analysis for High-Repetition-Rate HEDP (10 Hz to 1 kHz)"

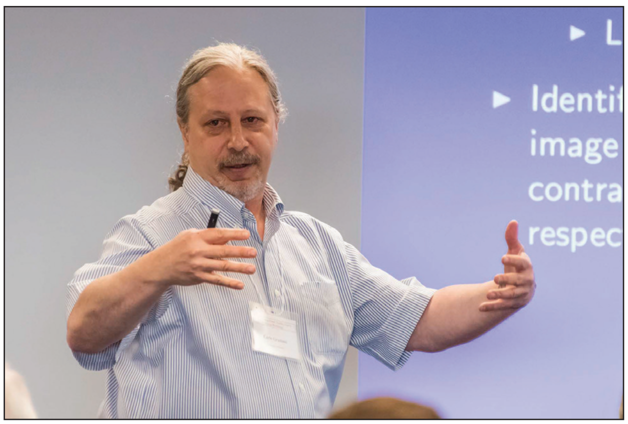

U2047JR

Figure 148.28
Carlo Graziani (University of Chicago) gave a talk on inferring morphology and the strength of magnetic fields from proton radiographs.

U2054JR

Figure 148.30
Patrick Knapp discussed research and career opportunities at Sandia National Laboratories.

U2048JR

Figure 148.29
Philip Nilson (LLE) gave a talk on high-resolving-power, ultrafast streaked x-ray spectroscopy on OMEGA EP.

U2053JR

Figure 148.31
Michael Campbell discussed research and career opportunities at LLE.

2nd prize: Jeffrey Fein, University of Michigan, "Modeling of OMEGA EP Experiments Studying *Z* Dependence of the Two-Plasmon–Decay Instability"

3rd prize: Samuel Totorica, Stanford University, "Non-Thermal Electron Energization from Magnetic Reconnection in Laser-Driven Plasmas"

Honorable-Mention Awards

Kevin George, Ohio State University, "Modifying the TNSA Ion Spectrum with Front-Surface Microstructures"

Amina Hussein, University of Michigan, "Optimization of Cold K-alpha Emission Using Copper Foams"

U2055JR

Figure 148.32
Student and postdoc poster awardees. From left to right, back row: Hans Rinderknecht, Alex Zylstra, Scott Feister, Jeffrey Fein, Samuel Totorica, and Hong Sio; front row: Willow Wan, Theodore Lane, and Amina Hussein. Also on the far right, front row are Maria Gatu Johnson and Craig Sangster who led the poster awardees selection process.

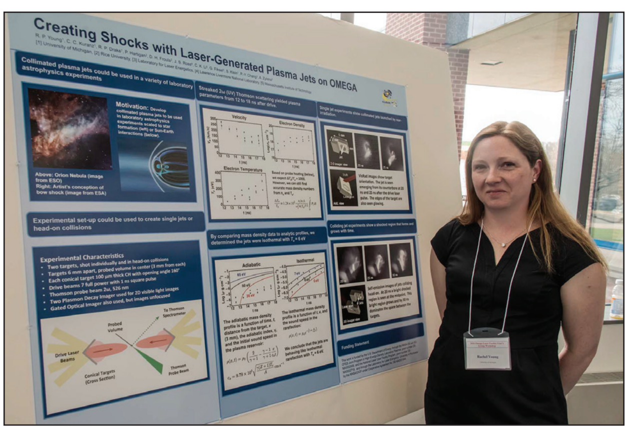

U2049JR

Figure 148.33
Rachel Young (University of Michigan) presented a poster on laser-generated plasma jets.

U2050JR

Figure 148.34
Federica Coppari (LLNL) discusses her poster on equation-of-state measurements on OMEGA.

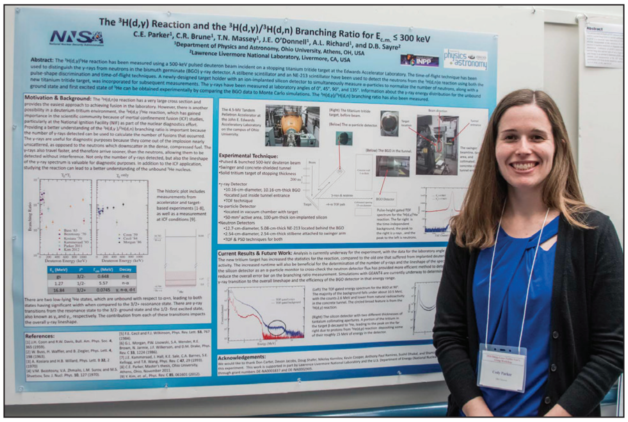

U2051JR

Figure 148.35
Cody Parker (Ohio State University) presented a poster on nuclear reactions with application for ICF diagnostics.

Theodore Lane, West Virginia University, "Improving the Fidelity of Interpreting Time-Averaged Spectra on Z for Development of a Multi-Element Stark-Broadening Diagnostic"

Mary Kate Ginnane and Ethan Turner, State University of New York at Geneseo, "Time-Resolved Tandem Faraday Cup Development for High-Energy TNSA Particles"

Willow Wan, University of Michigan, "Observation of Vortex Merger and Growth Inhibition in a Dual-Mode, Supersonic Kelvin–Helmholtz Instability Experiment"

Hong Sio, Massachusetts Institute of Technology, "Studies of Kinetic/Multi-Ion–Fluid Effects and Ion–Electron Equilibration in ICF Plasmas Using Multiple Nuclear and X-Ray Emission Histories"

<u>Postdoctoral Fellow Awards</u>

1st prize: Hans Rinderknecht, Lawrence Livermore National Laboratory, "Studies of Ion Species Separation in ICF-Relevant Plasmas at Omega"

2nd prize: Alex Zylstra, Los Alamos National Laboratory, "Studying Astrophysical Nucleosynthesis Using Inertially Confined Plasmas at Omega"

3rd prize: Siddarth Patankar, Lawrence Livermore National Laboratory, "Initial Results of Short-Pulse Laser Interactions with Optically Levitated Microdroplets"

Bylaws, Nominations, and Election

In the fall of 2015, members of OLUG approved the first set of bylaws for OLUG. Paul Drake (University of Michigan) gave a presentation on the bylaws and the approval process. Based on the guidelines established by the bylaws, Roberto Mancini (University of Nevada, Reno) led in the winter of 2016 the first nomination and election to select two new members for OLUG's Executive Committee (EC): one representative from a U.S. university/small business and one representative from a national laboratory/major business. To this end, a nominations committee was set up comprised of Roberto Mancini (Chair),

U2056JR

Figure 148.36
Paul Drake (University of Michigan) discussed the OLUG bylaws approved in the fall of 2015.

U2057JR

Figure 148.37
Roberto Mancini (University of Nevada, Reno) explained the nomination and election process carried out in the winter of 2016.

Tammy Ma (LLNL), and Farhat Beg (University of California, San Diego). This committee requested nominations from OLUG members from mid-January through mid-February of 2016. The election, which followed in February and March, resulted in the selection of Johan Frenje (MIT) and Mingsheng Wei (GA) as new members of the EC. Current members of OLUG's EC for April 2016–April 2017 include the following:

- Chair: Roberto Mancini (University of Nevada, Reno)
- University/small business: Paul Drake (University of Michigan), Johan Frenje (MIT), and Mark Koepke (West Virginia University)
- National laboratory/major business: Peter Celliers (LLNL), Kirk Flippo (LANL), and Mingsheng Wei (GA)
- Junior researcher: Alex Zylstra (LANL)
- Non-U.S. researcher: Peter Norreys (Rutherford Laboratory, U.K.)
- LLE, ex-officio: James Knauer

The first chairperson of OLUG, Richard Petrasso, has stepped down after leading OLUG for the eight years since its creation. The EC and the members of OLUG are very grateful to Richard Petrasso for his leadership, commitment, and generous dedication to making OLUG a success and serving as a role model for other facility users groups in the U.S. in the area of high-energy-density science.

Summary of Findings and Recommendations

An important outcome of OLUG's annual workshop is the list of Findings and Recommendations that OLUG submits for consideration to LLE's management. The list of 2016 Recommendations is summarized below, including those put forward by the postdocs and student panel.

1. A two-step upgrade of the magnetic-field capability on OMEGA: first, increase the magnetic field to 30 T within the next two years; second, a future enhancement to increase to 50 T.

2. Investigate the "straight-through" issue with the streaked x-ray spectrometer (SXS-SSCA) including the option of replacing the TIM-based streak camera (SSCA) with a newer/better camera.

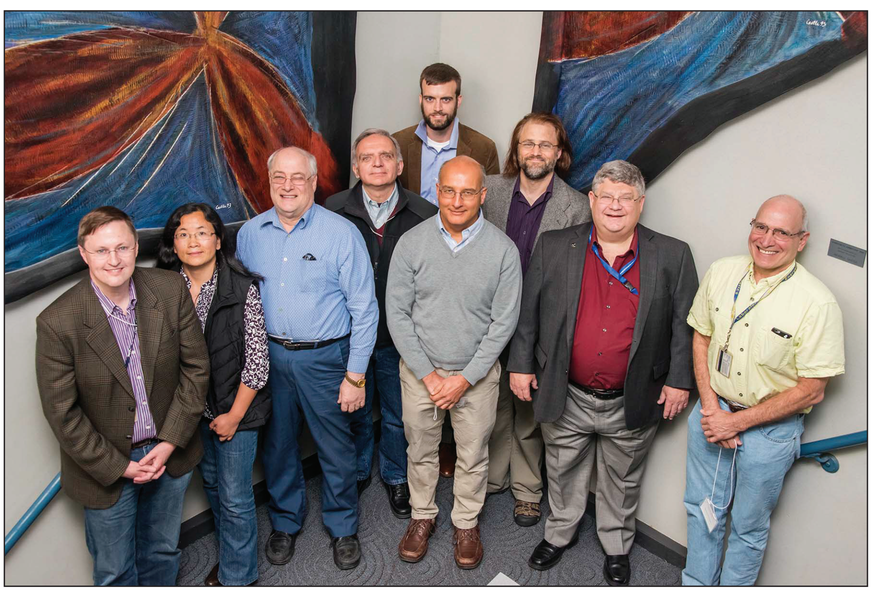

U2058JR

Figure 148.38
OLUG Executive Committee for April 2016–April 2017. From left to right: Johan Frenje (MIT), Mingsheng Wei (GA), James Knauer (LLE), Roberto Mancini (University of Nevada, Reno, Chair), Alex Zylstra (LANL), Peter Celliers (LLNL), Kirk Flippo (LANL), Paul Drake (University of Michigan), and past-chair Richard Petrasso (MIT). Not shown in the photo: Mark Koepke (West Virginia University) and Peter Norreys (Rutherford Laboratory, U.K.).

U2059JR

Figure 148.39
Paul Drake led the discussion on the **Findings and Recommendations**.

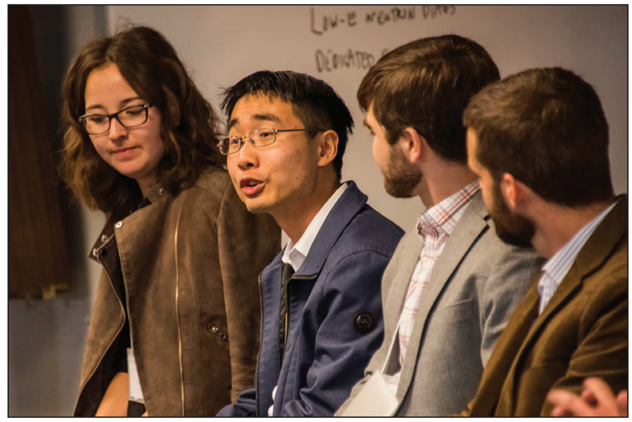

U2052JR

Figure 148.40
Students and postdocs are shown during their panel discussion session.

3. Make a second x-ray streak camera available on OMEGA with capabilities similar to those of SSCA.

4. Implement a Rochester Optical Streak System (ROSS) streak camera on OMEGA for the particle and x-ray temporal diagnostic (PXTD).

5. Use charge-coupled–device (CCD) detectors with the x-ray framing cameras on OMEGA EP.

6. Implement a standardized calibration procedure of the OMEGA optical Thomson-scattering system.

7. Implement faster framing cameras for Thomson-scattering measurements on OMEGA.

8. Undertake the necessary modifications on frequency conversion, final focusing optics, and distributed phase plates to enable a 2ω operation on one of the long-pulse beams of OMEGA EP.

9. Implement near-backscatter–imager (NBI) and time-integrated scatter calorimeter (SCAL) diagnostics on OMEGA EP.

10. Reconfigure the spherical-crystal-imaging (SCI) diagnostic hardware on OMEGA EP to a design similar to the SCI operational on OMEGA, where the line-of-sight block is a component held by the same ten-inch manipulator (TIM) and the detector is outside of the TIM.

11. Improve the projection capability of the OLUG Workshop conference room so that material being used in the discussion sessions can be projected from any Windows laptop or MacBook in the room.

12. Make several improvements to OMEGA's capability to measure low-energy neutron spectra in a DT background.

13. Enhance the active shock breakout (ASBO)/streaked optical pyrometer (SOP) diagnostic.

14. Install a planar cryogenic system on OMEGA EP to provide an additional capability that could complement the National Ignition Facility (NIF) capability and significantly broaden the possibilities for experiments in this area of study.

15. Consider adding plasma sacrificial mirrors to OMEGA EP.

16. Investigate the implementation of an enhanced laser pulse-shaping capability on OMEGA.

17. Allocate more resources to the CR39 etch/lab group to better support the increasing demand of this detector system on OMEGA and OMEGA EP experiments.

18. Consider making gas jet targets available for OMEGA and OMEGA EP.

19. Consider the development of a high-spectral-resolution x-ray spectrometer for OMEGA.

20. If possible, avoid parallel OLUG Workshop sessions in the future. We recommend that next year's evening session focus on x-ray imaging techniques. We appreciate the reinstatement of the national labs session on Friday and recommend additional opportunities for career-oriented interaction between young researchers and representatives of the laboratories—for example, during lunch or by creating an employment-opportunities board. The student/postdoc representative will organize these events at the 2017 workshop in consultation with the rest of the executive committee.

21. Continue the effort to improve and modernize web-based resources. We also recommend that LLE commits resources to development in two new areas: first, enhance the data downloading capability: exporting shot request form (SRF) configuration data as a "parseable file" (e.g., XML), providing diagnostic characterization information, and moving all results and analysis to the Principal Investigator (PI) computer; second, overhaul the data access permissions so that they are more reliable and potentially more granular, rather than blanket institution-based access.

ACKNOWLEDGMENT

This Omega Laser Facility Users Group Workshop was made possible in part by the generous support of the National Nuclear Security Administration of the U.S. Department of Energy for travel expenses of students and postdocs; by the MIT/Plasma Science and Fusion Center; and by the Laboratory for Laser Energetics for the use and availability of critical resources and support. In addition, OLUG thanks the LLE management for their responsiveness to our Findings and Recommendations. For capturing through his lens the workshop ambiance, OLUG thanks Eugene Kowaluk.

Submitted by Roberto Mancini, OLUG Chair.

LLE's Summer High School Research Program

During the summer of 2016, 13 students from Rochester-area high schools participated in the Laboratory for Laser Energetics' Summer High School Research Program. The goal of this program is to excite a group of high school students about careers in the areas of science and technology by exposing them to research in a state-of-the-art environment. Too often, students are exposed to "research" only through classroom laboratories, which have prescribed procedures and predictable results. In LLE's summer program, the students experience many of the trials, tribulations, and rewards of scientific research. By participating in research in a real environment, the students often become more excited about careers in science and technology. In addition, LLE gains from the contributions of the many highly talented students who are attracted to the program.

The students spent most of their time working on their individual research projects with members of LLE's technical staff. The projects were related to current research activities at LLE and covered a broad range of areas of interest including laser physics, computational modeling of implosion physics, experimental diagnostic development, experimental modeling and data analysis, physical chemistry, optical design, tritium capture and storage, cryogenic target characterization, and scientific web page development (see Table 148.VIII).

The students attended weekly seminars on technical topics associated with LLE's research. Topics this year included laser physics, fusion, holography, nonlinear optics, atomic force microscopy, optical instruments, and pulsed power. The students also received safety training, learned how to give scientific presentations, and were introduced to LLE's resources, especially the computational facilities.

The program culminated on 24 August with the "High School Student Summer Research Symposium," at which the students presented the results of their research to an audience including parents, teachers, and LLE staff. The students' written reports will be made available on the LLE Website and bound into a permanent record of their work that can be cited in scientific publications.

Three hundred and fifty-three high school students have now participated in the program since it began in 1989. This year's students were selected from approximately 60 applicants.

At the symposium LLE presented its 20th annual William D. Ryan Inspirational Teacher Award to Mrs. Shayne Watterson, a chemistry teacher at Penfield High School. This award is presented to a teacher who motivated one of the participants in LLE's Summer High School Research Program to study science, mathematics, or technology and includes a $1000 cash prize. Teachers are nominated by alumni of the summer program. Mrs. Watterson was nominated by Emma Garcia and Felix Weilacher, participants in the 2014 program. Emma wrote, "Mrs. Watterson inspired me and the rest of her classes every single day, regardless of the difficulty of the topic… Mrs. Watterson's enthusiasm for her subject is unmistakable… Plenty of times she came up with creative and fun ways for us to learn new concepts. For example, she made up an electromagnetic wave dance to show how the electric wave and the magnetic wave combine and move together." She noted that Mrs. Watterson "is concerned with the success of each of her students as individuals" and concluded by saying, "Mrs. Watterson is probably the best teacher I have ever had, and has showed me both how much fun science can be and how I can pursue it as a career." Felix said of Mrs. Watterson, "There are those who choose to make lives out of leading and inspiring future generations, and for their efforts our communities are certainly and greatly enriched." He noted that Mrs. Watterson "spent huge amounts of time with individual students, be it after school or during free periods, helping them steadily through areas they did not understand." He described Mrs. Watterson as "a truly inspirational teacher, who can affect a student in wonderful ways, pushing the student into new experiences, guiding the student through new layers of learning, and unlocking that student's potential."

Table 148.VIII: High School Student and Projects—Summer 2016.

Name	High School	Supervisor	Project Title
Kyle Bensink	Victor	D. W. Jacobs-Perkins	Post-Shot Data Analysis Tools for Cryogenic Target Shots
Lindsay Browning	Penfield	R. S. Craxton	Development of a Standardized Saturn Ring for Proton Backlighter Targets at the National Ignition Facility
James Hu	Brighton	R. W. Kidder	Using Social Media Technologies for Online Scientific Analysis and Collaboration
Webster Kehoe	Wilson Magnet	R. S. Craxton	Beam-Pointing Optimizations for OMEGA Implosions
Grace Lenhard	Prattsburgh	W. T. Shmayda	Characterizing a Cu/Mn Alloy for Extracting Oxygen from Inert Gas Streams
Joseph Mastrandrea	Webster Thomas	W. T. Shmayda	Measuring Hydrogen Pressure over a Palladium Bed
Nathan Morse	Allendale Columbia	M. J. Guardalben	OMEGA Frequency-Conversion Crystal Designs for Improved Power Balance
Sapna Ramesh	Pittsford Mendon	K. L. Marshall	Characterization of the Electrical Properties of Contaminated Dielectric Oils for Pulsed-Power Research
Archana Sharma	Webster Schroeder	A. Kalb	Design and Optimization of a Portable Wavefront Measurement System for Short-Coherent-Length Laser Beams
Jonah Simpson	Brighton	C. Stoeckl	Validating the Fast-Ion Energy Loss Model in the Monte Carlo Simulation Toolkit Geant4 and Simulating Laser-Driven Nuclear Reaction Experiments on OMEGA EP
Matthew Wang	Pittsford Sutherland	C. Stoeckl	Impulse Response Calibration of a Neutron Temporal Diagnostic Using the Multi-Terawatt Laser
Leah Xiao	Webster Schroeder	R. S. Craxton	Simulations of Laser-Driven Magnetized-Liner Inertial Fusion
Joy Zhang	Penfield	R. T. Janezic	Development of a Digital Microscope for the Characterization of Defects in Cryogenic DT-Filled Targets

FY16 Laser Facility Report

During FY16, the Omega Facility conducted 1414 target shots on OMEGA and 779 target shots on OMEGA EP for a total of 2193 target shots (Tables 148.IX and 148.X). OMEGA averaged 11.7 target shots per operating day with Availability and Experimental Effectiveness averages for FY16 of 95.6% and 96.6%, respectively.

OMEGA EP was operated extensively in FY16 for a variety of internal and external users. A total of 718 target shots were taken into the OMEGA EP target chamber and 61 joint target shots were taken into the OMEGA target chamber. OMEGA EP averaged 7.9 target shots per operating day with Availability and Experimental Effectiveness averages for FY16 of 96.9% and 95.8%, respectively.

Table 148.IX: OMEGA Laser System target shot summary for FY16.

Laboratory/ Program	Planned Number of Target Shots	Actual Number of Target Shots	ICF	Shots in Support of ICF	Non-ICF
CEA	44	55	—	—	55
HED	423.5	491	—	—	491
LANL	44	52	52	—	—
LBS	115.5	136	—	—	136
LLE	352	327	—	327	—
LLNL	77	75	75	—	—
NLUF	198	232	—	—	232
SNL	22	22	22	—	—
Calibration	0	24	—	24	—
Total	1276	1414	149	351	914

Table 148.X: OMEGA EP Laser System target shot summary for FY16.

Laboratory/ Program	Planned Number of Target Shots	Actual Number of Target Shots	ICF	Shots in Support of ICF	Non-ICF
HED	180	292	—	—	292
LBS	54	82	—	—	82
LLE	120	161	—	161	—
LLNL	12	14	14	—	—
NLUF	90	110	—	—	110
NRL	18	25	25	—	—
SNL	24	37	37	—	—
Calibration	0	58	—	58	—
Total	498	779	76	219	484

Highlights of Achievements in FY16

Spherical implosions on the OMEGA Laser System benefit from symmetric laser drive and uniform beam focal spots. As we continue to seek higher implosion pressures, we have embarked upon a system-wide campaign for improvements in subsystems to achieve improved power balance and uniformity.

In FY16, efforts have focused on temporally balancing the energy over 100-ps intervals of the pulse shape. To achieve this, each stage of beam splitters, spatial filters, and amplifiers must have the passive transmission losses and active gain balanced. An observed visible scatter (haze) has developed on several amplifier disks over 21 years of service, prompting investigation of transmission *in situ*. The haze is a scattering source for IR light and is a primary loss mechanism in the OMEGA system. Efforts in FY16 led to the discovery that this haze can be cleaned and the disks restored to pristine transmission characteristics. Since each amplifier exhibits a unique amount of haze, we will utilize system time in FY17 to systematically address the losses. Additionally, the spatial-filter transmission is affected by damage sites in the lenses. A tighter threshold for replacement was adopted in FY16 to minimize contributions to imbalance. We also completed development of a characterization tool to ensure quantitative measurement of the lens-damage site area within the beam aperture.

The OMEGA equivalent-target-plane diagnostic is a precision far-field laser instrument for characterizing the on-target beam uniformity. It has existed since FY01 and had been used to sample Beam 46 for 15 years. During FY16 it was changed from Beam 46 to Beam 56 to allow a second sample of the laser system. This capability will be used in FY17 to further study the on-target focal spot compared to x-ray images of the same beam recorded on an x-ray charge-coupled–device (CCD) diagnostic.

The relative phase of OMEGA smoothing by spectral dispersion (SSD) modulators gives an effective pointing shift to the on-target focal spot when SSD is used on picket pulses. This phenomenon led LLE to synchronize the modulators to the pulse shape. Previously, the co-timing has been set at the beginning of the day using target shots in an operationally costly manner. This year, a pulse shape was created that has a temporal profile matching the modulation period so that the majority of setup can be achieved before target shots and verified during the standard setup shots such as the pointing shot. Additionally, a streaked spectrometer at the output of the system has been fabricated and dedicated to SSD phase measurement, ensuring that drift does not limit this key aspect of focal-spot position during the campaign.

Several efforts have also been pursued to improve laser capabilities on OMEGA. The beam-to-beam timing system has been optimized to reduce the mean arrival time of the pulse to <3-ps root mean square (rms).[1] This method was demonstrated in FY15 and refined to enable quarterly calibration runs during FY16. The UV spectrometer focus was improved and spectrally calibrated using an in-house laser source matched to the primary wavelength. The OMEGA users identified a need for additional beam blocks to prevent blowthrough on the target chamber. Nine additional units were acquired, increasing the total available to 15.

LLE has supported laser-driven MagLIF (magnetized liner inertial fusion) experiments on OMEGA, including experiments where preheating the gas within a magnetized cylindrical target during compression is required. MagLIF on OMEGA utilizes 40 laser beams to compress a cylindrical target, one beam to preheat the fuel, and the magneto inertial fusion electrical discharge system (MIFEDS) to provide an axial magnetic field. A project was implemented in FY16 to improve the symmetry by properly orienting a single laser beam with respect to the compression beams. This symmetry is not readily available with the spherical symmetry of beams on OMEGA. The Beamline 35 pulse is redirected with the use of multiple mirrors to Port P9 and focused onto the cylindrical target using a newly acquired focus lens for the third-harmonic (351-nm) light. The energetics of Beam 35 are controlled by detuning frequency-conversion efficiency to achieve ~200 J in a 2-ns pulse.

The OMEGA EP short-pulse laser presents a number of challenges to operation because of the high fluence of the beam. Early in FY16, the lower-compressor diagnostic beam path was augmented with a large-aperture, neutral-density (ND) filter to reduce the accumulated *B*-integral distortions and enable the ability to diagnose the temporal and spectral characteristics of the signal path beam at higher energies. Significant improvements in the available uniformity of filter glass made it possible to calibrate the spatial transmission of this optic. This action ensured the safe operation of the laser at energies much closer to the upper-compressor capabilities.

Numerous improvements have been made to the OMEGA EP Laser System including an overhaul of the SBSS (stimulated Brillouin scattering suppression) system. This system ensures that acoustic waves are not generated during propagation of laser pulses by giving the beam a small amount of bandwidth to avoid the nonlinear Brillouin scattering effect. This effort reduced the amount of lost shot time from >600 min to <40 min per quarter. The short-pulse diagnostic package scanning autocorrelator was upgraded with an improved CCD detector replacing a photodiode, and the ultrafast temporal diagnostics (UTD) upgrade continued to explore the capabilities of pulse lengths between best compression (~700 fs) and 10 ps. The UTD scopes were ordered and will be installed in early FY17.

Additional diagnostic capabilities added in FY16 include a low-yield neutron time-of-flight diagnostic on the H15 port of OMEGA, covering a new range of neutron energies. The proton temporal diagnostic received a 3-cm nose cone, enabling one to more precisely measure DD and D^3He reaction history.

LLE has taken important steps in the development of future target diagnostics, one of which is the OMEGA EP subaperture backscatter system—an initial capability established in FY16. This hardware will measure the stimulated Brillouin and stimulated Raman scattering bands on a UV beam from the target. Measurements began in the fourth quarter and will be used to define the final system architecture.

Important time-integrated measurements of the high-resolution spectrometer diagnostic were completed in FY16. The shots collected data on scientific cameras (future use will include a streak camera for time-resolved measurements) using the two crystal options and paved the way for final design of the system.

The Experimental Operations and support groups have integrated several new key features to improve operational efficiency. The OMEGA Target Bay structure has been augmented with 600 ft^2 of additional decking space to make storage of the increasing ten-inch–manipulator diagnostic inventory more readily available. Additionally, the darkrooms have been outfitted with digital scanners to rapidly provide a moderate resolution image of film-based data to the Principal Investigator and aid in experimental direction during the campaign.

REFERENCES

1. W. R. Donaldson, J. Katz, R. Huff, E. M. Hill, J. H. Kelly, J. Kwiatkowski, R. B. Brannon, and R. Boni, Rev. Sci. Instrum. **87**, 053511 (2016).

National Laser Users' Facility and External Users' Programs

Under the facility governance plan implemented in FY08 to formalize the scheduling of the Omega Laser Facility as a National Nuclear Security Administration (NNSA) User Facility, Omega Laser Facility shots are allocated by campaign. The majority (68.2%) of the FY16 target shots were allocated to the Inertial Confinement Fusion (ICF) Campaign conducted by integrated teams from Lawrence Livermore National Laboratory (LLNL), Los Alamos National Laboratory (LANL), Naval Research Laboratory (NRL), Sandia National Laboratories (SNL), and LLE and the High-Energy-Density (HED) Campaigns conducted by teams led by scientists from the national laboratories, some with support from LLE.

The Fundamental Science Campaigns accounted for 25.5% of the Omega Facility target shots taken in FY16. Over 61% of these shots were dedicated experiments under the National Laser Users' Facility (NLUF) Program, and the remaining shots were allotted to the Laboratory Basic Science (LBS) Program, comprising peer-reviewed fundamental science experiments conducted by the national laboratories and by LLE.

The Omega Laser Facility was also used for several campaigns by teams from the Commissariat à l'énergie atomique et aux énergies (CEA) of France. These programs are conducted at the facility on the basis of special agreements put in place by Department of Energy (DOE)/NNSA and participating institutions.

The facility users during this year included 13 collaborative teams participating in the NLUF Program; 14 teams led by LLNL and LLE scientists participating in the LBS Program; many collaborative teams from the national laboratories and LLE conducting ICF experiments; investigators from LLNL, LANL, and LLE conducting experiments for high-energy-density–physics programs; and scientists and engineers from CEA.

In this article, we briefly review all the external user activity on OMEGA during FY16.

FY16 NLUF Program

FY16 was the second of a two-year period of performance for the NLUF projects approved for FY15–FY16 funding and Omega Laser Facility shot allocation. Thirteen NLUF projects (see Table 148.XI) were allotted Omega Laser Facility shot time and conducted a total of 342 target shots at the facility. The FY16 NLUF experiments are summarized in this section.

Fast-Electron Energy Coupling and Transport in Warm Dense Plasmas

Principal Investigators: F. N. Beg and C. M. Krauland (University of California, San Diego)
Co-investigators: M. S. Wei (General Atomics); J. J. Santos (Centre Lasers Intenses et Applications, Université Bordeaux); and W. Theobald (LLE)
Graduate Students: S. Zhang and J. Peebles (University of California, San Diego)

Understanding the transport physics of an intense relativistic electron beam in plasmas of varying density and temperature is crucial for many high-energy-density systems, including advanced ignition schemes (e.g., fast ignition and shock ignition) and energetic proton source generation. The fast-electron current (>MA) produced from petawatt laser–matter interaction is much greater than the Alfvén current, and while propagating in plasmas, this super-Alfvénic electron beam draws a return current of background electrons that acts as a neutralizing force. As the return current propagates in the target, resulting joule heating causes variations in the resistivity. Depending on the medium and the current density, either divergence-causing resistive filamentation instabilities or collimating resistive magnetic fields can occur. This award investigates fast-electron propagation in cold and pre-assembled large-volume plasmas to understand the role of resistive effects.

In FY16 experiments, we used OMEGA EP to examine electron-beam transport in allotropes of carbon. Samples of

Table 148.XI: NLUF proposals approved for shots at the Omega Laser Facility for FY15–FY16.

Principal Investigator	Institution	Title
F. N. Beg	University of California, San Diego	Fast-Electron Energy Coupling and Transport in Warm Dense Plasmas
A. Bhattacharjee	Princeton University	Dynamics of Magnetic Reconnection and Instabilities of Current Sheets in High-Energy-Density Plasmas
R. P. Drake	University of Michigan	Experimental Astrophysics on the Omega Laser Facility
T. Duffy	Princeton University	Dynamic Compression of Earth and Planetary Materials Using the OMEGA Laser
P. Hartigan	Rice University	Magnetic Accretion Shocks and Magnetospheres in the Laboratory
R. Jeanloz	University of California, Berkeley	Exploring the Quantum Mechanics of Dense Matter
K. Krushelnick	University of Michigan	X-Ray Measurements of Laser-Driven Relativistic Magnetic Reconnection Using OMEGA EP
D. Q. Lamb	University of Chicago	Nonlinear Amplification of Magnetic Fields in Laser-Produced Plasmas
E. P. Liang	Rice University	Creation of a Magnetized Jet Using a Hollow Ring of Laser Beams
R. D. Petrasso	Massachusetts Institute of Technology	Explorations of Inertial Confinement Fusion, High-Energy-Density Physics, and Laboratory Astrophysics
A. Spitkovsky	Princeton University	Generation of Collisionless Shocks in Laser-Produced Plasmas
M.-S. Wei	General Atomics	Hot-Electron Scaling in Long-Pulse Laser–Plasma Interactions Relevant to Shock Ignition
L. Willingale	University of Michigan	High-Energy Electron-Beam Acceleration from Underdense Plasma Using OMEGA EP

both single-crystal, chemical-vapor–deposition diamond and vitreous carbon were compared since the atomic ordering of a material can have a significant impact on resistivity itself. If the ions are highly disordered, as in the case of vitreous carbon, then electrons scatter incoherently and their mean free path limited to the mean inter-ionic distance results in high resistivity. We used the OMEGA EP IR sidelighter beam (850 J, 10 ps) to irradiate a 10-μm-thick coating of Al on both targets to produce the electron beam. Transport and energy deposition are inferred from the measured fast-electron–induced fluorescence emission of a Cu tracer layer on the opposite side of the carbon, seen in the target schematic of Fig. 148.41. We also compared the initially cold target shots to those that were shock heated from the high-energy, 4-ns-long pulse laser irradiation (~2×10^{14} W/cm^2) onto a 30-μm CH ablator. The shock propagated through the carbon layer toward the Al, creating a roughly uniform heated medium behind the front. The electron beam was then injected at various times relative to the shock location.

Our results show distinct differences in the divergence of hot electrons between the two initially cold samples. In data from a spherical crystal imager (SCI) tuned to Cu K_α (~8 keV), the short-pulse interaction with the Al target layer is recorded by the bright bremsstrahlung spot produced at the interaction. This provides a spatial fiducial for the 2-D, time-integrated Cu fluorescence images resulting from electrons moving through the target and impacting the Cu layer. SCI shows that strong resistive filamentation occurs in the vitreous carbon but not the diamond [Figs. 148.42(a) and 148.42(b)]. This is expected from the instability growth analysis that shows the higher resistivity leading to faster growth rates. When both targets are first heated via long-pulse irradiation, the background and high-angle divergence emission is significantly reduced and a more-focused beam is evidenced in the diagnostics. Figure 148.43(a) shows the difference in profiles for the cold versus heated high-density carbon, suggesting a collimating effect from magnetic-field growth. Similarly, in the vitreous carbon case, a more-localized emission is observed along the target axis but there is no evidence of filamentation. When the electron beam is injected into a fully shocked vitreous carbon layer, the Cu K_α yield is comparable to the high-density carbon case. Spectral analysis is ongoing but preliminary results suggest significant variation in temperature when the electron beam is injected at different delays. Particle-in-cell simulations are being performed to separate the effects of resistive heating and magnetic-field growth, including at target layer interfaces.

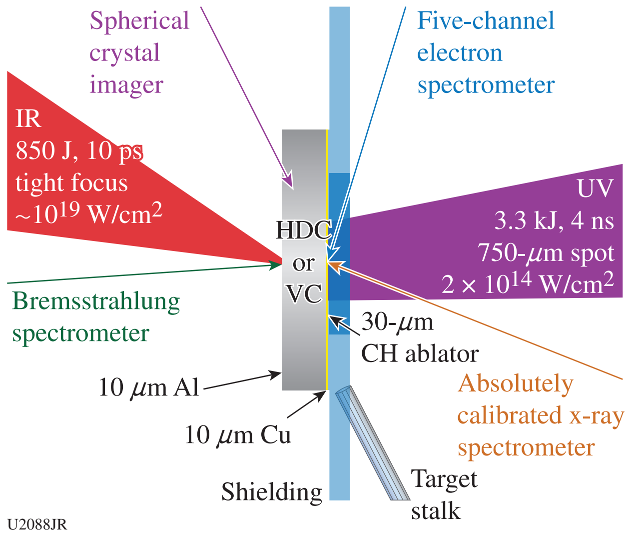

Figure 148.41
Schematic of the shock-heated sample experiment in the OMEGA EP chamber and the primary diagnostics detecting hot-electron characteristics. The targets were either high-density carbon (HDC) or vitreous carbon (VC). Some shots were performed without the UV beam in an otherwise identical configuration.

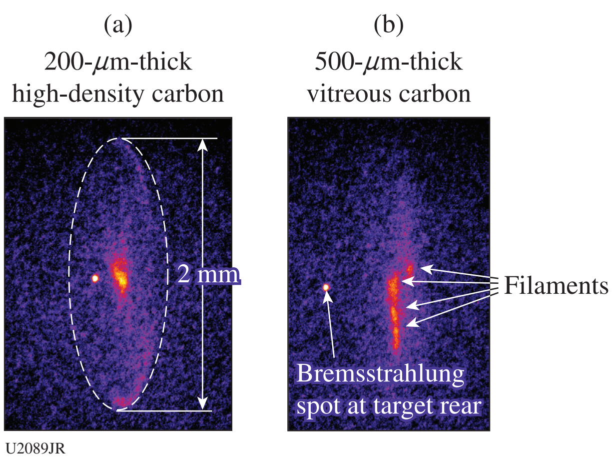

Figure 148.42
Spherical crystal imager (SCI)–measured Cu K_α images from short-pulse–only shots for (a) HDC and (b) VC. A spherical crystal imager (SCI) views the target 73.4° off of target normal.

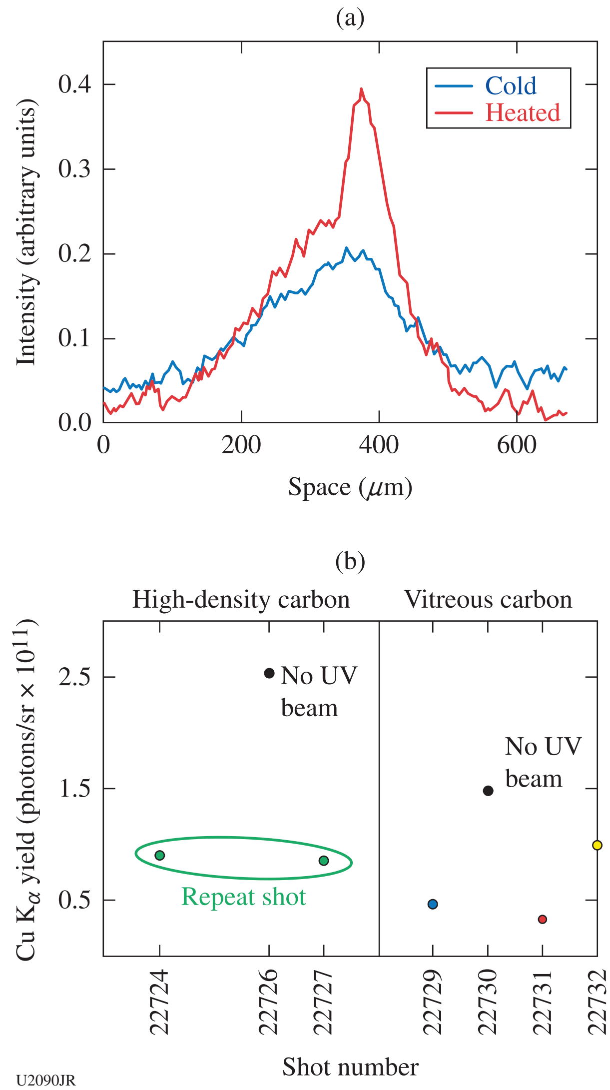

Figure 148.43
(a) SCI spatial profile of fluorescence emission from copper in HDC shots, showing evidence of a focused electron beam with bright localized emission when the target is initially shock heated. (b) Plot of Cu K_α photon yield calculated from spectra recorded on the calibrated zinc von Hamos x-ray spectrometer. While the overall signal drops when the targets are initially heated, this is likely caused by the refluxing of electrons over the entire target, as seen in the SCI data. The red, blue, and yellow dots correspond to a shock position 1/5, 2/3, and fully through the carbon target layer, respectively.

Multi-Nanosecond X-Ray Source Characterization on OMEGA

Principal Investigators: R. P. Drake, P. A. Keiter, and C. C. Kuranz (University of Michigan)
Co-investigators: D. Shvarts, Y. Elbaz, and G. Malamud (Negev Research Center); A. Frank and E. Blackman (University of Rochester); and B. van der Holst (University of Michigan)
Graduate students: J. Davis and R. Van Dervort (University of Michigan)

Soft x-ray sources provide a unique tool for probing and driving matter in high-energy-density systems. Our specific interest is using them for laboratory-astrophysics experiments driven by soft x rays at below 1 keV. To produce a readily characterized source of such x rays, we used a gold conversion foil, heated by high-energy laser beams, then acting as a quasi-blackbody emitter. Previous sources of this type had durations of 1 ns or less. Here, we used OMEGA to demonstrate a source with a duration of 6 ns. To optimize the source for this duration, we characterized the temporal and spatial emission from laser-heated foils of varying thickness.

Figure 148.44 shows a schematic of the experiments. The experiments used 0.5-, 0.75-, 1.0-, and 1.5-μm-thick foils, which were directly heated by a 2.0-kJ, 6-ns laser pulse produced by overlapping laser beams that were smoothed using SG5 phase plates, to produce a laser energy flux of 1×10^{14} W/cm^2. We measured the spatial profile of the x-ray emission using an x-ray framing camera with a soft x-ray nose cone to be able to image the x-ray emission in the 200- to 300-eV and 400- to 500-eV bands in addition to imaging the harder x rays. The Dante photodiode array measured the temporal characteristics of the emission with particular focus on the sub-keV energy bands [Fig. 148.44(b)].

We measured emission from both the irradiated and non-irradiated sides of the foil. The measurements of the irradiated side provided a baseline for future comparison when the source is used with a physics package and the emission from the non-irradiated side cannot be measured. From the Dante output we inferred a time-varying effective temperature, defined as the temperature of a blackbody source that would produce the observed energy flux. The thinnest foils (0.5 μm) produce an ~6-ns, 100-eV source. Thicker foils result in a lower effective temperature as well as a delay in the onset of emission. We were surprised to find the emission to be sustained for 6 ns with a foil as thin as 0.5 μm. Modeling of this case suggests that the laser heating creates and sustains a heated region throughout the gold, and that the foil density remains high enough to prevent the laser from penetrating through the foil up to 6 ns. As foil thickness increases, the effective temperature decreases significantly. The results were very reproducible.

We therefore have demonstrated that one can produce a simple, reliable x-ray source near 100-eV effective temperature, several nanoseconds in duration on OMEGA. We intend to use this source for laboratory-astrophysics experiments.

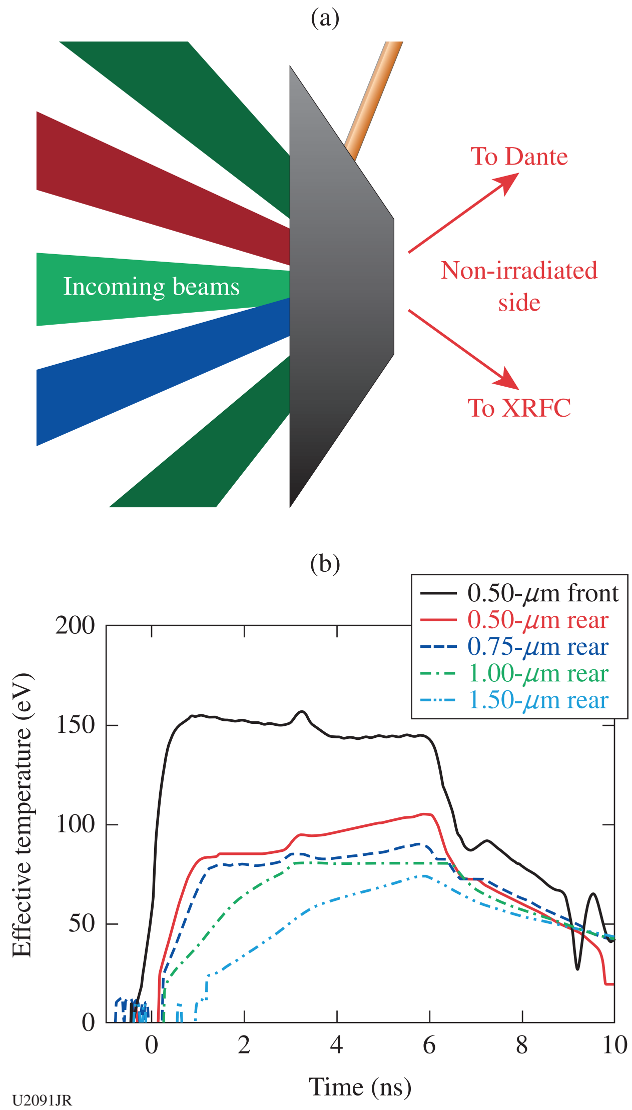

Figure 148.44
(a) Experimental schematic. The laser irradiates the left side of the gold, with Dante and the x-ray framing camera (XRFC) performing most measurements on the non-irradiated side. (b) Effective temperature versus time calculated from the Dante voltage signals. The onset slows and the peak effective temperature decreases as foil thickness increases.

Crystal Structure and Melting of a Laser-Shocked Fe–Si Alloy

Principal Investigators: T. S. Duffy (Princeton University) and R. G. Kraus (LLNL)
Co-investigators: R. F. Smith and F. Coppari (LLNL); J. K. Wicks (Princeton); and T. R. Boehly (LLE)
Graduate Student: M. G. Newman (California Institute of Technology)

The equations of state of potential Earth core alloys at pressures and temperatures near the solid–liquid coexistence curve are important for understanding dynamics at the inner core boundaries of the Earth and super-Earth extrasolar planets. Silicon is one of the most-promising candidates for the light element of the core. An iron–silicon alloy with composition Fe–15wt% Si (Fe–15Si) has been shown to phase separate at static high pressures into an Fe-rich hexagonal close-packed (hcp) phase and a cesium chloride structured (B2) phase.[1] This decomposition requires chemical diffusion of atoms, which is an inherently slow process. Previous studies of the structure and melting behavior of the iron silicide system have been limited to the more-modest temperatures and pressures that are attainable with a laser-heated diamond anvil cell. The OMEGA and OMEGA EP Laser Systems offer the capability to probe the iron silicide system at higher pressures and temperatures as well as dramatically different time scales (~1 ns versus ~1 h).

We have conducted a series of laser-driven shock-melt experiments on textured polycrystalline Fe–15Si samples on OMEGA and OMEGA EP. Measured particle velocities in the Fe–15Si samples using the line velocity interferometer system for any reflector (VISAR) were used to infer the thermodynamic state of the shocked samples. *In-situ* x-ray diffraction measurements using the powder x-ray diffraction image-plate (PXRDIP) diagnostic (Fig. 148.45) were used to probe the melting transition and investigate the decomposition of Fe–15Si into a Si-poor hcp phase and Si-rich B2 phase. Our work addresses potential kinetic effects of decomposition caused by the short time scale of laser-shock experiments. In addition, the thermodynamic data collected in these experiments add to our understanding of the equation of state of Fe–15Si, which is a candidate for the composition in Earth's outer core.

Our experimental results show a highly textured solid phase upon shock compression to pressures ranging from 170 to 300 GPa. The high degree of texturing makes it difficult to definitively identify the structure of the high-pressure solid phases, and both hcp and B2 phases are considered candidate structures. Upon shock compression above 300 GPa, the intense and highly textured solid diffraction peaks give way to diffuse scattering and loss of texture, consistent with melting along the Hugoniot (Fig. 148.46). This is the first direct determination of Hugoniot melting of a Fe–Si alloy. These measurements will enable us to place new constraints on the effect of alloying on the melting temperature and crystal structure of iron near-Earth core conditions.

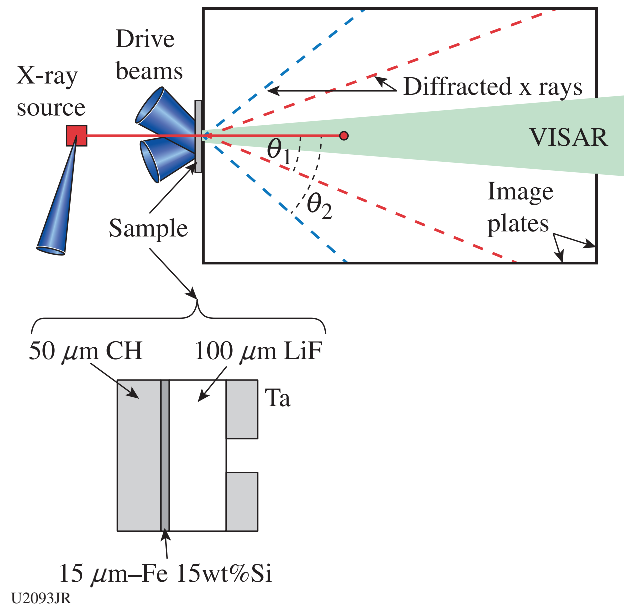

Figure 148.45
Schematic illustration of powder x-ray diffraction image-plate (PXRDIP) diagnostic for x-ray diffraction measurements on OMEGA and OMEGA EP. The diagnostic consists of a rectangular box whose interior is lined with image plates. X rays from a backlight source are used to probe the crystal structure of the laser-driven Fe–Si sample. The target package consists of an ablator, Fe–Si sample, and a LiF window mounted on a pinhole that serves to collimate the incident x rays. VISAR: velocity interferometer system for any reflector.

Dynamics of Magnetic Reconnection in High-Energy-Density Plasmas

Principal Investigators: W. Fox, D. Schaeffer, and A. Bhattacharjee (Princeton University); G. Fiksel (University of Michigan); and D. Haberberger (LLE)

We have developed and conducted experiments on OMEGA EP to study the phenomenon of magnetic reconnection. Magnetic reconnection occurs when regions of opposite directed magnetic fields in a plasma can interact and relax to a lower-energy state; it is an essential plasma-physics process in many systems that governs the storage and explosive release of magnetic energy in systems such as the Earth's magnetosphere,

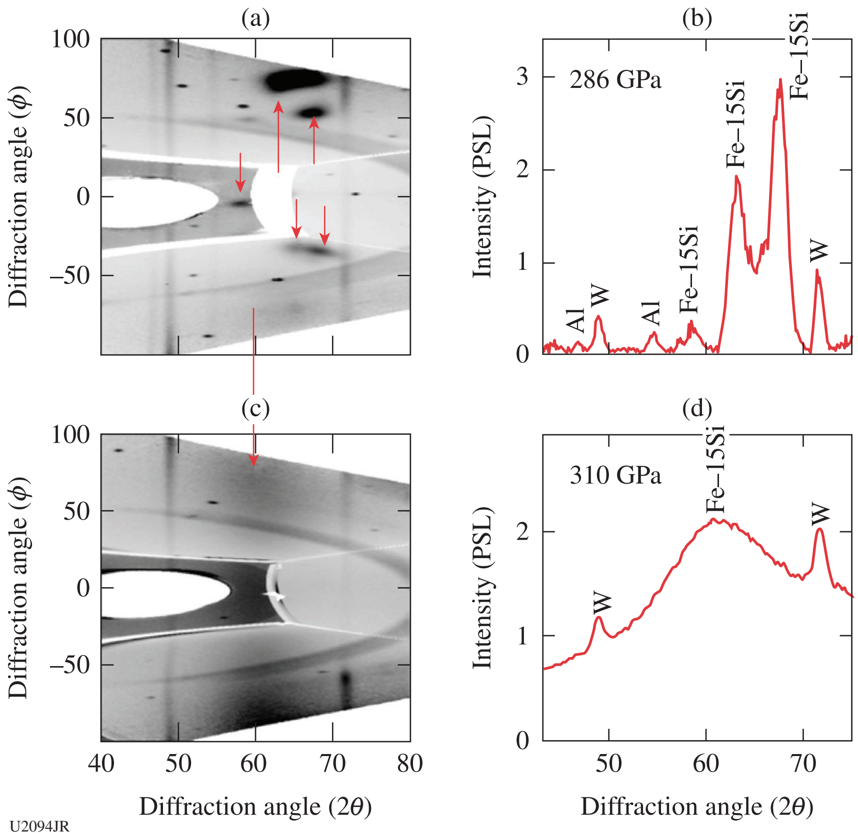

Figure 148.46
(a) Representative x-ray diffraction data for shocked Fe–15Si projected into 2θ versus ϕ space, which correspond to the polar and azimuthal angles about the incident wave vector, respectively. The red arrows point to the diffraction peaks associated with the shock-compressed sample. (b) The corresponding 1-D integrated diffraction patterns for these experiments. [(a) and (b)] At 286 GPa, textured diffraction peaks consistent with hcp/B2 Fe–Si are observed. [(c) and (d)] At 317 GPa, we observe diffuse scattering consistent with shock melting of the sample.

the solar corona, and magnetic-fusion devices. The energy thereby liberated can produce heat and flows and can cause a large number of particles to accelerate to high energies.

These experiments on OMEGA EP used an externally applied magnetic field of the order of 10 T as the seed field for reconnection. With an externally applied field, the fields undergoing reconnection are under experimental control, so it is possible to conduct experiments with variable fields and topologies.

We have successfully carried out two experimental shot days on OMEGA EP. These experiments used the magnetized colliding plasma platform developed by our group and first published in Ref. 2.

The first shot day used the angular filter refractometry diagnostic to observe the density evolution of the expanding plumes. These experimental results provide a measurement of the plasma density flowing with the magnetic field. This determines the plasma regime for reconnection and the flows and allows us to apply accurate initial conditions in our computation models of the colliding plumes and reconnection.

On the second shot day we used the proton radiography to obtain high-resolution images of the magnetic fields in the colliding plasmas. We successfully obtained data at both high- and low-temperature plasma conditions. These results were obtained very recently and are under analysis, but sample data are shown in Fig. 148.47. The data show proton-radiography measurements that are sensitive to the magnetic fields. Light to dark represents increasing fluence of the protons. We observe white "ribbons" on the edge of each expanding plume; each plume is a region of compressed magnetic field that is sufficiently strong enough (B ~ 25 T) to deflect the diagnostic protons off-detector and leave a white low-fluence area. We also observe thin, dark "caustics," which are regions where the protons are focused owing to large gradients of magnetic field. The results show a very rapid evolution of the current sheet from laminar to breaking up as the two plasmas collide, over only a very short time span (3.8 ns versus 4.0 ns). The fast breakup includes the generation of horizontal caustics, indicating the generation of multiple islands resulting from multiple reconnection sites. These results are presently being analyzed and compared with our particle-in-cell code.

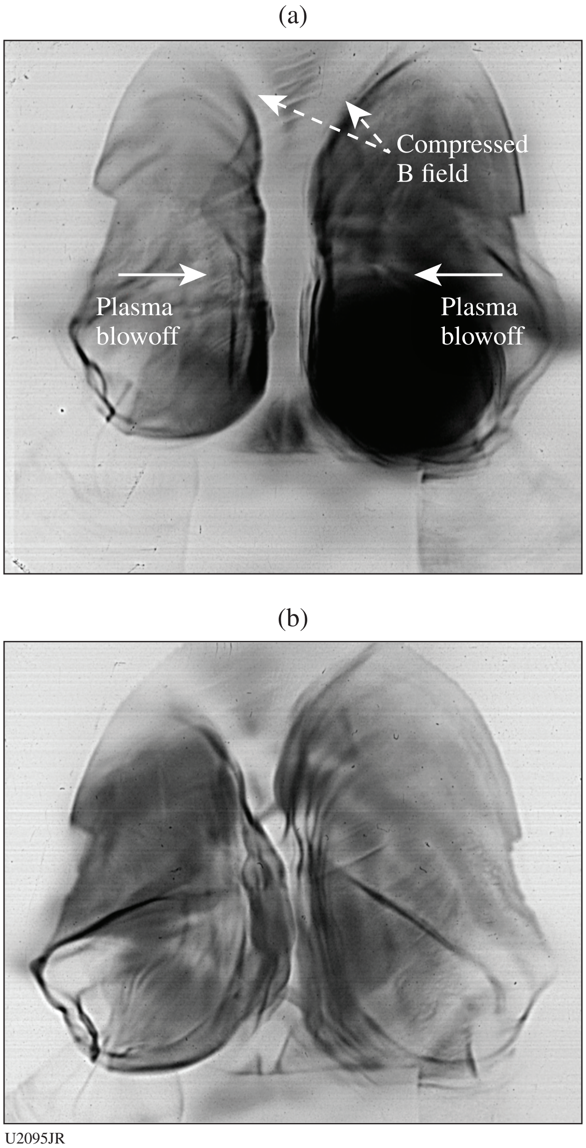

Figure 148.47
Fast evolution of the current sheet measure with proton radiography. The contrast indicates fluence of diagnostic protons, and white areas indicate regions where the magnetic field frozen into the plasma is strong enough to deflect the diagnostic protons off-film. (a) Evolution at 3.8 ns showing the formation of the current sheet as two plumes collide. (b) Evolution a short time later at 4.0 ns showing the fast breakup of the current sheet into smaller-scale structures.

Magnetized Accretion Shocks and Magnetospheres in the Laboratory

Principal Investigator: P. Hartigan (Rice University)
Co-investigators: C. C. Kuranz, G. Fiksel, J. Levesque, and R. Young (University of Michigan); J. M. Foster and P. Graham (Atomic Weapons Establishment; A. Frank (University of Rochester); A. Liao (Rice University); and C. K. Li and R. D. Petrasso [Massachusetts Institute of Technology (MIT)]

Our campaign seeks to develop experiments that feature strongly magnetized, high-Mach-number shock waves in a controlled laboratory environment. These experiments are motivated by the many astrophysical systems where magnetic fields play a key role in determining how supersonic flows interact with their surroundings. Examples include stellar winds, jets from young stars and black holes, interacting binary systems, accretion disks around young stars, planetary magnetospheres, and exoplanetary atmospheres that are subjected to both radiation and winds from their host stars.

Our previous work succeeded in making analogues for both a magnetized-accretion column and a planetary magnetosphere. The accretion-column experiments impacted a magnetized plume of supersonic plasma onto a surface, while the magnetosphere designs drove a supersonic flow (the laboratory equivalent of a solar wind) past a current-carrying wire (a planetary magnetosphere), with the goal to see if we could observe the enhanced magnetic pressure influence the offset of the bow shock from the surface of the wire. While both experiments showed promise, in both cases it was clear that the flow was too dense and too impulsive—the flow simply pushed the shock onto the surface of the obstacle.

To address this issue, we developed a new drive (Fig. 148.48) and performed a series of Thomson-scattering measurements in October 2015 to verify that the numerical models provided the desired ranges of density and velocity. Figure 148.48(b) highlights several regions in density and velocity that are unsuitable for the study of magnetized dynamical effects because the gas is too dense to be a plasma (mauve area), the field diffuses out of the material (green area), a shock does not form (blue area), the field is too strong to allow a shock to form (gray area), or the field is too weak to show dynamical effects (red area). We have found diagrams like that in Fig. 148.48 to be very useful in providing a broad overview of the plasma parameters associated with any experimental design. Our numerical models, verified by the Thomson-scattering data, show that the wind from the colliding flows remains in the desired range of parameter space for over 100 ns, equivalently 20× the characteristic dynamical time scale for laminar flow past the wire.

During the most recently completed shot day (in August 2016), we successfully acquired our first proton radiography images of the system (Fig. 148.49). These experiments used a dual-wire configuration for the target: one wire carrying current and the other one inactive. The images, still being analyzed, reveal a very sharp feature that we believe is a compressed magnetic layer in the dense zone behind the bow shock. These images have significantly better spatial resolution than the two-photon–decay imager (TPDI) optical images we have been using to date and appear to be an excellent diagnostic for these types of experiments. Our preliminary analysis implies that a radial flow from the wire, driven by irradiation from the foils, also affects the system dynamics. If confirmed, the system would then resemble an irradiated exoplanetary atmosphere embedded within a strong stellar wind. Differences between the thicknesses and intensities of the caustics for the 3-MeV and 15-MeV protons should provide clues as to the thickness of the magnetized shocked layer.

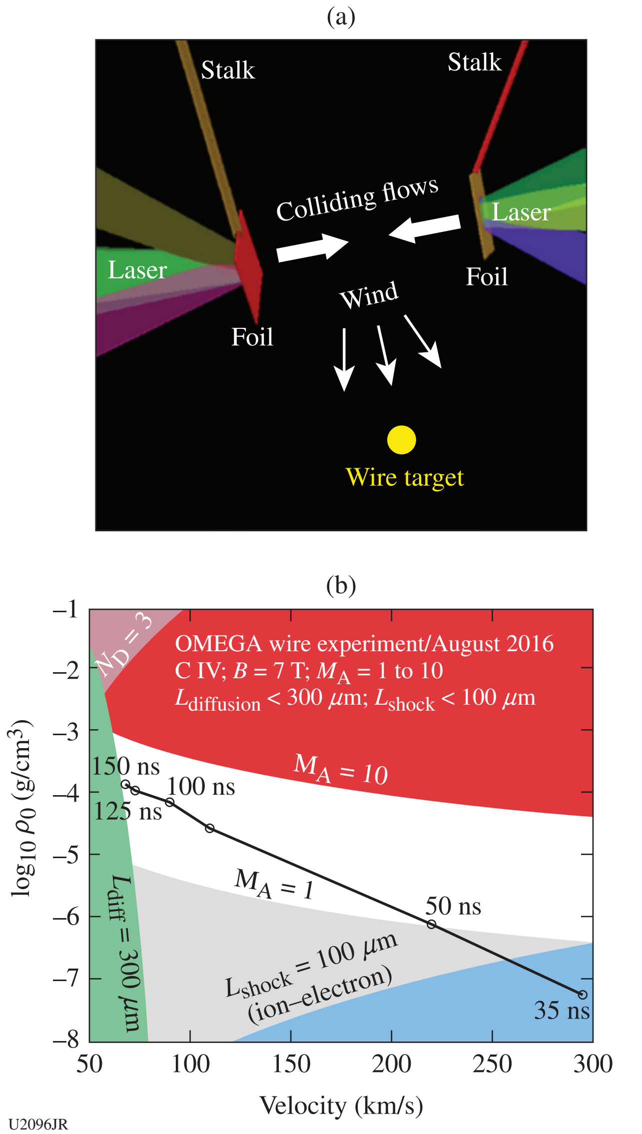

Figure 148.48
New drive design. (a) Design concept showing two colliding flows. Lasers irradiate graphite foils and create oppositely directed impulsive flows that collide and make a more-steady supersonic wind. Adjusting the angle between the two flows allows one control over both the density and velocity. (b) Parameter space for the drive. Shaded areas (green: magnetic diffusion; mauve: warm dense matter; blue: no shock formation; gray: sub-Alfvénic; and red: weak field) are not optimal for observing dynamical effects of fields. The line shows that the drive parameters remain in the correct regime for a time interval of over 100 ns.

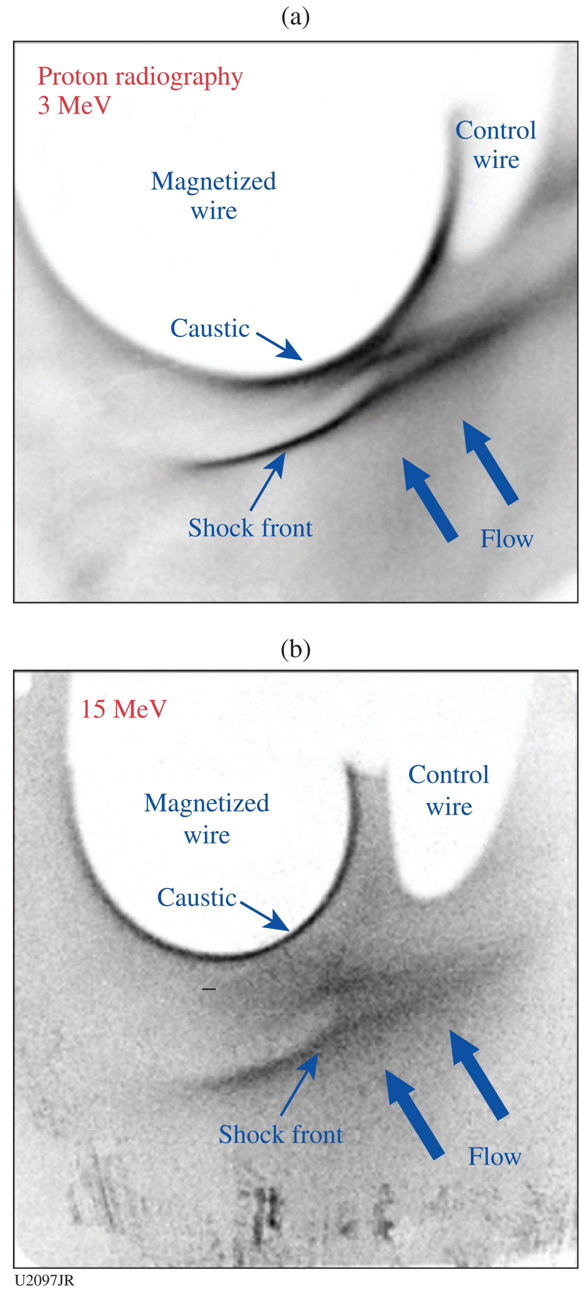

Figure 148.49
Proton radiographs of the wire magnetosphere experiment. The magnetic field from the current in the wire bends protons away from the wire to form a caustic, which is displaced more when the protons are less energetic. A second caustic forms as the magnetic field is compressed in the post-shock region.

The program currently supports the thesis work of three graduate students: R. Pierson and J. Levesque (University of Michigan) and A. Liao (Rice University). These students have been directly involved in the target designs, data analysis, and numerical modeling and on shot days have traveled to the Omega Laser Facility, where they have been involved with real-time decisions concerning the experiment.

Quantum Mechanical and Indirect Diamond Anvil Cell Campaigns

Principal Investigator: R. Jeanloz (University of California, Berkeley)

Co-investigators: P. Loubeyre and S. Brygoo (CEA); and M. Millot, J. R. Rygg, J. H. Eggert, P. M. Celliers, and G. W. Collins (LLNL)

In FY16, the University of California, Berkeley–CEA–LLNL team continued to explore the properties of warm dense hydrogen isotopes at extreme density using ultrafast optical diagnostics under shock compression. We conducted three half-days of experiments, using several-kJ, 1-ns drives to launch strong shocks in hydrogen precompressed to 15 GPa. Active shock breakout (ASBO, velocimetry) and streaked optical pyrometry (SOP) were used to monitor the shock-front velocity, reflectivity/absorptivity, and thermal emission during its travel in the hydrogen layer and in the quartz reference plate. Using impedance matching, new pressure–density–temperature equation-of-state data were obtained, and new data were collected on the metallization of hydrogen at unprecedented conditions approaching the predicted plasma-phase transition (PPT) (Fig. 148.50). In parallel, the team also developed a new approach for collecting multishock data on precompressed samples that allowed us to reach even higher densities in the vicinity of the PPT.

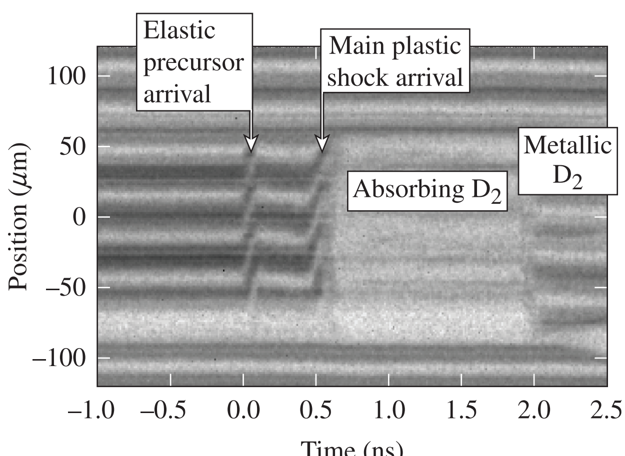

U2098JR

Figure 148.50
Raw velocimetry [active shock breakout (ASBO)] data for a multishock in deuterium precompressed to 13 GPa that will provide new insight into hydrogen's insulator-to-metal transition near the predicted plasma-phase transition. After the breakout of a two-shock structure from the diamond into the deuterium layer, D_2 becomes opaque before becoming reflecting (metallic) when the shock bounces off the second diamond anvil and sends a second shock into the D_2.

To pave the way for future National Ignition Facility (NIF) experiments, our team also started to develop an indirect-drive diamond anvil cell (DAC) platform on OMEGA using gold halfraums. Three half-day campaigns provided a wealth of information on this new platform and showed that a higher-pressure, highly planar shock could be obtained. Strong photoionization was always observed, however, even when using different halfraum geometries of drive configurations.

X-Ray Measurements of Laser-Driven Relativistic Magnetic Reconnection Using OMEGA EP

Principal Investigators: K. Krushelnick, A. Raymond, L. Willingale, A. Thomas, and T. Batson (University of Michigan); P. M. Nilson and C. Mileham (LLE); G. J. Williams and H. Chen (LLNL); and W. Fox (Princeton University)

Previous laser-driven magnetic-reconnection experiments used kilojoule-class, nanosecond-duration laser pulses (long-pulse regime) focused to moderate intensities $I \sim 10^{14}$ to 10^{15} W/cm^2 to heat a solid target and create two colliding plasmas. Azimuthal megagauss magnetic fields in each are driven together by frozen-in-flow, i.e., the bulk motion of the plasma, or hot-electron flows, resulting in electron acceleration by the reconnection fields to energies exceeding an order of magnitude larger than the thermal energy. This experimental regime allows for dimensionless parameter scalings with many astrophysical systems. Until now, however, the extremely energetic class of astrophysical phenomena, including high-energy pulsar winds, gamma-ray bursts, and jets from galactic nuclei, where the energy density of the reconnecting fields exceeds the rest mass energy density, has been inaccessible in the laboratory. This is the regime of relativistic reconnection, which results in much higher energies of accelerated electrons because of longer confinement of the charged particles within the acceleration region. With OMEGA EP we have been able to use laser pulses of much higher intensity ($I > 10^{18}$ W/cm^2) that generate a dense, relativistic electron plasma within the focal volume during the interaction with a solid foil target. In this regime, magnetic-field–generation mechanisms and transport are governed by the relativistic electron population and its dynamics. The expansion of the hot-electron plasma rapidly sets up a space-charge field at the target–vacuum interface, confining a large portion of the electrons to expand radially along the target surface. These currents generate an azimuthal magnetic field with ~100-MG magnitude expanding radially at about the speed of light. Generating two such interaction sites produces a reconnection geometry with plasma characteristics of the relativistic reconnection regime.

In these experiments an x-ray (copper K_α) imaging technique visualized the fast electrons accelerated in the reconnection region to provide spatial information about the extent of the current sheet and also allowed us to take time-resolved measurements of the x-ray emission. Our simulations show that the plasma density and magnetic-field characteristics in the reconnection region satisfy $\sigma > 1$, indicating these experiments are in the relativistic reconnection regime. The experiments focused two short-pulse laser beams onto micron-scale thick copper foil targets to focal spots separated by a distance x_{sep}. A generalized experimental schematic and diagram of the two-spot field geometry with corresponding magnetic and electric fields are depicted in Fig. 148.51. When the antiparallel magnetic fields meet in the midplane between the interaction sites, the field lines can break and reconnect within a reconnection layer, deflecting inflowing electrons and supporting a target-normal electric field supported by the Hall effect and by thermal pressure. This localized electric field generates a current sheet, with electrons being accelerated into the dense regions of the plasma. These fast electrons undergo ionizing collisions with atoms in the target and K-shell electrons are emitted (these atoms recombining on femtosecond time scales). K_α x-ray emission occurs as the L-shell electrons transition to

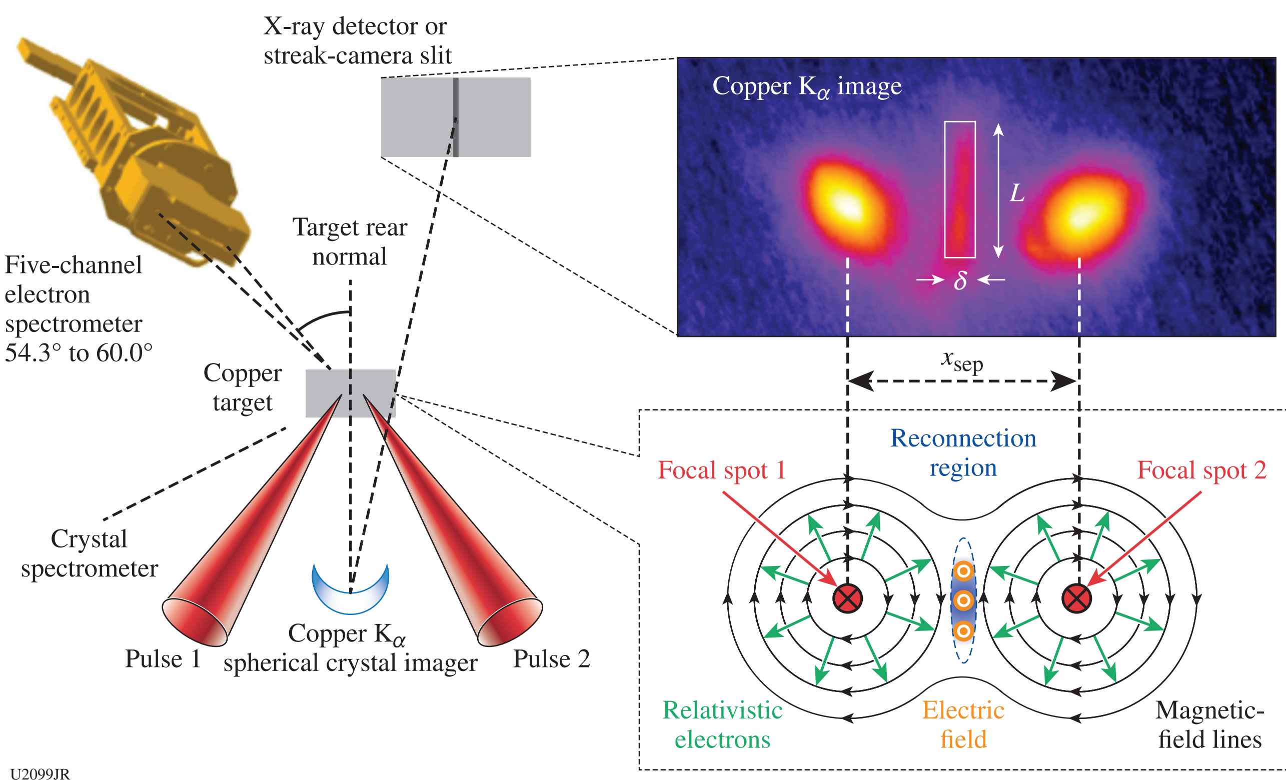

Figure 148.51
A schematic of the experimental geometry for the OMEGA EP experiments. The spherical crystal images x rays from the front side of the target onto a detector. A typical K_α image is shown with the reconnection layer highlighted in the white box with length (L) and width (δ) labeled. A physical picture of the interaction illustrates the two azimuthal magnetic fields expanding into the reconnection region where a target normal electric field accelerates the electrons into the dense target to generate the copper K_α emission in the midplane.

the K shell. Therefore, by imaging the K_α (8.048-keV) emission with a spherically bent quartz x-ray crystal, we are able to produce a map of the current sheet generated between the magnetic-field regions and therefore diagnose the reconnection process.

With this experimental geometry, separation scans of the focal spots were performed with the HERCULES laser at the University of Michigan (2-J, 40-fs pulses focused to extreme intensities 2×10^{18} W/cm^2 onto 12-μm copper foils) and OMEGA EP at LLE [500 J/1000 J, 20 ps focused to comparable intensities of (1 to 2) $\times 10^{18}$ W/cm^2 onto 50-μm copper foils]. Two bright K_α sources corresponding to the target heating within the focal volume were observed on both systems (Fig. 148.52). Additionally a separation-dependent enhancement of the K_α radiation at the midplane was measured corresponding to the current sheet. Detailed analysis of the midplane K photons with a von Hamos crystal spectrometer allowed us to estimate that they originated from within a cold, relatively deep plasma, consistent with a population of accelerated electrons in the midplane by the reconnection electric field. Further, x-ray pinhole camera images found no midplane emission between 2 to 6 keV, ruling out collisional heating between the two plasmas as a source of the K_α enhancement. Figure 148.53 shows the measured midplane signal (a) width and length and (b) normalized signal as a function of the focal separation. To search for additional signatures of electrons accelerated by the reconnection electric field, a five-channel electron spectrometer was utilized on OMEGA EP at the target rear (Fig. 148.54). It showed angularly dependent nonthermal features super-imposed on a quasi-Maxwellian energy distribution, suggesting rear target-normal accelerated electrons propagated through the target and escaped into vacuum. The nonthermal features were suppressed when a 100-ps delay was introduced between the pulses, supporting their association with reconnection.

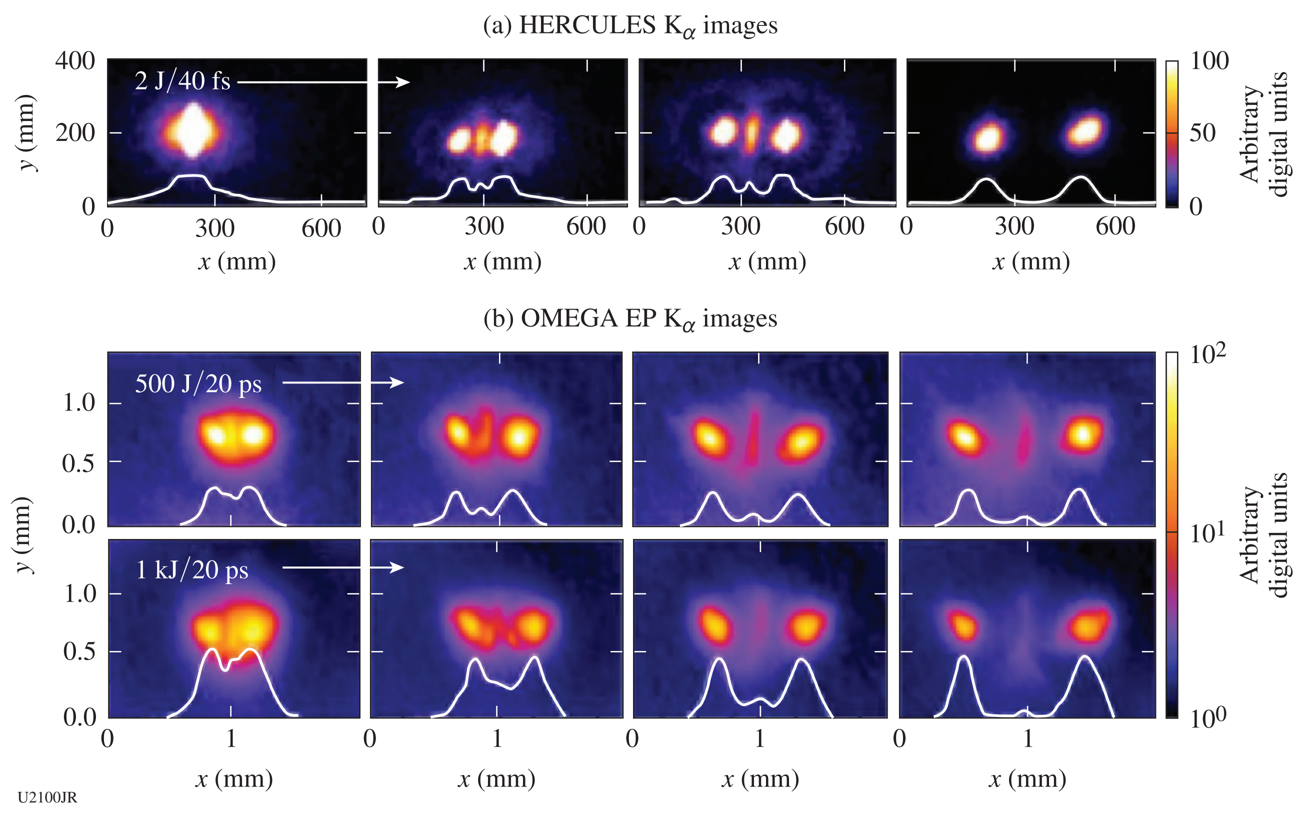

Figure 148.52
Front-side copper K_α images from focal-spot separation scans using (a) the HERCULES laser and (b) the OMEGA EP laser. The 50-μm horizontal lineouts are superimposed.

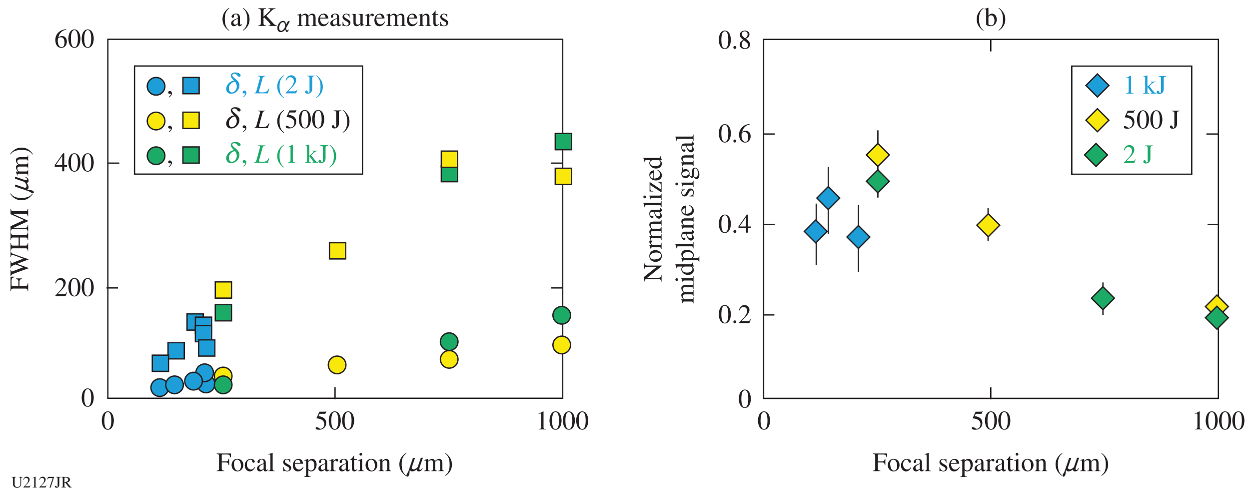

Figure 148.53
(a) The enhanced midplane signal full width at half maximum (FWHM) width (δ) and length (L) and (b) integrated signal normalized to the per-shot average of the integrated signal density from the focal-spot regions.

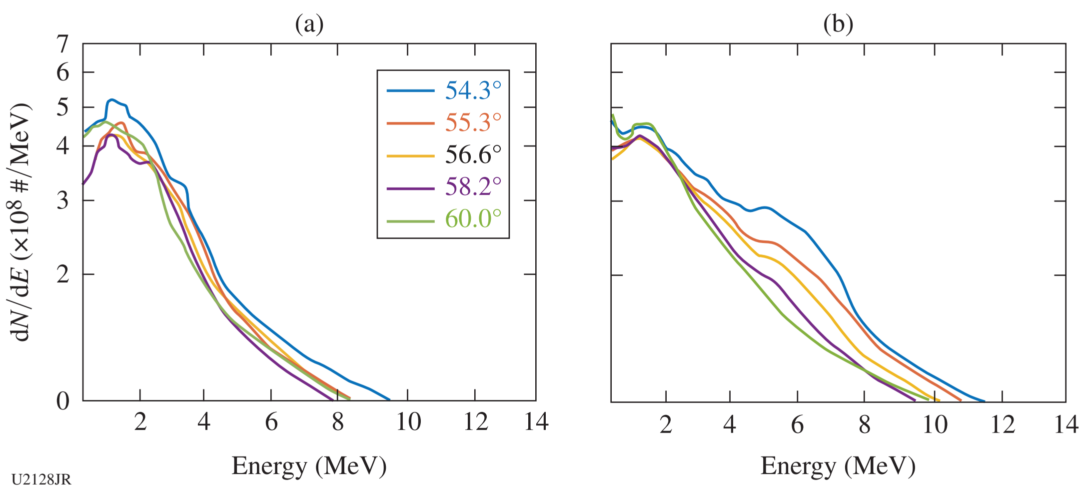

Figure 148.54
The electron spectra (for 500-μm separation) from the OMEGA EP multichannel spectrometer at angles from the transmitted laser axis in the case of (a) a 100-ps pulse-to-pulse delay (no reconnection) and (b) no pulse-to-pulse delay (reconnection).

Nonlinear Amplification of Magnetic Fields in Laser-Produced Plasmas

Principal Investigator: D. Lamb (University of Chicago)

The experiments we performed during our second shot day (10 August 2016) on the OMEGA laser studied the turbulent dynamo amplification of magnetic fields, a ubiquitous process in astrophysical systems, and the effects of magnetized turbulent plasmas on nonthermal particle diffusion and acceleration processes relevant to cosmic rays. The experiments utilized a platform [Fig. 148.55(a)] very similar to the one fielded on OMEGA during our very successful first shot day, during which we demonstrated nonlinear amplification by turbulent dynamo for the first time in a laboratory environment. We designed the experimental platform aided by numerical modeling effort on one of the nation's leading supercomputers [Fig. 148.55(c)] and it is uniquely fitted to generate turbulent plasmas in the large magnetic Reynolds numbers regime, where dynamo can operate. The configuration consists of two diametrically opposed foil targets, 8 mm apart, that are backlit with temporally

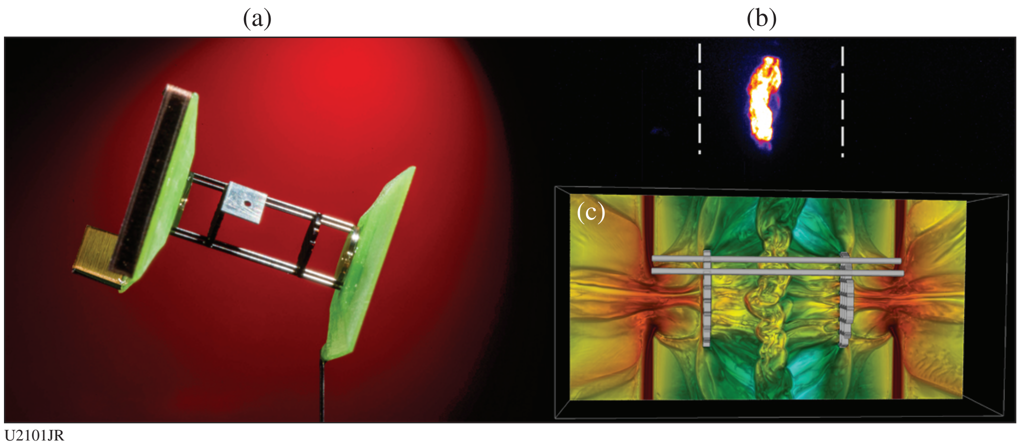

Figure 148.55
(a) Experimental platform of the National Laser Users' Facility (NLUF) Campaign to study turbulent dynamo amplification and nonthermal particle acceleration and diffusion, processes that occur in astrophysical environments like galaxy clusters. The assembly consisted of two polystyrene foils and a pair of meshes, held together by four boron rods. The foils and meshes were carefully designed and machined to optimize the conditions in the interaction region for turbulent field amplification. By changing the specifications of the grids, we are able to control the injection scale of the turbulence and the shape of the interaction region. The shields and flaps protect the interaction region, the imploding D^3He capsule, and the diagnostics from the direct view of the laser spots. The shield with the pinhole—on the side of one of the grids—made it possible to create collimated proton beams to investigate diffusion of charged particles by magnetized turbulence. (b) X-ray image of the interaction region after the collision. The flow exhibits strong turbulence and is considerably hot. The wealth of experimental diagnostics has made it possible to characterize the magnetized plasma, study the turbulent dynamo mechanism, and probe the physics behind the interaction of magnetized turbulence with charged particles. (c) Three-dimensional radiation–magnetohydrodynamic simulation of the experimental platform, performed with the multiphysics code *FLASH*. A large simulation campaign on Argonne National Laboratory's *Mira* BG/Q supercomputer guided us in the design of a platform capable of probing the turbulent dynamo regime. The figure displays a 3-D rendering of the simulated electron density (in cm^{-3}), after the jets collide.

stacked beams that deliver 5 kJ of energy on each side. The beams drive a pair of colliding plasma flows that carry seed magnetic fields, generated by the Biermann battery effect. The flows propagate through a pair of grids that destabilize the flow and produce turbulence with a driving scale defined by the grid specifications. By varying the latter we can assess the properties of turbulence injection. The turbulent flows meet at the center of the chamber to form a hot, turbulent interaction region where seed magnetic fields are amplified to saturation values. The magnetized turbulent flow is probed with pinhole-collimated proton beams to study spatial diffusion; we also measure the electron energy spectrum in search of particle acceleration signatures.

Our 13 shots have yielded a wealth of experimental data. The diagnostics we fielded made it possible to fully characterize the turbulent interaction region, quantify its energy budget and power spectrum, and study the effects of magnetized turbulence on diffusing and accelerating charged particles. More specifically, x-ray imaging [Fig. 148.55(b)] made it possible to directly visualize the turbulent region and explore how different grid specifications altered the dynamics of the flow interaction. From the x-ray intensity fluctuations we also reconstructed the density power spectrum of the turbulence and inferred its power law. Moreover, the time-resolved spectrum from the Thomson-scattering diagnostic yielded clear ion-acoustic features that allowed us to characterize the plasma properties, including ion and electron temperatures, turbulent and bulk flow velocity, and electron density. By coupling the Thomson-scattering diagnostic with a Wollaston prism, we were also able to separate the light's polarization into two orthogonal components and measure Faraday rotation caused by the magnetic field. In conjunction with proton radiography and the novel mapping techniques we developed, we were able to reconstruct the strength and topology of the magnetic field in space and time. By introducing a pinhole [Fig. 148.55(a)] in the path of the protons, we were also able to create a collimated proton beam that interacted with the electromagnetic fields of the turbulent plasma and spatially diffused, as cosmic rays would, with astrophysical turbulence. Lastly, by fielding the Osaka multichannel spectrometer, we were able to recover the energy spectrum of the electrons. This plenitude of experimental data is still under analysis and scrutiny and promises to expand our understanding of the puzzle that is astrophysical turbulence.

Creation of Magnetized Jet Using a Hollow Ring of Laser Beams
Principal Investigator: E. Liang (Rice University)

Progress toward the objectives of the project as listed in the original application has exceeded expectations. We carried out a one-day OMEGA laser experiment in December 2015, using 20 beams to form a hollow-ring focal pattern to create a magnetized jet from a flat plastic target. The hollow-ring radius varied from 0 to 800 μm. Eleven shots were completed successfully. Thomson-scattering (TS) diagnostics were used to measure the on-axis electron and ion densities, temperature, and flow velocity at 2.5 mm from laser target for each shot. The TS results confirmed the predictions of *FLASH* 2-D simulations, namely that the on-axis density, temperature, and velocity are highest for the 800-μm-radius ring and lowest for the 0-radius ring. Both 3-MeV and 14-MeV monoenergetic protons from D^3He capsule implosions were used to measure the magnetic-field geometry and magnitude in the jet via proton radiography. The results show much stronger and more filamentary magnetic fields embedded in the jet than *FLASH* 2-D simulation predictions. We deduced peak magnetic fields exceeding 10 T. This important and unexpected result means that the plasma properties of the hollow-ring jet, including its collisionality, will be significantly impacted by the self-generated magnetic field. Posters on the preliminary results were presented at both the Omega Laser Facility Users Group Workshop in April 2016 and the High-Energy-Density Laboratory Astrophysics (HEDLA) Stanford Linear Accelerator (SLAC) meeting in June 2016. A more-updated poster will be presented at the American Physical Society Division of Plasma Physics Conference in November 2016, in which details of the proton-radiography results and magnetic-field deconvolution will be discussed.

Explorations of Inertial Confinement Fusion, High-Energy-Density Physics, and Laboratory Astrophysics
Principal Investigators: R. D. Petrasso C. K. Li, and J. A. Frenje (MIT)
Co-investigators: F. H. Séguin and M. Gatu Johnson (MIT)

MIT work in FY16 included a wide range of experiments that applied proton radiography, charged-particle spectrometry, and neutron-spectrometry methods developed by MIT and collaborators to the study of laboratory astrophysics, high-energy-density physics (HEDP), and inertial confinement fusion (ICF) plasmas. Seventeen papers[3–19] about NLUF-related research were published in FY16 (four by students[4–7]) and many invited talks and contributed talks were presented at conferences.

Former MIT Ph.D. student Dr. M. J. Rosenberg (Fig. 148.56) won the 2016 Marshall N. Rosenbluth Outstanding Doctoral Thesis Award based on his 2014 thesis[20] entitled "Studies of Ion Kinetic Effects in Shock-Driven Inertial Confinement Fusion Implosions at OMEGA and the NIF and Magnetic Reconnections Using Laser-Produced Plasmas at OMEGA." He is only the second Ph.D. student supported by NNSA and/or the joint program to ever receive this prestigious award (the first was Dr. M. J.-E. Manuel, whose 2013 MIT thesis was also based on NLUF research). Dr. Rosenberg is now a Research Scientist at LLE.

U2102JR

Figure 148.56
Dr. M. J. Rosenberg, who won the 2016 Marshall N. Rosenbluth Outstanding Doctoral Thesis Award based on his 2014 thesis[20] entitled "Studies of Ion Kinetic Effects in Shock-Driven Inertial Confinement Fusion Implosions at OMEGA and the NIF and Magnetic Reconnections Using Laser-Produced Plasmas at OMEGA."

Two new Ph.D. students (R. Simpson and A. Rosenthal) and one new postdoc (C. Parker) have joined our division and are becoming active participants in the NLUF program. They work alongside continuing graduate students N. Kabadi, B. Lahmann, H. Sio, G. Sutcliffe, and C. Wink.

One of the major areas of research was the study of plasma jets and the effects of magnetic fields on their propagation. Of particular importance was a scaled laboratory experiment designed to shed light on jet dynamics in the Crab-nebula (as described in Ref. 3). The remarkable discovery by the Chandra X-Ray Observatory that the Crab nebula's jet periodically changes direction provides a challenge to our understanding of astrophysical jet dynamics. It had been suggested that this phenomenon may be the consequence of magnetic fields and magnetohydrodynamic instabilities, but experimental demonstration in a controlled laboratory environment was lacking. In the experiment (shown schematically in Fig. 148.57), high-power lasers were used to create a plasma jet that could be directly compared with the Crab jet through well-defined physical scaling laws. The jet generated its own embedded toroidal magnetic fields; as it moved, plasma instabilities resulted in multiple deflections of the propagation direction, mimicking the kink behavior of the Crab jet. The experiment was modeled with 3-D numerical simulations that showed exactly how the instability develops and results in changes of direction of the jet.

Other research and publication topics included the stopping of ions in plasmas,[19] utilizing charged fusion products from ICF implosions and measurements of their energy losses in passing through the ICF-capsule plasma with charged-particle spectrometers; this work is of great importance for ignition since it is relevant to the deposition of alpha-particle energy in burning fuel. In addition, studies of kinetic, multi-ion effects and ion–electron equilibration rates in ICF plasmas (e.g., Ref. 4) continued in the ongoing series of developments evolving from Ref. 20. Thermonuclear reactions at energies relevant to stellar nucleosynthesis and big-bang nucleosynthesis were studied using ICF implosions.[9] Effects of fuel-capsule shimming and drive asymmetry on ICF symmetry and yield were studied on OMEGA.[15,16]

Generation of Collisionless Shocks in Laser-Produced Plasmas

Principal Investigators: A. Spitkovsky (Princeton University) and C. Huntington (LLNL)

The FY16 MagShock EP Campaign was dedicated to the detection of collisionless magnetized shocks in ablated plasma flows. Such shocks form in supernova remnants and in the heliosphere, among others. The shock thickness is determined by the Larmor radius of the incoming protons, and the mean free path must be much longer. The setup is shown on Fig. 148.58. The experiments used the OMEGA EP Laser System in which a 3-D–printed Helmholz coil powered by MIFEDS (magneto-inertial fusion electrical discharge system) was inserted. Three targets were mounted on MIFEDS. A 400-J, 1-ns pulse was used to ablate plasma that propagated along the coil's magnetic field (this component is called "background" plasma). A 1.3-kJ, 1-ns pulse was used to drive fast flow orthogonal to the magnetic field [this component is called "piston" plasma (see Fig. 148.58)]. On some shots two piston plasmas were ablated with different time delays, but most shots

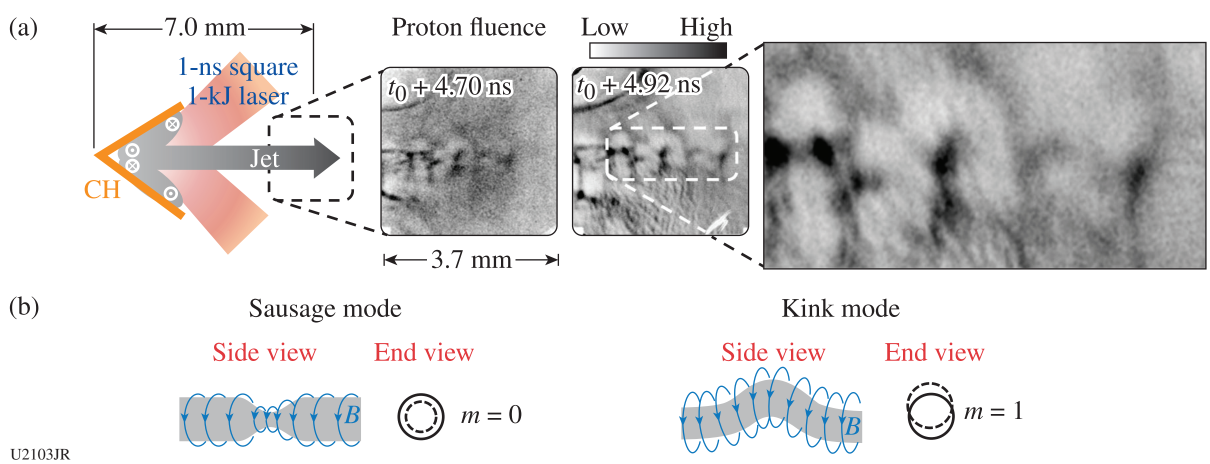

Figure 148.57
A scaled laboratory experiment that sheds light on the Crab-nebula jet dynamics.[1] (a) Schematic of a laser-beam–irradiated, cone-shaped target and the resulting plasma jet. Side-on (proton flux into the paper) radiographic images show the proton fluence distribution at t_0 + 4.70 ns with 14.7-MeV protons and at t_0 + 4.92 ns with 3-MeV protons, where t_0 is the time when the lasers turned on. The enlarged image shows a sequence of clumps and changes of jet direction. (b) Schematic illustrations of the fastest-growing magnetohydrodynamic current-driven instabilities: mode $m = 0$ (sausage, leading to jet propagation clumping) and $m = 1$ (kink, leading to jet direction changing). Higher modes ($m > 1$) are also expected to be excited, but they will have smaller effects and are not illustrated here.

used only one piston plasma. The interaction between the flows was expected to drive a compression in the background plasma and the magnetic field (see Fig. 148.59). At a strong-enough drive, this compression becomes a collisionless shock. We diagnosed this compression using proton radiography with target normal sheath acceleration (TNSA) from a short 10-ps laser pulse. The protons were recorded on CR39 film, which was our primary diagnostic. On some shots, a 4ω optical probe was also utilized.

Our experiments resulted in the detection of a magnetized collisionless shock propagating through the plasma. The main feature of the magnetic compression in the data was the appearance of a white band in the proton image, indicating additional deflection of the protons. The band was followed by a sharp caustic of enhanced proton concentration (Fig. 148.59). The band and the caustic propagated at 300 km/s. The thickness of the band allowed us to constrain the magnetic compression to 2.3, and the caustic was interpreted as the signature of the contact discontinuity between the piston and compressed background plasma. This compression ratio corresponds to a Mach-3 shock. The shock is in the collisionless regime since

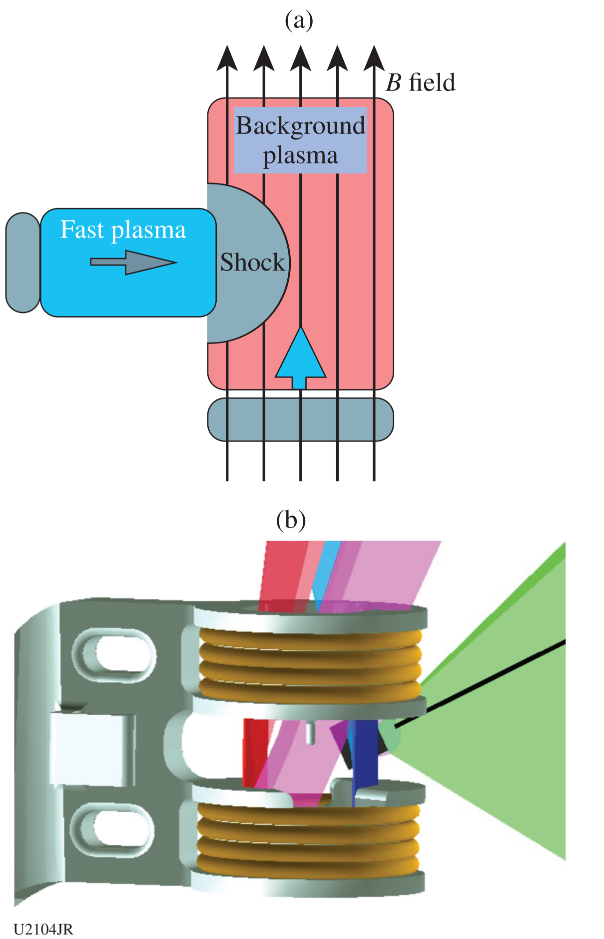

Figure 148.58
(a) Schematic of fast piston plasma interacting with a magnetized background plasma; (b) experimental setup.

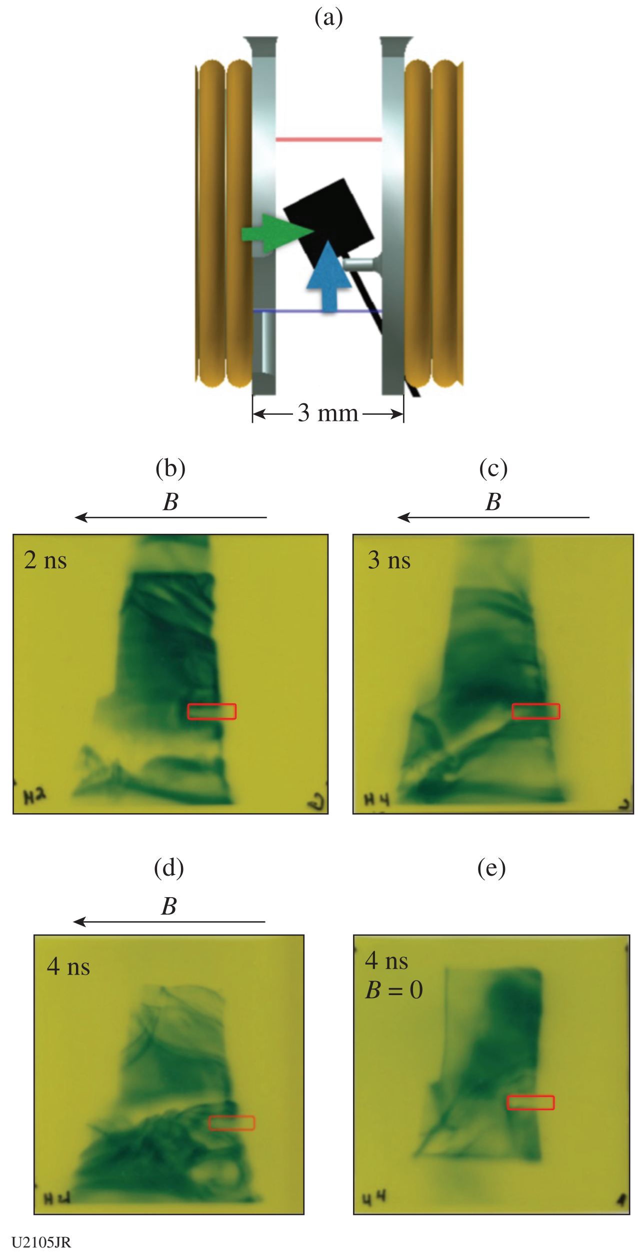

Figure 148.59
(a) View of the setup from the film. [(b)–(d)] Proton radiography of the interaction at different times. Notice the movement of the white band and the sharp caustic feature behind it. (e) The band is not present when the B field is off.

the mean free path of the background protons is larger than the size of the plasma. We have confirmed these results on several shots and have performed the time series study and the null shots of no B field, reverse B field, and individual piston and background plasma shots. These shots did not display the white compressional band, indicating that this feature is unique to the magnetized compressed plasma. We performed extensive numerical simulations of the experiment with particle-in-cell (PIC) simulations, including simulated proton radiography through the fields of the simulation. The experimental results agree quite well with the predictions of the simulations.

These findings are currently being readied for publication in Physical Review Letters. Some preliminary results from this campaign were presented at the 2016 HEDLA Conference.

We thank the OMEGA EP personnel for their assistance in planning and executing this campaign.

Hot-Electron Scaling in Long-Pulse Laser–Plasma Interaction Relevant to Shock Ignition

Principal Investigator: M. S. Wei (General Atomics)
Co-investigators: C. M. Krauland (General Atomics); S. Zhang, J. Peebles, F. N. Beg (University of California, San Diego); and W. Theobald, C. Ren, E. Borwick, J. Li, W. Seka, C. Stoeckl, R. Betti, and E. M. Campbell (LLE)

The shock-ignition (SI) fusion scheme requires launching a strong shock via a short-duration (0.5 to 1 ns), high-intensity (>5 $\times$ 10^{15} W/cm^{2}) spike laser pulse into a pre-assembled fuel to achieve ignition. Surpassing the threshold intensity for laser–plasma instabilities (LPI's) such as stimulated Brillouin scattering (SBS), stimulated Raman scattering (SRS), and two-plasmon decay (TPD), the coupling of spike pulse energy to the target is uncertain. Under these laser and plasma conditions, copious hot electrons can be produced. While very energetic electrons (>200 keV) could preheat the fuel and degrade compression, it is suggested that moderate energy electrons (50 to 100 keV) could benefit the SI scheme by increasing ablation pressure and augmenting the ignitor shock strength as they are stopped in the compressed high-density, low-Z ablator region. The objective of this General Atomics (GA) NLUF project in collaboration with the University of California, San Diego, and LLE is to systematically study the scaling of hot-electron generation with laser intensity, wavelength, and plasma condition (including target ablator material) in the SI-relevant regimes. Understanding LPI and the resultant hot-electron characteristics (total energy, temperature, and divergence) is important for the viability of the SI concept.

Our second-year NLUF experiment in 2016 was successfully conducted in the OMEGA chamber including both OMEGA-only shots and joint OMEGA and OMEGA EP shots, which provided the opportunity to evaluate hot-electron production and energy coupling in the SI-required spherical geometry. The experiment was built off of the strong spherical shock platform by using the same OMEGA 60 UV beams' pulse shape [0.35-TW, 0.8-ns square pulse with 1-ns low-power foot shown in Fig. 148.60(b)], but adding the high-energy OMEGA EP IR beam (0.1 ns, 2.7 kJ with nominal vacuum laser intensity of 2 $\times$ 10^{17} W/cm^{2}) at various timing delays in joint shots. Changing the injection time of the IR beam allowed us to alter the scale length and temperature of the corona plasma with which it interacted. In addition to measuring the IR-generated hot electrons and their energy coupling to the compressed target, we also measured electrons generated by the 60 UV beams alone with their overlapped high intensity of ~3 $\times$ 10^{15} W/cm^{2} by employing smoothing by spectral dispersion (SSD), a distributed polarization rotator (DPR), and an assortment of small phase plates. A schematic of the campaign is shown in Fig. 148.60(a). To facilitate hot-electron characterization including the spatial distribution in the target, experiments used a 485-μm-outer-diam sphere target [Fig. 148.60(c)] consisting of a 30-μm CH ablator layer and a low-density Cu foam ball. The novel GA-produced low-density, pure-Cu foam has a density of 1.2 g/cm^{3} (~13% of solid Cu) with $\leq$1-μm pore size.

Our results resolve successful coupling of IR beam energy to the spherically compressing target under various laser and target conditions. Figure 148.61 shows the measured Cu K_α emission from three different shots: (a) OMEGA only; (b) a joint shot with the IR beam at 0.9 ns, corresponding to the end of the low-intensity foot of the UV driver pulse; and (c) a joint shot with the IR beam at 1.8 ns, corresponding to the end of the UV beams. In the OMEGA-only shot, the observed Cu K_α emission spot excited by the UV beam–produced hot electrons had a characteristic ringlike pattern with a radius of ~150 μm corresponding to the location of the shock-compressed, high-density Cu foam region at 1.8 ns. In the joint shot with the OMEGA EP beam injected at the end of the OMEGA driver, additional Cu K_α emission caused by the OMEGA EP beam–produced hot electrons can be clearly seen on the compressed high-density Cu foam region along the OMEGA EP beam-propagation direction. The localized energy deposition shown in Figs. 148.61(a) and 148.61(c) suggests effective stopping of the UV beam– and IR beam–produced hot electrons by the high-density, compressed Cu foam shell with an areal density of 25 to 30 mg/cm^{2}, within which <100-keV electrons will be ranged out. In contrast, Cu K_α emission caused by

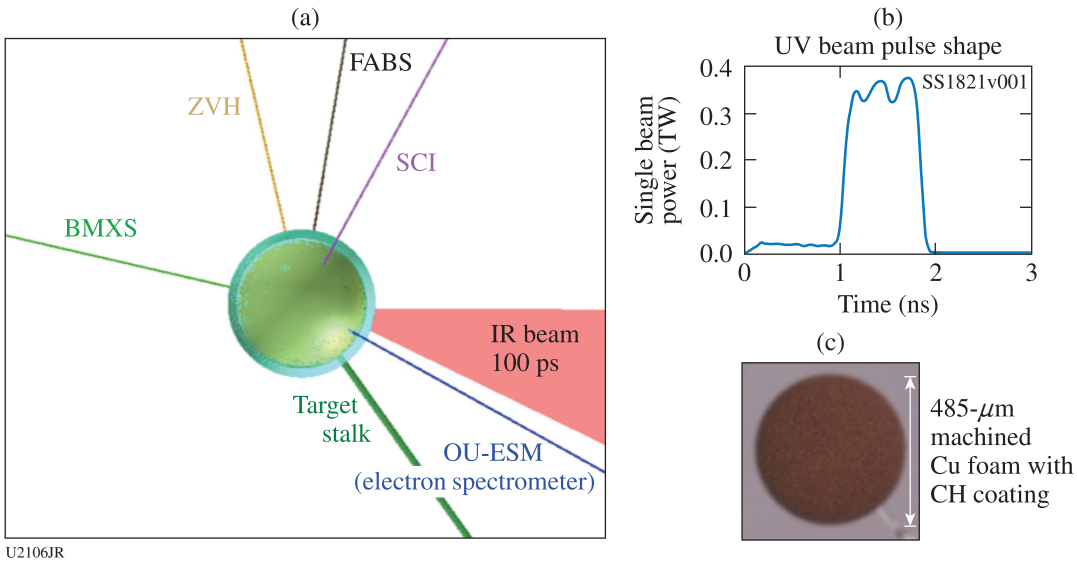

Figure 148.60
(a) Schematic of the joint shot experiment in the OMEGA chamber and the primary diagnostics detecting hot-electron–induced Cu K-shell fluorescence and bremsstrahlung radiation as a result of target irradiation by the OMEGA UV driver and OMEGA EP IR beam; (b) OMEGA pulse shape for 60 UV beams; (c) GA-made Cu foam sphere that is coated with 30 μm of CH as ablator. FABS: full-aperture backscatter station; ZVH: zinc von Hamos; BMXS: bremsstrahlung MeV x-ray spectrometer; OU EMS: Osaka University electron spectrometer.

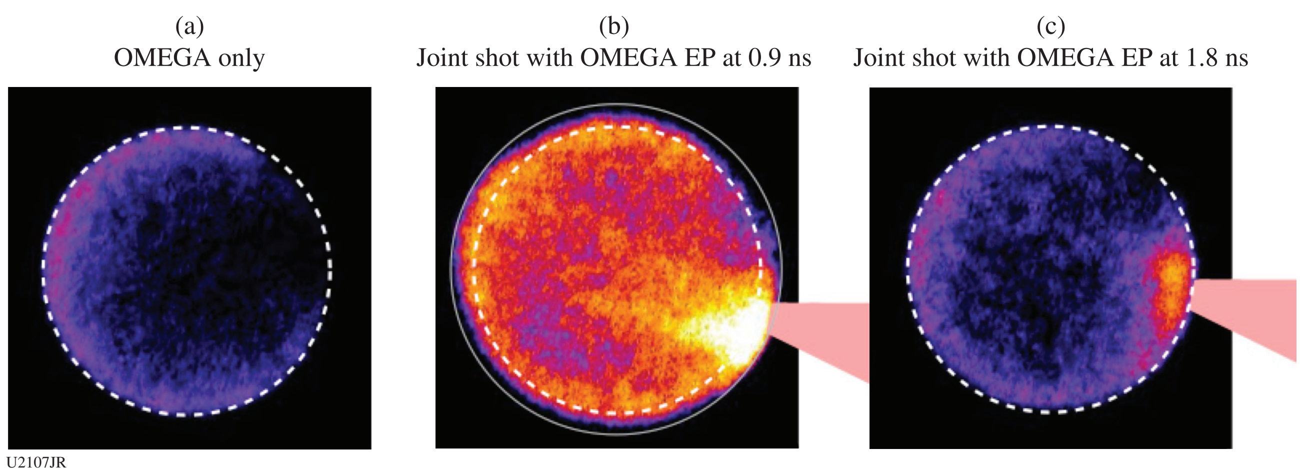

Figure 148.61
(a) SCI–measured Cu K_α images from an OMEGA-only shot; (b) a joint OMEGA and OMEGA EP shot with the OMEGA EP beam (represented by the red triangle with focal position in the corona plasma at $n_c/10$) at 0.9 ns; and (c) a joint shot with the OMEGA EP beam at 1.8 ns, respectively. The white dashed circle in each image has a radius of ~150 μm, corresponding to the radial location of the compressed Cu foam at 1.8 ns (the end of the OMEGA driver pulse). The solid circle in (b) has a radius of ~190 μm, indicating the compressed Cu target size at 0.9 ns.

hot electrons produced by the OMEGA EP IR beam injected at 0.9 ns into a short-scale-length, 1-keV corona plasma is observed from an ~200-μm target radius, corresponding to the location of the compressed Cu foam shell at the earlier time. Hot electrons produced by the IR beam can be seen penetrating through the compressed, dense Cu foam shell and being transported farther into the core. This is caused by the less-than-10-mg/cm^2 areal density of the compressed Cu foam shell at that time, where ~100-keV electrons will not be effectively stopped. It is also worth noting that this Cu K_α emission can be seen from the entire target, including the opposite side with the limb brightening. This may indicate the influence of hot-electron trajectories in the target by the self-generated electromagnetic fields. This phenomenon is much less prominent with the denser compressed shell in the joint shot with the OMEGA EP beam injected at 1.8 ns. The preliminary data clearly show that hot-electron generation and energy stopping strongly depend on the target conditions, which are visualized with the use of the novel low-density, mid-Z Cu foam target. The measured Cu K_α photon yield by the calibrated zinc von Hamos (ZVH) x-ray spectrometer agrees with the signal trend.

The streaked SRS data from the full-aperture backscatter station (FABS) diagnostic also captured sidescattered light from the IR beam's interaction with the long-scale-length plasma in all joint shots. Figure 148.62 shows the temporally and spectrally resolved backscattered light for the UV Beam 25 and sidescattered light from the IR beam (80° from the IR beam axis) for the same three shot cases: (a) an OMEGA-only shot, (b) a joint shot with the OMEGA EP beam at 0.9 ns, and (c) a joint shot with the OMEGA EP beam at 1.8 ns. An additional signal of the sidescattered light caused by the OMEGA EP IR beam in the joint shots is observed to emit near its 2ω (527 nm) and also in the spectrum range of 680 nm to 770 nm. An analysis of the scattered-light data is ongoing and will also be directly compared with the planned PIC simulations of LPI and the resultant hot-electron generation and transport. Other data analyses, including the bremsstrahlung spectrum data, are also in process and will provide information on hot-electron energy spectrum, temperature, and energy-coupling efficiency in the target to be similarly compared with simulations.

High-Energy Electron Beam Acceleration from Underdense Plasmas Using OMEGA EP

Principal investigators: L. Willingale, T. Batson, A. Raymond, and K. Krushelnick (University of Michigan); P. M. Nilson, D. H. Froula, D. Haberberger, A. Davies, and W. Theobald (LLE); J. G. Williams and H. Chen (LLNL); and A. V. Arefiev (University of Texas, Austin)

For intense, picosecond-scale lasers, propagation through underdense plasmas results in forces that expel electrons from along the laser axis, resulting in the formation of channels. Electrons can then be injected from the channel walls into the laser path, which results in the direct laser acceleration (DLA) of these electrons and the occurrence of a high-energy electron beam. Experiments performed on OMEGA EP studied the formation of a laser channel in an underdense CH plasma, as well as the spatial properties and energy of an electron beam created via DLA mechanisms. The 4ω optical probe diagnostic was used to characterize the density of the plasma plume, while proton radiography was used to observe the electromagnetic fields of the channel formation.

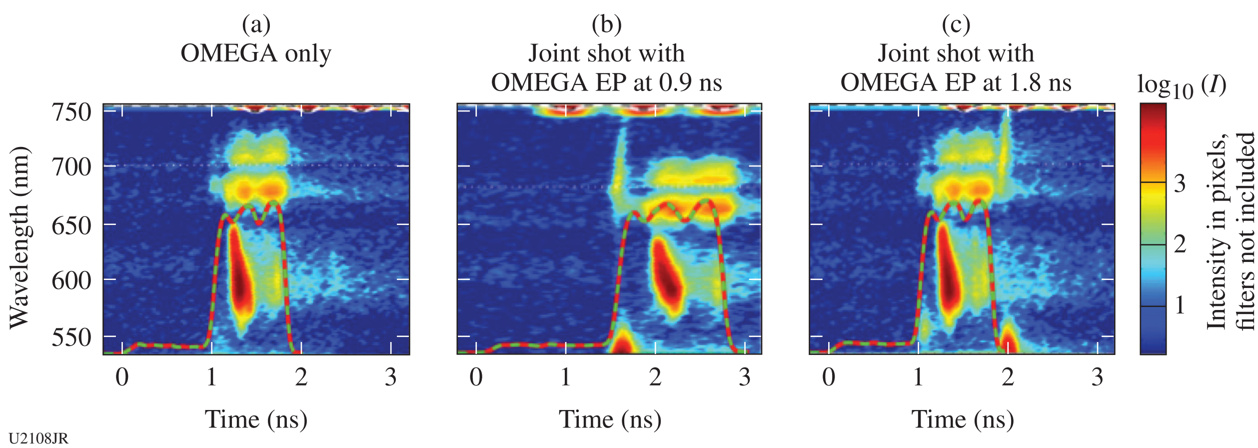

Figure 148.62
(a) Measured streaked stimulated Raman scattering (SRS) data in three typical shots: (a) OMEGA-only shot, [(b) and (c)] joint shots with the OMEGA EP beam at 0.9 ns and 1.8 ns, respectively. Sidescattered light from the OMEGA EP IR beam can be clearly seen in the joint shots.

The experiments used four of the OMEGA EP chamber's beams. A long-pulse UV beam (2.5 ns, 1200 J) ionized a CH target, creating an expanding plasma plume. After 2.5 ns, the backlighter (BL) [a short-pulse IR beam (0.7 ns, 400 J)] interacted with the plasma plume, creating a laser channel. The channel formation was imaged by two diagnostics. First, a short-pulse IR beam (sidelighter, 10 ps, 750 J) was focused on a Cu foil, creating a proton probe, which imaged electromagnetic fields onto radiochromic film (RCF). Secondly, the 4ω (263-nm) optical probe diagnostic was sent through target chamber center (TCC) to image the laser channel via shadowgraphy, the magnetic-field formation via polarimetry, and the density of the plasma channel via angular filter refractometry (AFR). The electrons propagated to a magnetic spectrometer where their energy was measured. Two target configurations have been used. In the first configuration, the CH target was ionized by the long-pulse UV beam and a plasma plume was allowed to propagate away from the target. The short-pulse main interaction beam then interacted with the plasma at a point 2 mm above the target. In the second configuration, a 1-mm-diam, 3-μm-thick CH disk was premanufactured to have a 400-μm-diam hole in the center. The pulse beam focused to a spot size of 800 μm, therefore centered on the hole. The plasma was allowed to flow toward the center of the disk, where the short-pulse main interaction beam was focused, thereby reducing diffraction of the intense laser pulse by plasma density gradients.

Protons generated via TNSA interactions with a Cu foil were deflected via the electromagnetic fields in the laser channel and imaged onto an RCF film stack located 8 cm away from the target interaction. The penetration depth of protons into the film pack was modeled with SRIM/TRIM, and time-of-flight calculations were used to map protons of a given energy to a given flight time from the Cu foil where they were born. Jitter of the order of 20 ps in the laser pulses made it impossible to achieve an exact timing relative to the short pulse; however, relative timing between each film in the proton stack was calculated. The channel was observed to have a length of 2 mm and a width of 0.49 mm (Fig. 148.63). These dimensions stayed constant over the 10 ps that they were visible on the film stack. In the normal geometry (Fig. 148.64), a region of high electric field is observed to expand from the target center at a velocity of 0.1 c. The formation of a laser channel inside an expanding plasma plume in an oblique target geometry and the resultant acceleration via DLA of high-energy electrons has been observed and appears to refract upward from the axis of the laser. Channel formation in a normal target configuration was also observed, with features specific to the presence of a high-

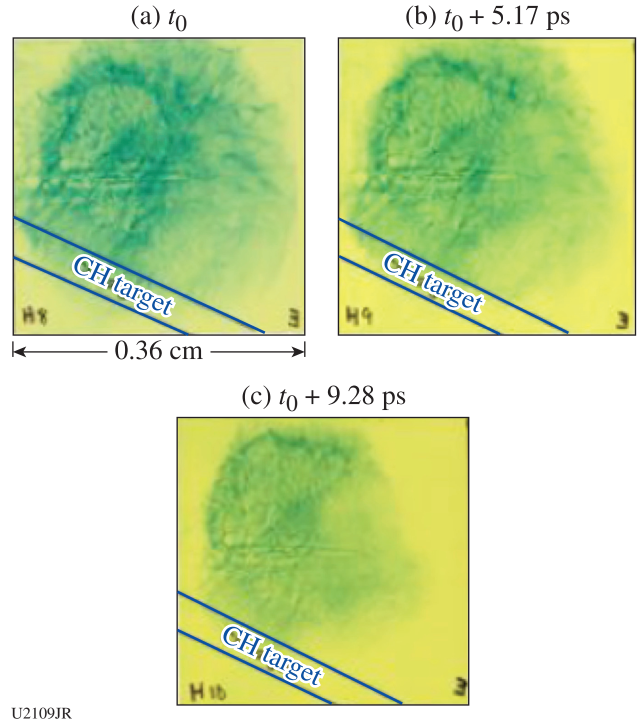

Figure 148.63
Proton images of a laser channel formed by oblique target geometry.

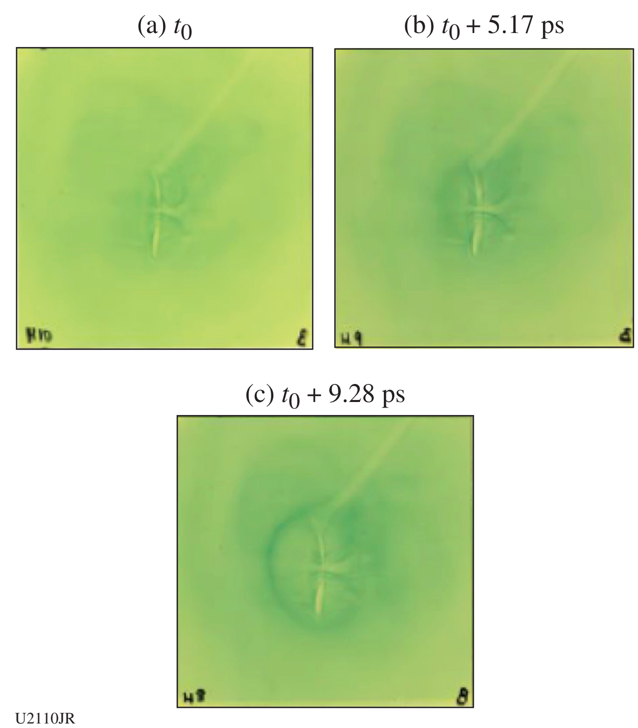

Figure 148.64
Proton images of target normal geometry

energy, short-pulse beam. Future work will focus on varying the plasma density in the channel and observing the channel in channel pointing and the energy of the accelerated electrons.

FY16 Laboratory Basic Science Studies

In FY16, LLE issued a solicitation for LBS proposals to be conducted in FY17. A total of 23 proposals were submitted. An independent committee reviewed and ranked the proposals; on the basis of these scores, 14 proposals were allocated 20 shot days at the Omega Laser Facility in FY17. Table 148.XII lists the approved FY17 LBS proposals.

Fourteen LBS projects previously approved for FY16 target shots were allotted Omega Laser Facility shot time and conducted a total of 218 target shots at the facility in FY16 (see Table 148.XIII). The FY16 LBS experiments are summarized in this section.

Ultrastrong Spherical Shocks for Nuclear and Material Science

Principal Investigators: R. Betti and W. Theobald (LLE)

This project applied the spherical strong shock (SSS) platform[21,22] to study material science at extreme pressures (several gigabars) and densities (several g/cm^3). The platform opens a new regime for HEDP and is also useful for applications to ICF since they make it possible to study ultrastrong shock generation for the shock-ignition scheme.

In UltraSSS-16A, we conducted experiments to study fundamental physics underlying the compression of a sample material in spherical geometry using the 60-beam OMEGA laser. Figure 148.65 shows a schematic of the experimental setup. The UV beams were focused on the surface of a 430-μm-diam solid CH target, which contained a small (50-μm-diam) sample material (Ti or Cu) precisely placed in the center. The targets were fabricated by GA, which also performed an extensive characterization of all the targets in the optical and x-ray regimes to demonstrate that the sample materials were placed better than 10 μm in the center of the CH sphere. A 1-ns square laser pulse with an intensity of 5×10^{15} W/cm^2 launched the spherical shock wave that converged in the sample. The pressure strongly increased because of the convergent geometry and the sample material was strongly heated and compressed, producing a short burst of x-ray emission. The x-ray emission was measured with several x-ray diagnostics including an x-ray framing camera and a streaked x-ray spectrograph. Figure 148.66 shows a measured time-resolved spectrum from a target with a Ti sample. The photon energy ranged from 4.5 keV to 8.5 keV and the time interval from 0.5 to 2.0 ns, where time zero is defined as the start of the laser pulse. The strong x-ray emission up to ~1.1 ns stems from the plasma corona outside of the CH sphere where most of the laser energy is absorbed. Once the laser was turned off, the coronal plasma quickly cooled and the x-ray emission from this region decayed. After

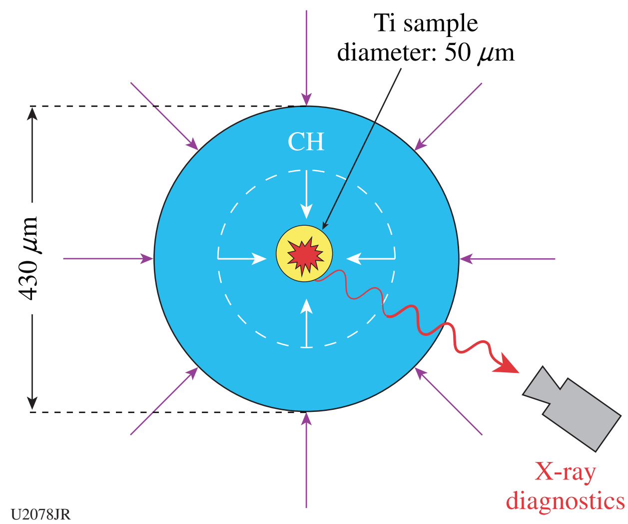

Figure 148.65
Schematic of the experimental setup of the ultrastrong spherical shock experiment. All 60 beams of the OMEGA laser were focused on the surface of a solid CH target, which contained a small sample material (Ti or Cu) precisely placed in the center. The x-ray emission from the sample material was measured and analyzed to obtain information on the achieved material condition.

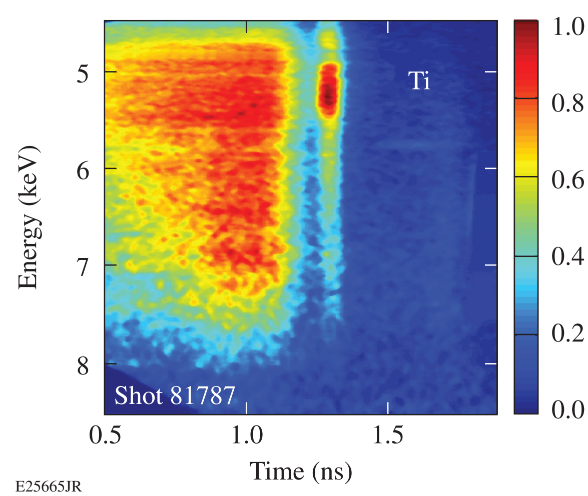

Figure 148.66
Measured time-resolved x-ray spectrum from a target with a Ti sample. The emission up to ~1.1 ns comes from the plasma corona, while the short burst at 1.3 ns is emitted from the heated and compressed Ti sample.

Table 148.XII: LBS Experiments approved for target shots at the Omega Laser Facility in FY17.

Principal Investigator	Title	Institution	Facility required	OMEGA shot days allocated	OMEGA EP shot days allocated
H. Chen	Exploring the Applications of Laser-Produced Relativistic Electron–Positron Pair-Plasma Jets	LLNL	OMEGA EP	0	1
A. R. Christopherson	Shock-Ignition Timing Measurements on OMEGA	LLE	OMEGA	1	0
J. R. Davies	Measuring the Nerst Effect and the Thermal Dynamo	LLE	OMEGA	1	0
T. Doeppner	Ionization Potential Lowering in Dense Plasma at Multi-100 Mbar	LLNL	OMEGA	1	0
D. E. Fratanduono	High-Pressure Polymorphism of Two High-Strength Ceramics: Boron Carbide (B_4C) and Silicon Carbide (SiC)	LLNL	OMEGA, OMEGA EP (not joint)	0	1
S. Jiang	Characterizing Pressure Ionization in Ramp-Compressed Materials with Electron-Induced Fluorescence	LLNL	OMEGA EP	0	1
D. Martinez	Imaging Cometary and Jet Flows on OMEGA EP	LLNL	OMEGA EP	0	1
M. Millot	Equation of State, Structure, and Optical Properties of Silicates	LLNL	OMEGA/ OMEGA EP	0	2
A. Pak	Probing the Field and Accelerated Ion Dynamics of Laser-Driven Electrostatic Shock Waves	LLNL	OMEGA EP	0	1
H.-S. Park	Study of the Dynamics of High Alfvénic Mach Number Plasma Interactions and Collisionless Shocks from Laser-Produced Plasmas	LLNL	OMEGA	2	0
H. G. Rinderknecht	Measurements of Kinetic Shock-Front Structure in Plasmas	LLNL	OMEGA	1	0
M. J. Rosenberg	Electron Energization During Magnetic Reconnection in HED Plasmas	LLE	OMEGA	1	0
M. B. Schneider	Radiative Properties of an Open L-Shell, non-LTE Plasma	LLNL	OMEGA	1	0
R. Smith	Thermal Conductivity of Fe and Fe-Si at Earth Core Conditions	LLNL	OMEGA	1.5	0
C. Wehrenberg	Probing the Extreme Deformation Mechanisms of Covalently Bonded Solids	LLNL	OMEGA	0.5	0
A. B. Zylstra	Charged-Particle Stopping Power and Scattering Measurements in Warm Dense Plasma	LANL	OMEGA	1	0

Table 148.XIII: LBS experiments approved for target shots at the Omega Laser Facility in FY16.

Principal Investigator	Title	Institution	Facility required	OMEGA shot days allocated	OMEGA EP shot days allocated	Joint shot days allocated
R. Betti	Ultrastrong Spherical Shocks for Nuclear and Materials Studies	LLE	OMEGA	1	0	–
J. H. Eggert	Development of Compressed Ultrafast Photography (CUP) Diagnostic for Dynamic Laser-Compression Experiments	LLNL	OMEGA EP	0	1	–
C. J. Forrest	Studies of (n,2n) Reactions of Light Nuclei at E_n = 14 MeV Using High-Energy-Density Laser Plasmas	LLE	OMEGA	1	0	–
P. Gourdain	High-Field–Assisted X-Ray Source	LLE	Joint	1	1	1
S. T. Ivancic	Integrated Channeling of High-Intensity Laser Beams in Implosions	LLE	Joint	1	1	1
A. E. Lazicki	Structural Studies of Electride Phases of High-Density Matter: Structures of Mg to Above 10 Mbar	LLNL	OMEGA	2	0	–
J. D. Moody	Characterization of Laser-Driven Magnetic Fields Using Proton Deflectometry	LLNL	OMEGA EP	0	2	–
P. M. Nilson	Study of Particle Energization During Magnetic Reconnection in High-Energy-Density Plasmas	LLE	OMEGA EP	0	2	–
A. Pak	Ion Acceleration from Laser-Driven Electrostatic Shock Waves	LLNL	OMEGA EP	0	1	–
H.-S. Park	Weibel Instabilities and Astrophysical Collisionless Shocks from Laser-Produced Plasmas	LLNL	OMEGA	2	0	–
Y. Ping	Pressure Ionization in Ramp-Compressed Materials	LLNL	OMEGA	1	0	–
C. Stoeckl	Spectroscopy of Neutrons Generated Through Nuclear Reactions with Light Ions in Short-Pulse Laser Experiments	LLE	OMEGA EP	0	1	–
W. Theobald	Proton Transport and Coupling into Shock-Compressed CH Targets for Proton Fast Ignition	LLE	OMEGA EP	0	1	–
C. E. Wehrenberg	Kinetics, Mechanism, and Shear Strain of the bcc-to-hcp Transition in Shock-Compressed Iron from Laue Diffraction	LLNL	OMEGA	1	0	–

a short time period of decreased x-ray emission, a short and intense burst is observed at 1.3 ns, indicative of the shock heating of the sample. The x-ray flash at 1.3 ns was emitted from the compressed and heated Ti sample.

Figure 148.67 shows the x-ray spectrum at 1.3 ns (blue) together with simulated spectra (red, yellow, and purple). Preliminary calculations were performed by our collaborators from the University of Las Palmas (Spain) with their code *ABAKO* to analyze the data. Assuming uniform conditions, a database of Ti spectra was computed within a range of mass densities of $\rho = 20$ to 200 g/cm^3 and temperatures $T = 400$ to 2400 eV for a uniformly compressed Ti sphere with radius $R = 10\ \mu$m. The assumed radius approximately matches the Ti core radius at the flash time according to a *LILAC* simulation of shot 81787. *ABAKO* calculations include a continuum-lowering effect, which has a strong impact for Ti conditions of interest, opacity effects based on escape factors to compute the atomic kinetics, and continuum broadening consistent with continuum lowering in order to calculate the emergent intensity. A simple χ^2 minimization was performed to obtain the best fit compared to the experimental spectrum (see Fig. 148.67). The comparison between measured and simulated spectra indicate that the core has been heated to a temperature of ~800 eV and compressed to a mass density of $\rho = 100$ g/cm^3. The analysis is ongoing and will include the input from radiation–hydrodynamic simulations. The *ABAKO* code will be used to post-process the *LILAC* simulation of shot 81787 and to compute the collection of emergent spectra during the flash time interval. A temperature of ~1 keV and a mass density of 100 g/cm^3 indicate that a pressure exceeding 1 Gbar has been reached inside the Ti sample.

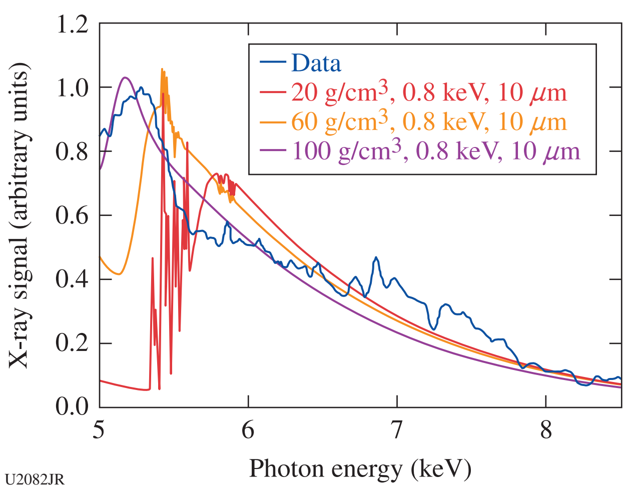

Figure 148.67
Comparison of the experimental x-ray spectrum from the Ti sample (blue) with calculations with the code *ABAKO*. A reasonable agreement was obtained for a temperature of ~800 eV and a mass density of $\rho = 100$ g/cm^3.

Development of a Compressed Ultrafast Photography Diagnostic for Time-Resolved Imaging of Dynamically Compressed Samples

Principal Investigators: J. H. Eggert and S. Ali (LLNL)
Co-investigator: D. E. Fratanduono (LLNL)

Late in FY16, one day on OMEGA EP was used to assess the feasibility of ultrafast optical imaging using coded images recorded by a Hamamatsu C7700 streak camera. The target design consisted of a plastic ablator and aluminum pusher driving a shock wave into a 2 × 2 grid of quartz samples of varying thicknesses, resulting in large-scale, spatially varying reflectivity changes as a function of time. A subset of the targets had an additional feature etched into the aluminum pusher layer to assess the resolution of the reconstructed series of images. Over the course of the day, data were collected with four different coded mask resolutions, three different streak-camera slit widths, and three different intensity levels on the camera. The full data set will enable one to assess the viability of the diagnostic and better determine the ideal experimental parameters for the diagnostic setup. Further analysis is required since the reconstruction of the images is nontrivial; however, the initial results are promising and suggest that this compressed ultrafast photography (CUP) diagnostic can provide images of the target with roughly 100-ps resolution.

Evaluation of the D(n,2n)p Reaction at 14.03 MeV with Modern* ab initio *Calculations

Principal Investigator: C. J. Forrest (LLE)

Nucleonic interactions with deuterium leading to a three-body breakup present important testing grounds for modern microscopic nuclear theory. The nuclear community has been studying these particular nucleon–nucleon (N–N) interactions over the past several decades. An accurate understanding of these processes is also of fundamental technological importance for the advancement of ICF research, tasked with demonstrating sustained thermonuclear D–T fusion in the laboratory. However, experimental data are scarce and incomplete, in particular, for energy spectra of neutrons from nD breakup occurring in thermonuclear ICF environment.

The neutron energy spectrum of the D(n,2n)p reaction has been measured (Fig. 148.68) using 14.03-MeV neutrons at a lab

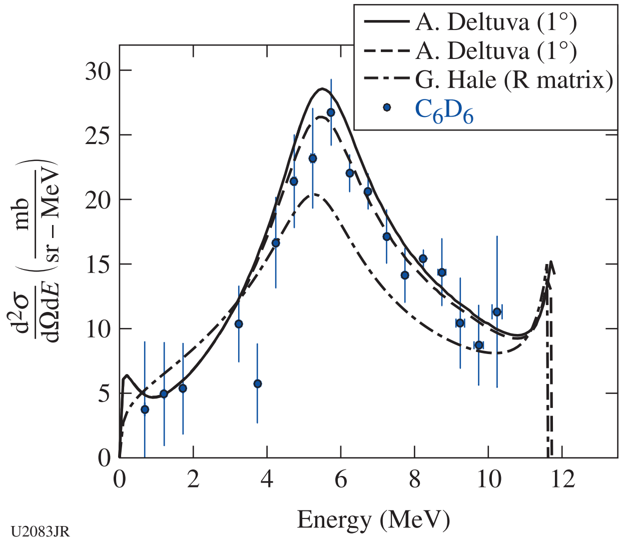

Figure 148.68
The measured cross section from a hexadeuterobenzene (C_6D_6) target (blue data points) shows good agreement with the modern *ab initio* calculation[23] outside the region at 3.75 MeV. An R-Matrix approach[24] is also compared with the inferred cross section with a larger discrepancy in the peak energy region ~5.5 MeV.

angle covering 0° to 7° using an ICF platform on OMEGA.[25] An ~100-ps-duration neutron burst from an imploding DT-filled glass-shell target was used to induce the breakup reaction in a nuclear interaction vessel that contained deuterated compounds positioned in-line with a high-resolution time-of-flight spectrometer. In these experiments, the double-differential cross section from deuterium breakup was measured in a lower-energy region (<2 MeV) and at a near-zero lab angle as compared to previous accelerator experiments. The results compare well with modern *ab initio* calculations, demonstrating that this theory can provide an accurate description of light-ion reactions.

High-Field–Assisted X-Ray Source
Principal Investigator: P.-A. Gourdain (LLE)

This experiment aimed at developing an assisted x-ray source using OMEGA as the imploder/pre-ionizer and OMEGA EP as the final ionizer. The goal of the 2016 campaign was to tune a cylindrical implosion driven by 36 beams and determine its quality, find the optimum timing to shoot OMEGA EP, and demonstrate feasibility of integration between MIFEDS coils/OMEGA/OMEGA EP to implode cylindrical geometries. All these goals were achieved successfully in one shot day.

Figure 148.69 shows that cylindrical implosions were achieved by using only 36 beams. The optimal timing was determined accurately. While we were able to record the Ar K-shell spectrum when OMEGA EP was turned off (shown in Fig. 148.70), spectra recorded with OMEGA EP turned on have a very poor signal-to-noise ratio. X rays from an unknown source, possibly e-beam bremsstrahlung, are believed to be responsible.

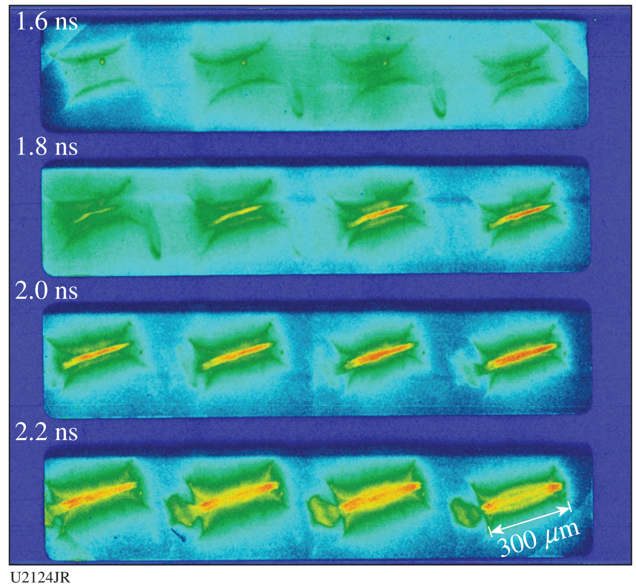

Figure 148.69
Framing-camera images showing the excellent cylindrical implosions. The last set of four frames shows a plasma plume created by OMEGA EP.

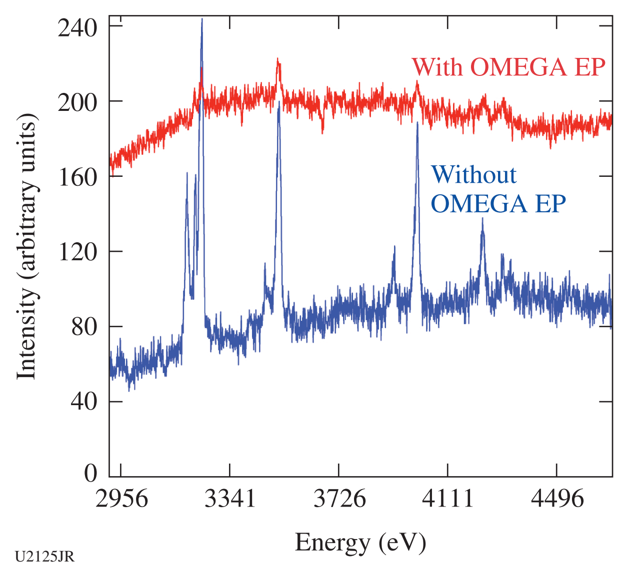

Figure 148.70
X-ray spectrum recorded by the end-on spectrometer in the Ar K-shell range with and without OMEGA EP.

Integrated Channeling of High-Intensity Laser Beams in Implosions
Principal Investigator: S. T. Ivancic (LLE)

This campaign studied the efficacy of heating a compressed OMEGA implosion with a co-propagated OMEGA EP channeling and heating beam. Sixty OMEGA beams imploded a CD capsule to a high areal density. The channeling and heating beams were timed to arrive at peak compression of the capsule. A new pulse shape that minimizes the coasting phase by using a triple-picket pulse and faster implosion velocity was implemented. The neutron yield from heated cores showed minimal additional neutrons generated from the addition of the heating pulse. Figure 148.71 displays a schematic of the experimental setup of the joint OMEGA/OMEGA EP experiment. A plastic shell is imploded by the 60 UV beams to create a high-density plasma with an extended corona. A 100-ps ("channeling") IR pulse is injected into the plasma, forming a channel followed by a high-intensity, 10-ps ("heating") pulse generating fast electrons at the channel wall. The shell consists of a 17-μm outer CH layer and a 23-μm inner deuterated plastic layer that is doped with 1% atomic density of Cu. The Cu doping provides K_{α} fluorescence x-ray emission at 8.048 keV when excited by fast electrons, which is imaged by an SCI. This technique visualizes the fast-electron energy deposition in the compressed shell. The 17-μm-thick CH ablator reduces the excitation of K_{α} fluorescence from direct interaction of the driver beams and eliminates the neutron background from the hot corona. Our experiments showed, however, that even with the undoped CH ablator, there is still some K_{α} radiation generated by the implosion. Other diagnostics include two electron spectrometers, an x-ray spectrometer, and neutron time-of-flight detectors to measure the thermonuclear fusion neutron yield from D–D reactions. The temporal evolution of the areal density was calculated with a 1-D simulation using the radiation–hydrodynamics code *LILAC* including cross-beam energy transfer (CBET) and nonlocal electron transport. Peak compression is predicted at 4.3 ns, where time zero is defined by the start of the drive pulse. The short pulses were injected at five times to bracket the peak compression. The electron spectrometers captured a very interesting trend in the spectrum of the escaped fast electrons for the different injection times. For an early injection of both pulses, copious amounts of MeV electrons were generated with a clear trend of decreasing fast-electron production for later injection times.

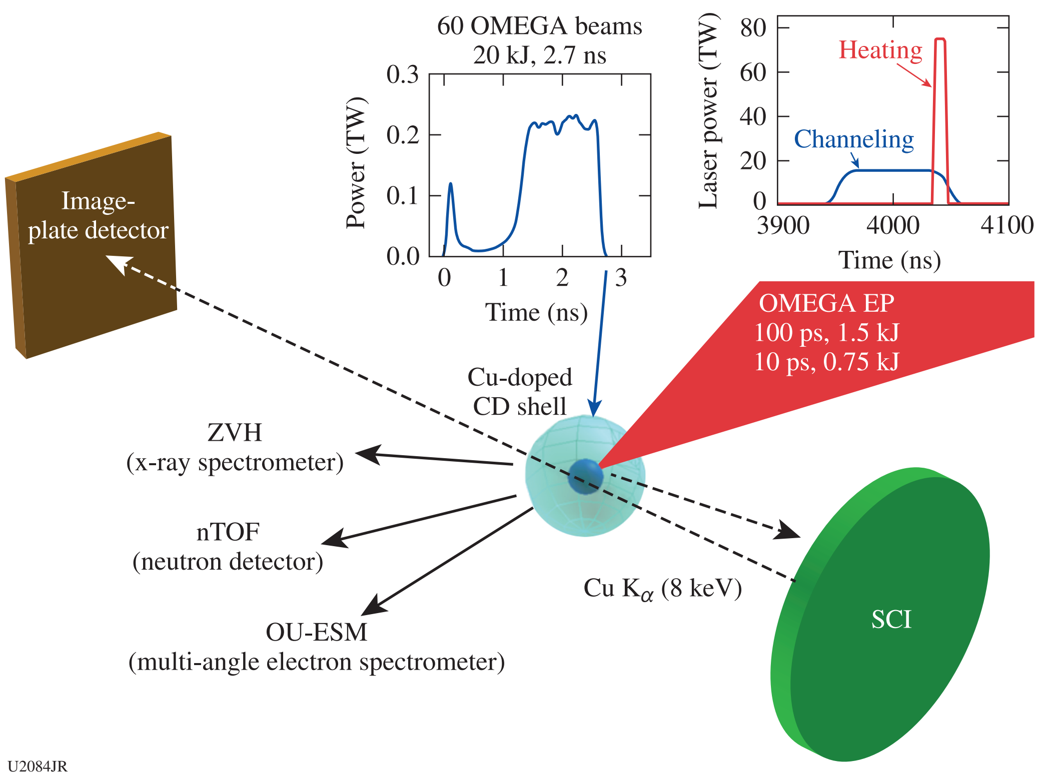

Figure 148.71
Schematic of experimental setup. nTOF: neutron time of flight.

The results of the integrated experiment showed indications of electron stopping in the core as it approached peak areal density. Figure 148.72 shows the trend observed in the Osaka University electron spectrometer data for the central (on-axis) channel as a function of injected electron time. As the target approaches peak areal density (4.5 ns), there is a dip in the escaped electrons between 1 and 3 MeV. This trend was observed only in the on-axis channel and not in the ±5° or 10° channels that do not pass through the dense core of the compressed target. These data suggest that the dense core of plasma is stopping some of the electron beam. The total electron yield for later short-pulse injection times is lower as well, indicating poorer coupling of energy from the high-intensity pulse into fast electrons. However, because of the high background levels in the Cu K_α images, the contribution from the IR-produced electrons was not directly observed in this campaign. A future experiment with a thicker ablator may protect the Cu fluor layer from direct irradiation by the drive beams with the extended pulse.

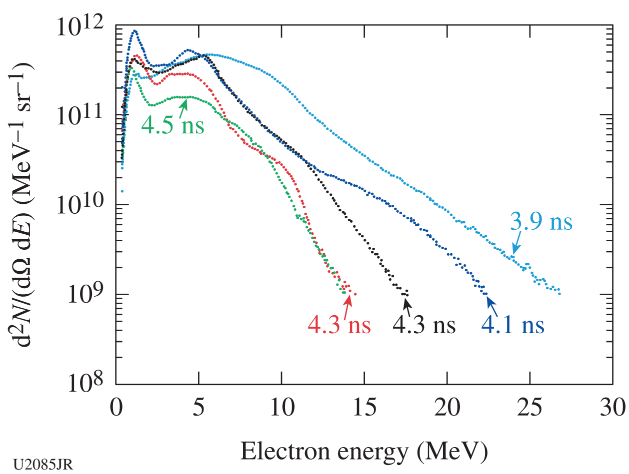

Figure 148.72
Transmitted electron spectrum through the compressed shell as a function of OMEGA EP injection time.

Structural Studies of Electride Phases of High-Density Matter: Structures of Mg to above 10 Mbar
Principal Investigator: A. E. Lazicki (LLNL)
Co-investigators: F. Coppari, R. Smith, R. Kraus, J. R. Rygg, D. E. Fratanduono, J. H. Eggert, and G. W. Collins (LLNL); M. McMahon, M. Gorman, and A. Coleman (University of Edinburgh); D. McGonegle and J. Wark (Oxford); and L. Peacock and S. Rothman (AWE)

This campaign sought theoretically predicted high-pressure phases of Mg, which have the interesting feature of density-driven electron localization in interstitial regions in the crystal lattice, occurring as a direct consequence of strong quantum mechanical constraints on the electronic wave functions of core and valence electrons at high compression. Three of these "electride" phases are predicted between 4 and 12 Mbar for magnesium.[26–28]

The experiment compressed solid Mg to the 10-Mbar pressure regime using ramped laser pulses and probed crystal structure using the PXRDIP diagnostic via transmission diffraction of He_α x rays from a metal foil backlighter (Fig. 148.73). Pressure in the sample was probed by measuring the target's free-surface velocity using VISAR and correlating it with a pressure state. Four half-days on OMEGA were used to optimize the target design, pulse shapes, and diagnostic filtering and timing and then to collect data between 2 and 15 Mbar. In spite of the very weak x-ray scattering strength of low-Z Mg, diffraction peaks were registered at up to 6 to 7 Mbar, above which pulse-length limitations hampered the ramp compression of the Mg, despite a high background resulting from ablation plasma x rays. Above 4 Mbar, the data indicate a new phase, albeit inconsistent with the theoretical predictions. These results are being used to design further measurements for the NIF.

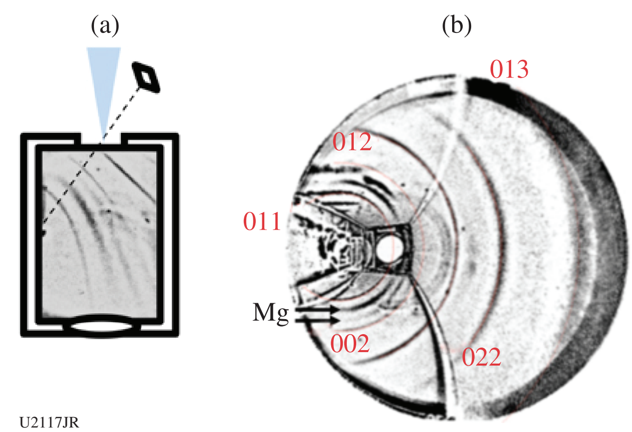

Figure 148.73
(a) Cross section of the PXRDIP diagnostic showing the laser drive in blue and the x-ray source incident ~45° into the image-plate chamber, where diffraction peaks are registered. (b) Image plates digitally warped into a stereographic projection to show the x-ray diffraction peaks from Mg near 400 GPa (indicated with arrows) and from an ambient Ta calibrant (marked with red lines).

Hohlraum Magnetization Using Laser-Driven Currents
Principal Investigators: J. D. Moody and B. Pollock (LLNL)
Co-investigators: J. S. Ross, D. Turnbull, C. Goyon, A. Hazi, G. Swadling, and W. Farmer (LLNL)

In FY16 the two-day LDMag Campaign on OMEGA EP continued a basic science investigation of the feasibility of using laser-generated currents to self-magnetize targets, such as future ICF hohlraums. These experiments substantially improved the proton deflectometry capability of previous campaigns to probe the fringing magnetic-field structure around the outside of the half-loop target shown in Fig. 148.74. On the open side of the loop are parallel plates, into one of which holes were placed so that the OMEGA EP long-pulse beams could shine through to produce a plasma at the surface of the second plate. Hot electrons from this plasma collect around the holes in the first plate, driving a current through the half-loop that connects the plates, and producing a magnetic field on the loop axis and in the surrounding volume.

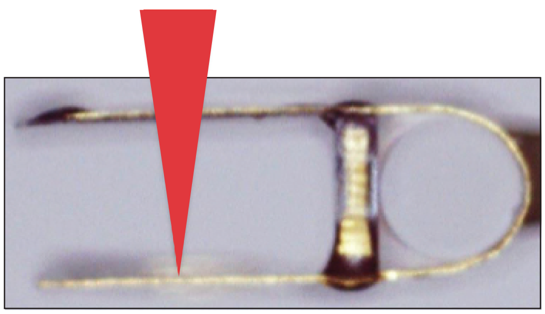
U2119JR

Figure 148.74
End-on view of geometry for hohlraum self-magnetization on OMEGA EP, with beam path shown schematically in red.

To probe these fields, protons are produced through the TNSA mechanism from the interaction of the two orthogonal OMEGA EP short-pulse beams with two separate, thin Au foil targets as shown in Fig. 148.75. Cu meshes impose fiducials in the proton images recorded on radiochromic film, providing detailed measurements of the field profile millimeters from the target. The loop structure was probed both along and across its axis by protons produced using the orthogonal short-pulse beams. Fields up to 200 T were inferred at the end of the 0.75- to 1-ns, 1-TW B-field drive laser pulses. The analysis of this recent experiment is ongoing and will inform the FY17 continuation of this effort.

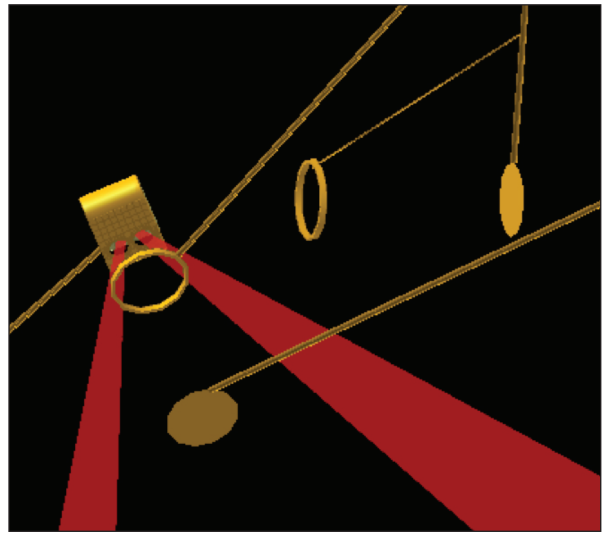
U2120JR

Figure 148.75
Geometry for proton deflectometry on OMEGA EP, with proton detectors (not shown) placed 8 cm behind and to the left of the B-field target.

Laser-Driven Electrostatic Shock-Wave Acceleration
Principal Investigator: A. Pak (LLNL)
Co-investigators: D. Haberberger (LLE) and T. Link (LLNL)

This shot day on OMEGA EP sought to create and image a relativistic collisionless electrostatic shock wave using a high-power, short-pulse laser. The astrophysical community is interested in understanding the plasma conditions under which these collisionless shocks form, the structure of their associated electric fields, and the resulting particle acceleration. It is also desirable to assess the viability of this new ion acceleration mechanism to produce an ion beam with the following properties: ~100 MeV per atomic mass unit, narrow energy spread $\Delta E/E$ ~10%, and high beam density ~10^{10} particles per bunch.

A summary of the experimental and diagnostic setup is shown in Figs. 148.76(a) and 148.76(b). An x-ray drive is first produced (or not) using a 1-ns laser pulse to irradiate a 25-μm-thick gold foil. The x-ray drive ablates and expands an initially 1.4-μm-thick CH target. After waiting ~500 ps for the peak plasma electron density to fall to ~5×10^{21} cm^{-3}, the backlighter beam drives the electrostatic shock wave to accelerate particles. The sidelighter beam then irradiates a second orthogonal proton source to probe the CH plasma. Figures 148.76(c)–148.76(e) and 148.76(f)–148.76(h) compare the accelerated proton beam profile, spectrum, and side-on proton radiography from, respec-

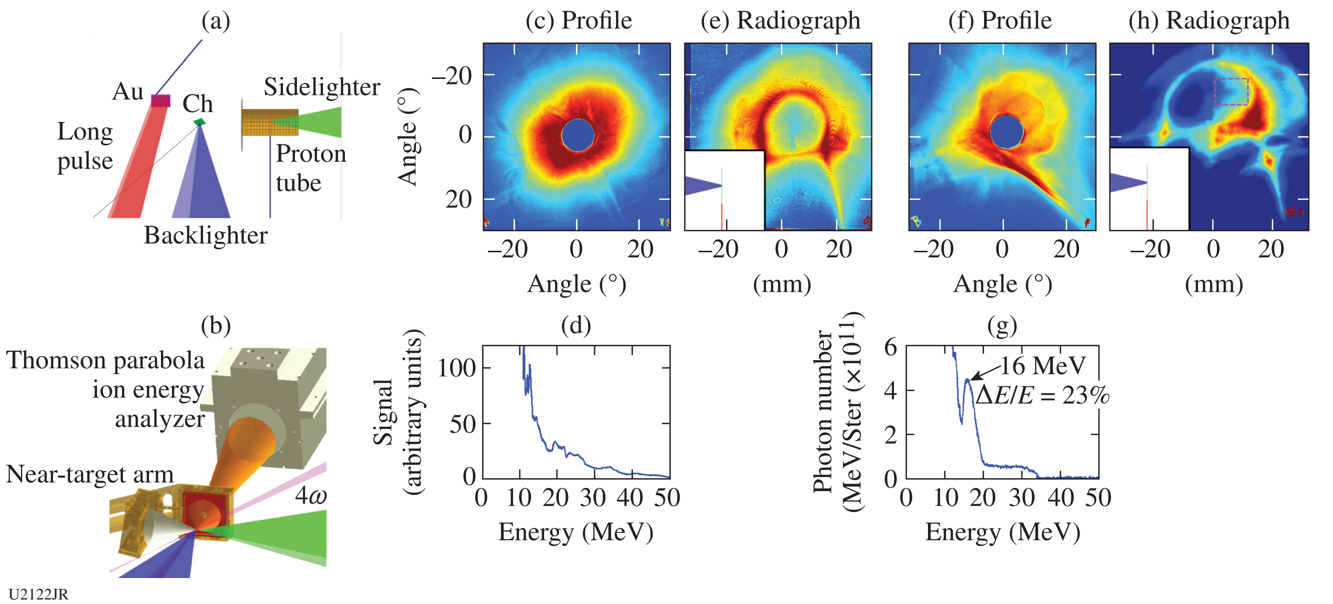

Figure 148.76
(a) Experimental configuration and (b) diagnostic suite. A long-pulse beam creates x rays to ablate an initially 1.4-μm-thick CH foil to tailor the plasma density profile. The short-pulse "backlighter" beam then drives the target, producing a proton beam via target-normal sheath acceleration (TNSA). Orthogonal to this, the "sidelighter" beam creates a second proton beam as a radiographic probe. [(c),(d)] TNSA proton beam profile and spectrum from direct drive of the CH foil, without x-ray preheat. The hole in the profile measurement transmits part of the beam to the Thomson parabola diagnostic. (e) Side-on proton radiograph of the TNSA field. [(f),(g)] TNSA beam profile and spectrum from an experiment with an x-ray tailored plasma density profile. (h) The resulting proton radiograph; the inset shows backlighter laser incident from the left, while the x-ray preheat comes from the right.

tively, an unperturbed foil and an expanded target. When the plasma density profile is first tailored with the x-ray drive, the proton spectrum exhibits a narrowband feature at ~16 MeV [Fig. 148.76(g)], and the side-on radiography shows a localized deficit in the probe beam. Both features are consistent with the generation of an electrostatic shock wave and are absent on the control experiment where an unperturbed target was used. Future work will focus on correlating the accelerated spectrum to the velocity of the electrostatic shock wave as inferred from the proton radiography data.

Astrophysical Collisionless Shock Experiments with Lasers (ACSEL)

Principal Investigators: H.-S. Park, C. M. Huntington, and G. F. Swadling (LLNL)

The ACSEL-16A and -16B experiments continued to investigate the formation of astrophysically relevant collisionless shocks in a diagnosable laboratory environment. These shots were carried out in support of the ongoing ACSEL effort at LLNL and with support of the broad, cross-institutional ACSEL collaboration. A total of 13 target shots were completed during ACSEL-16A and -14 during ACSEL-16B. The experiments primarily investigated interactions between beryllium targets, which were selected to provide a low-Z, single-species blowoff plasma in order to simplify Thomson-scattering analysis. Experiments also investigated end-on proton probing using thin foil targets and a new dish-shaped plastic target.

The experiments used OMEGA to heat the surfaces of a pair of opposing targets, launching counter-propagating plumes of high-velocity (~10^6-ms^{-1}), high-temperature (~keV) plasma. The parameters of the outflows are such that they are largely collisionless but with parameters amenable to the growth of instabilities, which can mediate the formation of a collisionless shock.

The interaction of the flows is diagnosed using a combination of (a) temporally resolved, single-point optical Thomson scattering and (b) proton radiography imaging. A D^3He exploding-pusher capsule provides a dichromatic (3.3- and 14.4-MeV) proton source for radiography, making it possible to probe at two separate times during each experiment. Images are recorded on CR39 nuclear track detectors whose processing and analysis are carried out by collaborators at MIT. Previous proton imaging data have detected the presence of complex magnetic-field structures. The field structures are observed to grow in strength as the experiment progresses; the observed filamentary structures are interpreted as being the result of the growth of the Weibel instability in the region where the flows collide and interpenetrate.

The primary goal of ACSEL-16A and -16B was to collect improved optical Thomson-scattering data by using the beryllium targets to provide single-species plasmas; this significantly simplifies the interpretation of the detailed structure of the scattered spectra. The Thomson-scattering diagnostic records features of both ion-acoustic waves and electron plasma waves; data from this diagnostic have been previously used to diagnose the interpenetration of the flows and to measure heating associated with the development of the two-stream instability. Figure 148.77 shows sample Thomson-scattering data from this campaign. High-quality data of the flow interactions at target separations of 4 and 5 mm were captured. Analysis of these data will reveal trends in the evolution of the plasma parameters of the interacting flows.

New experiments carried out in ACSEL-16B investigated a new target configuration. These targets were modified to a "dish" shape, allowing a significantly larger number of beams to impinge on the target within the facility's incident-angle constraints. This modification to the target geometry increased the density of the outflows by a factor of 10, as measured via Thomson scattering. This density scaling has the potential to allow one greater control in the pursuit of the formation of a mature collisionless shock.

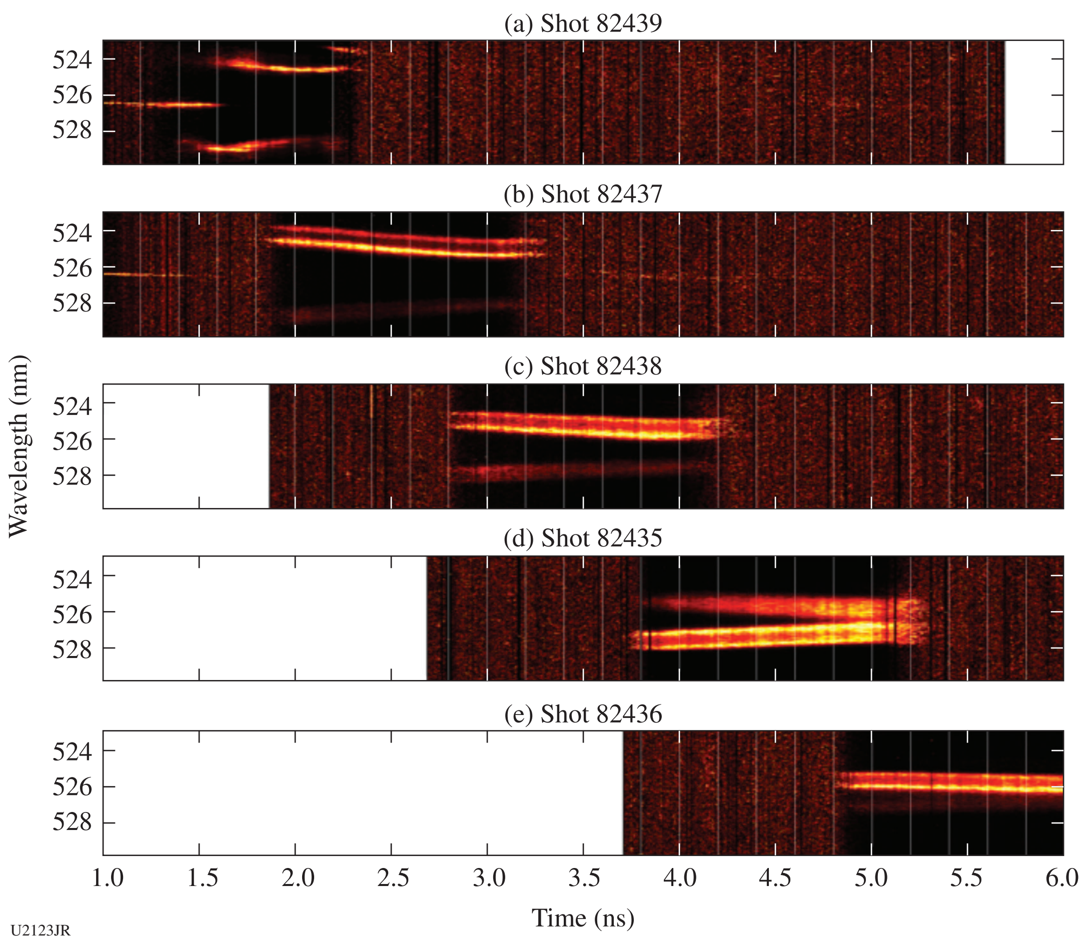

Figure 148.77
Thomson-scattering ion-acoustic wave time series, showing interpenetration of a pair of beryllium plasma flows.

Pressure Ionization in Ramp-Compressed Materials
Principal Investigators: Y. Ping and S. Jiang (LLNL)
Co-investigators: R. Shepherd and R. Heeter (LLNL)

The Pressure Ionization Campaign comprised two half-days on OMEGA during FY16. This campaign used ramp compression to compress an iron foil up to twice its original density, while keeping the temperature below 1 eV. The driver consisted of five laser pulses stacked in time. Separately, a spherical implosion provided a broadband x-ray backlighter. Both the absorption and fluorescence spectra were measured to study the energy shift of the Fe inner shells caused by pressure ionization. Figure 148.78(a) shows the measured absorption spectrum. At the top is a raw image from a 2× compression shot. X-ray filters of Fe, Mn, and Cr at the entrance slit of the spectrometer provided K-edge wavelength fiducials. The Fe K edge was measured for four different cases: undriven Fe, Fe with 2× and 1.5× compression, and liquid Fe. No obvious shift of the Fe K edge was observed in any of these cases. Figure 148.78(b) shows the fluorescence spectra measured using MSPEC (multipurpose spectrometer), in which K_α fluorescence was observed for the first time in ramp-compressed iron, despite noise and high background levels. The two top images in Fig. 148.78(b) show raw spectra processed by a despeckling technique. The two lines from right to left correspond to Fe K_α and Cu K_α (from an undriven Cu washer used to mount the iron sample). The Cu K_α line provides a reference to compare different shots. The plot of Fig. 148.78(b) compares the K_α peaks from liquid Fe (blue) and from solid Fe with 2× compression (red). There appears to be a slight shift in the K_α energy. Future experiments will improve the signal-to-noise ratio, use a higher-resolution spectrometer to confirm the energy change, and seek to measure the weaker K_β signal, which is more prone to a shift because of pressure ionization.

Spectroscopy of Neutrons Generated Through Nuclear Reactions with Light Ions in Short-Pulse Laser-Interaction Experiments
Principal Investigators: C. Stoeckl, U. Schroeder, T. C. Sangster, and C. J. Forrest (LLE)

The experimental objective of this project is to study nuclear reactions in light ions generated in short-pulse laser-interaction experiments. Planar deuterated plastic (CD) targets were irradiated with one short-pulse (10-ps) beam focused at the target's front surface. A second low-energy (100-J), long-pulse (100-ps)

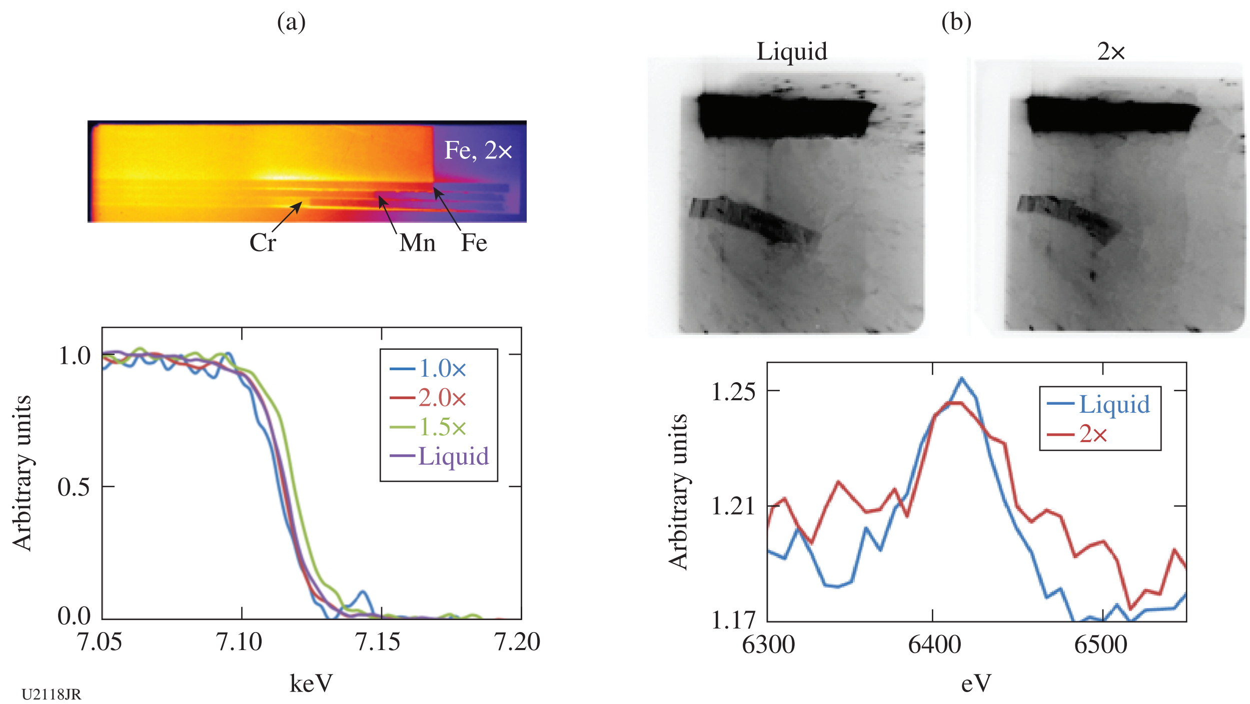

Figure 148.78
(a) A raw image of the measured absorption spectrum for 2× compressed Fe and measured Fe K edge under four different conditions. (b) Top: Measured MSPEC spectra, despeckled to reduce noise. Bottom: Lineouts of the Fe K_α feature for liquid and 2× compressed Fe.

UV beam was fired 0.5 ns ahead of the short-pulse beam to suppress proton acceleration on the front surface of the target. Charged particles, protons, and deuterons from the rear of the target create neutrons and charged particles through nuclear reactions in a second converter target placed closely behind the primary interaction target. The spectrum of the neutrons generated in the converter target is measured using a three-channel scintillator photomultiplier–based neutron time-of-flight detector system. Charged-particle detectors are used to measure the spectra of the primary particles.

The previous experiments in FY15 with CD primary and layered secondary targets with up to ten alternating layers of 25-μm-thick CD and 25-μm-thick Be foils showed clear evidence of both D–D fusion neutrons and neutrons from the $Be^9(d,n)B^{10}$ nuclear reaction. No secondary D–T fusion neutrons are observed from any tritium that would be generated in $Be^9(d,t)$ Be^8 neutron pickup reactions, which indicates that the cross section of this reaction is smaller than the calculated values.

The experiments with the layered CD/Be targets were continued in FY16, where one shot day was available. Three shots were taken with secondary targets at different laser intensities to measure the neutron spectrum and three shots without a secondary target to record the incident fast-ion spectrum. Again no neutrons from D–T fusion reactions were observed.

To be able to run realistic simulations of the OMEGA EP experiments, fusion cross sections based on the Bosch and Hale parametrization were added to the Monte Carlo particle transport framework Geant4. Geant4 already includes primary and secondary particle tracking and physics modules to describe the slowing down of the ion flow in the secondary target and neutron scattering in the target and detector.

First tests show that the Geant4 simulations correctly reproduce the relativistic kinematic of the D–D in-flight fusion reaction and the mean free path of the deuterons with respect to fusion reactions, if the simulations used enough particles that the statistical error becomes insignificant.

Figure 148.79 shows the calculated total neutron energy spectrum from a first preliminary simulation using a 4-MeV deuteron beam on a 1-g/cm^3 pure-deuterium target. A pure-deuterium target was chosen to improve the statistics.

Neutrons from both the primary D–D fusion (2 to 6 MeV) and the secondary D–T reaction (11 to 19 MeV) from the tritium produced in the d(d,t)p branch of the D–D reaction are visible. Out of the 8×10^9 incident primary particles, ~0.1% produce a primary fusion neutron and ~0.1% of the tritons produced in the primary reactions generate a secondary neutron. Because of the complex interaction between the energy loss of the fast ions (deuterons, tritons) in the target material and the energy dependence of the fusion cross section, these conversion efficiencies are difficult to predict accurately without these detailed simulations. Given that the dynamic range of our current detectors is ~100, these simulations indicate that it might not be feasible to detect those secondary neutrons with the present detector system on OMEGA EP.

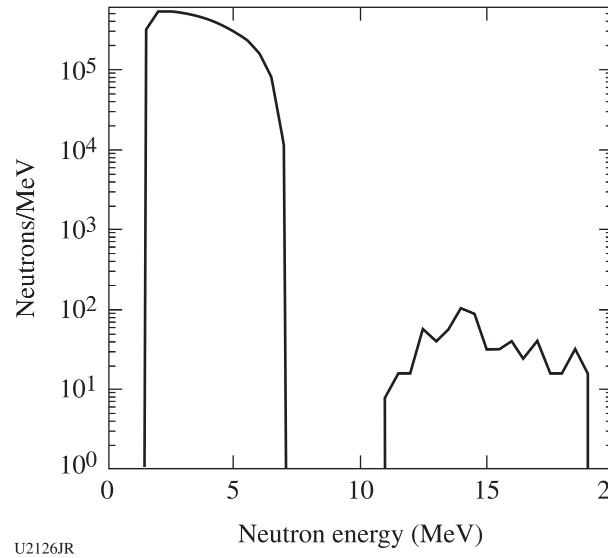

Figure 148.79
Neutron energy spectrum from a deuterium secondary target irradiated by a 4-MeV deuteron beam calculated by Geant4.

Proton Transport and Coupling into Shock-Compressed CH Targets for Proton Fast Ignition
Principal Investigator: W. Theobald (LLE)

A focused, laser-driven proton beam is an effective means for rapidly heating material and it remains a promising fast ignitor. However, there are unexplored topics that must be incorporated into an integrated proton fast-ignition scheme such as conversion efficiency to protons in a fully assembled target and transport of the high-current-density proton beam in shock-compressed fuel. In pTransEP-16A, we conducted experiments to study fundamental physics' underlying high-current proton beam production, transport, stopping, and energy coupling in reduced-scale, fast-ignition–relevant conditions using OMEGA EP. The two short-pulse beams were alternated with

700-J energy and 10-ps pulse duration to irradiate compound targets consisting of a curved source foil, a conducting cone to focus the beam, low-density resorcinol formaldehyde (RF) plastic foam (340 mg/cm^3) transport blocks, and 10-μm-thick Cu diagnostic layers on the top and rear sides. Integrated shots were also taken in which two long-pulse lasers were used to drive a quasi-planar shock to compress the RF in the probe beam path.

We shot targets of increasing complexity from a freestanding curved foil to the full compound integrated target. The proton spectrum was measured for each of the types using a stack of radiochromic film and a Thomson parabola ion energy analyzer. Figure 148.80 shows how the maximum proton energy decreased as target components were added. The maximum energy (shown here) and proton number (not shown) decreased as soon as material was added to the curved target. This is in line with our understanding from previous experimental and computational work that added target material is a sink for the energetic electrons that support accelerating fields on the target; however, the magnitude of the change is surprising. In fact, this reduction in energy gain is more significant than the stopping in the 0.34-g/cm^2 areal density of RF.

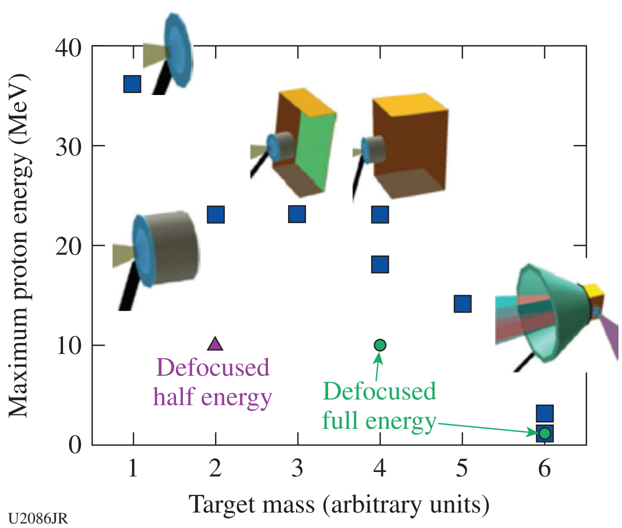

Figure 148.80
Maximum proton energy measured in the forward direction for the six target types investigated. The energy was highest for the freestanding target and lowest for the fully integrated target with a shock-compressed transport medium.

The coupling to the rear side of the target was also studied by observing Cu x-ray line emissions with a spectrometer (ZVH) and a monochromatic x-ray imager using an SCI. Example images from the latter (see Fig. 148.81) show the signature of a moderately well collimated beam (cone angle <20°) in the laser's forward direction.

The localized emission will be compared to the results of future transport simulations. The simulations will also be compared to the proton spectral measurements with and without the RF blocks.

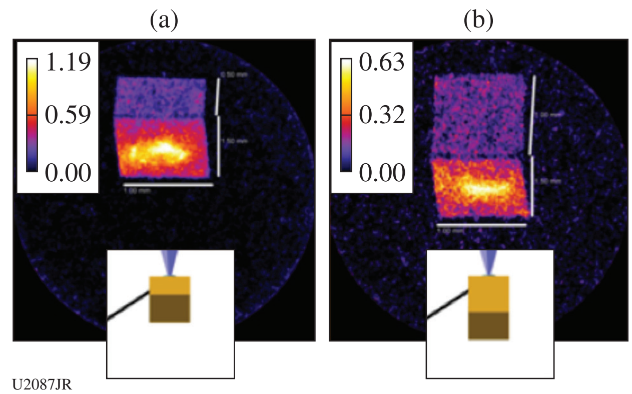

Figure 148.81
SCI images of 8.048-keV Cu K_α x-ray emission from Cu foils on the top and rear side of a plastic block. The block length was (a) 500 μm or (b) 1 mm. The insets show the target as viewed from the diagnostic. The signal consists of a relatively uniform background caused by refluxing energetic electrons and a forward-directed beam of protons.

Shear Stress and Mechanism of Phase Transition in Shock-Compressed Iron

Principal Investigator: C. E. Wehrenberg (LLNL)

The IronLaue-16 Campaign was the first campaign to use Laue diffraction to study the response of single-crystal iron to shock compression. As shock compression drives iron through a body-centered-cubic (bcc)–hexagonal phase transition, Laue diffraction can be used to determine the orientation of the transformed phase and therefore the mechanism of transformation. Additionally, Laue can measure the shear strain in the compressed state. In these shots, 32 OMEGA beams were used to drive an implosion of an empty CH capsule, creating a burst of broadband x rays during stagnation that are used for Laue diffraction. Separately, two beams were used to drive a shock into an ablator and the single-crystal sample. Excellent diffraction data were observed in several shots for a range of shock pressures. Figure 148.82 shows an example in which multiple diffraction spots from the shock-compressed iron are visible.

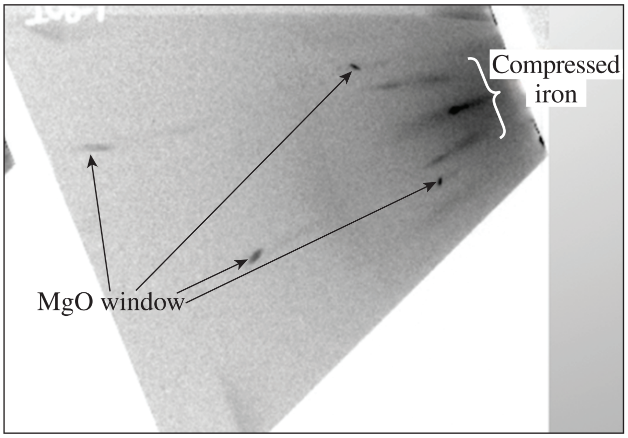

U2121JR

Figure 148.82
Example of Laue diffraction data showing multiple diffraction spots from shock-compressed iron.

FY16 LLNL Omega Facility Experiments
Principal Investigators: R. F. Heeter, S. J. Ali, P. M. Celliers, F. Coppari, J. H. Eggert, D. Erskine, A. Fernandez Panella, D. E. Fratanduono, C. M. Huntington, L. C. Jarrott, S. Jiang, R. G. Kraus, A. E. Lazicki, S. LePape, D. A. Martinez, J. M. McNaney, M. A. Millot, J. D. Moody, A. E. Pak, H.-S. Park, Y. Ping, B. B. Pollock, H. G. Rinderknecht, J. S. Ross, R. F. Smith, G. F. Swadling, C. E. Wehrenberg, G. W. Collins, O. L. Landen, A. Wan, and W. Hsing (LLNL); J. Benstead and M. Rubery (AWE); R. Hua (UCSD); and H. Sio (MIT)

In FY16, LLNL's High-Energy-Density (HED) Physics and Indirect-Drive Inertial Confinement Fusion (ICF-ID) Programs conducted several campaigns on the OMEGA and OMEGA EP Laser Systems, as well as campaigns that used the OMEGA and OMEGA EP beams jointly. Overall, these LLNL programs led 430 target shots in FY16, with 304 shots using only the OMEGA Laser System and 126 shots using only the OMEGA EP laser. Approximately 21% of the total number of shots (77 OMEGA shots and 14 OMEGA EP shots) supported the ICF-ID Campaign. The remaining 79% (227 OMEGA shots and 112 OMEGA EP shots) were dedicated to experiments for the HED Physics Campaign. Highlights of the various HED and ICF campaigns are summarized in the following reports.

In addition to these experiments, LLNL Principal Investigators (PI's) led a variety of Laboratory Basic Science Campaigns using OMEGA and OMEGA EP, including 81 target shots using only OMEGA and 42 shots using only OMEGA EP. The highlights of these are also summarized, following the ICF and HED campaigns.

Overall, LLNL PI's led a total of 553 shots at LLE in FY16. In addition, LLNL PI's also supported 57 NLUF shots on OMEGA and 31 NLUF shots on OMEGA EP, in collaboration with the academic community.

Indirect-Drive Inertial Confinement Fusion Experiments

Hydrodynamic Response from Oxygen Nonuniformities in Glow-Discharge Polymer Plastic
Principal Investigators: P. M. Celliers and S. J. Ali

Simulations and target characterization indicated that inhomogeneity in oxygen content could be a significant seed for Rayleigh–Taylor growth in NIF implosions using glow-discharge polymer (GDP) plastic shells. This has been indirectly supported by the observation of larger-than-expected in-flight modulations during NIF GDP capsule implosions along with the realization that such inhomogeneities can result from photo-induced oxygen uptake. To investigate the magnitude of the effect of these oxygen heterogeneities on the hydrodynamic response of GDP ablators, oxygen modulations were photo-induced in GDP foils by illuminating the foils with blue light through a periodic mask pattern. The foils were then fielded on OMEGA as ablators driven by a halfraum to replicate foot conditions on the NIF. The resulting optically reflective shock wave was observed using the OMEGA high-resolution velocimeter (OHRV), a 2-D single-gate measurement. Two-dimensional velocity maps were obtained for both oxygen-modulated and unmodulated samples, with the modulated samples showing clear evidence of the propagation of a rippled shock wave as a result of the photo-induced oxygen heterogeneity. A time series spanning approximately 2.3 to 4.2 ns after shock breakout from the GDP ablator into a poly (methyl methacrylate) (PMMA) witness layer was obtained and clearly showed that the decay in the amplitude of the perturbation was dependent on the perturbation wavelength, as expected.

Principal Hugoniot Measurements of Liquid Deuterium Above 100 GPa
Principal Investigator: A. Fernandez Panella

These two half-day campaigns using cryogenic targets on OMEGA investigated the principal Hugoniot of liquid deuterium at high precision above 100 GPa. This study was motivated by a systematic discrepancy between previous experimental data on different platforms (OMEGA, Z, and NIF keyhole data) and current equation-of-state (EOS) models above 100 GPa, with the data suggesting higher compression than models, including the current preferred EOS used in ICF simulations.[29] Experimental uncertainties of the existing data are too large, however, to rule out the models unambiguously. Examining this discrepancy is relevant as the first shock in an ICF implosion lies on the principal Hugoniot of the fuel. Recent diagnostic improvements along with the availability of the recent high-accuracy calibration of the quartz EOS standard[30] result in new experiments collecting data with much higher accuracy.

The first campaign carried out three measurements of shock-compressed deuterium along the principal Hugoniot at pressures ranging from 350 to 550 GPa, the highest pressures to date. The ablator material was 90-μm-thick beryllium and the targets were driven by a 2-ns flat, square laser pulse. VISAR was used as the main diagnostic to measure shock velocities. In the alpha-quartz reference material, shock velocities of 34 to 40 km/s were measured, and velocities of 50 to 64 km/s were obtained in the deuterium (Fig. 148.83). A summary of the data is shown in Fig. 148.84. Note the improvement of the data quality with respect to previous campaigns (e.g., D. Hicks 2009); the uncertainties in the shock velocities in the present campaign are a factor of 3 smaller.

The impedance-matching analysis relies on an accurate knowledge of the EOS of the standard material (alpha quartz) to determine the particle velocity, pressure, and density of the sample (shock-compressed deuterium). Because the new data extend beyond the valid range of the quartz calibration, two tabular quartz EOS models have been used to estimate the systematic uncertainty of the new data. The results are shown in Fig. 148.84. All the experimental data show higher compression along the Hugoniot (4.5 to 4.7) than the current EOS models predict (e.g., 4 to 4.3 with LEOS 1014 Kerley). This trend is similar to the previous data obtained at different facilities (Omega, Z, and the NIF), which also showed a similar discrepancy with current models beyond 100 GPa. Further analysis is underway to understand the systematic uncertainties and to understand the underlying reasons for such discrepancy with the models.

The second half-day in August was very successful as well. The addition of an extra quartz anvil to the target design enabled us to measure a re-shock and a second impedance data point. Four shots were taken that will complete the data set at lower shock pressures ($100 < P < 350$ GPa), where the Knudson–Desjarlais quartz calibration is more accurate.

Study of Interpenetrating Plasmas on OMEGA
Principal Investigator: S. Le Pape

The Near-Vacuum Campaign on the NIF has shown that radiation–hydrodynamic codes such as *HYDRA* do not accurately describe the collision of two high-velocity flows, e.g., ablated gold from the hohlraum wall and ablated carbon from the capsule, with relative velocity of 8×10^7 cm/s at an electron density of 10^{21}/cm^3. In this parameter space, radiation–hydrodynamic simulation predicts a stagnation of the two plasmas, leading to a density ridge at the materials' boundary; however, experimental data do not support this scenario. The main hypothesis to explain the discrepancy is that the flows'

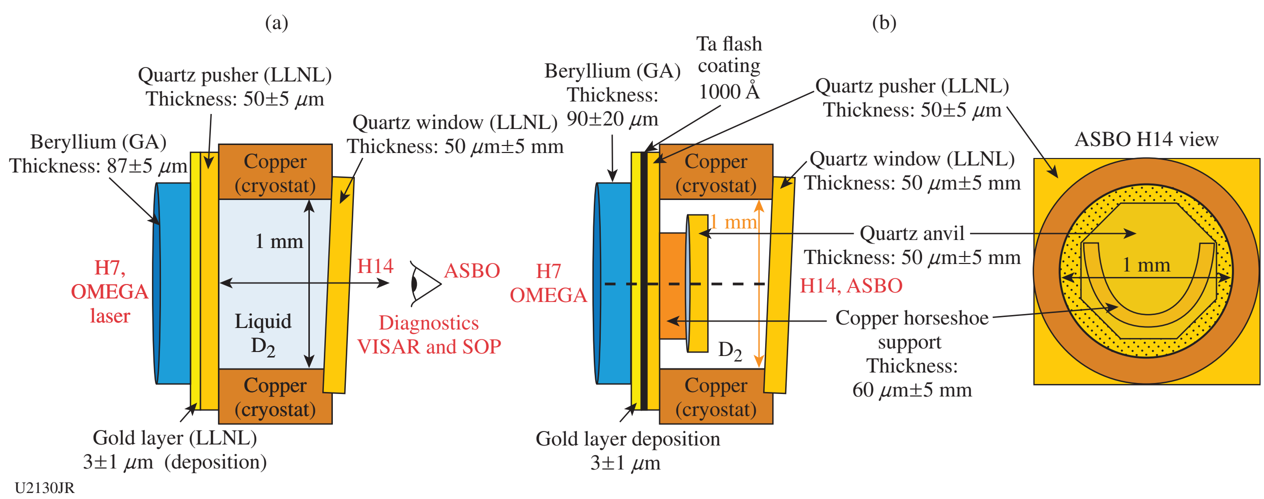

Figure 148.83
Schematic of the target design and experimental configuration for the (a) PCRYO-16A and (b) PCRYO-16B Campaigns, respectively.

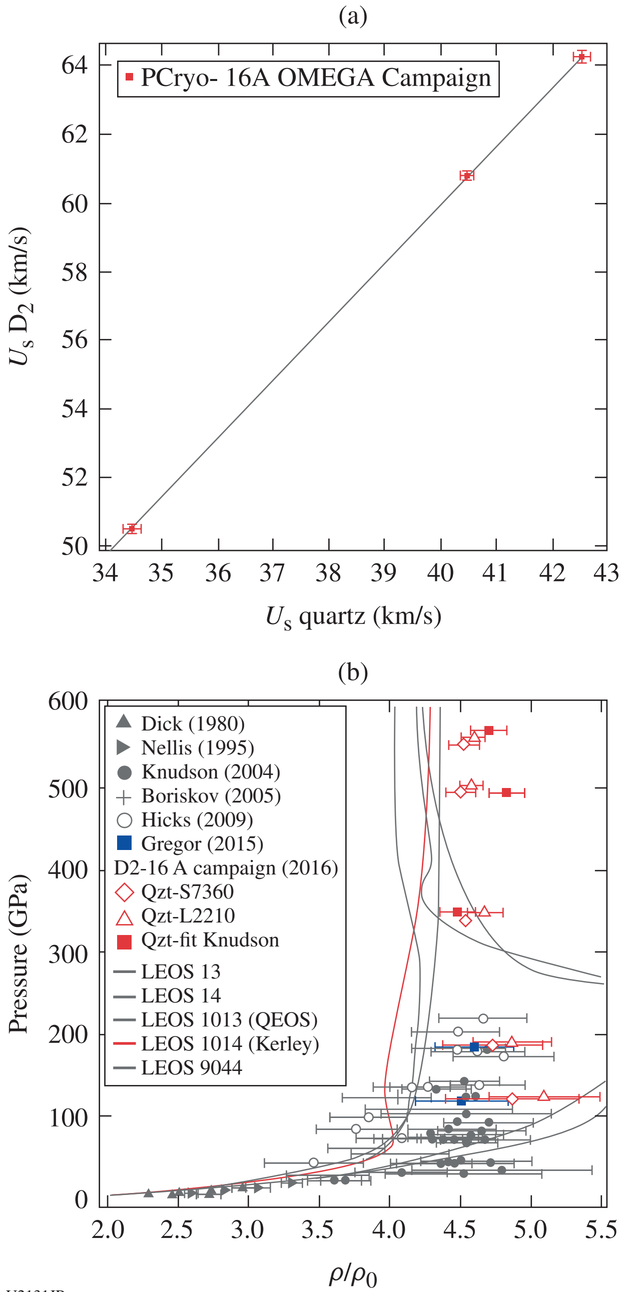

U2131JR

Figure 148.84
(a) Summary of the observables: transmitted shock velocity in D_2 versus incident shock velocity in quartz. (b) Pressure versus compression along the principal Hugoniot of liquid deuterium. Experimental data: vertical triangle by Dick *et al*., horizontal triangle by Nellis, filled circles by Knudson *et al*., crosses by Boriskov, open circles by Hicks *et al*., blue squares are recent data (not yet published) by M. Gregor *et al*. (LLE), red symbols this work (preliminary result) analyzed using the Knudson–Desjarlais quartz calibration and also using two tabular quartz EOS models (*SESAME* 7360, Kerley, and LEOS 2210).

interpenetration cannot be described by a fluid code but requires a full kinetic description at this high relative velocity and low density. To explore this, an OMEGA campaign was designed to emulate a near-vacuum hohlraum environment in a simpler geometry that would allow one to diagnose the material boundary using both optical Thomson scattering and time-resolved x-ray imaging. To reach NIF-relevant conditions, laser beams are used to irradiate both an outer ring of material ranging (depending on the shot) from low to high Z (carbon, aluminum, and gold) and an inner ring of high-density carbon (Fig. 148.85). The laser energy was also varied during the campaign.

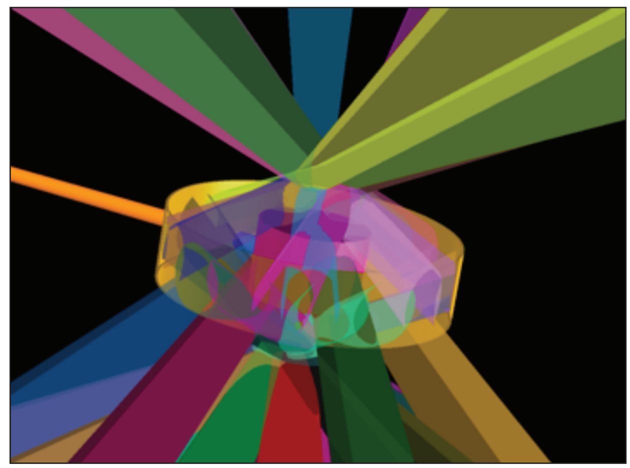

U2132JR

Figure 148.85
VISRAD view of the target geometry with laser beams.

High-quality data were obtained from both main diagnostics. Figure 148.86 illustrates that as the Z of the outer ring material is increased from carbon to gold, and plasma collisionality is increased, the material boundary becomes more apparent for the same laser drive and time.

Figure 148.87 shows ion-acoustic wave (IAW) and electron plasma wave (EPW) spectra. From these spectra, flow velocities, ion temperatures, electron densities, and flow compositions are deduced, providing a complete picture of the plasma parameters.

Broadband Proton Radiography of Shock Front in Gases
Principal Investigators: Y. Ping and R. Hua (LLNL)
Co-investigators: H. Sio (MIT); C. McGuffey and F. Beg (University of California–San Diego); and G. W. Collins (LLNL)

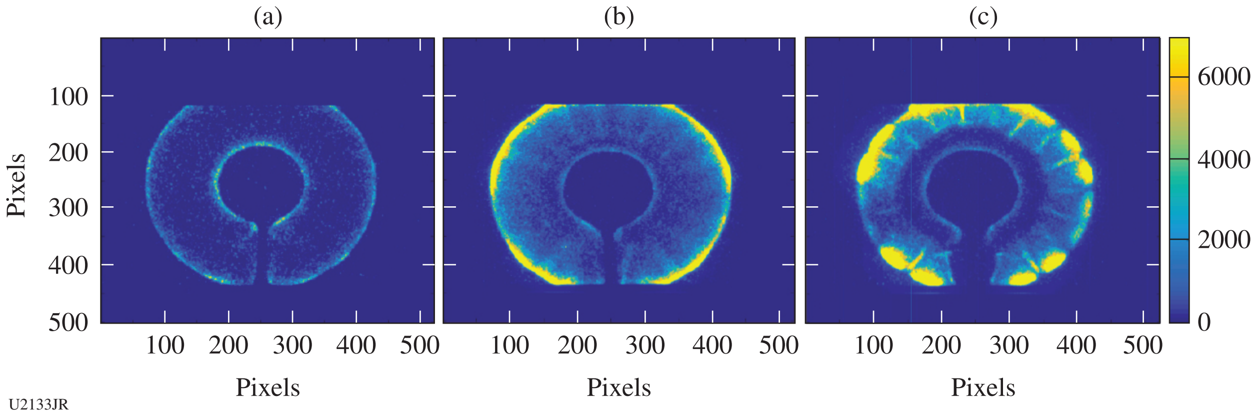

Figure 148.86
X-ray images at 0.9 ns for the three different rings: (a) carbon, (b) aluminum, and (c) gold. The center circle is the high-density carbon ring; the outer circle is the low- to high-*Z* ring.

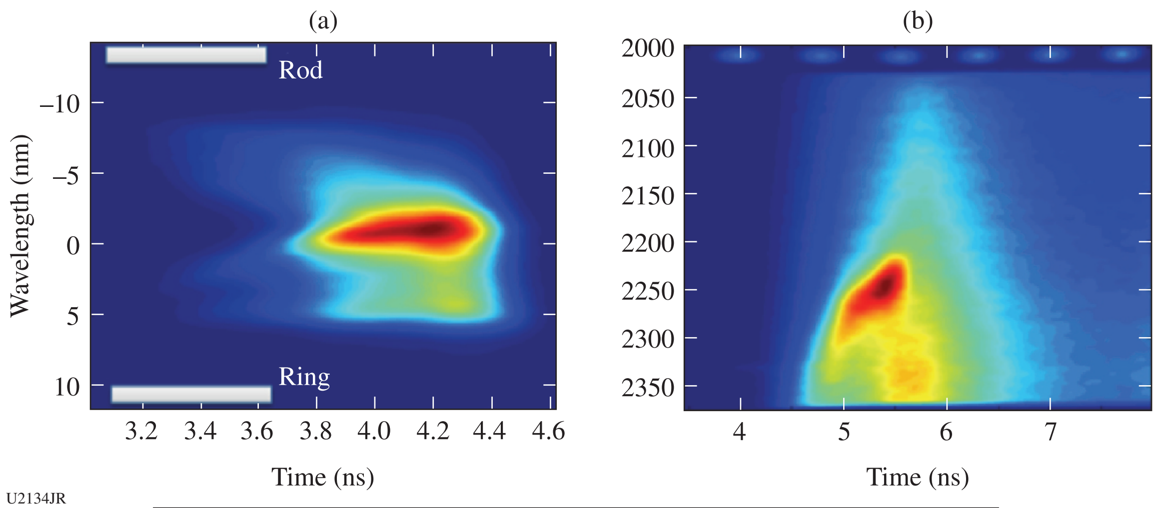

Figure 148.87
(a) Ion-acoustic wave (IAW) and (b) electron plasma wave (EPW) spectra for carbon into carbon.

This campaign is based on an experimental platform developed on OMEGA EP in FY15 to study shock-front structure and field effects in low-density systems. The broadband proton backlighter is generated by high-intensity, short-pulse interaction with metal foils through the well-known TNSA process. The shock is driven by three UV long-pulse beams in a gas cell with a CH ablator. Both shot days provided excellent proton radiographs and soft x-ray spectra of shock propagation in gases. Figure 148.88(a) displays proton radiographs with different-energy protons, showing clearly energy-dependent deflection of protons and complex structure at the shock front. A variable-spaced-grating (VSG) snout was added as a spectroscopic diagnostic for He–Ne mixtures. The spatially resolved spectra, shown in Fig. 148.88(b), provided shock velocity in a single shot and a constraint on shock temperature by Ne lines. A radiative precursor was also observed as indicated in Fig. 148.88(b) as the He-like Ne line extended beyond the shock front. A paper on this new platform has been submitted to Review of Scientific Instruments[31] and a radiograph analysis paper is in progress.

Studies of Kinetic and Multi-Ion-Fluid Effects in Inertial Confinement Fusion Implosions Using Nuclear-Reaction and X-Ray Emission Histories
Principal Investigator: H. Sio (MIT)

The motivations for the one-day DTHe3-16A Campaign on OMEGA were (1) to measure simultaneously the DT and D^3He reaction histories on the same instrument and (2) to measure multiple x-ray emission histories in different x-ray energy bands. By measuring the nuclear reaction histories, one can make a time-resolved comparison of the nuclear

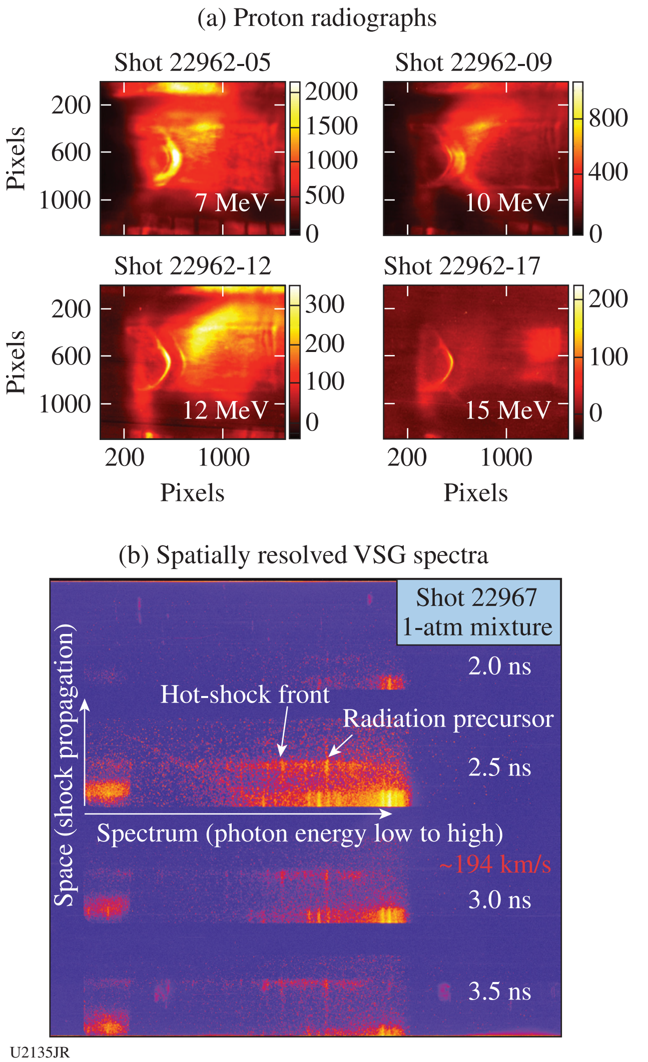

Figure 148.88
(a) Proton radiographs of a shock front in He gas showing energy-dependent structure; (b) spatially resolved spectra by a variable-spaced-grating (VSG) snout. Both shock front and radiative precursor were clearly observed.

rates as implosions transition from a more-hydrodynamic (~2.3-mg/cm^3 initial gas fill) to a more-kinetic (~0.3 mg/cm^3 initial gas fill) regime. Comparison with hydrodynamic and kinetic-ion simulations will be used to understand how plasma density and temperature profiles are altered by nonhydrodynamic effects during shock burn.

At the same time, the ratio of two different nuclear reaction histories will be used to infer a spatially averaged $T_i(t)$. X-ray emission histories in different x-ray energy bands will be used to infer a spatially averaged $T_e(t)$ from the slope of the bremsstrahlung continuum. Since both the nuclear reaction histories and the x-ray emission histories are simultaneously measured on the particle x-ray temporal diagnostic (PXTD), their relative cross timing is very well known (<10 ps). $T_i(t)$, $T_e(t)$, and their relaxation toward equilibrium will be used to measure the ion–electron (i–e) equilibration rate to experimentally validate the Coulomb logarithm for various plasma conditions.

In addition to the primary PXTD data (Fig. 148.89), other nuclear [wedge-range filter (WRF), charged-particle spectrometer (CPS), and proton-core imaging spectroscopy (PCIS)], optical (FABS), and x-ray [Dante, Sydor framing camera (SFC), and framed Kirkpatrick–Baez x-ray microscope (KB-FRAMED)] diagnostics also measured good data to constraint implosion trajectory, laser absorption, nuclear yields, ion temperatures, and x-ray output.

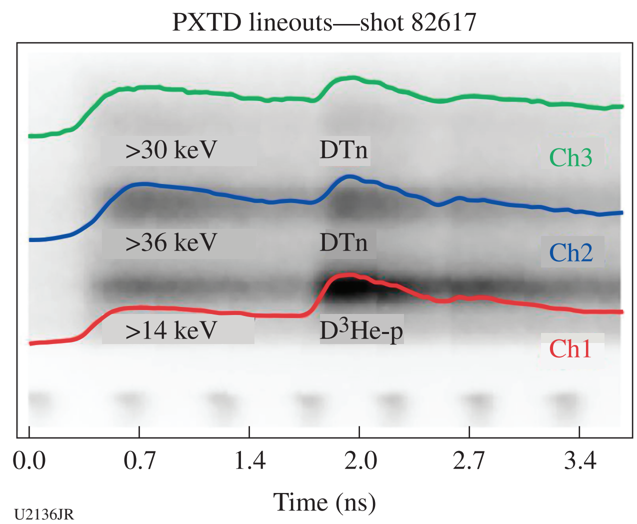

Figure 148.89
Particle x-ray temporal diagnostic (PXTD) channel lineouts on shot 82617. X-ray emission histories (in the energy band above 14, 30, and 36 keV) and nuclear reaction histories (DT, D^{3}He) are measured simultaneously on one streak. Each streak channel has its own filtering in front of, and light attenuation filter behind, the scintillator to equalize the signal relative to the other channels.

X-Ray Blanking Mitigation Experiments for the NIF Optical Thomson-Scattering Diagnostic

Principal Investigators: G. F. Swadling and J. S. Ross

The XRayBlanking-16A experiment was carried out to assess the risk posed to the NIF optical Thomson-scattering (OTS) diagnostic by x-ray–driven "blanking" of the optical debris shield, and to test a Xe gas x-ray shield design concept. A total of 11 target shots yielded high-quality data that addressed the threshold for x-ray blanking effects and demonstrated the feasibility of the Xe gas x-ray shield concept.

The radiation environment presented by NIF hohlraums is extreme; they typically produce radiation temperatures of ~300 eV, with soft x-ray (<3-keV) fluxes of ~10 to 20 TW sr^{-1}, and total time-integrated yields of ~60 kJ sr^{-1}. An optically transparent debris shield will be installed in front of the OTS collection telescope to protect it from target debris produced during shots. The optical layout constrains this shield to be <60 cm from the target, but at this distance, during a typical ignition-scale experiment, the window could receive a total time-integrated soft x-ray fluence of up to 16 J/cm^2. This fluence raises the potential for blanking of the debris shield–induced optical opacity caused by the effects of soft x-ray irradiation.

In the XRayBlanking-16A experiments, the OMEGA Laser System was used to heat a gold sphere target to produce soft x rays with a comparable spectrum and power to that produced by NIF hohlraums. The soft x-ray flux and spectrum were diagnosed using the OMEGA Dante diagnostic. Sample optics were exposed to this soft x-ray flux and their optical transmissions were measured using a 532-nm probe laser beam. Blanking was observed over a fluence range from 0.2 to 2.5 J/cm^2. This threshold falls significantly below the expected soft x-ray fluence onto the NIF OTS debris shield, indicating that measures are required to mitigate this effect.

An optically transparent but x-ray opaque Xe gas x-ray shield concept was tested. The x-ray shield successfully mitigated x-ray blanking of glass samples, demonstrating the feasibility of this concept (see Fig. 148.90). The x-ray shield concept will be applied to the NIF OTS.

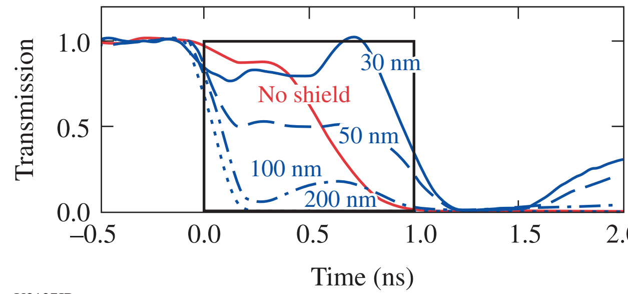

Figure 148.90
Example of 532-nm sample transmission data from XRayBlanking-16A. The black line shows the nominal square laser pulse shape. The red line shows the transmission of a sample in the absence of an x-ray shield. The sample was exposed to ~2.5 J/cm^2 of soft x rays over the duration of the experiment. The blue lines show transmission through samples protected by a 10-cm-long Xe gas shield at a pressure of 0.04 atm. The gas was contained by thin (30- to 200-nm) SiN membranes, which were themselves ablated by the soft x rays. For membranes ≤50 nm thick, the optical transmission was extended significantly relative to the unshielded sample. The thicker membranes appear not to have expanded sufficiently to allow transmission of the probe without significant absorption.

Measurements of Anisotropy in Non-LTE Low-Density Iron–Vanadium Plasmas

Principal Investigator: L. C. Jarrott

Co-Investigators: M. E. Foord, R. F. Heeter, D. A. Liedahl, M. A. Barrios Garcia, G. V. Brown, W. Gray, E. V. Marley, C. W. Mauche, K. Widmann, and M. B. Schneider

Accurate characterization of optical-depth effects, which create geometrical anisotropies in K-shell line emission from low-density non-LTE (local thermodynamic equilibrium) plasmas, is very important for improving line-ratio–based temperature measurements in hohlraums on the NIF, as well as OMEGA. This campaign built upon the established tamped-foil non-LTE platform on OMEGA, with specific goals to increase the laser intensity, verify the hydrodynamics of the target expansion, and provide a robust calibration of the x-ray spectrometers. Two target types were used: The primary target was a 10-μm-thick, 1000-μm-diam beryllium tamper containing a volumetrically equal mixture of iron and vanadium, 200 nm thick and 250 μm in diameter. The second target was a "null" where the beryllium tamper contained no sample material. Three beam–target orientations were used over the course of 13 shots. In the first configuration, an MSPEC spectrometer situated in TIM-2 and a gated pinhole imager in TIM-3 had an edge-on view of the target, while another MSPEC in TIM-6 and another pinhole imager in TIM-4 had a face-on view. In the second configuration, the target orientation with respect to TIM-2 and TIM-6 was reversed. In the third configuration, all primary TIM-based diagnostics had a viewing angle of 45° with respect to target normal. These three target–beam orientations provided an *in-situ* cross-calibration of the spectrometers and pinhole imagers. The data obtained from 13 shots included simultaneous, time-resolved edge-on and face-on measurements of (1) the iron and vanadium K-shell spectra and (2) the expanding plasma volume. The K-shell spectral data provided time-resolved electron temperature measurements of the expanding plasma, with preliminary analysis indicating $T_e >$ 2 keV, higher than previous campaigns (Fig. 148.91).

Optical Thomson-Scattering Measurements from Gas-Covered Au Spheres

Principal Investigator: J. S. Ross

Co-investigators: G. Swadling, R. Heeter, M. Rosen, K. Widmann, and J. Moody (LLNL); and D. H. Froula (LLE)

The GasCoSphere-16A Campaign performed "gas-covered," high-Z sphere experiments, with a gold-coated CH sphere

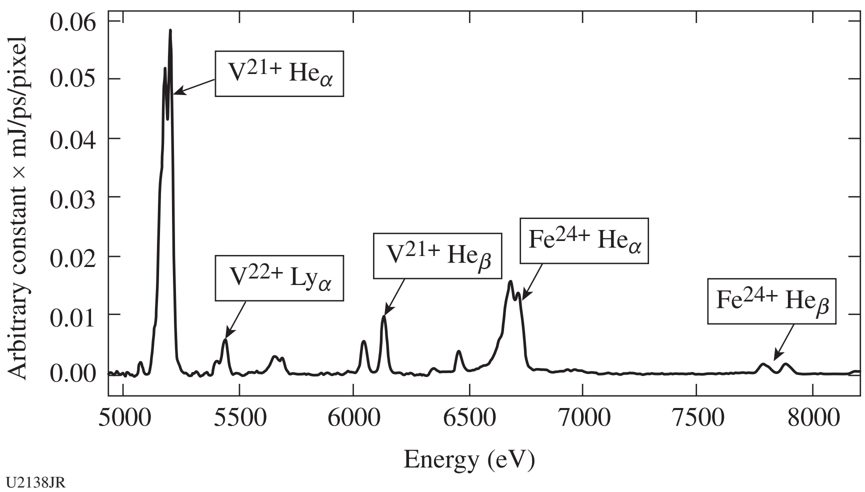

Figure 148.91
Spectrum measured by an MSPEC spectrometer of the x-ray emission from K-shell transitions in highly charged vanadium and iron. An electron temperature >2000 eV is inferred from the various line ratios.

placed inside of a gas bag and illuminated using a direct-drive geometry, to investigate atomic physics models, radiative properties of the laser-spot plasma, and the interpenetration of multi-ion–species plasmas relevant to ICF indirect-drive–ignition hohlraums. These experiments use a laser irradiation of 10^{14} to 10^{15} W/cm^2, similar to National Ignition Campaign hohlraums. The gas bag was filled with 1 atm of either propane or a 70/30 mix of propane and methane, achieving (respectively) initial electron densities of 7.5% and 6.0% of the critical density of the 3ω drive beams. With these conditions, the gold–gas interface mimics the interaction of a hohlraum's gold wall with the low-density hohlraum fill gas.

In these experiments, the plasma temperature and density at various radial positions in the blowoff plasma were characterized using optical Thomson scattering. The laser drive used a shaped laser pulse (1-ns square foot, 1-ns square peak) to reduce the shock produced by the gas-bag window. The electron temperature and density, the plasma flow velocity, and the average ionization state are inferred by fitting the theoretical Thomson-scattering form factor to the observed data. An example of the Thomson-scattering data from ion-acoustic fluctuations is shown in Fig. 148.92. The measured data are compared to post-shot simulations with and without a diffusion model in Fig. 148.93. The data and simulations show minimal

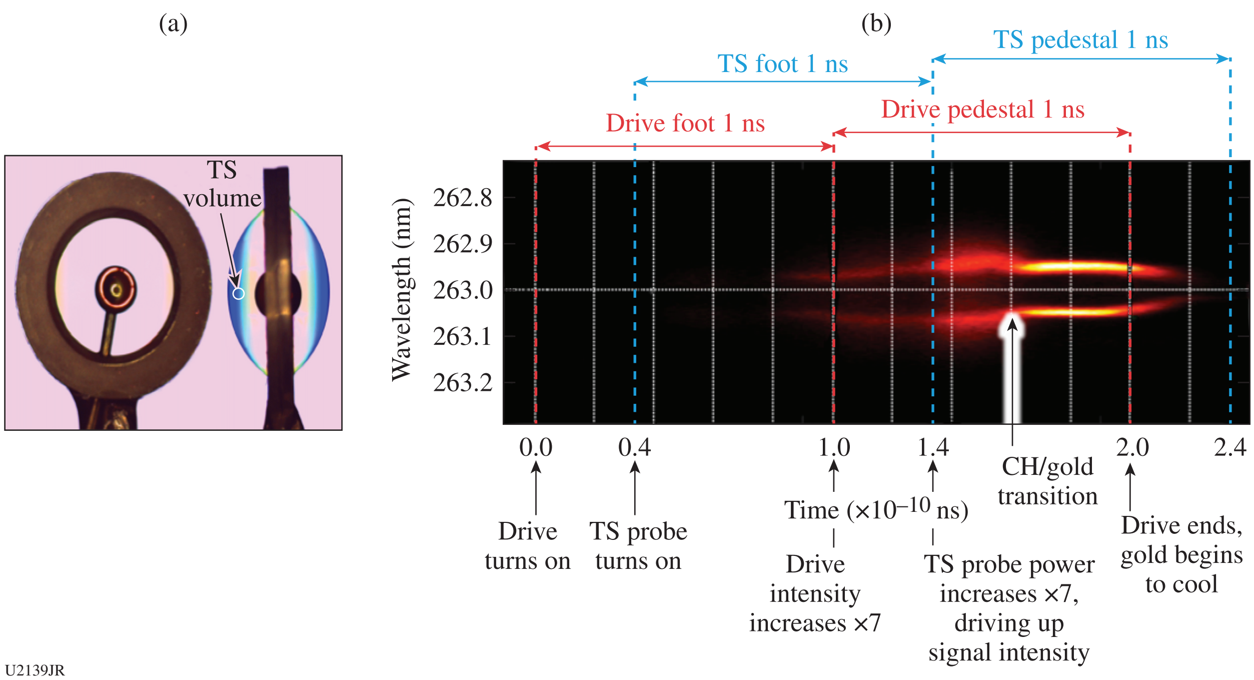

Figure 148.92
(a) A 1-mm-diam Au sphere centered in a 2.6-mm-diam gas bag. The location of the Thomson-scattering (TS) volume is shown. (b) This example of the Thomson-scattering ion feature indicates where the transition from scattering from Au to scattering from CH plasma is observed at 1.6 ns.

diffusion of Au into the low-*Z* CH plasma. Continued data analysis and simulations are in progress to better understand the plasma evolution and heat transport.

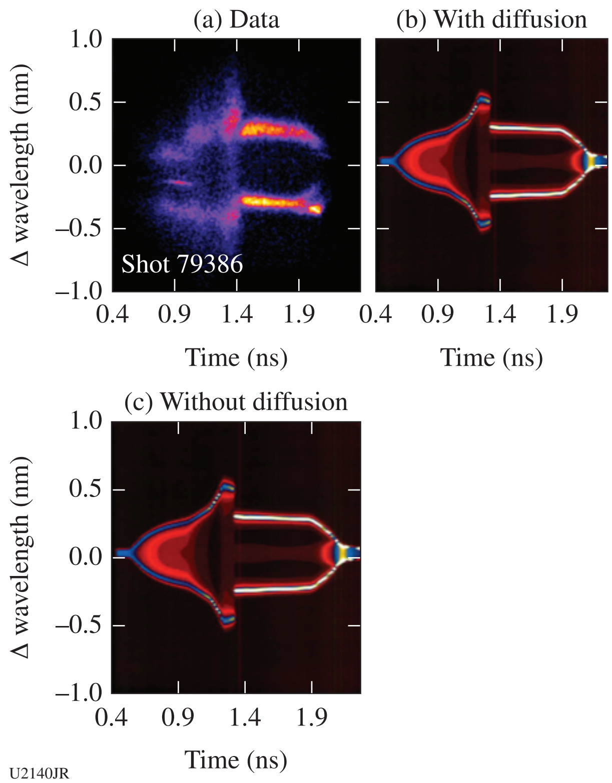

Figure 148.93
The (a) measured Thomson-scattering signal is compared to post-shot simulations (b) using or (c) not using a diffusion model to investigate the interpenetration of Au into the CH plasma.

High-Energy-Density Experiments

1. Material Equation of State Using Diffraction Techniques

Measurements of the High-Pressure Refractive Index of Magnesium Oxide Windows
Principal Investigator: R. F. Smith

Magnesium oxide (MgO) has the potential to be a good alternative to LiF as a window material in high-pressure EOS experiments. The goal of this half-day OMEGA campaign was to measure the refractive index of MgO to pressures up to 800 GPa, following the experiments and analytical techniques outlined in Ref. 32. The target design (shown in Fig. 148.94) consists of 100 μm of micrograined diamond with, on the rear surface, a half layer of 100-μm MgO [100] single crystal.

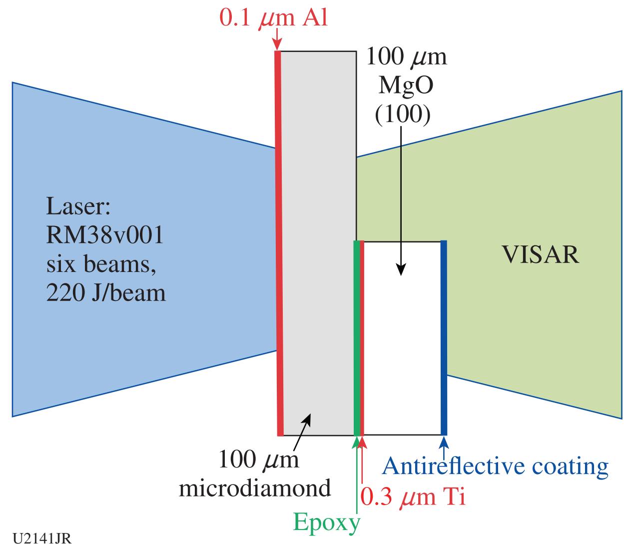

Figure 148.94
Target design for the MaxOxWindow-16A experiment.

A 0.3-μm Ti layer was coated onto the inner MgO surface to enhance reflectivity for VISAR measurements, and an antireflection coating was added to the rear surface. Target normal was oriented along the OMEGA H7–H14 axis. Six 23° beams with the RM38v001 pulse shape were incident onto the diamond ablator, using 220-J/beam, SG8 phase plates, and beam delays to achieve an ~7-ns ramped laser pulse. With this configuration a ramp compression wave with a peak pressure of 800 GPa was launched into the target assembly. The LLE-ASBO (VISAR) diagnostic could then simultaneously measure the diamond free-surface velocity and the diamond/MgO interface velocity. With knowledge of the sample thicknesses and the EOS of both diamond and MgO, one can compare the expected diamond/MgO interface velocity with the measured velocity. The discrepancies between the two can be then used to determine the density correction on the MgO refractive index with that of LiF (Ref. 32). Good-quality data were obtained on this campaign to support this analysis.

Ramp Compression of MgO and Development of Ge Diffraction Backlighter on OMEGA EP
Principal Investigator: R. F. Smith

The target and laser design for the W-MgO-DiffEP-16A Experimental Campaign is shown in Fig. 148.95(a). This campaign successfully demonstrated the capability of ramp compression of samples to high pressure on OMEGA EP [Fig. 148.95(c)]. With a slight variation of the target design

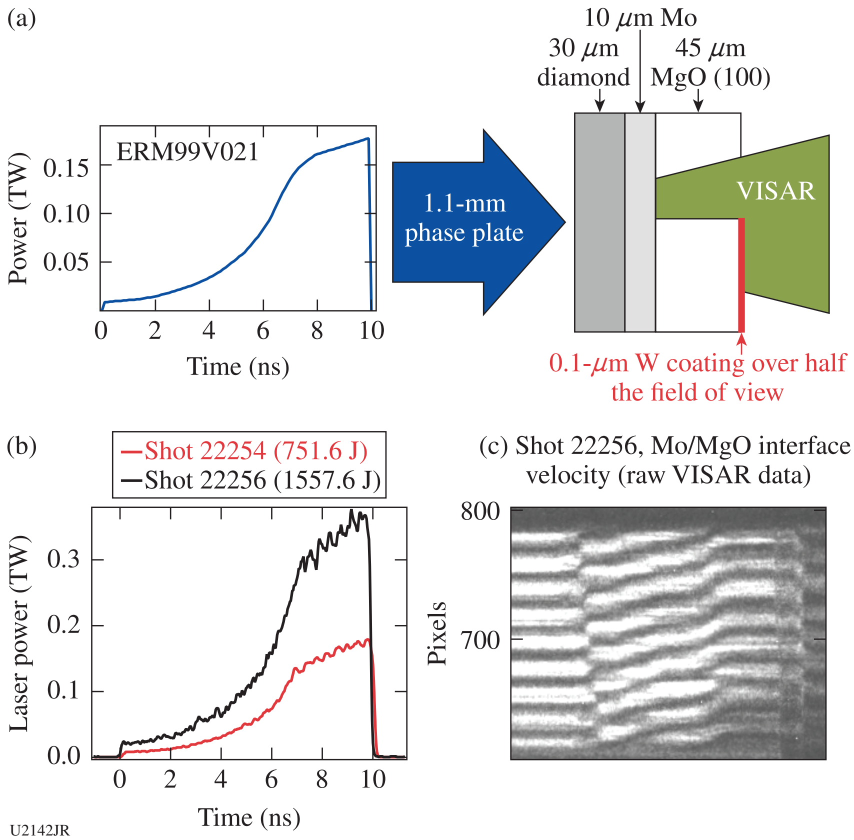

Figure 148.95
(a) Laser and target request for the W-MgO-DiffEP-16A shots. A 10-ns pulse (ERM99v021) was designed to compress to pressures of 500 GPa and then hold at that pressure. The target package consists of a 30-μm diamond ablator, a 10-μm Mo foil, and a 45-μm-thick MgO [100] window. Half of the MgO free surface was coated with 0.1 μm of W, such that the OMEGA EP VISAR diagnostic could simultaneously measure both the Mo/MgO interface velocity and the MgO free-surface velocity. (b) As-delivered laser power for two shots. (c) VISAR data from a shot successfully ramp compressing the MgO to several hundred GPa.

in Fig. 148.95(a), a 10-ns ramped pulse shape (ERM99v006) launched a steady shock into the MgO sample. By increasing the laser power (shock pressure) on a shot-to-shot basis, it was established that along the Hugoniot single crystal, MgO loses its 532-nm transmission at ~300 GPa; this is consistent with the onset of the B1–B2 phase transformation.

Simultaneously, this campaign tested the efficacy of a Ge He$_\alpha$ 10.2-keV source for x-ray diffraction measurements. The Ge target consisted of a 6-μm layer of Ge, coated onto a graphitic carbon substrate, and then illuminated with a 1-ns flattop pulse that delivered 1250 J into a 200-μm spot. Using this configuration, a strong He$_\alpha$ peak was measured and found to be sufficiently strong for use as a source in subsequent x-ray diffraction experiments.

Development of a New Platform for Measuring Recrystallization

Principal Investigators: F. Coppari and R. G. Kraus

The goal of this campaign is to develop a platform for measuring recrystallization of Pb through shock-ramp compression. By launching a first initial shock to compress the sample along the Hugoniot close to the melting pressure, letting it release into the liquid phase, and then recompressing it with a ramp compression across the solid–liquid phase boundary, one can measure high-pressure melting lines of materials. The phase of the Pb upon shock, release, and ramp compression is monitored by time-resolved x-ray diffraction. The onset of melting is identified by the appearance of a diffuse scattering pattern and the disappearance of the Bragg diffraction lines characteristic of the solid. The pressure is monitored by VISAR, looking at the interface between the Pb and a LiF window. This campaign tested for the first time the use of beryllium ablators in diffraction experiments at Omega. This was possible thanks to excellent support from the Omega staff to implement special procedures to avoid Be contamination of the diffraction diagnostic hardware and the image-plate media used to record the data. The behavior of Be ablators is relatively easy to capture with hydrocode simulations, improving predictive capabilities for this class of experiments. In this experiment it was possible to accurately tune the laser pulse shape and compress the Pb sample along this complicated shock/release/ramp path. Beryllium is also a highly efficient ablator, especially compared to standard plastic ablators, so the same pressure can be obtained with lower laser energy, with the added desirable effect of reducing the ablation x-ray background that may interfere with the diffraction measurements. On this recent OMEGA EP shot day, excellent diffraction data were obtained that will help inform future Omega and NIF campaigns.

How Much Do The Backlighter X-Rays Heat Unshocked Diffraction Samples?
Principal Investigator: D. Erskine
Co-investigator: J. H. Eggert

Recently many diffraction shots on the NIF using the TARDIS diffraction platform have successfully returned valuable information about the structure of materials under shock loading. These experiments use an x-ray backlighting source created by intensely illuminating a material such as Fe or Cu to produce K-shell x-ray lines. This illumination occurs while other laser illumination creates a pressure wave that moves through the sample. The x rays diffract from the compressed sample and the angular directions of the diffracted rays are recorded by a set of time-integrating imaging plates that surround the sample. Simultaneously, a pair of VISAR interferometers measure the Doppler velocity of the target surface and the velocity history reveals information about the shock loading of the target.

The question is, does the backlighting illumination itself cause enough heating in the sample to perturb these measurements? To find out, this experiment shot a set of diffraction targets that were *not* illuminated by the pressure drive lasers; only the backlighting x rays were used. If the temperature increase related to absorption of x rays is significant, the thermal expansion creates a velocity (and displacement) signature. The answer is yes, a small signal can be observed, but only at maximum OMEGA EP laser power to the backlighter and with thicker (50-μm) samples. This was established using one day of OMEGA EP time to deliver nine shots using various sample thicknesses and backlighter sources. No heating signature was observed for the first six shots using moderate backlighter laser power on either 5- or 50-μm-thick samples. On three shots, however, a small thermal expansion displacement was observed (Fig. 148.96) when the maximum amount of backlighter power was delivered onto a relatively thick sample. These data will be used to refine the design of upcoming diffraction measurements.

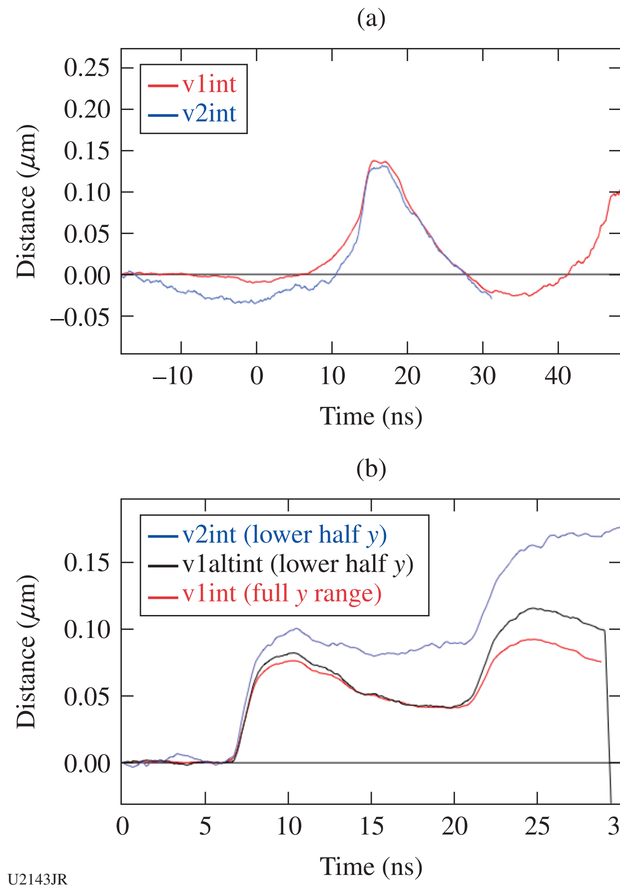

Figure 148.96
Measured displacement of diffraction sample's rear surface versus time, by integrating the VISAR velocity signal. Two VISAR's (1 = red, 2 = blue) monitor the same sample but have different record lengths. (a) Shot 22612 (Fe backlighter on 100 μm of Al). Good agreement between VISAR's was obtained. (b) Shot 22614 (Cu backlighter on 50 μm of Al). The discrepancy between the blue trace (VISAR2) and the red and black traces (integrating different regions on VISAR1) requires further investigation.

Development of* in-situ *Pressure Standard for Diffraction Experiments
Principal Investigator: F. Coppari
Co-investigator: J. H. Eggert

The goal of this campaign is to develop a new way to determine pressure in diffraction experiments, based on the use of an *in-situ* pressure gauge. By measuring the diffraction signal of a standard material (whose EOS is known) that has been compressed together with the sample, one can determine the pressure reached during ramp compression.

Currently, pressure is determined with VISAR measurements of diamond free-surface velocity; this method is in some cases ambiguous (e.g., because of the lack of reflectivity or shock formation). Cross checking the VISAR measurement with *in-situ* pressure determination, using the diffraction signal of a standard material, will improve the diffraction platform by providing a complementary way of determining the pressure state within the sample. In addition, combining pressure determination from VISAR and from the *in-situ* gauge can also provide information about the temperature of the sample by measuring the calibrant thermal expansion.

In this experiment, different pressure gauge materials (Au, Pt, and Mo) were tested in ramp compression to a moderate pressure (2 to 3 Mbar). Excellent-quality data were obtained. The Pt standard gave the best results because the diffraction signal was strong and untextured. Although this platform still needs some development effort before being used routinely in diffraction experiments, the data collected so far are extremely encouraging and suggest that the use of an *in-situ* pressure gauge can be a viable path forward in future x-ray diffraction measurements at both Omega and the NIF.

Development of Simultaneous Diffraction and EXAFS Measurements
Principal Investigator: F. Coppari
Co-investigators: Y. Ping and J. H. Eggert

Simultaneously measuring diffraction and extended x-ray absorption fine-structure (EXAFS) signals in the same shot will be an enormous advancement for laser-based materials experiments. Such capability would provide simultaneous probes of both the long-range (diffraction) and short-range (EXAFS) order of the material, as well as two complementary probes of the Debye–Waller factor to probe the temperature of a single material state.

The approach in this campaign used the PXRDIP diagnostic to measure diffraction and the x-ray spectrometer (XRS) to measure EXAFS. The challenge was to find a suitable backlighter that would generate both a monochromatic (for diffraction) and broadband (for EXAFS) x-ray source. Different schemes were tested out in the different campaigns, such as Kr-filled capsule implosions or illumination of a high-*Z* foil to exploit both the line and the continuum emission, but these initial schemes did not work for both diffraction and EXAFS. Success was achieved, however, in measuring simultaneous XRD and EXAFS by using a dual-material foil backlighter, where one side of the foil is optimized to generate He$_\alpha$ radiation for diffraction (i.e., Fe foil driven with six beams at 500 J and a 300-μm laser spot) and the other side is used to generate a broadband bremsstrahlung continuum for EXAFS (i.e., Ag foil driven with 13 beams at 500 J and best focus to maximize the laser intensity), as shown in Fig. 148.97. The sample material in these shots was a "diamond sandwich" with an Fe sample as typically used in ramp-compression experiments. Figure 148.97 also shows examples of the EXAFS and diffraction data.

Further development is needed to improve the data quality, but this result represents a big step forward in the study of dynamically compressed matter.

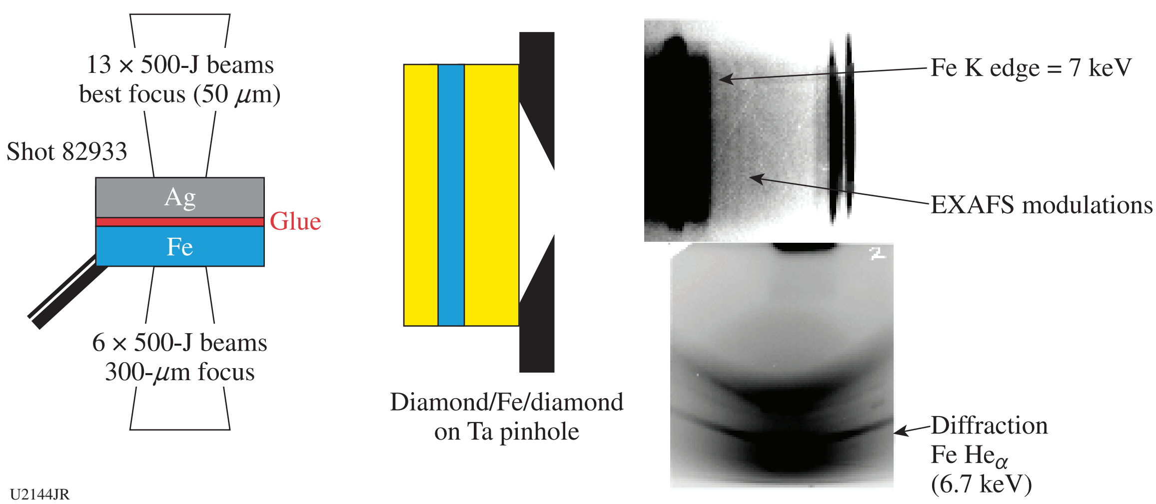

Figure 148.97
Schematic of the backlighter and target used in the XRD-EXAFS_16C Campaign to successfully measure simultaneous extended x-ray absorption fine structure (EXAFS) (top data) and diffraction (bottom) of an Fe foil sandwiched between a diamond ablator and a window.

2. Material Equation of State Using Other Techniques

Development of Spherically Convergent Equation-of-State Measurements
Principal Investigator: A. E. Lazicki
Co-investigators: D. Swift, A. Saunders, T. Doeppner, F. Coppari, R. London, D. Erskine, D. E. Fratanduono, P. M. Celliers, J. H. Eggert, G. W. Collins, H. Whitley, J. Castor, and J. Nilsen

This series of shots was designed to test and qualify a platform for measuring Hugoniot EOS at pressures much higher than can be achieved using a standard planar drive. This platform is intended to collect data in the >100-Mbar pressure regime, where currently very little data exist for any material, for the purpose of constraining EOS models.

The first two campaigns, GbarEOS-16A and -16B, used a hohlraum (indirect drive) to launch converging shock waves into solid spheres of CH_2, similar to an existing platform on the NIF but not yet in use on OMEGA. Along the axis of the hohlraum, backlit 2-D x-ray images of the imploding sphere were collected with a framing camera; streaked backlit images of a slice of the sphere, imaged through a slit in the hohlraum, were also recorded with a streak camera (Fig. 148.98). The radiographs yield density and shock velocity, which allow one to calculate the shock state using the Rankine–Hugoniot equations. The two campaigns experimented with variations in camera configuration, hohlraum gas fill, x-ray backlighter energies, and hohlraum drive energy. Usable data were collected on all diagnostics for a subset of the shots, indicating pressures between 30 to 200 Mbar, and analysis is in progress. In a subset of the shots, x-ray Thomson-scattering measurements were made using a spectrometer with a view along the hohlraum axis in an effort to constrain temperature as well. An analysis of these results has been published.[33] The third half-day campaign (GbarEOS-16C) used the OMEGA beams to directly ablate a sphere of deuterated plastic (CD) to drive the convergent shock wave, with the core material state assessed via radiography, x-ray Thomson scattering, and neutron-yield diagnostics. Results of these campaigns are being used to further optimize the platform to make more measurements in FY17.

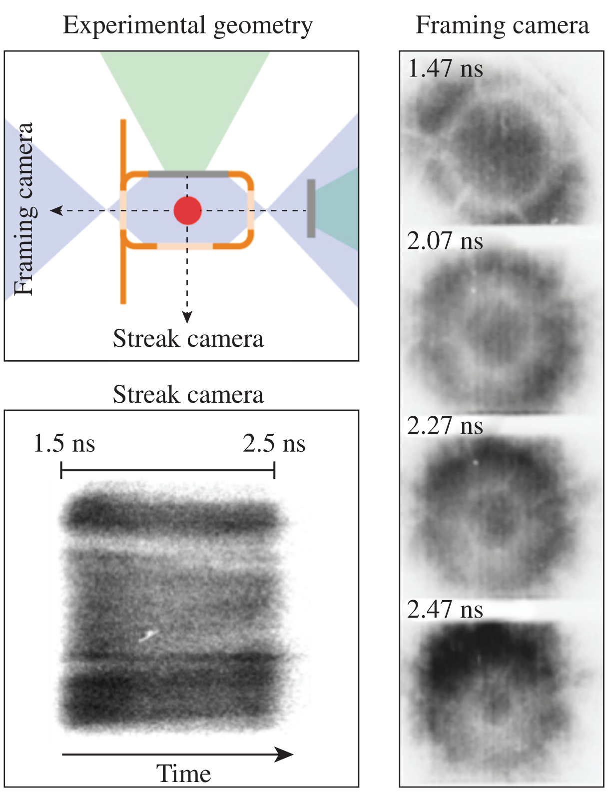

Figure 148.98
Experimental configuration and raw radiographs from a streak camera and framing camera for shot 79708.

Development of Conically Convergent Equation-of-State Measurements
Principal Investigator: A. E. Lazicki
Co-investigators: D. Swift, F. Coppari, R. London, D. Erskine, D. E. Fratanduono, P. M. Celliers, J. H. Eggert, G. W. Collins, H. Whitley, J. Castor, and J. Nilsen

This campaign was designed to test a conically convergent platform for measuring the Hugoniot EOS of arbitrary materials, including high-Z materials, at much higher pressures than can be achieved using a standard planar drive. This platform is intended to collect data in the >100-Mbar pressure regime, where currently very little data exist for any material, for the purpose of constraining EOS models.

To achieve the desired pressure amplification, this campaign experimented with convergent shock waves launched into a cone inset within a halfraum (Fig. 148.99). For appropriate cone angles, nonlinear reflections of the shock wave result in the formation of a Mach stem: a planar high-pressure shock that propagates along the axis of the halfraum. This concept has previously been demonstrated on high-explosives platforms[34] and proposed for a laser drive[35] but never previously tested.

One advantage of this geometry over a spherically convergent geometry is that since the Mach reflection is planar, it can be launched into a planar target package to make a traditional transit-time impedance-matching measurement using a velocimetry diagnostic.

One half-day of OMEGA shots was used to test three different cone angles using the VISAR and SOP diagnostics to register shock breakout times and profiles from the free surface of a CH (rexolite polystyrene) cone. Results indicate the formation of a Mach stem at pressures exceeding 200 Mbar. The data will be used to develop an EOS measurement on OMEGA in FY17, with extension to more-extreme conditions using NIF as well.

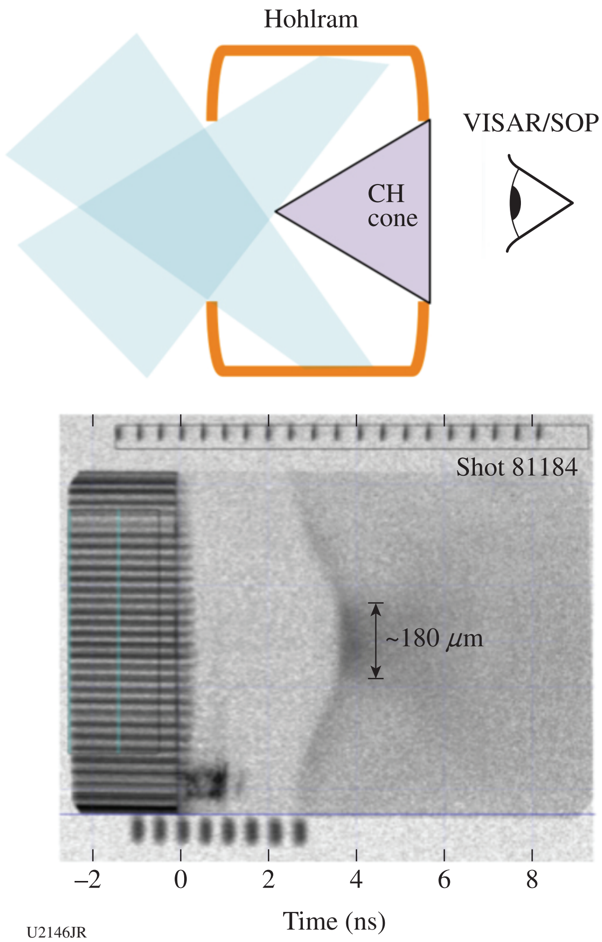

Figure 148.99
Experimental configuration and raw VISAR data showing the breakout time from a CH cone.

Ramp Equation-of-State Measurements on Gas-Encapsulated Samples
Principal Investigator: R. F. Smith
Co-investigator: D. E. Fratanduono

The goal of this campaign was to test a new target design in which the sample is encapsulated in a gaseous environment of nitrogen or argon. The target was designed to determine if the velocity at a diamond/gas interface was different from the velocity off a diamond/vacuum free surface.

The target was oriented along the H7–H14 axis (Fig. 148.100). Six OMEGA beams, incident 23° off axis with a 3.8-ns ramp laser pulse shape, were combined to generate an ~7-ns overall ramp compression drive in a diamond sample. Peak sample pressures of 800 GPa were generated. The ABSO (VISAR) diagnostic simultaneously measured the diamond/gas interface velocity and the diamond/MgO interface velocity. Using the diamond/MgO interface velocity, the known diamond thickness and the previously measured EOS of diamond, one can infer the diamond free-surface velocity. Discrepancies between the diamond/gas and calculated diamond free-surface velocities provide an indication as to the effect of gas encapsulation. During the half-day of shots, the gas pressure was varied to obtain a range of data to establish operating boundaries for future experiments with different sample materials.

Optical Blanking Test for Gas-Encapsulated Equation-of-State Measurements
Principal Investigator: D. E. Fratanduono
Co-investigator: R. Smith

Following up on the Gas-Encapsulation Ramp Campaign, this campaign continues to explore a new target design in which the sample is encapsulated in a gaseous environment. The target was designed to determine if a diamond/gas interface velocity differs from the velocity of a diamond/vacuum free surface. The new gas-fill capability on OMEGA EP was employed.

Eight experiments were performed to examine if a low-density gas would blank (become opaque to the VISAR probe beam) when ramp compressed using the UV lasers on OMEGA EP. Neon, xenon, argon, and nitrogen were examined at 1.0 atm and 1.5 atm. No issues were observed with neon, argon, and nitrogen. Blanking was observed in the xenon data. These data will be useful for designing future NIF experiments with encapsulated samples.

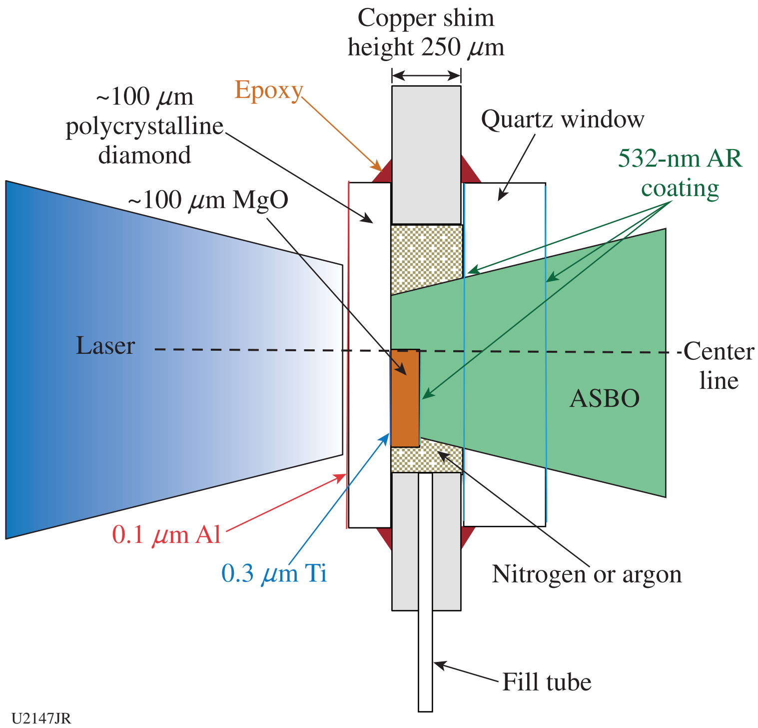

Figure 148.100
Target design for RampReverb-16B. AR: antireflective.

Development of a Platform for Equation-of-State Measurements Using Flyer-Plate Impact
Principal Investigator: F. Coppari
Co-investigators: R. London, P. M. Celliers, M. Millot, D. E. Fratanduono, A. Lazicki, and J. H. Eggert

The goal of this campaign is to develop a platform to accelerate diamond flyer plates to hypervelocity for EOS measurements. The conceptual design was to ramp compress a diamond plate on the end of a halfraum, using x-ray ablation to accelerate the diamond into vacuum. After propagating a known distance, the diamond flyer impacts a transparent diamond window. By measuring the diamond flyer-plate velocity prior to impact, together with the resulting shock velocity in the diamond witness, the principal Hugoniot of diamond can be determined *absolutely* (e.g., without requiring a known pressure reference), making it possible to develop diamond as a high-pressure EOS standard.

These FY16 shots pioneered the indirect-drive approach, which greatly improved planarity and resulted in more-homogeneous, smooth flyer acceleration compared to direct-drive flyer experiments in FY15. The maximum pressure achievable on OMEGA remains, however, below the onset of diamond reflectivity, so instead quartz was used as a window and reference. Issues with the diamond flyer breaking up before impact, because of spalling, arise when attempting to reach higher pressure. This currently prevents us from obtaining high-quality VISAR data (and high-precision EOS measurements) from a full-density diamond flyer. But since the technique appears promising, future campaigns will explore different flyer materials that could also become useful absolute EOS standards (i.e., Mo and Cu).

Backlighter Development for Extended X-Ray Absorption Fine Structure Measurements
Principal Investigator: F. Coppari
Co-investigators: Y. Ping, J. R. Rygg, and J. H. Eggert

EXAFS measurements require a bright, smooth broadband x-ray source for absorption spectroscopy near x-ray edges of the sample material. The x-ray radiation emitted by a capsule implosion meets these requirements and is currently used in laser-based EXAFS experiments. This x-ray emission decays rapidly, however, at higher photon energies, making it very challenging to measure EXAFS above 10 keV. To extend the x-ray energy range of laser-based EXAFS measurements, this campaign explored the possibility of using bremsstrahlung sources from foil backlighters driven at relatively high intensity. The specific goal of this campaign was to determine the optimum material and laser power configuration for this technique on OMEGA. Both Mo and Ag foils were tested, with laser intensity varying from 8×10^{16} W/cm^2 to 3×10^{17} W/cm^2. The source spectrum and size were measured for each shot.

The Ag foil driven with full intensity and tight laser focus is in fact somewhat brighter than the capsule backlighter above 10 keV (see Fig. 148.101). The bremsstrahlung backlighter's simplicity and potential for further improvement make this approach a valuable alternate x-ray source for high-energy EXAFS measurements.

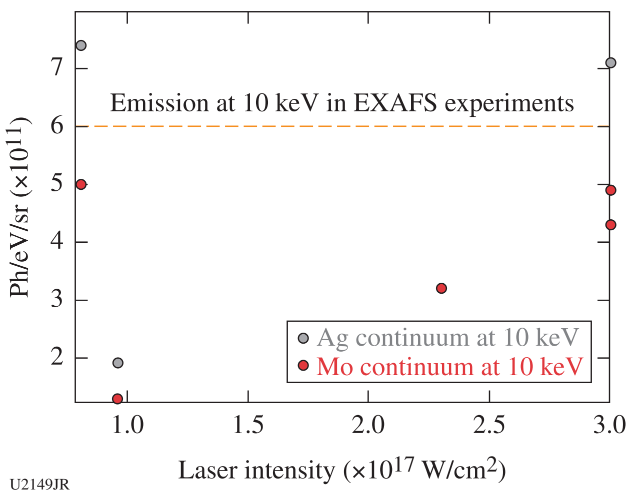

Figure 148.101
Brightness of Ag and Mo foils at 10 keV as a function of laser intensity. The dashed line represents the brightness of the capsule backlighter at 10 keV, currently used as an x-ray source for EXAFS measurements on OMEGA

Hugoniot Equation of State of Low-Density Porous Graphite
Principal Investigator: A. E. Lazicki
Co-investigators: F. Coppari, R. London, D. Swift, M. Millot, D. E. Fratanduono, H. Whitley, J. Castor, and J. Nilsen

This campaign was designed to probe a preheated Hugoniot EOS, using pore collapse of a porous material to generate preheating. The pressure and density of shocked states were determined by impedance matching with a quartz standard. As shown in Fig. 148.102, the samples were driven using the gas-filled hohlraum indirect-drive platform, and the VISAR and SOP diagnostics measured shock transit times in samples of porous graphite. Shock steadiness during transit through the graphite samples (which are opaque to the VISAR) was determined from a quartz witness sample placed next to the porous graphite, from which a continuous record of the shock speeed was simultaneously recorded. High-quality data were collected for 12 shots during two half-days in FY16; detailed analysis is underway.

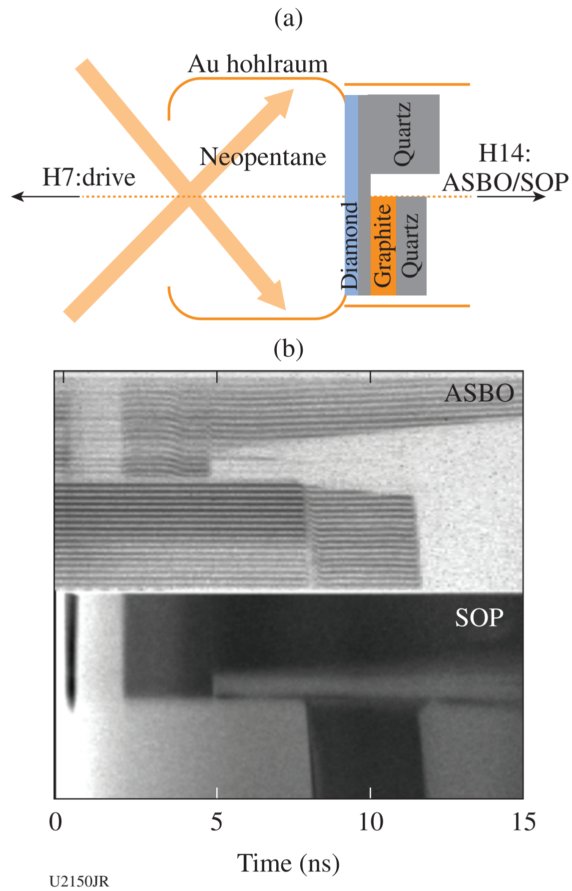

Figure 148.102
Experimental configuration and raw graphite EOS data for shot 80846.

3. Hydrodynamics

Mix-Width Measurements of Rayleigh–Taylor Bubbles in Opaque Foams
Principal Investigator: C. M. Huntington

The OMEGA Foam Bubbles Campaign addresses challenges in deeply nonlinear, multimode hydrodynamic-instability measurements. The interface between two materials of different densities may be susceptible to either Richtmyer–Meshkov (RM) or Rayleigh–Taylor (RT) instabilities if it is shocked or accelerated, respectively. These instabilities in turn drive mixing, where perturbations on the interface determine how the low- and high-density materials interpenetrate. This campaign aims to measure the extent of the interpenetration ("mix width") in cases where the perturbation is complex and the materials mix on small scales. This is achieved by carefully manipulating the properties of the materials in the system. Particular emphasis is placed on the densities, which set the instability growth rates, and on the x-ray opacity characteristics, which determine the contrast in the x-ray image used to diagnose the mix width.

A technique developed over many previous planar RT experiments uses a high-opacity material, often iodinated plastic, embedded in the plastic portion of the target that comprises the "high-density" part of the unstable interface. When driven by indirect drive from a halfraum, and then imaged with transmission x-ray radiography, the location of the high-opacity tracer material is clear and reveals the position of the high-density material in the system. This technique can obscure, however, the shape and extent of the low-density "bubbles" when the foam mixes with the doped plastic. In contrast to this, foam bubbles use an opaque *foam*, which when set next to the more-transparent plastic, highlights the extent of the *foam penetration into the plastic*. This system has identical hydrodynamic behavior as the traditional doped plastic/foam interface, but with inverse x-ray characteristics. The target for the Foam Bubbles Campaign includes both interfaces, ensuring that the entire system experiences the same acceleration. An example of the data collected is shown in Fig. 148.103. This image was generated using tilted, tapered, point-projection x-ray imaging and clearly shows the layers on each side of the split target. The extent of bubble penetration in an RT unstable system is a fundamental quantity, and this measurement will further our understanding of hydrodynamic systems, from ICF implosions to supernovae.

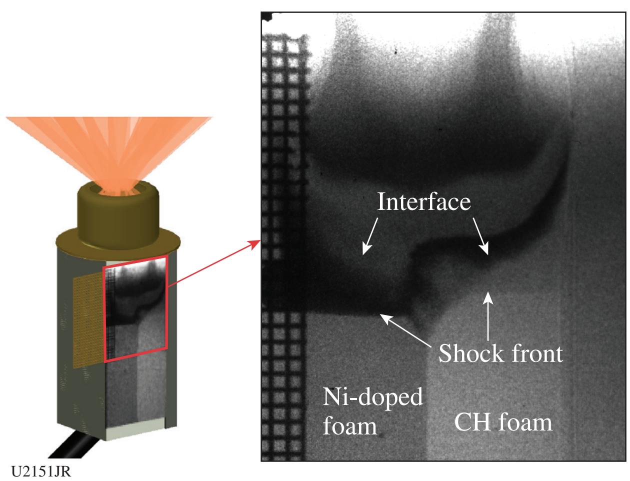

Figure 148.103
The indirectly driven target is shown, with an example of the data collected. The shock appears as a flat line across the foams, with the mixing evident at the foam/plastic interface downstream of the shock.

Development of a Radiography/VISAR Platform for Hydrodynamics Measurements

Principal Investigators: M. Rubery (AWE) and D. Martinez (LLNL)
Co-investigators: G. Glendinning (LLNL); and S. McAlpin, J. Benstead, and W. Garbett (AWE)

Continuing prior work on detailed radiography of hydrodynamic systems, hohlraum-driven experiments were performed over a half-day in FY16 by an LLNL/AWE collaboration using the OMEGA Laser System. The objectives for this campaign were to investigate the evolution of a driven interface using point-projection x-ray radiography, qualify a new simultaneous radiography/VISAR configuration, and obtain drive characterization data using the Dante diagnostic (Fig. 148.104).

For the radiography measurements, a point-projection backlighter was generated through a 20-μm pinhole along the "cranked" TIM-6 axis and recorded with a single-strip gated

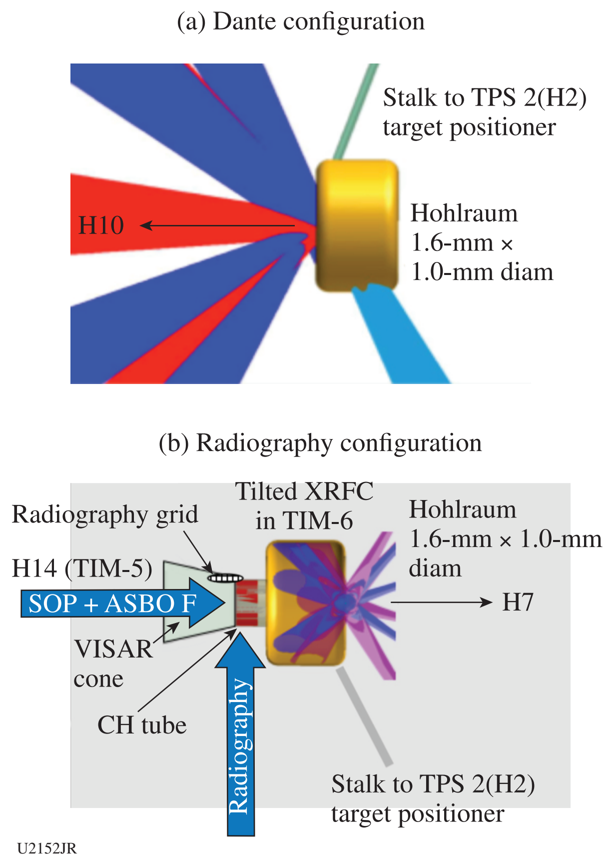

Figure 148.104
(a) Dante-optimized and (b) radiography/VISAR target configurations. TPS: Target Positioning System; XRFC: x-ray framing camera; SOP: streaked optical pyrometer; ASBO: active shock breakout; TIM: ten-inch manipulator.

imager. A quartz window with aluminum flash coating and a light shield cone were applied to the rear of one radiography target, allowing us to make a VISAR measurement along the TIM-5 (port H14) axis. Separate hohlraum drive measurements were performed with hohlraums oriented toward Dante along the H10 axis, using a simplified target with the physics package removed. A 75-J timing laser was incorporated into the Dante configuration to improve cross-timing of each Dante channel.

This half-day of experiments was successful, firing two radiography shots, four Dante shots, and one combined radiography/VISAR shot. Figure 148.105 shows the VISAR data from the combined radiography/VISAR design. Excellent data were recorded on all diagnostics and the experiments met the goals of the HED Program.

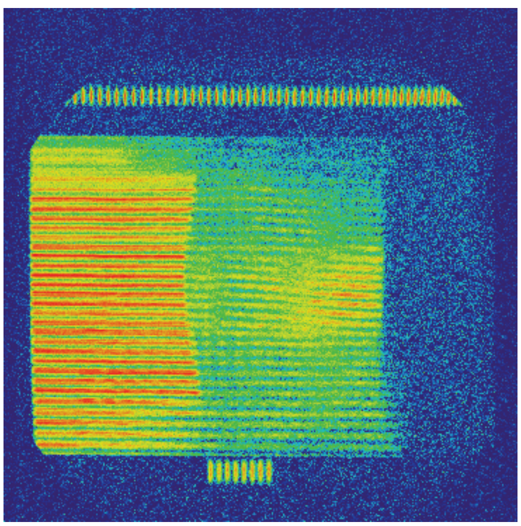

Figure 148.105
VISAR data confirming the success of the new dual radiography/VISAR target configuration.

Proton Heating of Copper Foam on OMEGA EP
Principal Investigator: J. Benstead (AWE)
Co-investigators: E. Gumbrell, P. Allan, S. McAlpin, M. Crook-Rubery, L. Hobbs, and W. Garbett (AWE)

This LLNL–AWE collaborative campaign studied the heating of a cylindrical puck of copper foam irradiated by a short-pulse–generated proton beam. The two major goals of the experiment were to measure the temperature distribution through the target and to quantify the extent of expansion of the rear surface.

The experimental setup is depicted in Fig. 148.106. A gold foil was irradiated with the OMEGA EP sidelighter (SL) short-pulse beam delivering 300 J over 0.7 ps. The SL produced a beam of protons and ions that were used to heat a copper foam puck positioned ~1.8 mm away. An aluminum foil was placed between the gold foil and the copper puck to improve heating by filtering out heavier ions and low-energy protons that would nonuniformly heat the target.

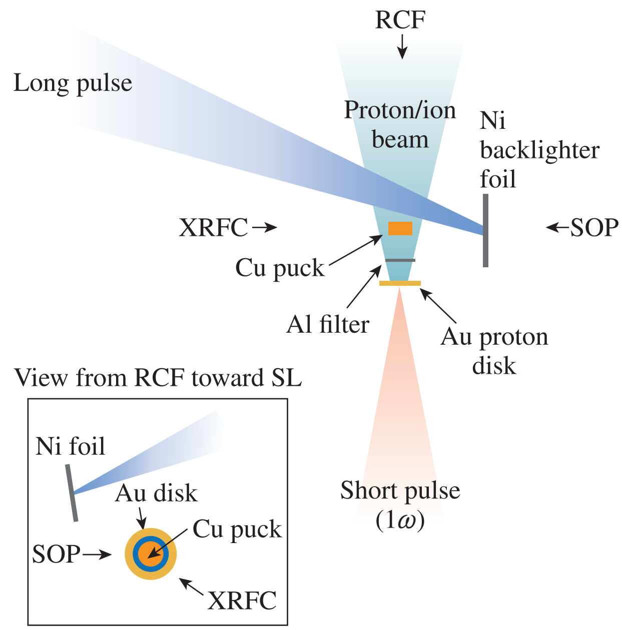

Figure 148.106
Experimental layout for proton-heating shots with combined x-ray radiography, SOP, and radiochromic film (RCF). For simplicity, only one backlighter beam (of the three used) is shown. SL: sidelighter.

The subsequent sample expansion was imaged with an x-ray radiography system. This experimental platform used a nickel area backlighter, irradiated with three long-pulse beams, coupled to an x-ray framing camera (XRFC), which imaged the backlit target. The backlighter (BL) beams were delayed with respect to the SL beam in order to observe the heated and expanded target at different times (see Fig. 148.107).

The SOP diagnostic was fielded orthogonally to the heating axis, with its imaging slit oriented such that the temperature through the central section of the disk could be measured front to rear over the first 5 ns of heating (see Fig. 148.108). In addition, an RCF stack measured the proton/ion beam spectrum on the shot.

In total, six shots were fired, with data acquired on the XRFC, RCF, and SOP diagnostics. The SOP indicated the front surface was significantly hotter, and expanding faster, than the rear surface over the first 5 ns. This agreed well with the XRFC data, which showed that the front surface had expanded while there was minimal rear-surface expansion on most shots.

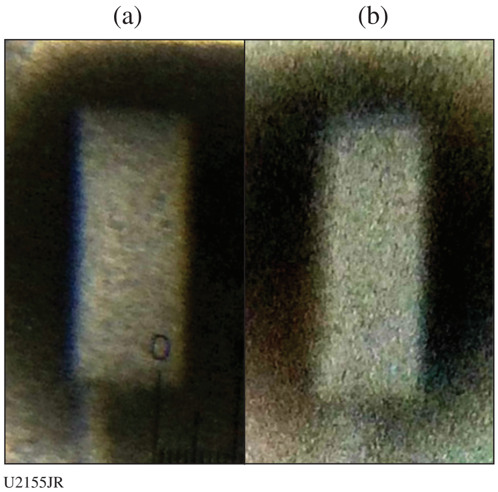

Figure 148.107
Gated x-ray imaging data from (a) an unheated and (b) a heated copper foam puck. For the heated shot, the backlighter was delayed by 20 ns. From this perspective, the protons propagate from left to right through the target. There is clear expansion of the front surface in (b).

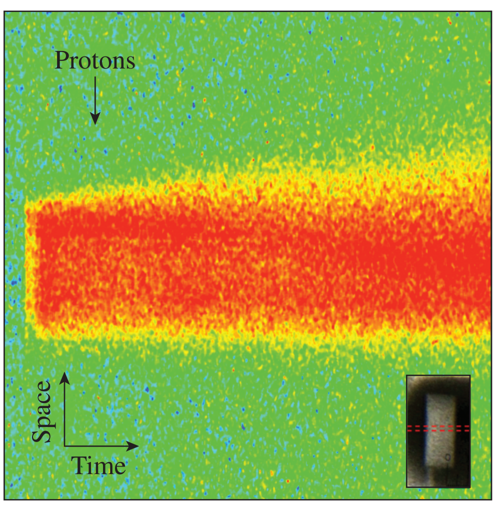

Figure 148.108
SOP data from a proton-heating shot. The insert shows the position and orientation of the SOP slit relative to the target. There is a clear difference between the expansion of the front (proton-facing) and rear surfaces.

4. Plasma Properties

Shock-Front Structure in Multispecies Plasmas
Principal Investigator: H. G. Rinderknecht
Co-investigators: H.-S. Park, S. Ross, S. Wilks, P. Amendt, and B. Remington (LLNL)

Two OMEGA shot days were dedicated to developing a new experimental platform for the study of shock-front structure in low-density plasmas composed of single- and multiple-ion species. In these experiments, 10 or 12 beams deliver 2.1 to 2.7 kJ in 0.6 ns to a thin ablator (2 μm SiO_2 or 5 μm CH) mounted to one end of a CH tube, launching a strong shock into a low-density gas (1 atm) contained within. After thin windows on two sides of the tube are destroyed by ~150 J of laser light, OMEGA's 4ω beam probes the shocked plasma and scatters light that is detected by the Thomson-scattering (TS) diagnostic. Figure 148.109(a) shows the experimental design used on the first day.

High-quality Thomson-scattering data were achieved on several shots, after tuning the destroyer-beam energy and the delay between the destroyer and probe beams. Figure 148.109(b) shows IAW features from a shocked plasma composed of H + 2%Ne, which shows the shock beginning to pass through the TS volume as blue-shifting of the scattered light. Lineouts shown in Fig. 148.109(c) uniquely demonstrate the evolution of a multispecies shock-front structure: the scattered-light feature associated with the hydrogen is blue-shifted (beginning to "shock up") while the peaked neon feature remains static. Analysis of these features shows the hydrogen is heated (T ~ 0.8 keV) and flowing (V ~ 250 μm/ns), while the Ne is cold (T ~ 0.1 keV) and still (V ~ 0)—a multifluid or kinetic phenomenon that cannot be captured in standard single-fluid models.

On the second shot day, single-species (H) and multispecies shocks (H + 2%C) were compared, using predominantly CH ablators. The CH ablators launched weaker shocks than the SiO_2. Further analysis of the TS data is in progress. These results will be used to constrain models of shock-front formation, which are sensitive to kinetic physics and relevant to the shock phase of capsule implosions. The shock-tube TS platform also makes more-detailed shock physics studies possible for laboratory astrophysics.

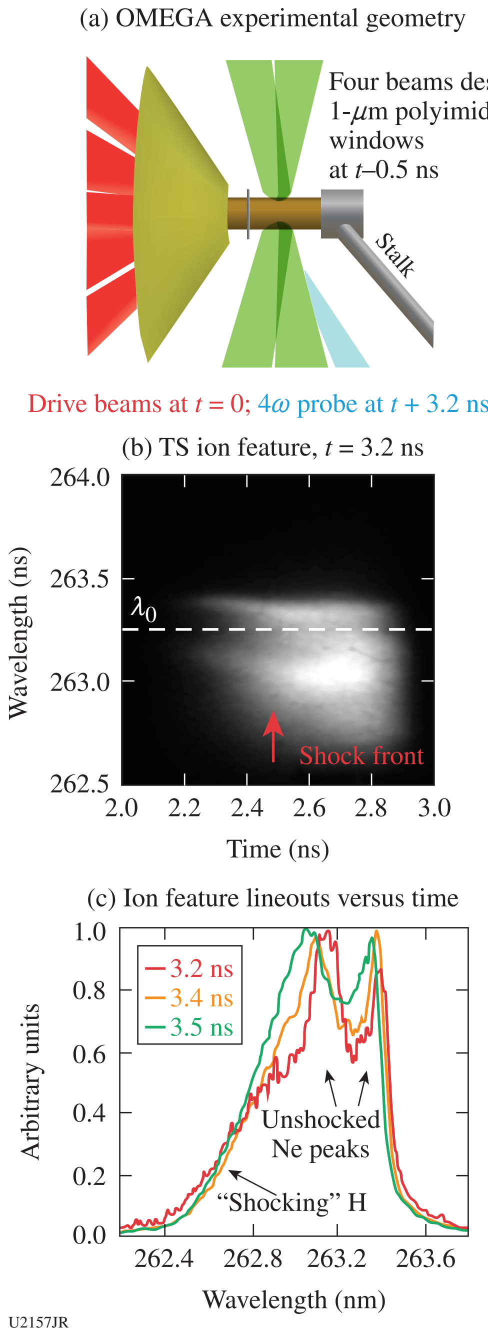

Figure 148.109
Experimental design and results for Thomson scattering (TS) in a shock tube on OMEGA. (a) A 2.1-mm-diam CH tube filled with 1 atm of H(0.98) + Ne(0.02) was shocked by 12 OMEGA beams driving an SiO_2 ablator. The 1-μm-thick CH windows were destroyed using 75 J each in 0.6 ns, allowing a 4ω probe beam and scattered light to pass. (b) Thomson-scattering ion feature recorded on this experiment, showing the evolution of the shock front. (c) Lineouts of the TS ion feature showing kinetic features in the shock evolution: differential velocity and temperature between the H and Ne ion species are observed.

Magnetized Collisionless Shocks for Weapons Effects
Principal Investigator: B. B. Pollock
Co-investigators: H.-S. Park, J. S. Ross, C. Huntington, and G. Swadling

In FY16 the MCLSWEffect Campaign on OMEGA continued an investigation of interpenetrating plasma flows in the presence of background magnetic fields. This campaign employed the MIFEDS pulsed-power magnetic-field system to provide a background field. As illustrated in Fig. 148.110, the field was directed along the direction of a low-density plasma plume that was produced inside the MIFEDS structure, into which a high-density plume was then expanded after a variable delay. The interaction region was probed with Thomson scattering and proton deflectometry to measure the plasma density, temperature, flow velocity, and field structure. This campaign increased the field of view for the proton diagnostic roughly threefold by inserting the proton detector much closer to the interaction than in previous experiments. The analysis of this recent experiment is ongoing and will inform the FY17 continuation of this effort.

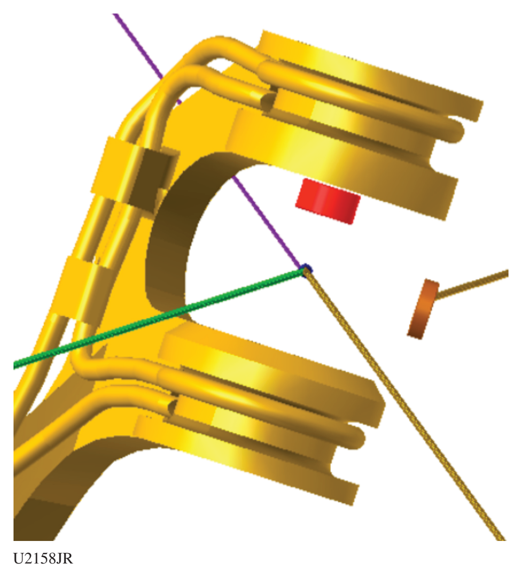

Figure 148.110
The magneto-inertial fusion electrical discharge system (MIFEDS) used in this campaign. The red disk on the upper surface is illuminated by four beams, producing a low-density plasma along the MIFEDS magnetic-field axis. The gold-colored disk on the right then provides the orthogonal plasma plume that interacts with the low-density plasma. The Thomson-scattering volume is at the intersection of the surface normal for these disks, while the proton radiography field of view slightly overfills the MIFEDS interior region.

X-Ray Spectroscopy of Fully Characterized Non-LTE Gold Plasmas

Principal Investigator: R. F. Heeter

Co-investigators: J. A. Emig, M. E. Foord, L. C. Jarrott, D. Liedahl, E. Marley, C. A. Mauche, M. B. Schneider, and K. Widmann

In pursuit of a more-precise understanding of the radiative properties of non-LTE gold, to improve the fidelity of hohlraum x-ray drive simulations for NIF experiments, the AuNLTE-16A Campaign continued a study of laser-heated beryllium-tamped gold/iron/vanadium foils. Prior measurements in FY13–FY15 suggest a need for refinements to an earlier benchmark,[36] involving a higher gold ionization versus temperature, but the plasma conditions and uniformity must be more fully understood. The FY16 campaign acquired both hydrodynamic expansion imaging data and detailed x-ray spectra for various laser-drive arrangements. Data obtained on 11 shots included simultaneous measurements of (1) time-resolved gold M-band spectra from 2 to 5.5 keV, (2) the plasma electron temperature via K-shell emission from helium-like and hydrogenic V and Fe ions, and (3) the plasma density from time-resolved face-on and edge-on imaging of the sample's expansion from its initial size. Preliminary analysis indicates electron temperatures at or above 1.5 keV were obtained, based on the presence of the Ly_α lines for V and Fe. Figure 148.111 provides a sample of the imaging data, which shows highly uniform M-band emission at 1.6 ns into the 3.2-ns laser drive, followed over the next 1 ns by an evolving bright spot suggestive of a radial compression-rarefaction wave. The radial feature is undergoing further investigation. Detailed analysis is expected to deliver improved M-band benchmark spectra for non-LTE models.

5. Material Dynamics and Strength

Copper Rayleigh–Taylor (CuRT) Growth Measurements

Principal Investigator: J. M. McNaney

Co-investigators: S. Prisbrey, H.-S. Park, C. M. Huntington, and C. E. Wehrenberg

The CuRT Campaign is part of the material strength effort, which is aimed at assessing the strength of various metals at high pressure and high strain rate. The goal of the CuRT platform is to measure RT growth of samples that behave "classically," meaning they can be fully modeled using a fluid description. In this series of experiments the intent is to measure RT growth in liquid copper at high pressure, with a second goal of demonstrating the dynamic range of the technique by measuring RT growth in solid copper. The FY16 shots made significant progress toward these goals.

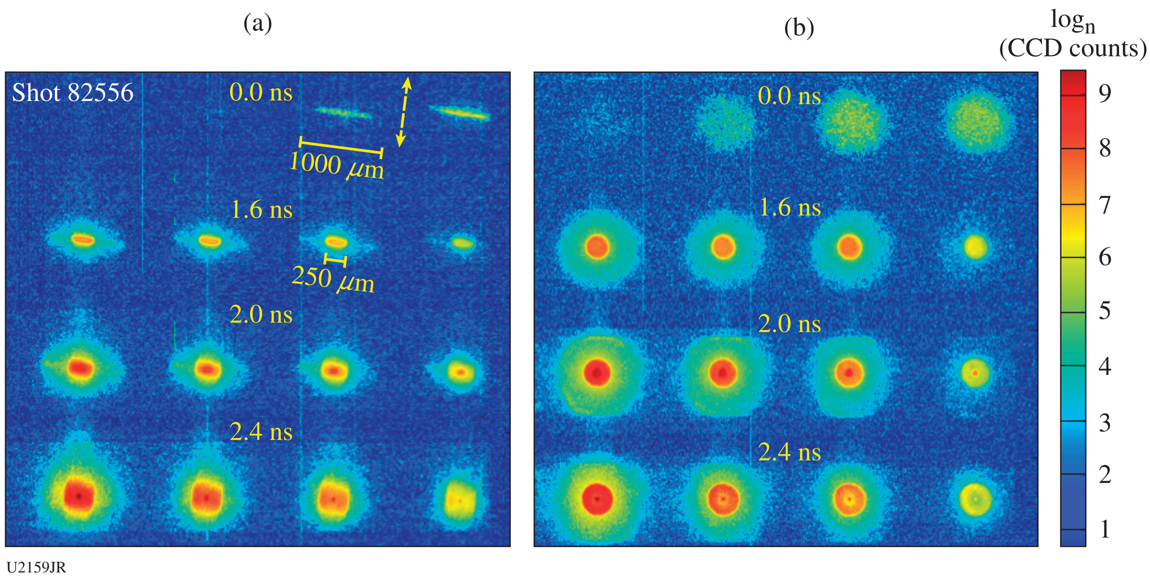

Figure 148.111
Log-scale rendering of gated x-ray images of the circular AuNLTE target. Images were obtained by viewing the target (a) edge-on and (b) face-on. The cameras were synchronized by observing laser turn-on (first row of images). Timing for each strip is labeled in the center, with the gate pulse propagating from left to right along each strip. Target dimensions are provided for the images in (a). The x-ray emission from the 250-μm-diam high-Z sample (orange–red) is visible inside the relatively weak signal from the 1000-μm-diam beryllium tamper (cyan halo). CCD: charge-coupled device.

Without the stabilization of strength, classical RT growth is characterized by a growth rate $\gamma = \sqrt{kgA_n}$, where k is the wavelength of the unstable mode, g is the acceleration, and the Atwood number A_n quantifies the magnitude of the density jump at the interface. Acceleration of the sample in this OMEGA EP experiment is provided by the stagnation of a releasing shocked plastic "reservoir," which is directly driven by ~1 to 2 kJ of laser energy, depending on the desired material condition. The growth of preimposed ripples is recorded using transmission x-ray radiography from a copper He_α slit backlighter source, where the opacity of the sample is calibrated to the ripple amplitude. The pre-shot metrology and measured ρr of the driven sample together yield the growth factor, which is compared to models of RT growth. A gold knife edge on the sample provides a measure of the modulation transfer function, and a step wedge creates an opacity look-up table on each shot, resulting in error bars of approximately ±10%.

In December 2015 a new set of large-spot phase plates was commissioned, and the drive was recalibrated to produce pressure conditions similar to those present during the shots earlier in 2015 with smaller laser spots. Excellent planarity was achieved (Fig. 148.112), and it was established that the laser energy was sufficient to reach the highest pressure condition necessary for the campaign.

Later in FY16, because of a target build that was out of specification, measurements of liquid phase RT growth were delayed, but the targets as built were sufficient to investigate solid-state copper behavior. RT growth data (Fig. 148.113) collected under very similar peak pressures in solid-state copper indicate that data collected using the smaller phase plate diverge from the large-phase-plate data at late times, likely caused by the loss of planarity and more-rapid drop off in ripple driving force. The analysis of this data is ongoing and modeling of the ripple growth is underway. Additional experiments are planned for FY17.

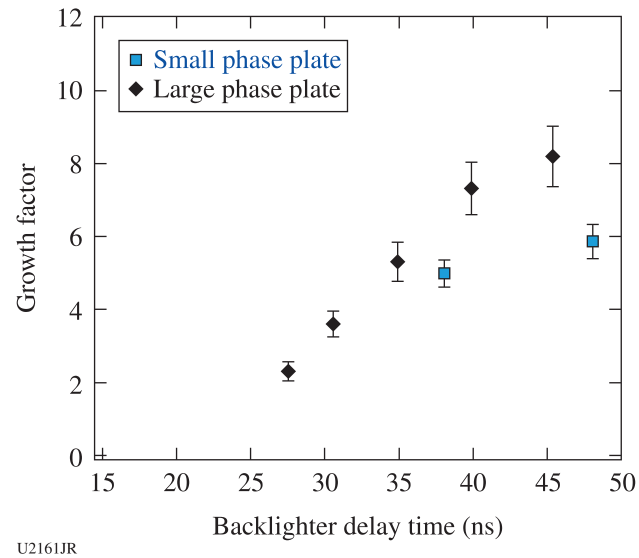

Figure 148.113
Growth factor data for solid copper using small and large phase plates.

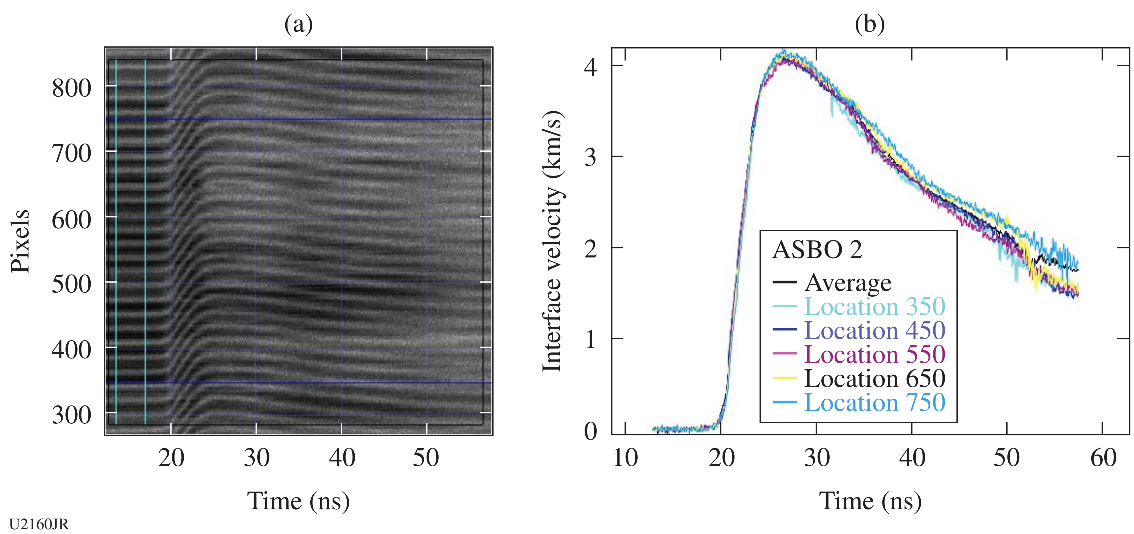

Figure 148.112
(a) The ASBO (VISAR) data from shot 24063 and (b) a series of lineouts taken across the image showing excellent planarity.

Evaluation of Additive-Manufactured Foams for Ramp-Compression Experiments
Principal Investigator: R. Smith

The four half-day AMFoam Campaigns evaluated the use of 3-D–printed or additive-manufactured foams as surrogates to carbonized resorcinol foams (CRF) in ramp-compression target designs, in support of ongoing material strength experiments on the NIF. The 3-D–printed foams were structured as follows: Individually printed lines were grouped into $100 \times 100 \times 16\text{-}\mu\text{m}^3$ "log pile" blocks, which in turn were stitched together to form 16-μm-thick, 1.7-mm-diam layers. Seven of the 16-μm layers were then stacked to arrive at cylindrical "AM foams" that were 1.7 mm in diameter and 112 μm tall. These foams were then glued onto a 25-μm Be + 180-μm 12% Br-doped CH ablator assembly. Following the ramp-compression platform described in Ref. 37, 15 beams of the OMEGA laser with 300 J in 2 ns drive through the ablator and launch the foam across a gap to send a ramp-compression wave into an Al/LiF sample (see Fig. 148.114, lower left), which is diagnosed using 1-D line VISAR viewing the sample off a semireflective mirror. In addition, at a controlled time after this compression begins, the OHRV (2-D VISAR probe) takes a 2-D snapshot of the reflectivity and velocity field with a spatial resolution of ~3 μm (Ref. 38). An example of the intensity field recorded on the 2-D VISAR is shown in Fig. 148.114, lower right. Over the course of the four campaigns the structure of the 3-D–printed foam was varied, with the goal of optimizing the temporal ramp profile.

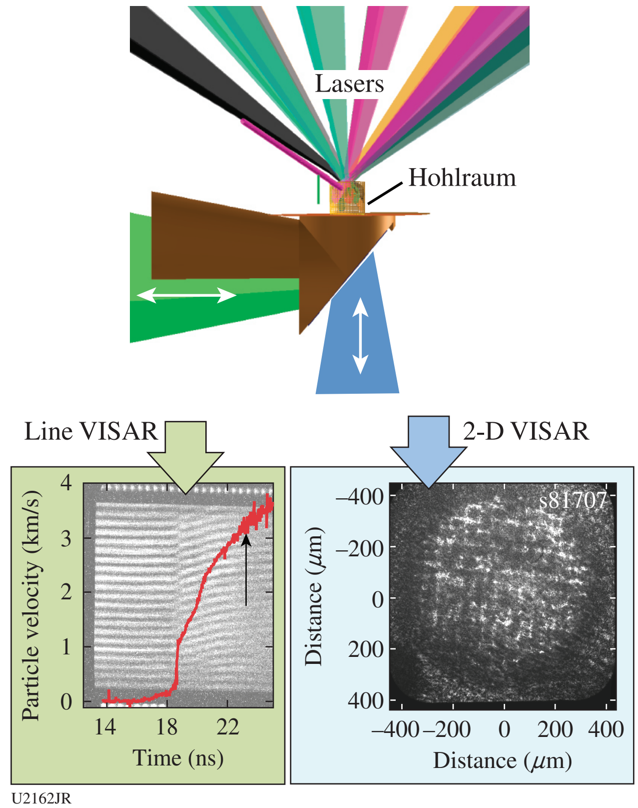

Figure 148.114
Schematic diagram describing the experimental setup for the AMFoam-17C/D campaigns, which combine the OMEGA high-resolution velocimeter (OHRV) and ASBO diagnostics on a single shot. The goal of these shots was to characterize the temporal and spatial drive associated with additive manufactured (3-D–printed) foam targets. The OHRV provided 2-D velocity measurement of the 3-D–printed foams at a snapshot in time. For the AMFoam-17A/B campaigns, only the ASBO (VISAR) diagnostic was used. The preliminary OHRV image (bottom right) shows a grid pattern consistent with the 3-D–printed foams' tiled pattern.

Development of an Experimental Platform for Reflection Diffraction Measurements During Shock or Ramp Compression
Principal Investigator: C. E. Wehrenberg

This campaign seeks to develop a platform for x-ray diffraction *in situ* during shock or ramp compression in a reflection geometry. To measure the strain state of a material in detail, it is necessary to probe the strain in several directions, yet diffraction experiments to date on OMEGA and the NIF have been limited to transmission diffraction in a narrow range of angles of incidence. The ability to measure diffraction in reflection geometry would greatly increase a diffraction experiment's sensitivity to shear strain.

In this campaign, one or two UV beams drove an Fe backlighter, while one or two UV beams drove a shock into an ablator and a sample (Ta or Fe). A 3-D–printed mount held both the sample and a pinhole to collimate the incoming x rays. A separate positioner held an image plate detector, and a shield attached to the backlighter prevented x rays from going straight through to the detector. The campaign tested several configurations for the backlighter shielding, pinhole, and detector filtering and also measured the background created by the sample drive. The campaign was successful in recording the first reflection diffraction signal, albeit a weak signal (as shown in Fig. 148.115). In future work shielding and collimation must be improved to in turn improve the diffraction resolution and signal-to-noise ratio.

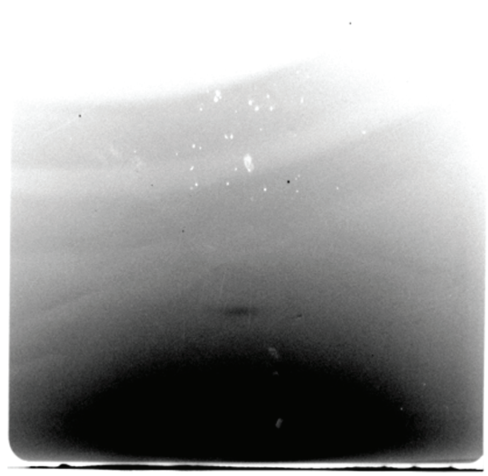

Figure 148.115
Diffraction pattern from a Ta sample in reflection geometry. The two "Saturn ring" broad diffraction lines near the top are an indication that improvements in the x-ray collimation are needed.

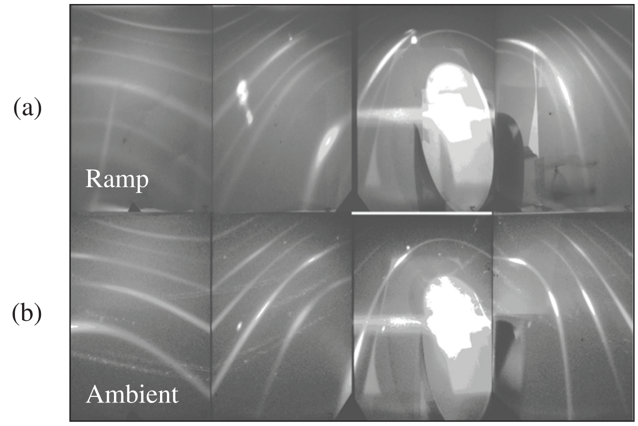

Figure 148.116
(a) Diffraction from (011) fiber-textured, ramp-compressed to 1.6 Mbar. (b) Diffraction from the same (011) fiber-textured sample under ambient conditions.

Understanding Plasticity Mechanisms in Ramp-Compressed Tantalum (OMEGA EP)
Principal Investigator: C. E. Wehrenberg

This campaign seeks to understand the mechanism for plasticity in ramp-compressed Ta, using x-ray diffraction (XRD) to track the texture change. The Ta samples initially had a sharp (011) fiber texture, which allowed one to easily detect subsequent texture changes that develop during compression. Since previous XRD campaigns studying Ta have encountered issues with the diffraction signal from the diamond pusher overlapping the expected Ta signal, this campaign developed a ramp drive using a Kapton ablator/pusher. This OMEGA EP campaign used two UV beams to drive a zinc backlighter and two more UV beams to drive a ramp wave through the Kapton ablator and into the Ta sample. Eight shots were performed, with the first four shots successfully demonstrating a ramp drive to 1.6 Mbar. Figure 148.116 compares the data from an ambient (static, undriven) sample and data from a 1.6-Mbar shot. The change in position of the azimuthal texture spots in the ramp-compressed pattern, when compared to the ambient one, will be used to determine the operative deformation mechanisms.

Understanding Plasticity Mechanisms in Shock-Compressed Tantalum (OMEGA)
Principal Investigator: C. E. Wehrenberg

This campaign seeks to understand the mechanism for plasticity in shock-compressed Ta, using XRD to track the texture change. Similar to the TaStrDiff-16A campaign on OMEGA EP, which used ramp compression, in this campaign on OMEGA the Ta samples initially had a sharp (011) fiber texture, which allowed one to easily detect subsequent texture changes that develop during compression. This campaign used 16 beams to drive a zinc backlighter, and two beams to drive a steady shock through the Kapton ablator and into the Ta sample. A total of 13 shots were performed, scanning a pressure range from 30 to 160 GPa. Figure 148.117 shows example data for an

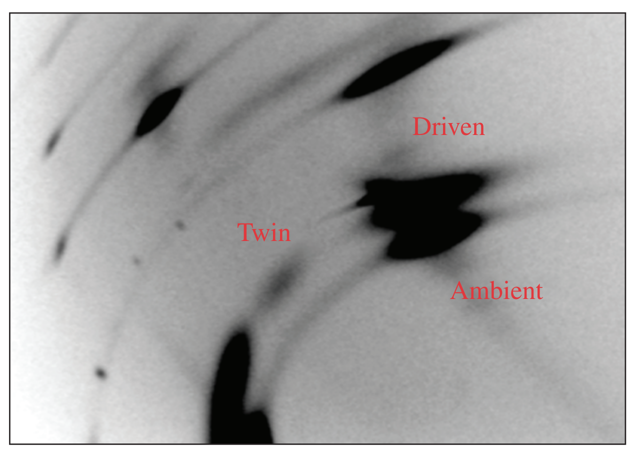

Figure 148.117
Diffraction data for (011) fiber-texture Ta, which has been shock compressed to ~80 GPa. The data were taken as the shock was in transit through the sample, so diffraction patterns from both ambient and compressed (driven) material are observed. A new texture component can be seen in the data from the compressed material, which corresponds to the twinning across the (112) plane.

~80-GPa shock. A new texture component is observed in the data that corresponds to twinning across the (112) plane, which produces a reorientation of the atomic lattice and therefore a change in the diffraction pattern. This type of driven data can now be used to determine the mechanism for plasticity during shock compression.

ACKNOWLEDGMENT

This work was performed under the auspices of the U.S. Department of Energy by Lawrence Livermore National Laboratory under Contract DE-AC52-07NA27344.

FY16 LANL Experimental Campaigns at the Omega Laser Facility

In FY16, Los Alamos National Laboratory (LANL) scientists carried out 22 shot days on the OMEGA and OMEGA EP Laser Systems in the areas of HED science and ICF. In HED we focused on the areas of radiation flow, hydrodynamic turbulent mix and burn, the equations of state of warm dense matter, and coupled Kelvin–Helmholtz (KH)/Richtmyer–Meshkov (RM) instability growth. Our ICF campaigns focused on the priority research directions (PRD's) of implosion phase mix and stagnation and burn, specifically as they pertain to laser direct drive (LDD). Several of our shot days also focused on transport properties in the kinetic regime. We continue to develop advanced diagnostics such as neutron imaging, gamma reaction history, and gas Cherenkov detectors. The following reports summarize our campaigns, their motivation, and the main results from this year.

Shear

The LANL Shear Campaign is examining instability growth and its transition to turbulence relevant to mix in ICF capsules using an experimental platform with counter-propagating flows about a shear interface to examine KH instability growth. The platform consists of a directly driven shock-tube target with an internal physics package. The physics package consists of two hemi-cylindrical foams separated by a layer of tracer material with gold plugs on opposing ends of the foams to limit shock propagation from the direct drive to only one end of the foam. This geometry collimates the shocks and sets a region of pressure-balanced shear flow at the center of the shock tube. Measurements of the tracer layer (shear interface) mixing dynamics are used to benchmark the LANL Besnard–Hazlow–Rauenzahn (BHR)[39] turbulence model. The mixing dynamics are characterized by measuring the mix width of the layer as well as examining multidimensional structure growth along the layer's surface.

The FY16 Shear Campaign continued an effort to examine instability and model initial condition parameter space by varying the characteristics of the target tracer layer. Both FY16 shot days were part of a three-shot-day study of instability mode growth caused by single-mode initial conditions, which employed sinusoidal tracer foils of various wavelengths as opposed to the previous flat and roughened foil campaigns. The sinusoids force instability growth by pre-seeding a coherent wavelength. In these experiments we observed (Fig. 148.118)

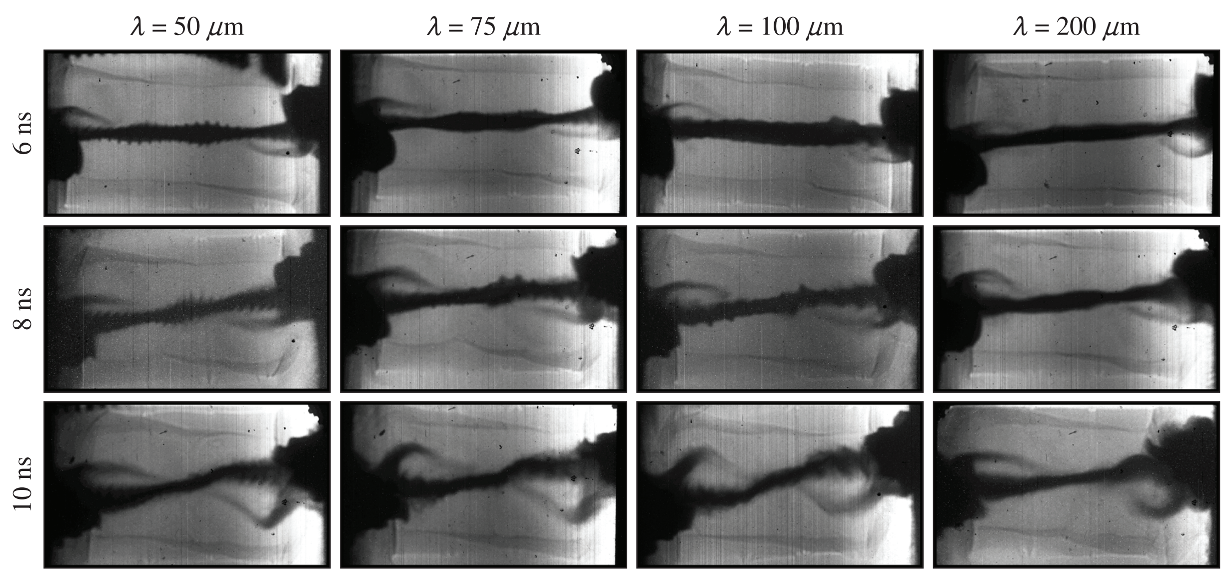

Figure 148.118
X-ray backlit images of a counter-flowing shear experiment showing the evolution of foil tracer layer at different perturbation wavelengths.

early-time (pre-shear) jets and "dust-up" structures, which are points of further study, as well as the persistence of the single-mode structures to late times in the experiment. The finished OMEGA mode growth study also confirms a most-unstable mode of $\lambda \approx 100$ to 150 μm, as predicted by observations of emergent rollers in our NIF experiment and a naïve application of the simple Rayleigh model.

Double-Shell Planar

The LANL Double-Shell Planar (DSPlanar) OMEGA Platform is part of the larger LANL Double-Shell Campaign. The DSPlanar experiments are intended to validate our ability to predict momentum transfer, hydrocoupling, and instability growth in a double-shell–relevant planar geometry. We choose to use a planar geometry since it is simpler to diagnose than full spherical implosions and can still give us an idea of how well the code simulates fundamental pieces of physics without the added complication of convergence. DSPlanar experiments serve a second purpose as a testing ground for the development of our target fabrication capability toward NIF double-shell capsules. DSPlanar target components will use similar materials as NIF double-shell targets but in a simpler-to-build geometry. We can use fabrication of these simpler parts as a first-pass test of our abilities and to identify where we require further R&D resources. The goals of this first DSPlanar shot day were to measure momentum transfer of an ablatively driven flyer into a mid-Z "inner shell" layer, as well as to test NIF-relevant ablator materials.

The DSPlanar target is an indirectly driven shock tube with a material stack approximating an unfolded double shell, with an ablator, a low-density foam cushion, an inner shell surrogate layer, and a final release foam. We varied on whether or not to include a tamper layer on the inner shell layer as part of our hydro-instability mitigation studies. The primary diagnostics for the FY16 DSPlanar day were edge-on streaked and imaging radiography (Fig. 148.119). The streaked radiography was designed so that measurements of inner shell preheat expansion, ablator velocity pre-impact, and system velocity post-impact for momentum transfer studies could be obtained. On this shot day we identified modifications to the platform required for good streak data and good imaging data. We also obtained data that compared our standard sample Be ablator targets and AlBeMet (Al/Be alloy) targets required to inform FY17 decisions about our NIF platform.

Marble

In the Marble project, nuclear reactants of an ICF implosion are initially separated via a spherical low-density CD foam matrix infused with a T_2 gas fill. Through advanced target fabrication, voids can be selectively etched into the foam core to control the initial separation scale. These cores are encapsulated within a machined ablator and imploded in 60-beam direct-drive implosions with the key measurements being D–T and D–D yields. In the FY16 OMEGA experiments, targets were

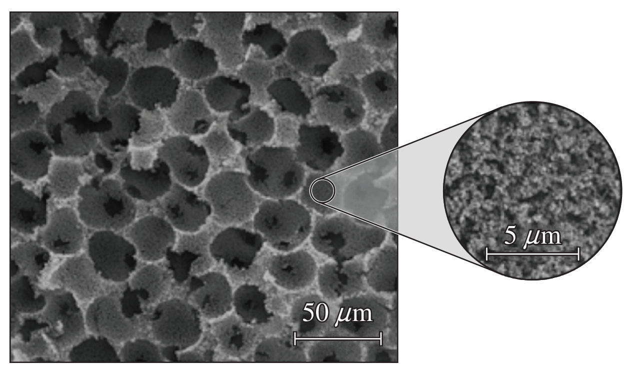

U2062JR

Figure 148.120
Marble CD foam with etched 30-μm voids.

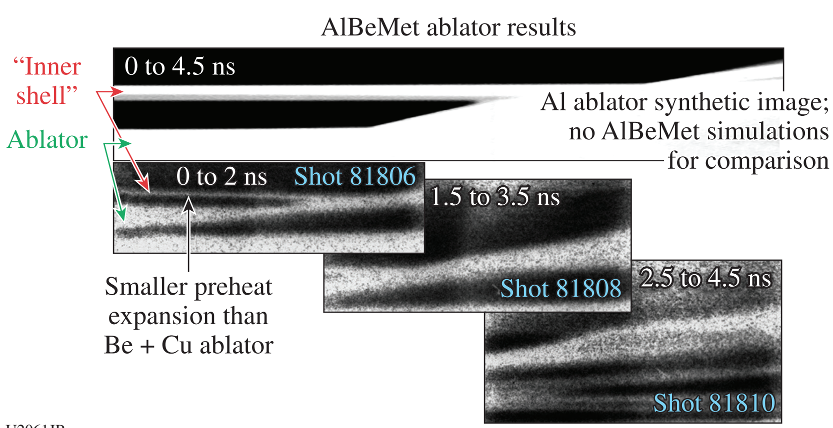

U2061JR

Figure 148.119
Backlit streak data viewing edge-on of the planar double-shell experiment

imploded with an intrinsic foam structure as well as foam with engineered voids. Figure 148.120 shows an image of such engineered foam. Most recently, target improvements (full deuteration, advanced machining) resulted in an order-of-magnitude increase of D–T and D–D yields. We are currently awaiting an estimate of as-shot conditions, which we will then use to calculate a normalized ratio of the yield of the D–T reactions to D–D reactions—the key metric for comparison to theory.

Marble Void Collapse

Marble is an experimental campaign intended to study the effects of heterogeneous mix on fusion burn. While designing the Marble implosion experiments, three questions emerged: First, how well do we understand the evolution of voids as the shock passes through? Is the evolution turbulent? Second, how well do we understand preheat inside our capsules? And finally, how accurate is the equation of state used for marble foams? To answer these questions, we designed an experimental campaign known as Marble Void Collapse. The idea was to take the well-understood shock-shear platform and modify it to answer these three questions. For the first type, a fine-cell 100-mg/cm^3 CH foam filled the Rexolite tube as shown in Fig. 148.121(a). Inside the foam, a sphere composed of iodine-doped CH foam (or tin-doped SiO_2 foam) was inserted. The density was chosen to be ~40 mg to give a similar Atwood number found in voids in the NIF foam capsules. The iodine (or tin) dopant provided a contrast with the vanadium and titanium backlighters. Figure 148.121(b) shows the second type, where a 6-μm-thick aluminum foil was embedded inside the shock tube to examine the expansion of the foil by preheat and measure the spread as the perturbed shock passed through the foil. The last type [shown in Fig. 148.121(c)] was filled with a marble CD foam where the void size was 50 μm in diameter. Throughout these three experiments, high-quality radiographic data were acquired. The experimental result shown in Fig. 148.121(d) appears to confirm that the evolution of the void is not turbulent as the initial shock passes, seen in simulation. Also, the shock timing between simulation and experiment is well matched. This suggests an accurate understanding of the fine-pore foam's equation of state. As shown in Fig. 148.121(e), preheat effect was examined by the expansion of aluminum foil before a shock arrives. Figure 148.121(f) shows the shock speed measured through marble foam (50-μm-diam pore size), which can be used to determine the equation of state of the marble foam.

CoaxDiff

The COAX Experimental Campaign on OMEGA develops an advanced radiation flow diagnostic that can be used to characterize the subsonic and supersonic radiation front to provide constraining data for physics models. The intention is to eventually move these experiments to the NIF. In these experiments, a halfraum is used to launch a radiation front down a cylindrical foam target (contained by a Be sleeve) (Fig. 148.122). The subsonic radiation front is measured by imaging, while spectroscopy of a doped insert in the target is utilized to study the supersonic form of the radiation front by observing its impact on the ionization balance of the dopant. Originally Ti was used and was able to provide constraining data to the shape of the radiation front by comparison to *PrismSPECT* simulations. However, Ti K-shell absorption spectra were unable to probe

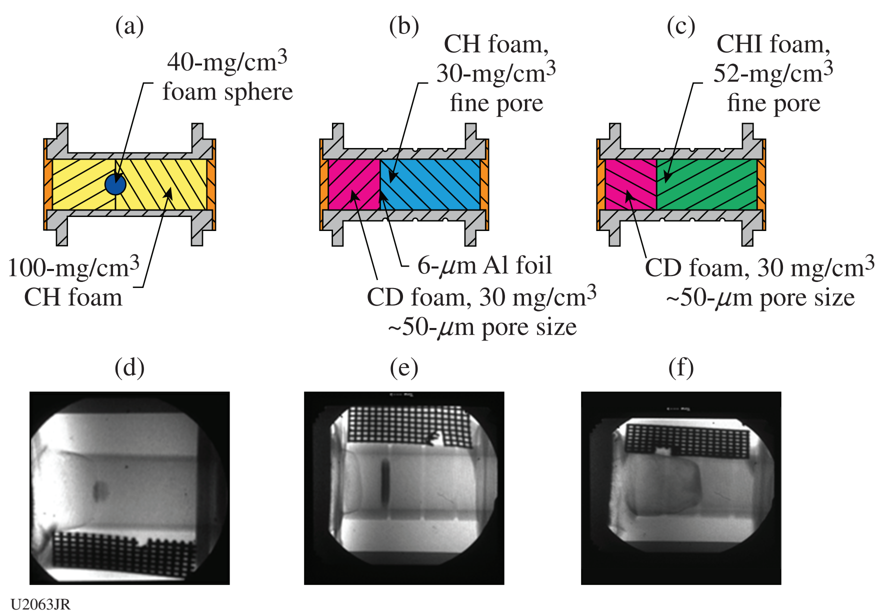

Figure 148.121
The three Marble Void Collapse setups [types (a), (b), and (c)]. (d) Evolution of void was not turbulent; (e) preheat effect was examined by the expansion of aluminum foil; (f) shock speed measured through marble foam (50-μm-diam pore size) can be used to determine the equation of state of marble foam.

the shape of the front at temperatures below 100 eV. To probe the potentially non-Planckian character of the radiation front below 100 eV, we elected to shift to a Sc dopant. Because Sc has a lower Z than Ti, it requires less energy to exceed the ionization potential; therefore K-shell absorption spectra will occur at lower photon energies and lower temperatures than Ti. For both elements, absorption spectra are observed when photons generated by the laser-driven backlighter pass through the target and interact with electrons in auto-ionizing states in the L shell, which enables them to transition to a hole in the inner shell. At the current photon energy range of the NIF-5 spectrometer, Ti $1s$–$2p$ and Ti $1s$–$3p$ spectra are observable, but only Sc $1s$–$3p$ spectra are observable.

Three shot days were dedicated to COAX in FY16. In October 2015 imaging data and absorption spectra were observed for Ti, and proof of principle was established for Sc by collecting Sc $1s$–$3p$ absorption spectra for the first time with the NIF-5 (Fig. 148.123). In April 2016 excellent image data of the doped aerogels were collected for both Ti- and Sc-doped foams, but issues with the spectroscopic backlighter resulted on only weak spectra being collected. In August a Kr-filled capsule backlighter design was successfully tested against a redesign of the previous wire backlighter, and a number of shots of strong Sc absorption spectra were collected using both backlighters. Initial data analysis suggests the T_e measured by the Sc was in the 75- to 90-eV range. No imaging data were collected in August, but we instead used the space to collect constraining information about the size, brightness, and symmetry of the capsule backlighter that would be used for the next set of experiments.

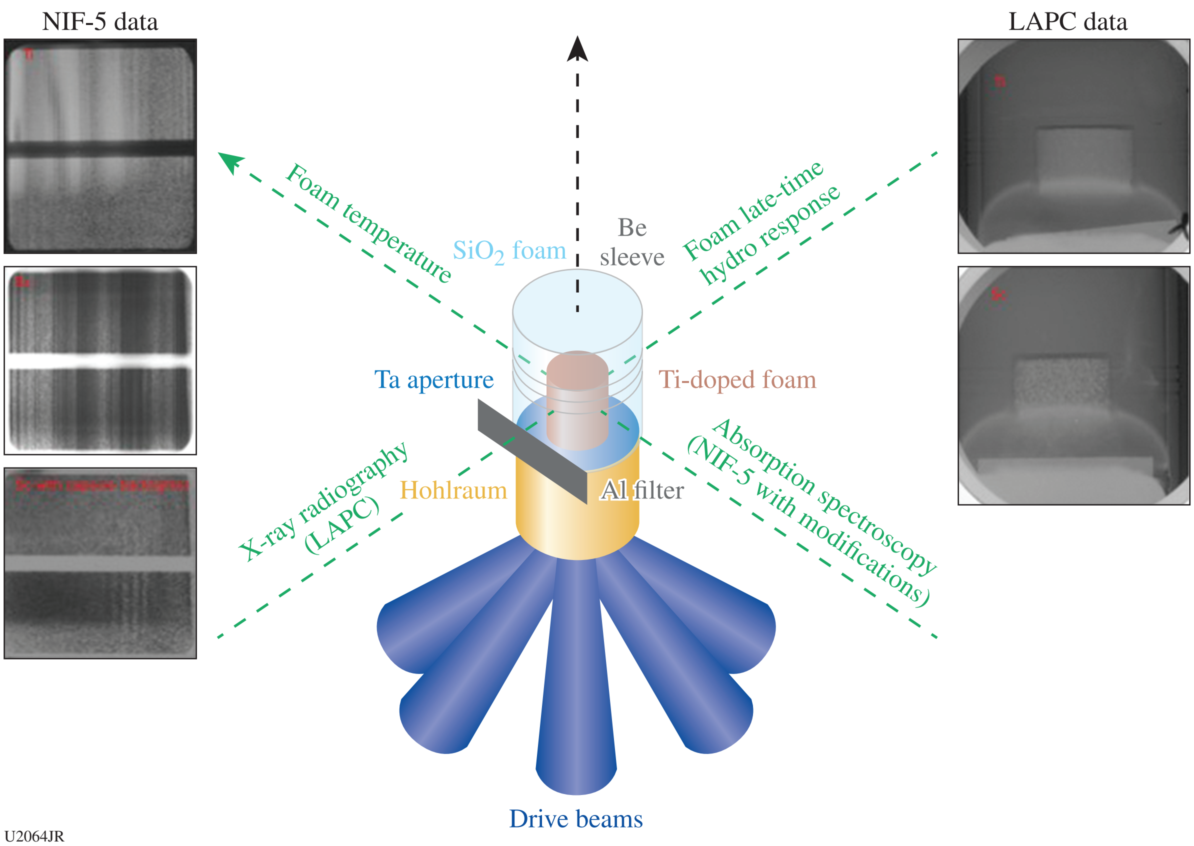

Figure 148.122
(a) Data collected for Ti from a prior year are compared to data from the latest shots with Sc in August. (b) Two radiographs from April with Sc- and Ti-doped aerogels. LAPC: LANL pinhole camera.

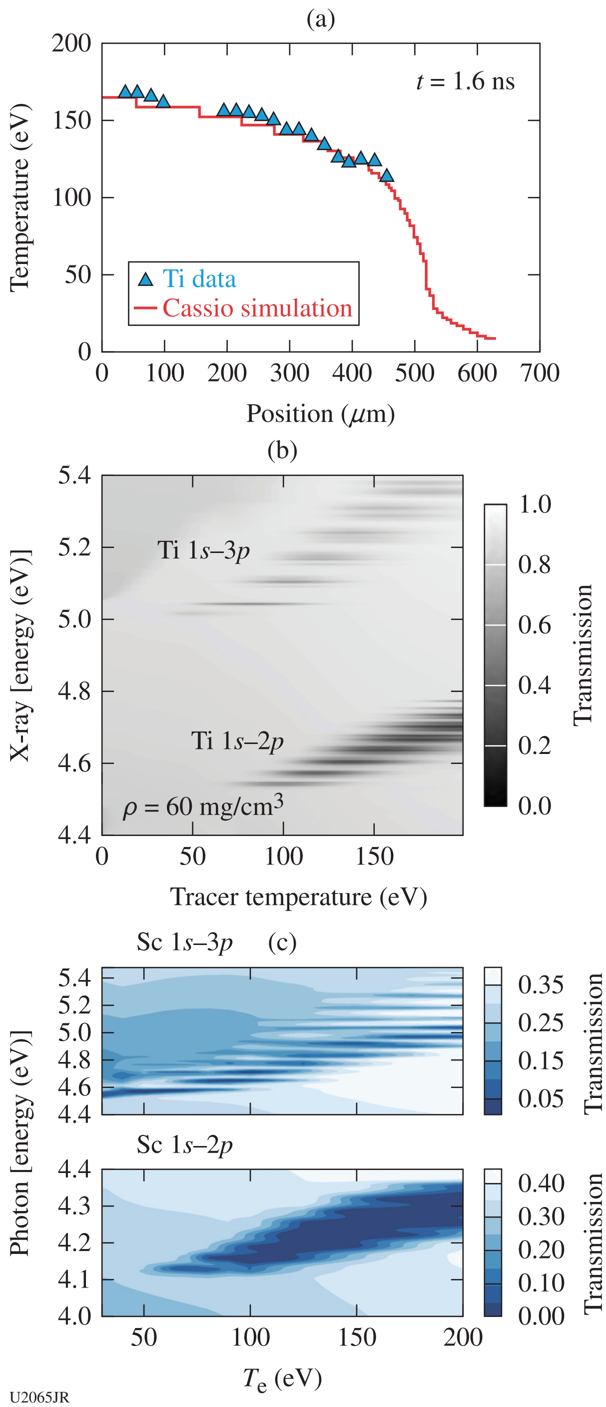

Figure 148.123
(a) The shape of the radiation front in simulation is compared to results from COAX experiments featuring Ti-doped aerogels. Simulated K-shell absorption spectra from *PrismSPECT* for (b) Ti and (c) Sc illustrate the change in temperature and photon energy distribution of lines for the same transitions in two different elements. These figures were presented at the 2016 High-Temperature Plasma Diagnostics Conference.

HEDmix

Anomalous low modes (particularly mode ~1) have been postulated as the cause of low hot-spot pressure of mid-adiabat implosions on OMEGA direct drive.[8,40] In the 2016 HED-MIX campaign, images captured emission signatures near stagnation, which are consistent with the presence of such hypothesized low-mode imbalance. The experiments used warm implosions with a Ti tracer at 1% by atom in the innermost 100 nm of the plastic shell. The Ti tracer emission was resolved spectrally using a unique imaging instrument termed the "multiple monochromatic imager" (MMI).[41] Figure 148.124(a) shows an image obtained from 5- to 6-keV Ti emission at time of peak neutron production. A mode-1 pattern appears in the emission and is quantified (~70% drop) in Fig. 148.124(b). Such a pattern appeared systematically within the day, although capsule mounting was excluded as the cause. Using 3-D modeling with LLE's *ASTER* code,[40] we found that such asymmetric emission results when such anomalous low modes are included in the drive. In the calculation, the emission drop results from reduced temperature on the overdriven side of the capsule where the tracer layer is compressed to a higher density. To quantifiably estimate this density imbalance from the data, first the measured spectrum is modeled [see Fig. 148.124(c)] to determine the tracer conditions from the emissive region ($n_e = 5.75 \times 10^{24}$ cm^{-3}, $T_e = 1350$ eV). Beginning with these conditions, Fig. 148.124(d) shows the reduction in observed emission as density increases and temperature is decreased under assumption of pressure balance. Similar to the type of density modulations observed in the simulation, the results suggest about 50% variation in density of the emissive layer across the observed mode-1 pattern.

HKMix

Mix is an important degradation mechanism for ICF and there is a programmatic need for strong benchmarks for mix models. A new experimental platform was developed, on this shot day and on THDGamma-16A, to study mix. Differentially thresholded gas Cherenkov detectors (GCD's) measure the γ-ray signal from a HT-fueled implosion with a deuterated shell, so that the HT burn comes from the core, while the D–T reactions occur from any mix of shell material into the hot spot. The detector with lower gas pressure (higher threshold) is more sensitive to the HT γ's. On this experiment, 860-μm-diam shells of 9- or 15-μm-thick plastic, with a 0.25-μm-thick inner deuterated layer, were filled with 9 atm of equimolar HT gas. A simultaneous forward fit to the two detectors was then used to infer both DT and HT burn histories. The data from shot 80348, which used a 15-μm-thick shell, are shown in Fig. 148.125. The difference in time between the core and mix burn will be used to constrain time-dependent mix models. In this shot, the mix signal (DT) comes about 70 ps later than the core (HT) burn. This result is corroborated by a second analysis technique that uses a surrogate shot without the deuterated layer, clearly showing that the core (HT) signal comes early. The data from the 9-μm-thick shells show, in contrast, that the mix (DT) signal

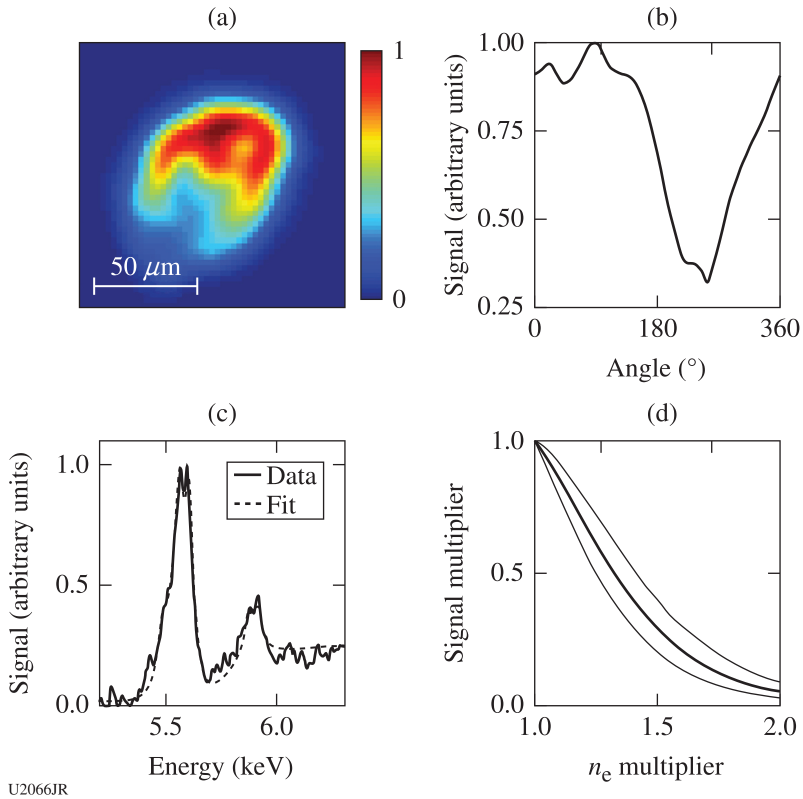

Figure 148.124
(a) Bang-time image of Ti emission from 5 to 6 keV; (b) peripheral signal versus angle; (c) measured multiple monochromatic imager (MMI) spectrum and fit; (d) modeled scaling of emission as density increases over nominal value from spectral fitting.

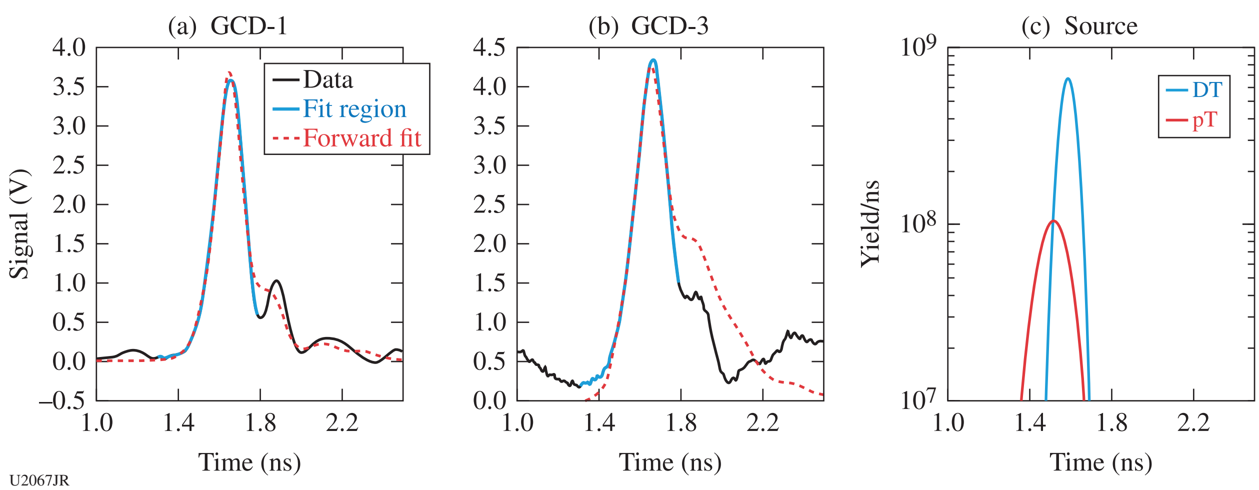

Figure 148.125
Cherenkov data from two detectors on shot 80348 using (a) 100 psi of CO_2 and (b) 30 psi of CO_2 on a mix shot. (c) The data are simultaneously forward fit using burn histories for pT and DT reactions to infer the difference in time between the core (pT) and mix (DT) burn.

comes earlier than the core burn, suggesting the importance of a nonhydrodynamic mix process. This technique will be used over future campaigns by varying implosion parameters to study mix under various conditions.

MSP

Measuring charged-particle stopping power (MSP) in dense plasmas relevant to ICF is challenging. The MSP-16A shot day tested a new technique based on measuring charged-particle downshift in the compressed shell of an implosion. The target design is shown in Fig. 148.126. A thick (25-μm) CH shell is imploded with a fuel mixture of D/T/^{3}He. The DT-n inelastically scatter on the C in the shell, producing 4.4-MeV γ rays that are detected with the GCD's, thereby measuring the areal density of the shell at peak burn. Simultaneously, the 15-MeV D^{3}He protons are emitted and slow down as they transit the shell. The proton downshift gives a measurement of the average stopping power in the shell. A preliminary proton spectrum (Fig. 148.126) shows the proton downshift from its birth energy. X-ray spectroscopy [Fig. 148.126(c)] was also used to characterize the plasma conditions in the shell, analyzing absorption lines produced by a 2% atomic Ti dopant in the shell. Analysis of the proton, x-ray, and γ-ray data is continuing.

ZSP

The ZSP-16A Campaign studied charged-particle stopping power in warm dense plasma. The experimental concept was based on previous successful experiments in Be samples.[42] The experimental concept is shown in Fig. 148.127(a). The subject target is a 500-μm-thick graphite cylinder, doped with 1% atomic Pd, which is placed inside a Ti-coated tube. The tube is illuminated by 30 of the OMEGA laser beams, and the

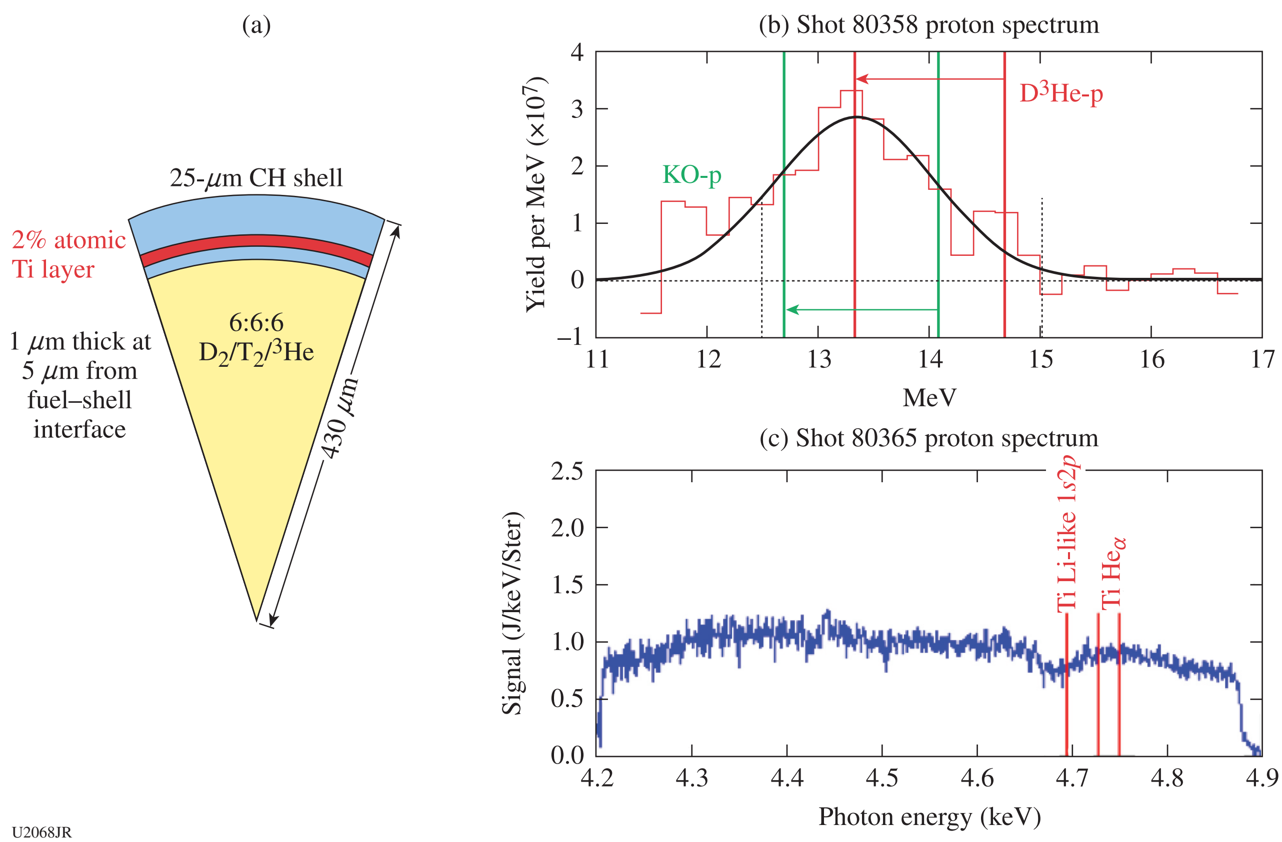

Figure 148.126
(a) Target pie diagram. (b) The D^{3}He proton spectrum measured on shot 80358, where the D^{3}He protons are downshifted from their birth energy by about 1.5 MeV. Knock-on (KO) protons are also observed, at lower energies, from elastic neutron scattering. (c) The Ti-doped layer in the shell is used for absorption spectroscopy to diagnose the shell's plasma conditions.

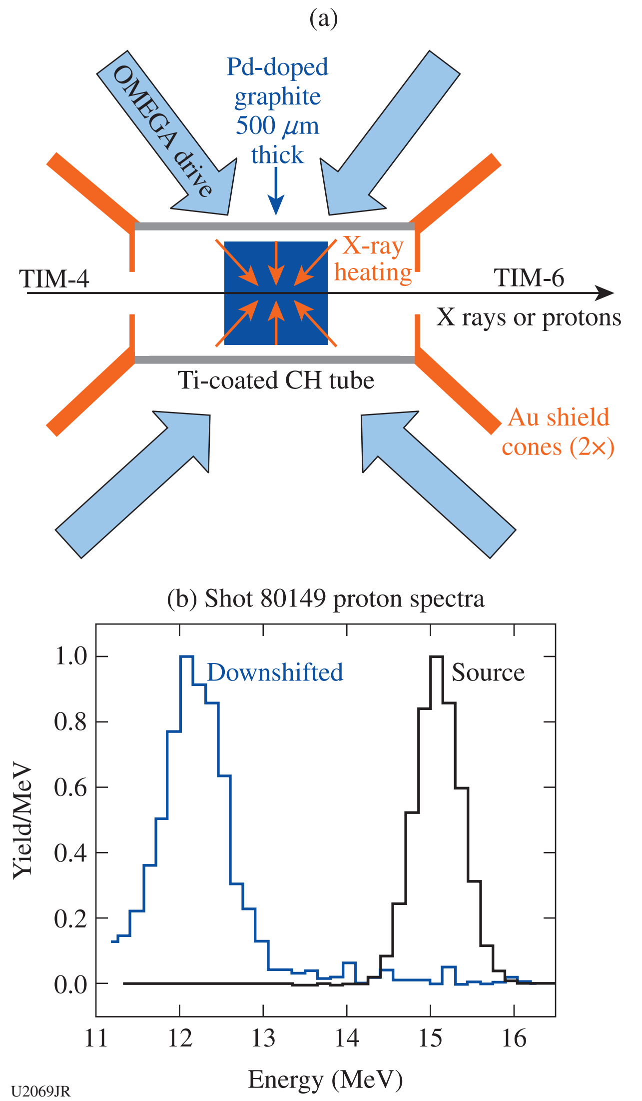

Figure 148.127
(a) ZSP-16A experimental schematic and (b) proton spectra. A cylindrical sample of Pd-doped graphite is heated isochorically by x rays generated at the outer surface of a Ti-coated tube. Probing protons or x rays sample the graphite along the axis. A sample proton spectrum from shot 80149 (peak normalized) is shown at right in (b).

Ti x-ray emission isochorically heats the graphite sample. Au shield cones are placed on each end of the cylinder to shield the diagnostic line of sight from the laser spots. The sample is probed by protons or x rays along the TIM-4/TIM-6 axis.

Preliminary proton data from shot 80149 are shown in Fig. 148.127(b). The proton source is a directly driven exploding pusher, which creates an isotropic flux of 15-MeV D^3He protons. The source spectrum is measured directly. The proton spectrum after transiting the graphite sample is also measured. The proton downshift is a direct measurement of the average stopping power in the sample. Additional proton data are being analyzed. X-ray absorption data from the Pd dopant will be analyzed to infer the plasma conditions.

THDGamma

The HT fusion reaction produces a mono-energetic γ ray at 19.8 MeV. Thresholded Cherenkov detectors, like the GCD's,[43] are relatively more sensitive to higher-energy γ than the DT γ [see Fig. 148.128(a)]. The THDGamma-16A Campaign was conducted to demonstrate the detection of HT γ and study the signals observed under different implosion conditions. CH

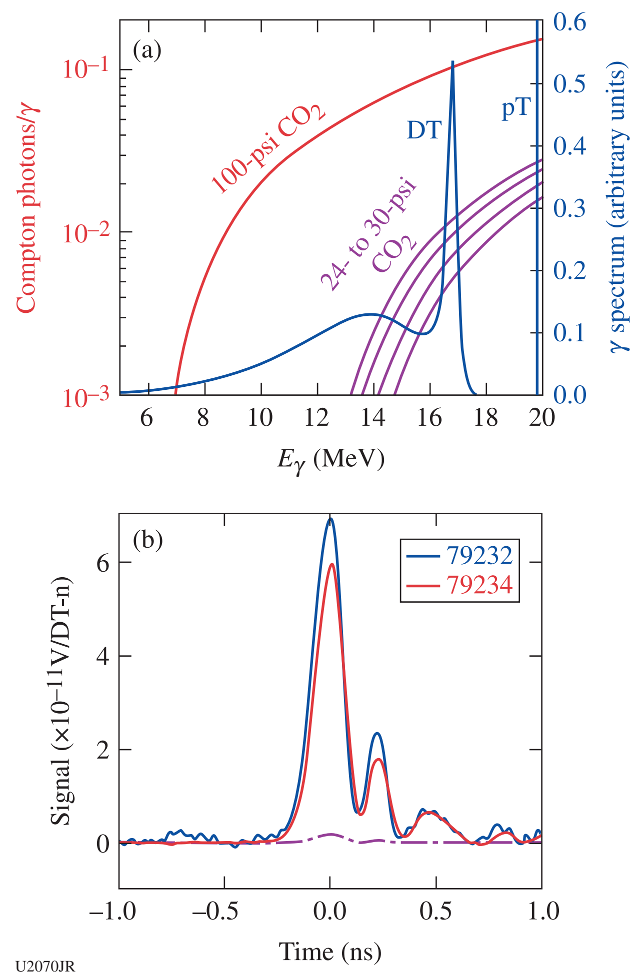

Figure 148.128
(a) Cherenkov detector response for various pressures of CO_2 gas compared to the γ-ray spectrum from DT and HT fusion. The detector's relative sensitivity to HT γ increases for the lower gas pressures. (b) Signal from two $H_2 + T_2$ fueled implosions, normalized to the DT-n yield. The GCD was fielded at 100-psi CO_2. The dashed curves represent the signal contribution from DT-γ based on the measured DT-n yield, from a 0.1% D impurity. The signal is dominated by HT-γ, the first definitive detection of these γ rays in ICF implosions.

shells (9 or 15 μm thick, 860 μm in diameter) were filled with an equimolar mixture of H and T, with either 0.1% or 2.0% D contamination. The shots with 0.1% D [Fig. 148.128(b)] show that the detector signal at 100 psi of CO_2 is dominated by the HT γ, as expected. This is the first definitive detection of these γ rays produced from an ICF implosion. As the D concentration is increased, in the initial gas fill or due to mix (e.g., from a CD shell), the relative importance of the DT γ contribution to the total signal increases. By using differentially thresholded detectors, both reactions may be measured simultaneously. This technique will be used in an upcoming LANL mix campaign. Preliminary shots with deuterated shells were also taken on this day and used to iterate the implosion design for the subsequent experiments (HKMix-16A).

WDFEOS

The WDFEOS experiment collects valuable information for understanding the equation of state of warm dense matter (WDM) under shocked conditions along the Hugoniot. The explored WDM conditions are relevant for ICF and the interiors of Jovian planets. On the WDFEOS shot date in February 2016, low-density CH foams under shock compression in the 1- to 4-Mbar range were studied using SOP and VISAR to measure shock velocity using shock breakout timing. After every VISAR/SOP shot there was an x-ray Thomson-scattering shot, with the imaging x-ray Thomson spectrometer (iXTS) looking at scattering from the Ni He$_\alpha$ line at 7.8 keV, timed based on the shock breakout of the prior shot. Note in Fig. 148.129 that the two types of targets have a different design to serve different purposes—the VISAR target includes a stepped foam to aid in the shock breakout measurement (Fig. 148.130), while the iXTS target includes a thin Ni foil used to probe the shocked foam with 7.8-keV x rays. The iXTS was used to primarily measure the temperature of the shocked foam.

An analysis of x-ray Thomson-scattering (XRTS) probe data (Fig. 148.131) so far demonstrates that as the shock progresses through the foam in time, there is a clear increase in T_e that appears as spectral broadening in the inelastic scattering feature. This also appears in time-integrated spectra within

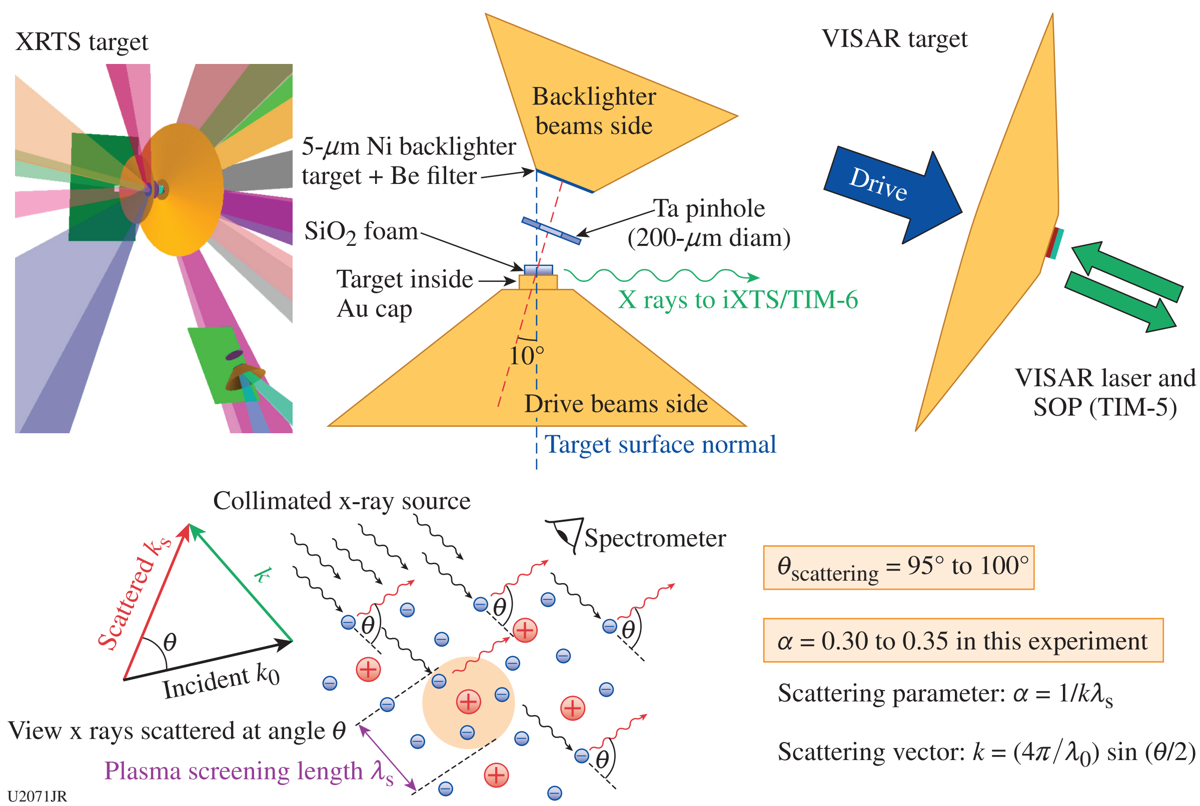

Figure 148.129
Schematics of the two types of targets used in WDFEOS experiments, as well as a simple explanation of the x-ray Thompson-scattering phenomenon. iXTS: imaging x-ray Thomson spectrometer.

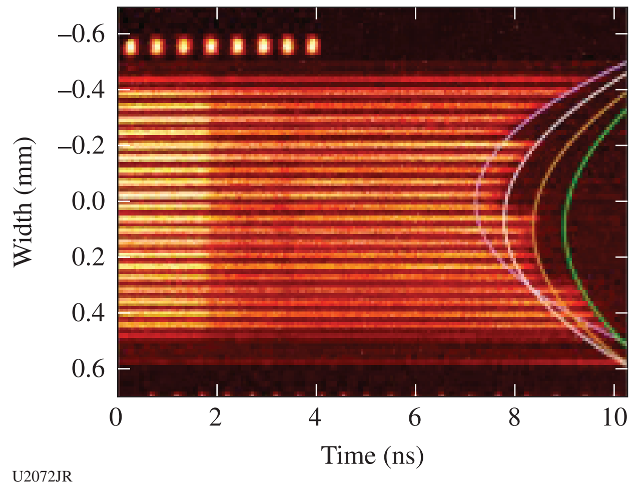

Figure 148.130
Parabolic fits to VISAR data determine shock velocity based on shock breakout time. For shot 80371, shock velocity is 82 to 95 km/s at 5.5 ns, 75 to 87 km/s at 6.0 ns, and 67 to 81 km/s at 6.5 ns.

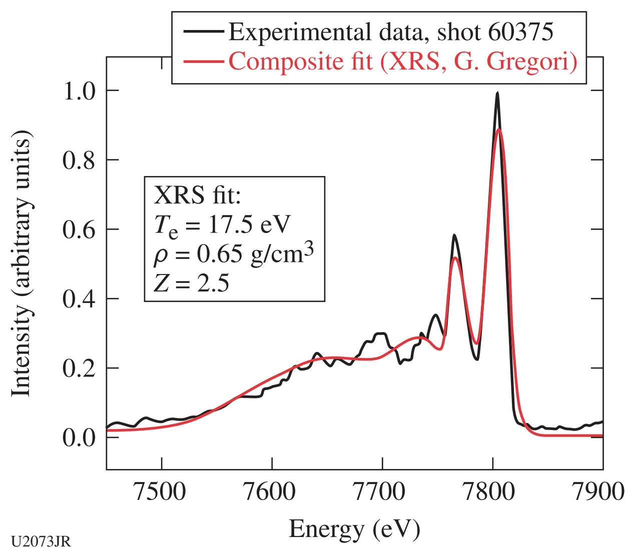

Figure 148.131
Temperature is determined by evaluating fits to the imaging x-ray Thomson spectrometer (iXTS) spectra after accounting for red-shift, contamination from blowoff plasma from the backlighter, and other corrections. XRS: x-ray scattering

the same shots (i.e., the shock propagates down, and upper profiles are wider and hotter). This increase of T_e with time is indicative of preheat. Simulations including up to 5 to 10 eV of preheat show little change to final temperature but expansion in the preheated foam reduces the initial density and results in higher shock speeds. This estimate is in agreement with SOP and VISAR analysis that shows higher shock speeds than previous experiments.

MixEOS-EP

Accurate simulations of fluid and plasma flows require accurate thermodynamic properties, which is typically represented by the EOS of the materials. For pure materials, the EOS may be represented by analytical models for idealized circumstances, or by tabular means, such as the *SESAME* tables. When a computational cell has a mixture of two or more fluids, however, the EOS is not well understood, particularly under the conditions of high-energy densities. For these mixed cells, mixture rules are typically used to provide the requisite information; however, the accuracy of these rules is uncertain. We have conducted experiments on OMEGA EP that provided EOS data, in the form of shock speed, of atomic mixtures of Ni and Al to study the mixed behavior and to validate various mixture rules used by our codes.

In our experiments we placed a quartz standard next to our test (NiAl) or reference (Al) metal specimen, all on top of a thick ablator material used to efficiently create high-pressure tens-of-Mbar shocks. The target geometry is shown in Fig. 148.132. With the ASBO, we measured the shock velocity inside the quartz standard as well as the shock transit time through our opaque metal test specimens. Since the EOS of quartz is well known, measuring the shock speed is sufficient to give us its shock pressure, which we also used to infer the shock pressure inside the ablator whose EOS we also assumed to be known (polystyrene and beryllium). Once the ablator shock pressure was known, along with any time-dependent variations as measured inside the quartz, we could apply that pressure in our simulations for each mixture rule and see which gave the closest prediction to the measured shock transit time through the test specimen. We repeated the experiments on Al reference specimens, whose EOS is assumed known, to verify the strategy was sound.

Figure 148.133 shows the as-built targets and raw ASBO streak-camera data for a CH ablator/NiAl target (OMEGA EP shot 22586) and a beryllium ablator/Al target (OMEGA EP shot 22587). The ASBO viewed at the center of the target across the quartz/specimen interface extending about 400 μm on either side. In these data we observed the time at which the shock front broke out of the ablator and entered the quartz witness, the subsequent shock velocity history in the quartz witness, the time the shock broke out of the specimen, and the subsequent shock velocity in the quartz after leaving the specimen. We measured shock velocities in our CH ablators of 43 km/s, which decreased to 35 km/s after entering the quartz due to differences in shock impedance at the interface. From measurements of shock transit time we found a shock velocity

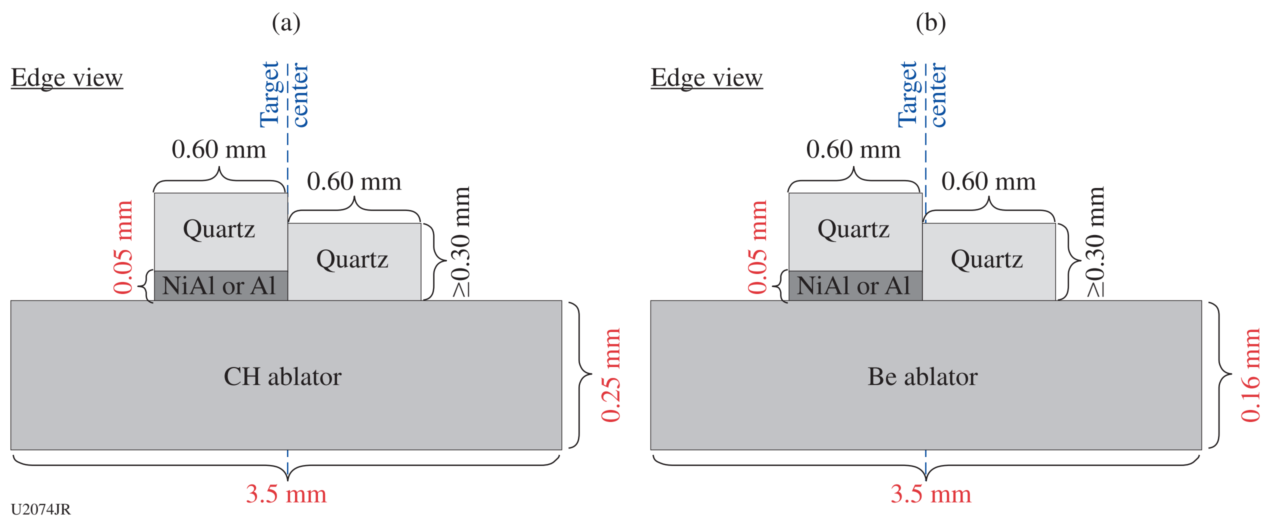

Figure 148.132
The two types of MixEOS targets used where specimens and quartz reference windows were placed on top of thick ablators designed to create steady shocks without wave reverberations.

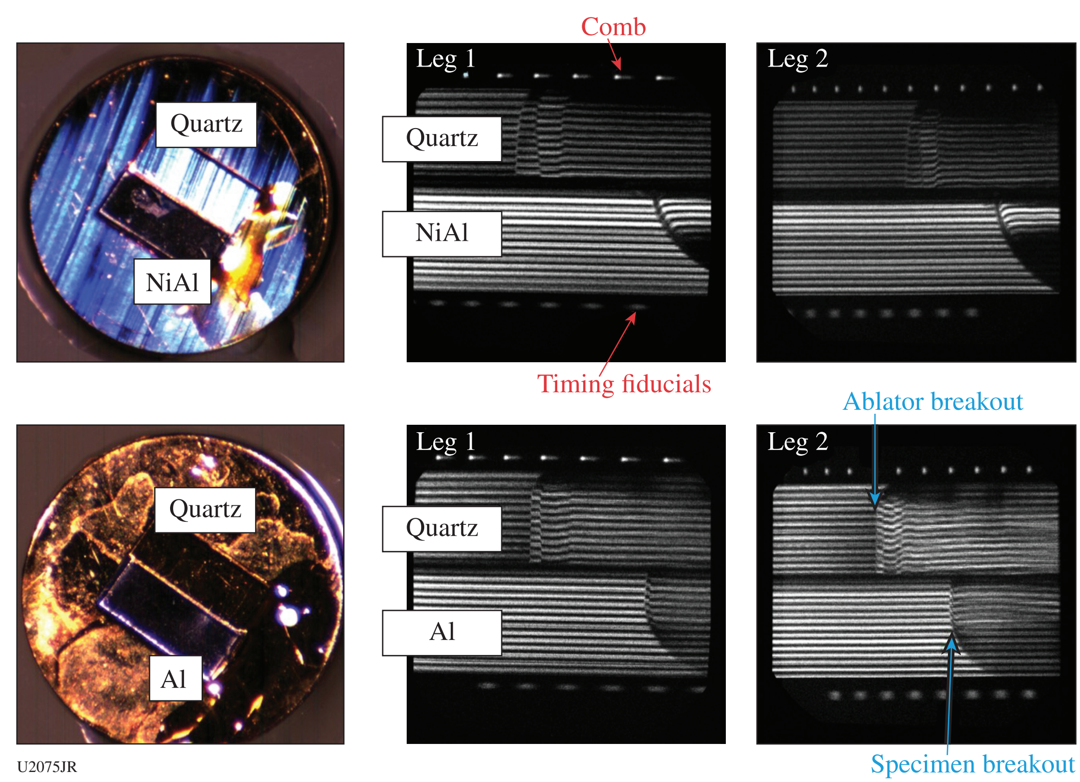

Figure 148.133
As-built targets and their ASBO streaked velocity data. Shock in the quartz is used to check steadiness and transit time through the specimen gives specimen shock velocity.

of about 36 km/s in Al specimens and 31 km/s in NiAl. This NiAl shock speed most closely matches the mixture rules of "additive volume" and ideal gas mixing.

ObliShock-EP

The mixing of modes between Rayleigh–Taylor (RT), Richtmeyer–Meshkov (RM), and Kelvin–Helmholtz (KH) instabilities occurs all across nature, from our terrestrial atmosphere and oceans[44] to astrophysical systems like accretion disks and supernovae.[45] The effects of shear on the growing spikes of the RT and RM processes is the reason for the production of the mushroom-like caps on these spikes[46] and can lead to a quicker onset and transition to turbulence.[47] Rarely is a flow interface purely shear or buoyancy driven; in the case of ICF, it is driven by a mix of passing shocks (RM), convergence (Bell–Plesset), and shearing shock flows (KH). The Oblique Shock Platform developed by LANL in collaboration with the University of Michigan aims to understand the interplay between the various instabilities.

The platform shown in Fig. 148.134 is designed to allow one to control the amount of shear with respect to RM/RT growth. This is accomplished by a variable tilt interface. A steeper slope allows for more KH shear to enter the problem. Depicted is a 0° [Fig. 148.134(a)] and a 30° tilt [Fig. 148.134(b)] as seen by the diagnostic; the 30° case shows the field of view of the diagnostic (green dashed circle). The interface has an embedded strip of iodinated CH (CHI) as a tracer layer for better imaging and is density matched at ~1.45 g/cm^3 to the surrounding polyimidamide (PIA) substrate (top hat, light blue). When shocked using three of the OMEGA EP beams at full power (~5 kJ) for 10 ns, the interface is pushed into a

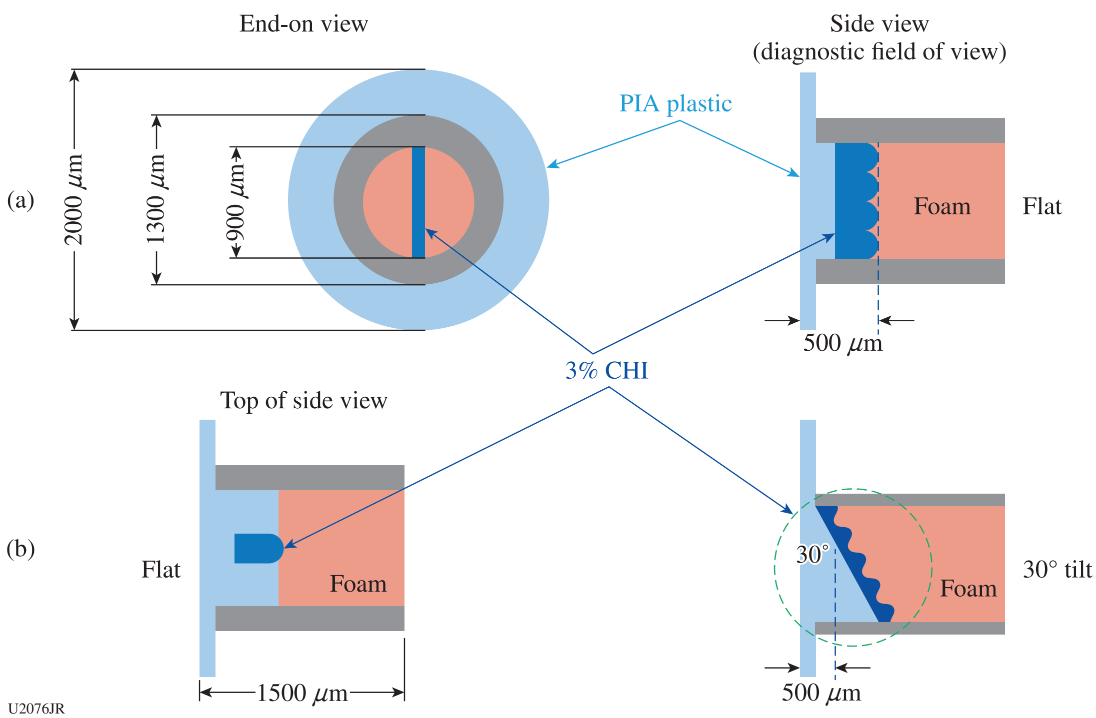

Figure 148.134
Setup of the OMEGA EP experiment. Three long-pulse 3ω beams of ~5 kJ each simultaneously irradiate the polyimidamide (PIA) ablator top-hat (light blue) and launch a shock into the experiment. A thin layer (100 μm) of density matched iodinated CH (CHI) (dark blue) is inserted into the PIA as a tracer layer for the perturbed interface inside a thin CH tube (gray). The tracer layer expands into a 100 mg/cm^3 foam (red). (a) A 0° tilt and (b) 30° tilt are illustrated. The interface evolution is then imaged at various times with the spherical crystal imager (SCI) using an 8-keV Cu K_α source driven by the fourth beam as a short-pulse (10-ps) backlighter. The area imaged by the SCI is indicated by the green dashed circle in the lower left 30° case. The field of view is shifted to follow the doped region as it transits the shock tube.

100-mg/cm^3 CH foam (Fig. 148.134, red) and is imaged using the OMEGA EP SCI from a short-pulse 10-ps Cu K_α backlighter onto image plates. The tracer layer is subject to several forces: shock acceleration, deceleration into the foam, deceleration and decompression from the laser turn-off rarefaction, and shear flow across the layer, which cause a complex interplay of RM, RT, and KH in the growth of the spikes and bubbles seeded into the experiment. This is an important part of LANL's turbulent mix-modeling strategy, including the implementation of a new modal model[48] coupled to the LANL HR[49] mix model.

The first set of experiments was used to understand the shock velocity in the PAI/CHI and foam, to gauge our accuracy in modeling the platform in the multiphysics code *RAGE*. The data from campaigns in FY15 were used to benchmark the platform.[50] Figure 148.135 shows the shock position from 1-D *RAGE* simulations, next to one point in time from the experiment, and the simulation. The FY16 campaigns have been focusing on the observing mode coupling from multimode sine waves and a band of modes to understand how the energy and growth are transferred from mode to mode.[51] The simulation shows similar growth of the layer and the characteristic turnover of the spikes caused by the shear across the layer but shows significantly more small-scale rollup than the experiment. The experiment is not well enough resolved to make out such small structures but clearly exhibits the same rollup feature, which was expected because of the shear component in the system. The agreement is surprising considering the code used a simple mass source as a pusher for the hydrodynamics, which is unphysical at late time since the laser turns off at 10 ns and a rarefaction wave starts to enter the experiment, where in the code the source is on for the full simulation. This rarefaction catches up to the individual vortices at different times as a result of the varying ablator thickness, and vortex size can be seen to grow as the rarefaction catches up with each vortex. Work is currently ongoing to assess the growth rate of the spikes and bubbles using a new laser package for the *RAGE* calculations to simulate the full system end-to-end.[52] This is the first step before using this data to help verify the modal model in a pure RT/RM configuration, i.e., 0°.

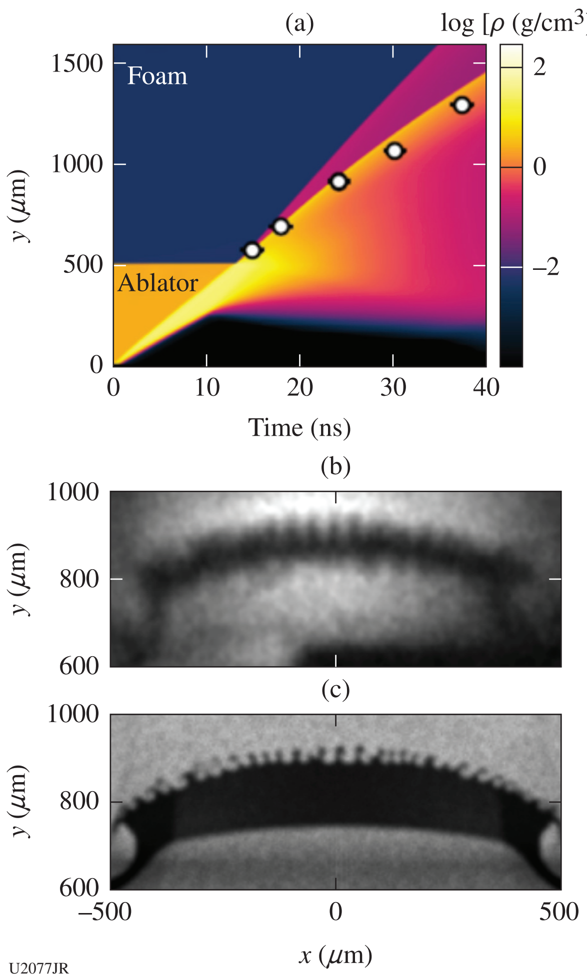

Figure 148.135
(a) Shock position/density jump as a function of time and images of the multimode band experiment (b) at 24 ns and (c) a 2-D *RAGE* simulation corresponding to the same time.

FY16 NRL Experimental Campaigns at the Omega Laser Facility

During FY16, NRL/LLE collaboration on laser imprint led to three successful shot days on OMEGA EP. A new method was devised to allow smooth preheating of the coating without installing a dedicated laser for preheating. It utilized soft x rays generated by a low-energy laser pulse on an auxiliary gold foil to heat and expand the coating on the main target. Streaked x-ray radiography shows that the x rays successfully expanded the coating in front of the plastic foil prior to arrival of the main laser drive. Well-resolved measurements of RT-amplified laser imprint (Fig. 148.136) were obtained on OMEGA EP, showing significant reduction of the target perturbations with the gold overcoat. Initial analysis shows further reduction when the coating is pre-expanded by the prepulse (Fig. 148.137).

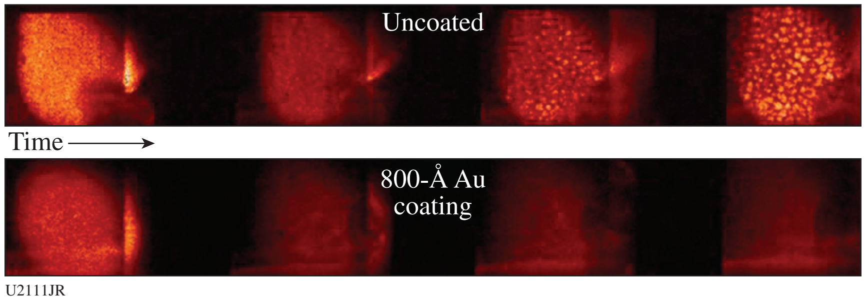

Figure 148.136
Measurements on OMEGA EP show laser imprint reduction with high-Z coating.

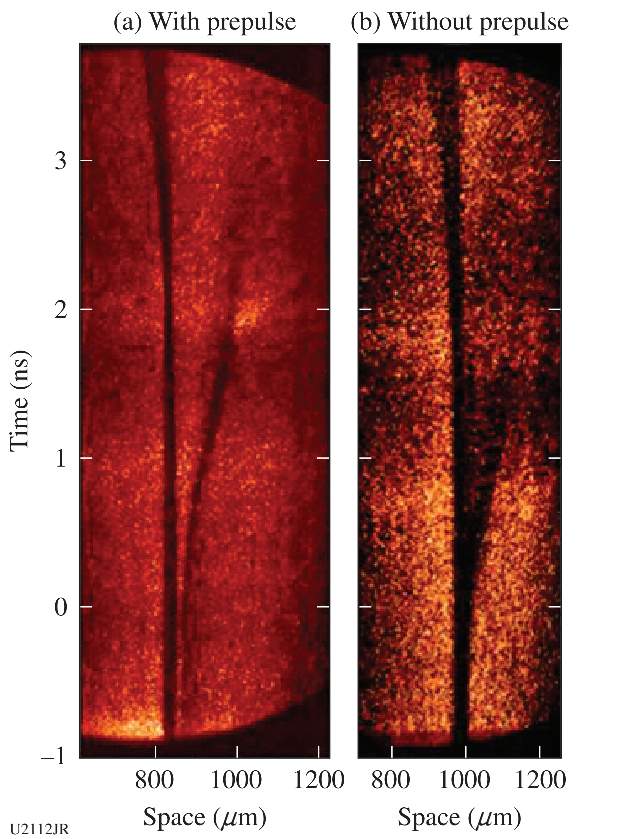

Figure 148.137
Gold coating is pre-expanded by an x-ray prepulse.

FY16 CEA Report on Omega Laser Facility Experiments

The Commissariat à l'énergie atomique et aux énergies (CEA) conducted 55 target shots on the OMEGA laser in FY16 for the campaigns discussed below.

Neutron-Induced Signals Generated on Coaxial Cables Exposed to OMEGA High-Yield Neutron Shots

Principal Investigators: J. L. Bourgade, J. L. Leray, B. Villette, O. Landoas, P. Leclerc, I. Lantuejoul-Thfoin, and J. E. Sauvestre (CEA-DAM-DIF)

Co-investigators: V. Yu. Glebov, T. C. Sangster, and G. Pien (LLE)

Since the first evidence of this effect in 2002 on OMEGA high-yield DT neutron shots,[53] it is now well demonstrated that high-pulsed, 14-MeV neutron irradiation can drive a transient current on various coaxial cables. Different geometries (based mainly on the same 0.141-in.-diam semi-rigid "SMA" coaxial cable with CF_4 dielectric) were used almost every year in the neutron "derby" on OMEGA since 2002 to better understand the current formation mechanisms.

In 2014 we selected a final experimental geometry that was able to induce a sufficient signal level with the neutron yield presently achievable on OMEGA direct-drive DT implosions ($Y_n \sim 10^{14}$). Since last year, the large effect of a weak magnetic field (~200 to 4000 Gauss) has been clearly demonstrated on this platform to generate a weaker current (by a factor of 12× less) at the same neutron irradiance than without it (see Ref. 54). These past results were obtained on coaxial cable embedded into a large amount of CHON, which was used to maintain the cable into its serpentine shape for inserting it into its protective cover tube.

In April 2016 the neutron derby shot day on OMEGA was used mainly to confirm results obtained in the past, which appear to show that the surrounding material of the coaxial cable under neutron irradiation induced a spurious signal that was larger than the internal signal generated only by the neutron interactions inside the coaxial cable.

According to our present hypothesis,[55] this current is mainly generated by traveling recoil nucleus into the coaxial cable, and we chose to switch the external support material from CHON to woven fiber glass and Macor ceramics. This change is driven by the fact that the heavier recoil nuclei ejected from these surrounding materials by the neutron knock-on processes is less energetic with a smaller range into matter than protons (CHON case) and therefore cannot penetrate the thin (~300-μm) Cu outside layer of our 0.141-in. coaxial cable (with CF_4 dielectric).

Figure 148.138(a) shows the FY15 coaxial cable embedded into the CHON epoxide glue as support material;

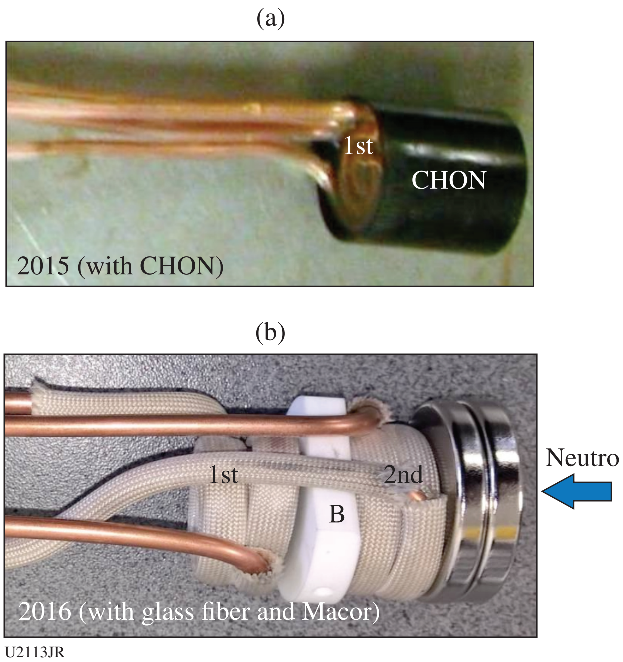

Figure 148.138
(a) FY15 coaxial cable serpentines embedded into CHON epoxide glue (the first serpentine without permanent magnet B but invisible though the epoxide glue and the plastic black cylinder). (b) FY16 coaxial cable serpentines with a woven glass fiber sheath (surrounding the 0.141-in. coaxial cable), the white Macor ceramic to maintain a permanent magnet disk (not visible), and the Fe-Nd-B permanent magnets (two silver disks at the far right).

Fig. 148.138(b) shows the FY16 coaxial cable geometry with this fiber glass–woven fastener and the Macor ceramics used to carry the magnets. In Fig. 148.138(a) the three permanent magnets are invisible, hidden by the black plastic cylinder. In Fig. 148.138(b) only two permanent magnets disks are clearly visible (marked "B"), and the last magnet used to create a larger magnetic field into the gap between them is placed in the middle of the white Macor ceramic.

This year two identical devices were fabricated with the fiber glass–woven sheath and the permanent magnets. On one device the magnetic field was canceled by heating the magnets above their Curie point. We chose to keep the unmagnetized magnets in the same place in order to have similar mass for the neutron interactions. These two identical devices were exposed on the same day to neutron shots on OMEGA by exchanging them into our CEA cart load between consecutive shots in the middle of the shot day.

Figure 148.139 shows the spectacular decreasing of the signal levels on OMEGA measured between 2014, 2015, and 2016 devices exposed on almost the same neutron flux (~3×10^{13} for 2014 and 2016 shots, and up to 7.5×10^{13} neutrons for 2015 shots —at the same distance of ~235 mm from the source).

If we compare the same scale (all the curves presented in Fig. 148.139 are normalized to the same value of 3×10^{13} neutrons/4π) the signals generated on a 50-Ω resistive charge—the largest current ever for this serpentine geometry—is generated by the one embedded into CHON without a magnetic field.

The signal differences of the two consecutives peaks (factor of ~2) are induced by a larger distance from the source (245 versus 239 mm, a factor of 1.05) for one of the serpentines (recorded here first in time by our choice) and also a larger neutron attenuation induced by the first serpentine (the CHON absorbing material used for fixing the serpentines in place and the permanent magnet and its plastic holder placed between the two serpentines as presented in Fig. 148.138). Nevertheless, Geant4 simulations performed to explain this difference were not sufficient to account for the signal level difference between the two serpentines and further calculations must be performed. For the glass fiber/Macor environment this measured difference is lower (by a factor of 1.2) because the neutron absorption is lower, resulting from less absorbing mass but still not accounted for in totality by the neutron absorption difference.

The glass fiber sheath/Macor without a magnetic-field device is the second in the row with a large reduction induced by replacing the outside material with fiber glass/Macor (factor of ~7.5 in our 2014/2015 shots comparison), confirming that surrounding CHON material generates a large part of the signal measured since first 2002 experiments.

A similar reduction factor has also been evaluated in the past on different coaxial cable geometries when CHON was replaced by a glass fiber sheath but have generated too weak signals even on the highest neutron yields achievable on OMEGA close to 10^{14} to be measured with enough accuracy. It is the first time since 2002 that such good data have been recorded and analyzed on different shots on OMEGA (three shots in 2016) on the same geometry with such accuracy for both magnetic field and higher atomic mass close materials. These clear measurements have also validated our choice of this new serpentine geometry used since 2013.

Finally the two devices with the magnetic field generate the lowest signals on this same neutron irradiation flux. For the *same* device without B field (2014) and magnetized again at Grenoble (Laboratoire National des Champs Magnétiques

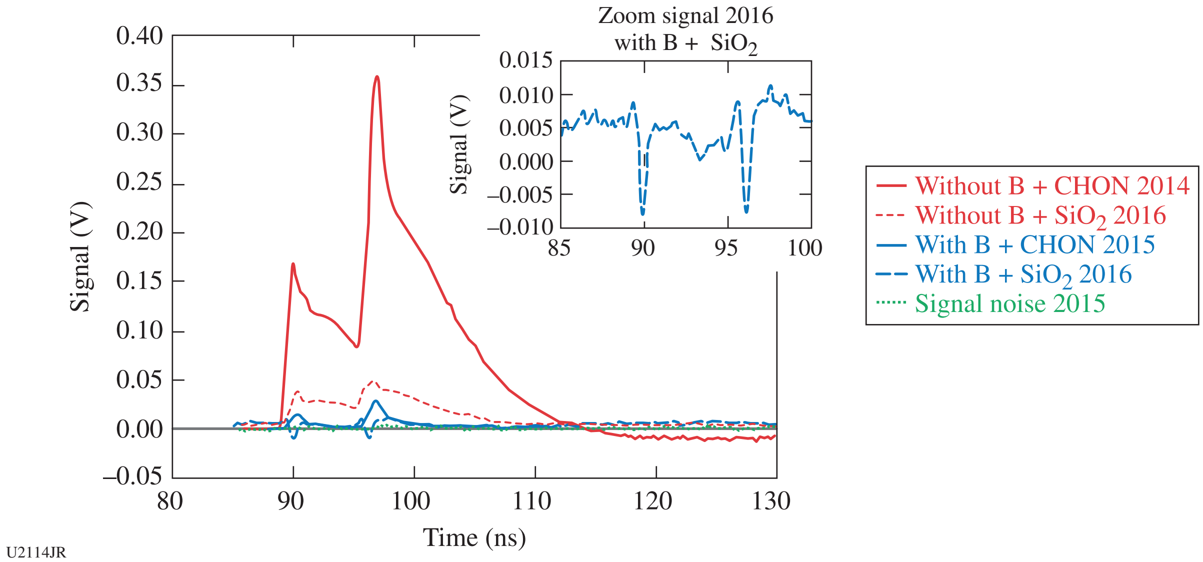

Figure 148.139
Summary of signal levels obtained since 2014 neutron derbies on the same geometry configuration "serpentine" on 0.141-in. coaxial cable with different configurations (with and without static magnetic field, with CHON and with glass fiber/Macor close environment). The lowest signal under neutron irradiation (normalized here for 3×10^{13} neutrons/4π) was obtained in the 2016 experiments by combining glass fiber/Macor close environment instead of CHON and by adding a static magnetic field. The two peaks are induced by two identical serpentines spaced electrically by a time delay coaxial cable of around 1.2 m (6 ns apart). The inset shows the weakest signal of 2016 around the 85- to 100-ns time window and the –10- to +15-mV range.

Intenses) in 2015, the reduction factor induced on both serpentines is even larger than for the outside material contribution (reduction factor of ~12).

The 2016 device (with glass fiber and Macor outside materials *and* with the magnetic field) shows the weakest current generation ever recorded. Fortunately it is just above the background level for these measurements (few mV peak to peak).

Moreover, the shape of this last signal is clearly different between the two identical devices. The one without a magnetic field always exhibits positive signals (as measured on all the geometries tested on OMEGA since 2002) while the magnetic field case exhibits more-complicated bipolar behaviors; therefore it is more difficult to derive a simple reduction factor from these two measurements. Nevertheless, if we try to crudely measure that value on the positive peaks only, this reduction factor is ~10.

Bipolar behaviors on the weakest signal obtained in 2016 (SiO_2 + B) can be analyzed as the following:

- The incoming neutrons interact with both the 3-mm-thick tungsten x-ray disc filter (added in front of the device to avoid any x rays below 200 keV generated by the laser–plasma interaction on the microballoon, to reach the cable) and the two permanent magnets (two 5-mm-thick disks), create a strong pulsed γ-ray source (duration estimated to ~400 ps including the neutron source duration, its Doppler broadening during their time of flight and their travel into the converting disks) by the neutron-to-gamma conversion into these high-Z and massive materials.

- The gamma rays can generate only negative peaks on coaxial cables [as measured on a pulsed hard x-ray generator and calculated with standard system-generated electromagnetic-pulse (SGEMP) effects simulations].[56] The two negative peaks seen in this case in Fig. 148.139 (into the right zoom) are almost equal in durations (FWHM ~ 600 ps) and value in both serpentines because the source is a large one (38 to 35 mm in diameter with respect to the 35-mm-diam serpentine wrap) placed close to them (2 mm for the first one and 7 mm for the second).

- The remaining positive signal (associated with the neutron interaction within the coaxial cable itself) is very weak (a few millivolt, so just above the signal background) and can be seen only on the second peak (associated to the serpentine placed closer from the source).

Finally a careful analysis of the signals presented in Fig. 148.139 shows little time change for the peak positions that can be related to different implosion bang times as measured by other OMEGA neutrons diagnostics as the neutron time of flight (nTOF). Those small time changes clearly show that the current is generated only by the neutron irradiation and no other energy vectors emitted by the implosions as gammas or hard x rays.

Moreover, to confirm the neutron origin of the measured signal, any or very few peaks are generated when the neutron yield is low (in the range of few 10^{12}) as recorded for instance in Fig. 148.139 labeled as "signal noise 2015" (where the yield for this specific shot was as low as 2.2×10^{12}).

These past yearly "neutron derby" experiments on the current generated during the OMEGA neutron irradiation on the 0.141-in. semi-rigid coaxial cable [widely used on the NIF and/or Laser Mégajoule (LMJ) to propagate fast electrical signals with their very large bandwidth up to few ten of GHz] are now well measured and their origin characterized. Some mitigation techniques were found to greatly reduce (by a factor of nearly 100) this spurious current:

- Avoid placing any CHON material in close proximity of the coaxial cable and replace any of these plastic materials by woven glass fiber and Macor–type ceramics as fixtures and holders if necessary.

- Add some permanent magnets (as Fe-Nd-B) along the coaxial cable able to maintain a few-hundred-Gauss magnetic field along the cable.

- With these precautions these coaxial cables widely used on our diagnostics signal transport can continue to be used even on the highest neutron flux perhaps achievable on the NIF and LMJ up to the ignition level (10^{17} to 10^{18} neutron yield at their 5-m-radius target chamber surface).

Progress in the Diamond Anvil Cell Target Setup for OMEGA

Principal Investigators: S. Brygoo and P. Loubeyre (CEA)
Co-investigators: R. Jeanloz (University of California, Berkeley); M. Millot, P. M. Celliers, and J H. Eggert (LLNL); and G. W. Collins, J. R. Rygg, and T. R. Boehly (LLE)

Measuring the properties of H and He and other simple molecular systems under deep planetary conditions has generated a great deal of interest.[58–59] The thermodynamical states there are qualified as warm dense matter, i.e., those of a plasma strongly correlated and with partly degenerated electrons. If the temperature is low enough, specifically in hydrogen, intriguing properties could be disclosed, like the possible existence of a plasma phase transition. To probe those states, pressures up to the TPa range must be generated but associated to temperatures below 1 eV. This range is well outside the principal Hugoniot of deuterium for which only pressures less than 0.1 TPa are associated to temperature below 1 eV.

The most-common technique for reaching off-Hugoniot states is to generate a multishock compression, through either reverberation between two anvils or a succession of small shocks. These two techniques make it possible to reach final pressures of several Mbar associated with temperatures close to an isentropic compression, but the thermodynamical state of the system is inferred indirectly using a hydro-simulation of the experiment. To keep the advantage of the single Hugoniot compression that provides a direct measurement of the final thermodynamical state by relating P, V, E values to the shock and particle velocities through the Rankine–Hugoniot equations, the CEA/UC Berkeley/LLNL/LLE team has developed a novel approach over the past ten years under the NLUF program. It is based on the concept of the diamond anvil cell (DAC) target, i.e., the sample is initially under an initial pressure of a few GPa. The Hugoniot curves generated from these precompressed initial states are therefore much cooler than the principal Hugoniot, which is illustrated in Fig. 148.140 for hydrogen, where different Hugoniot corresponding to different initial pressures are plotted.

The concept of the precompressed target is explained in Fig. 148.141. The figure of merit of this concept is the initial pressure that can be achieved using a thin-enough diamond window so that a strong shock can propagate to the sample. Since our first measurements on OMEGA, the initial pressure has been multiplied by a factor of 100, increasing from 0.16 GPa to 16 GPa. This increase has been made possible thanks to the evolution of the shape of the drive diamond going from a flat to a conical shape, which makes it possible to drastically increase the initial pressure for the same thickness. Also, to reduce the force on the diamond window, the culet size of the diamond anvil has been reduced. Increase of the initial pressure is consequently made at the expense of the diameter of the sample available. The evolution of the sample diameter is shown in Fig. 148.141. It should be stressed that even for a 100-μm-diam sample, the dimension of the sample for the 16-GPa initial pressure, the quality of the VISAR image remains good enough for an accurate analysis, made possible by OMEGA's constant

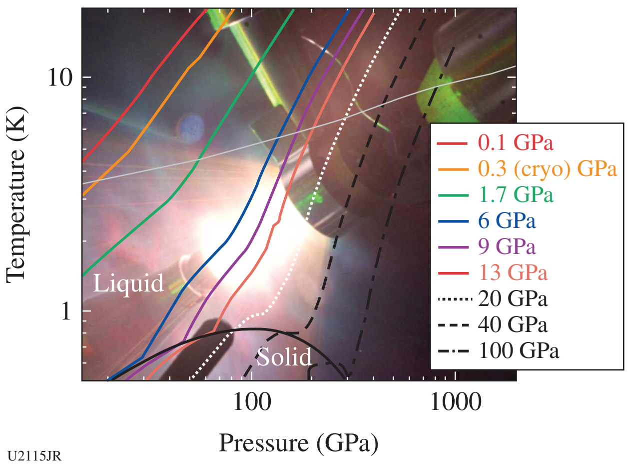

Figure 148.140
Precompressed H_2 Hugoniot curves associated with different initial pressures. By changing the initial pressure, a bundle of Hugoniot can be generated and consequently the equation of state can be measured over a large pressure–temperature phase domain. The colored Hugoniot are those that have been investigated on OMEGA up to now.

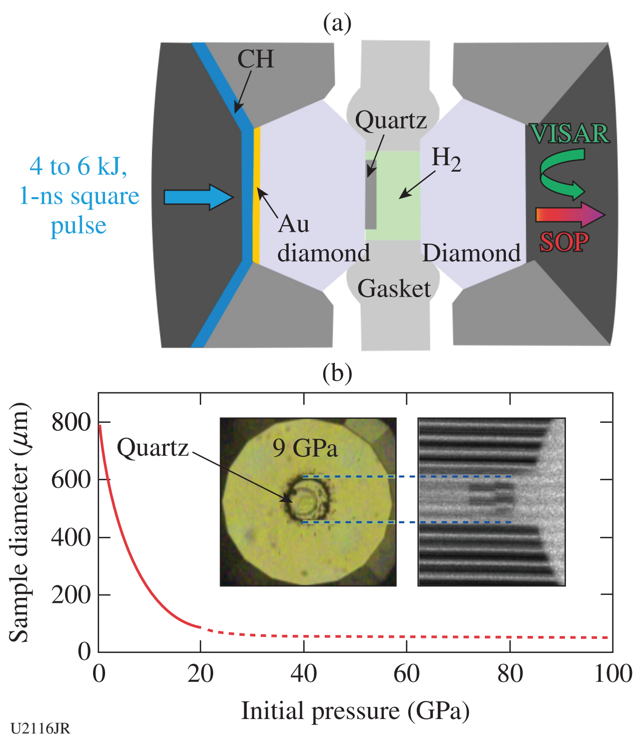

Figure 148.141
Evolution of the target over the years. (a) A typical target. (b) The diameter of the inside of a target as a function of the initial pressure. The inset represents the target before the shot and its associated VISAR image obtained for a 9-GPa precompression, respectively.

upgrade of the VISAR/SOP diagnostic. Finally, the laser-shock experiment on precompressed samples is analyzed using a quartz reference; this analysis framework has recently been improved. The roadmap of our effort on OMEGA is to continue the increase of the precompression and to extend the use of the precompressed target for simple molecular systems. Over the next two years, precompression of 40 GPa should be feasible.

Wall Motion Experiment on OMEGA

Principal Investigators: C. Courtois, L. Lecherbourg, and F. Girard

The objective of the experiment performed 15 September 2016 was to characterize the interaction between laser beams and expanded plasma from walls that occur in a halfraum. The expansion of the gold plasma wall produced by the external laser cone can indeed modify the propagation of laser beams of the internal cone and then directly affect the cavity energetics.

This OMEGA experiment is the second of this type (the first campaign was in June 2014). The cavity uses a double-wall design (one wall tilted by 30° relative to the second one) (see Fig. 148.142). At t_0, laser beams from the 21° and 59° cones (heating beams) are focused inside the cavity. The 59° cone is at the origin of the plasma bubbles of interest. At $t_0 + \delta t$, laser beams from the 42° cone (interaction beams) are focused inside the halfraum and propagate through the plasma bubbles that are more or less expanded, depending on the time delay δt and the methane gas filling pressure P. During the 2014 experiment, delays up to 1 ns were tested as a "3-D" pointing of the 59° cone beams. This 3-D pointing was chosen to maximize the size of the expanding plasma and, consequently, the interaction strength. The 2016 experiment tested longer delays (up to 2.2 ns) and also a 2-D pointing aimed at producing a more-cylindrical, expanding plasma wall.

On the opposite side of the laser entrance hole (LEH), the halfraum exhibits a window that gives direct access to the plasma bubbles (the interaction area). In the configuration called "P8" represented in Fig. 148.142, the interaction area is studied using an x-ray imager positioned in TIM-5. In the P5 configuration, the target is turned by 180° and the plasma bubbles are studied using the broadband x-ray spectrometers DMX and Dante.

In the P8 configuration, the hard x-ray imager in the TIM-5 provides access to the heating laser beam (59° cones) as it impacts on the halfraum walls. Hard x-ray emission is observed through an oblong observation window. Figure 148.143 shows experimental results obtained for δt = 1.4 ns and P = 1 bar. The maximum emission of the heating laser beams (59° cone) can be seen in Fig. 148.143(b). Persistence of the signal and features at t_0 + 3.3 ns [Fig. 148.143(c)] suggest 42° cone laser beam energy deposition inside the expanding plasma, producing hard x-ray emission.

The hard x-ray emission produced by the plasma bubbles (created by the heating beam from the 59° cone and the interaction beam during its propagation through this bubble) can be absolutely measured using the broadband x-ray spectrometers DMX and Dante [Fig. 148.144(b)]. The amplitude of the second peak associated with the interaction beam–deposited energy increases with the delay δt and decreases with the methane gas filling pressure P.

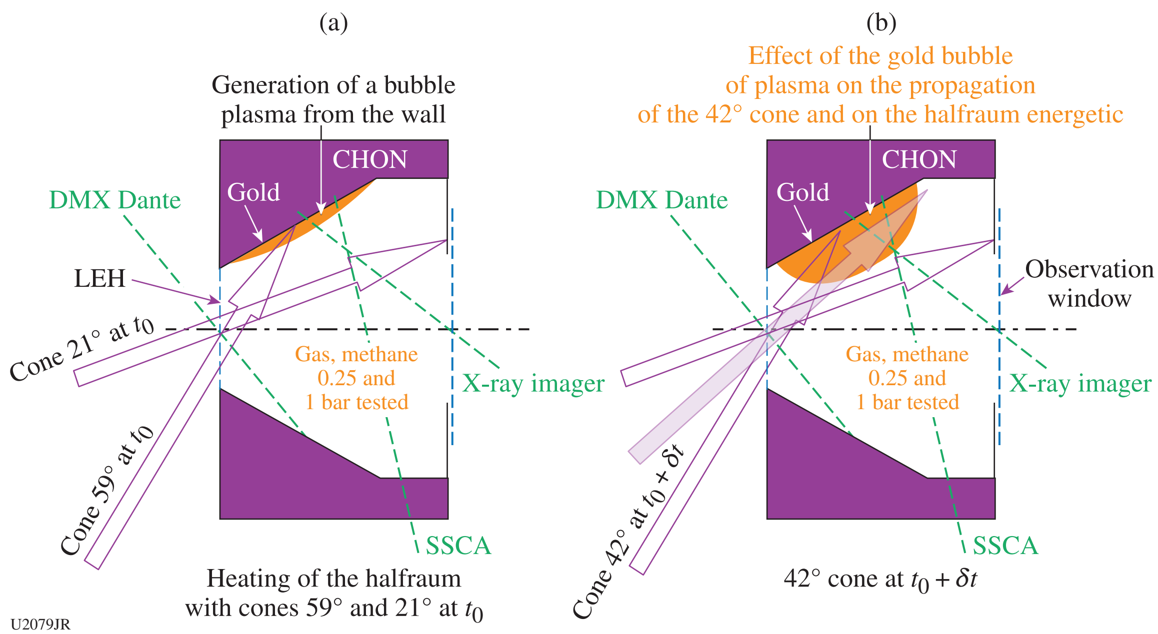

Figure 148.142
Principle of the experiment (P8 configuration). LEH: laser entrance hole.

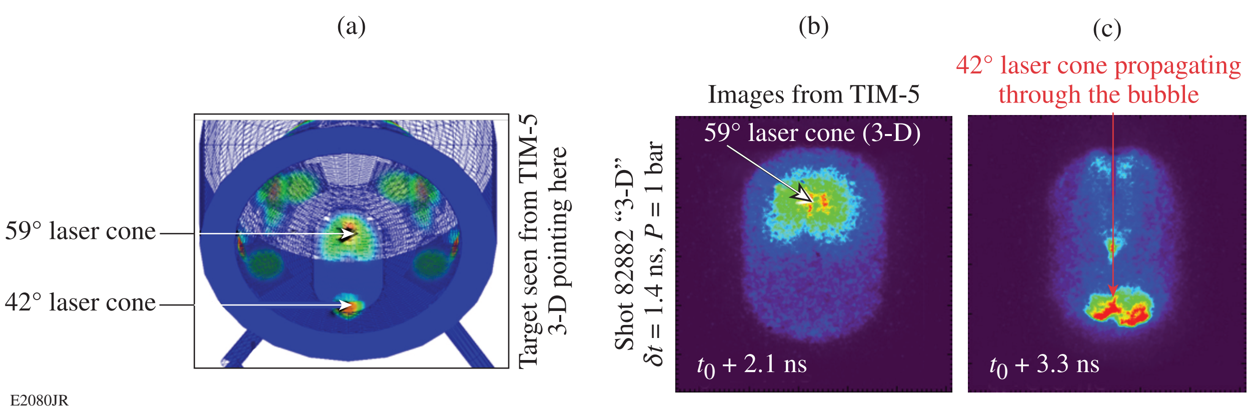

Figure 148.143
Images obtained with the hard x-ray imager in TIM-5 (P8 configuration).

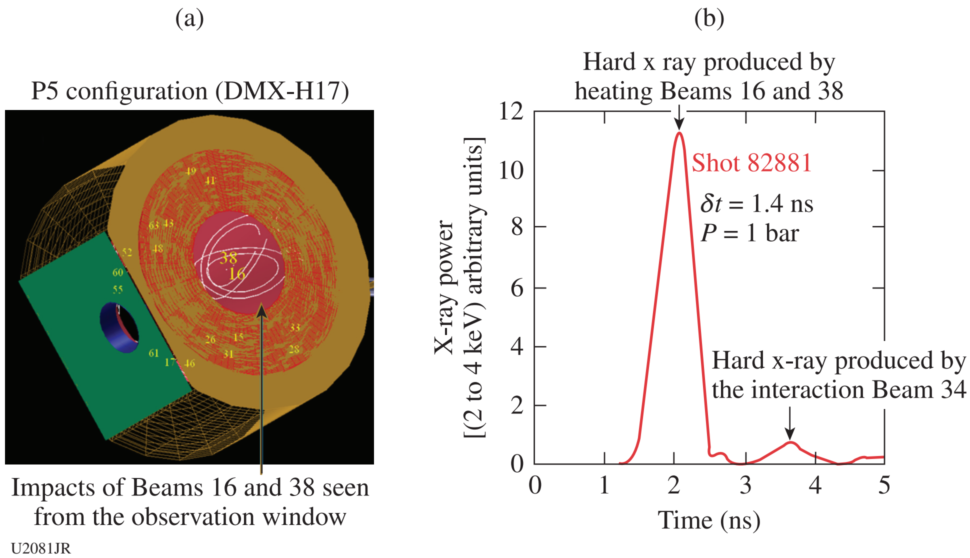

Figure 148.144
(a) Visrad image showing the target seen from DMX; (b) hard x-ray power (2 to 4 keV) measured by DMX.

REFERENCES

1. R. A. Fischer *et al*., Earth Planet. Sci. Lett. **373**, 54 (2013).

2. G. Fiksel, W. Fox, A. Bhattacharjee, D. H. Barnak, P.-Y. Chang, K. Germaschewski, S. X. Hu, and P. M. Nilson, Phys. Rev. Lett. **113**, 105003 (2014).

3. C. K. Li, P. Tzeferacos, D. Lamb, G. Gregori, P. A. Norreys, M. J. Rosenberg, R. K. Follett, D. H. Froula, M. Koenig, F. H. Séguin, J. A. Frenje, H. G. Rinderknecht, H. Sio, A. B. Zylstra, R. D. Petrasso, P. A. Amendt, H. S. Park, B. A. Remington, D. D. Ryutov, S. C. Wilks, R. Betti, A. Frank, S. X. Hu, T. C. Sangster, P. Hartigan, R. P. Drake, C. C. Kuranz, S. V. Lebedev, and N. C. Woolsey, Nat. Commun. **7**, 13081 (2016).

4. H. Sio, J. A. Frenje, J. Katz, C. Stoeckl, D. Weiner, M. Bedzyk, V. Glebov, C. Sorce, M. Gatu Johnson, H. G. Rinderknecht, A. B. Zylstra, T. C. Sangster, S. P. Regan, T. Kwan, A. Le, A. N. Simakov, W. T. Taitano, L. Chacòn, B. Keenan, R. Shah, G. Sutcliffe, and R. D. Petrasso, Rev. Sci. Instrum. **87**, 11D701 (2016).

5. N. V. Kabadi, H. Sio, V. Glebov, M. Gatu Johnson, A. MacPhee, J. A. Frenje, C. K. Li, F. Séguin, R. Petrasso, C. Forrest, J. Knauer, and H. G. Rinderknecht, Rev. Sci. Instrum. **87**, 11D817 (2016).

6. G. D. Sutcliffe, L. M. Milanese, D. Orozco, B. Lahmann, M. Gatu Johnson, F. H. Séguin, H. Sio, J. A. Frenje, C. K. Li, R. D. Petrasso, H.-S. Park, J. R. Rygg, D. T. Casey, R. Bionta, D. P. Turnbull, C. M. Huntington, J. S. Ross, A. B. Zylstra, M. J. Rosenberg, and V. Yu. Glebov, Rev. Sci. Instrum. **87**, 11D812 (2016).

7. B. Lahmann *et al*., Rev. Sci. Instrum. **87**, 11D801 (2016).

8. S. P. Regan, V. N. Goncharov, I. V. Igumenshchev, T. C. Sangster, R. Betti, A. Bose, T. R. Boehly, M. J. Bonino, E. M. Campbell, D. Cao, T. J. B. Collins, R. S. Craxton, A. K. Davis, J. A. Delettrez, D. H. Edgell, R. Epstein, C. J. Forrest, J. A. Frenje, D. H. Froula, M. Gatu Johnson, V. Yu. Glebov, D. R. Harding, M. Hohenberger, S. X. Hu, D. Jacobs-Perkins, R. T. Janezic, M. Karasik, R. L. Keck, J. H. Kelly, T. J. Kessler, J. P. Knauer, T. Z. Kosc, S. J. Loucks, J. A. Marozas, F. J. Marshall, R. L. McCrory, P. W. McKenty, D. D. Meyerhofer, D. T. Michel, J. F. Myatt, S. P. Obenschain, R. D. Petrasso, R. B. Radha, B. Rice, M. Rosenberg, A. J. Schmitt, M. J. Schmitt, W. Seka, W. T. Shmayda, M. J. Shoup, III, A. Shvydky, S. Skupsky, S. Solodov, C. Stoeckl, W. Theobald, J. Ulreich, M. D. Wittman, K. M. Woo, B. Yaakobi, and J. D. Zuegel, Phys. Rev. Lett. **117**, 025001 (2016); **117**, 059903(E) (2016).

9. A. B. Zylstra, H. W. Herrmann, M. Gatu Johnson, Y. H. Kim, J. A. Frenje, G. Hale, C. K. Li, M. Rubery, M. Paris, A. Bacher, C. R. Brune, C. Forrest, V. Yu. Glebov, R. Janezic, D. McNabb, A. Nikroo, J. Pino, T. C. Sangster, F. H. Séguin, W. Seka, H. Sio, C. Stoeckl, and R. D. Petrasso, Phys. Rev. Lett. **117**, 035002 (2016).

10. A. Bose, K. M. Woo, R. Betti, E. M. Campbell, D. Mangino, A. R. Christopherson, R. L. McCrory, R. Nora, S. P. Regan, V. N. Goncharov, T. C. Sangster, C. J. Forrest, J. Frenje, M. Gatu Johnson, V. Yu. Glebov, J. P. Knauer, F. J. Marshall, C. Stoeckl, and W. Theobald, Phys. Rev. E **94**, 011201(R) (2016).

11. A. B. Zylstra, J. A. Frenje, P. E. Grabowski, C. K. Li, G. W. Collins, P. Fitzsimmons, S. Glenzer, F. Graziani, S. B. Hansen, S. X. Hu, M. Gatu Johnson, P. Keiter, H. Reynolds, J. R. Rygg, F. H. Séguin, and R. D. Petrasso, J. Phys.: Conf. Ser. **717**, 012118 (2016).

12. Y. Kim, H. W. Herrmann, N. M. Hoffman, M. J. Schmitt, P. A. Bradley, S. Gales, C. J. Horsfield, M. Rubery, A. Leatherland, M. Gatu Johnson, J. Frenje, and V. Yu. Glebov, J. Phys.: Conf. Ser. **717**, 012030 (2016).

13. G. Kagan, H. W. Herrmann, Y.-H. Kim, M. J. Schmitt, P. Hakel, S. C. Hsu, N. M. Hoffman, D. Svyatsky, S. D. Baalrud, J. O. Daligault, H. Sio, A. B. Zylstra, M. J. Rosenberg, H. G. Rinderknecht, M. Gatu Johnson, J. A. Frenje, F. H. Séguin, C. K. Li, R. D. Petrasso, B. J. Albright, W. Taitano, G. A. Kyrala, P. A. Bradley, C.-K. Huang, C. J. McDevitt, L. Chacon, B. Srinivasan, A. M. McEvoy, T. R. Joshi, and C. S. Adams, J. Phys.: Conf. Ser. **717**, 012027 (2015).

14. P. B. Radha, V. N. Goncharov, M. Hohenberger, T. C. Sangster, R. Betti, R. S. Craxton, D. H. Edgell, R. Epstein, D. H. Froula, J. A. Marozas, F. J. Marshall, R. L. McCrory, P. W. McKenty, D. D. Meyerhofer,

D. T. Michel, S. X. Hu, W. Seka, A. Shvydky, S. Skupsky, J. A. Frenje, M. Gatu-Johnson, P. D. Petrasso, T. Ma, S. Le Pape, and A. J. Mackinnon, J. Phys.: Conf. Ser. **688**, 012006 (2016).

15. F. H. Séguin, C. K. Li, J. L. DeCiantis, J. A. Frenje, J. R. Rygg, R. D. Petrasso, F. J. Marshall, V. Smalyuk, V. Yu. Glebov, J. P. Knauer, T. C. Sangster, J. D. Kilkenny, and A. Nikroo, Phys. Plasmas **23**, 032705 (2016).

16. F. J. Marshall, P. B. Radha, M. J. Bonino, J. A. Delettrez, R. Epstein, V. Yu. Glebov, D. R. Harding, C. Stoeckl, J. A. Frenje, M. Gatu Johnson, F. H. Séguin, H. Sio, A. Zylstra, and E. Giraldez, Phys. Plasmas **23**, 012711 (2016).

17. S. Laffite, J. L. Bourgade, T. Caillaud, J. A. Delettrez, J. A. Frenje, F. Girard, V. Yu. Glebov, T. Joshi, O. Landoas, G. Legay, S. Lemaire, R. C. Mancini, F. J. Marshall, L. Masse, P. E. Masson-Laborde, D. T. Michel, F. Philippe, C. Reverdin, W. Seka, and V. Tassin, Phys. Plasmas **23**, 012706 (2016).

18. H. G. Rinderknecht, J. Rojas-Herrera, A. B. Zylstra, J. A. Frenje, M. Gatu Johnson, H. Sio, N. Sinenian, M. J. Rosenberg, C. K. Li, F. H. Séguin, R. D. Petrasso, T. Filkins, J. A. [Jeffrey] Steidle, J. A. [Jessica] Steidle, N. Traynor, and C. Freeman, Rev. Sci. Instrum. **86**, 123511 (2015).

19. J. A. Frenje, P. E. Grabowski, C. K. Li, F. H. Séguin, A. B. Zylstra, M. Gatu Johnson, R. D. Petrasso, V. Yu. Glebov, and T. C. Sangster, Phys. Rev. Lett. **115**, 205001 (2015).

20. M. Rosenberg, "Studies of Ion Kinetic Effects in Shock-Driven Inertial Confinement Fusion Implosions at OMEGA and the NIF and Magnetic Reconnection Using Laser-Produced Plasmas at OMEGA," Ph.D. thesis, Massachusetts Institute of Technology, 2014.

21. R. Nora, W. Theobald, R. Betti, F. J. Marshall, D. T. Michel, W. Seka, B. Yaakobi, M. Lafon, C. Stoeckl, J. A. Delettrez, A. A. Solodov, A. Casner, C. Reverdin, X. Ribeyre, A. Vallet, J. Peebles, F. N. Beg, and M. S. Wei, Phys. Rev. Lett. **114**, 045001 (2015).

22. W. Theobald, R. Nora, W. Seka, M. Lafon, K. S. Anderson, M. Hohenberger, F. J. Marshall, D. T. Michel, A. A. Solodov, C. Stoeckl, D. H. Edgell, B. Yaakobi, A. Casner, C. Reverdin, X. Ribeyre, A. Shvydky, A. Vallet, J. Peebles, F. N. Beg, M. S. Wei, and R. Betti, Phys. Plasmas **22**, 056310 (2015).

23. A. Deltuva, Institute of Theoretical Physics and Astronomy, Vilinus University, Vilinus, Lithuania, private communication (2015).

24. G. Hale, Los Alamos National Laboratory, private communication (2015).

25. T. R. Boehly, D. L. Brown, R. S. Craxton, R. L. Keck, J. P. Knauer, J. H. Kelly, T. J. Kessler, S. A. Kumpan, S. J. Loucks, S. A. Letzring, F. J. Marshall, R. L. McCrory, S. F. B. Morse, W. Seka, J. M. Soures, and C. P. Verdon, Opt. Commun. **133**, 495 (1997).

26. J. B. Neaton and N. W. Ashcroft, Nature **400**, 141 (1999).

27. Q. Liu, C. Fan, and R. Zhang, J. Appl. Phys. **105**, 123505 (2009).

28. C. J. Pickard and R. J. Needs, Nat. Mater. **9**, 624 (2010).

29. G. I. Kerley, Sandia National Laboratory, Albuquerque, NM, Report SAND2003-3613 (2003).

30. M. D. Knudson and M. P. Desjarlais, Phys. Rev. Lett. **103**, 225501 (2009).

31. H. Sio *et al*., "A Broadband Proton Backlighting Platform to Probe Shock Propagation in Low-Density Systems," submitted to Review of Scientific Instruments.

32. D. E. Fratanduono, T. R. Boehly, M. A. Barrios, D. D. Meyerhofer, J. H. Eggert, R. F. Smith, D. G. Hicks, P. M. Celliers, D. G. Braun, and G. W. Collins, J. Appl. Phys. **109**, 123521 (2011).

33. A. M. Saunders *et al*., Rev. Sci. Instrum. **87**, 11E724 (2016).

34. A. V. Bushman *et al*., *Intense Dynamic Loading of Condensed Matter* (Taylor & Francis, Washington, DC, 1993).

35. D. C. Swift and C. R. Ruiz, AIP Conf. Proc. **845**, 1297 (2006).

36. R. F. Heeter, S. B. Hansen, K. B. Fournier, M. E. Foord, D. H. Froula, A. J. Mackinnon, M. J. May, M. B. Schneider, and B. K. F. Young, Phys. Rev. Lett. **99**, 195001 (2007).

37. R. F. Smith, S. M. Pollaine, S. J. Moon, K. T. Lorenz, P. M. Celliers, J. H. Eggert, H.-S. Park, and G. W. Collins, Phys. Plasmas **14**, 057105 (2007).

38. R. F. Smith, C. A. Bolme, D. J. Erskine, P. M. Celliers, S. Ali, J. H. Eggert, S. L. Brygoo, B. D. Hammel, J. Wang, and G. W. Collins, J. Appl. Phys. **114**, 133504 (2013).

39. D. Besnard *et al*., Los Alamos National Laboratory, Los Alamos, NM, Report LA-12303-MS (1992).

40. I. V. Igumenshchev, V. N. Goncharov, F. J. Marshall, J. P. Knauer, E. M. Campbell, C. J. Forrest, D. H. Froula, V. Yu. Glebov, R. L. McCrory, S. P. Regan, T. C. Sangster, S. Skupsky, and C. Stoeckl, Phys. Plasmas **23**, 052702 (2016).

41. R. Tommasini, J. A. Koch, N. Izumi, L. A. Welser, R. C. Mancini, J. Delettrez, S. P. Regan, and V. Smalyuk, Proc. SPIE **6317**, 631716 (2006).

42. A. B. Zylstra, J. A. Frenje, P. E. Grabowski, C. K. Li, G. W. Collins, P. Fitzsimmons, S. Glenzer, F. Graziani, S. B. Hansen, S. X. Hu, M. Gatu Johnson, P. Keiter, H. Reynolds, J. R. Rygg, F. H. Séguin, and R. D. Petrasso, Phys. Rev. Lett. **114**, 215002 (2015).

43. H. W. Herrmann, Y. H. Kim, C. S. Young, V. E. Fatherley, F. E. Lopez, J. A. Oertel, R. M. Malone, M. S. Rubery, C. J. Horsfield, W. Stoeffl, A. B. Zylstra, W. T. Shmayda, and S. H. Batha, Rev. Sci. Instrum. **85**, 11E124 (2014).

44. W. R. Peltier and C. P. Caulfield, Annu. Rev. Fluid Mech. **35**, 135 (2003); J. D. Woods, J. Fluid Mech. **32**, 791 (1968).

45. D. P. Lathrop and C. B. Forest, Phys. Today **64**, 40 (2011); H. Xu *et al*., Astrophys. J. Lett. **698**, L14 (2009); S. A. Balbus and J. F. Hawley, Rev. Mod. Phys. **70**, 1 (1998); A. R. Bell, Mon. Not. R. Astron. Soc. **353**, 550 (2004); T. Ebisuzaki, T. Shigeyama, and K. Nomoto, Astrophys. J. Lett. **344**, L65 (1989); I. Hachisu *et al*., Astrophys. J. Lett. **358**, L57 (1990).

46. T. Yabe, H. Hoshino, and T. Tsuchiya, Phys. Rev. A **44**, 2756 (1991); N. J. Zabusky, Annu. Rev. Fluid Mech. **31**, 495 (1999).

47. Y. Zhou, H. F. Robey, and A. C. Buckingham, Phys. Rev. E **67**, 056305 (2003); Y. Zhou, Phys. Plasmas **14**, 082701 (2007).

48. B. Rollin and M. J. Andrews, J. Turbul. **14**, 77 (2013).

49. D. Besnard, F. H. Harlow, and R. Rauenzahn, Los Alamos National Laboratory, Los Alamos, NM, Report LA-10911-MS (1987).

50. G. Malamud *et al*., High Energy Density Phys. **9**, 122 (2013).

51. C. A. Di Stefano *et al*., submitted to Applied Physics Letters.

52. A. M. Rasmus *et al*., to be submitted to Physical Review Letters.

53. *LLE Review Quarterly Report* **96**, 284, Laboratory for Laser Energetics, University of Rochester, Rochester, NY, LLE Document No. DOE/SF/19460-509, NTIS Order No. PB2006-106668 (2003).

54. *LLE Review Quarterly Report* **144**, 280, Laboratory for Laser Energetics, University of Rochester, Rochester, NY, LLE Document No. DOE/NA/1944-1242 (2015).

55. J. L. Leray *et al*., IEEE Trans. Nucl. Sci. **59**, 1289 (2012).

56. J. L. Leray, S. Bazzoli, J. E. Sauvestre, and V. Yu. Glebov, IEEE Trans. Nucl. Sci. **55**, 3060 (2008).

57. R. Jeanloz, P. M. Celliers, G. W. Collins, J. H. Eggert, K. K. M. Lee, R. S. McWilliams, S. Brygoo, and P. Loubeyre, Proc. Natl. Acad. Sci. USA **104**, 9172 (2007).

58. P. Loubeyre, S. Brygoo, J. Eggert, P. M. Celliers, D. K. Spaulding, J. R. Rygg, T. R. Boehly, G. W. Collins, and R. Jeanloz, Phys. Rev. B **86**, 144115 (2012).

59. S. Brygoo, M. Millot, P. Loubeyre, A. E. Lazicki, S. Hamel, T. Qi, P. M. Celliers, F. Coppari, J. H. Eggert, D. E. Fratanduono, D. G. Hicks, J. R. Rygg, R. F. Smith, D. C. Swift, G. W. Collins, and R. Jeanloz, J. Appl. Phys. **118**, 195901 (2015).

Publications and Conference Presentations

Publications

Y. Akbas, A. Stern, L. Q. Zhang, Y. Alimi, A. M. Song, I. Iñiguez-de-la-Torre, J. Mateos, T. González, G. W. Wicks, and R. Sobolewski, "Ultrahigh Responsivity of Optically Active, Semiconducting Asymmetric Nano-Channel Diodes," J. Phys.: Conf. Ser. **647**, 012013 (2015).

M. Anthamatten, J. J. Ou, J. A. Weinfeld, and S. H. Chen, "Enthalpy Versus Entropy: What Drives Hard-Particle Ordering in Condensed Phases?" Chem. Phys. Lett. **660**, 18 (2016).

S.-W. Bahk, C. Dorrer, R. G. Roides, and J. Bromage, "Chromatic-Aberration Diagnostic Based on a Spectrally Resolved Lateral-Shearing Interferometer," Appl. Opt. **55**, 2413 (2016).

P. X. Belancourt, W. Theobald, P. A. Keiter, T. J. B. Collins, M. J. Bonino, P. M. Kozlowski, S. P. Regan, and R. P. Drake, "Demonstration of Imaging X-Ray Thomson Scattering on OMEGA EP," Rev. Sci. Instrum. **87**, 11E550 (2016).

R. Betti, A. R. Christopherson, A. Bose, and K. M. Woo, "Alpha Heating and Burning Plasmas in Inertial Confinement Fusion," J. Phys.: Conf. Ser. **717**, 012007 (2016).

R. Betti and O. A. Hurricane, "Inertial-Confinement Fusion with Lasers," Nat. Phys. **12**, 435 (2016).

A. Bose, K. M. Woo, R. Betti, E. M. Campbell, D. Mangino, A. R. Christopherson, R. L. McCrory, R. Nora, S. P. Regan, V. N. Goncharov, T. C. Sangster, C. J. Forrest, J. Frenje, M. Gatu Johnson, V. Yu. Glebov, J. P. Knauer, F. J. Marshall, C. Stoeckl, and W. Theobald, "Core Conditions for Alpha Heating Attained in Direct-Drive Inertial Confinement Fusion," Phys. Rev. E **94**, 011201(R) (2016).

B. P. Chock, T. B. Jones, and D. R. Harding, "Effect of a Surfactant on the Electric-Field Assembly of Oil-Water Emulsions for Making Foam Targets," Fusion Sci. Technol. **70**, 206 (2016).

T. J. B. Collins, J. A. Marozas, S. Skupsky, D. Cao, P. W. McKenty, J. A. Delettrez, and G. Moses, "Design Options for Polar-Direct-Drive Targets from Alpha Heating to Ignition," J. Phys.: Conf. Ser. **717**, 012012 (2016).

D. H. Crandall, "The Quest for Laboratory Inertial Fusion Burn in the United States," J. Phys.: Conf. Ser. **717**, 012001 (2016).

R. S. Craxton, K. S. Anderson, T. R. Boehly, V. N. Goncharov, D. R. Harding, J. P. Knauer, R. L. McCrory, P. W. McKenty, D. D. Meyerhofer, J. F. Myatt, A. J. Schmitt, J. D. Sethian, R. W. Short, S. Skupsky, W. Theobald, W. L. Kruer, K. Tanaka, R. Betti, T. J. B. Collins, J. A. Delettrez, S. X. Hu, J. A. Marozas, A. V. Maximov, D. T. Michel, P. B. Radha, S. P. Regan, T. C. Sangster, W. Seka, A. A. Solodov, J. M. Soures, C. Stoeckl, and J. D. Zuegel, "Direct-Drive Inertial Confinement Fusion: A Review," Phys. Plasmas **22**, 110501 (2015).

J. R. Davies, R. Betti, P.-Y. Chang, and G. Fiksel, "The Importance of Electrothermal Terms in Ohm's Law for Magnetized Spherical Implosions," Phys. Plasmas **22**, 112703 (2015).

A. K. Davis, D. Cao, D. T. Michel, M. Hohenberger, D. H. Edgell, R. Epstein, V. N. Goncharov, S. X. Hu, I. V. Igumenshchev, J. A. Marozas, A. V. Maximov, J. F. Myatt, P. B. Radha, S. P. Regan, T. C. Sangster, and D. H. Froula, "Isolating and Quantifying Cross-Beam Energy Transfer in Direct-Drive Implosions on OMEGA and the National Ignition Facility," Phys. Plasmas **23**, 056306 (2016) (invited).

A. K. Davis, D. T. Michel, R. S. Craxton, R. Epstein, M. Hohenberger, T. Mo, and D. H. Froula, "X-Ray Self-Emission Imaging Used to Diagnose 3-D Nonuniformities in Direct-Drive ICF Implosions," Rev. Sci. Instrum. **87**, 11E340 (2016).

W. R. Donaldson, J. Katz, R. Huff, E. M. Hill, J. H. Kelly, J. Kwiatkowski, R. B. Brannon, and R. Boni, "A Picosecond

Beam-Timing System for the OMEGA Laser," Rev. Sci. Instrum. **87**, 053511 (2016).

W. R. Donaldson, J. Katz, T. Z. Kosc, J. H. Kelly, E. M. Hill, and R. E. Bahr, "Enhancements to the Timing of the OMEGA Laser System to Improve Illumination Uniformity," Proc. SPIE **9966**, 996607 (2016).

C. Dorrer, A. Consentino, and D. Irwin, "Direct Optical Measurement of the On-Shot Incoherent Focal Spot and Intensity Contrast on the OMEGA EP Laser," Appl. Phys. B **122**, 156 (2016).

C. Dorrer, L. J. Waxer, A. Kalb, E. M. Hill, and J. Bromage, "Single-Shot High-Resolution Characterization of Optical Pulses by Spectral Phase Diversity," Opt. Express **23**, 33,116 (2015).

C. Dorrer, L. J. Waxer, A. Kalb, E. M. Hill, and J. Bromage, "Single-Shot, High-Resolution, Fiber-Based Phase-Diversity Photodetection of Optical Pulses," Proc. SPIE **9732**, 97320P (2016).

R. K. Follett, J. A. Delettrez, D. H. Edgell, V. N. Goncharov, R. J. Henchen, J. Katz, D. T. Michel, J. F. Myatt, J. Shaw, A. A. Solodov, C. Stoeckl, B. Yaakobi, and D. H. Froula, "Two-Plasmon Decay Mitigation in Direct-Drive Inertial-Confinement-Fusion Experiments Using Multilayer Targets," Phys. Rev. Lett. **116**, 155002 (2016).

R. K. Follett, J. A. Delettrez, D. H. Edgell, R. J. Henchen, J. Katz, J. F. Myatt, and D. H. Froula, "Plasma Characterization Using Ultraviolet Thomson Scattering from Ion-Acoustic and Electron Plasma Waves," Rev. Sci. Instrum. **87**, 11E401 (2016) (invited).

C. J. Forrest, V. Yu. Glebov, V. N. Goncharov, J. P. Knauer, P. B. Radha, S. P. Regan, M. H. Romanofsky, T. C. Sangster, M. J. Shoup III, and C. Stoeckl, "High-Dynamic-Range Neutron Time-of-Flight Detector Used to Infer the D(t,n)^{4}He and D(d,n)^{3}He Reaction Yield and Ion Temperature on OMEGA," Rev. Sci. Instrum. **87**, 11D814 (2016).

V. N. Goncharov, S. P. Regan, T. C. Sangster, R. Betti, T. R. Boehly, E. M. Campbell, J. A. Delettrez, D. H. Edgell, R. Epstein, C. J. Forrest, D. H. Froula, V. Yu. Glebov, D. R. Harding, S. X. Hu, I. V. Igumenshchev, F. J. Marshall, R. L. McCrory, D. T. Michel, J. F. Myatt, P. B. Radha, W. Seka, A. Shvydky, C. Stoeckl, W. Theobald, B. Yaakobi, and M. Gatu-Johnson, "Demonstrating Ignition Hydrodynamic Equivalence in Direct-Drive Cryogenic Implosions on OMEGA," J. Phys.: Conf. Ser. **717**, 012008 (2016).

D. R. Harding, D. C. Whitaker, and C. Fella, "Growth of a Solid DT Crystal from the Liquid Inside Inertial Confinement Fusion Targets," Fusion Sci. Technol. **70**, 173 (2016).

M. Hohenberger, A. Shvydky, J. A. Marozas, G. Fiksel, M. J. Bonino, D. Canning, T. J. B. Collins, C. Dorrer, T. J. Kessler, B. E. Kruschwitz, P. W. McKenty, D. D. Meyerhofer, S. P. Regan, T. C. Sangster, and J. D. Zuegel, "Optical Smoothing of Laser Imprinting in Planar-Target Experiments on OMEGA EP Using Multi-FM 1-D Smoothing by Spectral Dispersion," Phys. Plasmas **23**, 092702 (2016).

S. X. Hu, L. A. Collins, V. N. Goncharov, J. D. Kress, T. R. Boehly, R. Epstein, R. L. McCrory, and S. Skupsky, "First-Principles Studies on the Equation of State, Thermal Conductivity, and Opacity of Deuterium–Tritium (DT) and Polystyrene (CH) for Inertial Confinement Fusion Applications," J. Phys.: Conf. Ser. **717**, 012064 (2016).

S. X. Hu, L. A. Collins, V. N. Goncharov, J. D. Kress, R. L. McCrory, and S. Skupsky, "First-Principles Equation of State of Polystyrene and its Effect on Inertial Confinement Fusion Implosions," Phys. Rev. E **92**, 043104 (2015).

S. X. Hu, L. A. Collins, V. N. Goncharov, J. D. Kress, R. L. McCrory, and S. Skupsky, "First-Principles Investigations on Ionization and Thermal Conductivity of Polystyrene for Inertial Confinement Fusion Applications," Phys. Plasmas **23**, 042704 (2016).

S. X. Hu, B. Militzer, L. A. Collins, K. P. Driver, and J. D. Kress, "First-Principles Prediction of the Softening of the Silicon Shock Hugoniot Curve," Phys. Rev. B **94**, 094109 (2016).

I. V. Igumenshchev, V. N. Goncharov, F. J. Marshall, J. P. Knauer, E. M. Campbell, C. J. Forrest, D. H. Froula, V. Yu. Glebov, R. L. McCrory, S. P. Regan, T. C. Sangster, S. Skupsky, and C. Stoeckl, "Three-Dimensional Modeling of Direct-Drive Cryogenic Implosions on OMEGA," Phys. Plasmas **23**, 052702 (2016).

S. T. Ivancic, C. R. Stillman, D. Nelson, I. A. Begishev, C. Mileham, P. M. Nilson, and D. H. Froula, "Design of an Extreme Ultraviolet Spectrometer Suite to Characterize Rapidly Heated Solid Matter," Rev. Sci. Instrum. **87**, 11E538 (2016).

J. Katz, R. Boni, R. Rivlis, C. Muir, and D. H. Froula, "A Pulse-Front-Tilt–Compensated Streaked Optical Spectrometer with High Throughput and Picosecond Time Resolution," Rev. Sci. Instrum. **87**, 11E535 (2016).

Y. Kim, H. W. Herrmann, N. M. Hoffman, M. J. Schmitt, P. A. Bradley, S. Gales, C. J. Horsfield, M. Rubery, A. Leatherland, M. Gatu Johnson, J. A. Frenje, and V. Yu. Glebov, "Direct-Drive DT Implosions with Knudsen Number Variations," J. Phys.: Conf. Ser. **717**, 012030 (2016).

T. Z. Kosc, J. H. Kelly, E. M. Hill, and L. J. Waxer, "Design and Operation of the Multiple-Pulse Driver Line on the OMEGA Laser," J. Phys.: Conf. Ser. **717**, 012104 (2016).

J. A. Marozas, T. J. B. Collins, J. D. Zuegel, P. W. McKenty, D. Cao, S. Fochs, and P. B. Radha, "Continuous Distributed Phase-Plate Advances for High-Energy Laser Systems," J. Phys.: Conf. Ser. **717**, 012107 (2016).

F. J. Marshall, P. B. Radha, M. J. Bonino, J. A. Delettrez, R. Epstein, V. Yu. Glebov, D. R. Harding, C. Stoeckl, J. A. Frenje, M. Gatu Johnson, F. H. Séguin, H. Sio, A. Zylstra, and E. Giraldez, "Polar-Direct-Drive Experiments with Contoured-Shell Targets on OMEGA," Phys. Plasmas **23**, 012711 (2016).

K. L. Marshall, E. R. Sekera, and K. Xiao, "Computational Chemistry Modeling and Design of Photoswitchable Alignment Materials for Optically Addressable Liquid Crystal Devices," Proc. SPIE **9565**, 95650T (2015) (invited).

C. A. McCoy, M. C. Gregor, D. N. Polsin, D. E. Fratanduono, P. M. Celliers, T. R. Boehly, and D. D. Meyerhofer, "Shock-Wave Equation-of-State Measurements in Fused Silica Up to 1600 GPa," J. Appl. Phys. **119**, 215901 (2016).

J. F. Myatt, J. Shaw, V. N. Goncharov, J. Zhang, A. V. Maximov, R. W. Short, R. K. Follett, W. Seka, D. H. Edgell, and D. H. Froula, "Laser–Plasma Interaction in Direct-Drive Inertial Confinement Fusion," J. Phys.: Conf. Ser. **717**, 012040 (2016).

P. M. Nilson, F. Ehrne, C. Mileham, D. Mastrosimone, R. K. Jungquist, C. Taylor, C. R. Stillman, S. T. Ivancic, R. Boni, J. Hassett, D. J. Lonobile, R. W. Kidder, M. J. Shoup III, A. A. Solodov, C. Stoeckl, W. Theobald, D. H. Froula, K. W. Hill, L. Gao, M. Bitter, P. Efthimion, and D. D. Meyerhofer, "High-Resolving-Power X-Ray Spectrometer for the OMEGA EP Laser," Rev. Sci. Instrum. **87**, 11D504 (2016) (invited).

J. B. Oliver, C. Smith, J. Spaulding, A. L. Rigatti, B. Charles, S. Papernov, B. Taylor, J. Foster, C. W. Carr, R. Luthi, B. Hollingsworth, and D. Cross, "Glancing-Angle–Deposited Magnesium Oxide Films for High-Fluence Applications," Opt. Mater. Express **6**, 2291 (2016).

S. Papernov, A. A. Kozlov, J. B. Oliver, C. Smith, L. Jensen, D. Ristau, S. Günster, and H. Mädebach, "The Role of Film Interfaces in Near-Ultraviolet Absorption and Pulsed-Laser Damage in Ion-Beam–Sputtered Coatings Based on HfO_2/SiO_2 Thin-Film Pairs," Proc. SPIE **9632**, 96320B (2015).

B. W. Plansinis, W. R. Donaldson, and G. P. Agrawal, "Temporal Waveguides for Optical Pulses," J. Opt. Soc. Am. B **33**, 1112 (2016).

B. W. Plansinis, W. R. Donaldson, and G. P. Agrawal, "What is the Temporal Analog of Reflection and Refraction of Optical Beams?" Phys. Rev. Lett. **115**, 183901 (2015).

P. B. Radha, V. N. Goncharov, M. Hohenberger, T. C. Sangster, R. Betti, R. S. Craxton, D. H. Edgell, R. Epstein, D. H. Froula, J. A. Marozas, F. J. Marshall, R. L. McCrory, P. W. McKenty, D. D. Meyerhofer, D. T. Michel, S. X. Hu, W. Seka, A. Shvydky, S. Skupsky, J. A. Frenje, M. Gatu-Johnson, R. D. Petrasso, T. Ma, S. Le Pape, and A. J. Mackinnon, "Direct-Drive Implosion Physics: Results from OMEGA and the National Ignition Facility," J. Phys.: Conf. Ser. **688**, 012006 (2016).

P. B. Radha, M. Hohenberger, D. H. Edgell, J. A. Marozas, F. J. Marshall, D. T. Michel, M. J. Rosenberg, W. Seka, A. Shvydky, T. R. Boehly, T. J. B. Collins, E. M. Campbell, R. S. Craxton, J. A. Delettrez, S. N. Dixit, J. A. Frenje, D. H. Froula, V. N. Goncharov, S. X. Hu, J. P. Knauer, R. L. McCrory, P. W. McKenty, D. D. Meyerhofer, J. Moody, J. F. Myatt, R. D. Petrasso, S. P. Regan, T. C. Sangster, H. Sio, S. Skupsky, and A. Zylstra, "Direct Drive: Simulations and Results from the National Ignition Facility," Phys. Plasmas **23**, 056305 (2016) (invited).

P. B. Radha, M. Hohenberger, F. J. Marshall, D. T. Michel, J. Bates, T. R. Boehly, T. J. B. Collins, R. S. Craxton, J. A. Delettrez, S. N. Dixit, D. H. Edgell, J. A. Frenje, D. H. Froula, V. N. Goncharov, S. X. Hu, M. Karasik, J. P. Knauer,

S. LePape, J. A. Marozas, R. L. McCrory, P. W. McKenty, D. D. Meyerhofer, J. F. Myatt, S. Obenschein, R. D. Petrasso, S. P. Regan, M. J. Rosenberg, T. C. Sangster, W. Seka, A. Shvydky, H. Sio, S. Skupsky, and A. Zylstra, "Polar-Direct-Drive Experiments at the National Ignition Facility," J. Phys.: Conf. Ser. **717**, 012009 (2016).

S. P. Regan, V. N. Goncharov, I. V. Igumenshchev, T. C. Sangster, R. Betti, A. Bose, T. R. Boehly, M. J. Bonino, E. M. Campbell, D. Cao, T. J. B. Collins, R. S. Craxton, A. K. Davis, J. A. Delettrez, D. H. Edgell, R. Epstein, C. J. Forrest, J. A. Frenje, D. H. Froula, M. Gatu Johnson, V. Yu. Glebov, D. R. Harding, M. Hohenberger, S. X. Hu, D. Jacobs-Perkins, R. Janezic, M. Karasik, R. L. Keck, J. H. Kelly, T. J. Kessler, J. P. Knauer, T. Z. Kosc, S. J. Loucks, J. A. Marozas, F. J. Marshall, R. L. McCrory, P. W. McKenty, D. D. Meyerhofer, D. T. Michel, J. F. Myatt, S. P. Obenschain, R. D. Petrasso, P. B. Radha, B. Rice, M. J. Rosenberg, A. J. Schmitt, M. J. Schmitt, W. Seka, W. T. Shmayda, M. J. Shoup III, A. Shvydky, S. Skupsky, A. A. Solodov, C. Stoeckl, W. Theobald, J. Ulreich, M. D. Wittman, K. M. Woo, B. Yaakobi, and J. D. Zuegel, "Demonstration of Fuel Hot-Spot Pressure in Excess of 50 Gbar for Direct-Drive, Layered Deuterium-Tritium Implosions on OMEGA," Phys. Rev. Lett. **117**, 025001 (2016).

S. Salzman, L. J. Giannechini, H. J. Romanofsky, N. Golini, B. Taylor, S. D. Jacobs, and J. C. Lambropoulos, "Advanced Zirconia-Coated Carbonyl-Iron Particles for Acidic Magneto-rheological Finishing of Chemical-Vapor–Deposited ZnS and Other IR Materials," Proc. SPIE **9633**, 963307 (2015).

S. Salzman, H. J. Romanofsky, L. J. Giannechini, S. D. Jacobs, and J. C. Lambropoulus, "Magnetorheological Finishing of Chemical-Vapor Deposited Zinc Sulfide via Chemically and Mechanically Modified Fluids," Appl. Opt. **55**, 1481 (2016).

S. Salzman, H. J. Romanofsky, S. D. Jacobs, and J. C. Lambropoulos, "Surface–Texture Evolution of Different Chemical-Vapor-Deposited Zinc Sulfide Flats Polished with Various Magnetorheological Fluids," Prec. Eng. **43**, 257 (2016).

J. Serafini, Y. Akbas, L. Crandall, R. Bellman, C. Kosik Williams, and R. Sobolewski, "Nonequilibrium Carrier Dynamics in Ultrathin Si-on-Glass Films," J. Phys.: Conf. Ser. **647**, 012032 (2015).

J. Serafini, Y. Akbas, L. Crandall, R. Bellman, C. K. Williams, and R. Sobolewski, "Time-Resolved, Nonequilibrium Carrier Dynamics in Si-on-Glass Thin Films for Photovoltaic Cells," Semicond. Sci. Technol. **31**, 045006 (2016).

W. Shang, J. Yang, W. Zhang, Z. Li, B. Deng, Y. Dong, T. Zhu, C. Huang, X. Zhan, Y. Mei, L. Guo, R. Yu, S. Li, S. Jiang, S. Liu, F. Wang, Y. Ding, B. Zhang, and R. Betti, "Experimental Demonstration of Laser to X-Ray Conversion Enhancements with Low Density Gold Targets," Appl. Phys. Lett. **108**, 064102 (2016).

M. Sharpe, W. T. Shmayda, and W. U. Schröder, "Tritium Migration to the Surfaces of Type 316 Stainless Steel; Aluminum 6061; and Oxygen-Free, High-Conductivity Copper," Fusion Sci. Technol. **70**, 97 (2016).

W. T. Shmayda, M. Sharpe, A. M. Boyce, R. Shea, B. Petroski, and W. U. Schröder, "Dependence of Tritium Release From Stainless Steel on Temperature and Water Vapor," Fusion Sci. Technol. **68**, 766 (2015).

W. T. Shmayda, M. D. Wittman, R. F. Earley, J. L. Reid, and N. P. Redden, "The Laboratory for Laser Energetics' Hydrogen Isotope Separation System," Fusion Eng. Des. **109**, 128 (2016) (invited).

A. A. Solodov, M. J. Rosenberg, J. F. Myatt, R. Epstein, S. P. Regan, W. Seka, J. Shaw, M. Hohenberger, J. W. Bates, J. D. Moody, J. E. Ralph, D. P. Turnbull, and M. A. Barrios, "Hydrodynamic Simulations of Long-Scale-Length Plasmas for Two-Plasmon–Decay Planar-Target Experiments on the NIF," J. Phys.: Conf. Ser. **717**, 012053 (2016).

C. R. Stillman, P. M. Nilson, S. T. Ivancic, C. Mileham, I. A. Begishev, R. K. Junquist, D. J. Nelson, and D. H. Froula, "A Streaked X-Ray Spectroscopy Platform for Rapidly Heated, Near-Solid Density Plasmas," Rev. Sci. Instrum. **87**, 11E312 (2016) (invited).

C. Stoeckl, R. Boni, F. Ehrne, C. J. Forrest, V. Yu. Glebov, J. Katz, D. J. Lonobile, J. Magoon, S. P. Regan, M. J. Shoup III, A. Sorce, C. Sorce, T. C. Sangster, and D. Weiner, "Neutron Temporal Diagnostic for High-Yield Deuterium–Tritium Cryogenic Implosions on OMEGA," Rev. Sci. Instrum. **87**, 053501 (2016).

C. Stoeckl, W. Theobald, S. P. Regan, and M. H. Romanofsky, "Calibration of a Time-Resolved Hard-X-Ray Detector Using Radioactive Sources," Rev. Sci. Instrum. **87**, 11E323 (2016).

N. D. Viza, M. H. Romanofsky, M. J. Moynihan, and D. R. Harding, "The Effects of a Surfactant on the Operation of T-Junctions for Mass-Producing Foam Targets," Fusion Sci. Technol. **70**, 219 (2016).

H. Wen, A. V. Maximov, R. W. Short, J. F. Myatt, R. Yan, and C. Ren, "Two-Plasmon Decay Instability in Inhomogeneous Plasmas at Oblique Laser Incidence," Phys. Plasmas **23**, 092713 (2016).

R. Yan, R. Betti, J. Sanz, H. Aluie, B. Liu, and A. Frank, "Three-Dimensional Single-Mode Nonlinear Ablative Rayleigh–Taylor Instability," Phys. Plasmas **23**, 022701 (2016).

Omega External Users' Publications

R. Cristiano, L. Parlato, U. Nasti, M. Ejrnaes, H. Myoren, T. Taino, R. Sobolewski, and G. P. Pepe, "Superconductor/Ferromagnet Nanowires for Optical Photon Detection," IEEE Trans. Appl. Supercond. **26**, 2200104 (2016).

P. S. Datte, J. S. Ross, D. H. Froula, K. D. Daub, J. Galbraith, S. Glenzer, B. Hatch, J. Katz, J. Kilkenny, O. Landen, D. Manha, A. M. Manuel, W. Molander, D. Montgomery, J. Moody, G. F. Swadling, and J. Weaver, "The Design of the Optical Thomson Scattering Diagnostic for the National Ignition Facility," Rev. Sci. Instrum. **87**, 11E549 (2016).

P. Datte, J. S. Ross, D. Froula, J. Galbraith, S. Glenzer, B. Hatch, J. Kilkenny, O. Landen, A. M. Manuel, W. Molander, D. Montgomery, J. Moody, G. Swadling, J. Weaver, G. Vergel de Dios, and M. Vitalich, "The Preliminary Design of the Optical Thomson Scattering Diagnostic for the National Ignition Facility," J. Phys.: Conf. Ser. **717**, 012089 (2016).

B. Delormé, M. Olazabal-Loume, A. Casner, Ph. Nicolaï, D. T. Michel, G. Riazuelo, N. Borisenko, J. Breil, S. Fujioka, M. Grech, A. Orekhov, W. Seka, A. Sunahara, D. H. Froula, V. Goncharov, and V. T. Tikhonchuk, "Experimental Demonstration of Laser Imprint Reduction Using Underdense Foams," Phys. Plasmas **23**, 042701 (2016).

E. L. Dewald, F. Hartemann, P. Michel, J. Milovich, M. Hohenberger, A. Pak, O. L. Landen, L. Divol, H. F. Robey, O. A. Hurricane, T. Döppner, F. Albert, B. Bachmann, N. B. Meezan, A. J. MacKinnon, D. Callahan, and M. J. Edwards, "Generation and Beaming of Early Hot Electrons onto the Capsule in Laser-Driven Ignition Hohlraums," Phys. Rev. Lett. **116**, 075003 (2016).

T. Döppner, D. A. Callahan, O. A. Hurricane, D. E. Hinkel, T. Ma, H.-S. Park, L. F. Berzak Hopkins, D. T. Casey, P. Celliers, E. L. Dewald, T. R. Dittrich, S. W. Haan, A. L. Kritcher, A. MacPhee, S. Le Pape, A. Pak, P. K. Patel, P. T. Springer, J. D. Salmonson, R. Tommasini, L. R. Benedetti, E. Bond, D. K. Bradley, J. Caggiano, J. Church, S. Dixit, D. Edgell, M. J. Edwards, D. N. Fittinghoff, J. Frenje, M. Gatu Johnson, G. Grim, R. Hatarik, M. Havre, H. Herrmann, N. Izumi, S. F. Khan, J. L. Kline, J. Knauer, G. A. Kyrala, O. L. Landen, F. E. Merrill, J. Moody, A. S. Moore, A. Nikroo, J. E. Ralph, B. A. Remington, H. F. Robey, D. Sayre, M. Schneider, H. Streckert, R. Town, D. Turnbull, P. L. Volegov, A. Wan, K. Widmann, C. H. Wilde, and C. Yeamans, "Demonstration of High Performance in Layered Deuterium-Tritium Capsule Implosions in Uranium Hohlraums at the National Ignition Facility," Phys. Rev. Lett. **115**, 055001 (2015).

J. A. Frenje, P. E. Grabowski, C. K. Li, F. H. Séguin, A. B. Zylstra, M. Gatu Johnson, R. D. Petrasso, V. Yu. Glebov, and T. C. Sangster, "Measurements of Ion Stopping Around the Bragg Peak in High-Energy-Density Plasmas," J. Phys.: Conf. Ser. **647**, 012020 (2015).

L. Guazzotto and R. Betti, "Two-Fluid Equilibrium with Flow: FLOW2," Phys. Plasmas **22**, 092503 (2015).

A. J. Harvey-Thompson, A. B. Sefkow, T. N. Nagayama, M. S. Wei, E. M. Campbell, G. Fiksel, P.-Y. Chang, J. R. Davies, D. H. Barnak, V. Y. Glebov, P. Fitzsimmons, J. Fooks, and B. E. Blue, "Diagnosing Laser-Preheated Magnetized Plasmas Relevant to Magnetized Liner Inertial Fusion," Phys. Plasmas **22**, 122708 (2015).

O. A. Hurricane, D. A. Callahan, D. T. Casey, E. L. Dewald, T. R. Dittrich, T. Döppner, S. Haan, D. E. Hinkel, L. F. Berzak Hopkins, O. Jones, A. L. Kritcher, S. Le Pape, T. Ma, A. G. MacPhee, J. L. Milovich, J. Moody, A. Pak, H.-S. Park, P. K. Patel, J. E. Ralph, H. F. Robey, J. S. Ross, J. D. Salmonson, B. K. Spears, P. T. Springer, R. Tommasini, F. Albert, L. R. Benedetti, R. Bionta, E. Bond, D. K. Bradley, J. Caggiano,

P. M. Celliers, C. Cerjan, J. A. Church, R. Dylla-Spears, D. Edgell, M. J. Edwards, D. Fittinghoff, M. A. Barrios Garcia, A. Hamza, R. Hatarik, H. Herrmann, M. Hohenberger, D. Hoover, J. L. Kline, G. Kyrala, B. Kozioziemski, G. Grim, J. E. Field, J. Frenje, N. Izumi, M. Gatu Johnson, S. F. Khan, J. Knauer, T. Kohut, O. Landen, F. Merrill, P. Michel, A. Moore, S. R. Nagel, A. Nikroo, T. Parham, R. R. Rygg, D. Sayre, M. Schneider, D. Shaughnessy, D. Strozzi, R. P. J. Town, D. Turnbull, P. Volegov, A. Wan, K. Widmann, C. Wilde, and C. Yeamans, "Inertially Confined Fusion Plasmas Dominated by Alpha-Particle Self-Heating," Nat. Physics **12**, 800 (2016).

V. V. Ivanov, A. A. Anderson, and I. A. Begishev, "Four-Color Laser Diagnostics for *Z*-Pinch and Laser-Produced Plasma," Appl. Opt. **55**, 498 (2016).

L. C. Jarrott, M. S. Wei, C. McGuffey, A. A. Solodov, W. Theobald, B. Qiao, C. Stoeckl, R. Betti, H. Chen, J. Delettrez, T. Döppner, E. M. Giraldez, V. Y. Glebov, H. Habara, T. Iwawaki, M. H. Key, R. W. Luo, F. J. Marshall, H. S. McLean, C. Mileham, P. K. Patel, J. J. Santos, H. Sawada, R. B. Stephens, T. Yabuuchi, and F. N. Beg, "Visualizing Fast Electron Energy Transport into Laser-Compressed High-Density Fast-Ignition Targets," Nat. Phys. **12**, 499 (2016).

H. M. Johns, R. C. Mancini, T. Nagayama, D. C. Mayes, R. Tommasini, V. A. Smalyuk, S. P. Regan, and J. A. Delettrez, "Shell Stability and Conditions Analyzed Using a New Method of Extracting Shell Areal Density Maps from Spectrally Resolved Images of Direct-Drive Inertial Confinement Fusion Implosions," Phys. Plasmas **23**, 012709 (2016).

J. D. Kilkenny, P. M. Bell, D. K. Bradley, D. L. Bleuel, J. A. Caggiano, E. L. Dewald, W. W. Hsing, D. H. Kalantar, R. L. Kauffman, D. J. Larson, J. D. Moody, D. H. Schneider, M. B. Schneider, D. A. Shaughnessy, R. T. Shelton, W. Stoeffl, K. Widmann, C. B. Yeamans, S. H. Batha, G. P. Grim, H. W. Herrmann, F. E. Merrill, R. J. Leeper, J. A. Oertel, T. C. Sangster, D. H. Edgell, M. Hohenberger, V. Yu. Glebov, S. P. Regan, J. A. Frenje, M. Gatu-Johnson, R. D. Petrasso, H. G. Rinderknecht, A. B. Zylstra, G. W. Cooper, and C. Ruiz, "The National Ignition Facility Diagnostic Set at the Completion of the National Ignition Campaign, September 2012," Fusion Sci. Technol. **69**, 420 (2016).

J. D. Kilkenny, J. A. Caggiano, R. Hatarik, J. P. Knauer, D. B. Sayre, B. K. Spears, S. V. Weber, C. B. Yeamans, C. J. Cerjan, L. Divol, M. J. Eckart, V. Yu. Glebov, H. W. Herrmann, S. Le Pape, D. H. Munro, G. P. Grim, O. S. Jones, L. Berzak-Hopkins, M. Gatu-Johnson, A. J. Mackinnon, N. B. Meezan, D. T. Casey, J. A. Frenje, J. M. Mcnaney, R. Petrasso, H. Rinderknecht, W. Stoeffl, and A. B. Zylstra, "Understanding the Stagnation and Burn of Implosions on NIF," J. Phys.: Conf. Ser. **688**, 012048 (2016).

S. Laffite, J. L. Bourgade, T. Caillaud, J. A. Delettrez, J. A. Frenje, F. Girard, V. Yu. Glebov, T. Joshi, O. Landoas, G. Legay, S. Lemaire, R. C. Mancini, F. J. Marshall, L. Masse, P. E. Masson-Laborde, D. T. Michel, F. Philippe, C. Reverdin, W. Seka, and V. Tassin, "Time History Prediction of Direct-Drive Implosions on the Omega Facility," Phys. Plasmas **23**, 012706 (2016).

M. Margala, H. Wu, and R. Sobolewski, "Ballistic Deflection Transistors and Their Application to THz Amplification," J. Phys.: Conf. Ser. **647**, 012020 (2015).

P. E. Masson-Laborde, M. C. Monteil, V. Tassin, F. Philippe, P. Gauthier, A. Casner, S. Depierreux, C. Neuville, B. Villette, S. Lafite, P. Seytor, P. Fremerye, W. Seka, D. Teychenné, A. Debayle, D. Marion, P. Loiseau, and M. Casanova, "Laser Plasma Interaction on Rugby Hohlraum on the Omega Laser Facility: Comparison Between Cylinder, Rugby, and Elliptical Hohlraums," Phys. Plasmas **23**, 022703 (2016).

A. S. Moore, J. Benstead, M. F. Ahmed, J. Morton, T. M. Guymer, R. Soufli, T. Pardini, R. L. Hibbard, C. G. Bailey, P. M. Bell, S. Hau-Riege, M. Bedzyk, M. J. Shoup III, S. P. Regan, T. Agliata, R. Jungquist, D. W. Schmidt, L. B. Kot, W. J. Garbett, M. S. Rubery, J. W. Skidmore, E. Gullikson, and F. Salmassi, "Two-Color Spatial and Temporal Temperature Measurements Using a Streaked Soft X-Ray Imager," Rev. Sci. Instrum. **87**, 11E313 (2016).

Y. Ping, A. Fernandez-Panella, H. Sio, A. Correa, R. Shepherd, O. Landen, R. A. London, P. A. Sterne, H. D. Whitley, D. Fratanduono, T. R. Boehly, and G. W. Collins, "Differential Heating: A Versatile Method for Thermal Conductivity Measurements in High-Energy-Density Matter," Phys. Plasmas **22**, 092701 (2015).

M. J. Rosenberg, A. B. Zylstra, F. H. Séguin, H. G. Rinderknecht, J. A. Frenje, M. Gatu Johnson, H. Sio, C. J. Waugh, N. Sinenian, C. K. Li, R. D. Petrasso, S. LePape, T. Ma, A. J. Mackinnon, J. R. Rygg, P. A. Amendt, C. Bellei, L. R. Benedetti, L. Berzak Hopkins, R. M. Bionta, D. T. Casey, L. Divol, M. J. Edwards, S. Glenn, S. H. Glenzer, D. G. Hicks, J. R. Kimbrough, O. L. Landen, J. D. Lindl, A. MacPhee, J. M. McNaney, N. B. Meezan, J. D. Moody, M. J. Moran, H.-S. Park, J. Pino, B. A. Remington,

H. Robey, M. D. Rosen, S. C. Wilks, R. A. Zacharias, P. W. McKenty, M. Hohenberger, P. B. Radha, D. Edgell, F. J. Marshall, J. A. Delettrez, V. Yu. Glebov, R. Betti, V. N. Goncharov, J. P. Knauer, T. C. Sangster, H. W. Herrmann, N. M. Hoffman, G. A. Kyrala, R. J. Leeper, R. E. Olson, J. D. Kilkenny, and A. Nikroo, "A Direct-Drive Exploding-Pusher Implosion as the First Step in Development of a Monoenergetic Charged-Particle Backlighting Platform at the National Ignition Facility," High Energy Density Phys. **18**, 38 (2016).

J. S. Ross, P. Datte, L. Divol, J. Galbraith, D. H. Froula, S. H. Glenzer, B. Hatch, J. Katz, J. Kilkenny, O. Landen, A. M. Manuel, W. Molander, D. S. Montgomery, J. D. Moody, G. Swadling, and J. Weaver, "Simulated Performance of the Optical Thomson Scattering Diagnostic, Designed for the National Ignition Facility," Rev. Sci. Instrum. **87**, 11E510 (2016).

M. Rutkauskas, C. Farrell, C. Dorrer, K. L. Marshall, T. Crawford, T. R. Lundquist, P. Vedagarbha, K. Erington, D. Bodoh, and D. T. Reid, "Two-Photon Laser-Assisted Device Alteration in CMOS Integrated Circuits Using Linearly, Circularly and Radially Polarized Light," Microelectronics Reliability **60**, 62 (2016).

M. Rutkauskas, C. Farrell, C. Dorrer, K. L. Marshall, T. R. Lundquist, P. Vedagarbha, and D. T. Reid, "High-Resolution Subsurface Microscopy of CMOS Integrated Circuits Using Radially Polarized Light," Opt. Lett. **40**, 5502 (2015).

J. R. Rygg, A. B. Zylstra, F. H. Séguin, S. LePape, B. Bachmann, R. S. Craxton, E. M. Garcia, Y. Z. Kong, M. Gatu-Johnson, S. F. Khan, B. J. Lahmann, P. W. McKenty, R. D. Petrasso, H. G. Rinderknecht, M. J. Rosenberg, D. B. Sayre, and H. W. Sio, "Note: A Monoenergetic Proton Backlighter for the National Ignition Facility," Rev. Sci. Instrum. **86**, 116104 (2015).

S. A. Slutz, W. A. Stygar, M. R. Gomez, K. J. Peterson, A. B. Sefkow, D. B. Sinars, R. A. Vesey, E. M. Campbell, and R. Betti, "Scaling Magnetized Liner Inertial Fusion on Z and Future Pulsed-Power Accelerators," Phys. Plasmas **23**, 022702 (2016).

M. P. Valdivia, D. Stutman, C. Stoeckl, C. S. Mileham, I. A. Begishev, J. Bromage, and S. P. Regan, "A Talbot–Lau X-Ray Defelctometer as a High-Energy Density Plasma Diagnostic," IEEE Trans. Plasma Sci. **44**, 1592 (2016).

M. P. Valdivia, D. Stutman, C. Stoeckl, W. Theobald, C. Mileham, I. A. Begishev, J. Bromage, and S. P. Regan, "An X-Ray Backlit Talbot-Lau Deflectometer for High-Energy-Density Electron Density Diagnostics," Rev. Sci. Instrum. **87**, 023505 (2016).

J. Wang, F. Coppari, R. F. Smith, J. H. Eggert, A. E. Lazicki, D. E. Fratanduono, J. R. Rygg, T. R. Boehly, G. W. Collins, and T. S. Duffy, "X-Ray Diffraction of Molybdenum Under Shock Compression to 450 GPa," Phys. Rev. B **92**, 174114 (2015).

A. B. Zylstra, H. W. Herrmann, M. Gatu Johnson, Y. H. Kim, J. A. Frenje, G. Hale, C. K. Li, M. Rubery, M. Paris, A. Bacher, C. R. Brune, C. Forrest, V. Yu. Glebov, R. Janezic, D. McNabb, A. Nikroo, J. Pino, T. C. Sangster, F. H. Séguin, W. Seka, H. Sio, C. Stoeckl, and R. D. Petrasso, "Using Inertial Fusion Implosions to Measure the T + ^{3}He Fusion Cross Section at Nucleosynthesis-Relevant Energies," Phys. Rev. Lett. **117**, 035002 (2016).

Conference Presentations

D. Polsin, T. R. Boehly, S. Ivancic, M. C. Gregor, C. A. McCoy, D. D. Meyerhofer, D. E. Fratanduono, and P. M. Celliers, "Probing the Release of Shocked Material," Third High-Power Laser Workshop, Menlo Park, CA, 5–6 October 2015.

The following presentations were made at the Industrial Associates Fall 2015 Meeting, Rochester, NY, 12–13 October 2015:

B. W. Plansinis, G. P. Agrawal, and W. R. Donaldson, "Temporal Analog of Reflection and Refraction."

K. A. Sharma, T. A. Germer, J. D. Zuegel, and T. G. Brown, "A Review of Scattered Light Analysis for Distributed Polarization Rotators."

The following presentations were made at Optifab 2015, Rochester, NY, 12–15 October 2015:

S. Salzman, L. J. Giannechini, H. J. Romanofsky, N. Golini, B. Taylor, S. D. Jacobs, and J. C. Lambropoulos, "Advanced Zirconia-Coated Carbonyl-Iron Particles for Acidic Magnetorheological Finishing of Chemical-Vapor–Deposited ZnS and Other IR Materials."

K. Tinkham, T. Jacobs, M. Mayton, Z. Hobbs, K. L. Marshall, and S. D. Jacobs, "Cerium Oxide Polishing Slurry Reclamation Project: Characterization Techniques and Results."

W. T. Shmayda, "Tritium Operations at the Laboratory for Laser Energetics," Health Physics Society, Rochester, NY, 15 October 2015.

The following presentations were made at Frontiers in Optics, San Jose, CA, 18–22 October 2015:

T. Petersen and J. Bromage, "A High-Average-Power, Degenerate, 2.06 μm BiB_3O_6 Femtosecond Optical Parametric Oscillator."

B. W. Plansinis, G. P. Agrawal, and W. R. Donaldson, "Temporal Analog of Reflection and Refraction."

R. L. McCrory, "From ALPHA to OMEGA EP—The History of LLE," OSA Rochester Section, Rochester, NY, 27 October 2015.

W. Theobald, "Shock Ignition—An Alternative Concept for Laser Fusion," GSI Presentation, Darmstadt, Germany, 27 October 2015 (invited).

The following presentations were made at the Tritium Focus Group, Los Alamos, NM, 3–5 November 2015:

W. T. Shmayda, "Radiological Challenges at the Laboratory for Laser Energetics."

W. T. Shmayda, M. Sharpe, and M. Cody, "Modeling Tritium on Metal Surfaces."

W. R. Donaldson, "Electro-Optic Measurements on the OMEGA Laser System: How to do Small Science in a Big Science Environment," 39th Annual IEEE EDS Activities in Western New York Conference, Rochester, NY, 6 November 2015 (invited).

The following presentations were made at the 57th Annual Meeting of the APS Division of Plasma Physics, Savannah, GA, 16–20 November 2015:

K. S. Anderson, P. W. McKenty, A. Shvydky, J. P. Knauer, T. J. B. Collins, J. A. Delettrez, D. Keller, and M. M. Marinak, "Characterizing Hot-Spot Dynamics of Direct-Drive Cryogenic Implosions on OMEGA."

D. H. Barnak, R. Betti, P.-Y. Chang, and J. R. Davies, "First Results from Laser-Driven MagLIF Experiments on OMEGA: Time Evolution of Laser Gas Heating Using Soft X-Ray Diagnostics."

P. X. Belancourt, P. A. Keiter, R. P. Drake, W. Theobald, T. J. B. Collins, M. J. Bonino, and P. Kozlowski, "Equation-of-State Measurements of Resorcinol Formaldehyde Foam Using Imaging X-Ray Thomson Spectrometer."

T. R. Boehly, M. J. Rosenberg, M. Hohenberger, D. N. Polsin, P. B. Radha, A. Shvydky, V. N. Goncharov, D. R. Harding, S. P. Regan, T. C. Sangster, P. M. Celliers, D. E. Fratanduono, and S. N. Dixit, "Polar-Direct-Drive Shock-Timing Measurements at the National Ignition Facility."

A. Bose, R. Betti, K. M. Woo, A. R. Christopherson, and D. Shvarts, "Effects of Long- and Intermediate-Wavelength Asymmetries on Hot-Spot Energetics."

D. Cao, J. A. Marozas, T. J. B. Collins, P. B. Radha, and P. W. McKenty, "A New Immediate Far-Field Spot Design for Polar Direct Drive at the National Ignition Facility."

P.-Y. Chang, D. H. Barnak, R. Betti, E. M. Campbell, J. R. Davies, J. P. Knauer, K. J. Peterson, A. B. Sefkow, D. B. Sinars, S. A. Slutz, and G. Fiksel, "First Results from Laser-Driven MagLIF Experiments on OMEGA: Optimization of Illumination Uniformity."

A. R. Christopherson, A. Bose, K. M. Woo, J. Howard, K. S. Anderson, E. M. Campbell, J. A. Delettrez, V. N. Goncharov, F. J. Marshall, R. L. McCrory, S. P. Regan, T. C. Sangster, C. Stoeckl, W. Theobald, M. J. Edwards, R. Nora, B. K. Spears, J. Sanz, O. A. Hurricane, J. D. Lindl, P. K. Patel, and D. Shvarts, "Alpha Heating and Burning Plasmas in Inertial Confinement Fusion" (invited).

T. J. B. Collins, J. A. Marozas, S. Skupsky, D. Cao, P. W. McKenty, J. A. Delettrez, and G. Moses, "Design Options for Polar-Direct-Drive Targets: From Alpha Heating to Ignition."

R. S. Craxton, Y. Z. Kong, E. M. Garcia, P. Huang, J. Kinney, P. W. McKenty, R. Zhang, S. Le Pape, F. Coppari, R. F. Heeter, B. J. MacGowan, J. R. Rygg, and M. B. Schneider, "Beam-Pointing Designs for Exploding-Pusher Proton and X-Ray Backlighting Targets at the National Ignition Facility."

A. Davies, S. Bucht, J. Katz, D. Haberberger, J. Bromage, J. D. Zuegel, D. H. Froula, P. A. Norreys, R. Bingham, J. Saldler, R. Trines, and L. O. Silva, "A Tunable (1100-nm to 1500-nm) 50-mJ Laser Enables a Pump-Depleting Plasma-Wave Amplifier."

J. R. Davies, D. H. Barnak, R. Betti, E. M. Campbell, P.-Y. Chang, G. Fiksel, W. Seka, K. J. Peterson, A. B. Sefkow, D. B. Sinars, and S. A. Slutz, "First Results from Laser-Driven MagLIF Experiments on OMEGA: Backscatter and Transmission Measurements of Laser Preheating."

A. K. Davis, D. Cao, D. T. Michel, D. H. Edgell, R. Epstein, V. N. Goncharov, M. Hohenberger, S. X. Hu, I. V. Igumenshchev, J. A. Marozas, A. V. Maximov, J. F. Myatt, P. B. Radha, S. P. Regan, T. C. Sangster, J. G. Shaw, D. H. Froula, M. Lafon, J. D. Moody, and R. J. Wallace, "Angularly Resolved Mass Ablation Rate and Ablation-Front-Trajectory Measurements at the Omega Laser and National Ignition Facilities" (invited).

J. A. Delettrez, B. Yaakobi, J. F. Myatt, and D. H. Edgell, "Recent Advances in the Transport Modeling of Two-Plasmon–Decay Electrons in the 1-D Hydrodynamic Code *LILAC*."

T. Eckert, A. Gula, L. Vincett, M. Yuly, S. J. Padalino, M. Russ, A. Simone, D. Ellison, M. Bienstck, H. Desmitt, T. C. Sangster, and S. P. Regan, "Efficiency Calibration for Measuring the ^{12}C(n,2n)^{11}C Cross-Section."

D. H. Edgell, R. K. Follett, V. N. Goncharov, I. V. Igumenshchev, J. Katz, J. F. Myatt, W. Seka, and D. H. Froula, "Diagnosing Cross-Beam Energy Transfer Using Beamlets of Unabsorbed Light from Direct-Drive Implosions."

R. Epstein, M. J. Rosenberg, A. A. Solodov, J. F. Myatt, S. P. Regan, W. Seka, M. Hohenberger, M. A. Barrios, and J. D. Moody, "Application and Analysis of the Isoelectronic Line Ratio Temperature Diagnostic in a Planar Ablating-Plasma Experiment at the National Ignition Facility."

T. M. Filkins, J. A. Steidle, R. Ward, C. Freeman, T. C. Sangster, and S. P. Regan, "Radiochromic Film Sensitivity Calibrations Using Ion Beams from a Palletron Accelerator."

R. K. Follett, J. G. Shaw, D. H. Edgell, R. J. Henchen, S. X. Hu, J. Katz, D. T. Michel, J. F. Myatt, A. A. Solodov, C. Stoeckl, B. Yaakobi, and D. H. Froula, "Modeling Hot-Electron Measurements in Multibeam Two-Plasmon–Decay Experiments."

C. J. Forrest, V. Yu. Glebov, J. P. Knauer, P. B. Radha, S. P. Regan, T. C. Sangster, C. Stoeckl, W. U. Schröeder, J. A. Frenje, M. Gatu Johnson, M. W. Paris, G. Hale, and A. B. Zylstra, "Neutron Induced Deuterium Breakup in Inertial Confinement Fusion at the Omega Laser Facility."

D. H. Froula, R. K. Follett, R. J. Henchen, V. N. Goncharov, D. T. Michel, A. A. Solodov, J. A. Delettrez, D. H. Edgell, B. Yaakobi, C. Stoeckl, and J. F. Myatt, "Mitigation of Two-Plasmon Decay in Direct-Drive Implosions Using Multilayer Targets."

V. Yu. Glebov, C. J. Forrest, J. P. Knauer, S. P. Regan, T. C. Sangster, and C. Stoeckl, "A New Neutron Time-of-Flight Detector for DT Yield and Ion-Temperature Measurements on OMEGA."

V. N. Goncharov, S. P. Regan, T. C. Sangster, R. Betti, T. R. Boehly, M. J. Bonino, E. M. Campbell, T. J. B. Collins, R. S. Craxton, J. A. Delettrez, D. H. Edgell, R. Epstein, C. J. Forrest, D. H. Froula, V. Yu. Glebov, D. R. Harding, S. X. Hu, I. V. Igumenshchev, R. T. Janezic, J. H. Kelly, T. J. Kessler, T. Z. Kosc, S. J. Loucks, J. A. Marozas, F. J. Marshall, R. L. McCrory, P. W. McKenty, D. D. Meyerhofer, D. T. Michel, J. F. Myatt, P. B. Radha, W. Seka, W. T. Shmayda, A. Shvydky, S. Skupsky, C. Stoeckl, W. Theobald, F. Weilacher, B. Yaakobi, J. A. Frenje, M. Gatu Johnson, R. D. Petrasso, S. P. Obenschain, and M. Karasik, "Cross-Beam Energy Transfer Mitigation in Cryogenic Implosions on OMEGA."

X. Gong, V. N. Goncharov, and I. V. Igumenshchev, "A 3-D Model of Hot-Spot Formation in Inertial Confinement Fusion Implosions."

M. C. Gregor, T. R. Boehly, C. A. McCoy, D. N. Polsin, D. D. Meyerhofer, D. E. Fratanduono, P. M. Celliers, and G. W. Collins, "The Release Behavior of Diamond Shocked to 25 Mbar."

D. Haberberger, D. H. Froula, S. X. Hu, C. Joshi, S. Tochitsky, C. Gong, F. Fiuza, and L. Silva, "Shock-Wave Acceleration of Ions on OMEGA EP."

R. J. Henchen, S. X. Hu, R. K. Follett, J. Katz, V. N. Goncharov, D. H. Froula, and W. Rozmus, "Heat-Flux Measurements from Collective Thomson-Scattering Spectra."

M. Hohenberger, A. Shvydky, P. B. Radha, M. J. Rosenberg, V. N. Goncharov, S. Le Pape, F. J. Marshall, D. T. Michel, J. P. Knauer, S. P. Regan, T. C. Sangster, S. R. Nagel, A. Nikroo, V. A. Smalyuk, and R. J. Wallace, "Hydrodynamic Instability Growth in Polar-Direct-Drive Implosions at the National Ignition Facility."

S. X. Hu, L. A. Collins, J. D. Kress, V. N. Goncharov, T. R. Boehly, R. L. McCrory, and S. Skupsky, "First-Principles Investigations on Thermal Conductivity and Average Ionization of CH Ablators Under Extreme Conditions."

I. V. Igumenshchev, V. N. Goncharov, F. J. Marshall, K. Silverstein, J. P. Knauer, D. H. Froula, and S. P. Regan, "Numerical Study of Large-Scale, Laser-Induced Nonuniformities in Cryogenic OMEGA Implosions."

S. Ivancic, P. M. Nilson, C. R. Stillman, C. Mileham, and D. H. Froula, "Design of an Extreme Ultraviolet Spectrometer Suite for Isochoric-Heated Warm-Dense-Matter Studies."

J. P. Knauer, M. Gatu Johnson, R. M. Bionta, E. J. Bond, D. K. Bradley, J. A. Caggiano, D. A. Callahan, D. T. Casey, C. J. Cerjan, T. Doeppner, M. J. Eckart, M. J. Edwards, J. A. Frenje, V. Yu. Glebov, G. P. Grim, E. P. Hartouni, R. Hatarik, D. E. Hinkel, O. A. Hurricane, W. W. Hsing, J. D. Kilkenny, A. Kritcher, O. L. Landen, S. Le Pape, T. Ma, A. J. Mackinnon, D. H. Munro, H.-S. Park, P. K. Patel, R. D. Petrasso, J. E. Ralph, B. A. Remington, T. C. Sangster, D. B. Sayre, B. K. Spears, and C. B. Yeamans, "Neutron Yield and Ion Temperature from DD and DT Fusion in National Ignition Facility High-Foot Implosions."

P. Lawson-Keister, J. Padawar-Curry, H. Visca, K. Fletcher, S. J. Padalino, T. C. Sangster, and S. P. Regan, "Characterizing ICF Neutron Scintillation Diagnostics on the nTOF Line at SUNY Geneseo."

J. Li, S. X. Hu, and C. Ren, "Effects of Laser–Plasma Instabilities on Hydro Evolution in Direct-Drive Inertial Confinement Fusion."

J. A. Marozas, T. J. B. Collins, P. W. McKenty, and J. D. Zuegel, "Improved Wavelength Detuning Cross-Beam Energy Transfer Mitigation Strategy for Polar Direct Drive at the National Ignition Facility."

F. J. Marshall, V. N. Goncharov, V. Yu. Glebov, S. P. Regan, T. C. Sangster, and C. Stoeckl, "Framed X-Ray Imaging of Cryogenic Target Implosion Cores on OMEGA."

A. V. Maximov, J. F. Myatt, R. W. Short, I. V. Igumenshchev, and W. Seka, "Beam Energy Exchange Driven by Incoherent Laser Beams with Frequency Detuning."

C. A. McCoy, M. C. Gregor, D. N. Polsin, T. R. Boehly, D. E. Fratanduono, P. M. Celliers, G. W. Collins, and D. D. Meyerhofer, "Measurements of Sound Velocity and Grüneisen Parameter in CH and MgO Shocked to TPa Pressures."

P. W. McKenty, J. A. Marozas, F. J. Marshall, J. Weaver, S. P. Obenschain, and A. J. Schmitt, "Evaluation of Wavelength Detuning to Mitigate Cross-Beam Energy Transfer Using the Nike Laser."

D. T. Michel, T. C. Sangster, V. N. Goncharov, A. K. Davis, I. V. Igumenshchev, R. Epstein, V. Yu. Glebov, S. X. Hu, D. D. Meyerhofer, S. P. Regan, W. Seka, A. Shvydky, C. Stoeckl, and D. H. Froula, "Measurements of the Conduction-Zone Length and Mass Ablation Rate in Cryogenic Direct-Drive Implosions on OMEGA to Restrict Thermal-Transport Models."

J. F. Myatt, J. G. Shaw, V. N. Goncharov, J. Zhang, A. V. Maximov, R. W. Short, R. K. Follett, W. Seka, D. H. Edgell, D. H. Froula, D. F. DuBois, D. A. Russell, and H. X. Vu, "A Numerical Model for Two-Plasmon–Decay Hot-Electron Production and Mitigation in Direct-Drive Implosions."

P. M. Nilson, G. Fiksel, C. Stoeckl, P. A. Jannimagi, C. Mileham, W. Theobald, J. R. Davies, J. F. Myatt, A. A. Solodov, D. H. Froula, R. Betti, and D. D. Meyerhofer, "Supersonic Propagation of a K-Shell Ionization Front in Metal Targets."

S. J. Padalino, A. Simone, E. Turner, M. K. Ginnane, M. Glisic, B. Kousar, A. Smith, T. C. Sangster, and S. P. Regan, "Time-Resolved Tandem Faraday Cup Development for High-Energy TNSA Particles."

D. N. Polsin, T. R. Boehly, S. Ivancic, M. C. Gregor, C. A. McCoy, K. S. Anderson, D. E. Fratanduono, P. M. Celliers, and D. D. Meyerhofer, "Probing the Release of Shocked Material."

P. B. Radha, M. Hohenberger, T. R. Boehly, T. J. B. Collins, R. S. Craxton, J. A. Delettrez, D. H. Edgell, D. H. Froula, V. N. Goncharov, S. X. Hu, J. P. Knauer, J. A. Marozas, F. J. Marshall, R. L. McCrory, P. W. McKenty, D. D. Meyerhofer, D. T. Michel, J. F. Myatt, S. P. Regan, M. J. Rosenberg, T. C. Sangster, W. Seka, A. Shvydky, S. Skupsky, J. A. Frenje, R. D. Petrasso, H. Sio, A. B. Zylstra, S. N. Dixit, S. Le Pape, J. W. Bates, M. Karasik, and S. P. Obenschein, "Direct Drive: Simulations and Experiments at the National Ignition Facility" (invited).

S. P. Regan, V. N. Goncharov, T. C. Sangster, R. Betti, T. R. Boehly, M. J. Bonino, E. M. Campbell, D. Cao, T. J. B. Collins, R. S. Craxton, A. K. Davis, J. A. Delettrez, D. H. Edgell, R. Epstein, C. J. Forrest, D. H. Froula, V. Yu. Glebov, D. R. Harding, M. Hohenberger, S. X. Hu, I. V. Igumenshchev, R. T. Janezic, J. H. Kelly, T. J. Kessler, J. P. Knauer, T. Z. Kosc, J. A. Marozas, F. J. Marshall, R. L. McCrory, P. W. McKenty, D. T. Michel, J. F. Myatt, P. B. Radha, M. J. Rosenberg, W. Seka, W. T. Shmayda, A. Shvydky, S. Skupsky, A. A. Solodov, C. Stoeckl, W. Theobald, M. D. Wittman, B. Yaakobi, J. D. Zuegel, J. A. Frenje, M. Gatu Johnson, R. D. Petrasso, S. P. Obenschain, M. Karasik, A. J. Schmitt, D. D. Meyerhofer, and M. J. Schmitt, "Energy Coupling and Hot-Spot Pressure in Direct-Drive Layered DT Implosions on OMEGA" (invited).

M. J. Rosenberg, A. A. Solodov, W. Seka, R. Epstein, J. F. Myatt, S. P. Regan, M. Hohenberger, T. J. B. Collins, D. P. Turnbull, P. Michel, J. D. Moody, J. E. Ralph, and M. A. Barrios, "Planar Two-Plasmon–Decay Experiments at Polar-Direct-Drive Ignition-Relevant Scale Lengths at the National Ignition Facility."

W. Seka, S. P. Regan, P. B. Radha, M. J. Rosenberg, M. Hohenberger, V. N. Goncharov, J. F. Myatt, J. E. Ralph, J. D. Moody, and D. P. Turnbull, "Stimulated Raman Scattering as Coronal T_e Diagnostic for Direct-Drive Experiments on the Current National Ignition Facility."

R. W. Short, A. V. Maximov, J. F. Myatt, W. Seka, and J. Zhang, "Absolute Two-Plasmon Decay and Stimulated Raman Scattering in Direct-Drive Irradiation Geometries."

A. Shvydky, M. Hohenberger, P. B. Radha, M. J. Rosenberg, R. S. Craxton, V. N. Goncharov, J. A. Marozas, F. J. Marshall, P. W. McKenty, S. P. Regan, and T. C. Sangster, "Numerical Simulations of Hydrodynamic Instability Growth and Imprint Experiments at the National Ignition Facility."

A. A. Solodov, M. J. Rosenberg, J. F. Myatt, R. Epstein, S. P. Regan, W. Seka, J. G. Shaw, M. Hohenberger, J. W. Bates, J. E. Moody, J. E. Ralph, D. P. Turnbull, and M. A. Barrios, "Modeling of Two-Plasmon–Decay Experiments at Direct-Drive Ignition-Relevant Plasma Conditions at the National Ignition Facility."

C. R. Stillman, P. M. Nilson, S. Ivancic, C. Mileham, D. D. Meyerhofer, D. H. Froula, M. E. Martin, and R. A. London, "X-Ray Spectroscopy of Rapidly Heated Buried-Aluminum Layers."

C. Stoeckl, C. J. Forrest, V. Yu. Glebov, T. C. Sangster, W. U. Schröder, and E. Henry, "Spectroscopy of Neutrons Generated Through Nuclear Reactions in Short-Pulse Laser Experiments."

A. Tantillo, M. C. Watson, E. Pogozelski, T. C. Sangster, and S. P. Regan, "Target Chamber Manipulator."

W. Theobald, R. Betti, W. Seka, A. Bose, D. T. Michel, C. Stoeckl, R. Yan, R. Nora, A. Casner, M. Lafon, X. Ribeyre, E. Llor-Aisa, A. Vallet, J. Peebles, F. N. Beg, and M. S. Wei, "Hot-Electron Generation in Various Ablator Materials at Shock-Ignition–Relevant Laser Intensities."

H. Wen, A. V. Maximov, R. Yan, C. Ren, J. Li, and J. F. Myatt, "Three-Dimensional Modeling of Laser–Plasma Interactions Near the Quarter-Critical Density in Plasmas."

M. P. Wiesner, R. Ume, J. G. McLean, T. C. Sangster, and S. P. Regan, "Enhancement of Particle Track Etch Rate in CR-39 by UV Exposure."

K. M. Woo, R. Betti, A. Bose, R. Epstein, J. A. Delettrez, K. S. Anderson, R. Yan, P.-Y. Chang, D. Jonathan, and M. Charissis, "Three-Dimensional Simulations of the Deceleration Phase of Inertial Fusion Implosions Using *DEC3D*."

R. Yan, R. Betti, J. Sanz, B. Liu, and A. Frank, "Three-Dimensional Single-Mode Nonlinear Ablative Rayleigh–Taylor Instability."

J. Zhang, J. F. Myatt, R. W. Short, A. V. Maximov, H. X. Vu, D. F. DuBois, and D. A. Russell, "Self-Consistent Calculation of Half-Harmonic Emission Generated by the Two-Plasmon–Decay Instability."

D. R. Harding, B. Chock, W. Wang, Z. Bei, and T. B. Jones, "Electric-Field–Assisted Motion of Low-Surface–Energy Fluid Droplets on Dielectric Surfaces," 2015 MRS Fall Meeting, Boston, MA, 29 November–4 December 2015.

E. M. Campbell, D. Haberberger, A. Davies, S.-W. Bahk, J. Bromage, J. D. Zuegel, D. H. Froula, J. Sadler, and P. A. Norreys, "Ultrahigh Brightness Laser Development at the Laboratory for Laser Energetics," George Washington University, Washington, DC, 14 December 2015.

R. L. McCrory, "Perspectives on Inertial Fusion Energy," Fusion Power Associates, Washington, DC, 16–17 December 2015.

M. J. Rosenberg, A. A. Solodov, W. Seka, R. Epstein, J. F. Myatt, S. P. Regan, M. Hohenberger, T. J. B. Collins, P. Michel, D. P. Turnbull, J. D. Moody, J. E. Ralph, M. A. Barrios, and J. W. Bates, "Planar Laser–Plasma Interaction Experiments at Direct-Drive Ignition-Relevant Scale Lengths at the National Ignition Facility," NIF User Group Meeting, Livermore, CA, 1–3 February 2016.

J. D. Zuegel, A. Agliata, S.-W. Bahk, I. A. Begishev, W. A. Bittle, T. Buczek, J. Bunkenburg, D. Canning, A. Consentino, D. Coppenbarger, R. Cuffney, C. Dorrer, J. Fini, D. H. Froula, G. Gates, M. J. Guardalben, D. Haberberger, S. Hadrich, C. Hall, H. Huang, R. K. Jungquist, C. Kellogg, T. J. Kessler, G. Kick, E. Kowaluk, B. E. Kruschwitz, T. Lewis, J. Magoon, J. Marciante, D. D. Meyerhofer, C. Mileham, M. Millecchia, S. F. B. Morse, P. M. Nilson, A. Okishev, J. B. Oliver, R. G. Peck, C. Rees, B. S. Rice, E. Riedle, A. L. Rigatti, C. Robillard, R. G. Roides, M. H. Romanofsky, J. Rothhardt, M. J. Shoup III, C. Smith, C. Stoeckl, R. Taylor, L. J. Waxer, and D. Weiner, "Technology Development and Prospects for 100-PW-Class Optical Parametric Chirped-Pulse Amplification Pumped by OMEGA EP," the 2nd International Symposium on High Power Laser Science and Engineering, Suzhou, China, 15–18 March 2016.

The following presentations were made at Industrial Associates, Rochester, NY, 21–22 March 2016:

L. E. McIntire, M. Divoky, W. H. Knox, S.-W. Bahk, and J. D. Zuegel, "High-Contrast, Closed-Loop Control of Continuous-Wave Laser Beam Profiles."

B. W. Plansinis, W. R. Donaldson, and G. P. Agrawal, "Controlling the Optical Pulse Spectrum with an Electro-Optic Phase Modulator."

B. W. Plansinis, W. R. Donaldson, and G. P. Agrawal, "Temporal Waveguiding Caused by Time Reflection and Refraction."

R. Betti, A. R. Christopherson, A. Bose, K. M. Woo, J. Howard, K. S. Anderson, E. M. Campbell, J. A. Delettrez, V. N. Goncharov, F. J. Marshall, R. L. McCrory, S. P. Regan, T. C. Sangster, C. Stoeckl, W. Theobald, M. J. Edwards, R. Nora, B. K. Spears, and J. Sanz, "The Most Unsolved Problem in Plasma Physics: Demonstrating a Burning Plasma in the Laboratory," Solved and Unsolved Problems in Plasma Physics, Princeton, NJ, 28–30 March 2016 (invited).

M. J. Rosenberg, V. Yu. Glebov, C. Stoeckl, W. Seka, F. J. Marshall, J. A. Delettrez, P. W. McKenty, M. Hohenberger, R. Betti, V. N. Goncharov, P. B. Radha, J. P. Knauer, T. C. Sangster, H. G. Rinderknecht, F. H. Séguin, A. B. Zylstra, J. A. Frenje, H. Sio, M. Gatu Johnson, C. K. Li, R. D. Petrasso, N. M. Hoffman, G. Kagan, H. W. Herrmann, R. E. Olson, P. A. Amendt, S. Le Pape, T. Ma, A. J. Mackinnon, J. R. Rygg, S. C. Wilks, L. Berzak Hopkins, D. T. Casey, O. L. Landen, J. D. Lindl, J. Pino, H. F. Robey, S. Atzeni, O. Larroche, and A. Nikroo, "Ion Kinetic Effects in Exploding-Pusher Implosions on OMEGA and the National Ignition Facility," ICF Kinetic Physics Workshop, Livermore, CA, 5–7 April 2016.

The following presentations were made at the 11th International Conference on Tritium Science and Technology, Charleston, SC, 17–22 April 2016:

C. Fagan, M. Sharpe, W. T. Shmayda, and W. U. Schröder, "The Impact of Hydrophobicity of Stainless-Steel Surfaces on Tritium Inventories."

M. Sharpe, C. Fagan, W. T. Shmayda, and W. U. Schröder, "Influence of Surface Modifications on the Adsorption and Absorption of Tritium into 316 Stainless Steel."

W. T. Shmayda, M. D. Wittman, J. L. Reid, and R. F. Earley, "Tritium Activities at the University of Rochester's Laboratory for Laser Energetics."

M. D. Wittman, W. T. Shmayda, J. L. Reid, N. Redden, R. F. Earley, J. Magoon, K. Heung, S. Xiao, T. Sessions, and S. Redd, "Isotope Separation System at the University of Rochester's Laboratory for Laser Energetics."

The following presentations were made at the 12th Direct Drive and Fast Ignition Workshop, Talence, France, 25–27 April 2016:

R. Betti, A. Bose, K. M. Woo, E. M. Campbell, A. R. Christopherson, R. L. McCrory, and R. Nora, "Fusion-Yield Extrapolation to Higher Laser Energies for Direct-Drive Inertial Fusion Including the Effect of Alpha Heating."

V. N. Goncharov, S. P. Regan, T. C. Sangster, R. Betti, T. R. Boehly, M. J. Bonino, E. M. Campbell, T. J. B. Collins, R. S. Craxton, A. K. Davis, J. A. Delettrez, D. H. Edgell, R. Epstein, C. J. Forrest, D. H. Froula, V. Yu. Glebov, D. R. Harding, S. X. Hu, I. V. Igumenshchev, R. T. Janezic, J. H. Kelly, T. J. Kessler, T. Z. Kosc, S. J. Loucks, J. A. Marozas, F. J. Marshall, R. L. McCrory, P. W. McKenty, D. T. Michel, J. F. Myatt, P. B. Radha, W. Seka, W. T. Shmayda, A. Shvydky, S. Skupsky, C. Stoeckl, W. Theobald, F. Weilacher, B. Yaakobi, D. D. Meyerhofer, J. A. Frenje, M. Gatu Johnson, R. D. Petrasso, S. P. Obenschain, and M. Karasik, "Status of Direct-Drive Research in the U.S."

I. V. Igumenshchev, V. N. Goncharov, F. J. Marshall, J. P. Knauer, E. M. Campbell, C. J. Forrest, D. H. Froula, V. Yu. Glebov, R. L. McCrory, T. C. Sangster, S. Skupsky, and C. Stoeckl, "Three-Dimensional Modeling of Direct-Drive Cryogenic Implosions on OMEGA."

P. B. Radha, "Direct Drive at the National Ignition Facility."

S. P. Regan, V. N. Goncharov, T. C. Sangster, R. Betti, T. R. Boehly, M. J. Bonino, E. M. Campbell, D. Cao, T. J. B. Collins, R. S. Craxton, A. K. Davis, J. A. Delettrez, D. H. Edgell, R. Epstein, C. J. Forrest, D. H. Froula, V. Yu. Glebov, D. R. Harding, M. Hohenberger, S. X. Hu, I. V. Igumenshchev, R. T. Janezic, J. H. Kelly, T. J. Kessler, J. P. Knauer, T. Z. Kosc, J. A. Marozas, F. J. Marshall, R. L. McCrory, P. W. McKenty, D. T. Michel, J. F. Myatt, P. B. Radha, M. J. Rosenberg, W. Seka, W. T. Shmayda, A. Shvydky, S. Skupsky, A. A. Solodov, C. Stoeckl, W. Theobald, M. D. Wittman, B. Yaakobi, J. D. Zuegel, J. A. Frenje, M. Gatu Johnson, R. D. Petrasso, S. P. Obenschain, M. Karasik, A. J. Schmitt, D. D. Meyerhofer, and M. J. Schmitt, "Demonstraton of 50-Gbar Hot-Spot Pressure and Reduction of Cross-Beam Energy Transfer for Direct-Drive, Layered Deuterium–Tritium Implosions on OMEGA."

W. Theobald, R. Betti, W. Seka, A. Bose, K. S. Anderson, M. Hohenberger, F. J. Marshall, D. T. Michel, A. Shvydky, A. A. Solodov, C. Stoeckl, D. H. Edgell, B. Yaakobi, R. Nora, A. Casner, M. Lafon, C. Reverdin, X. Ribeyre, E. Llor-aisa, A. Vallet, J. Peebles, F. N. Beg, and M. S. Wei, "Gigabar Shocks for Direct-Drive Shock-Ignition Fusion."

The following presentations were made at the Omega Laser Facility Users Group Workshop, Rochester, NY, 27–29 April 2016:

W. J. Armstrong, J. C. Puth, and R. Rombaut, "Target Diagnostic Timing Manager."

J. R. Davies, D. H. Barnak, R. Betti, E. M. Campbell, P.-Y. Chang, G. Fiksel, J. P. Knauer, S. P. Regan, A. Harvey-Thompson, K. J. Peterson, A. B. Sefkow, D. B. Sinars, and S. A. Slutz, "An Overview of Laser-Driven Magnetized Liner Inertial Fusion on OMEGA."

M. J. Guardalben, M. Spilatro, L. J. Waxer, and M. Barczys, "OMEGA EP UV Prediction Model for Enhanced Operational Performance."

E. M. Hill, G. Balonek, R. Cuffney, J. H. Kelly, and T. Z. Kosc, "OMEGA SSD Arbitrary Waveform Generation Installation and Activation."

E. M. Hill and J. C. Puth, "Omega Laser Facility and Diagnostic Timing Management."

S. Ivancic, D. Haberberger, P. Angland, M. Barczys, M. Bedzyk, R. Boni, R. Brown, R. S. Craxton, A. Davies, F. Ehrne, R. K. Jungquist, J. C. Puth, R. G. Roides, W. Seka, M. J. Shoup III, C. Stoeckl, W. Theobald, D. Weiner, and D. H. Froula, "Optical Diagnostic Suite (Schlieren, Interferometry, and Angular Filter Refractometry) on OMEGA EP Using a 10-ps, 263-nm Probe Beam."

R. Jungquist, "Short-Pulse Stray Light Management."

R. W. Kidder, A. Zeller, M. Charissis, P. Stoeckl, J. J. Rung, and R. Holderried, "The Principal Investigator Portal Provides a Gateway to Shot Information for External Users."

R. W. Kidder, A. Zeller, T. Meyer, P. Stoeckl, R. Pasols, and R. Holderried, "External User Access Through the LLE Principal Investigator Portal."

J. Kwiatkowski, M. Barczys, M. Bedzyk, A. Kalb, B. E. Kruschwitz, C. McMahon, T. Nguyen, A. L. Rigatti, and M. Sacchitella, "OMEGA EP Short-Pulse Ratiometer."

J. Kwiatkowski, E. M. Hill, B. Ehrich, M. Heimbueger, F. J. Marshall, and B. E. Kruschwitz, "OMEGA EP Pointing, Focusing, and Timing."

J. Kwiatkowski, S. J. Stagnitto, S. F. B. Morse, M. Labuzeta, and V. Guiliano, "Characterizing Debris-Shield Transmission Degradation and Estimating On-Target Energy."

D. Mastrosimone, A. Agliata, T. Buczek, D. J. Lonobile, M. J. Shoup III, and C. Sorce, "Enhanced Gas-Filled Capabilities for Ten-Inch-Manipulator–Based Target Positioners."

D. Mastrosimone, G. Fiksel, J. Magoon, A. Agliata, P.-Y. Chang, and D. H. Barnak, "Fielding MIFEDS on OMEGA."

S. F. B. Morse, "Omega Facility OLUG 2016 Update: Progress on Recommendations and Items of General Interest."

P. M. Nilson, F. Ehrne, C. Mileham, D. Mastrosimone, R. K. Jungquist, C. Taylor, R. Boni, J. Hassett, D. J. Lonobile, R. W. Kidder, M. J. Shoup III, A. A. Solodov, C. Stoeckl, and D. H. Froula, "High-Resolving Power, Ultrafast Streaked X-Ray Spectroscopy on OMEGA EP."

T. C. Sangster, K. S. Anderson, R. Betti, T. R. Boehly, B. Boni, M. J. Bonino, E. M. Campbell, D. Canning, D. Cao, T. J. B. Collins, R. S. Craxton, A. K. Davis, J. A. Delettrez, W. R. Donaldson, D. H. Edgell, R. Epstein, C. J. Forrest, D. H. Froula, V. Yu. Glebov, D. R. Harding, M. Hohenberger, S. X. Hu, H. Huang, I. V. Igumenshchev, R. T. Janezic, D. W. Jacobs-Perkins, J. Katz, R. L. Keck, J. H. Kelly, T. J. Kessler, B. E. Krushwitz, J. P. Knauer, T. Z. Kosc, S. J. Loucks, J. A. Marozas, F. J. Marshall, A. V. Maximov, R. L. McCrory, P. W. McKenty, D. T. Michel, S. F. B. Morse, J. F. Myatt, P. M. Nilson, J. C. Puth, P. B. Radha, B. S. Rice, M. J. Rosenberg, W. Seka, W. T. Shmayda, R. W. Short, A. Shvydky, M. J. Shoup III, S. Skupsky, A. A. Solodov, C. Sorce, S. Stagnito, C. Stoeckl, W. Theobald, J. Ulreich, M. D. Wittman, B. Yaakobi, J. D. Zuegel, J. A. Frenje, M. Gatu Johnson, R. D. Petrasso, H. Sio, B. Lahmann, M. A. Barrios, P. Bell, D. K. Bradley, D. A. Callahan, A. Carpenter, D. T. Casey, J. Celeste, M. Dayton, S. N. Dixit, C. Goyon, O. A. Hurricane, S. Le Pape, L. Masse, P. Michel, J. D. Moody, S. R. Nagel, A. Nikroo, R. Nora, L. Pickworth, J. E. Ralph, H. G. Rinderknecht, R. P. J. Town, D. P. Turnbull, R. J. Wallace, P. J. Wegner, M. Farrell, A. Greenwood, T. Hilsabeck, J. D. Kilkenny, N. Rice, M. Schoff, N. Petta, J. Hund, S. P. Obenschain, J. W. Bates, M. Karasik, A. J. Schmitt, J. Weaver, M. J. Schmitt, G. Rochau, J. Porter, M. Sanchez, L. Claus, G. Robertson, O. Looker, J. Hares, and T. Dymoke-Bradshaw, "Direct Drive 2020."

I. Seth and J. P. Knauer, "Analysis of Chemical Vapor Deposition Diamonds for Neutron Detection on OMEGA."

S. Stagnitto, M. Labuzeta, and C. Sorce, "Qualifying as an External Instrument Specialist/Technician at LLE."

X. K. Zhou and S. X. Hu, "Radiation Reaction of Electrons at Laser Intensities up to 10^{25} W/cm^2."

N. D. Viza, M. Wang, M. H. Romanofsky, and D. R. Harding, "Using Lab-on-Chip Technology to Mass Produce Inertial Fusion Energy Targets," Exploring Alternative Energy: CO_2 as a Resource, Rochester, NY, 29 April 2016.

The following presentations were made at the 46th Annual Anomalous Absorption Conference, Old Saybrook, CT, 1–6 May 2016:

D. H. Barnak, R. Betti, E. M. Campbell, P.-Y. Chang, J. R. Davies, G. Fiksel, J. P. Knauer, S. P. Regan, A. Harvey-Thompson, K. J. Peterson, A. B. Sefkow, D. B. Sinars, and S. A. Slutz, "Scaling Laser-Driven Magnetized Liner Inertial Fusion to the National Ignition Facility."

E. Borwick, S. X. Hu, J. Li, R. Yan, and C. Ren, "Full-Pulse Particle-in-Cell Simulations of Hot-Electron Generation in OMEGA Experiments."

S. Bucht, D. Haberberger, J. Bromage, and D. H. Froula, "Transforming the Idler for Use in Laser–Plasma Interaction Experiments."

E. M. Campbell, "The National Ignition Facility: An Unexpected Journey, Lessons to be Learned to Secure Projects of Scale, and Persepctives on the Future of Inertial Confinement Fusion Research."

A. Davies, J. Katz, S. Bucht, D. Haberberger, J. Bromage, J. D. Zuegel, D. H. Froula, J. Sadler, P. A. Norreys, R. Bingham, R. Trines, and L. O. Silva, "Thomson Scattering from Nonlinear Electron Plasma Waves."

J. R. Davies, D. H. Barnak, R. Betti, P.-Y. Chang, K. J. Peterson, A. B. Sefkow, D. B. Sinars, and S. A. Slutz, "An Overview of Laser-Driven Magnetized Linear Inertial Fusion on OMEGA."

A. K. Davis, D. T. Michel, S. X. Hu, R. Epstein, J. P. Knauer, and D. H. Froula, "Conduction-Zone Measurements Using X-Ray Self-Emission Images."

D. H. Edgell, R. K. Follett, J. Katz, J. F. Myatt, W. Seka, and D. H. Froula, "Polarization Dependence of Cross-Beam Energy Transfer in Unabsorbed Light Beamlets."

D. H. Froula, R. K. Follett, R. J. Henchen, V. N. Goncharov, A. A. Solodov, J. A. Delettrez, D. H. Edgell, B. Yaakobi, C. Stoeckl, and J. F. Myatt, "The Effect of Cross-Beam Energy Transfer on Two-Plasmon Decay in Direct-Drive Implosions."

D. Haberberger, D. H. Froula, A. Pak, A. Link, P. K. Patel, F. Fiuza, S. Ya. Tochitsky, and C. Joshi, "Shock-Wave Acceleration of Ions on OMEGA EP."

R. J. Henchen, S. X. Hu, W. Rozmus, J. Katz, and D. H. Froula, "Heat-Flux Measurements from Collective Thomson-Scattering Spectra."

J. Li, R. Yan, and C. Ren, "Density Modulation–Induced Absolute Laser–Plasma Instabilities: Simulations and Theory."

D. T. Michel, S. X. Hu, A. K. Davis, V. Yu. Glebov, V. N. Goncharov, I. V. Igumenshchev, P. B. Radha, C. Stoeckl, and D. H. Froula, "Measurements of the Effect of Adiabat on the Shell Thickness of Direct-Drive Implosions on OMEGA."

J. F. Myatt, J. G. Shaw, R. K. Follett, D. H. Edgell, V. N. Goncharov, A. V. Maximov, R. W. Short, W. Seka, and D. H. Froula, "A Wave-Based Model for Cross-Beam Energy Transfer in Inhomogeneous Plasmas."

C. Ren, J. Li, W.-D. Liu, and R. Yan, "Simulation of Stimulated Brillouin Scattering and Stimulated Raman Scattering in Shock Ignition."

M. J. Rosenberg, A. A. Solodov, W. Seka, R. Epstein, J. F. Myatt, S. P. Regan, M. Hohenberger, T. J. B. Collins, P. A. Michel, D. P. Turnbull, C. Goyon, J. D. Moody, J. E. Ralph, M. A. Barrios, and J. W. Bates, "Planar Laser–Plasma Interaction Experiments at Direct-Drive Ignition-Relevant Scale Lengths at the National Ignition Facility."

W. Seka, J. F. Myatt, V. N. Goncharov, R. Betti, S. P. Regan, A. V. Maximov, J. A. Delettrez, R. E. Bahr, A. A. Solodov, M. J. Rosenberg, A. Bose, and R. W. Short, "The Influence of Smoothing by Spectral Dispersion on Cross-Beam Energy Transfer."

R. W. Short, W. Seka, and J. F. Myatt, "Kinetic Analysis of Convective Stimulated Raman Scattering and Its Potential as a Temperature Diagnostic."

A. A. Solodov, M. J. Rosenberg, J. F. Myatt, R. Epstein, S. P. Regan, W. Seka, J. G. Shaw, M. Hohenberger, J. W. Bates, P. A. Michel, J. D. Moody, J. E. Ralph, D. P. Turnbull, and M. A. Barrios, "Modeling of Laser–Plasma Interaction Experiments at Direct-Drive Ignition-Relevant Plasma Conditions at the National Ignition Facility."

I. Seth and J. P. Knauer, "Analysis of Chemical-Vapor–Deposition Diamonds for Neutron Detection on OMEGA," Intel International Science and Engineering Fair, Phoenix, AZ, 8–13 May 2016.

G. Chen, A. Koroliov, R. Sherstha, and R. Sobolewski, "Terahertz Spectroscopy of Graphene-Polymer Nanocomposites," Frontiers in Materials Science for the 21st Century, Rochester, NY, 16 May 2016.

The following presentations were made at the 21st Topical Conference on High-Temperature Plasma Diagnostics, Madison, WI, 5–9 June 2016:

P. X. Belancourt, W. Theobald, P. A. Keiter, T. J. B. Collins, M. J. Bonino, P. Kozlowski, S. P. Regan, and R. P. Drake, "Demonstration of Imaging X-Ray Thomson Scattering on OMEGA EP."

A. K. Davis, D. T. Michel, R. S. Craxton, R. Epstein, M. Hohenberger, T. Mo, and D. H. Froula, "X-Ray Self-Emission Imaging Used to Diagnose 3-D Nonuniformities in Direct-Drive ICF Implosions."

R. K. Follett, J. A. Delettrez, R. J. Henchen, J. Katz, D. H. Edgell, J. F. Myatt, and D. H. Froula, "Plasma Characterization Using Ultraviolet Thomson Scattering from Ion-Acoustic and Electron Plasma Waves" (invited).

C. J. Forrest, V. Yu. Glebov, V. N. Goncharov, J. P. Knauer, P. B. Radha, S. P. Regan, M. H. Romanofsky, T. C. Sangster, M. J. Shoup III, and C. Stoeckl, "High-Dynamic-Range Neutron Time-of-Flight Detector Used to Infer the D(t,n)^{4}He and D(d,n)^{3}He Reaction Yield and Ion Temperature on OMEGA."

V. Yu. Glebov, R. Flight, C. J. Forrest, J. P. Knauer, S. P. Regan, M. H. Romanofsky, T. C. Sangster, and C. Stoeckl, "A New Microchannel-Plate Neutron Time-of-Flight Detector."

S. T. Ivancic, D. Nelson, P. M. Nilson, C. R. Stillman, C. Mileham, I. A. Begishev, and D. H. Froula, "Design of an Extreme Ultraviolet Spectrometer Suite for Characterization of Rapidly Heated Solid Matter."

J. Katz, R. Boni, A. Maltsev, C. Muir, M. H. Romanofsky, and D. H. Froula, "A Pulse-Front-Tilt–Compensated Streaked Optical Spectrometer with High Throughput and Picosecond Time Resolution."

J. P. Knauer, C. J. Forrest, V. Yu. Glebov, T. C. Sangster, and C. Stoeckl, "Three-Axis Neutron Time-of-Flight Measurement."

P. M. Nilson, F. Ehrne, C. Mileham, D. Mastrosimone, R. K. Jungquist, C. Taylor, C. R. Stillman, S. T. Ivancic, R. Boni, J. Hassett, D. J. Lonobile, R. W. Kidder, M. J. Shoup III, A. A. Solodov, C. Stoeckl, D. H. Froula, K. W. Hill, L. Gao, M. Bitter, P. Efthimion, and D. D. Meyerhofer, "High-Resolving-Power, Ultrafast Streaked X-Ray Spectroscopy on OMEGA EP" (invited).

C. Sorce, C. Stoeckl, J. Katz, R. Boni, F. Ehrne, C. J. Forrest, V. Yu. Glebov, D. J. Lonobile, S. P. Regan, M. J. Shoup III, A. Sorce, T. C. Sangster, D. Weiner, and J. Magoon, "A Neutron Temporal Diagnostic for High-Yield DT Cryogenic Implosions on OMEGA."

C. R. Stillman, P. M. Nilson, S. Ivancic, C. Mileham, I. A. Begishev, R. K. Junquist, and D. H. Froula, "A Streaked X-Ray Spectroscopy Platform for Rapidly Heated, Near-Solid Density Plasmas."

C. Stoeckl, W. Theobald, S. P. Regan, and M. H. Romanofsky, "Calibration of a Time-Resolved Hard X-Ray Detector Using Radioactive Sources."

W. Theobald, C. Sorce, M. Bedzyk, F. J. Marshall, C. Stoeckl, S. P. Regan, T. Hilsabeck, J. D. Kilkenny, D. Morris, M. Chung, J. Hares, T. Dymoke-Bradshaw, P. Bell, J. Celeste, A. Carpenter, M. Dayton, D. K. Bradley, M. C. Jackson, L. Pickworth, S. Nagel, G. Rochau, J. Porter, M. Sanchez, L. Claus, G. Robertson, and Q. Looker, "Conceptual Design of a Single-Line-of-Sight Time-Resolved X-Ray Imager on OMEGA."

The following presentations were made at CLEO 2016, San Jose, CA, 5–10 June 2016:

I. A. Begishev, J. Bromage, P. S. Datte, S. T. Yang, and J. D. Zuegel, "Record Fifth-Harmonic–Generation Efficiency Producing 211-nm Pulses Using Cesium Lithium Borate."

S. G. Demos, R. Levenson, F. Fereidouni, and Z. Harmany, "Slide-Free (But Not Necessarily Stain-Free) Microscopy via Ultraviolet Excitation."

C. Dorrer, W. A. Bittle, R. Cuffney, E. M. Hill, T. Z. Kosc, J. H. Kelly, and J. D. Zuegel, "High-Contrast, Time-Multiplexed Pulse-Shaping Systems."

C. Dorrer, Y. Li, and P. Fiala, "Focal-Spot Optimization by Polarization Modulation."

C. Dorrer, L. J. Waxer, A. Kalb, E. M. Hill, and J. Bromage, "Single-Shot, High-Resolution Fiber-Based Phase-Diversity Photodetection of Optical Pulses."

R. Betti, A. R. Christopherson, A. Bose, K. M. Woo, J. Howard, K. S. Anderson, E. M. Campbell, J. A. Delettrez, V. N. Goncharov, F. J. Marshall, R. L. McCrory, S. P. Regan, T. C. Sangster, C. Stoeckl, W. Theobald, M. J. Edwards, R. Nora, B. K. Spears, and J. Sanz, "Status and Prospects for Burning Plasmas via Laser Fusion," 43rd IEEE International Conference on Plasma Science, Banff, Alberta, Canada, 19–23 June 2016 (invited).

The following presentations were made at the 15th Meeting of the Tritium Users Group, Southampton, UK, 21–22 June 2016:

W. T. Shmayda, "Tritium Interaction with Stainless Steel."

W. T. Shmayda, M. D. Wittman, J. L. Reid, and R. F. Earley, "Tritium Activities at the University of Rochester's Laboratory for Laser Energetics."

C. R. Stillman, P. M. Nilson, S. T. Ivancic, C. Mileham, I. A. Begishev, R. K. Junquist, and D. H. Froula, "A Streaked X-Ray Spectroscopy Platform for Rapidly Heated, Near-Solid Density Plasmas," 2016 DOE NNSA Stewardship Science Graduate Fellowship Program, Las Vegas, NV, 27–30 June 2016.

C. J. Forrest, V. Yu. Glebov, J. P. Knauer, P. B. Radha, S. P. Regan, T. C. Sangster, C. Stoeckl, W. U. Schroeder, J. A. Frenje, M. Gatu Johnson, M. W. Paris, G. Hale, and A. B. Zylstra, "Neutron-Induced Break-up Reaction Using Deuterium Fusion Neutrons at the Omega Laser Facility," 2016 R-Matrix Workshop on Methods and Applications, Santa Fe, NM, 27 June–1 July 2016.

The following presentations were made at the CEA-NNSA Workshop, Rochester, NY, 29–30 June 2016:

I. A. Begishev, J. Bromage, J. D. Zuegel, P. S. Datte, and S. T. Yang, "Record Fifth-Harmonic–Generation Efficiency Producing 211-nm Pulses Using Cesium Lithium Borate."

V. Yu. Glebov, R. Flight, C. J. Forrest, J. P. Knauer, S. P. Regan, M. H. Romanofsky, T. C. Sangster, and C. Stoeckl, "A New Microchannel-Plate Neutron Time-of-Flight Detector."

P. M. Nilson, F. Ehrne, C. Mileham, D. Mastrosimone, R. K. Jungquist, C. Taylor, R. Boni, J. Hassett, C. R. Stillman, S. T. Ivancic, D. J. Lonobile, R. W. Kidder, M. J. Shoup III, A. A. Solodov, C. Stoeckl, D. H. Froula, K. M. Hill, L. Gao, M. Bitter, P. Efthimion, and D. D. Meyerhofer, "High-Resolving-Power, Ultrafast Streaked X-Ray Spectroscopy on OMEGA EP."

W. Theobald, C. Sorce, M. Bedzyk, F. J. Marshall, C. Stoeckl, S. P. Regan, T. Hilsabeck, J. D. Kilkenny, D. Morris, M. Chung, J. Hares, A. Dymoke-Bradshaw, P. Bell, J. Celeste, A. Carpenter, M. Dayton, D. K. Bradley, M. C. Jackson, L. Pickworth, S. Nagel, G. Rochau, J. Porter, M. Sanchez, L. Claus, G. Robertson, and Q. Looker, "Conceptual Design of a Single-Line-of-Sight Resolved X-Ray Imager on OMEGA."

V. N. Goncharov, S. P. Regan, E. M. Campbell, T. C. Sangster, P. B. Radha, J. F. Myatt, D. H. Froula, R. Betti, T. R. Boehly, J. A. Delettrez, D. H. Edgell, R. Epstein, C. J. Forrest, V. Yu. Glebov, D. R. Harding, S. X. Hu, I. V. Igumenshchev, F. J. Marshall, R. L. McCrory, D. T. Michel, W. Seka, A. Shvydky, C. Stoeckl, W. Theobald, and M. Gatu-Johnson, "National Direct-Drive Program on OMEGA and the National Ignition Facility," 43rd European Physical Society Conference on Plasma Physics, Leuven, Belgium, 4–8 July 2016 (invited).

D. Polsin, T. R. Boehly, J. A. Delettrez, M. C. Gregor, C. A. McCoy, B. Henderson, D. E. Fratanduono, R. Smith, R. Kraus, J. H. Eggert, R. Collins, F. Coppari, and P. M. Celliers, "Observation of Solid-Solid Phase Transitions in Pump-Compressed Aluminum," High-Pressure Research, Holderness, NH, 17–22 July 2016.

J. B. Oliver, C. Smith, B. Taylor, J. Spaulding, S. MacNally, and T. Shea, "Characterization of Glancing-Angle–Deposited Magnesium Oxide Films," Novel Optical Materials and Applications, Vancouver, British Columbia, Canada, 18–20 July 2016.

D. H. Froula, P. M. Nilson, S. T. Ivancic, C. R. Stillman, C. Mileham, I. A. Begishev, A. A. Solodov, R. K. Jungquist, R. Boni, D. Hassett, C. Stoeckl, W. Theobald, F. Ehrne, D. Mastrosimone, D. Nelson, C. Taylor, D. J. Lonobile, R. W. Kidder, M. J. Shoup III, K. W. Hill, L. Gao, M. Bitter, and P. C. Efthimion, "Understanding the Material Response to Powerful Energy Fluxes Driven by Picosecond Lasers at the Laboratory for Laser Energetics," JOWOG37, Aldermaston, UK, 18–22 July 2016.

J. D. Zuegel, J. Bromage, E. M. Campbell, W. Krupke, T. Y. Fan, D. H. Martz, P. Reeves-Hall, and W. Leemans, "High-Average-Power, Ultra-Intense Laser Technology for Laser-Plasma Acceleration," 17th Advanced Accelerator Concepts Workshop, National Harbor, MD, 31 July–5 August 2016.

W. T. Shmayda, J. Ulreich, R. Earley, and M. D. Wittman, "Filling Inertial Confinement Fusion Targets with DT Using Palladium Tritide," The 22nd Topical Meeting on the Technology of Fusion Energy (TOFE 2016), Philadelphia, PA, 22–25 August 2016.

W. R. Donaldson, J. Katz, T. Z. Kosc, J. H. Kelly, E. M. Hill, and R. E. Bahr, "Enhancements to the Timing of the OMEGA Laser System to Improve Illumination Uniformity," 2016 Optical Engineering and Applications, San Diego, CA, 28 August–1 September 2016.

E. M. Campbell, "Symmetric Illumination and Direct Drive at the National Ignition Facility," Symmetric Direct-Drive Study, Livermore, CA, 7–8 September 2016.

The following presentations were made at the 7th International Conference on Ultrahigh Intensity Lasers, Montebello, Quebec, Canada, 11–16 September 2016:

S.-W. Bahk, J. B. Oliver, R. K. Jungquist, J. Bromage, E. M. Schiesser, and J. P. Rolland "Beam-Transport Systems for Ultra-Broadband Lasers."

I. A. Begishev, S.-W. Bahk, R. Cuffney, C. Dorrer, D. Haberberger, D. H. Froula, C. Mileham, P. M. Nilson, C. Stoeckl, J. D. Zuegel, and J. Bromage, "Extensions to the Multi-Terawatt Laser for Laser Development and Plasma Physics Studies."

S. Bucht, D. Haberberger, J. Bromage, and D. H. Froula, "Transforming the Idler-to-Seed Raman Amplification."

C. Dorrer, L. J. Waxer, A. Kalb, E. M. Hill, and J. Bromage, "Temporal Characterization of Optical Pulses by Spectral Phase Diversity."

D. Haberberger, A. Davies, S. Bucht, J. Bromage, J. D. Zuegel, D. H. Froula, R. Trines, R. Bingham, and P. A. Norreys, "Plans for a Tunable Raman Amplifier at The Laboratory for Laser Energetics."

R. Betti, "Status and Prospects for Demonstrating Ignition via Laser Fusion," The 3rd International Conference on High Energy Density Physics (ICHEDP-3), Shenzhen, China, 23–26 September 2016.

The following presentations were made at the XLVIII Annual Symposium on Optical Materials for High-Power Lasers, Boulder, CO, 25–28 September 2016:

S. G. Demos, C. W. Carr, and D. A. Cross, "Electrostatic Effects Following Irradiation of Fused Silica Surfaces with Nanosecond Laser Pulses."

A. A. Kozlov, S. Papernov, J. B. Oliver, A. L. Rigatti, B. Taylor, B. Charles, and C. Smith, "Study of the Picosecond Laser Damage in HfO_2/SiO_2-Based Thin-Film Coatings in Vacuum."

UNIVERSITY *of* ROCHESTER